Master's thesis

NTNU
Norwegian University of Science and Technology
Faculty of Engineering
Department of Marine Technology

Christos Farantos

Improved VIV Prediction of Free Spanning Pipelines and Cables

Master's thesis in Maritime Engineering
Supervisor: Prof. Svein Sævik, NTNU, Assoc. Prof. Yanlin Shao, DTU, Dr. Jie Wu, SINTEF Ocean AS
June 2022

NTNU
Kunnskap for en bedre verden

DTU Technical University of Denmark

Christos Farantos

Improved VIV Prediction of Free Spanning Pipelines and Cables

Master's thesis in Maritime Engineering
Supervisor: Prof. Svein Sævik, NTNU, Assoc. Prof. Yanlin Shao, DTU, Dr. Jie Wu, SINTEF Ocean AS
June 2022

Norwegian University of Science and Technology
Faculty of Engineering
Department of Marine Technology

NTNU

Kunnskap for en bedre verden

NTNU Trondheim
Norwegian University of Science and Technology *Faculty of Engineering*
Department of Marine Technology

THESIS WORK SPRING 2022

for

Stud. Tech. Christos Farantos

Improved VIV Prediction of Free Spanning Pipelines and Cables

Forbedret beregning av virvelindusert respons av rørledninger og kabler i frie spenn

Vortex Induced Vibrations (VIV) can lead to fast accumulation of fatigue damage to offshore slender structure, such as free spanning pipelines and cables. A new empirical method for time domain (TD) calculation of VIV has been developed by NTNU. This method is capable of accounting for structural non-linearity and time-varying flow compared to the traditional frequency domain analyses. The master thesis work is to be carried out as a continuation of the project performed in Fall 2021. The major objective of the study is to validate the TD VIV prediction tool for free spanning pipelines and cables as a basis for evaluating non-linear damping and local stress effects at pipeline shoulders due to pipe-soil interaction. The master thesis scope is to include the following items:

1. Literature study on the fundamental theory of VIV and numerical prediction tools, relevant DnV rules and recommended practices related to riser & free-spanning pipeline VIV response analysis.
2. Establish relevant TD VIV models related to available experimental data
3. Based on available experimental data, evaluate the TD VIV performance with respect to chosen parameters with focus on both pure in-line and combined in-line & cross-flow responses.
4. Identify optimum parameter sets and criteria for switching from pure in-line to cross-flow induced in-line vibrations.
5. Establish a TD-VIV model for a realistic free-span scenario and by application of the optimum parameter sets obtained from the above.
6. Investigate the effects from damping due to soil interaction and effect of the non-linear boundary condition with respect to stresses and fatigue damage
7. Conclusions and recommendations for further work

The work scope may prove to be larger than initially anticipated. Subject to approval from the supervisors, topics may be deleted from the list above or reduced in extent.

In the thesis report, the candidate shall present her personal contribution to the resolution of problems within the scope of the thesis work

Theories and conclusions should be based on mathematical derivations and/or logic reasoning identifying the various steps in the deduction.

The candidate should utilise the existing possibilities for obtaining relevant literature.

NTNU
Norwegian University of Science and Technology
Faculty of Engineering
Department of Marine Technology

Thesis report format
The thesis report should be organised in a rational manner to give a clear exposition of results, assessments, and conclusions. The text should be brief and to the point, with a clear language. Telegraphic language should be avoided.

The report shall contain the following elements: A text defining the scope, preface, list of contents, summary, main body of thesis, conclusions with recommendations for further work, list of symbols and acronyms, references and (optional) appendices. All figures, tables and equations shall be numerated.

The supervisors may require that the candidate, in an early stage of the work, presents a written plan for the completion of the work.

The original contribution of the candidate and material taken from other sources shall be clearly defined. Work from other sources shall be properly referenced using an acknowledged referencing system.

The report shall be submitted in electronic format (.pdf):
- Signed by the candidate
- The text defining the scope shall be included (this document)
- Drawings and/or computer models that are not suited to be part of the report in terms of appendices shall be provided on separate (.zip) files.

Ownership
NTNU has according to the present rules the ownership of the thesis reports. Any use of the report has to be approved by NTNU (or external partner when this applies). The department has the right to use the report as if the work was carried out by a NTNU employee, if nothing else has been agreed in advance.

Thesis supervisors:

Prof. Svein Sævik, NTNU, Dr. Jie Wu, SINTEF Ocean, Assoc. Prof. Yanlin Shao, DTU

Deadline: June, 2022, the exact data according to student administration

Trondheim, December 7th , 2022

Svein Sævik

Candidate – date and signature:

Christos Farantos, December 7th 2022

Preface - Acknowledgement

This report is the outcome of my Master's Thesis work carried out at the Department of Marine Technology at the Norwegian University of Science and Technology during the Spring semester of 2022. This thesis is a continuation and a broader and in more depth investigation of the the preparatory project performed in Fall 2021.

The topic of this Master's Thesis is "Improved VIV Prediction of Free Spanning Pipelines and Cables". A big part of this work was devoted to the acquisition of a deeper knowledge and understanding of the Vortex-Induced Vibrations (VIV) phenomenon in general and to the familiarization with the time domain model developed recently at NTNU for the prediction of VIV (TD VIV model). Another important part of this work was to get familiar with the non-linear finite element software RIFLEX which is used in combination with the TD VIV model for the computation of vortex-induced vibrations. Although laboratory experiments were not conducted in the context of this Thesis work, getting to know a so complex non-linear finite element tool and being able to use it in order to simulate real-life VIV phenomena required an extensive research in both theoretical literature and practical experimental procedures and data. In this way, the present work unquestionably provided me with deep theoretical knowledge and the practical know-how necessary in order to be able to address a real problem related to an actual structure experiencing vortex-induced vibrations.

There are two persons who had a major contribution to the present work and to whom I would like to express my sincere gratitude: Professor Svein Sævik, Department of Marine Technology, NTNU and Dr. Jie Wu, Senior Research Scientist at SINTEF Ocean AS. Their guidance and recommendations during our weekly meetings were vital for accomplishing the goals of this work. In particular, their high level of reliability and availability should be highlighted, since there were several times during this work that their help was necessary, especially when the examined VIV cases had to be implemented in RIFLEX, and they were always there to provide me with their experience and their valuable advice. Finally, I would also like to thank my co-supervisor at DTU, Associate Professor Yanlin Shao, Department of Mechanical Engineering Fluid Mechanics, Coastal and Maritime Engineering, DTU, who is also the coordinator of my Master's Program at DTU and his help was crucial for the completion of my Master's Thesis work and of my Studies in general.

The readers of this report are advised to be familiar with the basic aspects of hydrodynamics and structural analysis. In particular, having a basic knowledge of the fundamental theory behind dynamic analysis of structural response in both the frequency and the time domain would be a great advantage and would make understanding the context of this report much easier. Moreover, an in advance knowledge of some basic VIV related concepts would also be advantageous although the basics are also presented in this work.

Abstract

This thesis presents the outcome of the work done in order to validate and calibrate the semi-empirical time domain tool developed recently at NTNU with the aim to predict the response of flexible marine structures experiencing Vortex-Induced Vibrations (VIV). The goal of this work was on the one hand to present the basic aspects and the fundamental theoretical knowledge related to VIV and the several existing methods for the estimation of it, and on the other hand to establish a time domain model (TD VIV model) capable of accurately capturing the dynamic response of a free spanning pipeline under VIV excitation. The focus of this analysis was both on the pure in-line (IL) VIV occurring at low reduced velocities and on the combined in-line and cross-flow (CF) vibrations, which are observed at higher reduced velocities.

The hydrodynamic force model considered in this thesis is based on the fact that the vortex-induced forces can be combined with Morison's equation in order to get the total fluid-induced forces. In this way, the drag term of Morison's equation is utilized in order to directly account for the damping term of the vortex-induced forces and hence the formulation of a separate damping model is not required. Another crucial part of this hydrodynamic load model is the determination of a well-established synchronization model, which is capable of capturing accurately the interaction between the vortex-shedding phenomenon and the response of the structure during the exceptionally important lock-in phenomenon. The basis of this hydrodynamic force model lies on the utilization of empirical hydrodynamic coefficients obtained via full- and model-scale experiments. The available results from three model Test Series were utilized for the validation and calibration of the developed TD VIV model. The two main goals of this calibration procedure were on the one hand to find one single set of hydrodynamic coefficients that gives results in good agreement with the reference data for all the examined Test Series and on the other hand to achieve this while using a sufficiently wide synchronization range in the in-line synchronization model in order to be able to use one single set of hydrodynamic parameters to account for both the pure IL and the CF-induced IL vibrations. For this reason, several sets of hydrodynamic parameters were examined. Subsequently, structural and numerical models of the examined pipelines were established and combined with the above hydrodynamic load model by means of the non-linear finite element software RIFLEX. Then, RIFLEX was utilized in order to perform the static and dynamic analyses of the examined cases.

The obtained results were compared with relevant experimental and numerical (calculated by the frequency domain model VIVANA) reference data. On the basis of this preliminary comparative study, the overall optimum parameter set for all three examined Test Series was identified. Subsequently, an in depth comparison between the results obtained using this optimum parameter set and the respective experimental data was conducted and it was found that the TD VIV model is able to capture quite accurately the VIV responses observed during the model tests with regard to all three examined Test Series. More specifically, although some non-negligible deviations between the experimental data and the results of the time domain analysis were observed during the aforementioned preliminary comparative study, this more detailed comparison showed that the results of the TD VIV model are in fact in good agreement with the actual response of the pipeline. The most important finding of this analysis was the fact that the TD VIV model was found to give improved results compared to other traditionally used methods of analysis of dynamic phenomena like VIV, such as the modal analysis and the frequency domain tools. Such methods are based on the linearization of such complex and inherent non-linear phenomena and consequently they inevitably often lead to unreasonable results, especially when high flow velocities are considered, for which the non-linear effects are more significant.

Finally, the last step of the present thesis was to utilize this validated and calibrated TD VIV model in order to investigate a realistic case of Vortex-Induced Vibrations in a free spanning pipeline, taking also into account the complex pipe-soil interaction, which was neglected in the previous analyses. The main focus of this analysis was on the investigation of the effects from damping due to pipe-soil interaction and the effect of the non-linear boundary conditions with respect to the induced stresses and the fatigue damage accumulation. For this reason, two different soil models, one Linear and one Non-Linear, were developed and then implemented into RIFLEX and two different levels of soil damping were examined. On the basis of these analyses, it was found that the two soil models give almost identical results with regard to the predicted dominant vibration frequencies both in the IL and the CF directions, while some more significant deviations were observed with regard to the predicted response amplitudes in both directions and the respective findings for the induced bending stresses and the accumulation of fatigue damage. These deviations were found to be especially profound in the vicinity of the shoulders and within the soil-supported part of the pipeline. Finally, it was found that the reduction of the level of soil damping does not influence the predicted vibration frequencies, while it affects considerably the rest of the examined VIV responses, ultimately increasing the above mentioned discrepancies between the two soil models.

Contents

List of Figures

List of Tables

Nomenclature

List of Acronyms

$1D$	One-dimensional
$2D$	Two-dimensional
$3D$	Three-dimensional
BL	Boundary layer
CF	Cross-Flow
CFD	Computational Fluid Dynamics
DNS	Direct Numerical Simulation
$DNVGL$	Det Norske Veritas and Germanischer Lloyd
$dofs$	Degrees-of-freedom
FD	Frequency Domain
FEM	Finite Element Method
FFT	Fast Fourier Transform
IL	In-Line
LES	Large Eddy Simulation
$RANS$	Reynolds-Averaged Navier-Stokes
TD	Time Domain
VIM	Vortex-Induced Motions
VIV	Vortex-Induced Viabrations
$WAFO$	Wave Analysis for Fatigue and Oceanography

List of Symbols

α	Parameter that determines the extent of the dependence of the IL force frequency on the respective CF frequency (initial IL synchronization model)
α_1	Mass-proportional damping coefficient
α_2	Stiffness-proportional damping coefficient
$\bar{F}_D$	Mean drag force
$\bar{F}_L$	Mean lift force

β, γ	Parameters determining the functional change in nodal displacement, velocity and acceleration vectors over the timestep Δt
β_D	Phase angle of the drag force
β_L	Phase angle of the lift force
Δt	Timestep
$\dot{\phi}_{exc,x}$	In-line instantaneous frequency
$\dot{\phi}_{exc,y}$	Cross-flow instantaneous frequency
$\dot{x}_{rel}$	Relative in-line velocity of the structure
$\dot{y}_{rel}$	Relative cross-flow velocity of the structure
$\hat{f}$	Non-dimensional oscillation frequency
$\hat{f}_{0,x}$	Non-dimensional in-line excitation frequency of maximum energy transfer
$\hat{f}_{0,y}$	Non-dimensional cross-flow excitation frequency of maximum energy transfer
$\hat{f}_{\text{max},x}$	Upper limit of the IL synchronization range
$\hat{f}_{\text{max},y}$	Upper limit of the CF synchronization range
$\hat{f}_{\text{min},x}$	Lower limit of the IL synchronization range
$\hat{f}_{\text{min},y}$	Lower limit of the CF synchronization range
$\hat{f}_{exc,x}$	Non-dimensional in-line excitation frequency used to denote the IL synchronization range
$\hat{f}_{exc,y}$	Non-dimensional cross-flow excitation frequency used to denote the CF synchronization range
λ_i	Modal damping ratio for mode number i
$\mathbf{C}$	System's damping matrix
$\mathbf{F}$	Total hydrodynamic force
$\mathbf{K}$	System's stiffness matrix
$\mathbf{M}$	System's mass matrix
$\mathbf{u_n}, \dot{\mathbf{u}}_\mathbf{n}$	Normal component of the incident flow velocity and acceleration vectors
$\mathbf{u_t}$	Tangential component of the incident flow velocity vector
$\mathbf{u}$	Incident flow velocity vector
$\mathbf{v_n}$	Relative flow velocity vector
ν	Kinematic viscosity of the fluid
ν	Poisson's ratio

ω	Oscillation frequency in rad/s
ω_n	Eigenfrequency for mode number n
$\phi_{\dot{x}_{rel}}$	Instantaneous phase angle of the structure's relative in-line velocity
$\phi_{\dot{y}_{rel}}$	Instantaneous phase angle of the structure's relative cross-flow velocity
$\phi_{exc,x}$	Instantaneous phase angle of the vortex-induced excitation force in the IL direction
$\phi_{exc,y}$	Instantaneous phase angle of the vortex-induced excitation force in the CF direction
ψ_n	Mode shape for mode number n
ρ	Density of the fluid
ρ_s/ρ	Specific mass ratio
θ_x	Instantaneous phase difference between the structure's relative in-line velocity and the in-line excitation force
θ_y	Instantaneous phase difference between the structure's relative cross-flow velocity and the cross-flow excitation force
ζ_{pipe}	Structural damping ratio of the pipe
ζ_{soil}	Soil damping ratio
A	Cross-sectional area of the examined cylinder or pipe
A_D	Amplitude of the oscillating component of the drag force
A_L	Amplitude of the oscillating component of the lift force
C_D	Non-dimensional drag coefficient
C_L	Non-dimensional lift coefficient
C_A	Added mass coefficient
$C_{d,y}$	Damping coefficient in the CF direction
C_L	Lateral dynamic stiffness factor
$C_{v,x}$	In-line vortex-induced excitation force coefficient
$C_{v,y}$	Cross-flow vortex-induced excitation force coefficient
C_V	Vertical dynamic stiffness factor
D	Diameter of the examined cylinder or pipe
EA	Axial stiffness
EI	Bending stiffness
F_D	Drag force
F_L	Lift force

f_n	Still water natural frequency for mode number n
f_s	Vortex shedding frequency
F_{add}	Added mass force (initially proposed TD VIV model)
$F_{damping}$	Damping force (initially proposed TD VIV model)
$F_{exc,x}$	In-line vortex-induced excitation force
$f_{exc,x}$	In-line excitation frequency
$F_{exc,y}$	Cross-flow vortex-induced excitation force
$f_{exc,y}$	Cross-flow excitation frequency
F_{exc}	Excitation force (initially proposed TD VIV model)
$f_{n,x}$	Still water natural frequency in the in-line direction for mode number n
$f_{n,y}$	Still water natural frequency in the cross-flow direction for mode number n
f_{osc}	Oscillation frequency
F_y	Hydrodynamic force in the CF direction (initially proposed TD VIV model)
G	Shear Modulus of the soil
k	Spring stiffness
k_i	Linearized spring stiffness at support no. i
$K_{L,d}$	Lateral Dynamic Soil Stiffness
$K_{L,s}$	Lateral Static Soil Stiffness
$K_{V,d}$	Vertical Dynamic Soil Stiffness
$K_{V,s}$	Vertical Static Soil Stiffness
KC	Keulegan-Carpenter number
L	Length of the pipe
L_f	Length of the free span
M	Bending moment
m	Dry mass
m^*	Mass ratio
$m_{a,0}$	Added mass in still water
m_a	Added mass in actual flow and oscillation conditions
$q(z,t)$	Space- and time-varying external load
Q	Shear force

Q_v Static vertical soil reaction force per unit length of pipe

Re Reynolds number

St Strouhal number

T End Tension (in some cases it can also represent the oscillation period)

t The time variable

U Incident flow velocity

U_R Reduced velocity

V Amplitude of the flow velocity oscillation

$x, \dot{x}, \ddot{x}$ Displacement, velocity and acceleration in the IL direction (initially proposed TD VIV model)

$y, \dot{y}, \ddot{y}$ Displacement, velocity and acceleration in the CF direction (initially proposed TD VIV model)

Y_n Modal weight for mode number n

z Vertical penetration of the pipe required to mobilize the soil reaction

$\mathbf{r}, \dot{\mathbf{r}}, \ddot{\mathbf{r}}$ Nodal displacement, velocity and acceleration vectors

$\mathbf{R^D}$ Damping force vector

$\mathbf{R^E}$ External force vector

$\mathbf{R^I}$ Inertia force vector

$\mathbf{R^S}$ Internal structural reaction force vector

$\mathbf{r}_{t+\Delta t}, \dot{\mathbf{r}}_{t+\Delta t}, \ddot{\mathbf{r}}_{t+\Delta t}$ Nodal displacement, velocity and acceleration vectors at the new timestep

$\mathbf{r}_t, \dot{\mathbf{r}}_t, \ddot{\mathbf{r}}_t$ Nodal displacement, velocity and acceleration vectors at the current timestep

$\mathbf{x_n}, \dot{\mathbf{x}}_\mathbf{n}, \ddot{\mathbf{x}}_\mathbf{n}$ Displacement, velocity and acceleration of the cylinder's response

1 Introduction

1.1 Background

When, slender cylindrical structures with circular cross section, such as risers, pipelines, mooring lines and power cables are exposed in a fluid flow, time-varying oscillating loads may be exerted on the structure due to flow separation and vortex shedding. Such forces may result in structural oscillations of such slender marine structures, a phenomenon typically referred to as Vortex-Induced Vibrations (VIV). VIV is a phenomenon of great importance when it comes to the dynamic analysis of risers and pipelines, since it induces non-negligible dynamic stresses on the structure, ultimately resulting in the accumulation of fatigue damage [3, 13]. Therefore, the accurate prediction of these time-varying stresses and the corresponding fatigue damage caused by VIV is of paramount significance for the design of safe structures, that is, for adequately determining their expected life time and thus avoiding premature failure.

It becomes immediately apparent that VIV is an extremely complicated phenomenon considering that the flow is characterised by unsteady separation and turbulence. The complexity is further enhanced by the fluid-structure interaction, since these vortex-induced structural vibrations of the structure in turn influence the flow itself. What is more, VIV is closely linked to a wide range of practical engineering applications, including the design of pipelines, risers, power cables and mooring lines for the offshore oil and gas industry and the design of wind turbines to name but a few. The complexity of this phenomenon combined with the increased interest of the industry makes VIV a really fascinating research field and for this reason, extensive research work has already been devoted to it in the past decades, as presented in numerous review papers for the subject [14, 15]. The most significant findings of all those years of research are summarised in the DNV GL VIV Best Practice [3].

In the early years, the vast majority of the research on the topic was experimental. This is totally anticipated, since the governing equation of the examined flow problem is the Navier-Stokes equation, which cannot be solved analytically, except for some extremely simplified cases, and also because the computational power available at that time was limited. The knowledge gained by such experiments and the obtained experimental data were crucial for the determination of representative empirical hydrodynamic coefficients, such as the added mass and the drag coefficients, which are the foundation of the most common VIV prediction tools even today. Subsequently, based on the aforementioned experimental findings, several semi-empirical VIV prediction models were proposed. The VIV prediction tools that are most widely used in the industry today are VIVA [16], SHEAR7 [17] and VIVANA [18]. Despite their many differences, they are all characterised by the fact that they operate in the frequency domain (FD), which is also their main downside. In other words, the dynamic equilibrium equation is solved in the frequency domain and thus only stationary flow conditions and linearized structures can be treated. Of course, this is acceptable for simple cases such as for simple beams in uniform incident flows. However, the dynamic analysis of risers and pipelines is a highly non-linear problem. Non-uniform flows (e.g. sheared current), the interaction of multiple dynamic loads (e.g. combination of currents and waves), time-varying boundary conditions (e.g. soil-pipe interaction), tension variations and large displacements are a few examples of real operational conditions with regard to risers and pipelines, which introduce significant non-linearities to the considered problem. These non-linear effects have to be accounted for in a VIV analysis in order to accurately capture the dynamic response of the actual structure and get reliable results.

To include such non-linearities, a time domain (TD) analysis is needed. A detailed description

of the fundamentals of non-linear dynamic analysis is presented by Langen and Sigbjörnsson in [19]. Moreover, the differences between the non-linear and the linear analyses of flexible pipes are highlighted by Fergestad and Løtveit in [20]. In the latter, relevant information for free spanning pipelines can also be found, while an extended summary of the Recommended Practices with regard to the free spanning pipelines is given in [21]. In recent years, several time domain prediction tools have been proposed. If these models are coupled to a non-linear structural model, they can account for the aforementioned non-linearities. One very promising semi-empirical time domain VIV model (TD VIV model) was developed at NTNU by the PhD students Mats Jørgen Thorsen [22, 23, 24, 25] and Jan Vidar Ulveseter [26] and is based on a synchronization load model for the vortex-induced forces. Combining it with a non-linear Finite Element Model (FEM) the above TD model has been proven to be capable of predicting quite accurately the VIV response of slender elastic structures with respect to various loading conditions. More specifically, uniform, sheared and oscillating flows were examined in [27] while the combination of current and irregular waves was considered in [28] and the results were in general satisfactory. Finally, it is worth noting that apart from the aforementioned semi-empirical VIV prediction models, another existing tool is Computational Fluid Dynamics (CFD), which is an integrated method for calculation of forces and response from first principles. However, CFD is computationally too expensive and as a result it is not widely used in the industry for practical applications, at least for the time being.

1.2 Objectives

The purpose of this Master's Thesis work is to serve as a continuation of the the preparatory project performed in Fall 2021. To be more precise, the main objective of the present work is the validation and calibration of the TD VIV prediction tool, which is a recently developed empirical method for time domain calculation of VIV, with the focus mainly on the prediction of the dynamic response of free spanning pipelines. This thesis focuses both on the pure in-line VIV occurring at low reduced velocities and on the combined in-line and cross-flow vibrations, which are observed at higher reduced velocities. The calibrated time domain VIV prediction tool will then serve as the basis for evaluating non-linear damping and local stress effects at the pipeline's shoulders due to the pipe-soil interaction. The overall objectives will be completed through a number of subgoals, as explained in the following:

- Familiarization and presentation of the fundamental theory of VIV, of the existing numerical prediction tools and of the relevant DNV Rules and Recommended Practices related to riser and free spanning pipeline VIV response analysis.
- Familiarization with the TD VIV prediction tool and the non-linear FEM software RIFLEX, which can be coupled through the SIMA software.
- Familiarization with the reference data provided in terms of experimental data and numerical results obtained by means of the frequency domain VIV prediction model VIVANA.
- Definition and description of the examined model tests in terms of mechanical properties, geometry and test conditions.
- Establishment of relevant TD VIV models related to the available experimental and numerical reference data and carrying out TD VIV simulations of some selected cases.
- Comparison of the obtained results with the reference data and evaluation of the TD VIV prediction tool's performance with respect to chosen parameters and with focus on both pure in-line and combined in-line and cross-flow responses.

- Identification of optimum hydrodynamic parameter sets.
- Establishment of a TD VIV model for a realistic free span scenario and application of the optimum parameter set obtained previously.
- Investigation of the effects of damping due to soil-pipe interaction and the effect of the non-linear boundary conditions with respect to the induced stresses and fatigue damage.
- Presentation of the main conclusions and recommendations for further improvements of the TD VIV prediction tool and for other interesting cases that could be studied in the future.

1.3 Thesis Structure

Chapter 2 provides a literature review and serves as an introduction to the fundamental aspects of VIV that are relevant for the present thesis. First and foremost, a concise presentation of the basic theory behind VIV with focus on both rigid and flexible cylinders takes place in order to explain the hydrodynamic phenomena observed when the cylinder is exposed to a fluid flow. Subsequently, the main characteristics, advantages and disadvantages of the existing methods for VIV prediction, including CFD and semi-empirical methods in the frequency and time domain, are briefly illustrated.

Chapter 3 gives a brief introduction in the subject of Pipe-Soil interaction based on DNV's Recommended Practice [6]. This chapter focuses on the Soil Stiffness and Damping Characteristics and presents some simplifications proposed in [6] with regard to the implementation of the above soil properties in free spanning pipeline analyses.

Chapter 4 describes the examined reference model tests with regard to the general set up, the geometry and the mechanical properties of the considered models, as well as to the examined environmental and loading conditions. Then, the basic aspects of an earlier study of these particular model tests, conducted by Passano, Wu and Larsen [7] by means of the frequency domain VIV prediction tool VIVANA, are briefly presented. Finally, the experimental data and the respective frequency domain numerical results of three relevant test series are chosen to serve as a benchmark for the evaluation and calibration of the examined TD VIV model.

Chapter 5 presents the methodology followed in the present work for the investigation and analysis of the above model tests so as to achieve the aforementioned objectives and extract reliable results. First of all, the implementation of the hydrodynamic load model and the numerical and the structural models are illustrated. Furthermore, description of the tools utilized in order to perform the TD VIV simulations, in terms of the RIFLEX software, and to evaluate the validity of the obtained results is given. Finally, the parameters used initially in terms of the hydrodynamic coefficients, excitation ranges and the structural damping model to name but a few are highlighted and the procedure followed subsequently for the calibration of the TD VIV model and the identification of the optimum parameter set is described.

Chapter 6 discusses the findings of the above simulations and compares the obtained results with the reference numerical and experimental data. Of course, it is needless to say that the findings are also evaluated with regard to what is physically expected. Then based on the above results the optimum parameter set for the calibration of the TD VIV model is identified.

Chapter 7 describes a realistic case of a free spanning pipeline resting on the actual seabed with regard to the general set up, the geometry and the mechanical properties of the considered pipeline, as well as to the examined environmental and loading conditions. Then, the methodology followed for the analysis of this realistic free spanning pipeline case is presented. First of all, the implementation of the hydrodynamic load model with the optimum parameter set identified previously and the numerical and the structural models for this realistic scenario are illustrated. Subsequently, the two different approaches, i.e. the Linear and the Non-Linear models, adopted in the present work in order to model the soil properties and the pipe-soil interaction are described, and their implementation in RIFLEX is also presented. Finally, the procedure followed afterwards in order to post-process the results obtained by the time domain simulations of the examined scenarios is briefly described.

Chapter 8 discusses the findings of the TD VIV simulations with regard to the realistic scenario focusing on the comparison and the investigation of the differences between the Linear and Non-linear soil models. The basis of this comparative study is the observed effects of the non-linear damping and the time-varying boundary conditions due to pipe-soil interaction with respect to local stress and fatigue damage accumulation in the vicinity of the pipeline's shoulders.

Chapter 9 summarizes the key results, concludes and gives recommendations for further work.

Appendix A presents plots of the total set of the obtained results regarding the calibration of the TD VIV model. That is, plots of all the obtained simulation data with regard to all three investigated model test series and for all the examined hydrodynamic parameter sets are illustrated.

Appendix B presents plots of the total set of the obtained results regarding the Realistic Free Span Scenario. That is, plots of all the obtained simulation data with regard to the two examined soil models, the two considered soil damping levels and the conducted comparative studies between the aforementioned results are illustrated.

2 Introduction to Vortex-Induced Vibrations (VIV)

In this chapter a literature review on the basic aspects of vortex-induced vibrations (VIV) is given. As already mentioned, this is a topic of increased interest and a substantial research effort has been devoted to it in the last decades. Therefore, in this chapter only a brief summary of all this work is presented. The focus is on both theoretical and experimental findings with regard to the behavior of rigid and flexible pipes when exposed to VIV. In this way it will be possible to better understand and explain the otherwise complex interaction between the pipe and the incident fluid flow. Subsequently, the focus of this chapter is shifted on the existing numerical tools for VIV prediction, including Computational Fluid Dynamics (CFD) and Frequency Domain (FD) semi-empirical methods. Finally, the development of the Time Domain (TD) model, which is the foundation of this work, is presented. At this point it is worth noting that among the massive available literature, most of this chapter was chosen to be based on the DNV VIV Best Practice [3], while some other sources were also utilized to a lesser extent such as [2, 25, 29, 30].

2.1 Fundamental VIV Theory

2.1.1 Flow past a circular cylinder - Vortex shedding phenomenon

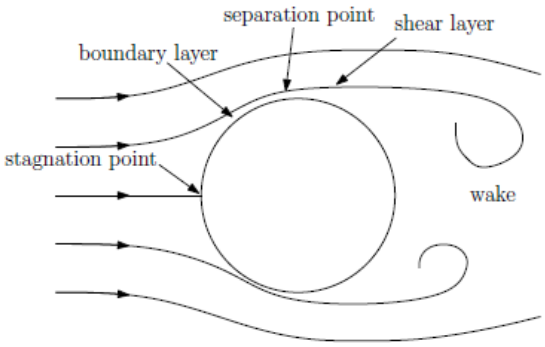

Figure 2.1: Steady flow past a fixed circular Cylinder

This section is based in [25, 29, 2, 30]. For the better understanding of the vortex shedding phenomenon the simplified case of a fixed circular cylinder exposed to a uniform steady flow is examined, as illustrated in Figure 2.1. According to potential flow theory, the impermeability and free-slip boundary conditions are valid on the body surface, meaning that the flow velocity normal to the cylinder's surface is equal to zero but a tangential velocity exists. However, in a real case the potential flow theory is not valid and the no-slip boundary condition applies on the body surface, indicating that the fluid velocity there must be equal to the cylinder's velocity and hence it must go to zero, since a fixed cylinder is considered. In other words, the fluid velocity must be reduced from its far field value to zero within a certain distance, $\delta(x)$, in the proximity of the body. The layer of fluid with thickness $\delta(x)$ is called boundary layer (BL) and within it non-negligible viscous effects are observed. This observation can be attributed to the fact that the shear/tangential stresses are proportional to the velocity gradient in the direction normal to the body surface. Therefore, the shear stresses take considerable values within the boundary layer, where large velocity gradients occur as the flow velocity reduces from the far field value to zero, and the smaller the boundary layer thickness is the larger the shear stresses are. The formation of the boundary layer is connected with an other important phenomenon, the flow separation, which is the detachment of the boundary layer in a wake. To elaborate on this, Figure 2.1 is

considered again. As the fluid moves downstream of the stagnation point, it actually flows in an adverse pressure gradient. The boundary layer separates when it has travelled far enough in an adverse pressure gradient that the speed of the boundary layer relative to the surface has stopped and reversed direction [31, 32]. That is at the flow separation point. Then the flow becomes detached from the surface, a shear layer is formed and the flow takes the forms of eddies and vortices. The above described phenomenon and thus the formation of vortices takes place both on the upper and on the lower side of the body but with opposite vorticity directions.

From all the above mentioned it becomes apparent that a critical parameter that governs the flow separation phenomenon and concequently the vortex shedding is the relative magnitude of the inertial and the viscous forces. A relevant non-dimentional parameter is the Reynolds number, which gives the ratio of those two forces and is given by Eq. 2.1.

$$Re = \frac{U \cdot D}{\nu} \tag{2.1}$$

where U is the velocity of the undisturbed incident flow, D is the characteristic length of the body (i.e. the diameter of the cylinder in the considered case) and ν is the kinematic viscosity of the fluid.

The Reynolds number is commonly used in order to classify the flow past a body in relevant regimes. According to Greco, [30], based on the value of Re four flow regimes can be distinguished with regard to a smooth circular cylinder as follows:

- Subcritical flow regime: $Re <\approx 2 \cdot 10^5$
- Critical flow regime: $\approx 2 \cdot 10^5 < Re <\approx 5 \cdot 10^5$
- Supercritical flow regime: $\approx 5 \cdot 10^5 < Re <\approx 3 \cdot 10^6$
- Transcritical flow regime: $Re >\approx 3 \cdot 10^6$

At this point it is worth noting that several different classifications have been proposed over the years, but the distinction of the flow into the four regimes presented above is the most widely acknowledged approach. Moreover, there might be some minor deviations between the researchers about the range of Reynolds number that corresponds to each regime. However, the purpose of this work is to get a better understanding of the phenomena that prevail when a cylinder is exposed to fluid flow and to highlight the differences between the four regimes and hence the exact value of Re where the transition from one regime to the next occurs is not of such importance in this context. Moreover, within those four main regimes, several subregimes have also been determined, as is explained in detail in Thorsen's Phd thesis [25]. Let us now examine the basic differences between those regimes using Figure 2.2 for a better visualization of them.

From Figure 2.2 it becomes clear that for low Reynolds numbers, where viscous forces prevail, the flow remains attached to the body, while for $Re > 5$ flow separation occurs and vortex shedding begins in both sides of the cylinder. In the starting process of the separated flow around the circular cylinder ($5 < Re < 40$), the vortical structures are released symmetrically from the two separation points, as described in detail previously. The frequency at which the vortex shedding phenomenon occurs is commonly referred to as the vortex shedding frequency f_s. A relevant non-dimentional parameter which is closely related to the vortex shedding frequency of a stationary cylinder is the Strouhal number, St. Provided that the Strouhal number is known

it becomes possible to predict the vortex shedding frequency for a fixed cylinder of arbitrary diameter (D) and incoming flow velocity (U) using Eq. 2.2.

$$St = \frac{f_s D}{U} \tag{2.2}$$

Subsequently, for $Re > 40$ due to the occurrence of some instabilities in the wake, an uneven growth of the two vortices is observed and as a result the smaller vortex is drawn by the larger one on the opposite side of the wake while at the same time the latter moves downstream following the flow and a new vortex emerges at its position. This process, in which vortices are shed alternatively from the two separation points is repeated in a loop and ultimately, the vortices travel along two parallel rows with opposite direction of rotation between eddies in one row and the other, which is commonly referred to as von Karman vortex street. As the Reynolds number increases turbulent phenomena are observed in the vortex street ($150 < Re < 300$) and for $Re > 300$ the street is fully turbulent. The process remains essentially unchanged for $300 < Re < 2 - 3 \cdot 10^5$ and this regime is referred to as subcritical. Most VIV related experiments takes place in this regime, while full scale cases easily will enter the critical and supercritical regimes [3]. Then in the critical flow regime ($2 \cdot 10^5 < Re < 5 \cdot 10^5$) a transition of the so far laminar boundary layer to turbulence is observed, but unexpectedly this phenomenon is focused only on the one side of the body resulting in a non-symmetrical flow. A further rise of the Reynolds number leads to a turbulent transition of the whole boundary layer, which is not fully turbulent yet, while the wake becomes narrower and more disorganized. This is referred to as the supercritical flow regime ($\approx 5 \cdot 10^5 < Re < \approx 3 \cdot 10^6$). Finally, in the transcritical flow regime ($Re > \approx 3 \cdot 10^6$) the boundary layer is fully turbulent.

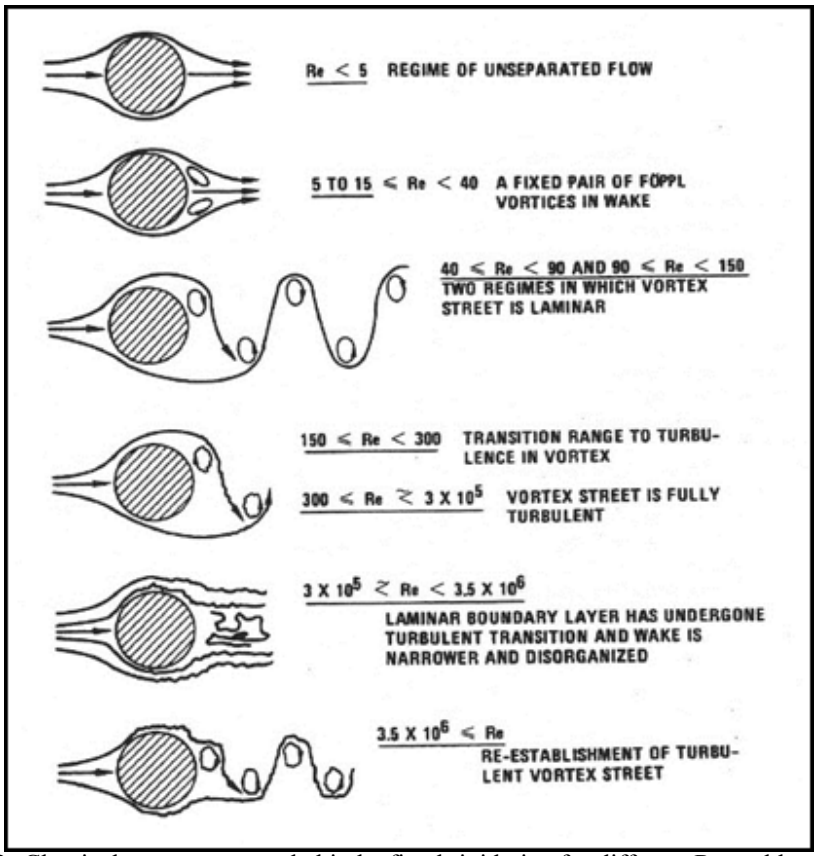

Figure 2.2: Classical vortex patterns behind a fixed rigid pipe for different Reynolds number [1]

2.1.2 Vortex shedding related forces

When a body is exposed to a stationary flow as examined in the previous section, pressure and shear stresses will be induced on the body. By integrating both contributions along the surface of the body, the respective fluid-induced force can be computed. This force is commonly divided in two components, one in the direction of the flow (in-line) and one in the direction perpendicular to the flow (cross-flow), which are referred to as drag force (F_D) and lift force (F_L) respectively, as illustrated in Figure 2.3. The amplitude of those forces per unit length is given by Eq. 2.3.

$$F_D = \frac{1}{2}\rho C_D D U^2 \quad , \quad F_L = \frac{1}{2}\rho C_L D U^2 \tag{2.3}$$

where ρ is the density of the fluid, D is the characteristic length of the body (i.e. the diameter of the cylinder in the considered case) and C_D and C_L are the non-dimensional drag and lift coefficients respectively.

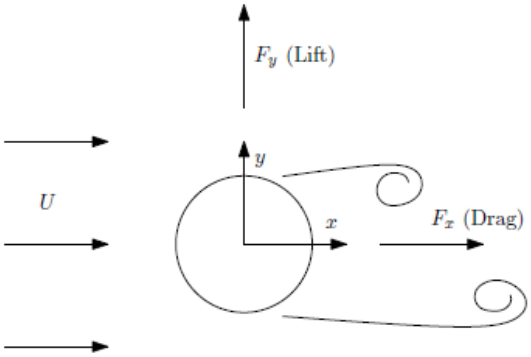

Figure 2.3: Lift and drag forces exerted on a fixed cylinder in stationary flow

When the considered body is symmetric, as in the examined case, the mean value of the above presented lift force is equal to zero. However, this is not true with regard to the drag force which has a considerable mean value, something that can mainly be attributed to the mean frictional terms and pressure losses around the cylinder (i.e. the significant pressure difference between the high pressure region in front of the cylinder near the stagnation point and the low pressure in the wake region). For a smooth cylinder a typical value for the drag coefficient in the subcritical regime is 1.2 [2]. At higher Reynolds numbers the flow separation takes place closer to the wake ultimately leading in a smaller wake region and thus pressure loss, which in turn results in lower drag coefficient values. Of course, the lift and drag forces do not only have mean values but a fluctuating component can also be determined. This statement can be justified by the fact that, when vortex shedding occurs, time-varying forces are exerted on the body due to the changes of the fluid pressure onto the body. If a single vortex shedding frequency is assumed, then the aforementioned pressure changes are almost periodic and the resulting oscillating parts of the forces can be approximated as sinusoidal with a certain amplitude A_D and A_L respectively. The oscillating component of the drag force is small relative to both the fluctuating lift force and to the mean drag force and oscillates at a frequency twice the vortex shedding frequency. On the other hand, the instantaneous fluctuating lift force oscillates at the vortex shedding frequency and takes considerable values with a typical lift coefficient at the subcritical flow regime of 1.35. The difference in the frequency of those two force components can mainly be attributed to the fact that the vortices, as already explained, are shed alternatively from the two separation points. For the lift, the change of the cylinder side where shedding occurs matters, because the lift is sensitive to variations in the transverse direction and thus its oscillation frequency is the same

as the shedding frequency. On the other hand, the change of the cylinder side where shedding occurs does not effect the drag,since it is only sensitive to variations in the current direction and therefore it oscillates at a frequency twice the shedding frequency [30]. The total time-varying drag and lift forces can be approximated by Eq.2.4, where it is highlighted that the drag force consists of a mean and a fluctuating part while the lift force does not have a mean component.

$$F_D(t) = \bar{F}_D + A_D cos(4\pi f_s t + \beta_D) \quad , \quad F_L(t) = A_L cos(2\pi f_s t + \beta_L) \tag{2.4}$$

where $\bar{F}_D$ is the mean drag force and β_D and β_L are the phase angles of the drag and lift force.

2.1.3 The results of the vortex shedding phenomenon

As explained in the previous section, when a fixed body is exposed to an incident flow, vortex-induced lift and drag forces are exerted on the body. Assuming now that the body is not restricted, the result of the aforementioned forces will be structural oscillations in both the cross-flow and the in-line directions. If the body oscillates at its natural frequency, these motions are regarded as resonant phenomena. Typically, those vortex-induced resonances are distinguished in two categories, the vortex-induced motions (VIM) and the vortex-induced vibrations (VIV). According to DNV's VIV Best Practice [3], these two phenomena are identical and their difference lies in the oscillation frequency. VIM is related to much longer motion periods than VIV and can occur on any bluff body exposed to currents (e.g. rigid body motions of floating structures like semi-submersibles and spar buoys). On the other hand, VIV mainly involves elastic motions of slender structures, such as pipes, risers and mooring lines, and is characterised by a considerably higher oscillation frequency. Taking all the above into consideration, it was chosen to not deal with VIM in the following.

As mentioned above, VIV can be regarded as a resonant phenomenon and therefore it occurs when the oscilation period of the vortex-induced forces are equal or close to the natural period of the body. Moreover, taking into account that, as previously shown, the oscillation frequency of the drag force is two times the vortex shedding frequency ($2f_s$), it becomes evident that in-line VIV occurs when this frequency becomes equal to the in-line natural frequency of the structure ($f_{n,x}$). Similarly, cross-flow VIV occurs when the oscillation frequency of the lift force, which is the vortex shedding frequency, becomes equal to the cross-flow natural frequency of the structure, that is when $f_s = f_{n,y}$. At this point it is worth noting that this is an extremely simplified approach and intends only to indicate approximately the frequency range where each of the two VIV modes occurs. In reality the occurrence of VIV is governed to a great extent by the so-called "lock-in" phenomenon. Lock-in can be explained in simple words by taking into account that, for a fixed cylinder, the vortex shedding frequency increases linearly with the incident flow velocity, as illustrated clearly in Eq.2.2. However, the structural oscillations of the cylinder interact with the vortex shedding procedure in such a way that the latter deviates from the linear relationship and synchronizes/locks with the cylinder motion and their frequencies become equal. A relevant non-dimensional parameter, which is closely related to the vortex shedding frequency and facilitates the understanding of lock-in, is the reduced velocity, U_R, which is given by Eq. 2.5.

$$U_R = \frac{U}{f_n D} \tag{2.5}$$

where U is the incident flow velocity, D is the diameter of the cylinder and f_n is the still water natural frequency of the body.

The significance of U_R in roughly predicting the occurrence of CF VIV and IL VIV can be easily understood if Eq.2.5 is combined with Eq. 2.2. Substituting $\frac{U}{D} = \frac{f_s}{St}$ from Eq. 2.2 in Eq. 2.5 yields:

$$U_R = \frac{f_s}{f_n}\frac{1}{St} \tag{2.6}$$

From Eq. 2.6 it becomes apparent that cross flow VIV occurs for $U_R = \frac{1}{St}$ (i.e. for $f_s = f_{n,y}$) and similarly IL VIV occurs for $U_R = \frac{1}{2St}$ (i.e. for $2f_s = f_{n,x}$). For example, assuming $St = 0.2$, which is a typical value within the subcritical flow regime, CF VIV is expected to occur at $U_R = 5$. Of course, this is a rough estimation of the VIV occurrence, but it seems to be in good agreement with relative experimental data. In Figure 2.4a, which is given in [21] and refers to CF VIV of a circular cylinder in water, it becomes apparent that the CF region extends from about $U_R = 2$ to about $U_R = 16$. Another interesting conclusion that can be reached by comparing this Figure with the respective results of CF VIV of a circular cylinder in air presented in [2], where the corresponding CF range is approximately $5 < U_R < 7$, is that VIV in water dramatically influences the natural period of the body, presumably due to changes of the added mass, something that is clearly presented in Figure 2.4b. Finally, as far as IL VIV is concerned, it is seen from Eq. 2.6 that it is related to lower reduced velocities, as illustrated clearly in Fig. 2.4c. Since IL VIV occurs at lower reduced velocities than CF VIV, it follows that there is a range of U_R where the considered body is vibrating only in the IL direction. This phenomenon is referred to as pure IL VIV and is of paramount importance especially with regard to free spanning pipelines.

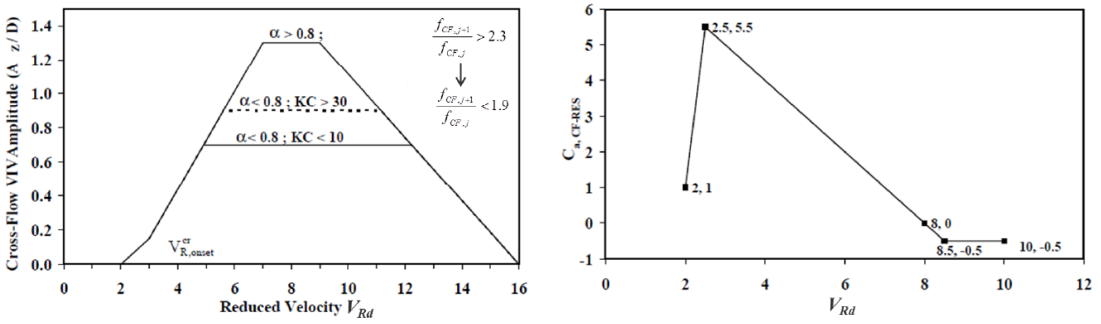

(a) CF VIV Response Amplitude vs Reduced Velocity

(b) Added mass coefficient vs Reduced Velocity

(c) IL VIV Response Amplitude vs Reduced Velocity

Figure 2.4: Illustration of the CF and IL VIV Response Amplitudes and the added mass coefficient as a function of the reduced velocity

2.2 VIV of Rigid and Flexible Cylinders

The rapid development of technology and the industrial domination in the last century led to a sharp increase in global energy needs, which at that time were covered almost entirely by fossil fuels and mainly by crude oil and its derivatives. The largest deposits of such forms of energy are located in the submarine space. In addition, the rapid depletion of such deposits and the rising awareness for the potential threats that such energy forms pose for the environment have turned global interest in the last decades in the exploitation of sustainable energy sources, including the installation of large offshore wind farms and wave energy absorption. Taking all the above mentioned facts into account, the oil and energy industry have invested a considerable amount of money in the research of relevant phenomena like VIV, which are threatening the survival of such expensive offshore energy related installations. According to DNV's VIV Best Practise, most of this research is based in model scale experiments, something that comes with the aforementioned downside that the examined cases are mainly limited within the subcritical flow regime, while full scale cases easily will enter the critical and supercritical regimes [3].

Moreover, since IL VIV response amplitudes have been shown to be much lower than the respective CF response amplitudes, the vast majority of the research used to be focused in CF VIV. However, more recent works (Baarholm et al. [33] and Vandiver et al. [15]) have proven that IL VIV, which is closely related with higher order harmonics, can contribute significantly to the total fatigue damage accumulation and thus should not be neglected. Finally, according to DNV's VIV Best Practise, in most of those experimental works, uniform and sheared flows were considered due to the fact that vortex-induced vibrations in time varying flow is still a very active research topic and the majority of the existing VIV prediction tools have not included such flows in their calculations yet. The experiments conducted in order to form the empirical basis for understanding VIV can be distinguished in four main types [3]:

- Rigid pipes with fixed supports
- Free oscillations of rigid pipes on elastic supports
- Forced oscillations of rigid pipes
- Slender elastic pipes in various flow conditions

2.2.1 Rigid pipes with fixed supports

The first VIV related experiments were with regard to rigid pipes with fixed supports and their main goal was to shed light on the prevailing phenomena when a stationary circular cylinder is exposed to incident fluid flow. This consists the most basic knowledge required for the understanding of the vortex shedding phenomenon and as such it has already been presented in depth in chapter 2.1, where it served as an introduction to VIV theory. Therefore, this type of experiments will not be treated in detail here but only some fundamental aspects will be reminded and elaborated further. More specifically, in chapter 2.1 it was noted that the vortex shedding phenomenon and the characteristics of the corresponding vortex street are closely related to two relevant non-dimensional parameters, the Reynolds number (Re) and the Strouhal number (St). What was not examined in chapter 2.1 is the dependence of St on the value of Re and the surface roughness of the examined cylinder. This was thoroughly investigated by Faltinsen and his findings are summarised in Figure 6.26 in [2], Figure 2.5.

Taking a closer look at Figure 2.5 it becomes apparent that St takes an almost steady value of 0.2 within the subcritical flow regime regardless of the examined roughness, while a strong

dependence of St on the surface roughness is evident in the critical flow regime. To be more precise, as far as smooth cylinders are concerned, the transition to the critical flow regime is accompanied by a sharp increase of St, while this is not true for cylinders with considerable surface roughness. However, it should be noted that real pipes used in practical offshore applications are characterised by a non-negligible surface roughness as a result of corrosion and marine growth. Therefore, the aforementioned radical rise of the vortex shedding frequency and the corresponding St is generally not accounted for in VIV analyses [3]. Finally, excluding again the case of a perfectly smooth pipe, in the supercritical and tanscritical flow regimes, St seems to be independent of the surface roughness and stabilizes to a value around 0.25.

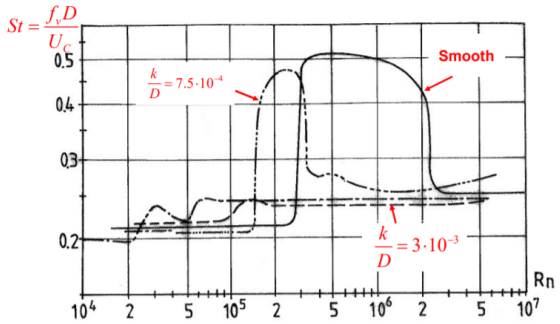

Figure 2.5: Strouhal number St of rough circular cylinders in steady incident flow for different surface roughness values k/D (k = average height of surface roughness, D = cylinder diameter, f_v = vortex shedding frequency, U_c flow velocity, $Rn = U_c D/\nu$ = Reynolds number) $-$ smooth; $-...-, k/D = 7.5 \cdot 10^{-4}$; $--, k/D = 3 \cdot 10^{-3}$; $-.-, k/D = 9 \cdot 10^{-3}$; $- - --, k/D = 3 \cdot 10^{-2}$ [2]

2.2.2 Free oscillations of rigid pipes on elastic supports

One of the three experimental setups illustrated in Figure 2.6 is usually used in order to perform free oscillation tests of rigid pipes on elastic supports, where a) corresponds to CF VIV, b) to IL VIV and c) to combined IL and CF VIV tests. The main objective of such free vibration experiments is to examine the amplitudes of the response and the phase differences between the response and the respective excitation force. Moreover, estimation of the values of the added mass coefficients becomes also possible through such experiments, although added mass coefficients are generally obtained via forced oscillation experiments.

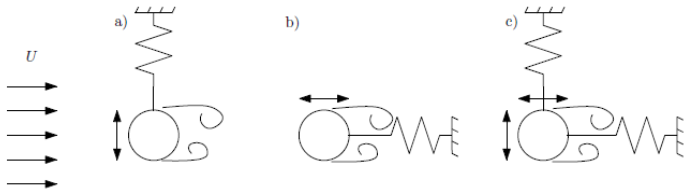

Figure 2.6: Typical VIV experiments with rigid cylinders on elastic supports: a) Cross-flow, b) In-line, c) Combined in-line and cross-flow

Since numerous different test conditions can be examined in such experiments, including different current velocities, pipe dimensions and mass and experimental apparatus' characteristics (e.g. different spring stiffness and natural frequencies), non dimensional parameters like the above introduced reduced velocity U_R are commonly used for an easier comparison of the obtained results. Apart from the vortex shedding frequency f_s, two more frequencies govern the dynamic response of the models presented in Figure 2.6. That is, the still water natural frequency f_n and the oscillation frequency f_{osc} or equivalently the non-dimensional oscillation frequency

$\hat{f}$ which are given in Eq. 2.7, Eq. 2.8 and Eq. 2.9 respectively.

$$f_n = \frac{1}{2\pi}\sqrt{\frac{k}{m + m_{a,0}}} \tag{2.7}$$

$$f_{osc} = \frac{1}{2\pi}\sqrt{\frac{k}{m + m_a}} \tag{2.8}$$

$$\hat{f} = \frac{f_{osc}D}{U} \tag{2.9}$$

where k is the spring stiffness, m is the dry mass which also includes the mass of the contents (e.g. the internal fluid in a pipe), $m_{a,0}$ is the added mass in still water and m_a is the added mass in actual flow and oscillation conditions. As was already noted in section 2.1.3, the oscillation frequency and the related added mass of a body that oscillates within a flowing fluid does not correspond to the respective still water added mass and natural frequency. Taking into account that the added mass is by definition the hydrodynamic force component that is in phase with the acceleration, it can in practice be calculated using experimental data and, as has already been shown in Figure 2.4b, it can vary significantly as a function of the reduced velocity and can even take negative values. This is attributed to the phase difference between the response and the respective hydrodynamic force. Furthermore, in order to better understand the dependence of the body's natural frequency on the variation of the added mass, a useful non-dimensional parameter is the mass ratio m^* given in Eq. 2.10, which is the ratio between the cylinder's dry mass and the mass of the displaced fluid and is used to distinguish the pipes into "heavy" and "light". Marine pipes are typically characterized by low mass ratio, since they are surrounded by sea water, which has a considerable density compared for example with the much thinner air. Changes to the added mass and thus to the natural frequency are much easier and more profound for "lighter" pipes [3].

$$m^* = \frac{4 \cdot m}{\pi \rho D^2} \tag{2.10}$$

In order to explain the various phenomena that take place during the occurrence of VIV, Figure 2.7 will be utilized, where the CF response amplitude to diameter ratio and the oscillation frequency to still water natural frequency ratio are presented as a function of the reduced velocity for an elastically supported pipe with low structural damping and low mass ratio. Initially, when vortex shedding begins, the oscillation frequency, which is in this case equal to the vortex shedding frequency, follows the Strouhal law (Eq. 2.2) and thus it increases linearly with the incident flow velocity or equivalently with the reduced velocity. However, when the oscillation frequency gets close to the still water natural frequency of the system, the previously mentioned lock-in phenomenon takes place and the two frequencies synchronize, as is shown in Figure 2.7b around $U_R = 5$. Then, and for an extended range of reduced velocities (lock-in range - $5 < U_R < 18$) the two frequencies attach to one another and the oscillation frequency does not comply with the Strouhal law in this region. Moreover, it becomes apparent that as the reduced velocity increases further, the natural frequency of the structure deviates from its still water value and increases as well, due to the changes of the added mass, as was already explained in detail. In other words and as has been shown in numerous experiments, within the lock-in range the oscillation frequency is equal to the true eigenfrequency of the structure (i.e. including the added mass correction) and thus the lock-in VIV is a true resonant phenomenon. From Figure 2.7a it becomes obvious that within the lock-in range the amplitude of the response increases dramatically. Further increase of the reduced velocity ($U_R > 18$) results in desynchronization of the two frequencies and the oscillation frequency follows again the Strouhal law while the

response amplitude reduces significantly.

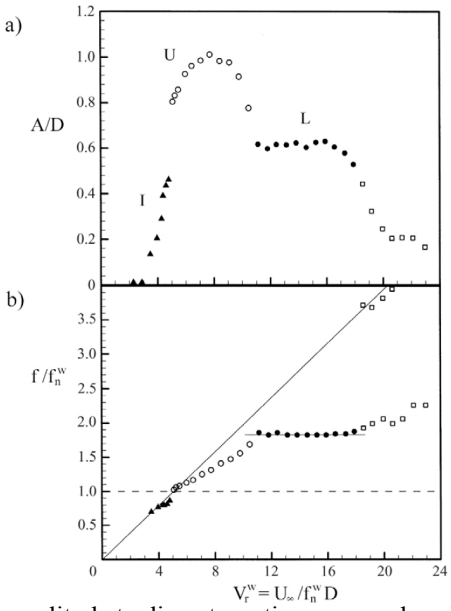

Figure 2.7: a) CF response amplitude to diameter ratio versus reduced velocity and b) oscillation frequency to still water natural frequency ratio versus reduced velocity of an elastically supported pipe with low structural damping and low mass ratio [3]

Another important feature of VIV is the fact that it is a self-limiting process, something that becomes evident in Figure 2.8. In the left plot, which corresponds to a pipe that is at rest when vortex shedding occurs, the response amplitude gradually increases until it reaches a steady state value. The opposite trend is observed in the right realization, where for larger initial amplitude than in steady state, the vortex shedding seems to result in a reduction of the response amplitude until again steady state is reached. This indicates that the excitation force coefficients have to be influenced by the response itself and they seem to take negative values when the initial response amplitude is relatively large and positive values for small amplitudes, while they seem to approach zero when steady state is reached. The behaviour of the excitation coefficients will be investigated more thoroughly in the following since they are mainly connected to forced oscillation experiments. Of course, such coefficients can be estimated from the initial transient part of free oscillation tests too, but this is not a common procedure.

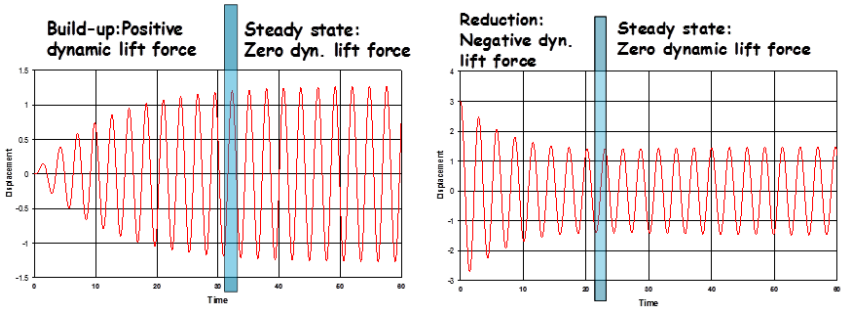

Figure 2.8: Time history of response oscillation for a cylinder with two different initial conditions [4]

So far, the above presented observations have been based to results corresponding to CF vibrations. However, the same trends can be extended to IL VIV as well, keeping in mind though that as a rule of thumb in-line response occurs at about two times the frequency of the cross-flow

response and that the lock-in range for IL VIV usually corresponds to lower reduced velocities. Finally, as far as the combined CF and IL VIV response is concerned, it was found by Triantafyllou et al. ([34]) that the presence of in-line response results in an increase in the respective cross-flow response, mainly due to the presence of IL VIV related higher order harmonics, and in an extension of the CF lock-in range to lower reduced velocities.

2.2.3 Forced oscillations of rigid pipes

The typical experimental setup used for forced oscillation tests is illustrated in Figure 2.9. In such experiments, the pipe is exposed to a uniform and steady onset flow and is forced to oscillate in a prescribed pattern either in the in-line or in the cross-flow direction, while combined IL and CF vibration is also possible. The main idea behind these experiments is based on the fact that the full scale data available are limited. Hence, instead of measuring the response of a pipe in order to estimate the corresponding loading pattern, these limited data are utilized so as to estimate representative trajectories of 2D cross sections of slender marine structures and then small deviations of those known responses are used in order to calculate the corresponding forces. In most cases the predefined response of the structure is approximated as a harmonic motion like the ones presented in Figure 2.9. Subsequently, the obtained hydrodynamic forces are split into components in phase with pipe's acceleration and velocity in each direction making in this way the calculation of the added mass and excitation coefficients possible for any combination of response amplitude and oscillation frequency of interest. Assuming that the considered response can be approximated by the expression of Figure 2.9 (Eq. 2.11), the procedure followed for the calculation of the aforementioned hydrodynamic coefficients can be briefly described as such:

$$x = x_0 sin(2\pi f_{osc} t) = x_0 \sin(\omega t), \quad \dot{x} = \omega x_0 \cos(\omega t), \quad \ddot{x} = -\omega^2 x_0 \sin(\omega t) \tag{2.11}$$

In most cases no damping and no restoring forces are introduced to the system and thus the harmonically oscillating cylinder experiences only inertial and hydrodynamic forces, the sum of which has to be equal to the total driving forces measured during the experiment.

$$m(-\omega^2 x_0 \sin(\omega t)) + F_{hydrodynamic} sin(\omega t + \epsilon) = F_{measured} \tag{2.12}$$

Dividing now the hydrodynamic force into one component in phase with the acceleration and one component in phase with the velocity yields:

$$(m + m_a)(-\omega^2 x_0 \sin(\omega t)) + F_e(\omega x_0 cos(\omega t)) = F_{measured} \tag{2.13}$$

Then it is straightforward how to compute the added mass m_a and the excitation force F_e for both IL and CF VIV. According to DNV's VIV Best Practice, attempts have also been made to estimate coefficients for combined IL and CF response but the complicated interaction between these two vibration types made the amount of required experiments too extensive and costly.

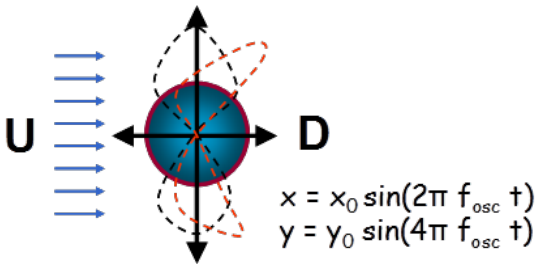

Figure 2.9: Typical experimental setup for forced oscillation tests of rigid pipes [3]

Results from forced oscillation experiments are usually illustrated as contour plots for the calculated hydrodynamic coefficients with the amplitude to diameter ratio A/D and the non-dimensional frequency $\hat{f}$ as the $y-$ and $x-$axes respectively as presented in Figure 2.10,where the bold lines represent conditions without excitation.

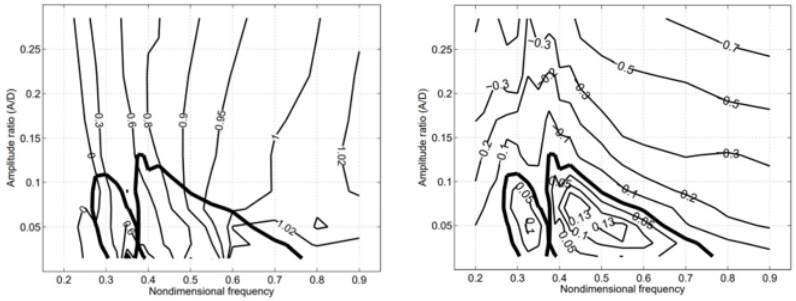

(a) Added mass coefficient (b) Excitation force coefficient

Figure 2.10: Contour plots of the in-line added mass and excitation force coefficients given in [5].

2.2.4 Slender elastic pipes

So far, the previously presented analysis has focused entirely on rigid pipes. However, in order to better understand and explain the dynamic properties and behaviour of real slender marine structures, which are far more complicated than the rigid cylinders, experiments on slender elastic pipes are necessary. This complexity is mainly attributed to the spatial response variability characterizing elastic pipes exposed to hydrodynamic loads like waves and currents. Such experiments are usually conducted on scaled models of real marine structures such as risers and pipelines. Contrary to the previous analysis, where the natural frequency was referring to the natural frequency of the test apparatus, since rigid pipes themselves have no elastic mode and thus natural frequency, elastic pipes have infinitely many natural frequencies, each of which corresponds to one vibration mode (mode shape). Therefore, the response of the examined structure is not characterized by one constant amplitude anymore, but instead the response varies in space and time. The maximum response of a flexible pipe is typically larger than the respective response of a rigid pipe under the same loading conditions. The experiments concerning elastic pipes are typically divided in three main groups [5]:

- Model tests of piles corresponding to cantilever beams
- Model tests of pipelines corresponding to beams where the bending stiffness is the dominant parameter that characterizes the response
- Model tests of risers corresponding to beams where the applied tension is the dominant parameter that characterizes the response

As pipelines are the main subject of this work, the following analysis will focus on this category. However, it should be noted that in most real-life cases regarding free spanning pipelines, a pretension is induced to the pipeline by the installation vessel during the pipe-laying procedure and adding a constant pretension in the system is the most widely used approach in free spanning pipeline analyses. On the basis of this statement, as will be explained in detail in chapters 4 - 5 and 7.1 - 7.2, the application of this additional axial pretension was considered for all the examined cases in the context of this thesis. For this reason, the effect of the axial tension on the dynamic behaviour of elastic pipes will also be discussed in the following. The existence of the pretension enables the occurrence of higher order modes and the excitation of multiple

eigenfrequencies and mode shapes. In order to accurately capture the dynamic response of elastic pipes, suitable devices like strain gauges and accelerometers are placed at selected positions along the pipe so as to record the CF and IL displacements and accelerations. Subsequently, the obtained data are utilized by means of modal analysis in order to determine the oscillation frequency and the respective vibration mode. At this point it is also worth noting that since pipelines are the main interest of this work, the following analysis will focus on pipes exposed to uniform steady currents considering that pipelines are positioned near the sea bottom and usually do not experience significantly varying incoming flow speeds along their length.

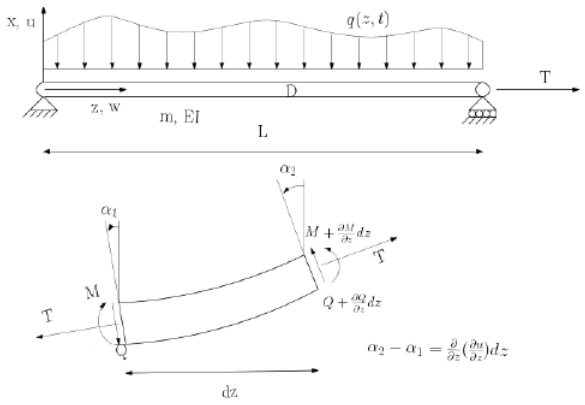

Figure 2.11: Schematic illustration of a pinned-pinned tensioned beam and the internal forces acting on a small deformed element with length dz

In order to better understand the dynamic behaviour of a slender elastic pipe, Figure 2.11 will be utilized, where a pinned-pinned beam (which is typically used as an approximation of an elastic pipe) with constant cross-sectional properties (i.e. constant diameter D, cross-sectional area A, mass distribution m and bending stiffness EI) and constant applied tension T is illustrated. Assuming that the shear deformations are negligible and considering only small lateral displacements, the dynamic equilibrium equation of such a beam can be formulated. First of all, the vertical force equilibrium applied to a strip dz of the beam as shown in Figure 2.11 yields:

$$T\frac{\partial^2 u}{\partial z^2} + \frac{\partial Q}{\partial z} + q(z,t) = m\frac{\partial^2 u}{\partial t^2} \tag{2.14}$$

where T is the applied tension, u is the lateral displacement, Q is the internal shear force, $q(z,t)$ the space- and time-varying external lateral load and m is the mass per unit length of the beam. Then, applying the moment equilibrium to the same strip dz the relation between the internal shear force Q and the bending moment $M = -EI\kappa$ can be obtained (Eq. 2.15), where $\kappa = \frac{\partial^2 u}{\partial z^2}$ is the curvature of the pipe.

$$Q = \frac{\partial M}{\partial z} = \frac{\partial}{\partial z}\left(-EI\frac{\partial^2 u}{\partial z^2}\right) \tag{2.15}$$

Finally, by substituting Eq. 2.15 in Eq. 2.14 the dynamic equilibrium equation can be established:

$$m\frac{\partial^2 u}{\partial t^2} - T\frac{\partial^2 u}{\partial z^2} + EI\frac{\partial^4 u}{\partial z^4} = q(z,t) \tag{2.16}$$

In order to find the natural frequencies of the considered pipe, the free vibration problem has to be examined. This can be done by finding the homogeneous solution of Eq. 2.16 or in other

words by setting the external loading in Eq.2.16 to zero as illustrated in Eq. 2.17.

$$m\frac{\partial^2 u}{\partial t^2} - T\frac{\partial^2 u}{\partial z^2} + EI\frac{\partial^4 u}{\partial z^4} = 0 \tag{2.17}$$

This type of homogeneous equations is commonly dealt with using separation of variables into spatial components $\psi_n(z)$, which are referred to as mode-shapes, and time-varying components $Y_n(t)$, which are usually referred to as modal weights and are simply some scaling factors that indicate the contribution of each mode-shape in the total response. In this way, and keeping in mind that a constant tension T is assumed and that pinned-pinned boundary conditions are considered meaning that both the displacements and the curvature at both ends are equal to zero, the solution to Eq. 2.17 can be written as:

$$u(z,t) = \sum_{n=1}^{\infty} \psi_n(z) Y_n(t) = \sum_{n=1}^{\infty} u_0 \sin\left(\frac{n\pi z}{L}\right) \sin\omega_n t, \quad n = 1, 2, 3, \ldots \tag{2.18}$$

where n refers to the vibration mode number. The first part of the above solution $\psi_n(z) = u_0 \sin\left(\frac{n\pi z}{L}\right)$ corresponds to the mode-shapes and expresses the variations of the response in space (i.e. along the length of the pipe) and has to satisfy the boundary conditions applied to the structure. The first 10 mode-shapes of a pinned-pinned flexible beam with constant tension are illustrated in Figure 2.12. Each mode-shape corresponds to one of the structures natural frequencies, which can be determined by inserting Eq. 2.18 in Eq. 2.17:

$$\omega_n = \frac{n\pi}{L}\sqrt{\frac{T}{m} + \left(\frac{n\pi}{L}\right)^2 \frac{EI}{m}}, \quad n = 1, 2, 3, \ldots \tag{2.19}$$

From Eq. 2.19 it becomes clear that the structure's natural frequencies increase with the mode number n. Moreover, two terms can be distinguished in Eq. 2.19. The first one is associated with the applied tension T and increases linearly with n, while the second term is related to the bending stiffness and is proportional to n^2. Therefore, the contribution of the bending term in the natural frequency becomes more and more profound as the mode number increases. Based on the relative contribution of those two terms in the natural frequency, the dynamic behaviour of the pipe is characterized as either tension dominated or as bending stiffness dominated.

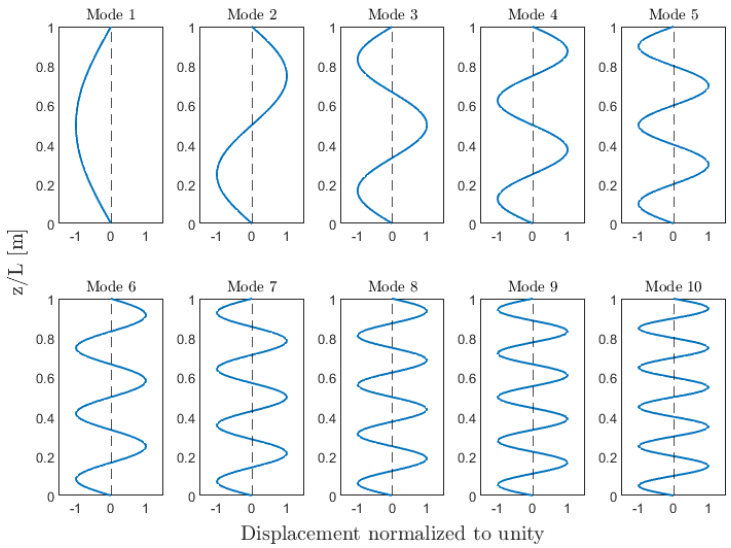

Figure 2.12: The first 10 mode shapes of a pinned-pinned flexible beam with constant tension

In order to better explain the effect of VIV in the dynamic behaviour of a flexible pipe, let as consider a flexible cylinder exposed to a uniform fluid flow and examine how its response changes as the incoming flow velocity increases. Since in this case, where a flexible pipe is considered, there is an infinite number of natural frequencies, the oscillation frequency can in practice synchronize with any of these frequencies resulting in a much more complicated dynamic behaviour than what was previously analysed regarding rigid pipes. Initially, for low current velocities, the oscillation frequency follows the Strouhal law (Eq. 2.2) and thus it increases linearly with the incident flow velocity leading in small amplitude vibrations. However, when the oscillation frequency gets close to the to the first eigenfrequency ω_1 of the system, the previously mentioned lock-in phenomenon takes place and the two frequencies synchronize. As long as the oscillation frequency is within the lock-in range with respect to ω_1 and since ω_1 is associated with the first vibration mode, high amplitude mode 1 vibrations can be observed. Further increase of the flow velocity results in desynchronization of the two frequencies, something that in the case of rigid pipes would mean that the oscillation frequency would follow the Strouhal law once again and the response amplitude would reduce significantly. However, when a flexible pipe is considered, the oscillation frequency might in fact be within the synchronization range with regard to the second natural frequency of the pipe ω_2 and the respective response amplitude will depend on the energy transfer between the fluid and the pipe and thus might become even higher. Taking all the above into account, it becomes obvious that in the case of flexible pipes the oscillation frequency might always be close and lock-in to one of the infinite many natural frequencies of the structure and thus vibrations of considerable amplitude might continue to be present at all higher flow velocities. At this point it is worth noting that the above analysis considered only the simple case of response at a single frequency. However, the VIV of flexible pipes is an even more complex phenomenon, since in reality, especially when the pipes are exposed in space-and time-varying ocean flows, numerous natural frequencies can be excited either simultaneously or over time, leading in a so-called ”multi-frequency” response [3]. Moreover, due to the fact that the incident flow velocity might vary along the length of the pipe, it has been observed ([35]) that the response of a flexible pipe can consist of either standing waves or travelling waves. Travelling waves seem to prevail in the regions of the pipe exposed to higher flow velocities and vice versa.

Another important feature of the VIV of flexible pipes is that apart from the fundamental cross-flow response at the vortex shedding frequency f_s and the fundamental in-line response at about twice the vortex shedding frequency $2f_s$, response associated with higher order harmonics is also often observed. This type of response is mainly related to IL VIV, since as already mentioned, non-negligible higher order harmonics are present in the lift force when the pipe is oscillating in the IL direction. The third harmonic associated with a frequency three times the vortex shedding frequency $3f_s$ is widely recognised as the most important higher order component. This feature of the VIV of flexible pipes is significant, because the third harmonic might be close to one of the structures natural frequencies and thus it might result in high frequency stresses and accumulation of fatigue damage. According to Wu et al. ([36, 37]) the stresses induced by the third harmonic can in a lot of cases be the dominant ones. Moreover, the contribution of the third harmonic was shown to be much more profound when the pipe is tension-dominated rather than bending stiffness dominated. This observation is closely related to another finding of the same research. That is, third harmonic induced stresses are more important when the response of the structure is stationary rather than chaotic or in other words at lower vibration modes which are tension dominated and not at high modes where the bending stiffness becomes significant. Finally, it was also shown that higher order VIV occurs when the response is characterized by travelling waves and not standing waves (i.e. for high flow velocity).

The existence of higher order harmonics can be of paramount importance with regard to free-spanning pipelines, in which pure IL VIV dominates and low mode vibrations are commonly observed, although it should be kept in mind that the applied tension in free spanning pipelines is usually much smaller than the one applied in risers for example and therefore the bending stiffness term prevails in Eq. 2.19. Another unique characteristic of free spanning pipelines is the existence of a sag in the middle of the pipe due to gravity, which can result in different natural frequencies in the two orthogonal directions (IL and CF). In particular, the existence of a long sag can highly influence the natural frequency in the CF direction, while the IL direction is practically unaffected. This phenomenon has been shown in many cases ([7]) to lead in mode 1 CF natural frequencies that are close or even higher than mode 2 IL natural frequencies and as a result simultaneous mode 1 vibrations have been observed in CF and IL directions, despite the fact that the IL vibration frequency is typically two times the CF frequency.

2.3 Existing VIV prediction tools

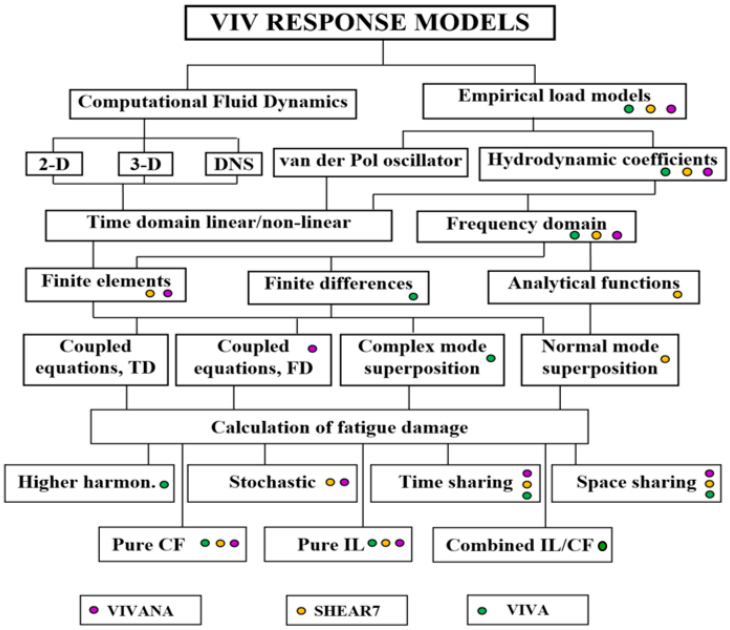

Figure 2.13: Overview of the available VIV response models [3].

In order to be able to accurately predict the results that VIV has on a flexible structure exposed to an incident fluid flow, two main models have to be established:

- An efficient hydrodynamic model that can accurately estimate the fluid induced hydrodynamic forces on the structure.
- A mathematical structural model that can accurately capture the resulting structural response of the structure in terms of displacements, velocities and accelerations.

The latter of the aforementioned models is not regarded as a serious problem nowadays, since typically the well-established and validated finite element method (FEM) is used. That is, the basic principles of structural mechanics such as force and moment equilibrium, continuity and material law are utilized in order to determine the equation of motion of the structure, which can then be solved either in the frequency domain or using time integration in the time domain, depending on the general formulation of the problem and the inherent non-linearities. In particular, slender marine structures like pipelines and risers are usually approximated as beam

elements. This results in rather simple structural models with a small number of participating degrees-of-freedom and hence the required computational time and cost is relatively low, taking also into account the increased computational power of today's computers. Contrary to this, establishing a reliable hydrodynamic force model can be quite challenging and for this reason several different VIV prediction tools have been proposed in the last several years. According to DNV's VIV Best Practice, the existing VIV prediction models can be classified in two main categories, the Computational Fluid Dynamics (CFD) and the empirical models which can be further distinguished in frequency and time domain models, as illustrated in Figure 2.13 [3].

2.3.1 Computational Fluid Dynamics (CFD)

Two of the most fundamental equations used to describe fluid flows and the resulting fluid induced motions and loads on structures, are the conservation equations for fluid mass and momentum. The momentum equation that describes the motion of fluids is the Navier–Stokes equation. By combining those two conservation laws, it is possible to estimate the entire flow field around a structure. Having calculated the flow velocity field surrounding the body, the fluid induced pressures and shear stresses can be computed and thus, integrating them along the wetted surface of the examined body, the fluid induced forces on the structure can be calculated. These are the foundations and the basic principles on which the first VIV prediction method, the Computational Fluid Dynamics, is based on.

In fact CFD is not just a numerical model but rather an entire scientific discipline, which focuses on the computation of the entire flow field in a region of the fluid based on the two aforementioned conservation laws. In order to do so various numerical methods have been proposed over the years, the main difference between which lies mainly on the way the examined fluid domain is discretized and on the turbulence model applied. According to Thorsen, the most widely used discretization methods are the finite difference method, the finite volume method and the finite element method, while the turbulence in the flow can be accounted for using a suitable turbulence model such as the Reynolds-Averaged Navier-Stokes (RANS) model and the Large Eddy Simulation (LES) model. Of course, the Navier-Stokes equations can be dealt with directly, without using one of the aforementioned turbulence models, using a procedure called Direct Numerical Simulation (DNS), but in order for this procedure to give reliable results, an extremely small time step and an immensely fine mesh are necessary [25]. Although CFD methods and especially 3D DNS simulations provide highly accurate and realistic results both with respect to the flow itself and to the corresponding structural response, CFD is regarded as computationally too demanding and hence it is not widely used in the industry for practical applications, at least for the time being. For this reason it will not be further analysed in the following.

2.3.2 Semi-empirical frequency domain models

Numerous semi-empirical frequency domain prediction tools exist, among which VIVA [16], SHEAR7 [17] and VIVANA [18] are considered state of the art and are the most widely used VIV prediction models in the industry today. As already mentioned, despite their many differences, they are all characterised by the fact that they operate in the frequency domain and that their operation relies heavily on the use of empirical hydrodynamic coefficients mainly with regard to the added mass, damping and excitation forces. More specifically, such frequency domain VIV prediction models typically consist of three main parts. The first one deals with the mathematical structural model which, as already explained in the beginning of this section, is usually based on a finite element model. The second one contains the hydrodynamic force

model, which focuses on the calculation of the fluid induced forces and solves the resulting dynamic equilibrium equation in the frequency domain using the frequency response method. The third part contains the database with the aforementioned empirical hydrodynamic coefficients, which are typically obtained by full- and model-scale experiments as described in detail in sections 2.2.2 and 2.2.3. The selection of the most appropriate coefficients is a quite challenging part of this process, since they typically depend on the frequency and amplitude of the oscillation.

The use of semi-empirical frequency domain VIV prediction tools is extremely widespread mainly due to the fact that solving the dynamic equilibrium equation in the frequency domain results in lower required computational time and power compared to time domain models and CFD methods. However, the fact that the dynamic equilibrium equation is solved in the frequency domain is at the same time a major downside of the frequency domain models, since only stationary flow conditions and linearized structures can be treated by this approach. Of course, this is acceptable for simple cases such as for simple beams in uniform incident flows. However, the dynamic analysis of risers and pipelines is a highly non-linear problem. Non-uniform flows (e.g. sheared current), the interaction of multiple dynamic loads (e.g. combination of currents and waves), time-varying boundary conditions (e.g. soil-pipe interaction), tension variations and large displacements are a few examples of real operational conditions with regard to risers and pipelines, which introduce significant non-linearities to the considered problem. These non-linear effects have to be accounted for in a VIV analysis in order to accurately capture the dynamic response of the actual structure and get reliable results. This is the reason why the main focus of the present work is related to time domain models. Nevertheless, because the study presented in chapter 4, which served as the basis for the elaboration and validation of the present thesis was conducted by means of the VIVANA VIV prediction tool, it would be advantageous for the better understanding of the aforementioned Case Study to give a brief description of the VIVANA analysis procedure here without getting into many details. VIVANA is a frequency domain VIV prediction model developed by SINTEF Ocean (former MARINTEK) for analyses of the VIV response of slender marine structures. The structure itself is approximated by a FEM model using mainly beam and bar elements. The most recent VIVANA versions are capable of analysing both pure CF and IL vibrations and the combined CF and IL VIV case. The main steps of the VIVANA analysis procedure are [18]:

- Static analysis by means of the RIFLEX software (which is coupled to VIVANA through the SIMA software) in order to find the static equilibrium position of the structure.
- Eigenvalue analysis in still water conditions to find the structure's natural frequencies and the respective vibration modes.
- Identification of possible excitation frequencies taking into account the dependence of the added mass on the structure's vibration. Hence an iteration procedure is necessary in order to match the added mass with the oscillation frequencies under VIV conditions. However, in the combined IL and CF case, it is assumed that the IL frequency is two times the CF frequency and a second iteration procedure is not needed.
- Determination of the excitation (lock-in) zones as a range of non-dimensional frequencies.
- Calculation of the response using the frequency response method.
- Post processing. In this step numerous operations can be performed based on what results the researcher is interested in (e.g. fatigue analysis, generation of plots).

2.3.3 Semi-empirical time domain models

As previously noted, the main drawback of the frequency domain models is that they can only deal with linearized structures exposed to stationary incident flows. In order to include the inherent non-linearities that characterize a realistic VIV case regarding a real non-linear marine structure, a time domain analysis is needed. Within the last decades, several time domain prediction tools have been proposed, which can account for the aforementioned non-linearities provided that they are coupled to a non-linear structural model. One such semi-empirical TD model is based on the concept of a wake oscillator, which was introduced by Zarantonello and Brikhoff in 1957 [38]. According to this concept, the vortex shedding phenomenon can be described by a single variable provided that it satisfies the van der Pol equation. Other worth mentioning TD VIV prediction models have been proposed by Finn in 1999 [39] and Maincon and Larsen in 2011 [40]. Moreover, as already mentioned in chapter 1, one very promising semi-empirical time domain VIV model (TD VIV model) was developed at NTNU by the PhD students Mats Jørgen Thorsen [22, 23, 24, 25] and Jan Vidar Ulveseter [26] and is based on a synchronization load model for the vortex-induced forces. This is the model that is going to be used in the present thesis and therefore it is the one that will be analysed in the following.

Pure CF and IL TD VIV models

As already mentioned, the basis of the TD VIV model is the existence of a synchronization load model to describe the vortex-induced forces. The TD VIV model utilizes strip theory in order to calculate the hydrodynamic forces exerted on a cross-section of the considered cylinder based on the velocity and acceleration of that particular cross-section. Several different formulations and modifications of the TD VIV model have been proposed over the years mainly by Thorsen and Ulveseter [22, 23, 24, 25, 27, 41, 42, 26, 28]. In order to demonstrate the basic principles of this synchronization load model, as a first step the initial model proposed by Thorsen with regard to pure CF VIV will be briefly introduced using the coordinate system presented in Figure 2.3. In this figure, the in-line direction is assumed to coincide with the x-axis and the cross-flow direction with the y-axis. The displacements, velocities and accelerations of the cross-section in the IL and CF directions will be denoted as $x, \dot{x}, \ddot{x}$ and $y, \dot{y}, \ddot{y}$ respectively. According to this initially proposed TD VIV model, the hydrodynamic force in the CF direction is given by:

$$F_y = F_{\text{exc}} + F_{\text{damping}} + F_{\text{add}} = \frac{1}{2}\rho D U^2 C_{v,y} \cos\phi_{exc,y} - \frac{1}{2}\rho D C_{d,y}|\dot{y}|\dot{y} - \rho\frac{\pi D^2}{4} C_A \ddot{y} \quad (2.20)$$

The first term of the right hand side in Eq. 2.20 corresponds to the excitation force, the second term to the damping force and the third term to the added mass force. As is the case throughout this work, ρ is the fluid density, D is the diameter of the cylinder and U is the incident flow velocity. Moreover, $\dot{y}, \ddot{y}$ are the velocity and acceleration in the CF direction, $C_{d,y}$ is the damping coefficient in the CF direction, C_A is the added mass coefficient and $C_{v,y}$ is the cross-flow vortex-induced excitation force coefficient, which is typically dependent on the ratio of the cross-flow response amplitude to the cylinder's diameter. Finally, $\phi_{exc,y}$ is the instantaneous phase angle of the vortex-induced excitation force. The three most significant parameters in Eq. 2.20 are $C_{v,y}, \phi_{exc,y}$ and $C_{d,y}$. As far as the damping coefficient is concerned, its estimation is based on the utilization of available experimental data. More specifically, the damping contribution measured in the experiment is used in order to determine an equivalent damping model by demanding that both the experimental and the equivalent damping result in the exact same energy dissipation over one oscillation period. With regard to the excitation force, establishing an accurate way to describe how it is connected/synchronized with the respective response of the cylinder or equivalently how its phase angle $\phi_{exc,y}$ changes relative to the phase of the response

is the foundation of the TD VIV model. However, since this is only the initial approach to establish such a model, it was preferred to demonstrate this connection/synchronization in detail with regard to the most up-to-date hydrodynamic force model.

The most up-to-date hydrodynamic force model is again based in strip theory and is again formulated in terms of the incoming flow field, the cylinder's response (velocity and acceleration) vectors and the aforementioned hydrodynamic coefficients. To demonstrate the fundamental principles of this TD VIV model Figure 2.14 will be used, where the most relevant parameters, coordinate systems and vector directions are illustrated. For each strip of the examined cylinder, the incident flow vector $\mathbf{u}$ is decomposed to one tangential, $\mathbf{u_t}$, and one normal, $\mathbf{u_n}$, component relative to this particular cross-section so as to neglect the tangential component in the following. In this way the examined fluid-body interaction problem can be simplified in the respective 2D problem in the cylinder plane $\mathbf{j_1 j_2}$, which describes the interaction between the hydrodynamic forces induced by the normal flow component $\mathbf{u_n}$ and the resulting response of the cylinder $\mathbf{x_n}$. At this point it should be highlighted that the drag force and the vortex shedding forces are expressed in a local coordinate system defined in such a way that the horizontal axis is always parallel to the relative flow velocity vector, $\mathbf{v_n} = \mathbf{u_n} - \dot{\mathbf{x}}_\mathbf{n}$, as illustrated in Figure 2.14. On this basis it becomes clear that the direction of these forces will constantly change following the changes in the direction of the relative flow vector. However, for the sake of simplicity, local CF and IL directions will be systematically referred to as simply CF and IL in the following.

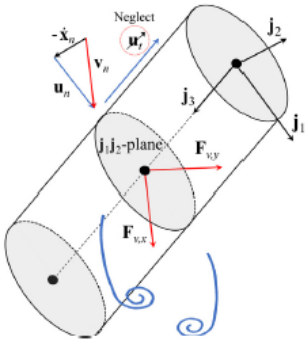

Figure 2.14: A cylinder strip with the relevant vectors and local coordinate system.

The main difference between this updated hydrodynamic force model and the previous ones is the fact that the vortex-induced forces are combined with Morison's equation in order to get the total fluid-induced forces. More specifically, in this model and contrary to what was the case previously, the drag term of Morison's equation is utilized in order to directly account for the damping force of Eq. 2.20 and hence the formulation of a separate damping model is not required. In this way, the mean-drag force exerted in the IL direction is also accounted for in this case. Based on all the above mentioned, the hydrodynamic loads acting on a cylinder strip (per unit length) with regard to a pure CF VIV problem can be expressed as such:

$$\mathbf{F} = \underbrace{\underbrace{(C_A+1)\,\rho\frac{\pi D^2}{4}\dot{\mathbf{u}}_\mathbf{n}}_{\text{Froude-Kriloff force}} - \underbrace{C_A\rho\frac{\pi D^2}{4}\ddot{\mathbf{x}}_\mathbf{n}}_{\text{Added mass force}} + \underbrace{\frac{1}{2}\rho D C_D\,|\mathbf{v_n}|\,\mathbf{v_n}}_{\text{Drag force}}}_{\text{Morison load terms}} + \underbrace{\frac{1}{2}\rho D C_{v,y}\,|\mathbf{v_n}|\,(\mathbf{j_3}\times\mathbf{v_n})\cos\phi_{exc,y}}_{\text{Cross-flow vortex shedding force }(\mathbf{F}_{v,y})} \tag{2.21}$$

where the first three terms correspond to the terms of the Morison's equation, the first of which is the Froude-Kriloff force, the second is the added mass force and the third the drag force. Moreover, C_A is the added mass coefficient, C_D is the drag coefficient and as usual ρ is the fluid density and D the cylinder's diameter. The remaining term in Eq. 2.21 corresponds to the cross-flow vortex-induced excitation force, where $C_{v,y}$ is the cross-flow vortex-induced excitation force coefficient and $\phi_{exc,y}$ is the instantaneous phase angle of the vortex-induced excitation force. At this point it is worth noting that so far only the cross-flow VIV case was treated. However, the exact same hydrodynamic force model can be used with regard to the pure IL VIV problem too. In this case the only change in Eq. 2.21 is in the vortex-induced excitation force term where the cross-flow vortex-induced excitation force coefficient $C_{v,y}$ and the instantaneous phase angle of the vortex-induced excitation force $\phi_{exc,y}$ have to be substituted by the respective IL parameters $C_{v,x}$ and $\phi_{exc,x}$ and the term $(\mathbf{j_3} \times \mathbf{v_n})$ has to be simplified to $\mathbf{v_n}$ as shown in Eq. 2.22.

$$\mathbf{F} = \underbrace{\underbrace{(C_A+1)\,\rho\frac{\pi D^2}{4}\dot{\mathbf{u}}_\mathbf{n}}_{\text{Froude-Kriloff force}} - \underbrace{C_A\rho\frac{\pi D^2}{4}\ddot{\mathbf{x}}_\mathbf{n}}_{\text{Added mass force}} + \underbrace{\frac{1}{2}\rho D C_D\,|\mathbf{v_n}|\,\mathbf{v_n}}_{\text{Drag force}}}_{\text{Morison load terms}} + \underbrace{\frac{1}{2}\rho D C_{v,x}\,|\mathbf{v_n}|\,\mathbf{v_n}\cos\phi_{exc,x}}_{\text{In-line vortex shedding force }(\mathbf{F}_{v,x})} \tag{2.22}$$

Combined CF and IL TD VIV models

So far the above presented TD VIV models account only for cross-flow or in-line vibrations separately. However, in reality when a flexible pipe is exposed to an incoming flow field, it is more common for these two types of oscillations to occur simultaneously than individually and therefore establishing a time domain VIV prediction model capable of accounting for those two combined phenomena is both very interesting and necessary. Such a combined CF and IL VIV model was first introduced by Ulveseter [28]. It is also worth noting that the most recent version of this model is also the one used for the purposes of the present work. The hydrodynamic load model or equivalently the expression for the hydrodynamic forces per unit length exerted on a strip of the cylinder can be calculated by simply combining the above presented pure CF model (Eq. 2.21) and pure IL model (Eq. 2.22) in order for the new model to include the contribution of the vortex-induced excitation forces in both directions. The hydrodynamic load model can then be expressed as such:

$$\mathbf{F} = \underbrace{\underbrace{(C_A+1)\,\rho\frac{\pi D^2}{4}\dot{\mathbf{u}}_\mathbf{n}}_{\text{Froude-Kriloff force}} - \underbrace{C_A\rho\frac{\pi D^2}{4}\ddot{\mathbf{x}}_\mathbf{n}}_{\text{Added mass force}} + \underbrace{\frac{1}{2}\rho D C_D\,|\mathbf{v_n}|\,\mathbf{v_n}}_{\text{Drag force}}}_{\text{Morison load terms}} + \underbrace{\underbrace{\frac{1}{2}\rho D C_{v,y}\,|\mathbf{v_n}|\,(\mathbf{j_3}\times\mathbf{v_n})\cos\phi_{exc,y}}_{\text{Cross-flow vortex shedding force }(\mathbf{F}_{v,y})} + \underbrace{\frac{1}{2}\rho D C_{v,x}\,|\mathbf{v_n}|\,\mathbf{v_n}\cos\phi_{exc,x}}_{\text{In-line vortex shedding force }(\mathbf{F}_{v,x})}}_{\text{Vortex-induced excitation terms}} \tag{2.23}$$

All the terms and parameters presented in Eq. 2.23 are the same as the ones used in Eq. 2.21 and Eq. 2.22 and there is no need of defining them again here. From Eq. 2.23 it becomes apparent that $C_{v,x}$ and $C_{v,y}$ are the two parameters that determine the magnitude of the vortex-induced excitation forces. However, it should be kept in mind that those forces are not constant but rather oscillatory and their oscillation is governed by the time-varying instantaneous phase an-

gles $\phi_{exc,x}$ and $\phi_{exc,y}$. These two angles introduce the aforementioned lock-in/synchronization phenomenon to the examined hydrodynamic force model. The basic idea behind this model is that in order to accurately simulate the lock-in phenomenon, a synchronization model has to be applied both in the IL and in the CF direction so as to ensure that the instantaneous frequency of the vortex shedding force can increase or decrease so that its phase can match the instantaneous phase of the cylinder's velocity [43]. For this reason, the instantaneous phase angles are the two basic parameters that will be used here in order to explain the synchronization model.

To begin with, these instantaneous phase angles vary continuously, but not in a constant rate, ultimately resulting in a corresponding varying excitation force frequency. Let us consider first the cross-flow instantaneous phase angle $\phi_{exc,y}$. The rate of change of this angle is typically referred to as the instantaneous frequency $\dot{\phi}_{exc,y} = \frac{d(\phi_{exc,y})}{dt}$ and is a function of the instantaneous phase difference θ_y between the phase of the relative cross-flow velocity of the cylinder $\phi_{\dot{\mathbf{y}}_{rel}}$ and the phase of the cross-flow vortex-induced excitation force $\phi_{exc,y}$, i.e. $\theta_y = \phi_{\dot{\mathbf{y}}_{rel}} - \phi_{exc,y}$. The relative cross-flow velocity of the cylinder is given by $\dot{\mathbf{y}}_{rel} = \dot{\mathbf{x}} \cdot \frac{\mathbf{j}_3 \times \mathbf{v}_n}{|\mathbf{v}_n|}$. The instantaneous phase of the relative cross-flow velocity, $\phi_{\dot{\mathbf{y}}_{rel}}$, must be numerically approximated at every time step of a time domain simulation [41]. The phase difference θ_y is the fundamental parameter that determines the relation between the vortex induced forces and the cylinder's response (i.e. velocity). In other words θ_y determines if the force is "ahead" of the velocity ($\theta_y < 0$) or is "trailing" the velocity ($\theta_y > 0$). Then the vortex-induced force has the ability to vary its frequency either reducing or increasing it so as to synchronize with the cylinder's velocity. However, this is possible only in a certain limited range of non-dimensional excitation frequencies $\hat{f}_{exc,y}$, the so-called "synchronization range". Within this range a considerable amount of energy is transferred to the cylinder by the fluid while the respective energy transfer outside of this range is almost negligible. The instantaneous frequency and the synchronization range for the above presented cross-flow case are given in Eq. 2.24 and Eq. 2.25 respectively [41].

$$\dot{\phi}_{exc,y} = \frac{d\phi_{\text{exc},y}}{dt} = 2\pi f_{\text{exc},y} = \frac{2\pi \left|\mathbf{v}_n\right|}{D} \hat{f}_{\text{exc},y} \tag{2.24}$$

$$\hat{f}_{\text{exc},y} = \begin{cases} \hat{f}_{0,y} + \left(\hat{f}_{\text{max},y} - \hat{f}_{0,y}\right) \sin\theta_y, & \theta_y \geq 0 \\ \hat{f}_{0,y} + \left(\hat{f}_{0,y} - \hat{f}_{\text{min},y}\right) \sin\theta_y, & \theta_y < 0 \end{cases} \tag{2.25}$$

where $\hat{f}_{\text{min},y}$ and $\hat{f}_{\text{max},y}$ specify the cross-flow synchronization range and $\hat{f}_{0,y}$ specifies the non-dimensional frequency of maximum energy transfer. More specifically, this means that for the CF VIV case, lock-in occurs in the non-dimensional frequency range $\hat{f}_{\text{min},y} \leq \hat{f}_{exc,y} \leq \hat{f}_{\text{max},y}$ while at $\hat{f}_{0,y}$ the CF vortex-induced excitation force is exactly in phase with the cylinder's CF velocity, i.e. $\theta_y = \phi_{\dot{\mathbf{y}}_{rel}} - \phi_{exc,y} = 0$.

With regard to the IL VIV case, two different types of in-line response can be distinguished. The first one corresponds to the pure in-line response and is associated with low current velocities. The synchronization model used for the simulation of the pure IL VIV phenomenon is exactly the same as the one presented above with regard to the CF VIV and is given below by Eq. 2.27 and Eq. 2.28 as part of the updated synchronization model used for the simulation of the combined CF and IL VIV phenomenon. The second type of IL response corresponds to the cross-flow induced in-line response observed at higher current velocities, where both CF and IL VIV are present. The latter type of response is mainly of interest and two different synchronization models have been proposed over the years. The first one was introduced by Ulveseter ([28])

and the basic idea behind it lies on the fact that according to the available experimental data, the frequency of the IL VIV is in most cases approximately two times the respective frequency of the CF VIV. On this basis, the instantaneous IL vortex-induced excitation force frequency $\dot{\phi}_{exc,x}$ can be calculated as a function of the respective CF frequency $\dot{\phi}_{exc,y}$ and the instantaneous phase difference θ_x between the phase of the relative in-line velocity of the cylinder $\phi_{\dot{\mathbf{x}}_{rel}}$ and the phase of the in-line vortex-induced excitation force $\phi_{exc,x}$, i.e. $\theta_x = \phi_{\dot{\mathbf{x}}_{rel}} - \phi_{exc,x}$ as illustrated in Eq. 2.26.

$$\dot{\phi}_{exc,x} = 2\dot{\phi}_{exc,y}\left(1 + \alpha \sin\left(\phi_{\dot{x}_{rel}} - \phi_{exc,x}\right)\right) \tag{2.26}$$

where α is a parameter that determines the extent of the dependence of the IL force frequency on the respective CF frequency. Typically α takes values very close to zero and in case $\alpha = 0$ then $\dot{\phi}_{exc,x} = 2 \cdot \dot{\phi}_{exc,y}$. Similarly to the CF case, the relative in-line velocity of the cylinder is given by $\dot{\mathbf{x}}_{rel} = \dot{\mathbf{x}} \cdot \frac{\mathbf{v}_n}{|\mathbf{v}_n|}$. The instantaneous phase of the relative in-line velocity, $\phi_{\dot{\mathbf{x}}_{rel}}$, must be numerically approximated at every time step of a time domain simulation [41].

The second synchronization model for the combined CF and IL VIV case was introduced by Kim ([43]), because, when he applied the previous model to simulate the Hanøytangen test, he obtained inaccurate results for the in-line response. This updated model is in fact the one used for the purposes of the present thesis and is based on the fact that the combined CF and IL VIV is the consequence of two resonant phenomena that occur in the two orthogonal directions simultaneously, but the respective resonances are independent of each other in terms of the natural frequencies in the two directions. On this basis, the synchronization model presented above was chosen again for the simulation of the CF VIV (i.e. Eq. 2.24 and Eq. 2.25), while a "new" synchronization model was formulated with regard to the cross-flow induced in-line vibrations as illustrated in Eq. 2.27 and Eq. 2.28.

$$\dot{\phi}_{exc,x} = \frac{d\phi_{\text{exc},x}}{dt} = 2\pi f_{\text{exc},x} = \frac{2\pi\,|\mathbf{v}_n|}{D}\hat{f}_{\text{exc},x} \tag{2.27}$$

$$\hat{f}_{\text{exc},x} = \begin{cases} \hat{f}_{0,x} + \left(\hat{f}_{\text{max},x} - \hat{f}_{0,x}\right)\sin\theta_x, & \theta_x \geq 0 \\ \hat{f}_{0,x} + \left(\hat{f}_{0,x} - \hat{f}_{\text{min},x}\right)\sin\theta_x, & \theta_x < 0 \end{cases} \tag{2.28}$$

where $\hat{f}_{\text{min},x}$ and $\hat{f}_{\text{max},x}$ specify the in-line synchronization range and $\hat{f}_{0,x}$ specifies the non-dimensional frequency of maximum energy transfer. More specifically, this means that for the IL VIV case lock-in occurs in the non-dimensional frequency range $\hat{f}_{\text{min},x} \leq \hat{f}_{exc,x} \leq \hat{f}_{\text{max},x}$ while at $\hat{f}_{0,x}$ the IL vortex-induced excitation force is exactly in phase with the cylinder's IL velocity, i.e. $\theta_x = \phi_{\dot{x}_{rel}} - \phi_{exc,x} = 0$.

Taking a closer look at Eq. 2.27 and Eq. 2.28, it becomes apparent that this in-line synchronization model is exactly the same as the one previously presented with respect to the CF VIV case and in fact is the synchronization model proposed by Ulveseter ([42]) for the pure IL VIV problem. The basic concept is that the same synchronization model can be used to predict both the pure IL induced force component and the IL force component related to the simultaneous presence of CF VIV. In that way, it will hopefully be possible simulate both pure in-line and cross-flow induced in-line vibrations using the same synchronization model by simply choosing a sufficiently wide synchronization range.

3 Pipe-Soil Interaction

It is a well known fact that submarine pipelines are one of the most widely used means of transporting oil and gas from offshore fields to oil storage platforms or directly to terminals in the main land. These offshore oil and gas fields are not always surrounded by a smooth and even seafloor and therefore laying the pipelines on uneven seabeds often cannot be avoided. The unevenness of the seabed can lead to the formation of several free spans along the pipeline. As already explained in detail previously, when such free spans are exposed to incident fluid flows, the vortex shedding phenomenon can take place leading in oscillating excitation forces being exerted on the pipeline. Then, depending on the properties of the soil, the flow conditions and the structural characteristics of the pipe itself, the frequency of this excitation force can get close to one of the pipe's natural frequencies and thus the "lock-in" phenomenon will take place leading in high amplitude resonant Vortex-Induced Vibrations. Typically, such resonant VIV phenomena result in high stress concentration at the shoulders of the free span, where the pipe is in contact with the seafloor. This high stress concentration at the shoulders combined with the high frequencies characterising the resonant VIV phenomena can lead to a non-negligible fatigue damage accumulation near the shoulders. Apart from the development of free spans, according to DNV's Recommended Practice, pipe-soil interaction is also crucial in several other typical pipeline scenarios such as lateral buckling, end expansion, pipeline walking, route-curve pullout, flow line anchoring, on-bottom stability and trawl impact to name but a few. It becomes therefore easily understood that the pipe-soil interaction is a key element in the assessment of exposed submarine pipelines [6].

As discussed previously, a reliable VIV prediction tool for pipelines has to be able to account for all the inherent non-linearities that characterise a realistic VIV scenario regarding a real slender marine structure like a free spanning pipeline. An important source of such non-linearities is the pipe-soil interaction. For example, if springs are used to model the seafloor in a submarine pipeline analysis, as is presently the common practice, the spring properties have to be non-linear so as on the one hand to restrict the pipe from penetrating the seafloor and on the other hand to account for the "lift off" phenomenon allowing the detachment and reattachment of the pipe to the seafloor during its oscillatory motion. The implementation of such a non-linear seafloor model will also result in non-linear/time-varying boundary conditions, since the position of the touch down point and the contact region between the pipe and the soil in general will be strongly dependent mainly on the actual time-varying response of the pipe and also on several other parameters, such as the fluctuation of the applied tension and the modification of the seabed's profile due to soil erosion and the interaction with the pipe itself. Moreover, including non-linear soil damping in the seafloor model can also have a significant effect on the response of the pipeline [6].

From all the aforementioned, it becomes clear that pipe-soil interaction is a really complicated subject and unfortunately, there are still many uncertainties with regard to the VIV response of a pipeline in close proximity to the seafloor for two main reasons. First of all, the basis of most existing VIV prediction tools is the use of empirical hydrodynamic coefficients obtained from model tests of rigid and flexible cylinders in infinite fluid. In such model tests the effect that the presence of a solid boundary close to the cylinder will inevitably have on the prevailing hydrodynamic conditions and the subsequent dynamic response of the cylinder are therefore neglected. Secondly, another even more important source of uncertainty is the fact that in order to accurately evaluate the pipe-soil interaction, a detailed knowledge of the soil properties along the pipeline route is essential and such information are in most cases neither available in advance nor easy

to obtain during the design stage of a project. According to DNV's Recommended Practice [6], "Soil variability is inevitable over large distances and is especially the case in the surficial soils. The variation in soil parameters seen in a pipeline development project is thus larger compared to traditional foundation design". For this reason, it is recommended in [6] that in-situ investigations should be planned for each specific pipeline scenario and these investigations should be tailor-made for the conditions encountered during the lifetime of the pipeline. Another important source of uncertainties regarding the soil properties is the fact that during the installation of a submarine pipeline, the soil in the vicinity of the pipe will inevitably be disturbed. Thus the seabed configuration and the soil stiffness and strength properties will be altered in this affected region. Of course, those installation-related effects are difficult to be predicted in the design stage. All in all, it is concluded in [6] that the level of uncertainty and the inherent complexity of the pipe-soil interaction is so high that simplifications and assumptions are required in order to develop reliable and efficient engineering models. In DNV's Recommended Practice the pipe-soil interaction responses are distinguished in the following five categories:

- Vertical Pipe-Soil Interaction - Embedment
- Axial Pipe-Soil Interaction - Axial Friction
- Lateral Pipe-Soil Interaction - Lateral Resistance
- Soil Stiffness
- Soil Damping

Table 3.1: Pipe-soil responses for exposed pipelines [6]

Response	**Description**
Embedment	The initial embedment is controlled by the soil conditions and the loads during and following installation. It has a significant influence on the subsequent axial and lateral response.
Axial friction	Axial breakout response: An initial peak in resistance that is mainly relevant to the first load response. Axial residual resistance: The large displacement response as the pipe expands or contracts. Cyclic axial response: The long term cyclic response under repeated expansion and contraction.
Lateral resistance	Lateral breakout response: An initial peak in resistance as the pipe first displaces from the as-installed position. Lateral residual resistance: The large displacement resistance. Cyclic lateral response: The long term cyclic response, when the pipe becomes embedded in a trench within a buckled pipe section and soil berms grow causing a rise in lateral resistance.
Soil stiffness	Vertical stiffness: Static and dynamic stiffness. Lateral stiffness: Static and dynamic stiffness.
Soil damping	Soil damping may be introduced in dynamic analyses.

A brief description of those five main categories of pipe-soil responses is given in Table 4-1 in [6], Table 3.1. Only the last two of those categories will be presented in more detail in the following because modelling the first three types of pipe-soil responses is extremely complicated and requires detailed knowledge of the soil properties and the pipeline's installation procedure, which is beyond the context of the present thesis. For this reason some simplified assumptions were made for the implementation of the Non-Linear seafloor model in the Realistic free span scenario in Chapter 7. To be more precise, as far as the Embedment is concerned, it was assumed that there is no initial penetration of the pipe in the seafloor and for simplicity it was also assumed that the contact between the pipe and the seabed takes place in only one point in each cross-section of the pipeline. This contact point was specified to be the middle of each cross-section

that is in contact with the seafloor. As for the two remaining pipe-soil interaction categories, the Axial Friction was entirely neglected in the following analysis, while the Lateral Resistance was for simplicity modelled using an unrealistically high friction coefficient $\mu = 500$ in order to prevent any slip occurrence between the seafloor and the pipe and thus to make sure that each time there is contact between the pipe and the seabed, the springs that are used to model the seafloor reaction in the lateral direction are activated representing the lateral dynamic soil stiffness. The Linear and Non-Linear soil models and their implementation in RIFLEX will be presented in more detail in sections 7.2.3 and 7.2.4 respectively.

3.1 Soil Stiffness

It is obvious that the stiffness of the seabed is strongly dependent on the material of the soil considered. According to DNV's Recommended Practice the soil material can be classified into two main categories, the Cohesive Soil or Clay and the Cohesionless Soil or Sand. The different soil materials are characterised by different properties, the most important of which for the evaluation of the soil stiffness are the shear strength, the soil submerged unit weight, the Poisson's ratio and the plasticity index among others. In case the non-linear response of the seabed cannot be taken into account explicitly into the evaluation of the soil stiffness it is recommended in [6] that elastic springs are used to model the seabed properties. These springs have to be able to account for the inherent non-linearity of the seafloor's response. Using this approach, the soil stiffness can be modelled as a secant stiffness representing the expected load level in the considered pipeline scenario. Moreover, for the correct evaluation of the soil stiffness it is recommended to distinguish between the Static Soil Stiffness, which is mainly associated with a static loading condition, and the Dynamic Soil Stiffness which is usually related to a cyclic unloading/re-loading condition [6].

3.1.1 Static Soil Stiffness

The static vertical stiffness $K_{V,s}$ is given by Eq. 3.1

$$K_{V,s} = \frac{Q_v}{z} \tag{3.1}$$

where Q_v is the static vertical soil reaction force per unit length of pipe and z is the vertical penetration of the pipe required to mobilize this reaction.

As already mentioned the vertical static soil stiffness is a secant stiffness representative of a static load condition like during the development of free spans due to soil erosion or during the installation of the pipeline as can be seen in Figure 3.1, where examples of equivalent secant stiffness are presented for different loading conditions.

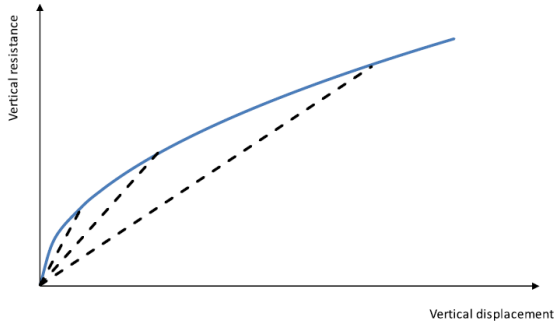

Figure 3.1: Examples of vertical static secant stiffness for different load levels [6].

As far as the static lateral stiffness, $K_{L,s}$, is concerned, it is recommended to be estimated using the models proposed in [6] for the estimation and establishment of fairly accurate lateral resistance curves. This procedure, as explained previously, is beyond the context of the present thesis and therefore it was decided to neglect the static lateral soil stiffness and use only the lateral dynamic stiffness for the implementation of the seafloor models in chapter 7.

3.1.2 Dynamic Soil Stiffness

The Vertical Dynamic Soil Stiffness, $K_{V,d}$, and the Lateral Dynamic Soil Stiffness, $K_{L,d}$ are given by Eq. 3.2 and Eq. 3.3 respectively.

$$K_{V,d} = \frac{0.88 \cdot G}{1 - \nu} \tag{3.2}$$

$$K_{L,d} = 0.76 \cdot G \cdot (1 + \nu) \tag{3.3}$$

where G is the soil's Shear Modulus and ν is the soil's Poisson's ratio. The above expressions "are based on elastic half space theory for a rectangular foundation under assumption of a pipe length that equals 10 times the contact width between pipe and soil", [6].

3.2 Soil Damping

It is commonly accepted that in general the soil damping depends strongly on the dynamic loads that the soil is subjected to. When a pipeline with bottom contact is considered, the damping contribution from the pipe-soil interaction can according to [6] be spit in two governing damping mechanisms:

- Radiation damping which is a result of propagating elastic waves.
- Material damping which is related to hysteresis effects that become evident in the vicinity of the contact region between the pipe and the seabed.

The radiation damping is of paramount importance with regard to high frequency oscillations since it is strongly dependent on the oscillation frequency. Therefore, the governing soil damping mechanism in free spanning pipeline cases is the material damping which depends mainly on the structural characteristics of the pipe and the material properties of the seabed. As already mentioned there is an increased level of uncertainty characterising the material properties of the seafloor, as for example the sea bottom can consist of clay, sand, rocks or even a combination of them resulting in a wide range of different possible seafloor properties, which in fact can also vary significantly along the route of the pipeline. Therefore, these uncertainties have to be taken into account when determining the damping contribution due to pipe-soil interaction. In [6] the use of modal analysis for the estimation of the level of soil damping is recommended. The case-specific modal soil damping ratio, ζ_{soil} is given by Eq. 3.4.

$$\zeta_{soil} = \frac{1}{4 \cdot \pi \cdot \mathrm{f_0}} \cdot \left(\frac{\int_\mathrm{L} \mathrm{c(s)} \phi^2(\mathrm{s}) \mathrm{ds}}{\int_\mathrm{L} \mathrm{m(s)} \phi^2(\mathrm{s}) \mathrm{ds}} \right) \tag{3.4}$$

where $c(s)$ is the soil damping per unit length, which depends on the energy balance between the maximum elastic energy stored by the soil during an oscillation cycle and the energy dissipated by a viscous damper in the same cycle [6].

In case of a FEM analysis where the pipe-soil interaction is modelled using discrete soil supports, the soil damping has to be modelled with discrete dampers and the damping coefficient, c_i, of

support no. i may be estimated using Eq. 3.5.

$$c_i = 2 \cdot \zeta_{soil,i} \cdot \frac{k_i}{\omega} \tag{3.5}$$

where k_i is the linearized spring stiffness at support no. i, ω is the angular frequency of the examined vibration mode and $\zeta_{soil,i}$ is the damping ratio corresponding to support no. i, which can be calculated by Eq. 3.6.

$$\zeta_{soil,i} = \frac{1}{4 \cdot \pi} \cdot \frac{E_{Dissipated}}{E_{Elastic}} \tag{3.6}$$

where $E_{Dissipated}$ is the energy dissipation at support no. i and $E_{Elastic}$ is the equivalent elastic energy at support no. i. This is clearly illustrated in Figure 3.2.

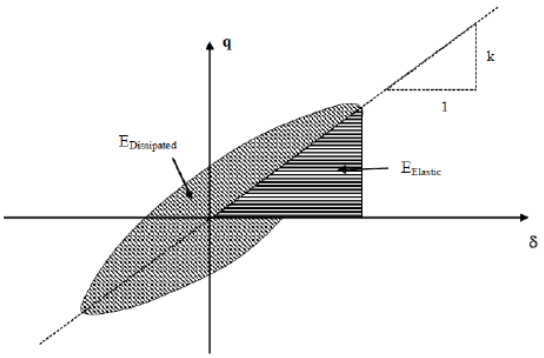

Figure 3.2: Energy dissipation at soil support, shown in the load-displacement space [6].

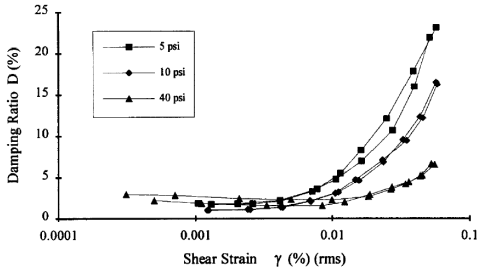

(a) Damping ratio $D(\%)$ vs. shear strain $\gamma(\%)$ (rms) at different confining pressures [44].

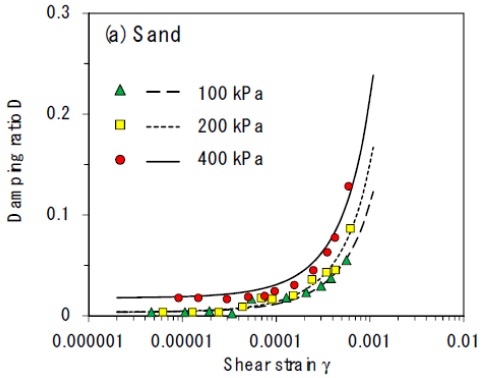

(b) Damping ratio D vs. shear strain γ at different confining pressures [45].

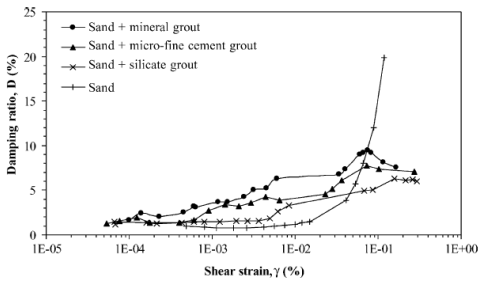

(c) Damping ratio $D(\%)$ vs. shear strain $\gamma(\%)$ [46].

Figure 3.3: Typical values of soil damping ratio for sand.

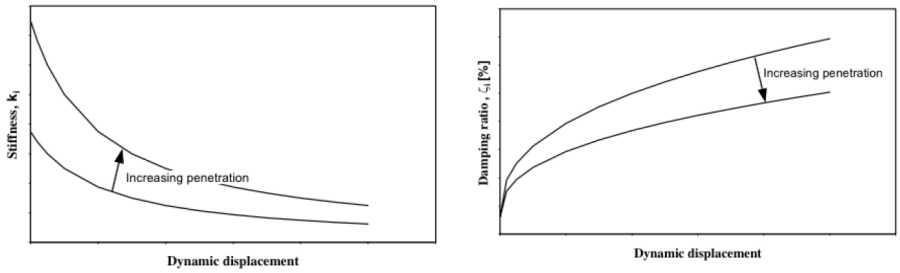

Figure 3.4: Non-linear characteristics of soil stiffness and damping [6].

Typical values of the level of soil damping for sands as a function of the applied shear strain found in literature are presented in Figure 3.3. From Figure 3.3 it becomes apparent that for typical values of shear strain between 0.05% and 0.1% the soil damping ratio takes values in the range of $10\% - 20\%$ while in some extreme cases values as low as 5% and as high as 25% can also be observed. Since the soil properties are highly non-linear, the characteristics of the springs and dampers used to model the supports will be a function of the support's displacements and hence iterations will be required in order to achieve good agreement between the spring stiffness and the damping ratio and the respective support's response. The relation between the spring's and damper's characteristics and the support's displacement is qualitatively shown in Figure 3.4.

3.3 Simplified Soil Stiffness for Free Spanning Pipelines

According to DNV's Recommended Practice, when a free spanning pipeline scenario is considered and the seabed profile is relatively simple, the Vertical Dynamic Soil Stiffness, $K_{V,d}$, and the Lateral Dynamic Soil Stiffness, $K_{L,d}$, can be estimated in a simplified manner by Eq. 3.7 and 3.8 respectively.

$$K_{V,d} = \frac{C_V}{1-\nu} \cdot (\frac{2}{3} \cdot \frac{\rho_s}{\rho} + \frac{1}{3}) \cdot \sqrt{D} \tag{3.7}$$

$$K_{L,d} = C_L \cdot (1+\nu) \cdot (\frac{2}{3} \cdot \frac{\rho_s}{\rho} + \frac{1}{3}) \cdot \sqrt{D} \tag{3.8}$$

where D is the outer diameter of the pipe including any coating, $\frac{\rho_s}{\rho}$ is the specific mass ratio between the pipe mass (not including added mass) and the displaced water, ν is the Poisson's ratio and the coefficients C_V and C_L are given in Tables 3.2 and 3.3 for different soil material types. In these Tables proposed values for the Vertical Static Soil Stiffness are also given.

Table 3.2: Simplified dynamic stiffness factor and static stiffness for pipe-soil interaction in sand [6]

Sand Type	Friction Angle, ϕ [°]	C_V $[kN/m^{5/2}]$	C_L $[kN/m^{5/2}]$	$K_{V,s}$ $[kN/m/m]$
Loose	28-30	10500	9000	250
Medium	30-36	14500	12500	530
Dense	36-41	21000	18000	1350

Table 3.3: Simplified dynamic stiffness factor and static stiffness for pipe-soil interaction in clay with OCR=1 [6]

Clay Type	Undrained Shear Strength, S_U $[kN/m^2]$	C_V $[kN/m^{5/2}]$	C_L $[kN/m^{5/2}]$	$K_{V,s}$ $[kN/m/m]$
Very Soft	<12.5	600	500	50-100
Soft	12.5-25	1400	1200	160-260
Firm	25-50	3000	2600	500-800
Stiff	50-100	4500	3900	1000-1600
Very Stiff	100-200	11000	9500	2000-3000
Hard	>200	12000	10500	2600-4200

4 Case Study for the calibration of the TD VIV model and the identification of optimum parameter sets

In this chapter the Case study that was the basis for the present analysis and served as a benchmark for the validation and calibration of the examined TD VIV model is described. More specifically, the general setup and the most relevant experimental data and results of the examined model tests are presented along with the respective findings of a previous study of the same model tests carried out by Passano, Wu and Larsen [7] by means of the frequency domain VIV prediction tool VIVANA. The considered model tests correspond to a series of laboratory experiments carried out in SINTEF Ocean's facilities as part of a broader research effort aimed at better understanding and explaining the phenomenon of VIV in free spanning pipelines. The experiments were conducted with scaled models of real pipelines and were focused on both IL and CF vibrations. The reason that made it necessary to carry out the above research program is the fact that in order to take advantage of a newly discovered gas reservoir offshore Norway, the pipelines necessary for the transportation of the gas from the field to the shore had to be laid on a very uneven seabed. This would inevitably result in the formation of a large number of free spans of considerable length along the pipeline. The existence of such free spans could then possibly lead in the emergence of vortex-induced vibrations which as already explained can pose a serious threat to the pipelines' survival and reduce their expected lifetime, mainly due to the accumulation of fatigue damage. Therefore efficient and accurate VIV prediction methods were necessary, the development of which required in turn the existence of an extensive database. This case study is based on the work of Passano, Wu and Larsen [7] and SINTEF Ocean's reports with regard to the findings of the model tests [47, 9, 48, 8].

4.1 General setup

The experimental apparatus used during the model tests is illustrated in Figure 4.1. The examined pipe was supported by a 12 m long truss girder. On the one edge of the pipe a pretension regulator and an axial stiffness regulator were implemented, while the other end was instrumented so that the applied pretension could be measured. Below the pipe several adjustable supports were used in order to make it possible to modify the active free span length and thus examine both single span and multi span pipelines. Ten sets of strain gauges were used in order to measure the curvature with regard to both IL and CF directions and two MacReflex video cameras were also used to measure the IL and CF displacements. Subsequently, using modal analysis it became possible to produce time series of the IL and CF response, snapshots of the pipeline's displacements at given time instants and also to compute and report modal participation factors with respect to both IL and CF response as presented in detail in [9, 48]. The interaction between the pipe and the uniform incident current flow was modelled by towing the pipe in calm water and the different current velocities were determined by varying the towing speed.

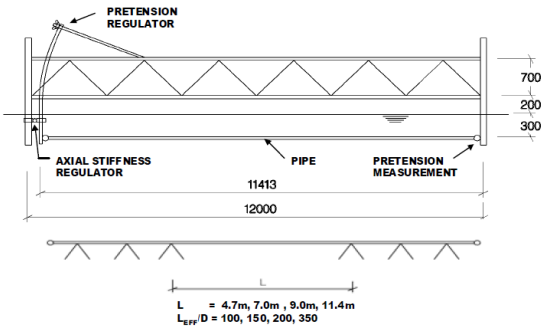

Figure 4.1: Experimental setup [7].

The examined model tests were divided in three phases. In the first two phases the same pipe model was used, while in the third one a modified model with slightly larger diameter was utilized in order to comply with the updated specifications of the pipeline that was actually going to be used in the gas field. Among the total amount of experiments, only three series were presented in [7], Test Series 10, Test Series 42 and Test Series 75. These three test series were also selected for this case study and were used for benchmarking and validating the results obtained in the present thesis. Therefore, only these test series are going to be treated in the following. The most relevant data for the models used during these three series of experiments are given in Table 4.1. At this point it is worth noting that there are some deviations between the values of the end spring stiffness (i.e. the stiffness of the axial spring applied at the one end of the pipe model) reported in Passano, Wu and Larsen's paper, [7], and the respective values given in SINTEF Ocean's reports and it was chosen to present the values that SINTEF Ocean reported in Table 4.1. As far as Test Series 10 is concerned, there were no clamps implemented in this series and therefore only a single span of 11.413 m was present in the experiments. The applied static pretension was set to $T = 67.8$ N and the stiffness of the axial spring implemented at the left end of the pipe was 2.3 kN/m. In Test Series 42 six sets of clamps were applied at positions 1.208 m , 2.215 m, 3.324 m, 8.053 m, 9.262 m and 10.170 m resulting in an active free span length of 4.729 m. The static pretension was set to $T = 51.5$ N and an end spring stiffness of 19.53 kN/m was applied. Last but not least, as for Test Series 75, eighteen sets of clamps were applied leaving an active free span length of 3.421 m. The clamps were positioned at approximately 0.5 m intervals on either side of the free span as shown in Figure 4.2. The static pretension was set to $T = 50$ N and an end spring stiffness of 20.04 kN/m was applied.

Table 4.1: Model test data [7].

Parameter	Test Series 10	Test Series 42	Test Series 75	Units
Length, L	11.413	11.413	11.413	m
Free span Length, L_f	11.413	4.729	3.421	m
Diameter, D	0.0326	0.0326	0.03511	m
Bend. Stiffness, EI	0.203	0.203	0.203	kNm^2
Axial stiffness, EA	5000	5000	5000	kN
Static Tension, T	67.8	51.5	50.0	N
Dry mass, m	1.147	1.147	1.307	kg/m
End spring stiffness, k	2.3	19.53	20.04	kN/m

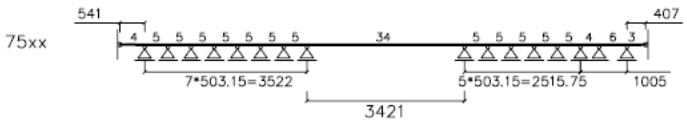

Figure 4.2: Span Configuration and clamp positions for Test Series 75 [8]

As far as the frequency domain analysis conducted by means of VIVANA in [7] is concerned, a finite element model consisting of 116 beam elements was utilized to model the pipe used in the experiments regarding Test Series 10 and 42, while 181 beam elements were used for Test Series 75. Moreover, the pure IL VIV and the combined CF and IL VIV phenomena, that were observed during the experiments, were treated separately in VIVANA. This means that different sets of IL excitation load coefficients were used in the two cases. Another difference of those two models lies in the way that the eigenfrequencies and the respective added mass coefficients were calculated. That is, in the pure IL VIV model (valid only for low current velocities without CF VIV) the eigenfrequencies and the added mass coefficients were computed based on the work

of Aronsen [5]. In the case of combined CF and IL VIV first the eigenfrequencies in the CF direction were calculated, then the respective CF added mass coefficients were calibrated in order to be consistent with the above eigenfrequencies and finally the IL added mass coefficients were adjusted in order to obtain IL eigenfrequencies that are two times the CF response frequency. This calibration procedure for the IL added mass is formulated in such a way that when the target frequency is between two still-water IL eigenfrequencies, the program tends to give IL response at the higher of the two possible mode shapes [7]. Finally, it should be noted that the VIV model used in [7] neglects the interaction between the response calculation at CF and IL frequencies.

4.2 Experimental data and frequency domain analysis results

In this section the most relevant experimental results obtained during the above described model tests with regard to Test Series 10, 42 and 75 are presented along with the respective findings of the frequency domain analysis conducted by Passano, Wu and Larsen using the FD VIV prediction tool VIVANA.

4.2.1 Test Series 10

In Figure 4.3 the response frequencies, the vibration mode numbers and the maximum response amplitudes normalized by the pipe's diameter observed during the experiments and the frequency domain analysis with regard both to the in-line and the cross-flow direction are illustrated. From the numerically obtained results given in this figure only those corresponding to the combined CF and IL VIV case (red and blue lines respectively) will be discussed in the following, since although the results of the pure IL VIV (green line) agree well with the experiments, they correspond to only two experimental values and thus the sample is not sufficient for safe conclusions. Moreover, snapshots of the response in both directions corresponding both to the experimental measurements and the numerical results are presented in Figure 4.4.

From Figures 4.3a and 4.3b it becomes apparent that both the model tests and the FD analysis give approximately the same results with regard to the CF response frequencies and vibration modes, predicting a stepwise increase of the mode number from mode 1 to mode 3. Contrary to this though, the numerically computed IL frequency does not agree with the experiments for the cases where the measured IL frequency was not equal to twice the respective CF frequency, something totally expected since such a behavior could not be captured by the above presented formulation of the combined CF and IL VIV model used in VIVANA. This is evident for current velocities of about 0.076 and 0.104 m/s where the experimental IL frequency was found to be three times the respective CF frequency. These two velocities seem to give problematic results for the IL vibration modes too, since the experiments gave mode 3 at 0.076 m/s and mode 2 at 0.104 m/s, while the frequency domain analysis predicted the exact opposite modes. In general, as far as the IL vibration modes are concerned, although both experiments and the frequency domain analysis go through mode 1, 2, 3 and 4, the latter predicts a stepwise increase of the modes as a function of the current velocity, while the experiments gave a somewhat more "random" behaviour. Finally, from Figure 4.3c it becomes apparent that in general, the numerically obtained results for the maximum response in the IL direction seem to be in good agreement with the experiments, although VIVANA seems to slightly underestimate the IL response. Contrary to this, VIVANA seems to constantly overestimate the CF response and this deviation from the experiments becomes maximum for current velocity 0.76 m/s, where the experiments give CF response amplitude smaller even that that of the IL response. As already mentioned, at this specific velocity the experiments gave IL frequency three times bigger than the respective CF frequency and a combination of CF mode 1 and IL mode 3, something that could not be pre-

dicted by the used frequency domain model. Moreover, this observation also indicates that there is a significant interaction between the vibration frequencies in the two direction. Therefore, the observed discrepancies between the experimental and numerical results could be attributed up to a point to the fact that this interaction is neglected in VIVANA.

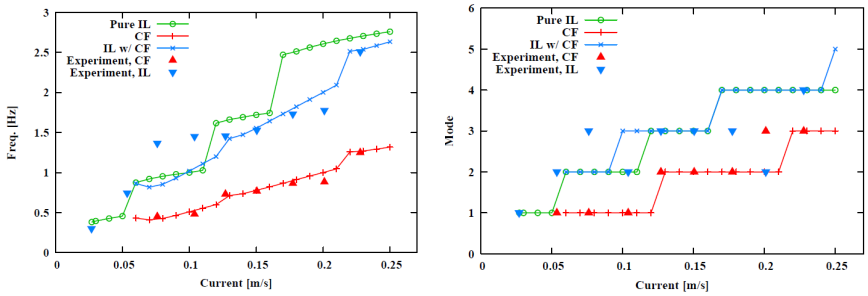

(a) Response Frequency vs Current Velocity

(b) Response Mode vs Current Velocity

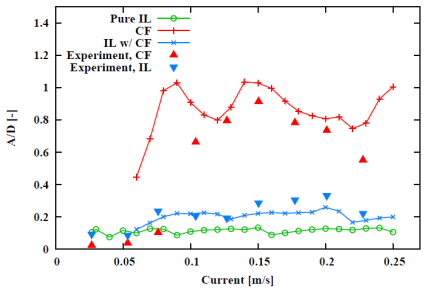

(c) Maximum response amplitude normalized by the pipe's diameter vs Current Velocity

Figure 4.3: Comparative plots of the fundamental experimental results and the respective findings of the frequency domain analysis for Test Series 10 given in [7].

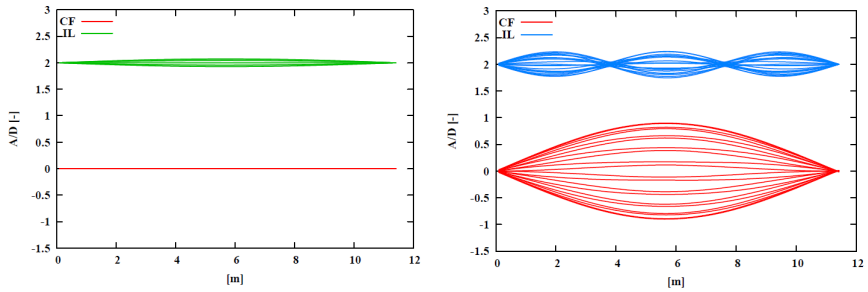

(a) Response snapshots from the FD analysis with 0.04 m/s current.

(b) Response snapshots from the FD analysis with 0.1 m/s current.

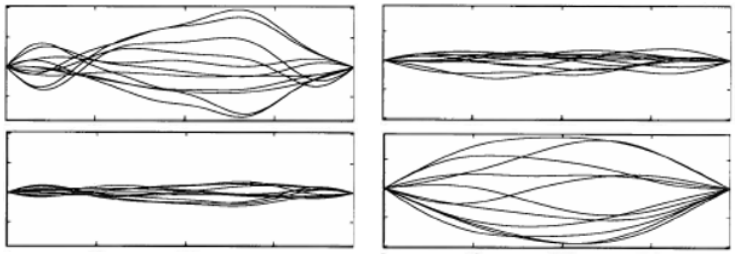

(c) Response snapshots from the model test with 0.027 m/s current.

(d) Response snapshots from the model test with 0.104 m/s current.

Figure 4.4: Response snapshots from the FD analysis and the model tests for Series 10 given in [7, 9]

Snapshots of the response predicted by the frequency domain analysis corresponding to current velocities of 0.04 m/s and 0.1 m/s are illustrated in Figures 4.4a and 4.4b respectively. It becomes obvious that at 0.04 m/s CF vibrations are not present while small amplitude mode 1 IL vibrations can be observed. Moreover, from Figure 4.4b it becomes apparent that mode 1 cross-flow Vibrations dominate the response for a current velocity of 0.1 m/s while at the same time non-negligible mode 3 IL vibrations can be observed. These observations seem to be in good agreement with the respective experimental results measured for current velocity of 0.104 ($\approx$0.1) m/s, where a dominant mode 1 cross-flow vibration is apparent while the respective IL response has a much smaller amplitude and can be characterized mainly by a mode 3 vibration pattern (although not as clear as predicted by the numerical analysis), as illustrated in Figure 4.4d. Contrary to this though, from Figure 4.4c it becomes obvious that although the response at current velocity 0.027 m/s is dominated by a quite clear mode 1 IL vibration, there is also a very small and in practice almost negligible (maximum A/D = 0.04) mode 1 CF vibration observed, something that was not captured via the FD analyses.

4.2.2 Test Series 42

In Figure 4.5 the response frequencies, the vibration mode numbers and the maximum response amplitudes normalized by the pipe's diameter observed during the experiments and the frequency domain analysis with regard both to the in-line and the cross-flow direction are illustrated. Moreover, snapshots of the response in both directions corresponding both to the experimental measurements and the numerical results are presented in Figure 4.6.

As far as the numerically obtained results by means of VIVANA are concerned, it becomes obvious from Figure 4.5 that CF vibrations are captured for the first time at a current velocity of 0.16 m/s and therefore up to this velocity the FD results for the pure IL vibrations are valid (i.e. green lines in the Figure), while for higher velocities the results of the combined IL and CF VIVANA model should be used (blue and red lines). Taking a closer look in Figure 4.5b it is clear that with regard to the CF response both the experimental and the numerical results give mode 1 vibrations for the whole range of the examined velocities. As for the IL direction now, during the experiments mode 1 IL vibrations were observed for velocities below 0.4 m/s while mode 2 became dominant above 0.4 m/s. Around 0.4 m/s two experiments were conducted one of which gave mode 1 as the dominant vibration mode while mode 2 response was observed during the second trial. Moreover, as far as the pure IL FD model is concerned, it seems to be in good agreement with the experiments for current velocities up to 0.22 m/s, which is way above the onset point for CF vibrations, predicting mode 1 IL response, while for even higher velocities mode 2 becomes dominant. However, the pure IL model is not valid at this higher part of the examined velocity range. Contrary to this though, the combined CF and IL FD model gives dominant mode 2 IL response for all the considered current velocities and therefore it agrees with the experiments only for the higher examined velocities above 0.4 m/s.

In Figure 4.5a the same trends that were observed for the dominant mode become apparent for the dominant response frequencies in the IL direction as well. To be more precise, the pure IL FD model agrees again very well with the experimental results for current velocities up to 0.22 m/s, while above this velocity, where it is again noted that this model is not valid and should not be used, it deviates significantly from the experimental data. As for the combined CF and IL VIVANA model, it gives similar results in both directions. That is that it follows the same trend as the experimental results in terms of the way the dominant vibration frequency varies as a function of the current velocity predicting an increase of the dominant frequency for higher

induced current velocities with an almost constant slope. However, the numerical results with regard to both the IL and the CF response constantly overestimate the dominant vibration frequency for the whole range of examined current velocities apart from the higher part above 0.4 m/s where they seem to be in quite good agreement with the experiments.

Finally, from Figure 4.5c the above observations can up to a point be also verified in terms of the maximum response amplitude both in the IL and the CF directions. More specifically, the pure IL FD model gives again very good results with regard to the maximum predicted response amplitude in the IL direction for the whole range of current velocities where this model is applicable and even beyond this range. Contrary to this though, the numerical results obtained by the combined CF and IL VIVANA model seems to be in fairly good agreement with the experimental results only for current velocities higher that 0.4 m/s and this is true with respect to both the IL and the CF predicted vibration amplitude. For the whole range of lower current velocities the numerically obtained results underestimate the IL response amplitude. As for the CF response now, the frequency domain analyses overestimate the maximum CF vibration amplitude for current velocities below 0.3 m/s and underestimates it in the range of current velocities between 0.3 and 0.4 m/s. The most profound deviations between the experimental data and the numerically predicted response amplitudes in the CF direction are observed at the current velocity range of 0.24-0.27 m/s, where the FD analyses give the maximum CF response of about 1.05 D while the experimentally measured response is much smaller and takes values between approximately 0.65 D and 0.8 D, and at the current velocity of 0.35 m/s, where the highest CF amplitude of 1.21 D was measured during the experiments while the respective numerical prediction is only 0.8 D. As for the IL direction, the most significant discrepancy is observed at 0.3 m/s where the maximum IL response of almost 0.4 D was captured experimentally while the respective numerically calculated vibration amplitude is equal to about 0.22 D.

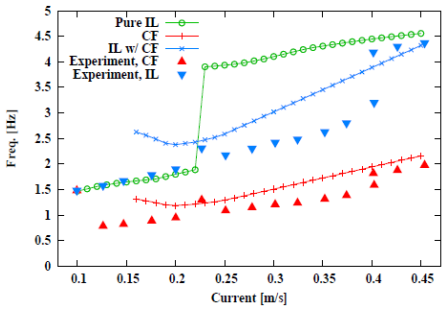

(a) Response Frequency vs Current Velocity

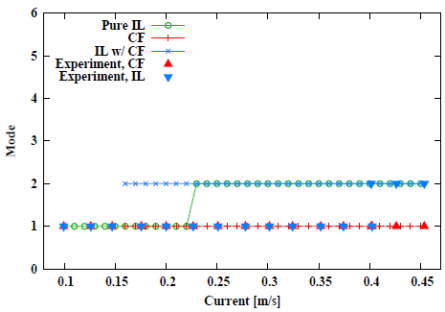

(b) Response Mode vs Current Velocity

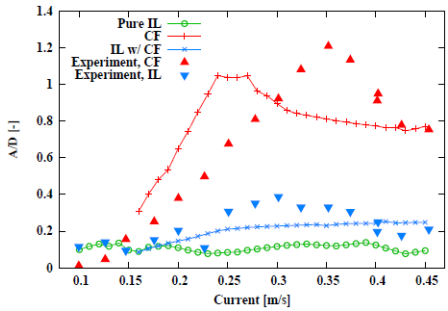

(c) Maximum response amplitude normalized by the pipe's diameter vs Current Velocity

Figure 4.5: Comparative plots of the fundamental experimental results and the respective findings of the frequency domain analysis for Test Series 42 given in [7].

Snapshots of the response predicted by the frequency domain analysis corresponding to current velocity of 0.23 m/s are illustrated in Figure 4.6a, where clear mode 1 and mode 2 vibrations can be observed in the CF and IL directions respectively. Moreover, snapshots calculated from the measured response of the model test at 0.2267 m/s are shown in Figures 4.6b and 4.6c for two different time periods. Both figures show a clear CF mode 1 response while in the IL direction the participation of both mode 1 and mode 2 becomes apparent.

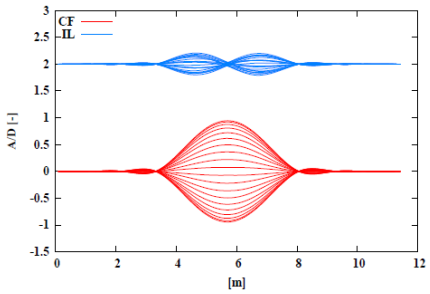

(a) Response snapshots from the FD analysis with 0.23 m/s current.

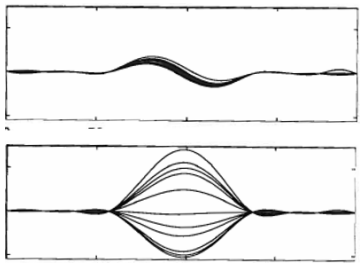

(b) Response snapshots from the model test with 0.2267 m/s current.

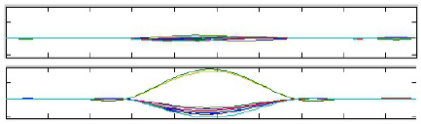

(c) Response snapshots from the model test with 0.2267 m/s current at a different time.

Figure 4.6: Response snapshots from the FD analysis and the model tests for Series 42 given in [7, 9]

4.2.3 Test Series 75

In Figure 4.7 the response frequencies, the vibration mode numbers and the maximum response amplitudes normalized by the pipe's diameter observed during the experiments and the frequency domain analysis with regard both to the in-line and the cross-flow direction are illustrated. Moreover, snapshots of the response in both directions corresponding both to the experimental measurements and the numerical results are presented in Figure 4.8.

Taking a closer look at Figure 4.7 it becomes obvious that the frequency domain analyses capture the onset of CF vibrations with regard to Test Series 75 at 0.31 m/s. Hence, the FD results for the pure IL vibrations (i.e. green lines in the Figure) should only be considered for current velocities below this limit, while the combined IL and CF VIVANA model (blue and red lines) is valid only with respect to current velocities above and including 0.31 m/s. Moreover, it should be noted that the results obtained by means of VIVANA should be taken into account only for velocities up to 0.46 m/s because convergence problems emerged for higher velocities and the respective simulations can be regarded as failed.

As a general remark, it becomes clear from Figure 4.7 that the main observations made previously with regard to Test Series 42 are also valid in this case too. To be more precise, from Figure 4.7b it becomes apparent that as far as the CF response is concerned, both the experimental and the numerical results give mode 1 vibrations for the whole range of the examined velocities. This is also true for the IL vibration mode observed during the model test as well as to the IL mode predicted by the pure IL FD model up to 0.44 m/s. This corresponds to current velocities covering the whole span for which this model is valid and also much higher velocities too. Contrary to this though, the results obtained by means of the combined CF and IL VIVANA

model deviate from the aforementioned observations, predicting dominant IL vibrations of mode 2 for all examined current velocities. The same trends can also be observed in Figure 4.7a with regard to the dominant response frequencies in the IL direction as well. To be more precise, the pure IL FD model agrees again very well with the experimental results for current velocities well beyond the onset point of the CF response up to 0.44 m/s, while above this velocity, where this model should not be considered anyway, it deviates significantly from the experimental data. As for the combined CF and IL VIVANA model, it seems to constantly overestimate the dominant vibration frequency of the pipe with respect to both the IL and the CF directions and for all the examined current velocities. Finally, as far as the response amplitude is concerned, the pure IL frequency domain analyses seem to be again in good agreement with the experimental results for the whole span of current velocities for which this model is applicable and also gives quite good estimations for higher velocities up to 0.35 m/s too. In contrast, the combined CF and IL VIVANA model predicts considerably higher responses in the CF direction compared to the model test data for all the considered current velocities. Last but not least, it is worth noting that even though this combined model deviates significantly from the experimental results in terms of the predicted dominant IL vibration mode and frequencies, the estimated values for the maximum response amplitude in the IL direction seem to be fairly accurate for the whole range of the examined current velocities (i.e. up to 0.46 m/s, before the calculations eventually fail).

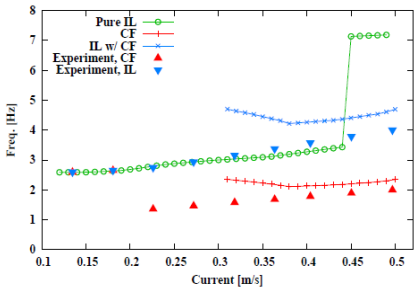

(a) Response Frequency vs Current Velocity

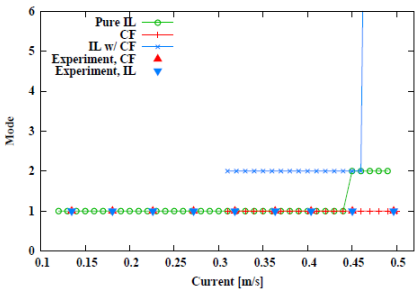

(b) Response Mode vs Current Velocity

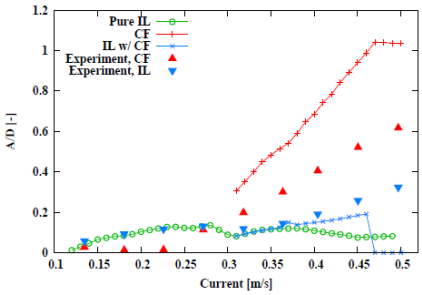

(c) Maximum response amplitude normalized by the pipe's diameter vs Current Velocity

Figure 4.7: Comparative plots of the fundamental experimental results and the respective findings of the frequency domain analysis for Test Series 75 given in [7].

Snapshots of the response predicted by the frequency domain analysis corresponding to current velocity of 0.27 m/s are illustrated in Figure 4.8a, where clear mode 1 vibrations are predicted by the pure IL frequency domain model while CF vibrations are not captured at such a low current velocity. Moreover, snapshots calculated from the measured response of the model test at 0.272 m/s are shown in Figure 4.8b where it is apparent that mode 1 vibrations dominate the pipeline's response both in the IL and in the CF directions.

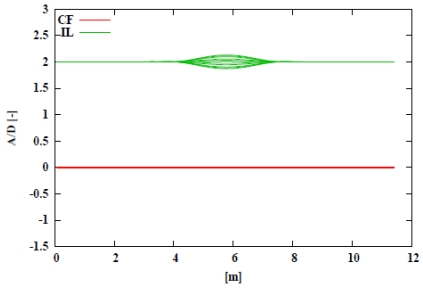

(a) Response snapshots from the FD analysis with 0.27 m/s current.

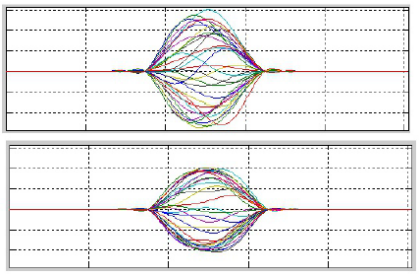

(b) Response snapshots from the model test with 0.272 m/s current.

Figure 4.8: Response snapshots from the FD analysis and the model tests for Series 75 given in [7, 8]

5 Method of Analysis of the Case Study

In this chapter the methodology followed in order to implement in RIFLEX the VIV cases investigated in the present thesis so as to calibrate the TD VIV prediction tool and the procedure adopted to obtain the respective results is presented. As a first step, the hydrodynamic load model used for the simulation of the examined VIV phenomena is established and the hydrodynamic coefficients chosen initially as part of the preparatory project performed in Fall 2021, in which only the model tests corresponding to Test Series 10 were considered and which will be hereafter referred to as Project Thesis, are presented. Subsequently, the structural and numerical models used in order to approximate the actual free spanning pipeline cases are illustrated. Then the fundamental theory behind and the structure of the RIFLEX software is briefly described before illustrating the implementation of the hydrodynamic and structural models into RIFLEX and carrying out the TD VIV analyses. Finally, the procedure followed in order to calibrate the TD VIV model and post-process, analyse and assess the obtained results is also presented.

5.1 Hydrodynamic load model

As explained in detail previously, in order to be able to account for the inherent non-linearities that characterize a realistic VIV case, time domain analysis is needed. For this reason, the updated synchronization load model for combined CF and IL VIV that was introduced by Kim and was thoroughly analysed in section 2.3.3 was utilized. In order to use this TD VIV model suitable empirical hydrodynamic drag, added mass and vortex-induced excitation force coefficients had to be chosen. Typically these coefficients depend on the Reynolds number, the surface roughness (neglected here as the examined pipeline is assumed to be smooth) and the Keulegan-Carpenter number (KC), which is a non-dimensional parameter that describes the relative importance of the drag forces over inertia forces for bluff objects in an oscillatory fluid flow or equivalently for objects that oscillate in a fluid at rest, and is given in Eq. 5.1.

$$KC = \frac{VT}{D} \tag{5.1}$$

where V is the amplitude of the flow velocity oscillation (or the amplitude of the object's velocity, in case of an oscillating object), T is the period of oscillation and D is a characteristic length scale of the object (i.e. the diameter of the pipe in our case).

As far as the hydrodynamic drag coefficient is concerned, two components can be distinguished. The first one is the tangential component which is mainly attributed to skin friction and for most practical applications is considered negligible. Contrary to this though, the normal component of the drag coefficient typically takes considerable values as illustrated in Figure 5.1. Taking into account that on the one hand a smooth pipe is examined and on the other hand that the considered Reynolds number is within the subcritical flow regime, from Figure 5.1 the value of the normal component of the hydrodynamic drag coefficient is found equal to 1.2. Moreover, keeping in mind that the drag coefficient is also dependent on the KC number, the findings of Sarpkaya ([49]) were also utilized before deciding on its value. According to those findings the value of the drag coefficient for a fixed rigid smooth circular cylinder varies between 0.5 and 2.0 as a function of the considered KC and Re numbers. Finally it should be noted that both Figure 5.1 and Sarpkaya's findings correspond to fixed rigid cylinders. However, since the main purpose of this thesis is to conduct an analysis so as to validate the applicability of the updated TD VIV model in the case of free spanning pipelines and also taking into account that it is widely accepted that using the value of 1.2 presented above for rigid cylinders in VIV analyses of flexible structures gives conservative results, this value of the drag coefficient was

considered as a reasonable estimation.

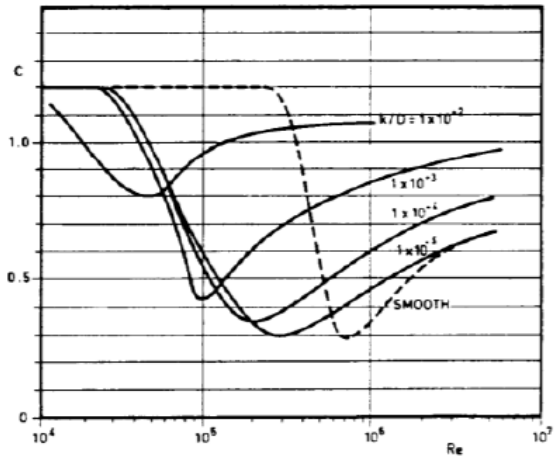

Figure 5.1: Drag coefficient for fixed circular cylinder in uniform flow for various roughness values.

As for the added mass coefficient now, its tangential component is also considered negligible for most practical applications of smooth cylinders, while based on potential flow theory the value of the normal added mass coefficient of a circular cross-section is typically taken equal to 1.0. Finally the last step before being able to implement the hydrodynamic load model in the RIFLEX software is to determine suitable vortex-induced excitation force coefficients and synchronization parameters both for the in-line and for the cross-flow direction. As a first estimation, these coefficients were initially chosen in the context of the Project Thesis to be equal to those determined by Kim in [43] despite the fact that in this paper the VIV response of a deep-water vertical riser is examined and not the response of a free spanning pipeline. The reason for this choice was that it was the only available research where the new updated synchronization load model for combined CF and IL VIV response was implemented. The only change applied to Kim's TD VIV model parameters is that the upper limit of the IL synchronization range $\hat{f}_{\text{max},x}$ was extended from 0.7 used in [43] to 0.9 so as to be sure that the chosen synchronization range is sufficiently wide to capture both pure in-line and cross-flow induced in-line vibrations. All the relevant hydrodynamic parameters chosen and implemented in the TD VIV model for the purposes of the Project Thesis' work are summarised in Table 5.1.

Table 5.1: Hydrodynamic parameters used in the TD VIV model in Project Thesis

Parameter	**Value**
Quadratic drag coefficient in tangential direction $[-]$	0
Quadratic drag coefficient in normal direction $[-]$	1.2
Added mass coefficient in tangential direction $[-]$	0
Added mass coefficient in normal direction $[-]$	1
Hydrodynamic diameter [m]	0.0326
$C_{v,y}[-]$	0.85
$C_{v,x}[-]$	0.75
$\hat{f}_{0,y}[-]$	0.144
$\hat{f}_{\text{min},y}[-]$	0.08
$\hat{f}_{\text{max},y}[-]$	0.208
$\hat{f}_{0,x}[-]$	0.5
$\hat{f}_{\text{min},x}[-]$	0.1
$\hat{f}_{\text{max},x}[-]$	0.9

5.2 Structural and numerical model

A Finite Element Method (FEM) was utilized in order to model the free spanning pipelines investigated in this thesis. The FEM model is mainly characterized by the system mass, damping and stiffness matrices **M**, **C** and **K** respectively. The global Rayleigh damping formulation was used in order to establish the structural damping model, according to which the damping matrix is determined as a linear combination of the global mass and stiffness matrices as shown in Eq. 5.2.

$$\mathbf{C} = \alpha_1 \mathbf{M} + \alpha_2 \mathbf{K} \tag{5.2}$$

where the parameters α_1 and α_2 are referred to as the mass- and stiffness-proportional damping coefficients, respectively.

One of the main benefits of the above formulation is that it makes the implementation and specification of the structural damping level computationally convenient. However, the most significant feature of the global Rayleigh damping formulation is that it gives a damping matrix that is orthogonal with respect to the eigenvectors and thus the modal damping can be expressed in terms of the damping coefficients as illustrated in Eq. 5.3. This equation is typically used for linear dynamic systems but it can also serve as a reference for specification of Rayleigh damping for nonlinear dynamic systems.

$$\lambda_i = \frac{1}{2}\left[\frac{\alpha_1}{\omega_i} + \alpha_2 \omega_i\right] \tag{5.3}$$

Here λ_i is the modal damping ratio relative to critical and ω_i is the eigenfrequency. The damping term proportional to the mass matrix is typically omitted in order to avoid unphysical structural damping due to rigid body motions (i.e. $\alpha_1 = 0$) and this approach was also used in this thesis. Therefore the only term left is the stiffness-proportional damping, $\alpha_2 \boldsymbol{K}$, which corresponds to a modal damping ratio, $\lambda_i = \frac{\alpha_2 \omega_i}{2}$. Based on the information about the level of structural damping of the models used in the experiments that are given in [47, 9, 48, 8], the value of $\lambda_i \leq 0.004$ was used. At this point it is worth noting that since several different current velocities were examined in this thesis for each considered model test series, a different value of α_2 was chosen for each one of them. Moreover, it should be noted that although the value of $\lambda_i \leq 0.004$ was given in SINTEF Ocean's reports as a representative damping ratio for both the IL and CF directions, it was found in the detailed experimental data that this value is in fact more representative for the IL direction, while in the CF direction some decay test gave somewhat higher and others somewhat lower damping ratio leading ultimately in an average value of 0.4%. For this reason and also keeping in mind that the fundamental IL frequency is typically approximated as twice the fundamental CF frequency, the value of α_2 for each current velocity was chosen such that it corresponds to damping ratios below 0.4% of critical damping at all fundamental IL frequencies (or equivalently at two times the fundamental CF frequency). Typically it is the fundamental CF frequency that is used for the calibration of α_2 but in this case the above approach was chosen because of the aforementioned findings and also because it was preferred to have an under-damped structure than an over-damped one in order to get more realistic results. More specifically, the value of α_2 for each current velocity U and each examined test series was calculated based on the respective vortex shedding frequency as such:

$$2 \cdot f_{s,i} = 2 \cdot \frac{U_i \cdot St}{D} \rightarrow \omega_i = 2\pi \cdot (2 \cdot f_{s,i}) \rightarrow \alpha_{2,i} = \frac{2 \cdot \lambda_i}{\omega_i} \tag{5.4}$$

where the subscript i corresponds to the different current velocities examined, St is the Strouhal number, for which the typical value for subcritical flow of 0.2 was used, and the value of $\lambda_i =$

0.004 was used for all current velocities. The obtained results with regard to Test Series 10, Test Series 42 and Test Series 75 are summarized in Tables 5.2, 5.3 and 5.4 respectively.

Table 5.2: Test Series 10: Stiffness-proportional damping coefficients for the examined current velocities

U[m/s]	0.025	0.03	0.04	0.05	0.06	0.07
α_2[s/rad]	0.004151	0.003459	0.002594	0.002075	0.001729	0.001482
U[m/s]	0.08	0.09	0.10	0.11	0.12	0.13
α_2[s/rad]	0.001297	0.001153	0.001038	0.000943	0.000865	0.000798
U[m/s]	0.14	0.15	0.16	0.17	0.18	0.19
α_2[s/rad]	0.000741	0.000692	0.000649	0.00061	0.000576	0.000546
U[m/s]	0.20	0.21	0.22	0.23	0.24	0.25
α_2[s/rad]	0.000519	0.000494	0.000472	0.000451	0.000432	0.000415

Table 5.3: Test Series 42: Stiffness-proportional damping coefficients for the examined current velocities

U[m/s]	0.10	0.11	0.12	0.13	0.14	0.15
α_2[s/rad]	0.001038	0.000943	0.000865	0.000798	0.000741	0.000692
U[m/s]	0.16	0.17	0.18	0.19	0.20	0.21
α_2[s/rad]	0.000649	0.00061	0.000576	0.000546	0.000519	0.000494
U[m/s]	0.22	0.23	0.24	0.25	0.26	0.27
α_2[s/rad]	0.000472	0.000451	0.000432	0.000415	0.000399	0.000384
U[m/s]	0.28	0.29	0.30	0.31	0.32	0.33
α_2[s/rad]	0.000371	0.000358	0.000346	0.000335	0.000324	0.000314
U[m/s]	0.34	0.35	0.36	0.37	0.38	0.39
α_2[s/rad]	0.000305	0.000296	0.000288	0.00028	0.000273	0.000266
U[m/s]	0.40	0.41	0.42	0.43	0.44	0.45
α_2[s/rad]	0.000259	0.000253	0.000247	0.000241	0.000236	0.000231

Table 5.4: Test Series 75: Stiffness-proportional damping coefficients for the examined current velocities

U[m/s]	0.12	0.13	0.14	0.15	0.16	0.17
α_2[s/rad]	0.000865	0.000798	0.000741	0.000692	0.000649	0.00061
U[m/s]	0.18	0.19	0.20	0.21	0.22	0.23
α_2[s/rad]	0.000576	0.000546	0.000519	0.000494	0.000472	0.000451
U[m/s]	0.24	0.25	0.26	0.27	0.28	0.29
α_2[s/rad]	0.000432	0.000415	0.000399	0.000384	0.000371	0.000358
U[m/s]	0.30	0.31	0.32	0.33	0.34	0.35
α_2[s/rad]	0.000346	0.000335	0.000324	0.000314	0.000305	0.000296
U[m/s]	0.36	0.37	0.38	0.39	0.40	0.41
α_2[s/rad]	0.000288	0.00028	0.000273	0.000266	0.000259	0.000253
U[m/s]	0.42	0.43	0.44	0.45	0.46	0.47
α_2[s/rad]	0.000247	0.000241	0.000236	0.000231	0.000226	0.000221
U[m/s]	0.48	0.49	0.50			
α_2[s/rad]	0.000216	0.000212	0.000208			

Having now formulated the structural damping model, the next step was to establish the actual numerical/structural model. For the FEM representation of the structure, beam elements based on the small strain theory were used. As for the discretization of the examined structure in finite beam elements, it was chosen to use the discretization used in [7] where the same model

tests were investigated by means of the frequency domain VIV prediction model VIVANA. That is, the pipeline was modelled as a beam consisting of 116 beam elements regarding Test Series 10 and 42 and of 181 beam elements with respect to Test Series 75. At this point it should be noted that a convergence study with regard to the number of beam elements was not conducted in the context of this thesis. However, the examined structure is approximated as a very simple pinned-pinned tensioned beam with an additional axial spring applied to one of its ends. Moreover, according to the findings in [7], the highest vibration mode observed both during the experiments and via the frequency domain analysis was mode 5 and was regarding Test Series 10 while the highest observed vibration mode for the other two Test Series was mode 2. So using 116 and 181 beam elements to model the pipeline means that more than 20 elements are contained in each half wave length of a mode shape of Test Series 10 and more than 50 elements are contained in each half wave length of a mode shape of Test Series 42 and 75. Taking all the aforementioned facts into account it was concluded that using 116 and 181 beam elements for the respective Test Series should be adequate in order to accurately capture the dynamic response of the structure.

Moreover, as far as Test Series 42 and 75 are concerned, the clamps used during the experiments to reduce the active span length of the models were modelled in RIFLEX as stiff springs in y- and z-directions. The stiffness of those springs was chosen high enough (i.e. $9 \cdot 10^6 N/m$ for Test Series 42 and $24.26 kN/m$ for Test Series 75) to prevent displacement of the pipe at the clamp positions since the clamp arrangements used in the experiments provided high stiffness in the IL and CF directions and low to no stiffness in the axial direction of the pipeline. In fact, the exact same approach was implemented during the post-processing procedure of the experimental results by SINTEF Ocean. To be more precise, RIFLEX was also used by SINTEF Ocean so as to model the considered experiments and obtain the system's natural frequencies and mode shapes that were required during modal analysis of the obtained experimental results. For this purpose, springs were used to model the clamps and the exact same spring configurations and characteristics were used in the present thesis too.

What is more, for the computation of the dynamic response of the structure, numerical stepwise time integration of the dynamic equilibrium equation was conducted. For each examined Test Series, the same timestep and simulation length were chosen for all the considered current velocities. The size of the timestep was chosen based on the highest fundamental cross-flow frequency, which corresponds to the highest examined current velocity, while the simulation length was chosen based on the lowest fundamental cross-flow frequency corresponding to the lowest current velocity. The vortex shedding frequency was used as the fundamental cross-flow frequency. In particular, as far as Test Series 10 is concerned, the timestep was chosen to be equal to 0.05s so that for the highest current velocity at least 10 timesteps to be contained in one oscillation period, and the simulation length was set to 3650s so that for the lowest current velocity at least 500 periods to be simulated. Moreover, in order to be sure that the transient effects are not included in the calculations, the first 650s of the simulation were removed. This corresponds to 100 periods for the lowest current velocity, which was considered to be enough to remove all transients from the obtained results. The exact same procedure was followed for the other two considered Test series in order to determine the timestep, the simulation length and the part of the simulation that had to be removed from the obtained results in order to remove all possible transient effects. The implemented values for all three Test Series are summarized in Table 5.5. The pure Newton-Raphson method was used in order to conduct equilibrium iterations at each timestep while a maximum number of 10 iterations per timestep and a desired displacement accuracy of 10^{-5} were defined. As for the static analysis, it was based on an in-

cremental loading procedure where a loading sequence of Global Spring Activation, Specified Forces, Volume Forces and Current Forces with 10 increments for each load type was applied to the structure. The pure Newton-Raphson method was used again with a maximum number of 30, 30, 100 and 55 iterations for the four aforementioned load types respectively and a desired displacement accuracy of 10^{-7}.

Table 5.5: Implemented values for timestep size, simulation length and removed transient time.

	Timestep [s]	**Simulation Length [s]**	**Removed Time [s]**
Test Series 10	0.05	3650	650
Test Series 42	0.025	980	180
Test Series 75	0.025	850	150

5.3 The RIFLEX software

The hydrodynamic load model and the structural/numerical model presented in sections 5.1 and 5.2 respectively are coupled through the non-linear finite element software RIFLEX in order to perform the static and dynamic analysis of the examined structure. RIFLEX is a powerful tool developed for the analysis of slender marine structures including among others flexible marine risers, umbilicals, pipelines and mooring lines. Here only some fundamental aspects of the theoretical basis and structure of RIFLEX focused exclusively in the needs of the present thesis will be briefly described and then the implementation of the hydrodynamic and structural model into RIFLEX will be presented. For a more detailed description of the features and capabilities of RIFLEX one should refer to the RIFLEX User Guide and Theory Manual [50, 51].

5.3.1 RIFLEX theory basis

As already mentioned in section 5.2, for the FEM representation of the examined structure, beam elements based on the small strain theory were used. According to [51] the finite element model is formulated on the basis of the principle of virtual displacements and for the description of the beam's deformation pattern, the co-rotated ghost reference (or "co-rotated total Lagrange") formulation is utilized, in which the "Green strain" is used as the strain measure while the respective stress measure is the "2nd Piola Kirchoff" stress. For each element there is a co-rotated reference system that follows the element as a rigid body referring to the initial configuration. The orientation of the element system is defined by continuously updating it's orthonormal transformation matrix. As far as the beam elements themselves are concerned, they are modelled as 3D elements with 6 degrees-of-freedom (dofs) (i.e. 3 translational and 3 rotational) at each node.
As mentioned previously, RIFLEX was used in order to carry out both the static and the dynamic analysis of the structure and the non-linear formulation was chosen for both calculations. The static analysis is based on solving the system of equations given in Eq. 5.5, where $\boldsymbol{r}$ is the nodal displacement vector containing all the system's dofs, $\boldsymbol{R}^S(\boldsymbol{r})$ is the internal structural reaction force vector where the contributions from all the elements are assembled and $\boldsymbol{R}^E(\boldsymbol{r})$ is the external force vector including the contributions from all the elements. Keeping in mind that typically there will be a non-linear relation between the two above load vectors and the nodal displacement vector, the main goal of the above procedure is to find the nodal displacement vector so that the complete system is in static equilibrium. Eq. 5.5 is solved numerically using the so-called incremental-iterative procedure with Euler-Cauchy incrementation. To be more precise, an incremental stepwise loading procedure is applied, where the external loading is accumulated in a number of small load increments in order to iteratively find the static configuration at each load step using the displacement vector from the previous load increment as the initial solution. The equilibrium iterations are performed using the Newton-Raphson method as mentioned in

the previous section.

$$\boldsymbol{R}^S(\boldsymbol{r}) = \boldsymbol{R}^E(\boldsymbol{r}) \tag{5.5}$$

As far as the non-linear time domain dynamic analysis is concerned, it is based on solving the following non-linear system of differential equations:

$$\boldsymbol{R}^I(\boldsymbol{r}, \ddot{\boldsymbol{r}}, \boldsymbol{t}) + \boldsymbol{R}^D(\boldsymbol{r}, \dot{\boldsymbol{r}}, \boldsymbol{t}) + \boldsymbol{R}^S(\boldsymbol{r}, \boldsymbol{t}) = \boldsymbol{R}^E(\boldsymbol{r}, \dot{\boldsymbol{r}}, \boldsymbol{t}) \tag{5.6}$$

Here $\boldsymbol{r}$, $\dot{\boldsymbol{r}}$ and $\ddot{\boldsymbol{r}}$ are the displacement, velocity and acceleration vectors respectively. $\boldsymbol{R}^I$ is the inertia force vector which includes the contributions of the structural mass forces, the mass forces accounting for the internal fluid and the added mass forces which are the result of the acceleration of the surrounding fluid due to the presence and motion of the structure. $\boldsymbol{R}^D$ is the damping force vector accounting both for the internal structural damping and the hydrodynamic damping. $\boldsymbol{R}^S$ is the internal structural reaction force vector which was already introduced in Eq. 5.5 and finally $\boldsymbol{R}^E$ is the external force vector which apart from the static loads introduced in Eq. 5.5 in this case also includes the time-varying forces exerted on the structure.

In order to solve Eq. 5.6 a step by step numerical integration procedure is performed. More specifically, a Newton-Raphson type of equilibrium iteration method is applied at each time step so as to solve the incremental dynamic equilibrium equations. The numerical time integration procedure is based on the Newmark β-family which considers a constant timestep Δt throughout the analysis. According to this method the displacement, the velocity and the acceleration at the new timestep $t + \Delta t$ are estimated in terms of the respective values at the previous timestep t as such:

$$\begin{aligned} \dot{\boldsymbol{r}}_{t+\Delta t} &= \dot{\boldsymbol{r}}_t + (1-\gamma)\ddot{\boldsymbol{r}}_t \Delta t + \gamma \ddot{\boldsymbol{r}}_{t+\Delta t} \Delta t \\ \boldsymbol{r}_{t+\Delta t} &= \boldsymbol{r}_t + \dot{\boldsymbol{r}}_t \Delta t + \left(\tfrac{1}{2} - \beta\right) \ddot{\boldsymbol{r}}_t (\Delta t)^2 + \beta \boldsymbol{r}_{t+\Delta t} (\Delta t)^2 \end{aligned} \tag{5.7}$$

where γ and β are parameters determining the functional change in displacement, velocity and acceleration vectors over the time step Δt. The most widely used values for γ and β are $\gamma = \frac{1}{2}$ and $\beta = \frac{1}{4}$ because the first one makes sure that no artificial/numerical damping is implemented in the solution and the second one gives an unconditionally stable integration method.

5.3.2 RIFLEX structure

The RIFLEX program system contains 5 modules which communicate with each other through the file system as illustrated in Figure 5.2. These five modules are called INPMOD, STAMOD, DYNMOD, FREMOD and OUTMOD and a brief description of them is given in the following.

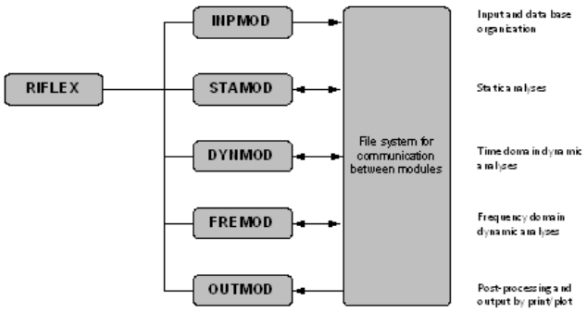

Figure 5.2: Structure of program system

INPMOD: This module reads and stores the input data provided by the user in order to be used in the subsequent analyses. There are two ways to import data to INPMOD. Initially this was only

possible via a batch mode where prestructured input files were imported to INPMOD. However, in the most recent versions of RIFLEX a complete and very user friendly interface has been implemented and therefore the user is able to provide the input data manually one at a time. The input data should contain all the information that is relevant for carrying out the subsequent static and dynamic analyses including information about the geometry of the examined structure, the considered environmental conditions, the discretization and the characteristics of the finite element model of the structure (e.g. number of elements, nodes and dofs, element type etc.), the material and mechanical properties and the applied boundary and loading conditions to name but a few. INPMOD has to be run only once and then various different analyses can be performed without rerunning INPMOD, provided that the input data have not been modified.

STAMOD: This module is responsible for performing static analyses. It reads the input data stored in relevant databases by INPMOD and generates the element mesh, the initial stressfree configuration and other key data necessary for performing static analysis using a finite element method.

DYNMOD: This module is responsible for performing time domain dynamic analyses using the results obtained by the previously conducted static analysis and other relevant input data stored by INPMOD such as the considered environmental and time-varying loading conditions. The obtained results consist of time series of the dynamic response, natural frequencies and mode shapes which are then stored on files of several different types in order to be post-processed either via the OUTMOD module within RIFLEX or via other applicable software like MATLAB and PYTHON.

FREMOD: This module is associated with frequency domain analyses and therefore is not relevant in the context of the present thesis and will not be further analysed.

OUTMOD: This module is used for post-processing the results obtained by running the rest of the modules including creating plots and performing spectral analysis and fatigue analysis to name but a few. It is also possible to export the obtained results in various file types in order to further analyse them using other applicable software. The OUTMOD module was not utilized for this thesis since the obtained results were post-processed directly after the static and dynamic analyses by means of the MATLAB software.

5.3.3 Implementation of the examined case in RIFLEX

In order to run the static and dynamic analyses for the examined pipeline cases the hydrodynamic and structural models presented in sections 5.1 and 5.2 were implemented into RIFLEX following a number of steps. To begin with, the first step was to define the considered environment and environmental conditions. The depth of the sea area was set to 600m and the examined beam was positioned in the middle of this depth so as to be unaffected by both the free surface and the sea bottom as this was also the case during the experiments presented in chapter 4. Then an incident current flow along the y-direction (i.e. normal to the beam axis) was introduced as steady and uniform all over the considered sea area and several different current velocities were examined as already presented in Tables 5.2 - 5.4. At this point it is worth noting that in order to run a dynamic analysis in RIFLEX it is necessary to define a sea state in terms of incident free surface waves too. However, since only a current flow is investigated in this thesis the significant wave height of the aforementioned waves was set to a very small value ($10^{-5}[m]$) in order to not influence the results at all. Subsequently the cross-sectional properties of the beam were defined.

More specifically, the beam sections were modelled as axisymmetric cross-sections. In this stage the mass coefficient $m = 1.147[kg/m]$ for Test Series 10 and 42 or $m = 1.307[kg/m]$ for Test Series 75 was defined along with the hydrodynamic diameter of the pipeline $D = 0.0326[m]$ or $D = 0.03511[m]$ for the respective Test Series and the material and mechanical properties of the beam, including the bending stiffness $EI = 203[N \cdot m^2]$, the axial stiffness $EA = 5 \cdot 10^6[N]$ and the torsional stiffness which was taken equal to $10000[N \cdot m^2/rad]$. Moreover, in this stage the hydrodynamic load model presented in section 5.1 was also chosen as the TD VIV model for combined CF and IL VIV with independent IL and CF synchronization and the hydrodynamic parameters, as presented for example in Table 5.1 with regard to the Project Thesis' case, were also given here as input.

The next step was to create two supernodes to serve as the two edges of the beam with coordinates $z = -300[m]$, $y = 0[m]$ and $x_1 = 0[m]$ and $x_2 = 11.413[m]$ respectively so that the considered beam to be horizontal with length $L = 11.413[m]$. Moreover, the boundary conditions were imposed using these supernodes. More precisely, as far as the end node is concerned, all the translational dofs and the rotation around the x-axis were fixed while the other two rotations were free. As for the first node now, the only difference in the applied boundary conditions is that the axial translation was also free because this is the node where the axial spring is attached and where the pretension $T = 67.8/51.5/50[N]$ was applied as explained in detail in sections 4.1 and 5.2. Finally, a "line" and a respective "linetype" were created in order to model the beam and in this step the structural model presented in section 5.2 was implemented. That is that the beam was decomposed into 116/181 beam elements and 117/182 nodes all with the same cross-sectional properties and then as far as Test Series 42 and 75 are concerned global springs were attached to the nodes corresponding to the clamp positions as described above. Having implemented the hydrodynamic and the structural model in RIFLEX the static and dynamic analysis were then performed based on the procedures described in sections 5.3.1 and 5.3.2.

5.4 Post-processing and calibration procedure

In this section, the calibration procedure adopted in the present thesis and the methodology followed after running the dynamic and static analyses in RIFLEX in order to post-process the obtained results and compare them with the respective reference data presented in section 4.2 is described.

5.4.1 Calibration Procedure

In order to be able to calibrate the proposed TD VIV prediction tool to give good results with respect to all three of the examined Test Series several different sets of hydrodynamic parameters were tested. The Hydrodynamic parameters applied in the Project Thesis with regard to Test Series 10 that are illustrated in Table 5.1 were used as a starting point of the calibration procedure followed in the present Thesis. For this reason and also in order to make it easier to realize the improvement that this calibration procedure has brought to the obtained results, a brief presentation of the main findings and the conclusions that where reached in the Project Thesis will be presented in section 6.1.1 although this analysis was not conducted in the context of the present work. At this point it is worth mentioning that during the Project Thesis's work SINTEF Ocean's reports with regard to the findings of the model tests, [47, 9, 48, 8], were not available and the Project Thesis was based entirely on the data given by Passano, Wu and Larsen in [7]. As already mentioned there was a considerable difference between the end spring stiffness value presented in this paper, 34.4 kN/m, compared to the correct value of 2.3 kN/m. Using this extremely high spring stiffness resulted in an unphysical response of the pipeline and hence

it was decided during the Project Thesis' work to not use an axial spring at all, something that improved the results considerably. So the first step of the calibration procedure was to correct this mistake with regard to Test Series 10 and apply the correct end spring stiffness while using the same hydrodynamic parameters as given in Table 5.1. The obtained results are illustrated in section 6.1.1 too. Then the same hydrodynamic parameters were applied to the other two Test series in order to serve as a starting point for the calibration of those Test Series too (Sections 6.2.1 and 6.3.1).

Subsequently, a series of different sets of hydrodynamic parameters was examined. Most of the parameters presented in Table 5.1 were kept fixed throughout this analysis since they have already been tested and validated in numerous other research works with regard to both free spanning pipelines and vertical risers. So the only parameters that were varied during this calibration procedure were regarding the synchronization ranges applied in the IL and CF hydrodynamic force model. There were two main goals. The first one was to find one single set of parameters that gives results in good agreement with the reference data for all the examined Test Series. The second goal was to be able to achieve the first goal while using a sufficiently wide synchronization range in the in-line synchronization model in order to be able to use one single set of hydrodynamic parameters to account for both the pure IL and the CF-induced IL vibrations. For this reason, it was decided to keep the lower and upper limits of the synchronization ranges both in the IL ($\hat{f}_{\text{min},x}$ and $\hat{f}_{\text{max},x}$) and the CF ($\hat{f}_{\text{min},y}$ and $\hat{f}_{\text{max},y}$) direction fixed and equal to the values given in Table 5.1 and vary only the values of the the non-dimensional frequency of maximum energy transfer in the two directions, $\hat{f}_{0,x}$ and $\hat{f}_{0,y}$. The whole series of hydrodynamic parameter sets examined during this calibration procedure are summarized in Table 5.6.

Table 5.6: The whole series of parameter sets examined during the calibration procedure

Parameter Set No.	$\hat{f}_{\text{min},y}[-]$	$\hat{f}_{0,y}[-]$	$\hat{f}_{\text{max},y}[-]$	$\hat{f}_{\text{min},x}[-]$	$\hat{f}_{0,x}[-]$	$\hat{f}_{\text{max},x}[-]$
1	0.08	0.144	0.208	0.1	0.5	0.9
2	0.08	0.144	0.208	0.1	0.216	0.9
3	0.08	0.144	0.208	0.1	0.252	0.9
4	0.08	0.12	0.208	0.1	0.288	0.9
5	0.08	0.144	0.208	0.1	0.288	0.9
6	0.08	0.144	0.208	0.1	0.324	0.9
7	0.08	0.12	0.208	0.1	0.36	0.9
8	0.08	0.144	0.208	0.1	0.36	0.9
9	0.08	0.12	0.208	0.1	0.396	0.9
10	0.08	0.144	0.208	0.1	0.396	0.9

5.4.2 Post-Processing Procedure

Having run the simulations for each examined case (i.e. for each examined Test Series, current velocity and hydrodynamic parameter set) following the procedure described in the previous sections of this chapter, the obtained results with regard to the nodal displacements in the global x-, y- and z-direction for all nodes and every timestep were stored and written into ASCII-files so as to be post-processed by means of the MATLAB software. As already explained in section 5.2, the first step of this post-processing procedure was to remove the first part of the simulation from the raw data in order to be sure that any possible transient effects will not be included in the subsequent calculations. Then the response time series were plotted so as to visually verify that indeed the transients were no longer present in the remaining data series. Furthermore, the nodal displacements corresponding to the IL and the CF direction were stored separately. For each current velocity, the mean value of the displacement of each node in both directions was

subtracted by the corresponding response time series. In this way, the static equilibrium response of the beam in both directions was removed from the obtained data and thus the remaining data series correspond exclusively to the dynamic response of the structure. Having performed all the aforementioned preliminary steps, the remaining time series are now ready to be used for the actual analysis of the simulation results.

First of all, for each current velocity the maximum amplitude of the response in both directions as well as the respective positions along the pipe were found. Then for each simulation case, the response time series corresponding to the nodes where the maximum amplitude in each direction was observed were used in order to produce the respective response spectra. For this reason, a Fast Fourier Transform (FFT) algorithm was applied in MATLAB. More specifically in order to verify the correct implementation of this transformation from the time domain to the frequency domain several different FFT functions were used, among which it is worth giving special mention to the FFT routine provided within the WAFO Matlab toolbox. The obtained response spectra where subsequently utilized in order to identify for each simulation case the active response frequencies both in the in-line and the cross-flow direction and to compare them with the respective reference data. To be more precise, the dominating frequencies for the in-line and cross-flow directions were taken in the context of the present thesis as the peak frequencies in the response spectra corresponding to the positions along the pipe where the maximum amplitudes were measured in each direction. Finally, the dominant vibration modes in both directions for each examined case were identified by plotting snapshots of the calculated response and visually observing their shape. In other words, if the shape of the snapshot for example resembled a half sinusoidal wave, mode 1 was considered as the dominant vibration mode.

6 Results of the calibration procedure, Discussion and Identification of the optimum parameter sets

After establishing the hydrodynamic load model (TD VIV model) and the structural and numerical model as presented in sections 5.1 and 5.2 respectively, they were then implemented in RIFLEX following the procedure described in section 5.3.3. Subsequently, the static and dynamic analyses were run by means of RIFLEX for all three examined Test Series and for all the chosen sets of hydrodynamic parameters, which are given in Table 5.6 in section 5.4.1. The obtained results in terms of calculated nodal displacements were written in ASCII-files. Then, the MATLAB software was utilized in order to post-process the above data as described in detail in section 5.4.2. The most relevant results of this post-processing procedure are presented in sections 6.1, 6.2 and 6.3 with regard to Test Series 10, 42 and 75 respectively and the optimum set of hydrodynamic coefficients with regard to all three Test Series is identified. Finally, in section 6.4 the results corresponding to these optimum parameters are compared in more detail with the respective experimental data.

6.1 Test Series 10

6.1.1 Project Thesis' Results and the updated results after correcting the applied end spring stiffness

As mentioned in section 5.4.1 the Hydrodynamic parameters applied in the Project Thesis with regard to Test Series 10, which are given in Table 5.1, were used as a starting point for the calibration procedure followed in the present Thesis for all three Test Series. Moreover, as explained in detail in section 5.4.1, due to the wrong value of the end spring stiffness that was reported in [7] for Test Series 10, it was decided during the Project Thesis's work to completely neglect the use of the axial spring. So the first step of this calibration procedure with regard to Test Series 10 was to correct this mistake and apply the correct end spring stiffness while using again the same set of hydrodynamic parameters. In Figure 6.2 the response frequencies, the vibration mode numbers and the maximum response amplitudes normalized by the pipe's diameter that were calculated by means of the time domain analysis conducted during the Project Thesis's work are illustrated. The respective experimental results and the findings of the frequency domain analysis performed by Passano, Wu and Larsen are also presented in this Figure for an easier comparison. These results correspond both to the cross-flow and the in-line vibrations. The experimental and the frequency domain data presented in this section were extracted from Figure 4.3, which was described in detail in section 4.2. Moreover, in Figure 6.1 the updated results obtained during the present work are also illustrated. This Figure corresponds to the same set of hydrodynamic coefficients but considers the right value of the end spring stiffness. At this point it is worth noting that, since the findings of Figure 6.2 were not obtained in the context of the present work, they will not be analysed in depth in the following and the focus will be on the detailed description of the updated results shown in Figure 6.1. However, in order to better understand the improvement that the implementation of the correct boundary conditions brought to the results, the main differences between the two Figures will be highlighted in the following analysis.

To begin with, taking a closer look at Figure 6.1d it becomes apparent that as far as the lower examined current velocities up to 0.13 m/s are concerned, the IL vibration modes predicted by the TD VIV model are in general in very good agreement with both the experimental data and the respective findings of the frequency domain analysis. To be more precise, the TD VIV model seems to predict a stepwise increase of the IL vibration modes as the current velocity becomes

higher, something that can also be observed for the frequency domain analysis presented in Figures 4.3b and 6.1d. However, contrary to what is true both for the experiments and for the FD VIV model, which go through modes 1, 2, 3 and 4, the time domain analysis gives higher order IL vibration modes at the highest considered current velocities. As for the the cross-flow vibration modes, the TD VIV model agrees well both with the experiments and with the frequency domain analysis for all the considered current velocities up to 0.2 m/s. However, the TD VIV model is not able to predict the third CF vibration mode that was observed during the model tests and was also verified by the FD VIV model for the highest examined current velocities. At this point it is worth mentioning that all the above observations with regard to the CF and IL vibration modes are also valid with respect to the initial results obtained during the Project Thesis work and are illustrated in Figure 6.2c. It is clear that the change of the boundary conditions did not affect the predicted vibration modes, since the respective findings are almost identical and only some minor differences in the velocities for which the transition from one mode to the next one occurs can be observed. The above observations can also be verified by the respective findings of the time domain analysis with regard to the predicted dominant vibration frequencies in the IL and CF directions, as presented in Figures 6.1a, 6.1b and 6.1c.

At this point it is worth noting that a multi-frequency response is predicted by the TD VIV model for all three examined Test Series and for most of the examined current velocities, especially with regard to the IL response. This phenomenon is found to be much more profound with regard to Test Series 10, since this Test Series is characterised by the largest length to diameter ratio ($L/D = 11.413/0.0326 \approx 350$) and thus the examined pipeline is extremely slender and resembles more to a cable than to a real-life marine pipeline. The existence of multi-frequency response is something totally expected when a slender marine structure is investigated. As explained in detail in section 2.2.4, slender marine structures are far more complicated than the simple rigid cylinders, mainly due to the spatial response variability characterizing elastic structures exposed to hydrodynamic loads like waves and currents. This spatial response variability, combined with the fact that in most typical real-life pipeline applications there is also an axial pretension applied to the pipeline as a result of the pipe laying procedure, enables the occurrence of higher order modes and the excitation of multiple eigenfrequencies and mode shapes as the time goes by, and also enables the simultaneous excitation of multiple eigenfrequencies and mode shapes at different positions along the pipeline. Moreover, it should be reminded that the dominating frequencies for the in-line and cross-flow directions were taken in the context of the present thesis as the peak frequencies in the response spectra corresponding to the positions along the pipe where the maximum amplitudes were measured in each direction. The results of this process are illustrated in the following in plots like Figure 6.1a. However, because of the aforementioned multi-frequency response, which was also evident during the experiments as will be discussed in detail in section 6.4, it was found that for all three Test series and for several current velocities there are more than one dominant peaks present in the response spectra. For this reason, in order to better present all the important frequency contents that were present during the experiments and are also captured by the TD VIV model, additional plots were created, which are in the following named as ”modified”, and in which, instead of the frequency corresponding to the highest peak in the response spectrum, when several dominant peaks are present, the frequency corresponding to the second or even to the third highest peak is presented. For example, in Figure 6.1 three such plots are presented. In Figure 6.1a the dominant response frequencies (i.e. corresponding to the highest peaks in the response spectra) are given, in Figure 6.1c the frequencies of the peaks that are closer to the respective experimental results are presented and in Figure 6.1b the frequencies of the peaks that correspond to the dominant vibration modes, which were identified based on snapshots of the captured response and are also presented

in Figure 6.1d, are illustrated. In Figure 6.3 the IL response spectra corresponding to $U = 0.15$ m/s and $U = 0.2$ m/s are illustrated indicatively, and it becomes evident that indeed several significant peaks are present in the response spectra.

From Figures 6.1a, 6.1b and 6.1c it becomes apparent that as far as the cross-flow response frequency is concerned, the results of the time domain analysis seem to be in good agreement both with the experiments and the frequency domain results. The maximum discrepancy with the experiments is observed for the highest tested current velocity of 0.228 m/s, where the experimental results give a CF frequency of 1.2 Hz while the respective CF frequency predicted by the TD VIV model is 0.953 Hz. At this point it is worth noting that the TD VIV model also predicts the existence of cross-flow vibrations even for the lowest examined current velocities. As becomes clear from Figure 6.1e, these vibrations are characterised by an extremely small amplitude and therefore could have been neglected. However, it was preferred to include them in these Figures for the sake of completeness and because CF vibrations with amplitude of the same order of magnitude were also observed during the model tests for the lowest tested towing speeds (see Figure 6.1e) although the corresponding CF frequency was not reported in [7].

As for the IL frequency, based on Figures 6.1a, 6.1b and 6.1c, the time domain results seem to agree well with the experiments and to be much better than the respective findings of the FD VIV model for current velocities up to 0.13 m/s, for which only one dominant peak is present in the obtained IL response spectra. This is a really important finding, since it proves that the TD VIV model is in fact able to accurately capture the IL response frequency in the range of current velocities between 0.07 and 0.1 m/s, where the frequency domain analysis presented in [7] failed. It should be reminded that, as explained in detail in section 4.2, in this velocity range the experiments give IL frequency three times higher than the respective CF frequency making it impossible for the FD VIV model to predict this behaviour. Moreover, in the range of current velocities between 0.07 and 0.13 m/s, both the experiments and the TD VIV model give IL vibration frequencies corresponding to the third IL vibration mode, as is also shown in Figure 6.1d. For higher current velocities between 0.13 and 0.18 m/s, the experiments still give mode 3 IL vibrations and hence IL frequencies of about the same magnitude. The dominant IL vibration frequencies predicted by the TD VIV model for this range of current velocities seem to be almost identical to the experimental ones, as is clearly illustrated in Figures 6.1a and 6.1c. However, based on the snapshots of the calculated IL response, a dominant contribution of mode 4 vibrations becomes evident for this range of current velocities. This becomes also apparent from the existence of significant peaks at higher frequencies in the obtained response spectra for these velocities. These higher frequencies that agree with the observed vibration shapes are presented in Figure 6.1b.

Furthermore, for current velocities above 0.18 m/s the experiments give again mode 3 IL vibrations and quite low vibration frequency, except for the highest examined velocity for which mode 4 IL response and a somewhat higher vibration frequency were captured during the model tests. Contrary to this, the results of the time domain analysis for the IL frequency, which are given in Figure 6.1a, seem to be extremely unstable with frequent and intense ups and downs in this velocity range. This is a result of the aforementioned multi-frequency response, since the simultaneous participation of mode 3,4,5 and 6 IL vibrations becomes apparent in the calculated response snapshots. In these snapshots, it became clear that mode 5 vibrations dominate the response for velocities between 0.19-0.22 m/s while mode 6 is the dominant one for even higher velocities. The captured frequencies corresponding to mode 3 IL response and are thus in agreement with the experimental results are shown in Figure 6.1c, while the respective fre-

quencies corresponding to the dominant vibration modes 5 and 6 are presented in Figure 6.1b. Finally, from all the above observation and also keeping in mind that the discrepancies in the IL frequency are observed only for high current velocities, where considerable and fully developed CF vibrations are also present, it becomes apparent that the problem of this synchronization model lies mainly in the way the interaction between the two phenomena is captured. More specifically, it could be concluded that the deviations from the experiments can mainly be attributed to the synchronization parameters used for the above analysis. This could mean that the chosen non-dimensional frequencies of maximum energy transfer $\hat{f}_{0,x}$ and $\hat{f}_{0,y}$ are not optimal, ultimately leading in the prediction of unrealistically high response frequencies. For this reason, $\hat{f}_{0,x}$ and $\hat{f}_{0,y}$ were the only parameters that were examined in the context of the following calibration procedure.

As illustrated in Figure 6.1e, and contrary to what was observed so far with regard to the response frequency and the vibration modes, the response amplitude in the in-line direction calculated by means of the TD VIV model in general seems to be in good agreement both with the experiments and with the findings of the frequency domain analysis. The maximum deviations from the experimental data are found at current velocities of 0.128 m/s and 0.2 m/s, where the maximum IL response amplitude was found during the experiments to be equal to 0.155D and to 0.3D respectively, while the respective results obtained by means of the TD VIV model are 0.254D and 0.17D. As far as the response amplitudes in the cross-flow direction are concerned, the findings of the TD VIV model are in quite good agreement with the respective results from the frequency domain analysis. More specifically, the TD analysis overestimates the CF response for most of the examined current velocities, something that is especially apparent for current velocities between 0.05 and 0.08 m/s. In this range the TD VIV model gives rapidly increasing values for the maximum CF response amplitude leading to a significant CF amplitude of 0.83D at 0.08 m/s, while the corresponding experimental values are extremely small and in fact they are even lower than the respective IL response amplitudes. This range of velocities corresponds to the transition region from the pure IL VIV phenomenon to the combined CF and IL VIV and the TD VIV model seems to predict that this transition starts at somewhat lower current velocity than what was observed during the model tests. However, it should be noted that this transition region is generally accepted to be the most difficult region to predict, as the limited relevant experimental data available increase the uncertainty in the selection of appropriate empirical coefficients necessary for the establishment of a reliable VIV prediction tool. Moreover, important deviations between the experimental data and the CF response predicted by the TD VIV model become also apparent for the higher part of the considered current velocity range, where the time domain analysis gives some of the higher values of CF vibration amplitude, while a reduction of the CF response was observed during the experiments. Finally, a really important finding has to do with the fact that both the experiments and the TD analysis give exactly the same CF response amplitude at the velocity of 0.15 m/s, for which the maximum CF response was captured during the model tests.

What is more, as for the improvement that the correction of the boundary conditions brought to the obtained results for the vibration frequencies, from Figures 6.2a - 6.2b, it becomes apparent that the changes in the CF direction are negligible. As for the IL direction, it becomes evident that for the highest part of the examined velocities above 0.14 m/s, the response is again characterized by the simultaneous existence of multiple vibration modes which in this case is much more profound than what is observed in the updated results. However, the most important improvement is observed for the velocities of 0.11 and 0.12 m/s, for which during the Project Thesis an unphysical almost zero IL frequency was predicted, something that was fixed after the

implementation of the correct end spring stiffness. This also led to a significant improvement of the predicted IL response amplitude for those two velocities, as is shown clearly in Figure 6.2d. Finally, it also becomes clear that the implementation of the correct boundary conditions resulted in the prediction of the transition from the pure IL to the combined CF and IL phenomenon at higher current velocities, ultimately leading in a considerable improvement of the obtained results for the CF response amplitude with regard to the lower examined current velocities.

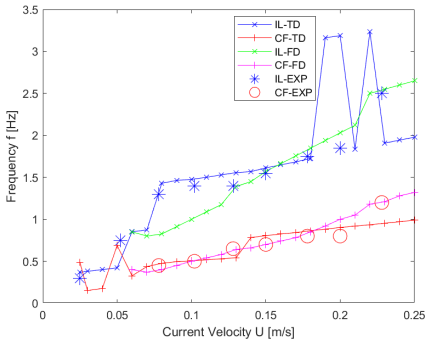

(a) Response Frequency vs Current Velocity

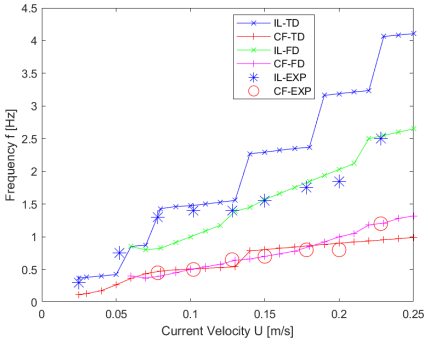

(b) Response Frequency vs Current Velocity (modified)

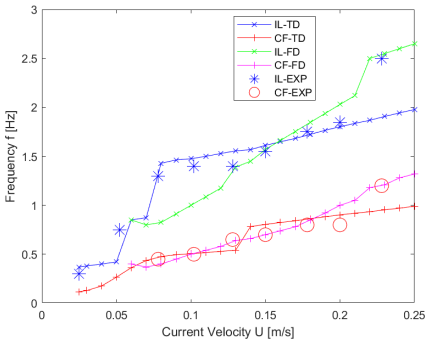

(c) Response Frequency vs Current Velocity (modified)

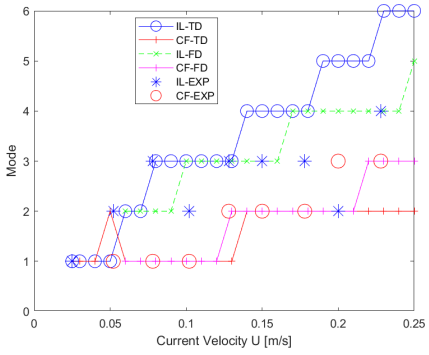

(d) Response Mode vs Current Velocity

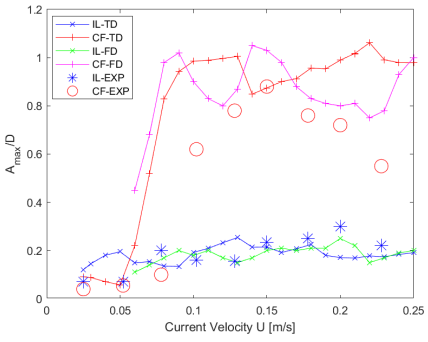

(e) Maximum response amplitude normalized by the pipe's diameter vs Current Velocity

Figure 6.1: Comparative plots of the fundamental experimental results and the respective findings of the frequency domain analysis conducted in [7] and the time domain analysis conducted in this thesis for Parameter Set No. 1.

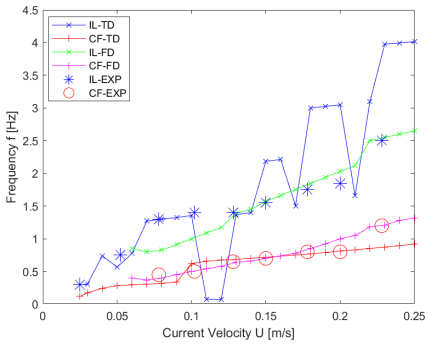

(a) Response Frequency vs Current Velocity

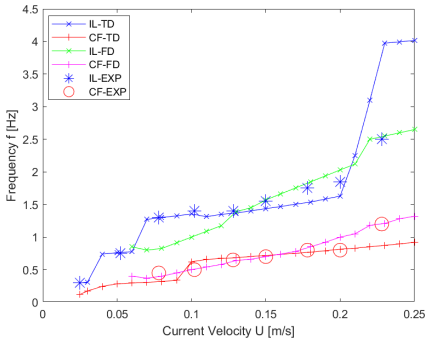

(b) Response Frequency vs Current Velocity (modified)

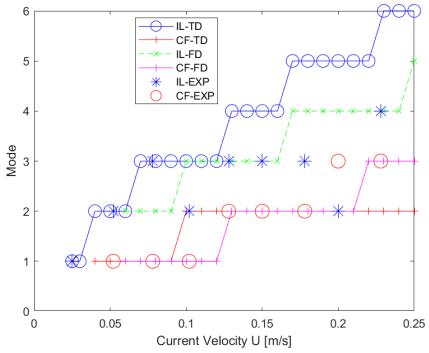

(c) Response Mode vs Current Velocity

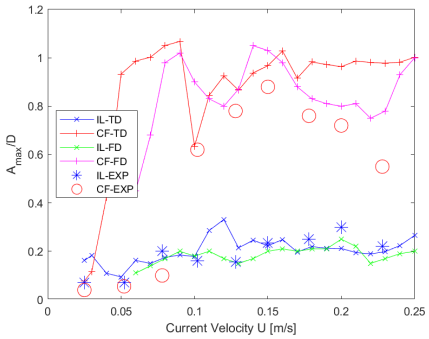

(d) Maximum response amplitude normalized by the pipe's diameter vs Current Velocity

Figure 6.2: Comparative plots of the fundamental experimental results and the respective findings of the frequency domain analysis conducted in [7] and the time domain analysis conducted in the context of the Project Thesis.

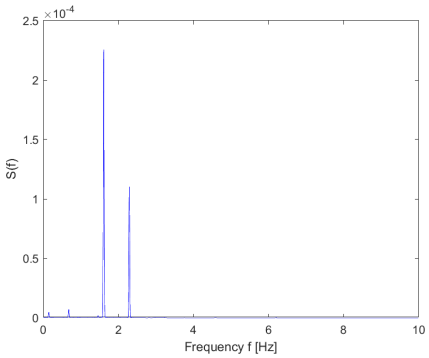

(a) $U = 0.15$ m/s.

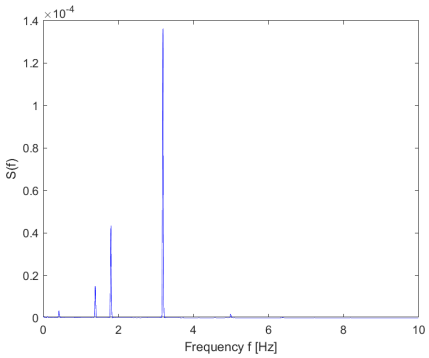

(b) $U = 0.2$ m/s.

Figure 6.3: Response spectra corresponding to the IL vibrations at velocities (a) 0.15 and (b) 0.2 m/s.

Finally, in Figure 6.4 snapshots of the response predicted by the time domain analysis corresponding to current velocities of 0.025 m/s and 0.1 m/s are illustrated. As already mentioned previously, contrary to the findings of the frequency domain analysis which give that below 0.06 m/s CF vibrations are not present, the TD VIV model and the experiments predict the existence of extremely low amplitude mode 1 CF vibrations even at the lowest examined current velocities (see also Figures 6.1e and 6.1d). At the lowest velocity, both the experiments and the time domain and frequency domain analyses give mode 1 vibrations in the in-line direction too. What is more, from Figures 6.4b, 4.4b and 4.4d regarding current velocity $U = 0.1$ m/s, it

becomes apparent that all three methods of analysis are again in total agreement predicting clear and dominant mode 1 CF vibrations and mode 3 IL vibrations. However, it should be noted that there was not a clear IL vibration mode observed during the experiments, but there was instead a vibration pattern with influences from modes 1,2 and 3.

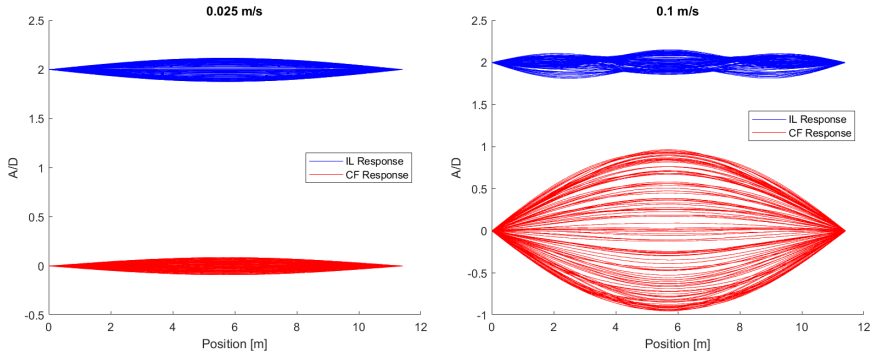

(a) $U = 0.025$ m/s. (b) $U = 0.1$ m/s.

Figure 6.4: Response snapshots from the time domain analysis with velocities (a) 0.025 and (b) 0.1 m/s.

6.1.2 The best two of the examined parameter sets

Having now analysed in detail the results that the TD VIV model gives with regard to the initial set of hydrodynamic parameters, the next step of this analysis is to test several different sets of parameters in order to calibrate the proposed TD VIV prediction tool to capture more accurately the VIV response observed during the experiments. In the following only the findings corresponding to the two parameter sets that give the most improved results will be presented. That is, Parameter Set No. 7 and Parameter Set No. 8. The corresponding hydrodynamic coefficients are given in Table 5.6. The obtained results corresponding to all the examined parameter sets can be found in Appendix A.1 (Figures A.1 - A.11). As a general remark, it can be concluded on the basis of this calibration procedure that the reduction of the values of $\hat{f}_{0,x}$ and $\hat{f}_{0,y}$ results on the one hand in the prediction of smaller values for the dominant vibration frequencies in both directions and on the other hand in a small increase in the obtained results for the response amplitudes in both directions. Moreover, it becomes also clear that in general reducing the values of $\hat{f}_{0,x}$ and $\hat{f}_{0,y}$ leads in the prediction of the transition from the pure IL to the combined CF and IL phenomenon at slightly higher current velocities. For these reasons, and also keeping in mind that in section 6.1.1 it was found that when the initial set of hydrodynamic parameters is used the TD VIV model overestimates the IL response frequencies (especially for the higher part of the examined velocity range) and that it predicts the transition from the pure IL to the combined CF and IL response at lower velocities than what was observed during the model test, it was decided to examine only lower values for both $\hat{f}_{0,x}$ and $\hat{f}_{0,y}$.

The response frequencies, the vibration mode numbers and the maximum response amplitudes normalized by the pipe's diameter that were calculated by means of the time domain analysis with regard to Parameter Set No.7 and Parameter Set No.8 are illustrated in Figures 6.5 and 6.6 respectively. The respective experimental results and the findings of the frequency domain analysis performed by Passano, Wu and Larsen are also presented in these Figures for an easier comparison. At this point it should be noted that the existence of the aforementioned multi-frequency response becomes also evident in Figures 6.5 and 6.6, especially with regard to the IL direction. However, for those two parameter sets this phenomenon is not as profound as was observed in section 6.1.1 for the initially examined hydrodynamic coefficients. For this reason,

the same approach that was described above was also followed for the analysis of the present cases. That is, in Figures 6.5a and 6.6a the dominant response frequencies (i.e. corresponding to the highest peaks in the response spectra) with respect to Parameter Set No. 7 and Parameter Set No. 8 are illustrated respectively. However, for several of the examined current velocities more than one dominant peaks are present in the obtained response spectra and in fact these secondary peaks are found to correspond to the dominant vibration mode observed in the calculated snapshots. So, in Figures 6.5b and 6.6b the response frequencies corresponding to the second highest peaks in the response spectra are presented. Of course, this applies only for the current velocities for which this multi-frequency response is observed.

At a first glance at Figures 6.5 and 6.6, it becomes apparent that these two parameter sets give very similar results, something totally expected since the only difference between those two parameter sets is the value of $\hat{f}_{0,y}$, while the rest of the considered hydrodynamic coefficients are the same. More specifically, taking a closer look at Figures 6.5c and 6.6c it becomes apparent that the IL vibration modes predicted by the TD VIV model are in very good agreement with both the experimental data and the respective findings of the frequency domain analysis for the whole range of the examined current velocities. To be more precise, the TD VIV model seems to predict for both examined parameter sets a stepwise increase of the IL vibration modes as the current velocity becomes higher, going through modes 1, 2, 3 and 4 for velocities up to 0.23 m/s. For the two highest velocities the TD VIV model gives dominant mode 5 IL response, something that is also verified by the FD analysis in [7], while there are not experimental data available for these velocities. As far as the deviations between the two parameter sets and also between the time domain analysis results and the respective experiments are concerned, some minor differences in the velocities for which the transition from one mode to the next one occurs can be observed. To be more precise, both parameter sets predict that the change from mode 1 to mode 2 and from mode 2 to mode 3 IL response takes place at slightly higher velocities than what was observed during the model tests. As a result, Parameter Set No. 7 seems to be able to predict mode 2 IL vibrations at the velocity of 0.1 m/s, something that was also observed experimentally but is not predicted by Parameter Set No. 8. Finally, both parameter sets cannot predict the drop of the dominant IL vibration from mode 3 to mode 2 at the velocity of 0.2 m/s. These two specific velocities for which the above discrepancies become evident will be examined in more detail in section 6.4 with regard to the overall optimum parameter set. As for the the cross-flow vibration modes, the exact same findings that were presented in section 6.1.1 become also evident here, since for both examined parameter sets, the TD VIV model agrees well both with the experiments and with the frequency domain analysis for all the considered current velocities up to 0.2 m/s, but it is not able to predict the third CF vibration mode that was observed during the model tests for the highest examined current velocities.

The above observations can also be verified by the respective findings of the time domain analysis with regard to the predicted dominant vibration frequencies in the IL and CF directions, as presented in Figures 6.5a - 6.5b and 6.6a - 6.6b. From these Figures it becomes apparent that for both examined parameter sets, the TD VIV model seems to predict dominant IL and CF vibration frequencies that are in general in very good agreement with the respective experimental data. To be more precise, as far as the CF response frequencies are concerned, it becomes clear that Parameter Set No. 8 gives slightly better results than Parameter Set No. 7, since, because of the smaller value of $\hat{f}_{0,y}$, the latter seems to constantly underestimate the dominant CF vibration frequencies for the whole range of the examined current velocities. As for the IL direction, Parameter Set No. 8 gives again improved results compared to the other case, since it predicts almost the same dominant IL vibration frequencies as observed during the experiments.

More specifically, in Figure 6.6a it becomes clear that the most important deviations between the experiments and Parameter Set No. 8 can be observed at the lower considered velocities as well as for the velocities of 0.1 and 0.2 m/s, for which differences with regard to the predicted vibration modes were also observed previously. As far as the lowest velocities are concerned, the fact that the change from mode 1 to mode 2 and from mode 2 to mode 3 IL response takes place at slightly higher velocities results in the prediction of lower response frequencies in this velocity range. As for the velocities of 0.1 and 0.2 m/s, the differences between the numerical results and the experimental data can mainly be attributed to the existence of multi-frequency IL response at these velocities, since it becomes apparent in Figure 6.6b that, when the frequencies corresponding to the second highest peak in the response spectra obtained for these two velocities are used instead, the results of the TD VIV model are almost identical to the experimental data. Finally, as far as Parameter Set No. 7 is concerned, much more profound deviations from the experiments can be observed in Figure 6.5a. Apart from the lowest examined velocities for which the same issues and explanations that were analysed for Parameter Set No. 8 are also valid, significant differences between the numerical results and the experimental data can also be observed for the whole range of current velocities above 0.15 m/s. For this velocity range the existence of multi-frequency response is again observed, however in this case using the second highest peak frequency in the respective response spectra does not improve much the obtained results with regard to the predicted IL response frequency, as illustrated in Figure 6.5b, although this Figure is in agreement with the predicted dominant IL vibration modes (see Figure 6.5c).

What is more, as illustrated in Figures 6.5d and 6.6d, both examined parameter sets seem to give quite good results with regard to the predicted IL response amplitudes. More specifically, Parameter Set No. 7 seems to constantly give somewhat higher values for the IL vibration amplitude than what was observed during the model tests. Contrary to this, Parameter Set No. 8 for some velocities slightly underestimates the experimental data and for some velocities it slightly overestimates them. However, a very significant finding has to do with the fact that Parameter Set No. 8 overestimates the IL response amplitude for the velocity range between 0.025 m/s and 0.08 m/s for which it predicts lower response frequency than the experiments while the exact opposite behaviour can be observe for velocities around 0.2 m/s. This observation indicates that in fact Parameter Set No. 8 will ultimately give better results for the respective fatigue damage accumulation than Parameter Set No. 7, which constantly overestimates the IL response amplitude regardless of the corresponding vibration frequency. As for the the cross-flow response amplitudes, the exact same findings that were presented in section 6.1.1 become also evident here, since the TD analysis overestimates the CF response for the whole range of the examined current velocities, something that is especially apparent for lowest velocities. To be more precise, the smaller value of $\hat{f}_{0,y}$ used in Parameter Set No. 7 led on the one hand to the shift of the corresponding curve to the right and consequently to improved results for the lower considered velocities compared to the respective findings for Parameter Set No. 8. On the other hand though, this also resulted in the prediction of much higher CF response amplitudes for the rest of the examined velocities above 0.08 m/s when Parameter Set No. 7 is used. This is a very significant finding, since the CF vibrations are almost negligible for the lower part of the examined current velocities, while they dominate the total response at higher velocities. So ultimately, from all the above mentioned observations and differences between the results obtained using Parameter Set No. 7 and Parameter Set No. 8, it can be concluded that as far as Test Series 10 is concerned, Parameter Set No. 8 is the optimum parameter set and captures the VIV response observed during the model tests quite accurately.

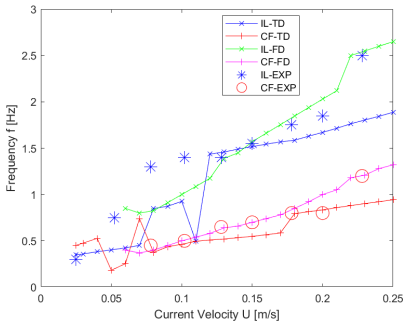

(a) Response Frequency vs Current Velocity

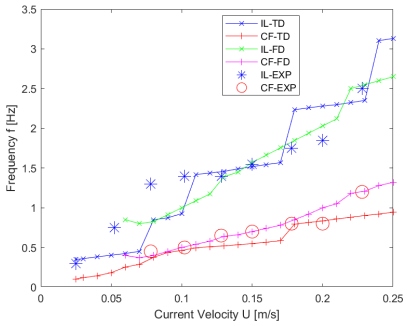

(b) Response Frequency vs Current Velocity (modified)

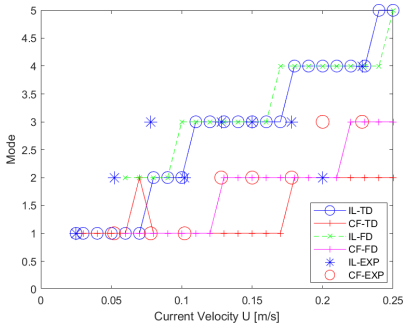

(c) Response Mode vs Current Velocity

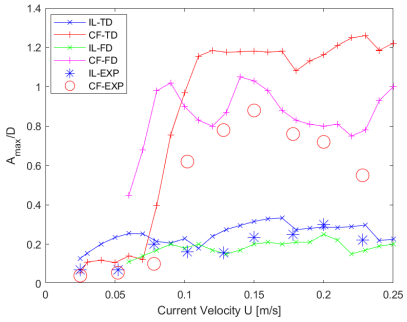

(d) Maximum response amplitude normalized by the pipe's diameter vs Current Velocity

Figure 6.5: Comparative plots of the fundamental results for Parameter Set No. 7.

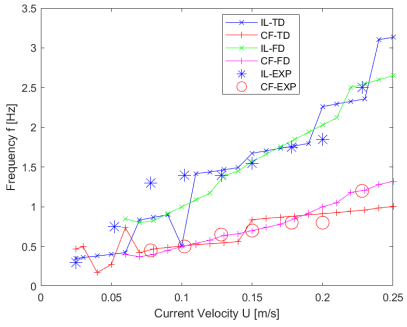

(a) Response Frequency vs Current Velocity

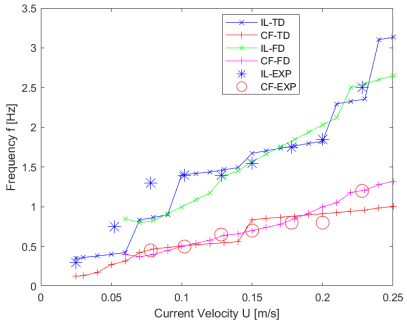

(b) Response Frequency vs Current Velocity (modified)

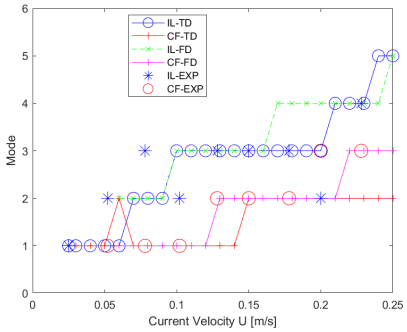

(c) Response Mode vs Current Velocity

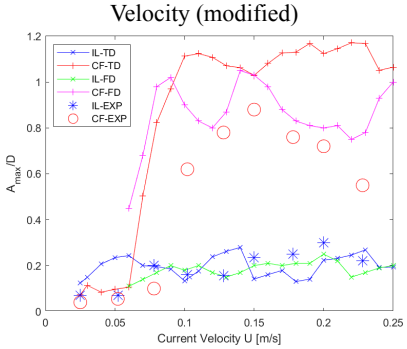

(d) Maximum response amplitude normalized by the pipe's diameter vs Current Velocity

Figure 6.6: Comparative plots of the fundamental results for Parameter Set No. 8.

6.2 Test Series 42

6.2.1 Application of initial hydrodynamic parameters in Test Series 42

As mentioned in section 5.4.1, the initial hydrodynamic coefficients that were used during the Project Thesis work, which correspond to Parameter Set No. 1 in Table 5.6, were also implemented with regard to Test Series 42 in order to serve as a starting point for the following calibration procedure. The response frequencies, the vibration mode numbers and the maximum response amplitudes normalized by the pipe's diameter that were calculated by means of the time domain analysis with regard to Parameter Set No.1 are illustrated in Figure 6.7 along with the respective experimental results and the findings of the frequency domain analysis performed by Passano, Wu and Larsen. Moreover, the same approach that was described in the previous sections was also followed for the analysis of the present case. That is, in Figure 6.7a the dominant response frequencies (i.e. corresponding to the highest peaks in the response spectra) are given, in Figure 6.7b the frequencies of the peaks that are closer to the respective experimental results are presented and in Figure 6.7c the frequencies of the peaks that correspond to the dominant vibration modes, which were identified based on snapshots of the captured response and are also presented in Figure 6.7d, are illustrated.

At a first glance at Figure 6.7, it becomes apparent that the results of the TD VIV model with regard to Test Series 42 are in quite good agreement with the respective experimental data as far as the CF response is concerned. However, some significant deviations can be observed with regard to the IL direction. More specifically, from Figures 6.7a - 6.7c it becomes clear that the predicted CF response frequencies are almost identical to those observed during the experiments for the whole range of the examined current velocities. Contrary to this, from Figure 6.7a it becomes evident that for velocities above 0.17 m/s the dominant IL response frequency predicted by the time domain analysis is much higher than the respective experimental results. At this point it is worth mentioning that for these velocities several significant peaks are present in the obtained IL response spectra. However, when the peak frequencies corresponding to the the dominant vibration modes identified on the basis of the obtained response snapshots are considered, the TD results give even higher IL response frequencies, as is clearly illustrated in Figure 6.7c. Nevertheless, there are also peaks in the response spectra at frequencies that are in better agreement with the experimentally estimated dominant IL response frequencies, as is shown in Figure 6.7b, but even in this Figure some non-negligible deviations from the experiments can also be observed. The above observations can also be verified by the respective findings of the time domain analysis with regard to the predicted dominant vibration modes in the IL and CF directions, as presented in Figure 6.7d. To be more precise, both the experiments and the frequency domain and time domain analyses give mode 1 CF vibrations for the whole range of examined velocities. As for the IL response, the experimental results give dominant mode 1 vibrations in the IL direction too for current velocities up to 0.4 m/s, while for the two highest velocities mode 2 IL response was captured during the model tests. Contrary to this, the frequency domain analysis predicts mode 2 IL vibrations for all the considered velocities, while the TD VIV model gives mode 2 IL response between 0.18 and 0.26 m/s and mode 3 vibrations for even higher velocities.

What is more, as illustrated in Figure 6.7e, the results of the time domain analysis with regard to the maximum CF response amplitude seem to be in quite good agreement with the respective experimental data for current velocities up to 0.3 m/s. As for the higher velocities, the TD VIV model seems to underestimate the CF response amplitudes in the range of current velocities between 0.31 and 0.4 m/s while it overestimates it for even higher velocities. The maximum deviation between the TD VIV model and the experiments can be observed at the velocities of

0.35 m/s and 0.45 m/s. At 0.35 m/s the maximum CF response amplitude of 1.2D was captured during the model tests, while the TD VIV model predicts a considerably smaller amplitude of 0.96D. The exact opposite trend becomes evident at 0.45 m/s, where the TD VIV model gives the maximum CF response amplitude of 1.025D, while the respective experimental result is only 0.75D. Finally, as far as the maximum IL response amplitudes are concerned, the time domain analysis gives quite good results for the lowest (0.1 m/s - 0.18 m/s) and the highest (0.4 m/s - 0.45 m/s) parts of the examined current velocity range, while for the intermediate current velocities, the TD VIV model constantly underestimates the maximum IL response amplitudes. In Figure 6.7e, the maximum deviation from the model tests becomes evident at the velocity of 0.3 m/s, for which the maximum IL response amplitude of 0.38D was captured during the experiments, while a vastly smaller amplitude of 0.14D is predicted by the time domain analysis.

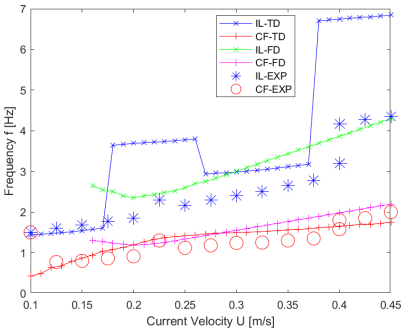

(a) Response Frequency vs Current Velocity

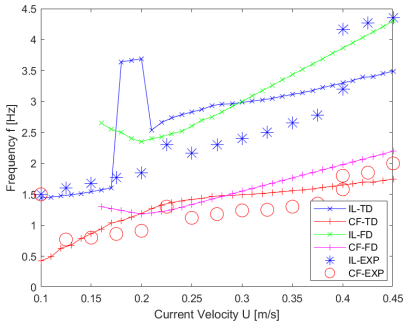

(b) Response Frequency vs Current Velocity (modified)

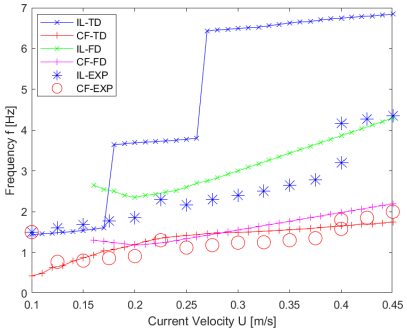

(c) Response Frequency vs Current Velocity (modified)

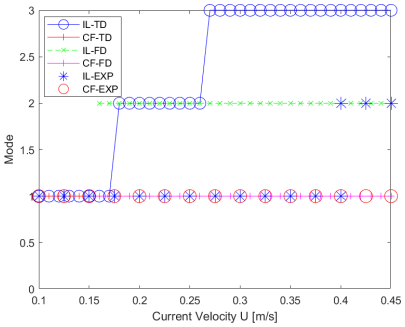

(d) Response Mode vs Current Velocity

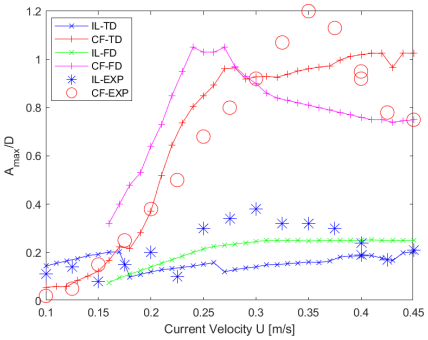

(e) Maximum response amplitude normalized by the pipe's diameter vs Current Velocity

Figure 6.7: Comparative plots of the fundamental results for Parameter Set No. 1.

6.2.2 The best two of the examined parameter sets

As was also the case in section 6.1.2, in the following only the findings corresponding to the two parameter sets that give the most improved results compared to the findings presented in section 6.2.1 regarding the initially used hydrodynamic coefficients will be presented. These are again Parameter Set No. 7 and Parameter Set No. 8. The obtained results corresponding to all the examined parameter sets can be found in Appendix A.2 (Figures A.12 - A.21). Moreover, it should be noted that the reduction of the values of $\hat{f}_{0,x}$ and $\hat{f}_{0,y}$ was found to have more or less the above mentioned effects on the estimated VIV response leading again in the prediction of smaller values for the dominant vibration frequencies in both directions and also in a small increase in the obtained results for the response amplitudes in both directions. The response frequencies, the vibration mode numbers and the maximum response amplitudes normalized by the pipe's diameter that were calculated by means of the time domain analysis with regard to Parameter Set No.7 and Parameter Set No.8 are illustrated in Figures 6.8 and 6.9 respectively along with the respective experimental results and the findings of the frequency domain analysis. In Figures 6.8a and 6.9a the dominant response frequencies (i.e. corresponding to the highest peaks in the response spectra) with respect to Parameter Set No. 7 and Parameter Set No. 8 are illustrated respectively. However, for current velocities above 0.2 m/s, more than one dominant peaks are again present in the obtained response spectra. So, in Figures 6.8b and 6.9b the response frequencies corresponding to the second highest peaks are presented.

At a first glance at Figures 6.8 and 6.9, it becomes apparent that these two parameter sets give again very similar results. More specifically, as far as the IL response is concerned the results obtained by the TD VIV model using these two parameter sets are almost identical. To begin with, taking a closer look at Figures 6.8a, 6.8c, 6.9a and 6.9c it becomes clear that both parameter sets seem to give very good results with regard to the dominant IL vibration frequencies and modes for the lower part of the examined current velocity range up to about 0.2 m/s. For higher velocities, both parameter sets in general seem to predict much higher IL response frequencies and as a result they also give dominant IL vibration mode 2 for the velocity range between 0.2 m/s and 0.42 m/s and mode 3 for the highest current velocities. Contrary to this, the results of the model tests give dominant mode 1 vibrations in the IL direction for current velocities up to 0.4 m/s and only for the two highest velocities that were tested during the experiments mode 2 IL response was captured. The only significant difference between the two parameter sets can be observed with regard to the predicted IL response frequency at the two highest current velocities, for which Parameter Set No. 7 underestimates the experimental results, while the opposite is true for Parameter Set No. 8. Moreover, another interesting finding, which also proves the similarity of the results of those two parameter sets with regard to the IL response, is the fact that both parameter sets predict approximately the same secondary peak frequencies for the whole range of relevant current velocities apart from the two highest velocities. This is clearly shown in Figures 6.8b and 6.9b, where both parameter sets seem to give much better results when the secondary peak frequencies are considered. Finally, as far as the maximum IL response amplitudes are concerned, it becomes apparent from Figures 6.8d and 6.9d that the findings of section 6.2.1 can be observed for both parameter sets examined here too. More specifically, the time domain analysis gives again quite good results for the lowest (0.1 m/s - 0.22 m/s) and the highest (0.4 m/s - 0.45 m/s) parts of the examined current velocity range but it constantly underestimates the maximum IL response amplitudes for the intermediate velocities.

What is more, as far as the CF response is concerned, it becomes evident that both parameter sets are in very good agreement with the respective experimental findings. To be more precise, from

Figures 6.8c and 6.9c, it becomes clear that both parameter sets give mode 1 CF vibrations for the whole range of examined velocities, something that was also observed during the model tests. Furthermore, in Figures 6.8a - 6.8b and 6.9a - 6.9b, it is seen that both parameter sets predict CF response frequencies that are almost identical to the experimental data. Nevertheless, because of the smaller value of $\hat{f}_{0,y}$ used for Parameter Set No. 7, it seems to slightly underestimate the CF response frequency for the lower and higher parts of the examined current velocity range and to give almost perfect results for intermediate velocities, while the exact opposite trend is apparent with regard to Parameter Set No. 8. Finally, the most important differences between the two parameter sets regards the predicted maximum CF response amplitudes and especially for current velocities below 0.3 m/s. This becomes apparent in Figures 6.8d and 6.9d. For this velocity range, Parameter Set No. 7 seems to slightly underestimate the CF response amplitude while the opposite is true for Parameter Set No. 8. However, for higher velocities the obtained results are quite similar. More specifically, both parameter sets accurately capture the maximum CF response amplitude of 1.2D that was observed at 0.35 m/s during the experiments. Above this velocity, both parameter sets overestimate the CF response, although it should be noted that Parameter Set No. 8 seems to give slightly better results for such high velocities. To sum up, from all the above mentioned observations, it is clear that the results obtained using these two parameter sets are almost identical and both of them capture the VIV response observed during the model tests quite accurately, especially with regard to the CF direction. However, based mainly on the fact that the only important difference between the two parameter sets is that Parameter Set No. 7 slightly underestimates the CF response amplitude for current velocities below 0.3 m/s, it can be concluded that as far as Test Series 42 is concerned, the optimum parameter set from the engineering point of view is Parameter Set No. 8, which gives somewhat more conservative results.

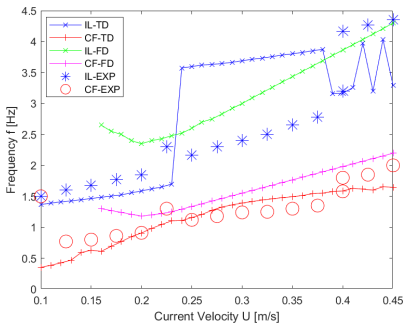

(a) Response Frequency vs Current Velocity

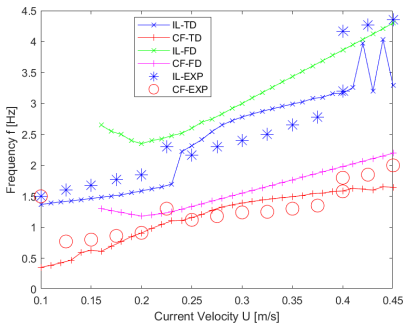

(b) Response Frequency vs Current Velocity (modified)

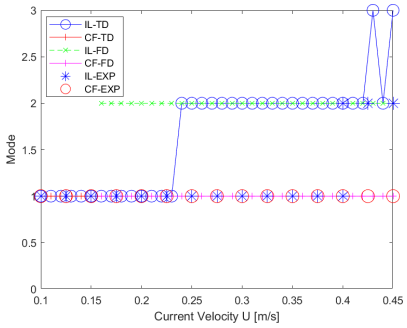

(c) Response Mode vs Current Velocity

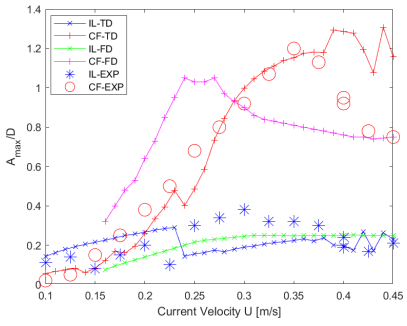

(d) Maximum response amplitude normalized by the pipe's diameter vs Current Velocity

Figure 6.8: Comparative plots of the fundamental results for Parameter Set No. 7.

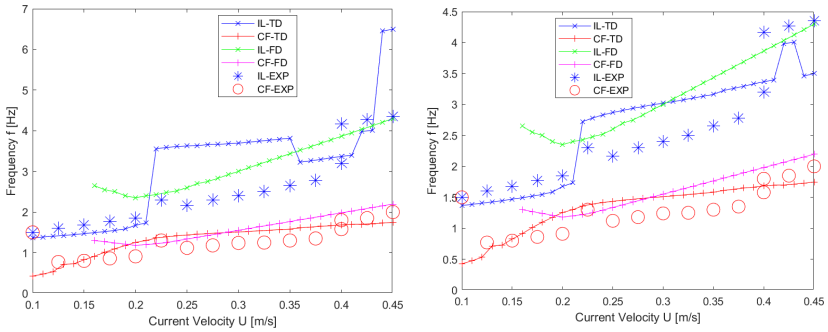

(a) Response Frequency vs Current Velocity

(b) Response Frequency vs Current Velocity (modified)

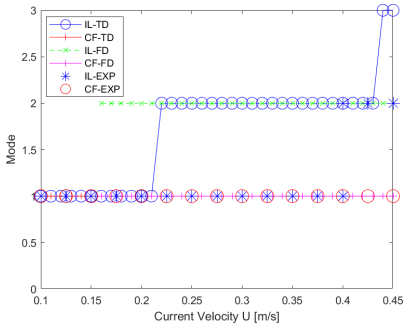

(c) Response Mode vs Current Velocity

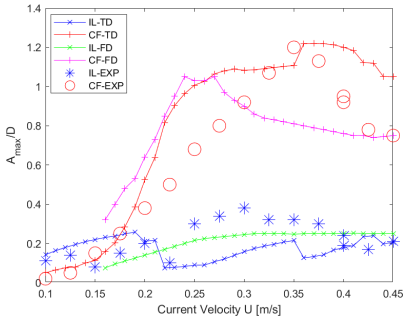

(d) Maximum response amplitude normalized by the pipe's diameter vs Current Velocity

Figure 6.9: Comparative plots of the fundamental results for Parameter Set No. 8.

6.3 Test Series 75

6.3.1 Application of the initial hydrodynamic parameters in Test Series 75

The time domain results for the response frequencies, the vibration mode numbers and the maximum response amplitudes normalized by the pipe's diameter regarding Test Series 75 and the initially used Parameter Set No.1 are illustrated in Figure 6.10 along with the respective experimental results and the findings of the frequency domain analysis. The results presented in this Figure will serve again as a starting point for the following calibration procedure. Following the same process as in the previous sections, in Figure 6.10a the dominant response frequencies (i.e. corresponding to the highest peaks in the response spectra) are given, while in Figures 6.10b and 6.10c the frequencies of the second and third highest peaks are presented respectively.

At a first glance at Figure 6.10, it becomes clear with respect to both the CF and the IL direction that the results of the time domain analysis regarding Test Series 75 are in quite good agreement with the respective experimental data for some of the examined current velocities but some non-negligible deviations from the experiments can also be observed. More specifically, as far as the CF response is concerned, it becomes apparent from Figures 6.10a, 6.10b, 6.10c and 6.10d that the results of the TD VIV model seem to be almost identical with the respective experimental data with regard to the predicted dominant CF response frequencies, while at the same time all three methods of analysis give mode 1 CF vibrations for the whole range of the examined velocities. However, in Figure 6.10e, some significant discrepancies between the numerically obtained results for the maximum CF response amplitudes and the respective values captured during the model tests become evident. To be more precise, although the TD VIV model gives an increasing trend for higher velocities, something that was also observed during the experiments,

it seems to constantly overestimate the CF response for all the considered current velocities. This deviation from the experiments becomes more and more profound as the current velocity increases, giving the maximum discrepancies at the highest part of velocity range between 0.45 m/s and 0.5 m/s, for which the TD VIV model predicts CF response amplitudes of about 0.95D-1.1D, while the respective experimental findings are about 0.52D-0.62D.

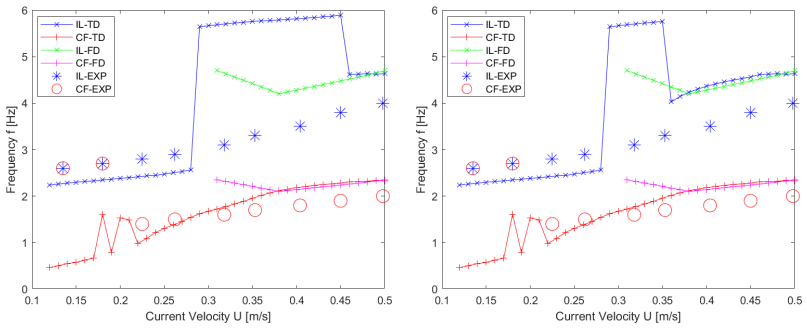

(a) Response Frequency vs Current Velocity

(b) Response Frequency vs Current Velocity (modified)

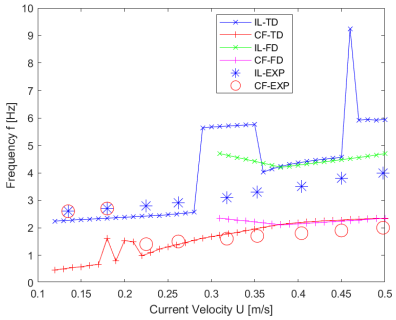

(c) Response Frequency vs Current Velocity (modified)

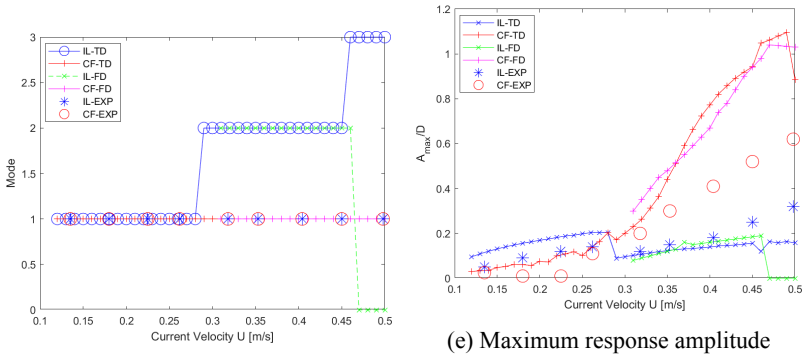

(d) Response Mode vs Current Velocity

(e) Maximum response amplitude normalized by the pipe's diameter vs Current Velocity

Figure 6.10: Comparative plots of the fundamental results for Parameter Set No. 1.

What is more, from Figures 6.10a, 6.10b, 6.10c and 6.10d it becomes clear that the results of the time domain analysis in general seem to be in quite good agreement with the respective experimental findings with regard to the predicted dominant IL response frequencies and the corresponding vibration modes for the lower part of the examined current velocity range up to 0.28 m/s. For higher velocities, the TD VIV model constantly overestimates significantly the IL response frequencies and as a result it predicts mode 2 dominant IL response for the range of current velocities between 0.29 m/s and 0.45 m/s and mode 3 IL response for even higher velocities. Contrary to this, during the experiments only dominant mode 1 IL vibrations were

observed. Finally, as far as the results for the maximum IL response amplitudes are concerned, in Figure 6.10e it can be seen that in general the findings of the time domain analysis agree quite well with the benchmark data. More specifically, the TD VIV model seems to slightly overestimate the IL response for the lower examined velocities up to 0.28 m/s, while the opposite behaviour becomes evident for higher velocities. The maximum deviation from the experiments can be observed at the highest examined velocity of 0.5 m/s, for which the numerically obtained IL response amplitude is equal to 0.158D while two times larger response of 0.32D was measured during the model tests.

6.3.2 The best two of the examined parameter sets

As was also the case for the other two Test Series which were analysed above, it was again found that Parameter Set No. 7 and Parameter Set No. 8 give the most improved results compared to the findings presented in section 6.3.1 and hence only the results corresponding to these two parameter sets will be presented in the following. The obtained results corresponding to all the examined parameter sets can be found in Appendix A.3 (Figures A.22 - A.31). The same observations, as described in detail previously, became again evident with regard to the effects that the reduction of the values of $\hat{f}_{0,x}$ and $\hat{f}_{0,y}$ has on the obtained results for the VIV responses and therefore they will not be further analysed here. The response frequencies, the vibration mode numbers and the maximum response amplitudes normalized by the pipe's diameter that were calculated by means of the time domain analysis with regard to Parameter Set No.7 and Parameter Set No.8 are illustrated in Figures 6.11 and 6.12 respectively along with the respective experimental results and the findings of the frequency domain analysis. In Figures 6.11a and 6.12a the dominant response frequencies (i.e. corresponding to the highest peaks in the response spectra) with respect to Parameter Set No. 7 and Parameter Set No. 8 are illustrated respectively, while in Figures 6.11b and 6.12b the response frequencies corresponding to the second highest peaks in the response spectra are presented. At this point it should be noted that, contrary to what was true with regard to Test Series 10 and 42, when Test Series 75 is considered, more than one dominant peaks are present in the response spectra obtained for several examined current velocities both with regard to the IL and to the CF directions.

On the basis of Figures 6.11 and 6.12, it becomes apparent that these two parameter sets give almost identical results with regard to the predicted IL response, while the observed differences are much more profound in the CF direction. More specifically, as far as the IL direction is concerned, from Figures 6.11a and 6.12a, it becomes clear that Parameter Set No. 7 and Parameter Set No. 8 predict somewhat lower dominant IL response frequencies than what was observed during the experiments for current velocities below 0.4 m/s and 0.38 m/s respectively, while the opposite trend becomes evident for higher velocities, for which both parameter sets overestimate significantly the IL response frequencies. Moreover, the existence of multi-frequency IL response above the aforementioned velocities can be verified by taking a closer look at Figures 6.11b and 6.12b with regard to both examined parameter sets. If for these velocity ranges the second highest peak frequencies are considered instead of the dominant ones, the predicted IL response frequencies seem to improve drastically. This is especially apparent for Parameter Set No. 7, which under the above assumption seems to be in almost perfect agreement with the experimental findings for the higher examined velocities. Furthermore, based on Figures 6.11c and 6.12c, it can be seen that both parameter sets give dominant mode 1 IL vibrations for the lower part of the examined velocity range, while the aforementioned overestimation of the IL frequency at higher velocities ultimately results in the prediction of mode 2 IL response there, something that is not in accordance with the respective findings of the model tests. As far as

the maximum IL response amplitudes are concerned, it becomes clear from Figures 6.11d and 6.12d that both parameter sets overestimate the predicted IL response amplitudes for the lower tested velocities, while the exact opposite behaviour can be observed at the higher part of the examined velocity range. Finally, as was also found in section 6.3.1 with regard to the initially used hydrodynamic coefficients, for both parameter sets the maximum discrepancies between the reference data and the numerically obtained results are observed at the highest velocity of 0.5 m/s, for which much smaller IL response amplitudes are predicted by the TD VIV model.

What is more, from Figures 6.11 and 6.12 it becomes evident that the results of the time domain analysis with regard to the CF response are for both parameter sets much closer to the reference data than what was observed previously for the IL direction. To be more precise, from Figures 6.11c and 6.12c it becomes clear that both parameter sets give mode 1 CF vibrations for the whole range of examined velocities, something that was also observed during the model tests. Furthermore, from Figures 6.11a and 6.12a it becomes clear that both parameter sets predict CF response frequencies that in general can be regarded as a fairly good approximation of the benchmark data. More specifically, due to the effect of the smaller value of $\hat{f}_{0,y}$ used for Parameter Set No. 7, it seems to constantly underestimate the CF response frequency for current velocities below 0.42 m/s while it gives almost perfect results for higher velocities. As for Parameter Set No. 8, it predicts the CF response frequencies very accurately for current velocities up to 0.3 m/s while it seems to slightly overestimate them above this velocity. However, it is worth mentioning that, as far as Test Series 75 is concerned, due to the aforementioned multi-frequency response that is present in the CF direction too, using the secondary peak frequencies improves the obtained results for the CF response frequencies considerably for both examined parameter sets, as is shown clearly in Figures 6.11b and 6.12b. Finally, from Figures 6.11d and 6.12d, it becomes evident that, when Parameter Set No. 8 is considered, the TD VIV model in general seems to overestimate the CF response for all the considered current velocities and this deviation from the experiments becomes more and more profound as the current velocity increases. As for Parameter Set No. 7, it seems to agree very well with the model tests. More precisely, it seems again to slightly overestimate the CF response for the lower and higher parts of the examined current velocity range, while it gives somewhat lower values of maximum CF response amplitude for intermediate current velocities between 0.3 m/s and 0.42 m/s, which is in contrast to the previous findings with regard to Parameter Set No. 8.

To sum up, from all the above mentioned observations, it is clear that the results obtained using Parameter Set No. 7 and Parameter Set No. 8 are almost identical with regard to the IL direction, while the observed behaviour for the CF direction is a bit more complicated. To be more precise, Parameter Set No. 8 seems to be in better agreement with the experimental data as far as the predicted CF vibration frequencies are concerned, while the opposite is true for the CF response amplitudes. So in order to be able to identify the best parameter set with regard to Test Series 75, an additional and very important finding has also to be taken into account. That is, for current velocities between 0.3 m/s and 0.42 m/s, Parameter Set No. 7 underestimates both the CF response frequencies and the respective vibration amplitudes. This is a clear indication that the fatigue damage accumulation will also be considerably underestimated for this velocity range in case this parameter set is implemented. For this reason, it can be concluded that, as far as Test Series 75 is concerned, the optimum parameter set from the engineering point of view is Parameter Set No. 8, which gives somewhat more conservative results. Finally, taking all the findings of sections 6.1.2, 6.2.2 and 6.3.2 into consideration, it becomes clear that the overall optimum parameter set for all three examined Test Series is Parameter Set No. 8 and therefore this parameter set will be utilized in the continuation of this Master's Thesis.

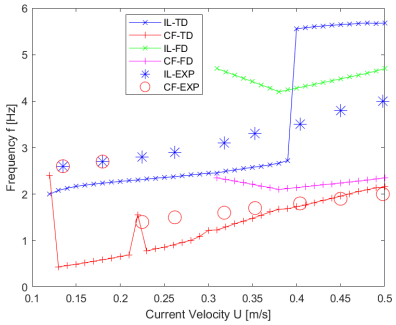

(a) Response Frequency vs Current Velocity

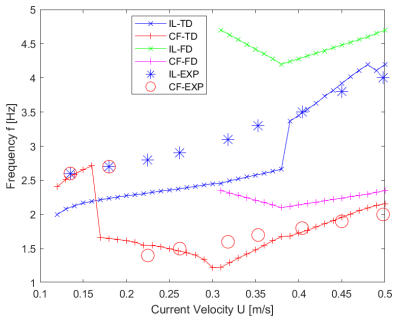

(b) Response Frequency vs Current Velocity (modified)

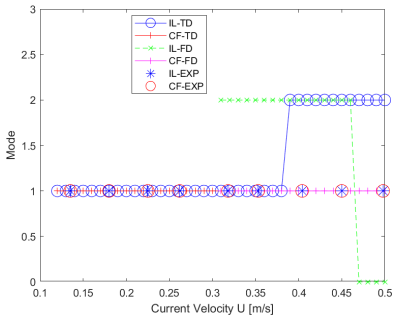

(c) Response Mode vs Current Velocity

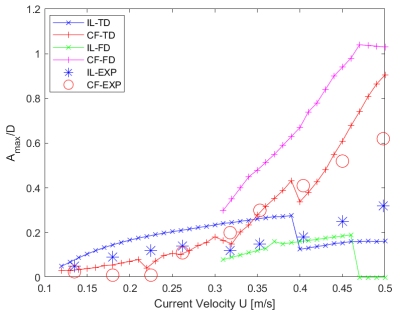

(d) Maximum response amplitude normalized by the pipe's diameter vs Current Velocity

Figure 6.11: Comparative plots of the fundamental results for Parameter Set No. 7.

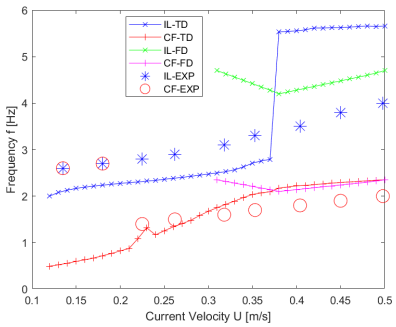

(a) Response Frequency vs Current Velocity

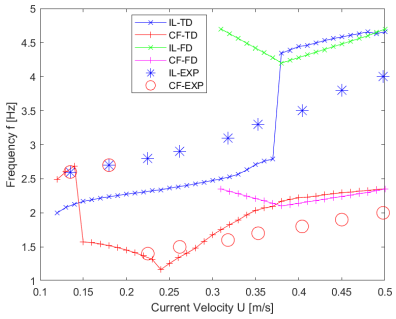

(b) Response Frequency vs Current Velocity (modified)

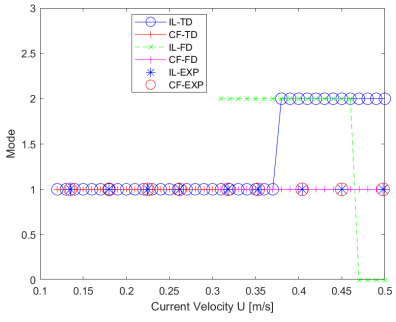

(c) Response Mode vs Current Velocity

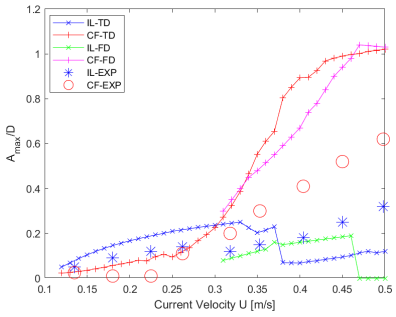

(d) Maximum response amplitude normalized by the pipe's diameter vs Current Velocity

Figure 6.12: Comparative plots of the fundamental results for Parameter Set No. 8.

6.4 In depth comparison between the results of the overall optimum Parameter Set and the experimental data

In sections 6.1 - 6.3 the overall optimum parameter set was identified by comparing the results obtained by means of the TD VIV model with the respective experimental data and the findings of the frequency domain analysis as they were presented by Passano, Wu and Larsen in [7]. The next step of this analysis was to verify that the chosen parameter set is indeed able to capture accurately the VIV responses observed during the model tests with regard to all three examined Test Series. In order to do so the results of the time domain analysis were compared in more depth with the experimental findings based entirely on the more detailed results reported by SINTEF Ocean in [47, 9, 48, 8]. The procedure followed by SINTEF Ocean in order to perform the modal analysis and obtain the aforementioned results is described in detail in [47, 9, 48, 8] and can be summarised in a few words as follows:

The estimation of the responses of the pipeline is based on the so-called "modal decomposition", which is based on the assumption that any time-dependent shape of the pipe can be expressed as a sum of eigenfunctions. Eigenfunctions of displacement ($\mathrm{e}_1^d(x), \mathrm{e}_2^d(x), \mathrm{e}_3^d(x), \ldots \quad x \in [0, L]$) and rotation ($\mathrm{e}_1^r(x), \mathrm{e}_2^r(x), \mathrm{e}_3^r(x), \ldots \quad x \in [0, L]$) were obtained using RIFLEX. Subsequently, eigenfunctions of curvature were estimated as such:

$$\mathrm{e}_i^c(x) = \frac{d\mathrm{e}_i^r(x)}{dx} = \frac{d^2\mathrm{e}_i^d(x)}{dx^2}, \quad i = 1, 2, 3, \ldots \tag{6.1}$$

Then, the curvature measurements at the positions of the strain gauges ($x_1, x_2, \ldots, x_{10}$) were written as a linear superposition of the above calculated curvature eigenfunctions and corresponding modal weights ($q_i(t), i = 1, 2, 3 \ldots$) as such:

$$m_i(t) = q_1(t)\mathrm{e}_1^c(x_i) + q_2(t)\mathrm{e}_2^c(x_i) + q_3(t)\mathrm{e}_3^c(x_1) + \ldots . \quad i = 1, 2, \ldots, 10 \tag{6.2}$$

So ultimately the system of equations of Eq. 6.3 was solved for the modal weights, and the displacements ($d(x,t)$) and the curvature ($c(x,t)$) at any given point were calculated by Eq. 6.4 - 6.5.

$$\begin{bmatrix} m_1(t) \\ m_2(t) \\ \vdots \\ m_{10}(t) \end{bmatrix} = \begin{bmatrix} e_1^c(x_1) & e_2^c(x_1) & \cdots & e_n^c(x_1) \\ e_1^c(x_2) & e_2^c(x_2) & \cdots & e_n^c(x_2) \\ \vdots & \vdots & & \vdots \\ e_1^c(x_{10}) & e_2^c(x_{10}) & \cdots & e_n^c(x_{10}) \end{bmatrix} \cdot \begin{bmatrix} q_1(t) \\ q_2(t) \\ \vdots \\ q_n(t) \end{bmatrix} \tag{6.3}$$

$$d(x,t) = q_1(t)\mathrm{e}_1^d(x) + q_2(t)\mathrm{e}_2^d(x) + \ldots + q_n(t)\mathrm{e}_n^d(x) \tag{6.4}$$

$$c(x,t) = q_1(t)\mathrm{e}_1^c(x) + q_2(t)\mathrm{e}_2^c(x) + \ldots + q_n(t)\mathrm{e}_n^c(x) \tag{6.5}$$

The results of the above procedure with regard to the modal weights, the frequency of the dominant vibration mode as well as of the rest of the active modes and the response amplitude for each one of the active modes were reported in [47, 9, 48, 8] in the form of tables and aggregate plots in full scale. For an easier comparison of the respective findings of the time domain analysis, which were presented in the previous sections, with these experimental results, the latter were transformed back to model scale and are summarized in Figures 6.13 - 6.14 and 6.15 - 6.16 with regard to Test Series 10 and Test Series 42 respectively. At this point it is worth noting that, because Test Series 75 was part of phase 3 of the experimental procedure, the way the obtained results were reported by SINTEF Ocean in [8] was different than for the previous Test Series and unfortunately only the data for the response amplitude for each one of the active modes were available. These results are summarized in Figure 6.17.

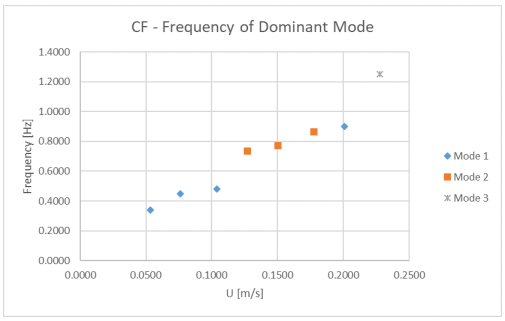

(a) CF - Frequency of Dominant Mode

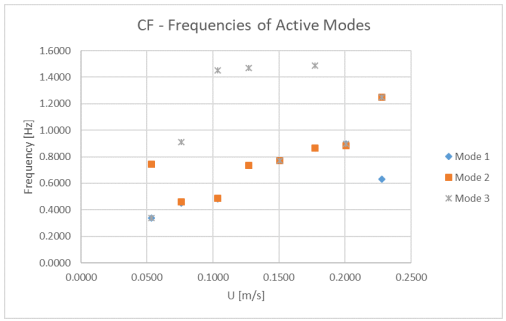

(b) CF - Frequencies of Active Modes

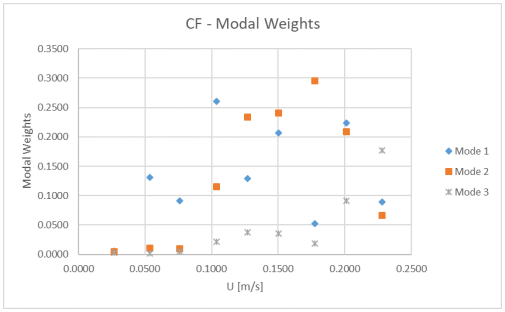

(c) CF - Modal Weights

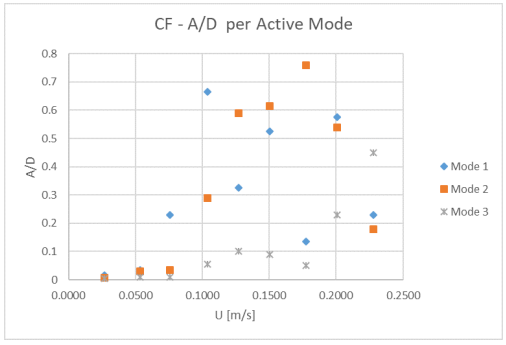

(d) Amplitude normalized by the pipe's diameter per Mode

Figure 6.13: Summary of the experimental results for the CF direction obtained via modal analysis for Test Series 10

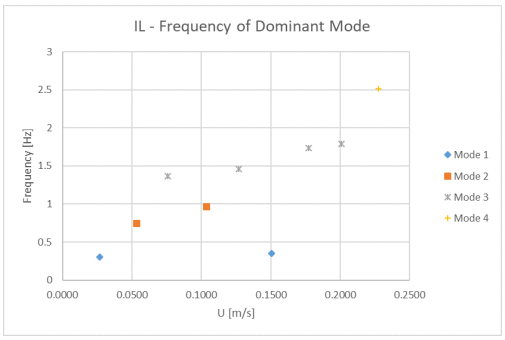

(a) IL - Frequency of Dominant Mode

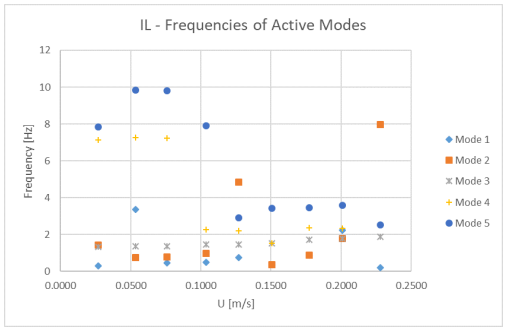

(b) IL - Frequencies of Active Modes

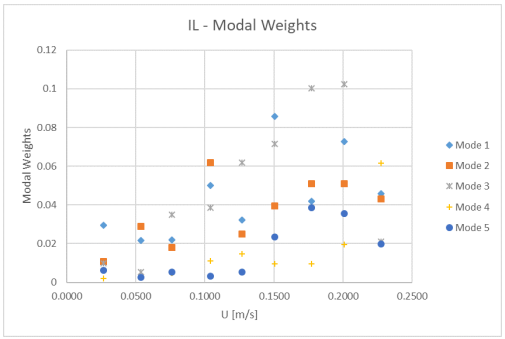

(c) IL - Modal Weights

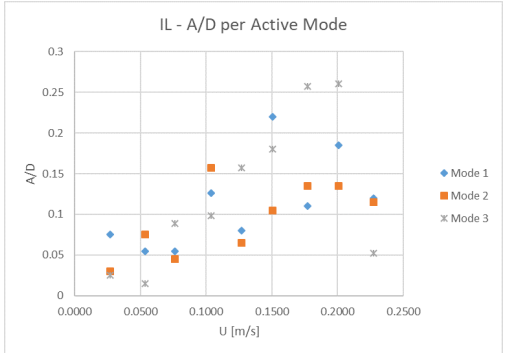

(d) IL - Amplitude normalized by the pipe's diameter per Mode

Figure 6.14: Summary of the experimental results for the IL direction obtained via modal analysis for Test Series 10

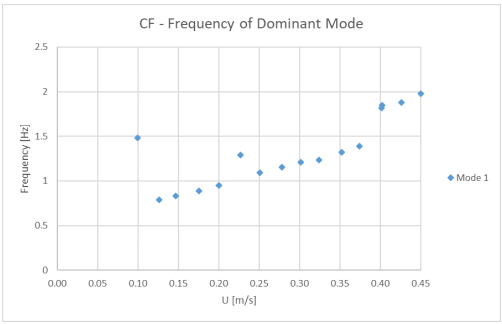

(a) CF - Frequency of Dominant Mode

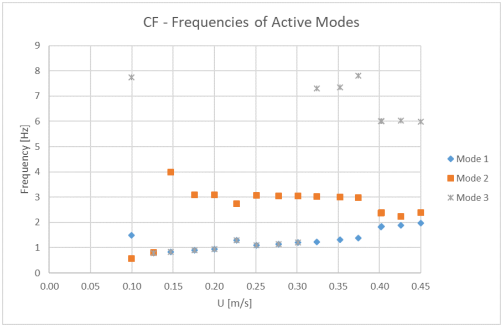

(b) CF - Frequencies of Active Modes

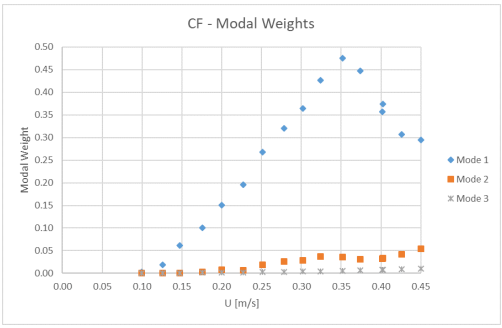

(c) CF - Modal Weights

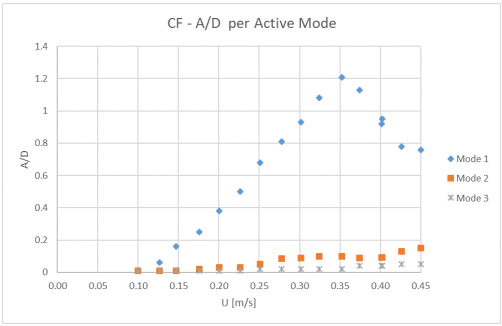

(d) Amplitude normalized by the pipe's diameter per Mode

Figure 6.15: Summary of the experimental results for the CF direction obtained via modal analysis for Test Series 42

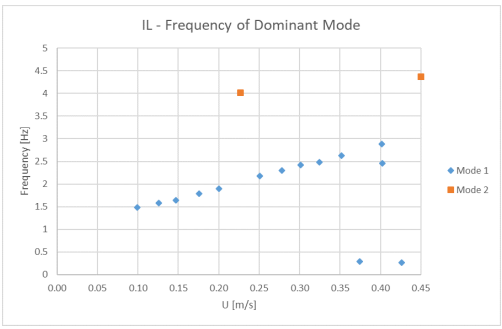

(a) IL - Frequency of Dominant Mode

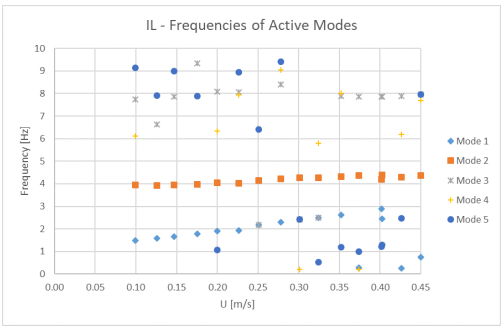

(b) IL - Frequencies of Active Modes

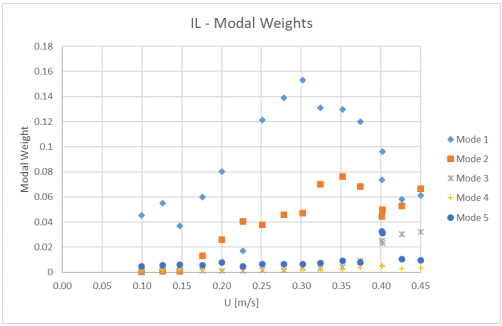

(c) IL - Modal Weights

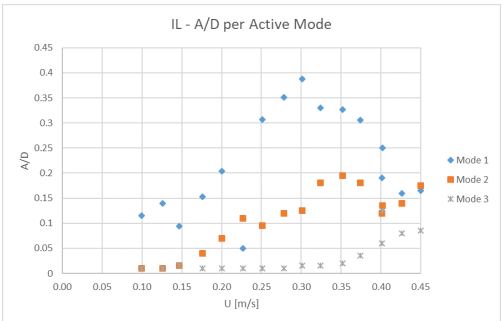

(d) IL - Amplitude normalized by the pipe's diameter per Mode

Figure 6.16: Summary of the experimental results for the IL direction obtained via modal analysis for Test Series 42

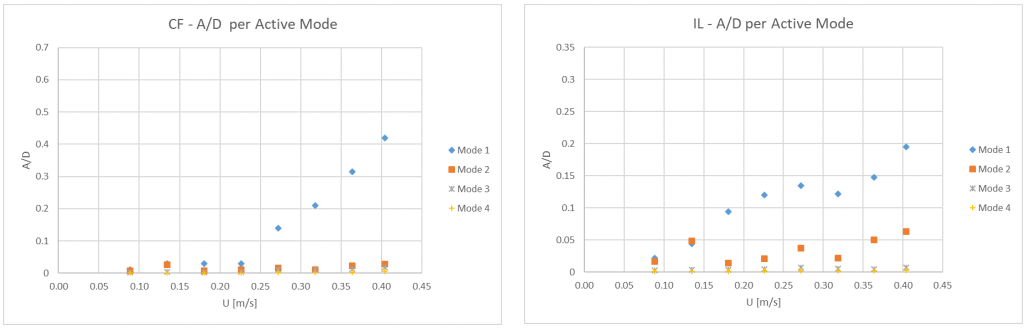

(a) Amplitude normalized by the pipe's diameter per Mode

(b) IL - Amplitude normalized by the pipe's diameter per Mode

Figure 6.17: Summary of the experimental results regarding the response amplitude normalized by the pipe's diameter per Mode for Test Series 75

AS a general remark, it becomes apparent from Figures 6.13 - 6.17 that for all three Test Series and both for the IL and CF directions more than one active vibration modes can be observed for several of the examined current velocities, something that verifies the above findings regarding the existence of multi-frequency response. Moreover, the most interesting finding of those Figures is the fact that there are some non-negligible deviations between the results of modal analysis presented here and the respective results presented by Passano, Wu and Larsen in [7] with regard to the total response of the pipeline that was measured during the model tests. For the sake of simplicity the results reported by SINTEF Ocean in [47, 9, 48, 8] will be hereafter be referred to as "the results of the modal analysis", while the respective findings of Passano, Wu and Larsen will be referred to as "the experimental results reported in [7]".

At this point it should be noted that, although the work of Passano, Wu and Larsen was based on the results of the modal analysis reported by SINTEF Ocean in [47, 9, 48, 8] too, Passano, Wu and Larsen also had access to additional data (e.g. the measurements of the strain gauges and the video recordings of the experiments to name but a few) and in this way they were able to calculate more accurately the actual total response of the pipeline, which was then reported in [7] and was also described in detail in the previous sections of the present thesis. Contrary to this, only the results of the modal analysis regarding the response of each mode separately were available for the purposes of this Master's Thesis and are presented in Figures 6.13 - 6.17. For this reason, it was preferred to use the data presented in [7] in the previous sections in order to calibrate the TD VIV model, taking into account that, due to the fact that modal analysis is a simplified way of analysing complex phenomena like VIV of flexible pipelines, there are some limitations on the level of accuracy of the obtained results. For this reason, there are several results that seem to be unphysical in the above presented Figures. For example, from Figures 6.14a and 6.14c it becomes apparent with regard to Test Series 10 and velocity 0.15 m/s, that modal analysis gives dominant mode 1 IL vibrations, while non negligible contributions from mode 3, mode 2, mode 4, mode 5 can also be observed. Moreover, from Figure 6.14b, it becomes evident that modal analysis gives the same frequency for modes 1 and 2 ($\approx 0.35Hz$) and modes 3 and 4 ($\approx 1.5Hz$). This is obviously not correct, something that becomes even more clear by observing that modal analysis at the same time gives mode 3 dominant IL vibrations with frequencies a bit lower and a bit higher that 1.5 Hz for the previous and the next examined velocity respectively. This issue was corrected by Passano, Wu and Larsen, who presented the right value of dominant IL frequency of about 1.5 Hz corresponding to mode 3 response, as is illustrated in Figure 6.6 and is also predicted by the TD VIV model.

However, there are also some cases for which such unreasonable results still remain present in the values reported by Passano, Wu and Larsen, and in fact these are the cases for which some significant deviations were observed between these results and the respective findings of the TD VIV model. So, the following analysis will focus entirely on a few specific velocities for each Test Series for which considerable differences between the experimental results and the TD VIV model were observed in the previous sections. All the available data obtained by means of the modal analysis, the TD VIV model and the experimental results presented by Passano, Wu and Larsen will be utilized in order to get a better understanding of the actual response of the pipeline and to see how accurate the TD VIV model is. More specifically, as far as Test Series 10 is concerned, the results corresponding to the velocities of 0.05 m/s, 0.1 m/s and 0.2 m/s will be examined. In Figures 6.18, 6.20 and 6.22 the experimentally obtained response time series (both with full length and zoomed at a smaller time interval) along with the respective response spectra and snapshots of the measured response and the time series (both with full length and zoomed at a smaller time interval) along with the respective spectra of the calculated modal weights are illustrated with regard to both the CF and the IL directions for the three aforementioned current velocities (Note: These Figure are in Full scale and not in model scale). In Figures 6.19, 6.21 and 6.23 the numerically obtained response time series (both with full length and zoomed at a smaller time interval) along with the respective response spectra and snapshots of the response calculated by the TD VIV model are illustrated with regard to both the CF and the IL directions for the same three velocities (Note: These Figure are in model scale).

To begin with, it was found using RIFLEX that the still water natural frequencies of the pipeline examined for Test Series 10 are 0.37, 0.85, 1.5, 2.38 and 3.495 Hz for the first 5 IL vibration modes and 0.495, 0.85 and 1.5 Hz for the first three CF vibration modes. Moreover, as far as the IL direction is concerned, it is found in Figure 6.6 that for the velocity of 0.05 m/s, the experimental data presented in [7] give dominant mode 2 IL vibrations with the corresponding frequency being equal to 0.75 Hz. Moreover, from the same Figure and also from Figure 6.19a, it becomes apparent that the TD VIV model gives dominant mode 1 IL vibrations at 0.4 Hz with a much smaller contribution from mode 2 IL vibrations at 0.8 Hz. Finally, modal analysis gives significant contributions from modes 2 and 1 at frequencies of 0.75 Hz and 3.37 Hz respectively and a much smaller contribution from the rest of the IL modes, as is clearly shown in Figures 6.14b and 6.14c. Of course the frequency of 3.37 Hz obtained via modal analysis for mode 1 is clearly wrong. However, from the spectrum in Figure 6.18c, it becomes apparent that as far as mode 1 is concerned, apart from a broad peak at the wrong frequency of 3.37 Hz (0.8171 Hz in full scale), a clear peak of the same height can be observed at the correct frequency of about 0.4 Hz ($\approx$ 0.096 Hz in full scale). So all in all, it can be concluded that the results of the TD VIV model are quite accurate, since the participation of both mode 1 and mode 2 and the correct vibration frequencies are predicted, and the only difference has to do with the percentage of contribution from each mode. This becomes also apparent from Figures 6.18b and 6.19b, where it is clear that contribution from both IL mode 1 and IL mode 2 response was captured during the experiments, while mode 1 IL vibrations dominate the response predicted by the TD VIV model. As for the CF direction, it becomes clear that the results of the time domain analysis are almost identical to the experimental data. More specifically, from Figures 6.13b and 6.13c, it is clear that modal analysis gives dominant mode 1 CF vibration at the frequency of 0.33 Hz and a small contribution from mode 2 at 0.74 Hz. The exact same observations become evident from the obtained CF response spectrum presented in Figure 6.19a, where a broad peak around 0.33 Hz can be observed (i.e. a dominant peak at 0.27 Hz and a smaller one at 0.4 Hz) and a secondary peak becomes cleat at 0.67 Hz corresponding to mode 2. Moreover, the fact that the results of the TD VIV model with regard to the CF direction are almost perfect becomes apparent

by comparing the CF response spectrum and the respective snapshot that were captured during the experiments (see Figures 6.18a and 6.18b) with the respective results of the time domain analysis illustrated in Figures 6.19a and 6.19b, which are almost identical.

What is more, as far as the velocity of 0.1 m/s is concerned, it is found in Figure 6.6 that the experimental data reported in [7] give dominant mode 2 IL vibrations, but the value reported for the dominant IL response frequency is equal to 1.45 Hz, which in fact corresponds to the third IL mode. Therefore, it is clear that there is a disagreement between these results. Furthermore, as far as the results of modal analysis are concerned, it becomes clear from Figures 6.14b, 6.14c and 6.20c that modes 1, 2 and 3 are all present in the observed IL response, with the largest contribution coming from mode 2. Mode 1 also contributes significantly to the IL response, while the importance of mode 3 seems to be somewhat smaller. Moreover, from these Figures it is also clear that modal analysis gives the correct frequencies for each of the aforementioned vibration modes. That is, mode 1 corresponds to 0.481 Hz, mode 2 to 0.97 Hz and mode 3 to 1.45 Hz. However, in order to get a better understanding of the actual IL response observed during the experiments, one should also focus in Figures 6.20b and 6.20a, in which snapshots of the actual response and the respective response spectra are illustrated. From Figure 6.20b it becomes clear that all three aforementioned IL modes were present during the model tests and in fact mode 3 seems to dominate the captured response. Moreover, from the IL response spectrum of Figure 6.20a it becomes apparent that, if one neglects the noise that can be observed at the lowest frequencies, because of the fact that the transient effects have not been removed from this Figure, the highest peak in the spectrum can be observed at the frequency of 0.481 Hz (i.e. 0.1165 Hz in full scale), the second highest peak at 1.45 Hz (i.e. 0.3517 Hz in full scale) and the third peak at 0.97 Hz (i.e. 0.2339 Hz in full scale). The findings of Figures 6.20b and 6.20a are in total agreement with the respective results of the time domain analysis, since in Figure 6.21a the highest peak in the IL response spectrum can be observed at the frequency of 0.5 Hz, the second highest peak at 1.4 Hz and the third peak at 1.01 Hz, while in Figure 6.21b the contribution of all three modes in the IL response becomes apparent and again mode 3 seems to dominate the calculated response. So it can be concluded that the TD VIV model captures very accurately the IL response observed during the model tests and in fact the results of the time domain analysis seem to be better than the respective findings of the traditionally used modal analysis.

As for the CF direction, it becomes clear that the results of the time domain analysis are almost identical to the experimental data, since all three methods of analysis give clear mode 1 CF vibrations at the frequency of 0.5 Hz. However, it becomes again apparent that modal analysis is a simplified method of analysis which is accompanied by a lot of limitations and an increased level of uncertainty. This becomes evident from Figures 6.13b, 6.13c and 6.20d, where apart from the dominant mode 1 CF vibrations, a significant contribution of mode 2 CF response is reported. However, modal analysis gives exactly the same CF vibration frequency for both mode 1 and mode 2, something that is unreasonable and verifies that in fact only mode 1 CF vibrations are present in the pipeline's response. This becomes apparent from Figures 6.20b and 6.21b, in which clear mode 1 CF vibrations can be observed in the response snapshots captured during the experiments and the snapshots calculated using the TD VIV model.

Finally, as far as the velocity of 0.2 m/s is concerned, it is found in Figure 6.6 that the experimental data reported in [7] are again unphysical. More specifically, the experiments seem to give dominant mode 2 IL vibrations at the velocity of 0.2 m/s, but the value reported for the dominant IL response frequency is equal to 1.85 Hz which again corresponds to the third IL mode. Furthermore, as far as the results of modal analysis are concerned, it becomes clear from

Figures 6.14b, 6.14c and 6.22c that modes 1, 2, 3, 4 and 5 are all present in the observed IL response, with the largest contribution coming from mode 3 instead. Modes 1 and 2 also contribute significantly to the IL response, while the importance of modes 4 and 5 seems to be somewhat smaller. Moreover, from these Figures it is also clear that modal analysis gives the exact same frequency for modes 1 and 4 ($\approx 2.3Hz$) and modes 2 and 3 ($\approx 1.8Hz$). This is obviously not correct, since the frequencies of 1.8 Hz and 2.3 Hz clearly correspond to mode 3 and mode 4 IL vibrations respectively. Therefore, from all the above observations, it becomes apparent that actually mode 3 and mode 4 vibrations dominate the IL response, something that verifies that the dominant IL vibration frequency of 1.85 Hz reported in [7] is indeed quite accurate, but it should correspond to mode 3 response and not to mode 2. These observation are also verified by the actual IL response observed during the experiments, which is illustrated in Figures 6.22b and 6.22a in terms of snapshots captured during the model tests and the respective response spectra. From Figure 6.22b it becomes clear that both mode 3 and mode 4 dominate the IL response of the pipeline, while in the IL response spectrum of Figure 6.22a (neglecting again the noise at the lowest frequencies), one dominant peak can be observed at the frequency of 1.94 Hz (i.e. 0.47 Hz in full scale), which is in fact in-between the frequencies of 1.8 Hz and 2.3 Hz corresponding to modes 3 and 4 respectively. All the above findings are in total agreement with the respective results of the time domain analysis, since in Figure 6.23a two dominant peaks corresponding to mode 3 and 4 IL response become apparent in the IL response spectrum at the frequencies of 1.824 Hz and 2.261 Hz. Moreover, a much smaller peak can also be observed at 0.436 Hz which corresponds to mode 1 IL vibrations. Finally, Figure 6.23b is almost identical to Figure 6.22b, since in both figures the dominant contribution from both modes 3 and 4 to the IL response becomes apparent. So, it becomes clear that the TD VIV model captures very accurately the IL response observed during the model tests and in fact it can again be concluded that the results of the time domain analysis seem to be better than the respective findings of the traditionally used modal analysis.

As for the CF direction, the TD VIV model seems to be again able to capture perfectly the response of the pipeline that was observed during the model tests. To be more precise, in Figure 6.6 it is found that the experimental data reported in [7] are unphysical with regard to the CF response at 0.2 m/s too. More specifically, the experiments seem to give dominant mode 3 CF vibrations at this velocity, but the value reported for the dominant CF response frequency is equal to 0.88 Hz, which clearly corresponds to the second CF mode. Furthermore, modal analysis seems again to give problematic results, since from Figures 6.13b, 6.13c and 6.22d it becomes clear that modal analysis gives non-negligible contribution from modes 1, 2 and 3 to the CF response of the pipeline. However, in Figure 6.13b the exact same frequency of $\approx 0.9Hz$ is reported for all three above mentioned modes. So taking into account that the dominant CF frequency of about 0.9 Hz is reported for the experimental results both in [7] and in the above results of modal analysis, it can be concluded that the actual response of the pipeline in the CF direction is dominated by second mode vibrations at frequency of about 0.9 Hz. These observations are also verified by the actual CF response illustrated in Figures 6.22b and 6.22a, in the first of which it becomes clear that the CF response is characterized by dominant mode 2 vibrations, while in the latter Figure one dominant peak at 0.9 Hz (i.e. 0.2178 Hz in full scale) can be observed. Finally, the findings of the TD VIV model are in total agreement with the above observations. This is illustrated clearly in Figures 6.23a and 6.22b where the dominant contribution of mode 2 in the CF response becomes immediately apparent and the respective vibration frequency is equal to 0.91 Hz.

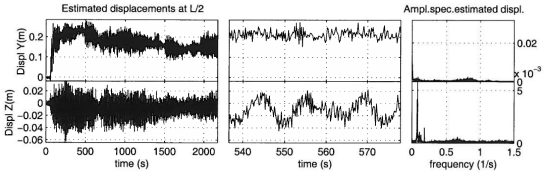

(a) Response Time Series and Spectra

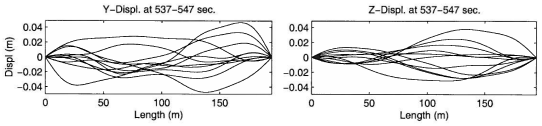

(b) Response Snapshots

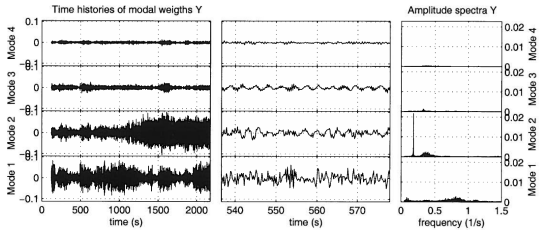

(c) IL - Modal Weights Time Series and Spectra

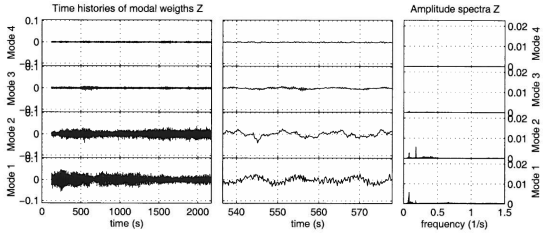

(d) CF - Modal Weights Time Series and Spectra

Figure 6.18: Summary of the experimental results for Test Series 10 at 0.05 m/s

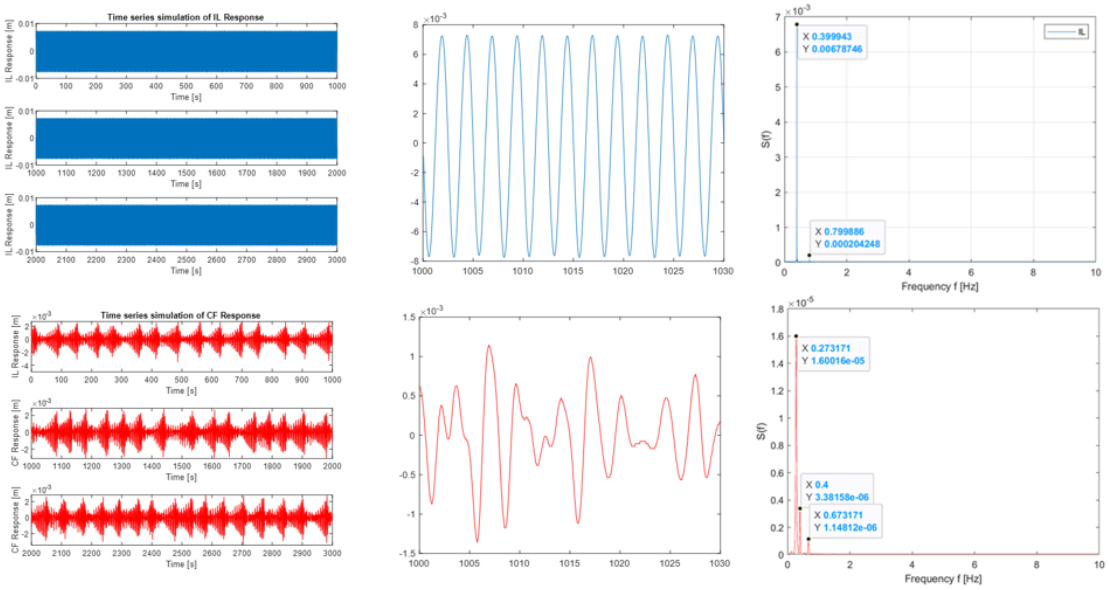

(a) Response Time Series and Spectra

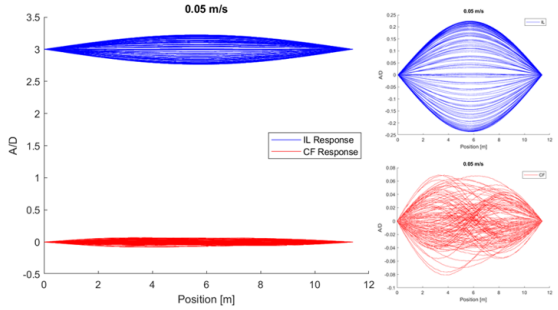

(b) Response Snapshots

Figure 6.19: Summary of the time domain analysis results for Test Series 10 at 0.05 m/s

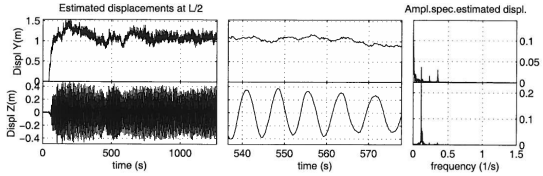

(a) Response Time Series and Spectra

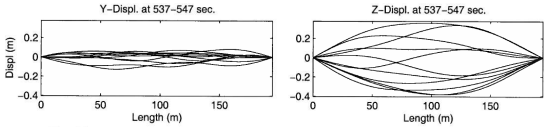

(b) Response Snapshots

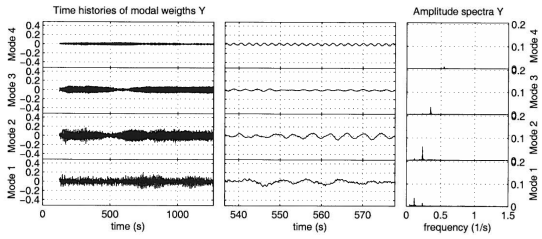

(c) IL - Modal Weights Time Series and Spectra

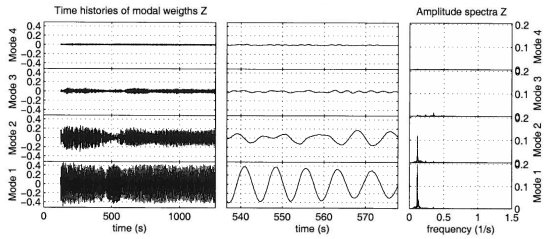

(d) CF - Modal Weights Time Series and Spectra

Figure 6.20: Summary of the experimental results for Test Series 10 at 0.1 m/s

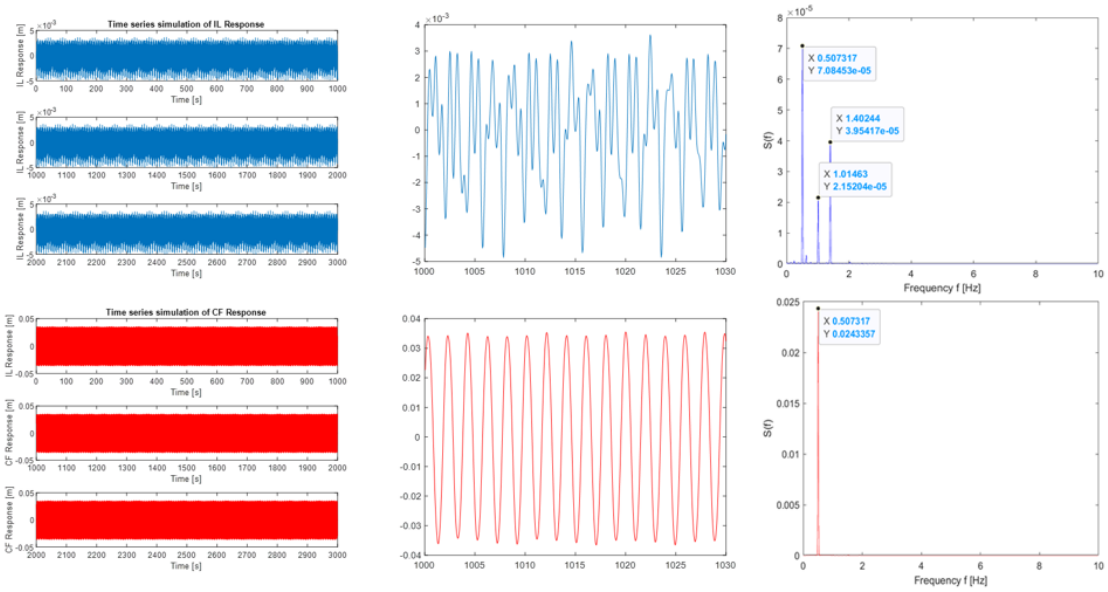

(a) Response Time Series and Spectra

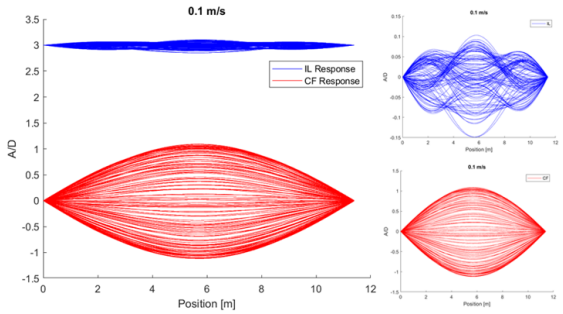

(b) Response Snapshots

Figure 6.21: Summary of the time domain analysis results for Test Series 10 at 0.1 m/s

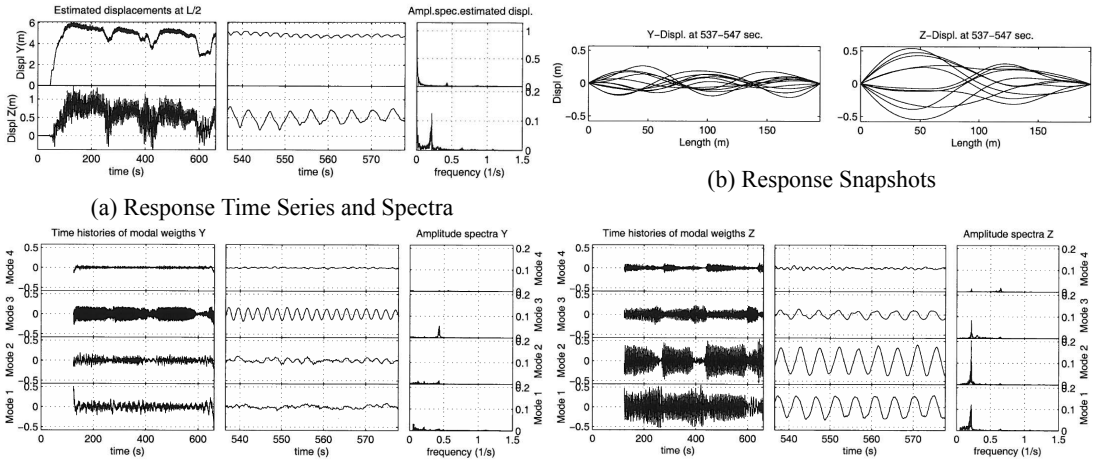

(a) Response Time Series and Spectra

(b) Response Snapshots

(c) IL - Modal Weights Time Series and Spectra

(d) CF - Modal Weights Time Series and Spectra

Figure 6.22: Summary of the experimental results for Test Series 10 at 0.2 m/s

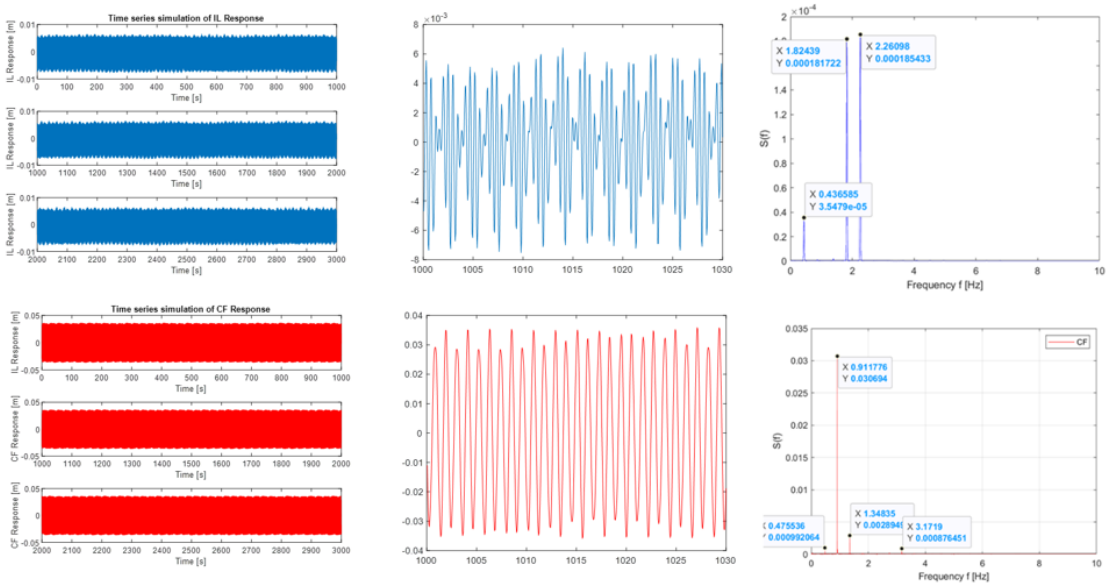

(a) Response Time Series and Spectra

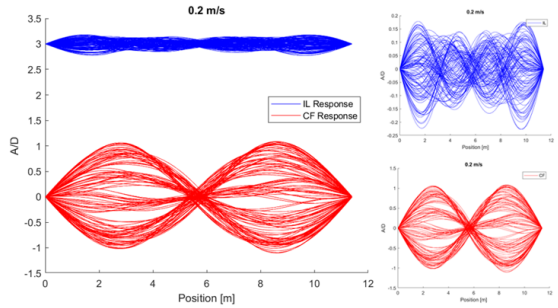

(b) Response Snapshots

Figure 6.23: Summary of the time domain analysis results for Test Series 10 at 0.2 m/s

As far as Test Series 42 is concerned, the results corresponding to the velocities of 0.2267 m/s, 0.4 m/s and 0.426 m/s will be examined. In Figures 6.24, 6.26 and 6.28 the experimentally obtained response time Series (both with full length and zoomed at a smaller time interval) along with the respective response spectra and snapshots of the measured response and the time series (both with full length and zoomed at a smaller time interval) along with the respective spectra of the calculated modal weights are illustrated with regard to both the CF and the IL directions for the three aforementioned current velocities (Note: These Figure are in Full scale and not in model scale). At this point it should also be noted that for the velocity of 0.4 m/s two separate experiments were conducted. However, because the results of the modal analysis for those two experiments were found to be almost identical, only one of them will be presented in the following. The second one can be found in Figure A.33 in Appendix A.4. In Figures 6.25, 6.27 and 6.29 the numerically obtained response time Series (both with full length and zoomed at a smaller time interval) along with the respective response spectra and snapshots of the response calculated by the TD VIV model are illustrated with regard to both the CF and the IL directions for the velocities of 0.22 m/s, 0.4 m/s and 0.42 m/s (Note: These Figures are in model scale). Finally, it should be noted that, because the velocities of 0.2267 m/s and 0.426 m/s, for which experiments were conducted, are in-between the velocities that were examined numerically, the TD results of the velocities of 0.23 m/s and 0.43 m/s were also examined but were found to be identical to those observed at 0.22 and 0.42 m/s respectively and thus will not be presented in the following. These results can be found in Figures A.32 and A.34 in Appendix A.4.

To begin with, it was found using RIFLEX that the still water natural frequencies of the pipeline examined for Test Series 42 are 1.45, 3.876 and 7.542 Hz for the first 3 vibration modes with regard to both the CF and the IL directions. Moreover, as far as the IL direction is concerned, it is found in Figure 6.9 that for the velocity of 0.2267 m/s, the experimental data presented in [7] give dominant mode 1 IL vibrations with the corresponding frequency being equal to 2.31 Hz. However, this frequency is in-between the above given values of 1.45 Hz and 3.876 Hz that correspond to mode 1 and mode 2 vibrations respectively. Contrary to this, from Figures 6.16a, 6.16b, 6.16c and 6.24c it becomes apparent that modal analysis gives that the IL response is dominated by mode 2 vibrations at the frequency of 4.015 Hz. Moreover, a non-negligible contribution from mode 1 IL vibrations at frequency of 1.927 Hz can also be observed. Again, in order to get a better understanding of the actual IL response observed during the experiments, one should also focus in Figures 6.24b and 6.24a in which snapshots of the actual response and the respective response spectra are illustrated. From Figure 6.24b it becomes evident that the IL response of the pipeline is characterized by an almost clear mode 2 vibration. However, the results presented in the IL response spectrum are somewhat more complicated, since a very broad-banded peak can be observed around the frequency of 2 Hz (i.e. 0.5 Hz in full scale). This broad-banded peak seams to extend from about 1.2 Hz (i.e. 0.3 Hz in full scale) to about 2.9 Hz (i.e. 0.7 Hz in full scale). From all the above findings, it can be concluded that the actual IL response is characterized by the existence of a multi-frequency response with significant contributions predominantly from mode 2 and to a lower degree from mode 1. These observations seem to be in quite good agreement with the respective findings of the time domain analysis, since in the IL response spectrum of Figure 6.25a the observed peaks cover the whole range of frequencies between which the aforementioned broad-banded peak of Figure 6.24a extends. More specifically, a dominant peak becomes evident at 3.558 Hz corresponding to mode 2 IL vibrations, a secondary peak can be observed at the frequency of 2.724 Hz, which is in-between the frequencies of mode 1 and mode 2, and a third peak becomes evident at 1.669 Hz corresponding to mode 1 IL response. Finally, in Figure 6.25b, almost clear mode 2 IL vibrations can be observed, something that is in total agreement with the respective findings of Figure 6.24b. As

for the CF direction, it becomes apparent that the results of the time domain analysis are almost identical to the experimental data. More specifically, from Figures 6.15b, 6.15c and 6.24d, it is seen that modal analysis gives clear and dominant mode 1 CF vibrations at the frequency of 1.3 Hz (i.e. 0.315 Hz in full scale). The exact same observations become evident in the CF response spectrum presented in Figure 6.25a which was obtained using the TD VIV model, where a clear peak at 1.36 Hz can be observed. Moreover, the fact that the results of the TD VIV model with regard to the CF direction are almost perfect becomes apparent by comparing the CF response spectrum and the respective snapshot that were captured during the experiments (see Figures 6.24a and 6.24b) with the respective results of the time domain analysis illustrated in Figures 6.25a and 6.25b, which are almost identical.

What is more, regarding the velocity of 0.4 m/s, it becomes clear that this specific velocity gives the most complicated response, especially with regard to the IL direction, and this is probably the reason why two tests were performed for this specific velocity. First of all, as far as the simpler CF response is concerned, it becomes apparent that the results of the time domain analysis are in very good agreement with the experimental data, since all three methods of analysis give clear mode 1 CF vibrations. More specifically, the experimental data reported in [7] give dominant CF response frequency of 1.58 Hz and 1.8 Hz with regard to the first and second experiments respectively. Furthermore, modal analysis gives dominant CF vibration frequencies of 1.82 and 1.85 Hz respectively, as is shown clearly in Figure 6.15a. Finally, from Figures 6.27a and 6.27b, it becomes apparent that the CF response predicted by the TD VIV model is characterised by clear mode 1 vibrations at frequency of 1.684 Hz.

Contrary to this, the response obtained for the IL direction is much more complicated and several unphysical results can be observed both with regard to the experimental data reported in [7] and to the results of modal analysis. To begin with, it is found in Figure 6.9, that the experimental data reported in [7] give dominant mode 1 IL vibrations and vibration frequency of 3.2 Hz for the first experiment, while dominant mode 2 IL vibrations and vibration frequency of 4.19 Hz was reported for the second experiment. Furthermore, as far as the results of modal analysis are concerned, it becomes clear from Figures 6.16b, 6.16c and 6.26c with regard to both performed experiments, that there is a significant contribution to the IL response of the pipeline from modes 1, 2, 5 and 3 in decreasing order of importance. However, taking a closer look in the vibration frequencies reported for each one of the aforementioned modes (see Figure 6.16b), it becomes immediately apparent that the results of modal analysis are unphysical. To be more precise, according to the results of modal analysis, vibration frequency of about 2.65 Hz is given for mode 1 which is reported as the dominant vibration mode. This frequency is between the above mentioned values of 1.45 and 3.876 Hz, which correspond to mode 1 and mode 2 respectively. Moreover, the correct frequency of about 4.2 Hz is reported for the second most important mode 2 IL vibrations. The third most contributing mode seems to be mode 5, for which the frequency of about 1.25 Hz is reported. Therefore, it is clear that the third most contributing mode is in fact mode 1. Finally, mode 3 seems to contribute to the IL response but to a smaller degree and for this mode the correct frequency of about 7.85 Hz is reported. From all the above findings, it can be concluded that the actual IL response is characterized by the existence of a multi-frequency response with significant contributions predominantly from mode 2 and to a lower degree from modes 1 and 3. These observations are also verified by the snapshots of the IL response that were captured during the experiments and are illustrated in Figure 6.26b. Finally, all the above findings seem to be in very good agreement with the results obtained using the TD VIV model. To be more precise, in Figure 6.27a a dominant peak becomes evident at 3.368 Hz corresponding to mode 2 IL vibrations, a secondary peak can be observed at the frequency of 6.375 Hz

which is in-between the frequencies of mode 2 and mode 3 but closer to mode 3 and a third peak becomes evident at 1.684 Hz corresponding to mode 1 IL response. Finally, Figure 6.27b seems to be in total agreement with Figure 6.26b, since in both Figures the contribution from all three aforementioned modes to the IL response of the pipeline is evident.

Finally, as far as the velocity of 0.426 m/s is concerned, in general the same observations as for the velocity of 0.4 m/s become evident. To begin with, as far as the CF response is concerned, it becomes apparent that the results of the time domain analysis are in very good agreement with the experimental data, since all three methods of analysis give clear mode 1 CF vibrations. More specifically, the experimental data reported in [7] give dominant CF response frequency of 1.85 Hz, the modal analysis gives 1.88 Hz and the TD VIV model predicts a slightly lower value for the dominant CF response frequency of 1.7 Hz, as is shown clearly in Figures 6.15a and 6.9. Finally, from Figures 6.28b and 6.27b it becomes apparent that the snapshots of CF response captured during the model tests and the respective snapshots calculated by the TD VIV model are almost identical. As for the IL direction, in Figure 6.9 it is found that the experimental data reported in [7] give dominant mode 2 IL vibrations and vibration frequency of 4.27 Hz. Furthermore, as far as the results of modal analysis are concerned, it becomes clear from Figures 6.16b, 6.16c and 6.28c that there is a significant contribution to the IL response of the pipeline from modes 1, 2, 3 and 5 in decreasing order of importance. However, taking a closer look in the vibration frequencies reported for each one of the aforementioned modes (see Figure 6.16b), it becomes immediately apparent that the results of modal analysis are again unphysical. To be more precise, according to the results of modal analysis, vibration frequency of 0.269 Hz is given for mode 1 which is reported as the dominant vibration mode. It is obvious that this frequency is totally unphysical and does not correspond to any vibration mode. Moreover, the correct frequencies of 4.3 Hz and 7.88 Hz are reported for the second and third IL vibration modes. Finally, the wrong frequency of 2.47 Hz is reported with regard to mode 5, which in practice is in-between the above mentioned values of 1.45 and 3.876 Hz which correspond to mode 1 and mode 2 respectively. From all the above findings, it can be concluded that the actual IL response is characterized by the existence of a multi-frequency response, in which the dominant contribution comes from mode 2, while modes 1 and 3 are also present but to a much smaller degree. These observations are also verified by the snapshots of the IL response that were captured during the experiments, in which almost clear mode 2 IL vibrations can be observed, as is shown in Figure 6.28b. Moreover, all the above findings seem to be in quite good agreement with the results obtained using the TD VIV model. To be more precise, in Figure 6.29a a dominant peak becomes evident at 3.98 Hz corresponding to mode 2 IL vibrations, a secondary peak can be observed at the frequency of 3.39 Hz which is in-between the frequencies of mode 1 and mode 2 but closer to mode 2 and a third and much smaller peak becomes evident at 1.7 Hz corresponding to mode 1 IL response. Finally, Figure 6.29b seems to be in total agreement with Figure 6.28b, giving again almost clear mode 2 IL response.

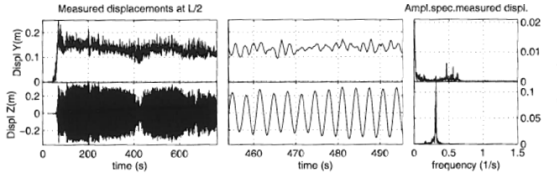

(a) Response Time Series and Spectra

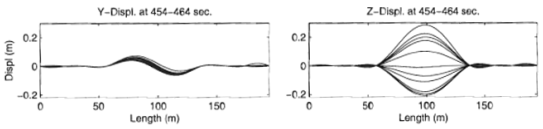

(b) Response Snapshots

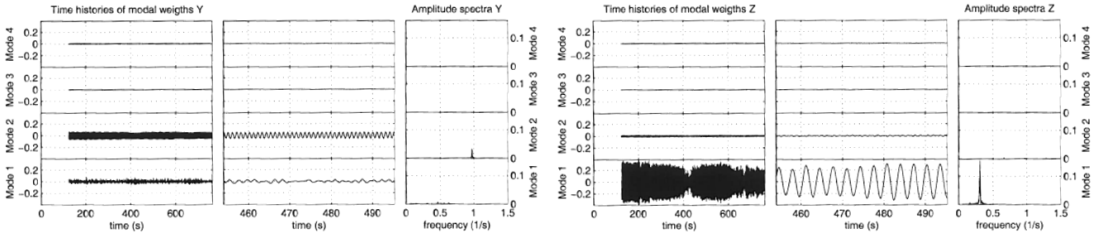

(c) IL - Modal Weights Time Series and Spectra

(d) CF - Modal Weights Time Series and Spectra

Figure 6.24: Summary of the experimental results for Test Series 42 at 0.2267 m/s

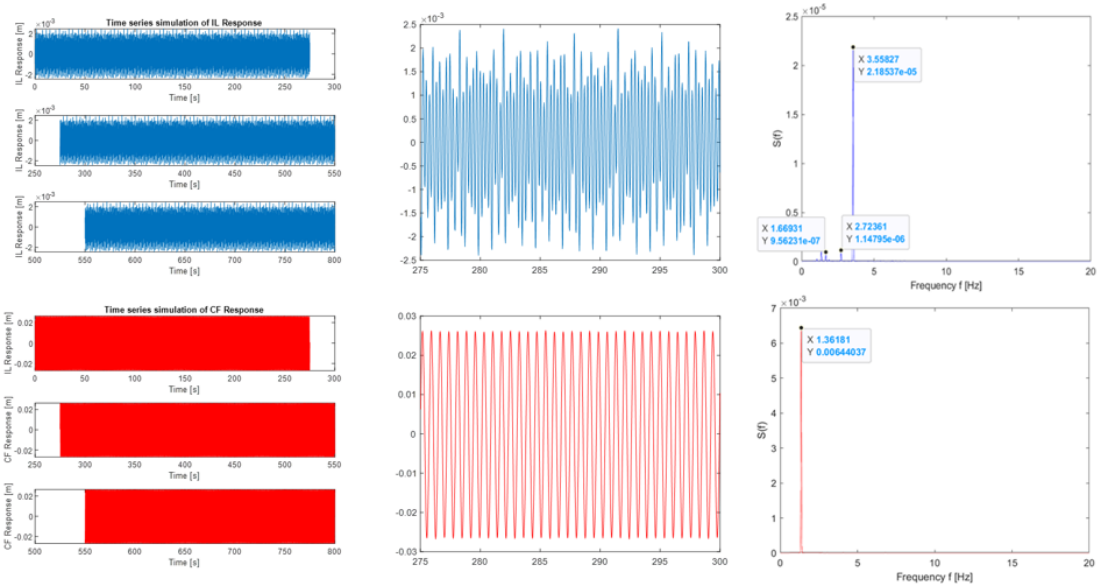

(a) Response Time Series and Spectra

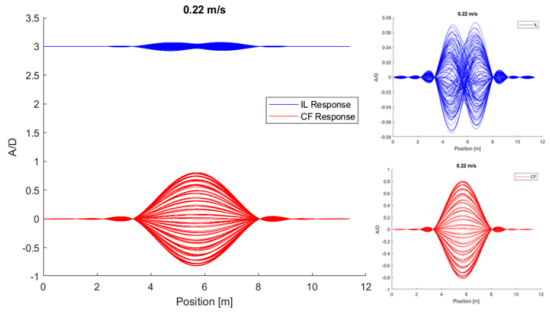

(b) Response Snapshots

Figure 6.25: Summary of the time domain analysis results for Test Series 42 at 0.22 m/s

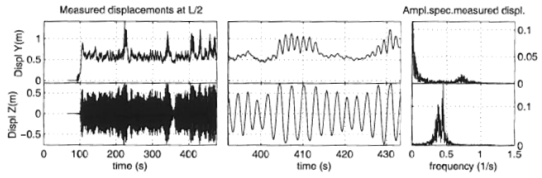

(a) Response Time Series and Spectra

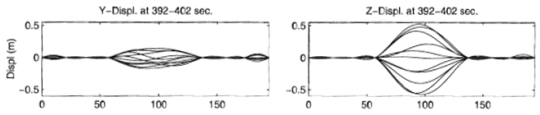

(b) Response Snapshots

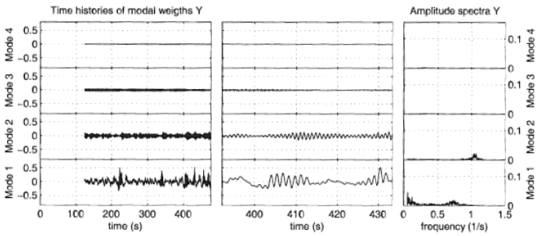

(c) IL - Modal Weights Time Series and Spectra

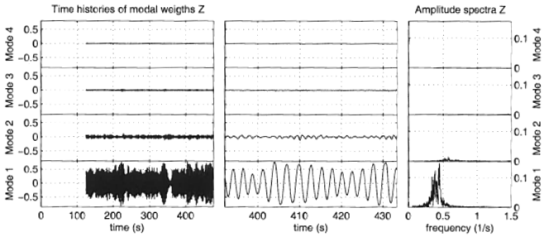

(d) CF - Modal Weights Time Series and Spectra

Figure 6.26: Summary of the experimental results for Test Series 42 at 0.4 m/s

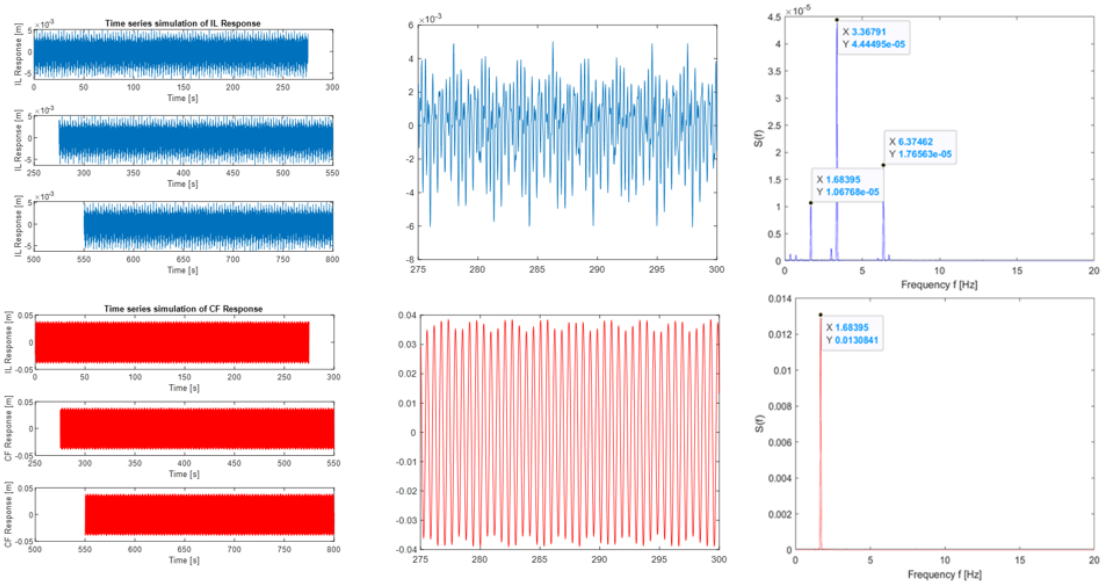

(a) Response Time Series and Spectra

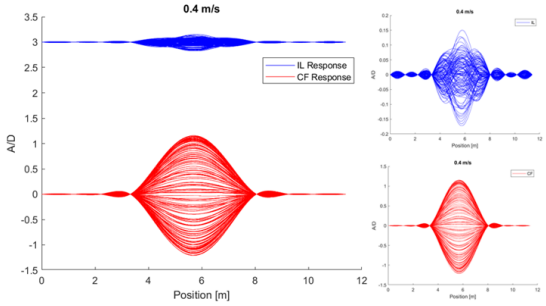

(b) Response Snapshots

Figure 6.27: Summary of the time domain analysis results for Test Series 42 at 0.4 m/s

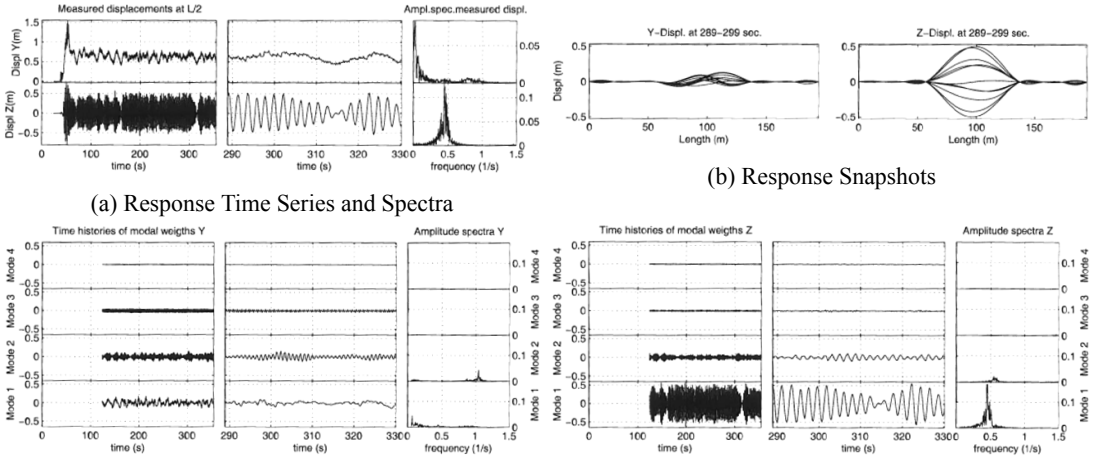

(a) Response Time Series and Spectra

(b) Response Snapshots

(c) IL - Modal Weights Time Series and Spectra

(d) CF - Modal Weights Time Series and Spectra

Figure 6.28: Summary of the experimental results for Test Series 42 at 0.426 m/s

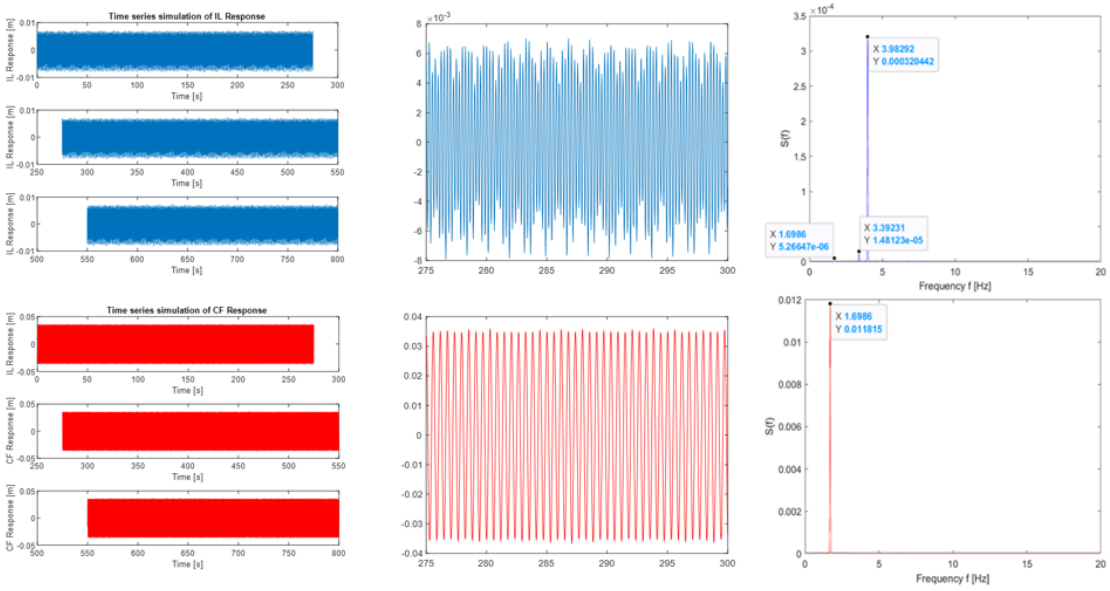

(a) Response Time Series and Spectra

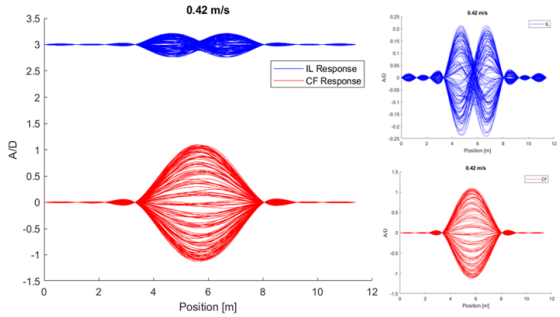

(b) Response Snapshots

Figure 6.29: Summary of the time domain analysis results for Test Series 42 at 0.42 m/s

Finally, as far as Test Series 75 is concerned, it was explained above that, due to the fact that these model tests were part of phase 3 of the experimental procedure, limited data were reported in [8] with regard to this Test Series. For this reason, more detailed experimental results were available only for the velocities of 0.27 m/s and 0.4 m/s and these two velocities are the ones that are going to be investigated in the following. In Figures 6.30 and 6.32, snapshots of the measured response that were captured during the model tests and the time series (both with full length and zoomed at a smaller time interval) along with the respective spectra of the calculated modal weights are illustrated with regard to both the CF and the IL directions for the two aforementioned current velocities (Note: These Figures are in Full scale and not in model scale). Moreover, in Figures 6.31 and 6.33, the numerically obtained response spectra and snapshots of the response calculated by the TD VIV model are illustrated with regard to both the CF and the IL directions for the same two velocities (Note: These Figures are in model scale).

To begin with, it was found using RIFLEX that the still water natural frequencies of the pipeline examined for Test Series 75 are 2.347 and 5.794 Hz for the first 2 vibration modes with regard to both the CF and the IL directions. Moreover, as far as the IL direction is concerned, it is found in Figure 6.12 that for the velocity of 0.27 m/s the experimental data presented in [7] give dominant mode 1 IL vibrations with the corresponding frequency being equal to 2.9 Hz. These findings are in total agreement with the respective results of the modal analysis and the time domain analysis, since from Figures 6.30b and 6.31a it becomes apparent that both methods of analysis give that the IL response is dominated by mode 1 vibrations at the frequencies of 2.936 Hz (i.e. 0.6241 Hz in full scale) and 2.4 Hz respectively. This is also verified by the snapshots of the actual response that where captured during the model tests and the respective snapshots calculated by means of the TD VIV model, since in Figures 6.30a and 6.31b it is clear that that the IL response of the pipeline is characterised by clear mode 1 vibrations. As for the CF direction, it becomes apparent that the results of the time domain analysis are again in very good agreement with the experimental data, since all three methods of analysis give clear mode 1 CF vibrations. More specifically, the experimental data reported in [7] give dominant CF response frequency of 1.48 Hz, while modal analysis gives dominant CF vibration frequency of 1.4644 Hz (i.e. 0.3113 Hz in full scale), as is shown clearly in Figures 6.12 and 6.30b respectively. Finally, from Figure 6.31a it becomes clear that there is only one dominant peak in the CF response spectrum predicted by the TD VIV model at the frequency of 1.4 Hz. The snapshots of the actual response that where captured during the model tests and the respective snapshots calculated by means of the TD VIV model are again almost identical, since in Figures 6.30a and 6.31b it is apparent that that the CF response of the pipeline is characterised by clear mode 1 vibrations too. Finally it is worth noting that, as becomes evident from the above presented results, all three methods of analysis give dominant CF vibration frequency of about 1.4 - 1.5 Hz, which is much smaller than the frequency of 2.347 HZ that was found using RIFLEX to correspond to mode 1 vibrations and was also verified by the results obtained for the IL direction. This observation can mainly attributed to the fact that at the velocity of 0.27 m/s the CF response is extremely small and for this reason the FD VIV model was not able to capture any CF response at all at this velocity. Nevertheless though, it also becomes clear that the TD VIV model is indeed capable of accurately capturing the actual response of the pipeline even in cases that the VIV phenomenon is too weak to be captured by other typically used models.

Finally, as far as the velocity of 0.4 m/s is concerned, it becomes clear that the results of the time domain analysis are in quite good agreement with the experimental data with regard to the CF response, while some more significant deviations can be observed for the IL direction. First of all, as far as the simpler CF response is concerned, it becomes apparent that all three methods of

analysis give clear mode 1 CF vibrations. More specifically, the experimental data reported in [7] give dominant CF response frequency of 1.8 Hz, while modal analysis gives dominant CF vibration frequency of 1.7848 Hz (i.e. 0.3794 Hz in full scale), as is shown clearly in Figures 6.12 and 6.32c respectively. Finally, from Figure 6.33a it becomes apparent that there is only one dominant peak in the CF response spectrum predicted by the TD VIV model at the frequency of 2.22 Hz. The snapshots of the actual response that where captured during the model tests and the respective snapshots calculated by means of the TD VIV model are again almost identical, since in Figures 6.32a and 6.33b it is clear that the CF response of the pipeline is characterised by clear mode 1 vibrations. Contrary to this, the response obtained for the IL direction is somewhat more complicated. To begin with, it is found in Figure 6.12 that the experimental data reported in [7] give dominant mode 1 IL vibrations and vibration frequency of 3.5 Hz. Furthermore, as far as the results of the modal analysis are concerned, it becomes clear from Figure 6.32b that the IL response of the pipeline is dominated by mode 1 vibrations at the frequency of 3.5689 Hz (i.e. 0.75865 Hz in full scale). However, there seems to be a small deviation between the above presented findings and the actual IL response of the pipeline that was captured during the experiments and snapshots of which are illustrated in Figure 6.32a. From this Figure it becomes evident that the actual IL response is characterized by the existence of a multi-frequency response with significant contributions from both mode 1 and mode 2. This observation can also explain the fact that the dominant IL response frequencies of 3.5 Hz and 3.5689 Hz that were reported in [7] and in SINTEF Ocean's report are in fact between the above mentioned values of 2.347 and 5.794 Hz, which correspond to mode 1 and mode 2 respectively. Finally, all the above findings seem to be in very good agreement with the results obtained using the TD VIV model. To be more precise, in Figure 6.33a a dominant peak becomes evident at 5.55 Hz corresponding to mode 2 IL vibrations, a secondary peak can be observed at the frequency of 2.222 Hz which corresponds to mode 1 IL response and several additional peaks of significant height become evident at frequencies between the two aforementioned values (at 3.33 Hz and at 4.44 Hz). The fact, that there are several important peaks in the obtained response spectrum covering the whole range of frequencies form clear mode 1 to clear mode 2 IL vibrations, proves the existence of the aforementioned multi-frequency response. Finally, Figure 6.33b seems to be in very good agreement with Figure 6.32a since in both Figures the contribution from both mode 1 and mode 2 to the IL response of the pipeline is evident.

To sum up, from all the findings and the analyses presented in this section, it becomes clear that, when the previously identified optimum parameter set is implemented, the TD VIV model is able to capture accurately the VIV responses observed during the model tests with regard to all three examined Test Series. More specifically, the detailed comparison conducted in this section proved that, even for the velocities for which some significant deviations between the experimental data and the results of the time domain analysis were observed in sections 6.1 - 6.3 for the three Test Series, the results of the TD VIV model are in very good agreement with the actual response of the pipeline. In fact, it became clear that the results of the time domain analysis seem to be even better than the respective findings of other traditionally used methods such as modal analysis and frequency domain analysis.

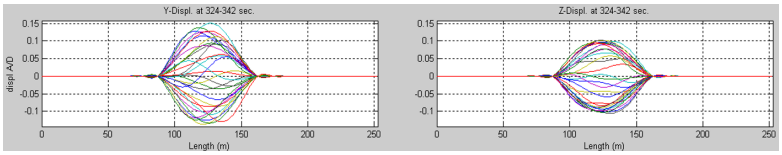

(a) Response Snapshots

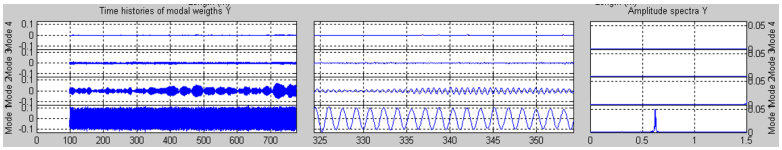

(b) IL - Modal Weights Time Series and Spectra

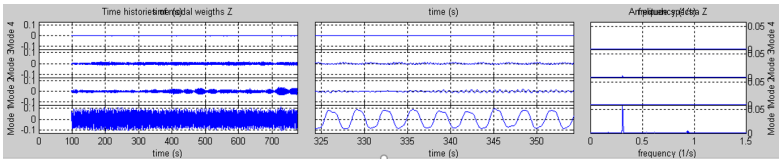

(c) CF - Modal Weights Time Series and Spectra

Figure 6.30: Summary of the experimental results for Test Series 75 at 0.27 m/s

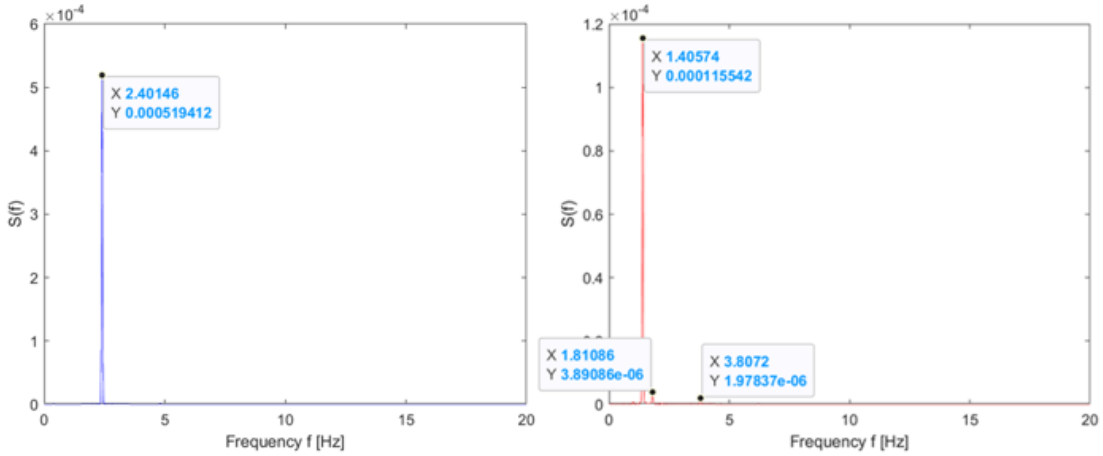

(a) Response Time Series and Spectra

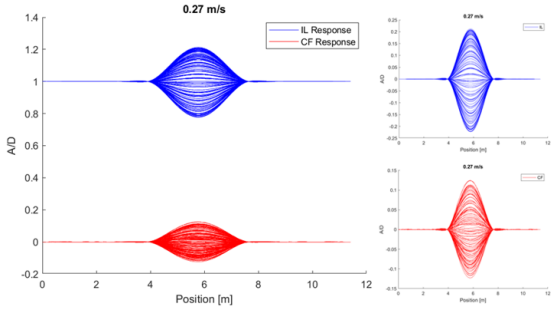

(b) Response Snapshots

Figure 6.31: Summary of the time domain analysis results for Test Series 75 at 0.27 m/s

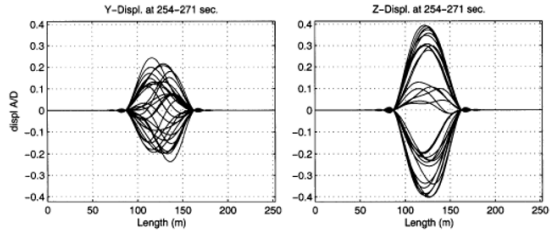

(a) Response Snapshots

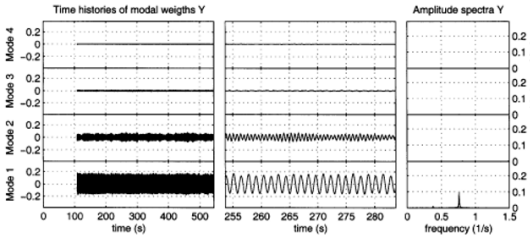

(b) IL - Modal Weights Time Series and Spectra

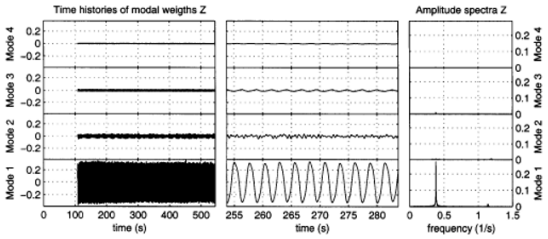

(c) CF - Modal Weights Time Series and Spectra

Figure 6.32: Summary of the experimental results for Test Series 75 at 0.4 m/s

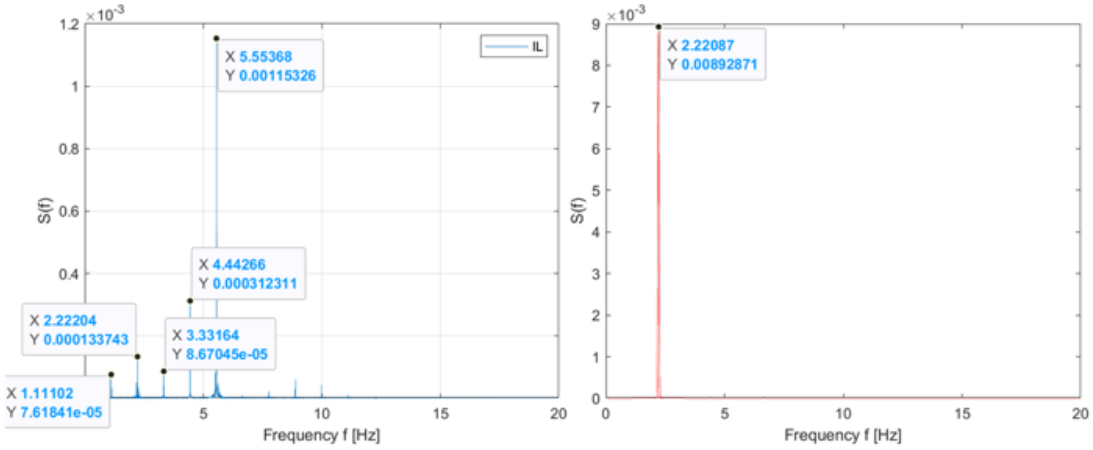

(a) Response Time Series and Spectra

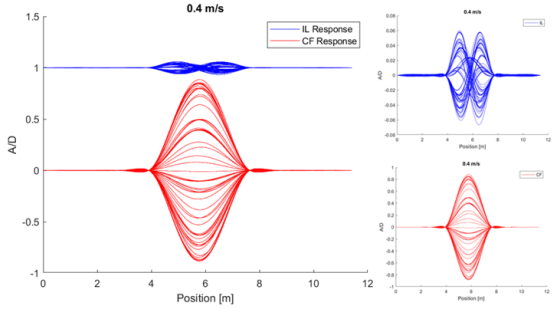

(b) Response Snapshots

Figure 6.33: Summary of the time domain analysis results for Test Series 75 at 0.4 m/s

7 Realistic free span Scenario

In this chapter the Realistic Free Span Scenario that was investigated in the context of the present thesis is described. More specifically, the general setup and the examined environmental and loading conditions are presented first and subsequently the methodology followed in order to implement into RIFLEX the Realistic free span case is illustrated.

7.1 General setup

The Realistic free span case examined in the present thesis is mainly based on the work of Wu et al., [11, 12], the focus of which was on the prediction of pure IL responses of a free spanning pipeline with partial strake coverage. The aforementioned analysis consisted of two parts, an experimental investigation of the subject in terms of model tests and a numerical case study of a typical full-scaled pipeline that was conducted by means of the VIVANA-FD frequency domain VIV prediction tool. Although the main goal of the study presented in [11, 12] was to assess the effectiveness of partial strake coverage for the considered case, the VIV response of a typical bare pipeline was also simulated in order to determine the sufficient strake coverage level that can fully suppress pure IL VIV responses. This particular bare pipeline case served as the basis of the analysis carried out in the present thesis. To be more precise, the exact same structural properties of the pipeline as presented in [11, 12] were also applied in the present study. However, some modifications had to be implemented mainly in terms of environmental and loading conditions in order to better serve the purposes of this Master's Thesis. The structural properties of the examined pipeline and the soil properties of the seafloor are summarised in Tables 7.1 and 7.2 respectively. Moreover, the configuration of the pipeline and the profile of the seabed are illustrated in Figure 7.1.

Table 7.1: Structural properties of the pipeline [11, 12]

Parameters	**Value**	**Unit**
Pipe inner diameter	0.5758	m
Concrete outer diameter	0.69	m
Hydrodynamic diameter, D	0.702	m
Free span length, L	54	m
Anti-corrosion mass	17	kg/m
Concrete mass	184	kg/m
Steel pipe mass	250	kg/m
Specific mass ratio ρ_s/ρ	1.223	-
Elastic modulus of steel, E_S	$2.07\text{E}+05$	MPa
Elastic modulus of concrete, E_C	$3.07\text{E}+04$	MPa
Second moments of area, steel, I_S	$1.40\text{E}-03$	m^4
Second moments of area, concrete, I_C	$4.33\text{E}-03$	m^4
Steel pipe bending stiffness, EI_S	$2.90\text{E}+08$	Nm^2
Concrete bending stiffness, EI_C	$1.33\text{E}+08$	Nm^2
Structure damping ratio ζ_{pipe}	1.5%	-

Table 7.2: Soil properties for medium sand [11, 12]

Parameters	Value	Unit
Vertical dynamic stiffness factor, C_V	$1.45E+07$	$N/m^{5/2}$
Lateral dynamic stiffness factor, C_L	$1.25E+07$	$N/m^{5/2}$
Poisson's ratio, ν	0.5	-
Soil damping ratio ζ_{soil}	8%/22%	-

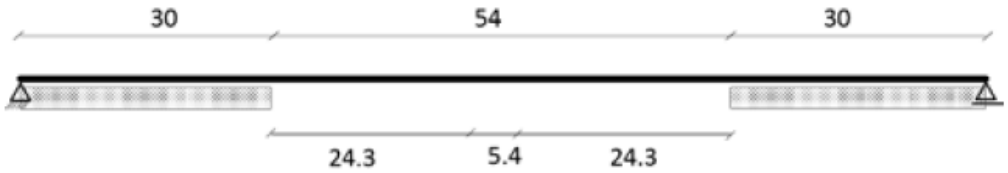

(a) Pipeline Configuration

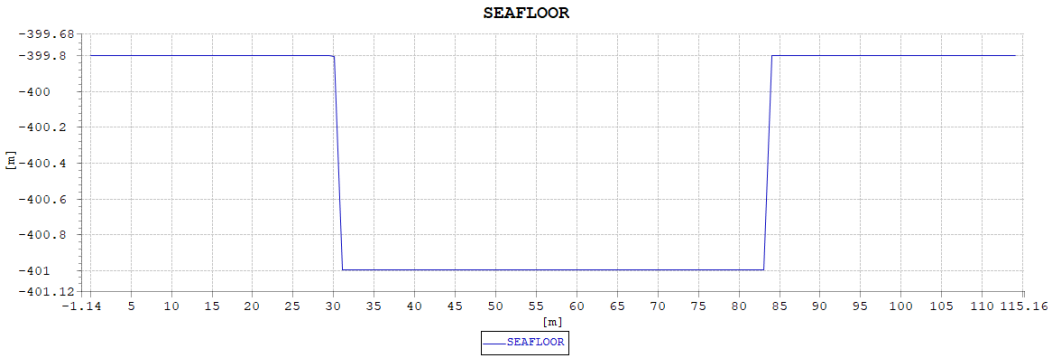

(b) Seabed Profile

Figure 7.1: Description of the examined pipeline case's configuration

There are three main deviations from the original scenario, with regard to the applied axial force, the range of current velocities examined and the value of the considered soil damping ratio. As far as the axial force is concerned, in [11, 12] a compressive force of $1.3 \cdot 10^6 N$ was applied at the one end of the pipeline. Contrary to this, it was preferred to use a pretension of the same magnitude in the following analysis. The reason behind this decision was that a compressive force can in fact occur in a real-life pipeline only in case the seabed under the pipeline is extremely uneven. In such a case, it might not be possible to lay the pipeline in a straight-line route, but instead a route shape resembling a "snake" may in practice occur. So between two consecutive points where the curvature of the pipeline changes sign such a compressive force can be observed. However, this is a quite rare scenario, while in most cases with regard to free spanning pipelines a pretension is induced to the pipeline by the installation vessel during the laying procedure and the application of a constant pretension is the most widely used approach in free spanning pipeline analyses.

As for the current velocities, it should be kept in mind that only the pure IL response was investigated in [11, 12] and as a result really low current velocities were examined, corresponding to a range of reduced velocities between 0 and 2.5, in which only mode 1 IL vibrations can be observed, while there is no CF response present. Contrary to this, the initial goal of the present work was to cover the whole range of reduced velocities in which VIV phenomena can occur (i.e. $U_R = 1-10$) so as to examine both pure IL and CF-induced IL responses and also to hopefully be able to capture higher mode vibrations too. So it was initially attempted to examine a

range of current velocities between 0.5 and 4.4 m/s, which corresponds to the aforementioned range of reduced velocities, but this approach unfortunately failed for two main reasons. The first problem had to do with the fact that in the original pipeline configuration given in [11, 12], the end of the pipeline, where the axial force was applied, was free to move in the axial direction. So using that high current velocities resulted in inducing extremely high current loads in the IL direction. However, at the same time there was also a non-negligible axial component. This axial force led to an unrestricted axial motion of the pipeline's end node, which eventually resulted in the failure of the static and dynamic analyses. In order to address this issue a quite stiff axial spring was applied in this node and the problem was solved.

However, the implementation of this axial spring did not solve and in fact it made worse the second problem that led to the failure of this attempt to examine extremely high current velocities. That is, for current velocities above 2.3 m/s the results of the TD VIV analysis gave a dominant frequency of 0 Hz with regard to the pipeline's IL response, as illustrated for example in Figure 7.2a. This dominant zero frequency component was present both before and after implementing the axial spring in the considered system. When there is no axial spring applied, this observation can mainly be attributed to the fact that the unrealistically high induced current loads in the IL direction lead in turn to an extremely high curvature of the pipeline, which ultimately suppresses the ability of the pipeline to vibrate as a result of the increased tension and geometric stiffness in the system. On the other hand, the implementation of the axial spring results in the reduction of the aforementioned curvature, but at the same time it also leads to a constantly increasing tension in the system and consequently in higher natural frequencies as the examined current velocity becomes higher. This is because of the axial component of the current induced loads that was mentioned in the previous paragraph as the reason of the first observed problem. The ultimate result of the above argument is that as the system's natural frequency increases with the current velocity, there is a velocity limit (around 2.3-2.4 m/s in the present case) above which the natural frequency becomes so high that it is no longer within the synchronization range and therefore the vortex shedding phenomenon cannot take place and there are no vortex-induced vibrations to be observed. Of course this zero frequency component can be removed by the application of a high-pass filter as illustrated in Figure 7.2b but unfortunately this filtering procedure had no effect on the estimated distribution of bending stresses in the IL direction which exhibits a chaotic behavior at high current velocities as presented clearly in Figure 7.3. For all the aforementioned reasons, it was decided to not use the axial spring (as was anyway initially intended) and investigate only current velocities below 2.4 m/s, which was found that in most cases was the limit above which the above described issues occur (although in some cases the high curvature problem problem started at a bit lower velocities as will be shown in the following). The reasoning behind the above decision can be easily understood if one takes also into account that 2.4 m/s is already an unrealistically high value of current velocity, which will probably never be observed in real life and even if such a strong current ever occurs the duration of such a phenomenon will be so limited that the resulting fatigue damage accumulation would not be the most significant problem to be addressed.

Finally, as far as the soil damping ratio is concerned, in [11, 12] the value of $\zeta_{soil} = 10\%$ was used. However, as already presented in section 3.2 and in Figure 3.3, the level of soil damping for sands typically takes values between 10% and 20%, while in some extreme cases values as low as 5% and as high as 25% can also be observed. For this reason, it was preferred, instead of the value of 10% used by Wu et. al., to examine two cases, one at the lower and one at the upper limit of the above range using the values of $\zeta_{soil} = 8\%$ and $\zeta_{soil} = 22\%$ respectively.

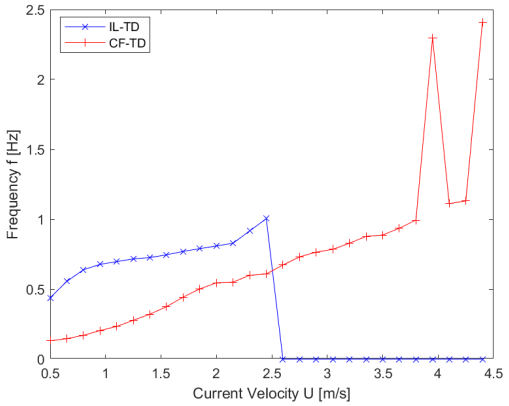

(a) Response Frequency vs Current Velocity

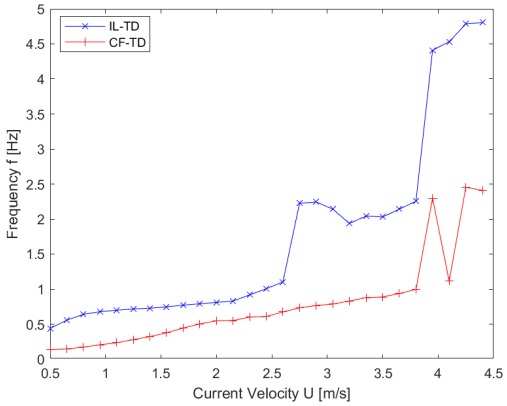

(b) Response Frequency vs Current Velocity (filtered)

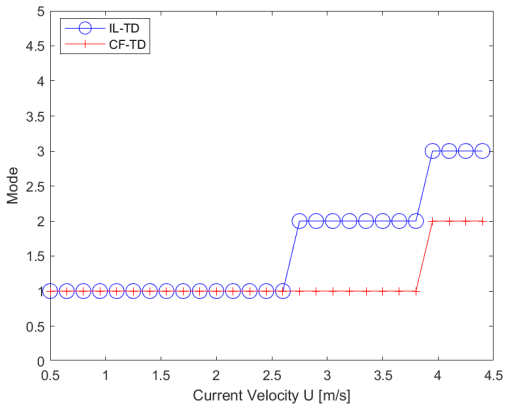

(c) Response Mode vs Current Velocity

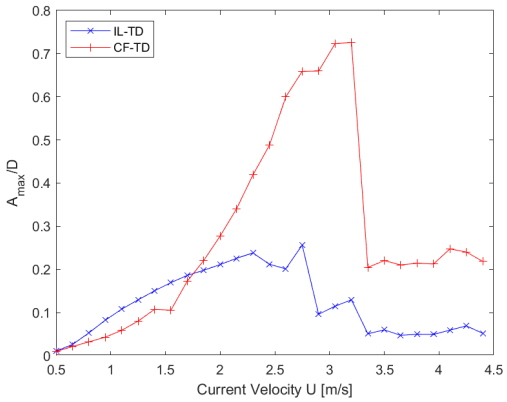

(d) Maximum response amplitude normalized by the pipe's diameter vs Current Velocity

Figure 7.2: Indicative results of the time domain analysis when extremely high current velocities are examined.

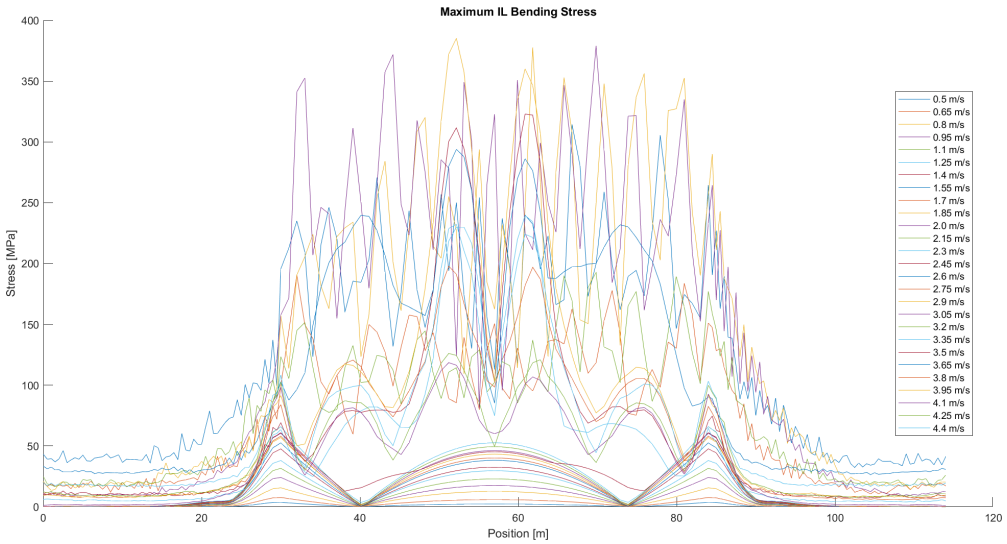

Figure 7.3: Distribution of the bending stresses in the IL direction along the pipeline

7.2 Method of Analysis of the Realistic free span Scenario

In this section the procedure followed for the implementation of this Realistic free span scenario in RIFLEX is described. As a first step the hydrodynamic load model used for the simulation of the examined VIV phenomena is established and the chosen hydrodynamic coefficients are presented. Then, the structural and numerical models used in order to approximate the actual free spanning pipeline are illustrated, followed by a detailed description of the Linear and Non-Linear soil models that were developed and used for the purposes of this analysis. Finally, the steps followed in order post-process, analyse and assess the obtained results are also presented.

7.2.1 Hydrodynamic load model and Implementation in RIFLEX

As was also the case for all the other analyses performed previously as part of the calibration procedure of the TD VIV model, the updated synchronization load model for combined CF and IL VIV that was introduced by Kim and was thoroughly analysed in section 2.3.3 was again utilised for carrying out the necessary simulations with regard to this realistic free span scenario. However, the differences between the pipeline currently investigated and the previous pipeline models had to be taken into account before deciding on the values of the required hydrodynamic coefficients.

As far as the hydrodynamic drag coefficient is concerned, its tangential component was again regarded negligible and was set equal to zero. As for the more significant normal component, some important differences between the present and the previous cases had to be highlighted before being able to choose a reasonable value. More specifically, in the present case a realistic full-scaled pipeline is examined, contrary to the idealized model-scaled pipelines investigated previously. As a result, the pipe could no longer be regarded as smooth but a value of surface roughness of at least $\kappa/D = 3.6 \cdot 10^{-3}$ had to be used. This value was reported in [11, 12] as an approximation of the surface roughness of the concrete coating when the bare rough pipe was investigated. If the marine growth, which will inevitably affect the surface roughness of the pipeline during its life time, is to be considered as well, it becomes obvious that an even higher value of κ/D should be used. Moreover, using the hydrodynamic diameter of this realistic pipe $D = 0.702m$ and the range of current velocities $U = 0.5 - 2.4m/s$ that are going to be examined, the range of Reynold's numbers $Re = 3.34 \cdot 10^5 - 1.6 \cdot 10^6$ is found, which corresponds to the Critical and Supercritical flow regimes. Taking all the aforementioned into account, from Figure 5.1 and considering the line corresponding to $\kappa/D = 1 \cdot 10^{-2}$, it is found that the drag coefficient takes values between approximately 1.05 and 1.1. However, taking into consideration that Figure 5.1 is based on the findings of experiments conducted with fixed rigid cylinders and not with flexible structures, the more conservative value of 1.2 that was used in the previous analyses was also chosen in this realistic scenario too.

As for the added mass coefficient, contrary to what was true for the previous cases, the value of 1.0 was used for both the tangential and the normal components of the added mass coefficient. At this point it should be noted that, as was explained in section 5.1, the tangential component of the added mass coefficient is typically considered negligible for most practical applications. However, the value of 1.0 was used in [11, 12] because the pipe investigated in this Realistic Scenario is not smooth, although the tangential component of the added mass coefficient is typically considered negligible even for rough pipes. Moreover, taking into account that the motions of the pipeline in the axial direction are negligible, it was concluded that the effect of this parameter in the response of the pipeline will be negligible too. For this reason, it was decided to use the value of 1.0 in order to not deviate from the reference study presented in [11, 12]. Finally,

the last step before being able to implement the hydrodynamic load model in RIFLEX was to determine suitable vortex-induced excitation force coefficients and synchronization parameters both for the in-line and for the cross-flow direction. For the purposes of this analysis the optimum parameters that were identified in chapter 6 were used. All the relevant hydrodynamic parameters implemented in the TD VIV model for the analysis of the realistic free span case are summarised in Table 7.3.

Table 7.3: Hydrodynamic parameters used in the TD VIV model for the analysis of the Realistic Scenario

Parameter	**Value**
Quadratic drag coefficient in tangential direction $[-]$	0
Quadratic drag coefficient in normal direction $[-]$	1.2
Added mass coefficient in tangential direction $[-]$	1.0
Added mass coefficient in normal direction $[-]$	1.0
Hydrodynamic diameter [m]	0.702
$C_{v,y}[-]$	0.85
$C_{v,x}[-]$	0.75
$\hat{f}_{0,y}[-]$	0.144
$\hat{f}_{\min,y}[-]$	0.08
$\hat{f}_{\max,y}[-]$	0.208
$\hat{f}_{0,x}[-]$	0.36
$\hat{f}_{\min,x}[-]$	0.1
$\hat{f}_{\max,x}[-]$	0.9

7.2.2 Structural and Numerical Models and Implementation in RIFLEX

In general, the same procedure as described in section 5.2 was followed again with regard to the Realistic Free Span Scenario. To be more precise, a Finite Element Method (FEM), in which the examined model is mainly characterized by the system mass, **M**, damping, **C** and stiffness, **K**, matrices, was again utilized so as to model the free spanning pipeline. Similarly, the global Rayleigh damping formulation illustrated in Eq. 5.2 was used again in order to establish the structural damping model. For the considered damping ratio, the value of $\lambda_i \leq 0.015$ that was reported in [11, 12] was used in the following analyses too. Since several different current velocities were examined in this thesis, a different value of the stiffness-proportional damping coefficient, α_2, was chosen for each one of them. The value of α_2 for each current velocity was chosen such that it corresponds to damping ratios below 1.5% of critical damping at all fundamental CF frequencies, since this approach was adopted in [11, 12] too. More specifically, the value of α_2 for each current velocity U was calculated based on the respective vortex shedding frequency using Eq. 5.4, in which the typical value for supercritical flow of $St = 0.25$ was used for the Strouhal number and the value of $\lambda_i = 0.015$ was used for all current velocities. The obtained results are summarized in Table 7.4.

Table 7.4: Realistic Scenario: Stiffness-proportional damping coefficients for the examined current velocities

U[m/s]	0.5	0.6	0.7	0.8	0.9
α_2[s/rad]	0.026814	0.022345	0.019153	0.016759	0.014897
U[m/s]	1.0	1.1	1.2	1.3	1.4
α_2[s/rad]	0.013407	0.012188	0.011173	0.010313	0.009577
U[m/s]	1.5	1.6	1.7	1.8	1.9
α_2[s/rad]	0.008938	0.00838	0.007887	0.007448	0.007056
U[m/s]	2.0	2.1	2.2	2.3	2.4
α_2[s/rad]	0.006704	0.006384	0.006094	0.005829	0.005586

For the FEM representation of the structure, beam elements based on the small strain theory were used again. As for the discretization of the examined structure in finite beam elements, it was chosen to use the discretization used in [11, 12] where the same pipeline was investigated by means of the frequency domain VIV prediction tool VIVANA. That is, the pipeline was modelled as an 114 m long beam consisting of 174 beam elements. More precisely, the middle part of this beam that corresponds to the free span was discretized in 54 beam elements with total length of 54 m (approximate element length of 1 m). Moreover 60 beam elements with total length of 30 m (element length of 0.5 m) were added at each side of the free span in order to model the part of the pipeline that rests on the seafloor.

What is more, for the computation of the dynamic response of the structure, numerical stepwise time integration of the dynamic equilibrium equation was again conducted.The same timestep and simulation length were chosen for all the considered current velocities. The size of the timestep was chosen equal to 0.025 s while the simulation length was equal to 2300 s. The pure Newton-Raphson method was used in order to conduct equilibrium iterations at each timestep, while a maximum number of 50 iterations per timestep and a desired displacement accuracy of 10^{-5} were defined. Moreover, RIFLEX's option for automatic subdivision of the timestep, in case the required accuracy is not obtained with the original timestep, was also activated. As for the static analysis, it was based on an incremental loading procedure. The applied loading sequence was a bit different when the Non-Linear soil model was used than when the Linear soil model was considered as will be explained in detail in sections 7.2.4 and 7.2.3. More specifically, the loading sequence of Bottom Friction Forces, Specified Forces, Volume Forces, Current Forces and Global Spring Activation with 50, 50, 10, 10 and 1 increments for each respective load type was applied to the structure when the Non-Linear soil model was implemented. The pure Newton-Raphson method was used again with a maximum number of 20, 20, 10, 10 and 10 iterations for the five aforementioned load types respectively and a desired displacement accuracy of 10^{-6}. For the case of the Linear soil model, a loading sequence of Specified Forces, Volume Forces, Global Spring Activation and Current Forces with 50, 10, 1 and 10 increments for each respective load type was applied to the structure. The pure Newton-Raphson method was used with a maximum number of 20, 10, 10 and 10 iterations for the four aforementioned load types respectively and a desired displacement accuracy of 10^{-6}.

7.2.3 Linear Soil Model and Implementation in RIFLEX

For the development and implementation of the Linear soil model that was required for the purposes of the present thesis, the same approach as in [11, 12], where the VIV response of the same pipeline was investigated by means of the frequency domain VIV prediction tool VIVANA, was followed. To be more precise, the stiffness and damping characteristics of the considered soil were approximated by discrete linear springs and dampers applied at every second nodal point. As far as the Vertical Dynamic Soil Stiffness, $K_{V,d}$, and the Lateral Dynamic Soil Stiffness, $K_{L,d}$, are concerned, they were calculated using Eq. 3.7 and Eq. 3.8 respectively as is proposed in DNV's Recommended Practice, when a free spanning pipeline scenario is considered and the seabed profile is relatively simple [6]. These calculations are given in Eq. 7.1 and Eq. 7.2 respectively.

$$K_{V,d} = \frac{C_V}{1-\nu}\cdot\left(\frac{2}{3}\cdot\frac{\rho_s}{\rho}+\frac{1}{3}\right)\cdot\sqrt{D} = \frac{1.45\cdot 10^7}{1-0.5}\cdot\left(\frac{2}{3}\cdot 1.223+\frac{1}{3}\right)\cdot\sqrt{0.702} = 2.791\cdot 10^7\,\frac{N}{m^2} \quad (7.1)$$

$$K_{L,d} = C_L \cdot (1+\nu) \cdot (\frac{2}{3} \cdot \frac{\rho_s}{\rho} + \frac{1}{3}) \cdot \sqrt{D} \Rightarrow$$
$$K_{L,d} = 1.25 \cdot 10^7 \cdot (1+0.5) \cdot (\frac{2}{3} \cdot 1.223 + \frac{1}{3}) \cdot \sqrt{0.702} \Rightarrow \quad (7.2)$$
$$K_{L,d} = 1.804 \cdot 10^7 \frac{N}{m^2}$$

where the values for the outer diameter of the pipe including any coating $D = 0.702m$, the specific mass ratio between the pipe's mass (not including added mass) and the displaced water $\frac{\rho_s}{\rho} = 1.223$, the Poisson's ratio $\nu = 0.5$ and the Vertical and Lateral Dynamic Stiffness factors $C_V = 1.45\text{E}+07\ \text{N/m}^{5/2}$ and $C_L = 1.25\text{E}+07\ \text{N/m}^{5/2}$ are given in Tables 7.1 and 7.2.

Subsequently the stiffness, k_i, of each one of the aforementioned discrete linear springs i, was calculated as $K_{V,d}$ or $K_{L,d}$ (depending on whether this is a vertical or a lateral spring) times a tributary length. This tributary length was taken to be equal to twice the element length (i.e. 1.0 m) everywhere within the soil-supported zone. However, at the shoulders of the span (i.e. at the transition from the soil-supported to the free spanning condition) and at the two ends of the pipeline, the tributary length was taken to be equal to the element length (i.e. 0.5 m).

Finally, it should be noted that the Vertical and Lateral Static Soil Stiffness were neglected in [11, 12], which is also true for the present thesis as far as the Lateral Static Soil Stiffness is concerned. However, the Vertical Static Soil Stiffness was used in the present work and it was modelled in the exact same way as it was modelled in the Non-Linear soil model and will be described in detail in section 7.2.4. The reason behind this decision is that, using the same model to approximate the Vertical Static Soil Stiffness, the exact same static configurations were achieved for both examined soil models and therefore the same starting point was used for the respective dynamic analyses, which are the main interest of the present thesis.

As far as the damping coefficients of the used discrete dampers are concerned, they were calculated using Eq. 3.5 as is proposed in DNV's Recommended Practice for cases in which a FEM analysis is conducted and the pipe-soil interaction is modelled using discrete soil supports [6]. These calculations are given in Eq. 7.3 and Eq. 7.4 for soil damping ratios $\zeta_{soil} = 8\%$ and $\zeta_{soil} = 22\%$ respectively.

$$c_i = 2 \cdot \zeta_{soil} \cdot \frac{k_i}{\omega} = 2 \cdot 0.08 \cdot \frac{2.791 \cdot 10^7}{2\pi \cdot 0.6984} = 1.018 \cdot 10^6 \frac{Ns}{m} \quad (7.3)$$

$$c_i = 2 \cdot \zeta_{soil} \cdot \frac{k_i}{\omega} = 2 \cdot 0.22 \cdot \frac{2.791 \cdot 10^7}{2\pi \cdot 0.6984} = 2.798 \cdot 10^6 \frac{Ns}{m} \quad (7.4)$$

where k_i is the above calculated spring stiffness at support no. i, $\omega = 2\pi \cdot 0.6984$ is the first angular natural frequency of the pipeline, which was estimated using RIFLEX.

7.2.4 Non-Linear Soil Model and Implementation in RIFLEX

For the development and implementation of the Non-Linear soil model that was required for the purposes of the present thesis, in general the same approach as for the Linear soil model was followed. To be more precise, the stiffness and damping characteristics of the considered soil were again approximated by discrete springs and dampers, but instead of using linear springs and dampers, bi-linear springs and dampers were used. As far as the Vertical Dynamic Soil Stiffness, $K_{V,d}$, and the Lateral Dynamic Soil Stiffness, $K_{L,d}$, are concerned, they were calculated using Eq. 3.7 and Eq. 3.8 respectively and their values are given in Eq. 7.1 and Eq. 7.2 respectively in

section 7.2.3. As for the Vertical Static Soil Stiffness, $K_{V,s} = 530kN/m^2$, its value was taken from Table 3.2 considering medium sand properties, while the Lateral Static Soil Stiffness was again neglected as in the Linear soil model and in [11, 12] as well. In order to model the aforementioned soil properties, both the so-called "Seafloor Spring Contact" component of RIFLEX and additional bi-linear springs and dampers were utilized.

RIFLEX's "Seafloor Spring Contact" component uses bi-linear springs and dampers both in the vertical and the lateral directions. That means that, when there is contact between the pipeline and the seafloor, springs and dampers corresponding to the stiffness and damping properties of the soil are activated in both directions, while they are deactivated when there is not contact, as for example in a "lift off" situation. According to RIFLEX's User Manual, [50], in the lateral direction, apart from the cases where there is no pipe-soil contact, sliding of the pipe can also occur when the lateral spring force reaches the friction force value, resulting in the spring - damper deactivation. Springs and dampers will be reinstated if the pipeline starts sliding in the opposite direction, or if the friction force increases and is greater than the spring force. Similarly, the additional bi-linear springs and dampers were defined in such a way that they are active when the node at which they are applied is in contact with the seafloor or equivalently when the spring is in compression and they are deactivated when during the pipeline's motion the node is not in contact with the seafloor or equivalently when the spring is in tension.

The additional bi-linear springs and dampers were utilized in the Non-Linear Soil model so as to model the Vertical Dynamic Soil Stiffness and Damping. The "Seafloor Spring Contact" component was used in order to model the Vertical Static Soil Stiffness and the Lateral Dynamic Soil Stiffness and Damping within this Non-linear Soil model, while it was used so as to model the Vertical Static Soil Stiffness alone within the Linear Soil model. The reason that led to the decision to model the Vertical Static Soil Stiffness using the "Seafloor Spring Contact" component is the fact that in order to get the right static configuration, the Vertical Static Soil Stiffness had to be active before activating the Volume Forces (i.e. the weight of the pipeline) and before activating the Vertical Dynamic Soil Stiffness within the static analysis. In this way, the weight of the pipeline is handled exclusively by the springs corresponding to the Vertical Static Soil Stiffness, while afterwards when the rest of the springs that correspond to the Vertical Dynamic Soil Stiffness are activated, the pipeline is already in equilibrium and hence the "dynamic" springs do not induce any additional force. In RIFLEX this could be determined by specifying a suitable loading sequence for the static analysis (see also section 7.2.2), in which the Volume Forces are activated before activating the Global Spring Forces (Note: the Global Springs are the linear springs in the Linear soil model and the bi-linear springs in the Non-Linear model) and by taking advantage of the fact that when the "Seafloor Spring Contact" component is used in RIFLEX, it is always active throughout the analysis (i.e. from the start until the end of the analysis). What is more, as far as the reason why it was decided to use the "Seafloor Spring Contact" component to model the Lateral Dynamic Soil Stiffness too within the Non-Linear model is concerned, that is because separate bi-linear springs could not be utilized for this purpose, since the seafloor exerts forces both in the positive and in the negative lateral directions when there is contact between the pipe and the seabed. Therefore, having contact or not could not be related to the springs being in tension or in compression, as is the case in the vertical direction. Consequently, the use of the "Seafloor Spring Contact" component was necessary, since, when it is used, RIFLEX automatically captures when and where there is contact between the pipe and the seafloor and springs and dampers are activated there. Finally, it should be noted that when the Linear soil model is used, the Global Spring Forces have to be activated before activating the Current Forces within the static analysis something that is not necessary with regard to the Non-Linear model. That is

because only the Lateral Dynamic Soil Stiffness is considered in the present thesis, which in the linear soil model is approximated as linear lateral springs. Therefore, the global springs have to be activated in advance, so as to handle the current loads induced in the lateral direction. Contrary to this, the Lateral Dynamic Soil Stiffness is modelled by the "Seafloor Spring Contact" component in the Non-Linear model and hence the global springs can in fact be activated after the current loads.

So in the Non-Linear soil model, the stiffness of the additional bi-linear springs was set equal to $k_i = 2.791 \cdot 10^7 \frac{N}{m}$ when there is contact between the pipe and the seafloor. The above value is the same as the Vertical Dynamic Soil Stiffness and the respective value used in the Linear Soil model, since the springs are positioned in 1 m intervals. When there is not contact, this value was set equal to zero. Similarly, the respective damping coefficients were set equal to $1.018 \cdot 10^6 \frac{Ns}{m}$ for $\zeta_{soil} = 8\%$ or to $2.798 \cdot 10^6 \frac{Ns}{m}$ for $\zeta_{soil} = 22\%$ when there is contact and equal to 0 when there is not contact. Moreover, for both considered soil models, the above mentioned value of $K_{V,s} = 530kN/m^2$ was given as input for the stiffness normal to the seafloor in the "Seafloor Spring Contact" component, while the damping coefficient normal to the seafloor was set equal to zero, since the static properties are considered in the vertical direction. In the Non-Linear soil model, additional properties were specified for the lateral direction. That is, the above calculated value for the Lateral Dynamic Soil Stiffness $K_{L,d} = 1.804 \cdot 10^7 \frac{N}{m^2}$ was specified here. Moreover, the value of the seafloor damping coefficient in lateral direction was also specified here to be equal to $1.018 \cdot 10^6 \frac{Ns}{m^2}$ for 8% soil damping ratio and to $2.798 \cdot 10^6 \frac{Ns}{m^2}$ for 22% soil damping ratio. These values of the seafloor damping coefficient are the same as used in the Linear Soil model for each discrete damper, since the dampers were positioned in 1 m intervals in that model. Finally, the seafloor friction coefficient was also specified to be equal to an unrealistically high value of $\mu = 500$.

At this point it is worth noting that the initial goal was to use a realistic friction coefficient $\mu = 0.7$. However, for current velocities of 1.1 m/s and above, using this friction coefficient resulted in the pipeline sliding on the seafloor even within the static analysis, for which only the current loads are considered in the IL direction (i.e. without considering the vortex-induced loads). This ultimately led in the failure of the static analysis, since the solution could not converge. This observation is totally expected. In order to show this, the pipeline can be approximated as a beam simply supported at the two shoulders. The weight per unit length of the pipeline in air including the weight of the contents (i.e. the gas) as exported from RIFLEX is equal to 4759 N/m, while the total buoyancy per unit length of the pipeline is equal to 3892 N/m. This results to a vertical force exerted to the seafloor equal to:

$$F_{vertical} = 4759 - 3892 = 867 \frac{N}{m} \tag{7.5}$$

According to Morisson's equation and considering that a steady flow is considered, the in-line force induced by the current per unit length of the pipeline can be calculated as such:

$$F_{current} = \frac{1}{2} \rho C_D D U^2 = \frac{1}{2} 1025 \cdot 1.2 \cdot 0.702 \cdot U^2 = 431.73 \cdot U^2 \tag{7.6}$$

In order for the pipeline to slide, the above current force has to be higher or equal to the vertical force exerted to the seabed times the friction coefficient:

$$F_{current} \geq F_{vertical} \cdot \mu \Rightarrow 431.73 \cdot U^2 \geq 867 \cdot 0.7 \Rightarrow U \geq 1.1856 \frac{m}{s} \tag{7.7}$$

The small difference between the result of Eq. 7.7 and the actual velocity of 1.1 m/s for which the pipeline starts to slide is because the above presented calculation is a simplification of the real case treated in RIFLEX. Moreover, taking into account that within the dynamic analysis non-negligible VIV loads will also be added to the above current loads, it becomes obvious that sliding will in fact occur at even lower current velocities within the dynamic analysis. Therefore, the realistic friction coefficient could only be used in case only low velocities below 1 m/s were going to be examined. However, at such low velocities, there is no significant CF response present. For this reason, it was decided to use the above unrealistic value for the friction coefficient in order to be able to restrict the pipeline from sliding at least for the lower part of the considered current velocities. In fact, for the case of $\zeta_{soil} = 22\%$ the pipeline did not slide for the whole range of the examined current velocities ($U = 0.5 - 2.4m/s$), while for the case of $\zeta_{soil} = 8\%$ pipeline sliding was observed only for velocities above 2.0 m/s and only within the dynamic analysis. Using this high friction coefficient, it was of course not possible to capture the difference between the two soil models with regard to modelling the lateral soil properties using linear springs (Linear Model) and Coulomb Friction Model (Non-linear Model), but it was necessary in order to be able to extend the analysis to higher current velocities and examine the interaction between CF and IL response. So the only difference between the two soil models in terms of the lateral soil properties has to do exclusively with the existence or not of contact between the pipe and the seafloor, since in the Linear model the springs and dampers are always active while in the Non-linear model there has to be contact for them to be activated.

7.2.5 Post-processing procedure

Having run the simulations for each examined case (i.e. for each current velocity, soil model and soil damping ratio) following the procedure described in the previous sections of this chapter, the most relevant results and responses had to be computed and stored so as to be afterwards post-processed by means of the MATLAB software.. At this point it is worth noting that using the TD VIV prediction tool coupled to the RIFLEX software through SIMA it is possible among others to obtain directly time series of nodal displacements, element curvature, element forces and moments and local cross-sectional stresses at every time step. This possibility comes with the benefit that there is no need to perform mode identification and to conduct modal analysis in order to be later able to combine the modal results and compute the total responses and hence it reduces significantly the level of uncertainty of the analysis. In order to decrease the computational time and also to save some data storage space, it was preferred to calculate and store only the nodal displacements and the element curvature time series. More specifically, the data obtained directly by the TD VIV prediction tool were:

- Nodal displacements in the global x-, y- and z- directions for all nodes. The results after every time step were written in ASCII-files.
- The element curvature about the y- and z-axis at both element ends for every beam element. The results after every time step were written in ASCII-files.

In general the same preliminary steps that were described in section 5.4.2 were followed here too so as to prepare the above time series for the subsequent analysis and assessment of the simulation results. To be more precise, the first step of the post-processing procedure was to remove the first part of the simulation from the raw data in order to be sure that any possible transient effects will not be included in the subsequent calculations. For this reason, the first 600 s of the total 2300 s of simulation time were removed. This corresponds to more than 100 periods for the lowest fundamental cross-flow frequency, which was considered to be enough

to remove all transients from the obtained results. Then the response time series were plotted so as to visually verify that indeed the transients were no longer present in the remaining data series.

Calculation of the Response Amplitudes and the dominant Vibration Frequencies
Having removed all transients, the remaining time series are now ready to be used for the actual analysis of the simulation results. First of all, the nodal displacements corresponding to the IL and the CF direction were stored separately. Contrary to what was true in section 5.4.2, for this Realistic scenario, the mean value of the displacement of each node in both directions was not subtracted by the corresponding response time series. That is because in this case, when the Non-linear soil model is used, the response in both directions is no longer symmetric because of the ”lift off” phenomenon that takes place in the CF direction and the effect that this phenomenon has in the IL response too. Therefore, in order to be able to capture the aforementioned phenomena and to visually illustrate the difference between the two examined soil models, the total response had to be used instead of a response that is modified to have zero mean value. Subsequently, following the procedure given in 5.4.2, the maximum amplitude of the response in both directions as well as the respective positions along the pipe were found for each current velocity. Then, for each simulation case, the response time series, corresponding to the nodes where the maximum amplitude in each direction was observed, were used in order to produce the respective response spectra. For this reason, a Fast Fourier Transform (FFT) algorithm was applied in MATLAB and more precisely the FFT routine provided within the WAFO Matlab toolbox was again applied. The obtained response spectra were then utilized in order to identify for each simulation case the active response frequencies both in the in-line and the cross-flow direction. The dominating frequencies for the in-line and cross-flow directions were again taken as the peak frequencies in the response spectra corresponding to the positions along the pipe where the maximum amplitudes were measured in each direction. Finally, the dominant vibration modes in both directions for each examined case were again identified by plotting snapshots of the calculated response and visually observing their shape. However, contrary to the previous cases, only mode 1 vibrations were observed in both directions and for all the examined cases (i.e. for all the considered current velocities, soil models and soil damping ratios).

Stress Calculation
In this section, the procedure followed in order to calculate the time series of the stress distribution along the examined pipeline is described. In the previous section, the procedure followed in order to calculate, store and remove all transients from the curvature time series was described. Subsequently, the remaining curvature data were utilized in order to calculate the time series of the stress distribution using MATLAB. First of all, taking into account that the produced stress time series are going to be used to estimate the fatigue damage accumulation and considering that only dynamic loads are of interest in a fatigue analysis, the static curvature was removed from the curvature time series and therefore only the variations of the curvature because of the dynamic response of the structure were considered. Moreover, it is worth noting that the fatigue damage accumulation and the stress distribution at the outer fiber of the steel pipe are of interest and therefore the external coating was neglected in the stress and fatigue damage calculation procedures.

Typically, the stresses induced in a pipe’s cross-section can be split in a shear stress component and an axial stress component. The shear stress is constant around the circumference of each cross-section and can be calculated by Eq. 7.8.

$$\tau_{xy} = \frac{M_x}{I_x} R_S \tag{7.8}$$

where M_x is the torsional moment, I_x is the polar moment of inertia of the steel pipe's cross section and R_S is the outer radius of the steel pipe. At this point it should be noted that the magnitude and the variations of the shear stress were found to be negligible compared to the axial stress and were therefore neglected in the following analysis.

The axial stress σ_{xx} at a point of a thin-walled circular cross-section is generally a function of the local loads and the angular position within the cross-section and can be calculated by Eq. 7.9.

$$\sigma_{xx} = \frac{N_x}{A_S} + \frac{M_y}{I_y} z + \frac{M_z}{I_z} y = \frac{N_x}{A_S} + \frac{M_y}{I_y} R_S \sin\theta + \frac{M_z}{I_z} R_S \cos\theta \tag{7.9}$$

where N_x is the applied axial force, A_S is the cross-sectional area of the steel pipe, M_y and I_y are the moment and the second moment of area around the y-axis respectively and similarly M_z and I_z are the moment and the second moment of area around the z-axis.

It is worth noting that, as was the case for the shear stress too, the variation of the stress because of the applied axial force (i.e. the N_x-term in Eq. 7.9) is typically considered to be of secondary importance compared to the so-called flexural stress (i.e. the last two terms in Eq. 7.9) and was hence neglected in the following analysis. The flexural stresses were evaluated at 8 points around the circumference of the steel pipe's cross section. However, the interest of the present thesis is focused only in the induced stresses in the cross-flow, σ_{CF}, and in-line, σ_{IL}, directions, corresponding to the stresses induced at the outer fiber of the cross section at angles $\theta = 90°$and $\theta = 0°$respectively. Moreover, since, as explained previously, the time series of the element curvatures about the y- and z-axis were extracted as outputs from the TD VIV prediction tool, it would be more relevant to calculate the cross-flow and in-line stresses directly in terms of the curvatures rather than the moments. For this purpose, the relation between the curvature and the moment given in Eq. 2.15 can be utilized and the cross-flow and in-line stresses can be calculated by Eq. 7.10.

$$\sigma_{CF} = E_S \cdot \kappa_y \frac{D_S}{2} \quad , \quad \sigma_{IL} = E_S \cdot \kappa_z \frac{D_S}{2} \tag{7.10}$$

where E_S is the Young's modulus of steel, κ_y and κ_z are the curvature around y- and z- axis respectively and D_S is the steel pipe's outer diameter.

Fatigue Damage Calculation

It is a well-known fact that offshore structures are exposed to cyclic dynamic loads as a result of the simultaneous action of wave, current and wind loads. Although the magnitude of such environmental loads is typically much lower than the structure's yield strength, the fact that these loads are characterised by a cyclic behaviour can lead to the degradation of the material properties of the structure in microscopic level. That is, imperfections in the material's microstructure can occur, leading in turn in the development and gradual growth of cracks over time. If the cyclic loading continues, the initially microscopic cracks can grow to such an extent that the resulting degradation of the material's properties can lead to the cross-section not being able to bear the induced loads and premature failure may occur far below the yield limit. This is because damage is accumulated cycle by cycle, a phenomenon referred to as fatigue, and is a common issue with regard to marine structures [52].

When estimating the accumulated fatigue damage and the expected lifetime of a structure in a fatigue analysis, apart from the prevailing environmental conditions, detailed data about the long term stress distribution along the structure and the material properties of the structure, a material response model is also required in order to evaluate the structural response in the induced loading and stresses. There are two main methods that are typically used to determine the material response model, the fracture mechanics approach and the SN-curve approach. The first of them is based on the investigation of the crack development and propagation mechanisms and on the estimation of the local stress concentration in the vicinity of the crack. The SN-curve approach is the most widely used method and it is the method implemented in the present thesis and thus it will be described in more detail in the following.

SN-curve approach

In the SN-curves, the stress range is plotted against the number of cycles that would lead to failure if loading of constant magnitude was applied. SN-curves are available for different environments (i.e. in air, in water with cathodic protection, in water without corrosion protection), geometries and load directions and also for different probabilities of failure [53]. These diagrams are based on data obtained from laboratory experiments on specimens of simple geometry which were subjected to stress ranges of varying magnitude until failure occurred [54]. The relation between the number of cycles to failure, N, and the respective stress range, $\Delta\sigma$, which forms the SN-curves is given in Eq. 7.11 or in log-log scale in Eq. 7.12.

$$N = K \cdot \Delta\sigma^{-m} \tag{7.11}$$

$$N = \log(K) - m \cdot \log(\Delta\sigma) \tag{7.12}$$

where m is the slope of the SN-curve and $\log(K)$ is the interception between the SN-Curve and the $\log(N)$ axis. An one-sloped SN-curve was utilized for the estimation of the fatigue damage accumulation in the Realistic free span scenario with parameters: $m = 3$ and $\log(K) = 11.63$.

Rainflow Counting

In most engineering applications, simple periodic loading cases with constant amplitude are examined and therefore the Guassian distribution with zero mean value is regarded as a good assumption for the stress time histories and the resulting vibrations [53]. In a realistic vibration case though, as in Vortex-Induced Vibration cases, stress ranges of infinite different magnitudes can in fact occur. Consequently, in order to be able to utilize the SN-curves for the estimation of the fatigue damage accumulation, all the induced stress cycles and the corresponding stress ranges that are present in the measured stress signal have to be determined and counted. Several techniques have been proposed in order to convert the random load spectra to simpler cycles. One such approach is cycle counting. The goal of this cycle counting procedure is to split the total stress signal, which is in most cases rather broad banded, into discrete stress cycles, in order to be subsequently able to estimate the damage caused by each loading event independently [54]. There are numerous cycle counting techniques such as the level crossing cycle counting, the peak counting method, the simple-range counting method, the rainflow counting method, the range-pair counting method and the two-parametric fatigue characteristics method to name but a few [55, 56, 57, 58, 59]. The rainflow counting technique is the most widely used cycle counting method and it is the method implemented in the present thesis. The procedure followed in the rainflow counting method to determine all the measured stress cycles and the corresponding stress ranges is visually illustrated in Figure 7.4 and is as such [54]:

- Rainflows are initiated at the start of the time series and successively at the inside of every

peak and valley.

- A rainflow which started at a peak (or a valley) continues dropping down until a peak more positive (or a valley more negative) than the peak (or the valley) from which it initiated from is reached at the opposite side. This is shown in Figure 7.4a by the counted half-cycles 1-2-4, 2-3, 4-5-7, 5-6 and 8-9.
- Another reason for a rainflow to stop is meeting a rainflow coming from a roof above. This is shown in Figure 7.4a by the counted half-cycles 3-2', 6-5' and 9-8'.
- Finally, a rainflow has of course to be terminated at the end of the time series. This is shown in Figure 7.4a by the counted half-cycle 7-8-10.
- The horizontal length of each rainflow is counted as a half cycle corresponding to that stress range.

The rainflow counting routine provided within the WAFO Matlab toolbox was utilized for the purposes of the present thesis.

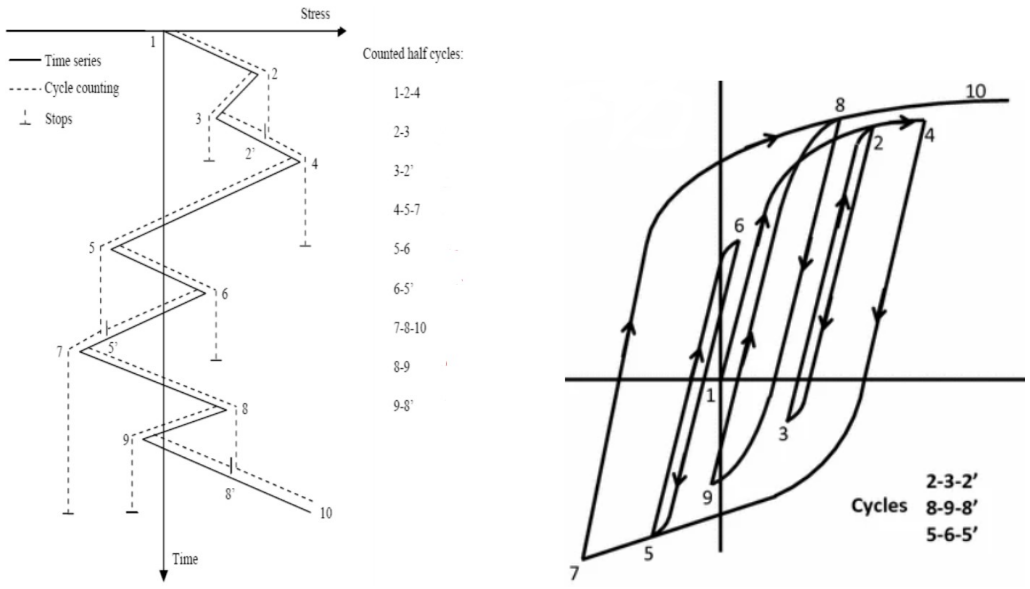

(a) Load sequence (b) Stress-strain history

Figure 7.4: Visual illustration of the Rainflow counting method [10]

The Palmgren-Miner rule

The most widely used method for the evaluation of the accumulated fatigue damage on a structure over a certain time period is the Palmgren-Miner rule, which is based on the assumption that the fatigue damage is linearly accumulated. Before being able to utilize the Palmgren-Miner rule, a cycle counting technique has to be applied to the examined long-term stress time history, as described previously, and the stress distribution over the considered period of time has to be transformed into a stress histogram of the counted stress cycles and the corresponding stress ranges, as illustrated in Figure 7.5. Then according to the Palmgren-Miner rule the total accumulated fatigue damage D can be calculated as such:

$$D = \sum \frac{n_i}{N_i} \tag{7.13}$$

where n_i is the number of cycles corresponding to the stress range block no. i and N_i is the number of cycles with constant-amplitude which would cause failure for this stress range, as found from the SN-curve. Summation is applied over all load cases i. When $D \geq 1$ the structure fails due to fatigue damage.

At this point it is worth noting that the one-year accumulated fatigue damage D_{year} is examined in the present thesis for two main reasons. First of all, typical time series of measured stress signals have duration of some minutes, while the offshore structures are designed to have a much larger operational life. Secondly and most importantly, the interest of the present thesis is not focused on the actual value of the accumulated fatigue damage, since unrealistically high values of current velocities are examined, which will probably never be observed in real life, and even if such strong currents ever occur, the duration of such a phenomenon will be so limited that the fatigue damage would not be the important issue, but rather the ultimate limit state would be of interest. Instead, the main goal of this thesis is to investigate the differences in the fatigue damage induced in the structure when the Linear and the Non-Linear soil models are implemented. Therefore, it was preferred to use the one-year fatigue damage in order to get higher damage accumulation and thus to be easier to identify the differences between the two approaches. The one-year fatigue damage accumulation can be calculated as such:

$$D_{year} = \sum \frac{n_{i,year}}{N_i} \quad , \quad n_{i,year} = \frac{n_i \cdot 365 \cdot 24 \cdot 60 \cdot 60}{t} \tag{7.14}$$

where t is the total length of the measured stress time series.

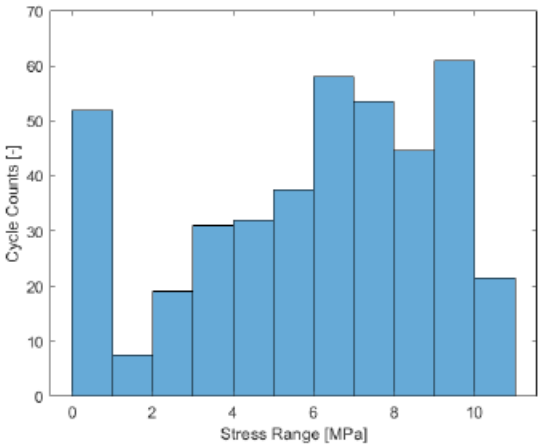

Figure 7.5: A typical Stress Histogram obtained by a cycle counting technique.

8 Results and Discussion for the Realistic Case Scenario

After establishing and implementing in RIFLEX the hydrodynamic load model (TD VIV model) and the rest of the models presented in sections 7.2.1 - 7.2.4, the static and dynamic analyses were run by means of RIFLEX. The obtained simulation results in terms of calculated nodal displacements and element curvatures were written in ASCII-files. Then, the MATLAB software was utilized in order to post-process the obtained data as described in detail in section 7.2.5. The results of this post-processing procedure are presented in the following sections. More specifically, the results obtained for soil damping ratio $\zeta_{soil} = 22\%$ are presented in section 8.1, where a comparison between the findings of the Linear and Non-Linear soil models is conducted. Similarly, a comparative study with regard to the results obtained for soil damping ratio $\zeta_{soil} = 8\%$ is presented in section 8.2. Finally, an overall comparison of all four examined cases, focusing on the effects of the two different levels of soil damping examined, is presented in section 8.3.

8.1 Comparative Study - Soil Damping Ratio 0.22

In this section, a comparative study between the most relevant of the results obtained using the Non-Linear and Linear soil models with regard to soil damping ratio $\zeta_{soil} = 22\%$ is conducted. The total set of findings with regard to soil damping ratio $\zeta_{soil} = 22\%$ (also including the results presented in this section) can be found in Appendices B.1, B.2 and B.3, where the results corresponding to the Non-Linear soil model alone, to the Linear soil model alone and the comparative study between the two soil models are presented respectively. The main goal of this section is on the one hand to describe the observed trends in terms of how the characteristics of the VIV response change as a function of the examined current velocity and on the other hand to compare in detail the obtained results with respect to the two different soil models in order to identify the differences between the two soil models. In Figure 8.1, the dominant response frequencies and the maximum response amplitudes normalized by the pipe's diameter that were calculated by means of the time domain VIV analysis with regard to both examined soil models and considering the soil damping ratio $\zeta_{soil} = 22\%$ are illustrated.

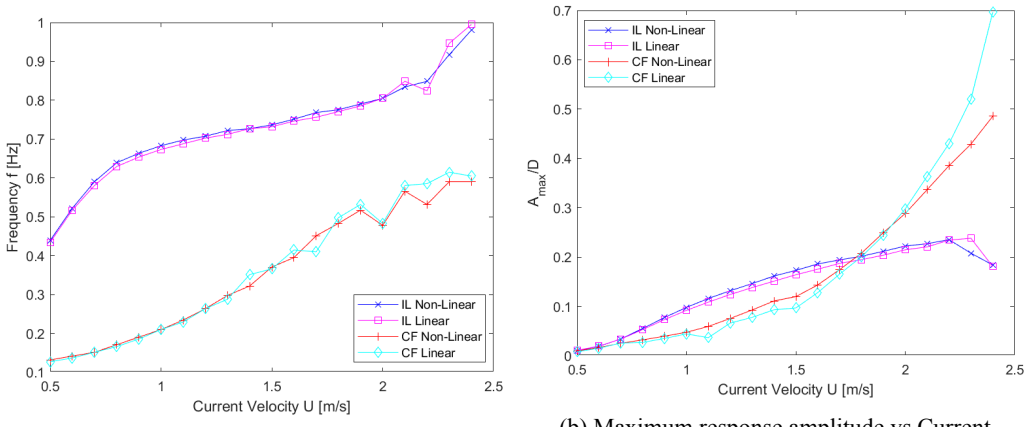

(a) Response Frequency vs Current Velocity

(b) Maximum response amplitude vs Current Velocity

Figure 8.1: Plots of the dominant response frequencies and the maximum response amplitudes for the Non-Linear and Linear soil models and $\zeta_{soil} = 22\%$.

At a first glance in Figure 8.1 it becomes evident that in general, the exact same trends, in terms of how the dominant response frequencies and the maximum response amplitudes in both the CF and IL directions change as a function of the current velocity, can be observed with regard to both examined soil models. To be more precise, from Figure 8.1a, it becomes apparent that for both the IL and CF responses, the dominant vibration frequency increases as the examined

current velocity becomes higher. More specifically, as far as the CF response is concerned, this increase in dominant frequency in general seems to follow an almost constant slope, although for the higher velocities some local ups and downs can be observed. With regard to the Non-Linear model, these indentations become evident for velocities above 1.8 m/s, while they are shifted to slightly lower velocities between 1.5 m/s and 2.1 m/s when the Linear model is considered. Contrary to this, it becomes apparent that the observed trends for the two soil models with regard to the dominant IL response frequency are almost identical. More specifically, for both soil models, the IL dominant response frequency increases radically for the lower range of the examined current velocities up to 0.8 m/s. Afterwards, it continues to follow an upward course but with a clearly smaller slope which is kept almost constant for the most of the remaining current velocities until the value of 2.2 m/s is reached. For even higher velocities, a rapid increase of the dominant vibration frequency becomes evident with approximately the same slope as was observed for the lower considered current velocities. The only notable difference between the two soil models is the fact that, although both models predict that the dominant IL response frequency generally increases with the current velocity, a small drop can also be observed at the velocity of 2.2 m/s when the Linear model is used. Moreover, as far as the difference between the vibration frequencies in the two directions is concerned, the results of the two soil models seem to be in quite good agreement. For the lowest velocity, the IL frequency is about 3.3-3.4 times higher than the CF frequency. This ratio gradually increases until it reaches the value of $\frac{f_{IL}}{f_{CF}} \approx 3.9$ at 0.7 m/s and then starts to slowly decrease until it becomes equal to 2 at 1.5 m/s. Afterwards, for the range of current velocities $1.6 - 2.4$ m/s, this ratio seems to change more randomly, because of the ups and down observed with regard to both models, and takes values in the range of $\frac{f_{IL}}{f_{CF}} \approx 1.4 - 1.9$.

What is more, as far as the main trends observed with regard to the maximum response amplitude are concerned, taking a closer look at Figure 8.1b, a very good agreement between the two soil models becomes again apparent. First and foremost, it is seen that both models give that the IL response is higher than the CF response at the lower range of the examined velocities (up to about 1.7-1.8 m/s), while for the highest range of current velocities, the CF vibrations become dominant, as expected. Furthermore, it becomes clear that the CF response amplitude rises and in fact at a rapidly increasing rate for higher current velocities, taking its maximum value at 2.4 m/s. On the contrary, the IL response amplitude rises with a gradually dropping rate as the current velocity becomes higher, up to the velocity of 2.2 m/s. Above this velocity, one significant deviation between the two soil models becomes evident. That is, the Non-Linear soil model predicts a fast drop of the IL response amplitude for current velocities above 2.2 m/s, while this reduction in the IL response is evident only for the highest examined velocity of 2.4 m/s when the Linear model is considered. As a result, the Non-Linear and the Linear models give the the highest IL response amplitude at the velocity of 2.2 m/s and 2.3 m/s respectively. However, at this point it should be noted that for the highest current velocity of 2.4 m/s, extremely high curvature of the pipeline was again observed with regard to both examined soil models. This observation can be mainly attributed to the fact that, as explained in detail in section 7.1, when the considered current velocity is really large, it results in very high current loads in the IL direction, which lead in turn to an extremely high curvature of the pipeline. This results in having increased tension in the system, which ultimately suppresses the ability of the pipeline to vibrate. This is the reason why a non-negligible zero frequency component became evident in the response spectrum of this specific current velocity, which however was not so big as to dominate the response as in other examined cases related to even higher velocities (see for example Figure 7.2). Moreover, this issue also led to significant convergence problems for this velocity, since a lot of timestep subdivisions were required in order for the solution to converge,

while for the rest of the examined current velocities either much less timestep subdivisions were required or there was no need for timestep subdivision at all. All the above problems ultimately resulted in an unrealistic distribution of bending stress and fatigue damage in the IL direction with regard to the velocity of 2.4 m/s which does not follow the trends observed for the rest of the velocities and can be characterized as chaotic. This is clearly shown in Figures B.26 and B.27b in Appendix B.1 with regard to the Non-Linear model and in Figures B.50 and B.51b in Appendix B.2 for the Linear model. For all these reasons the respective results were regarded as unreliable and hence they will not be treated in the following. The full set of the obtained results including the velocity of 2.4 m/s can be found in Appendices B.1-B.2.

Based on the above presented main trends, it becomes evident that there seems to be a very good agreement between the results of the two soil models. However, some non-negligible deviations can also be observed, especially with regard to the CF response. To be more precise, as far as the IL dominant vibration frequency is concerned, it becomes clear from Figure 8.1a that the Non-linear soil model seems to give slightly higher frequencies than the Linear model for current velocities up to 2.0 m/s, but the deviations are very small and range from 0% at 1.4 m/s and 2.0 m/s to the maximum difference of 1.65% at 0.7 m/s. For higher velocities, a more random behavior can be observed, with the Linear soil model giving 1.75% and 3.19% higher frequency at 2.1 and 2.3 m/s respectively and the Non-linear model giving 2.87% higher frequency at 2.2 m/s. As for the CF vibration frequency, the Non-linear soil model predicts slightly higher frequencies for the lower part of the examined current velocities up to 1.3 m/s. The maximum deviation in this region is observed at 0.5 m/s and is found to be equal to 3.7%. For the upper part of the current velocity range the opposite trend is observed, with the Linear model giving constantly higher CF vibration frequency for all the velocities above 1.7 m/s. The maximum discrepancy between the two models for the higher part of the examined velocities is observed at 2.2 m/s and is equal to 10.1%. Finally, the most important deviations between the two models with regard to the CF vibration frequency are found in a small range of current velocities between 1.3 and 1.8 m/s, where the higher frequency is given alternatively by the two models. By comparing the results from the two models, it was found that the difference of the two models is equal to -3.3% at 1.3 m/s, $+9.1\%$ at 1.4 m/s, -1.3% at 1.5 m/s, $+4.94\%$ at 1.6 m/s, , -9.2% at 1.7 and , $+3\%$ at 1.8 m/s where the ”-” sign means that the Non-linear model gives higher frequency and the ”+” sign the opposite. This observation can up to a point be explained by the fact that in this range of current velocities, the responses in the CF and IL directions have more or less the same amplitude and therefore a more complicated interaction between the two responses might take place in these velocities.

From Figure 8.1b it becomes apparent with regard to the maximum IL response amplitude that the Non-linear soil model seems to give slightly higher amplitudes than the Linear model for the whole range of current velocities up to 2.2 m/s, apart from the two lowest velocities for which the Linear model predicts a bit higher IL response. It should be noted though, that for the two lowest velocities, both models give extremely low response amplitudes of about $1\% - 2\%$ of the pipe's diameter and hence these results are not really important in practice. In general, the calculated deviations with regard to the above velocity range are again very small, with the maximum discrepancy of 6.4% being observed at 1.1 and 1.4 m/s. As for the highest examined velocity of 2.3 m/s, the aforementioned drop of the IL response amplitude becomes evident with regard to the Non-linear model, ultimately resulting in the prediction of 14.54% lower IL vibration amplitude than the Linear model. As far as the CF response amplitude is concerned, it becomes clear from Figure 8.1b that the Non-Linear soil model constantly predicts somewhat higher CF response amplitudes for current velocities below 2.0 m/s. The maximum deviation for this ve-

locity range was observed at 1.1 m/s and was found equal to 38.25%. However, it should be noted that the discrepancy is not that big as it appears to be. This can be easily understood by comparing the actual response amplitudes predicted by the two models, which are 0.037 D for the Linear model and 0.059 D for the Non-Linear model. From these values, it becomes obvious that at so low velocities the CF response is extremely small and not really important. The CF response becomes of interest in practice for velocities above 1.3-1.4 m/s, where the CF response amplitude is higher than 0.1 D. Of course, for the range of current velocities between 1.3 and 1.9 m/s, the Non-linear model still predicts higher CF response, however the maximum deviation from the respective results of the Linear Model in this range is equal to 19% at 1.5 m/s and it becomes smaller for higher velocities. Finally, for the range of current velocities above 1.9 m/s, the rate of increase of the maximum CF response amplitude with the current velocity seems to be much higher with regard to the Linear model than for the Non-linear one, something that in turn results in significant deviations between the respective results. The maximum discrepancy was observed at the highest examined velocity of 2.3 m/s and was found equal to 21.19%.

The above observations are totally expected and can mainly be attributed to whether the ”lift off” phenomenon takes place or not. More specifically, as far as the IL response is concerned, for the lower range of the considered current velocities for which the IL vibrations are dominant, negligible differences between the two soil models can be observed. This can be explained by the fact that for such low velocities the CF response and consequently the effect of the ”lift off” phenomenon is limited. Moreover, for higher current velocities, although some more profound deviations with regard to the IL direction can be observed, these discrepancies are still small. The reason for this is that the ”lift off” phenomenon is not expected to affect dramatically the IL response at the midspan, which is the point where the maximum response amplitude was observed, as reported in Figure 8.1. Instead, the effect of the ”lift off” phenomenon on the IL response is expected to be much more profound locally near the shoulders and within the soil-supported part of the pipeline, something that will become clear in the following, where snapshots of the response and the distribution of the bending stress and the fatigue damage along the pipeline are presented. Contrary to this, the ”lift off” phenomenon influences significantly the CF response even in the vicinity of the midspan. So, for the higher examined velocities for which the CF response is dominant, it becomes apparent that the Linear model predicts much higher responses at the midspan. This observation is totally reasonable since when the Non-Linear model is used, the pipeline can detach from the seabed above the shoulders and this fact leads to a bigger active free span. As a result, the vertical forces induced in the pipeline are distributed to an extended part of the pipeline (beyond the initial free span). This in turn leads to an alleviation of forces in the middle of the free span and thus the respective response is smaller than when the Linear model is used, for which the ends of the initial free span are basically restricted to stay in place.

In Figures 8.2 - 8.5 comparative snapshots of the response predicted by the TD VIV model with respect to both the CF and the IL directions (subfigures (a) and (c) in the aforementioned Figures) are presented for four indicative current velocities along with zoomed images focusing on the details of the respective responses near the left shoulder of the pipeline (subfigures (b) and (d) in the aforementioned Figures). Moreover, additional snapshots corresponding to the timesteps for which the maximum (i.e. most positive) and minimum (i.e. most negative) responses for both directions were observed are illustrated in Figures 8.6 - 8.9 for the same four current velocities along with zoomed images focusing on the details of the respective responses near the left shoulder of the pipeline. Comparative snapshots for the whole range of the examined velocities can be found in Appendix B.3 (Figures B.56 - B.95).

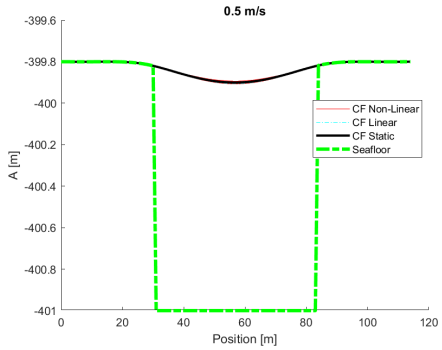

(a) CF - 0.5 m/s

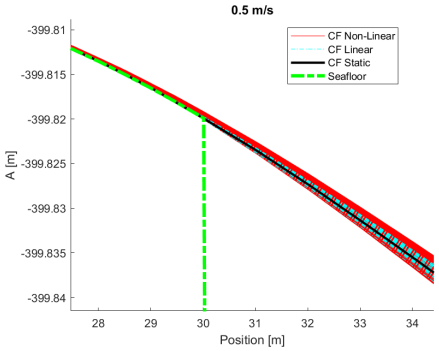

(b) CF - 0.5 m/s (zoom at the left shoulder)

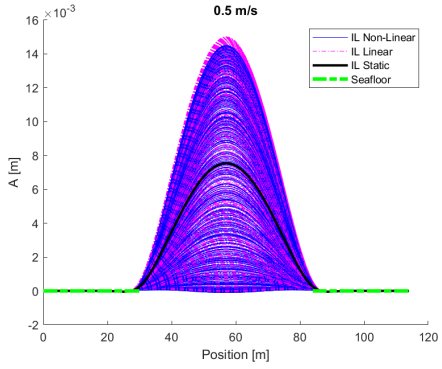

(c) IL - 0.5 m/s

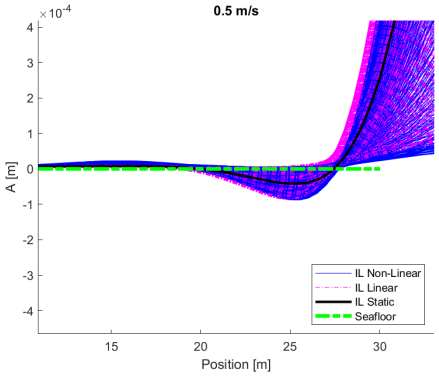

(d) IL - 0.5 m/s (zoom at the left shoulder)

Figure 8.2: Comparative snapshots of the calculated responses for the two soil models at 0.5 m/s.

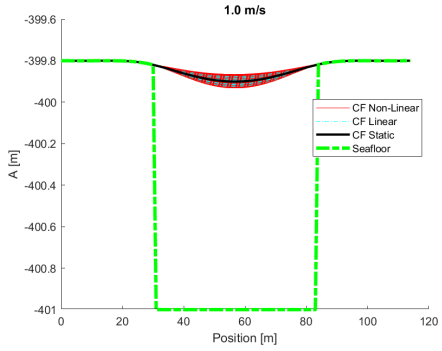

(a) CF - 1.0 m/s

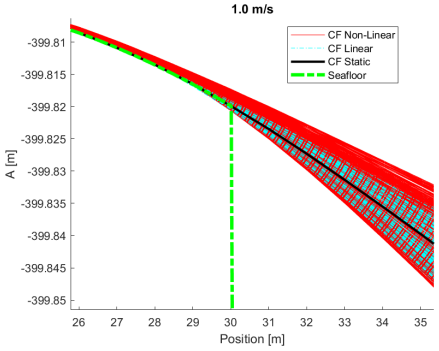

(b) CF - 1.0 m/s (zoom at the left shoulder)

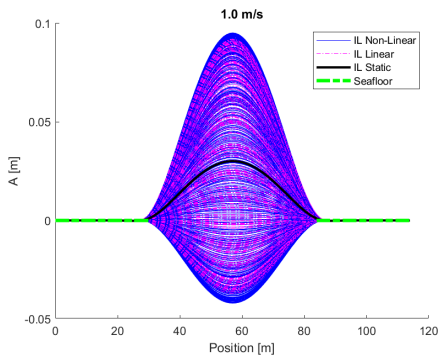

(c) IL - 1.0 m/s

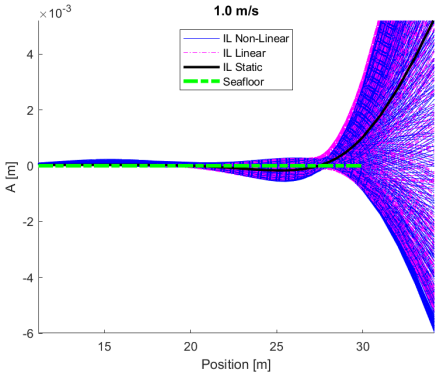

(d) IL - 1.0 m/s (zoom at the left shoulder)

Figure 8.3: Comparative snapshots of the calculated responses for the two soil models at 1.0 m/s.

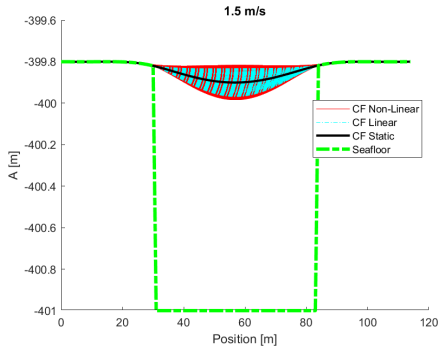

(a) CF - 1.5 m/s

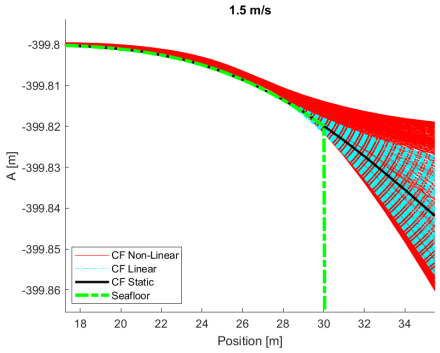

(b) CF - 1.5 m/s (zoom at the left shoulder)

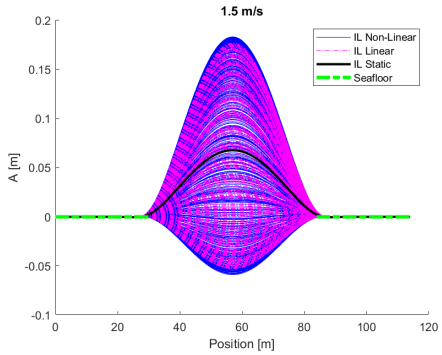

(c) IL - 1.5 m/s

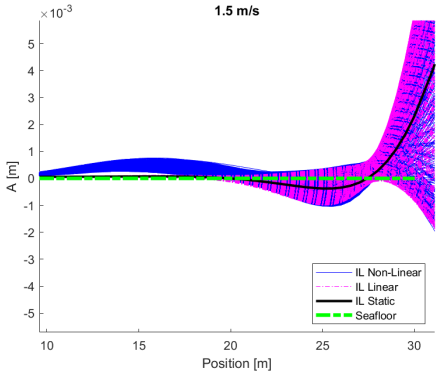

(d) IL - 1.5 m/s (zoom at the left shoulder)

Figure 8.4: Comparative snapshots of the calculated responses for the two soil models at 1.5 m/s.

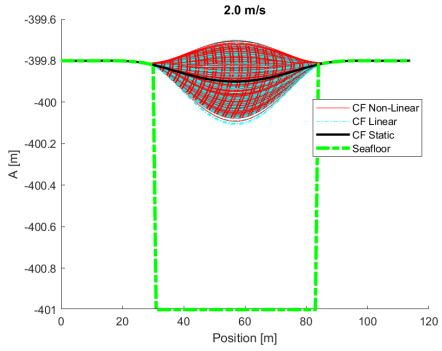

(a) CF - 2.0 m/s

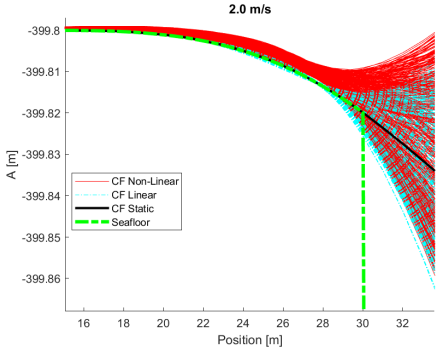

(b) CF - 2.0 m/s (zoom at the left shoulder)

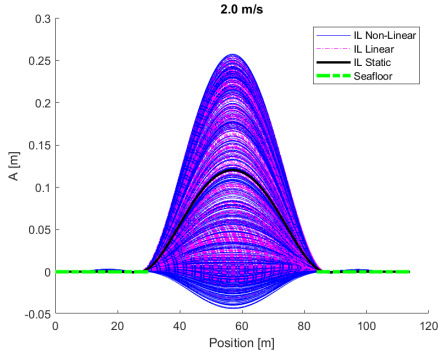

(c) IL - 2.0 m/s

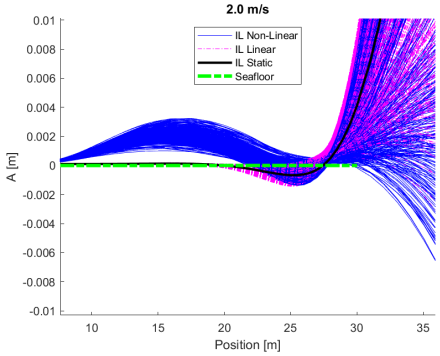

(d) IL - 2.0 m/s (zoom at the left shoulder)

Figure 8.5: Comparative snapshots of the calculated responses for the two soil models at 2.0 m/s.

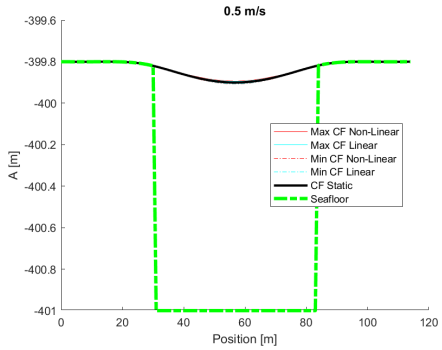

(a) CF - 0.5 m/s

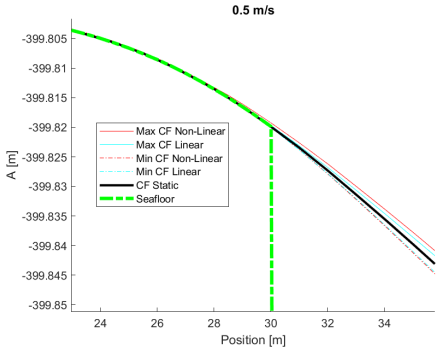

(b) CF - 0.5 m/s (zoom at the left shoulder)

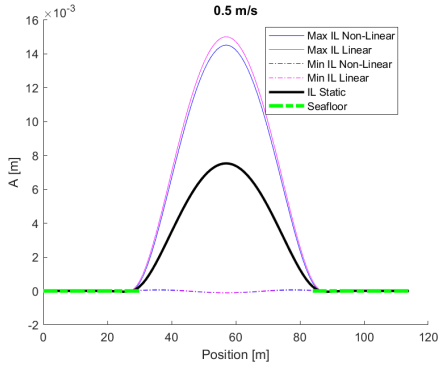

(c) IL - 0.5 m/s

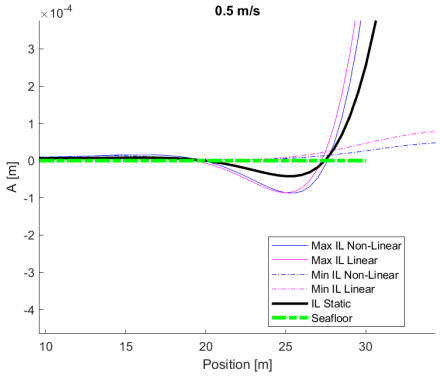

(d) IL - 0.5 m/s (zoom at the left shoulder)

Figure 8.6: Comparative snapshots of the max and min responses for the two soil models at 0.5 m/s.

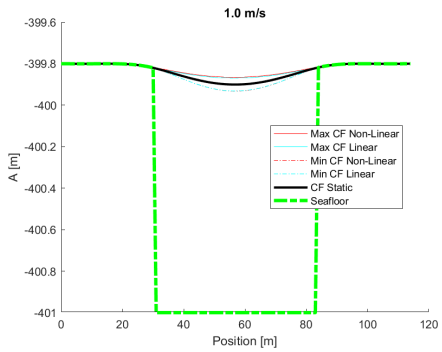

(a) CF - 1.0 m/s

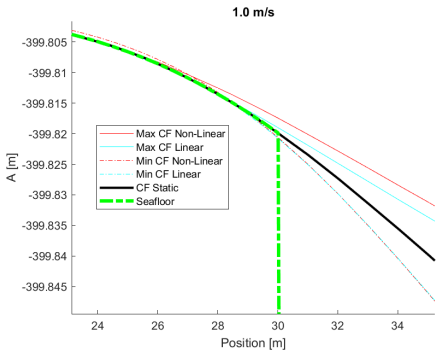

(b) CF - 1.0 m/s (zoom at the left shoulder)

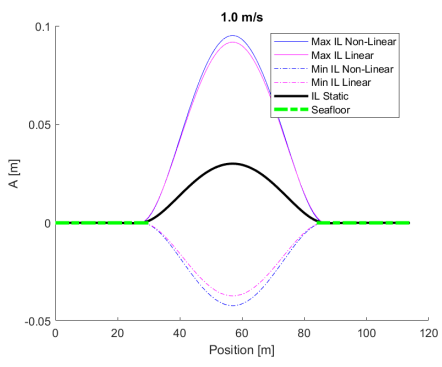

(c) IL - 1.0 m/s

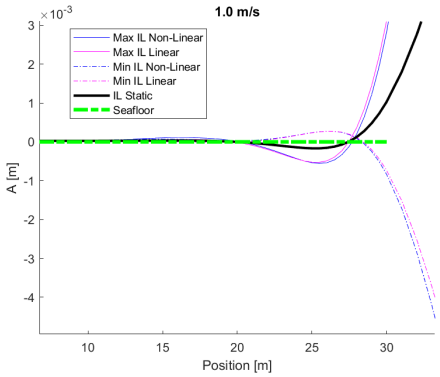

(d) IL - 1.0 m/s (zoom at the left shoulder)

Figure 8.7: Comparative snapshots of the max and min responses for the two soil models at 1.0 m/s.

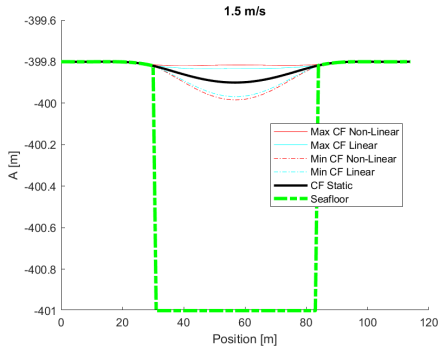

(a) CF - 1.5 m/s

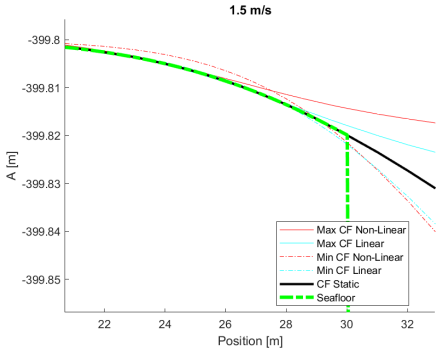

(b) CF - 1.5 m/s (zoom at the left shoulder)

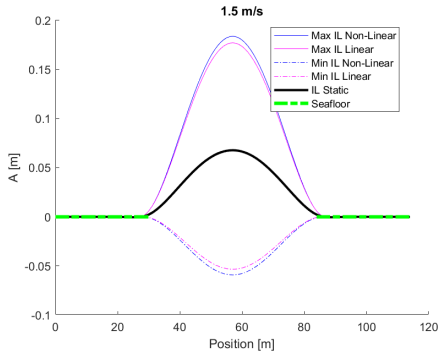

(c) IL - 1.5 m/s

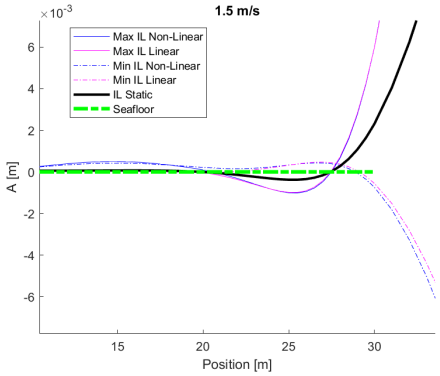

(d) IL - 1.5 m/s (zoom at the left shoulder)

Figure 8.8: Comparative snapshots of the max and min responses for the two soil models at 1.5 m/s.

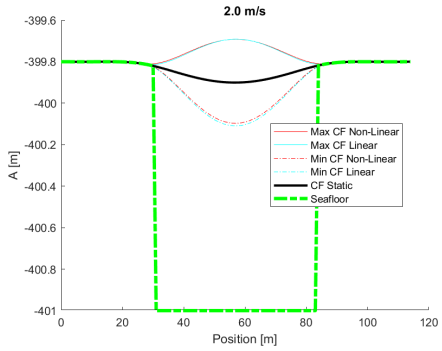

(a) CF - 2.0 m/s

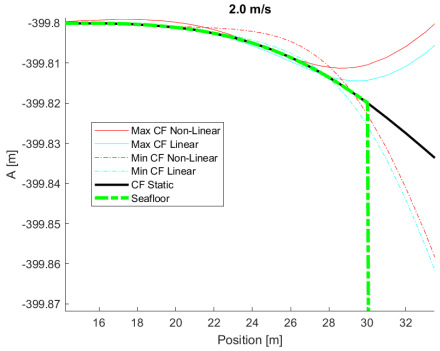

(b) CF - 2.0 m/s (zoom at the left shoulder)

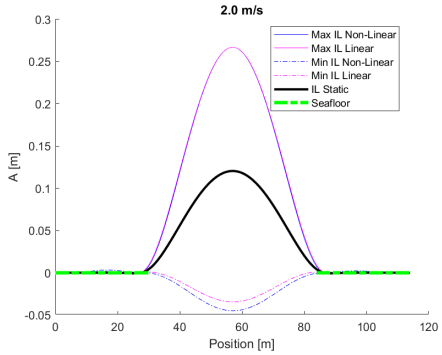

(c) IL - 2.0 m/s

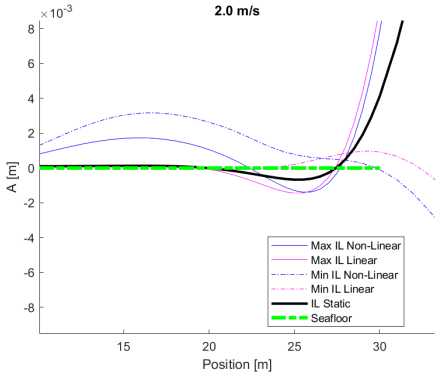

(d) IL - 2.0 m/s (zoom at the left shoulder)

Figure 8.9: Comparative snapshots of the max and min responses for the two soil models at 2.0 m/s.

At first glance, it becomes apparent that the response snapshots illustrated in Figures 8.2 - 8.5 are in very good agreement with the previously analysed main trends of the CF and IL VIV responses presented in Figure 8.1, since for both examined soil models, a clear mode 1 vibration can be observed with regard to both the IL and the CF directions and for the whole range of examined current velocities. In addition, it becomes clear that the amplitude of these responses gradually increases with the current velocity. However, from these Figures, the difference between the two soil models and the significant effect of the ”lift off” phenomenon become also apparent. As far as the CF response is concerned, taking a closer look at the details of the CF response near the shoulder presented in Figures 8.2b, 8.3b, 8.4b and 8.5b, it becomes clear that the Linear model gives a perfectly symmetric response about the static configuration. This is a clear proof that there is no ”lift off” present in this case in which the Linear soil model is used. Contrary to this the response predicted by the Non-Linear model is not symmetric due to the non-linear pipe-soil contact. More specifically, the two models give approximately the same CF response when it comes to the response in the negative direction (i.e. downwards), something totally expected since the soil springs are active in both models when the pipeline tries to penetrate to the seabed moving downwards. However, the response in the positive direction predicted by the Non-linear model near the shoulder is much higher (i.e. there is a significant spreading of the response), since there is no reaction force from the soil when the pipeline moves upwards and is not in contact with the seabed, which is a clear proof of the existence of the ”lift off” phenomenon. The fact that the pipeline is indeed able to lift up and detach from the seafloor, when the Non-Linear soil model is considered, becomes also apparent by the existence of important CF response above the seabed within the soil-supported part of the pipeline even far away from the free span, something that is not true with regard to the Linear model. As for the minor vibrations that can be observed within the first 1-2 m of the shoulder when the Linear soil model is used, this observation can be explained by the fact that the seafloor is modelled by springs. Therefore, because of the forces that are induced at the shoulders due to the motion of the pipeline, some minor movement of the seabed/springs is inevitable, but it is clear that this movement is perfectly symmetric. Finally, from Figure 8.2b, it is clear that a small ”lift off” can be observed even at the lowest examined current velocity and the effect of this phenomenon becomes more and more profound as the velocity increases.

What is more, as far as the IL response is concerned, it is again evident that there is a significant spreading of the IL response near the shoulder when the Non-Linear model is used. However, in this case, the difference between the two models is found in the negative IL direction. This is clearly illustrated in Figures 8.5c and 8.5d, while it is not that apparent in Figures 8.2c - 8.4c and 8.2d - 8.4d, since as explained above a significant CF response and consequently high current velocity is required in order for the ”lift off” phenomenon to have a profound effect in the IL direction. The fact that the Linear model gives much smaller responses in the negative IL direction near the shoulder can be explained by the fact that the lateral soil springs are always active in this model and they always react to the motion of the pipeline in both directions. Contrary to this, when the Non-Linear model is used and there is not contact between the seafloor and the pipe, the lateral springs are deactivated. In this case, the only forces exerted on the pipeline are the time varying VIV loads (i.e. they change both in magnitude and in direction in time) and the mean current loads (i.e. with constant magnitude and always in the positive direction). So when the VIV loads are induced in the negative direction, and since there is no spring force applied as in the case of the Linear model, they oppose to the mean current loads leading the pipeline to move towards the negative direction (i.e. away from the static configuration) and when the VIV loads become larger than the mean current loads, the IL response takes negative values. As for the reason why this spreading takes place predominantly in the negative direction,

it could be attributed to the fact that at such high current velocities, the static configuration is characterized by an extremely curved pipeline as shown in Figures 8.5c and 8.5d. Because of this high curvature there is increased tension and geometric stiffness in the system. This fact combined with the bending stiffness of the pipeline itself, makes it difficult for the pipeline to move further towards the positive direction and to become even more curved. In contrast, when the VIV loads are negative and the pipeline starts moving towards the negative IL direction, the pipeline curvature and consequently the tension in the system decrease making it possible for the pipeline to move further away from the static configuration.

Finally, the most important difference between the IL response predicted by the two soil models is the fact that when the Non-Linear model is considered, there is a considerable IL response above the seafloor that extends far away from the end of the free span, something that is in general not present for the Linear model. The fact that the Linear model mostly predicts no IL response within the soil-supported part of the pipeline is explained by the existence of the lateral soil springs which are always active in the Linear model and which restrict the motion of the pipeline's segment above the seabed. However, small vibrations in the IL direction become also evident within the soil-supported part of the pipeline in the zoomed images, but these vibrations are restricted in a small region in the vicinity of the shoulders and are again totally symmetric about the static configuration. This observation can be attributed to the inevitable deformation of the springs used to model the soil properties under the excitation of the current loads, as explained in detail previously. As far as the Non-Linear model is concerned, the above observation can be explained more easily by also taking a closer look at Figures 8.6, 8.7, 8.8 and 8.9. To be more precise, from Figures 8.6b, 8.7b, 8.8b and 8.9b which correspond to the CF response near the shoulder, it becomes evident that when the Non-Linear model is used, there are two touch-down points between the pipeline and the seabed, both when the response is in the positive and in the negative directions. This is a result of the ability of the pipeline to detach and lift up from the seafloor. So when the pipeline during its vibration gets in touch with seabed at the first touch-down point, the part of the pipeline that is further away from the free span lifts up until it reattaches to the seafloor at the second contact point. This is a result of the pipeline's bending stiffness and is also amplified by the fact that the TD VIV model is applied in the soil-supported region of the pipeline too as will be explained in detail in the following paragraph. This response is not possible to be captured by the Linear model because of the existence of the vertical soil springs which are always active and suppress both the upward and the downward motion of the pipeline. So, since there is a significant part of the pipeline that is not in contact with the seafloor, a considerable IL response can be developed when the Non-Linear soil model is used and this is one of the main differences between the two models. Finally, in Figures 8.6b, 8.7b, 8.8b and 8.9b it is evident that because of the "lift off" phenomenon the first touch-down point in the Non-linear model is further away from the end of the initial free span than the one and only contact point in the Linear model.

At this point it is worth mentioning that the fact that there is significant CF and IL response even far away from the edge of the free span is a bit exaggerated in this thesis compared to a real-life case. The reason for this is that in all the analyses that were conducted in the context of the present thesis, the TD VIV model was applied to the whole length of the pipeline and not only to the free span, in order to be able to capture the aforementioned "lift off" phenomenon. However, typically a gap of at least half diameter between the seabed and the pipeline is required in order for the vortex shedding phenomenon to occur. Therefore, it would be more correct to apply the TD VIV model only to the actual active free span and to use another model (e.g. the Morison's load model) for the rest of the pipeline. However, as the pipeline vibrates and because

of the ”lift off” phenomenon, the position of the touch-down point and consequently the active free span length constantly changes and these variations are more significant as the current velocities increase. So considering the number of different current velocities and cases that had to be examined, it was decided that such an analysis would be too complicated and tedious and beyond the context of the present thesis. For all these reasons and also taking into account that the main goal of this analysis is to compare the two soil models, it was decided to apply the TD VIV model to the whole pipeline for all the simulations and thus to be able to capture this ”lift off” phenomenon and observe the differences between the two soil models.

In Figures 8.10 - 8.12 the calculated distribution of the bending stresses and the respective fatigue damage accumulation along the pipeline both in the IL and the CF directions are illustrated with respect to the Non-Linear soil model and for soil damping ratio $\zeta_{soil} = 22\%$. The respective findings with regard to the Linear soil model are presented in Figures 8.13 - 8.15. As a first step, these results are given here separately for the two soil models in order to observe the main trends with regard to the distribution of the bending stresses and the fatigue damage along the pipeline when the two soil models are considered and also to describe the way these findings change as a function of the examined current velocity. Moreover, in Figures 8.16 - 8.18, comparative plots of the calculated distribution of the bending stresses and the respective fatigue damage accumulation are illustrated for two indicative current velocities for an easier identification of the main differences between the two examined soil models. The respective findings for other examined current velocities can be found in Appendix B.3 (Figures B.99 - B.108).

At this point it is worth noting that in Figures 8.10a and 8.10b for the curve corresponding to 1.7 m/s, a smaller timestep of 0.01 s was required instead of the initial timestep of 0.025 s that was used for the rest of the velocities. The reason for this is that, as is shown clearly in Figures B.25a and B.25b, when the initial timestep was used, the obtained curve for the velocity of 1.7 m/s, although it follows the same trend as the rest of the curves, it presents some indentation along the free span. This phenomenon was also observed for the other three examined cases. More specifically, this was also observed for the Linear model and $\zeta_{soil} = 22\%$ at 1.5 m/s but at a smaller degree (see Figures B.52a and B.52b), and for both soil models at a small extent at 1.5 m/s and predominantly at 1.8 m/s when the soil damping ratio of $\zeta_{soil} = 8\%$ was used (see Figures B.133a and B.133b and Figures B.160a, B.160b and B.162a for the Non-Linear and the Linear soil models respectively). One possible explanation of this peculiar behaviour at these velocities could be the fact that for all the examined cases, the CF and IL responses become almost equal in this velocity range and therefore, as has already been mentioned, the complicated interaction between the two vibrations makes the prediction of the VIV responses much more difficult at these velocities. In order to solve this problem, initially it was examined if there are any convergence problems present at these velocities, but this was not the case. So eventually it was decided to use an even smaller timestep for these cases, hoping that this might result in capturing this complex interaction more accurately and indeed this smaller timestep solved the above problem. So, in the following the results obtained using the smaller timestep will be presented for these problematic cases.

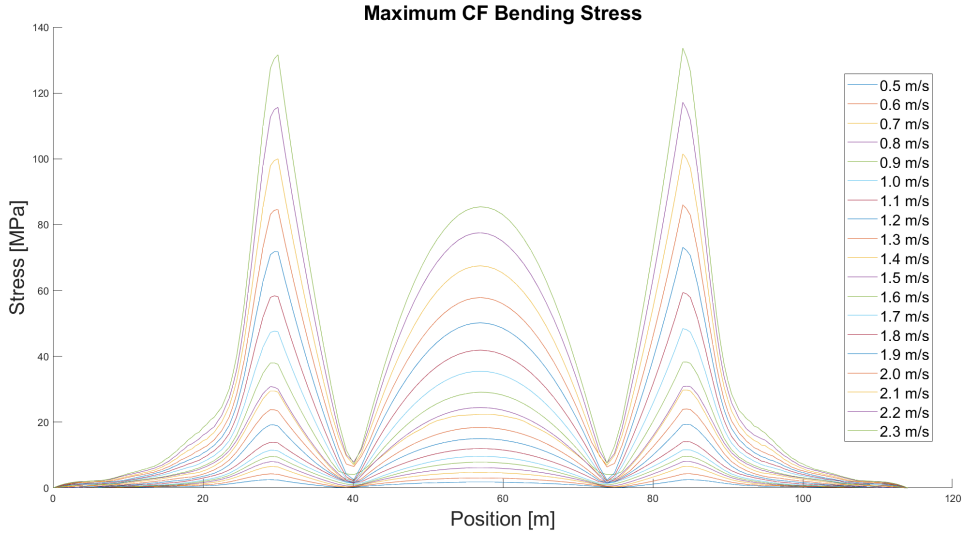

(a) CF - Maximum Bending Stress

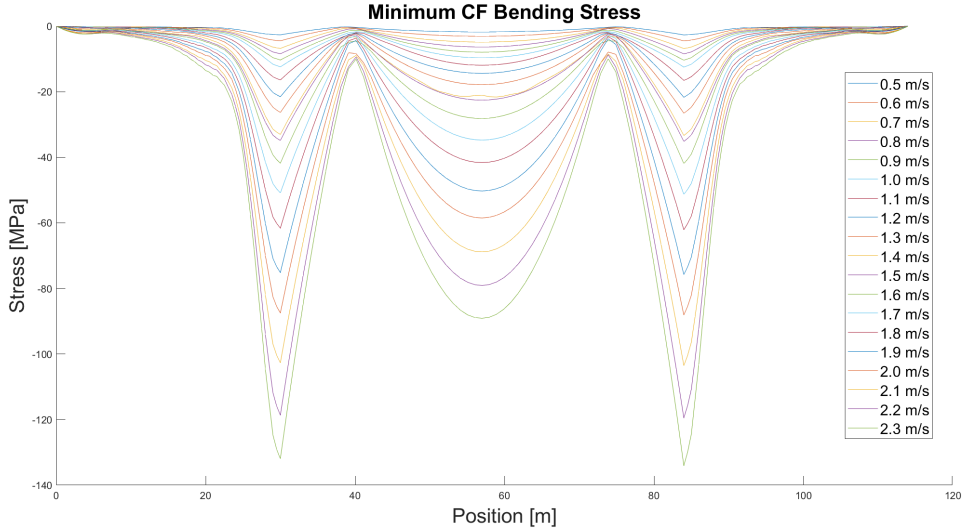

(b) CF - Minimum Bending Stress

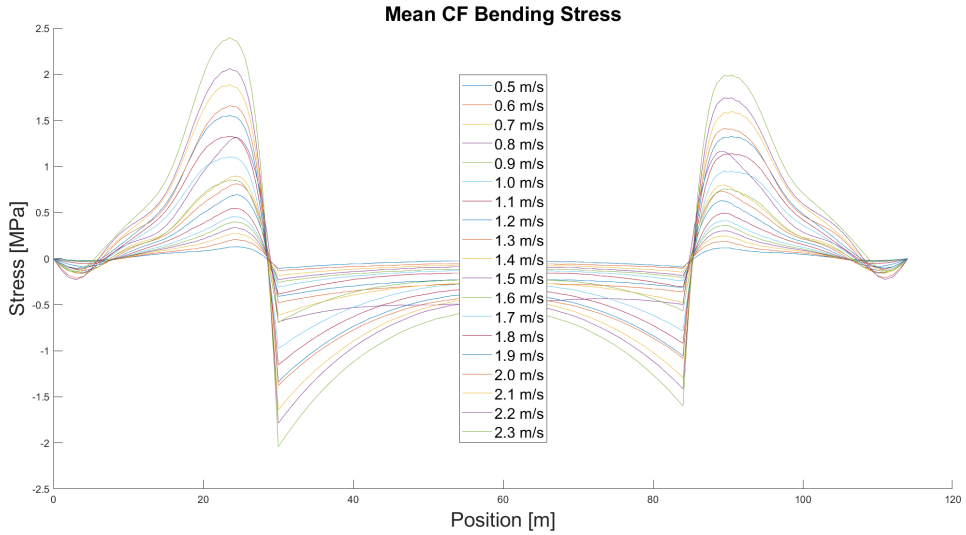

(c) CF - Mean Bending Stress

Figure 8.10: Plots of the calculated bending stress distribution in the CF direction for the Non-linear soil model and $\zeta_{soil} = 22\%$.

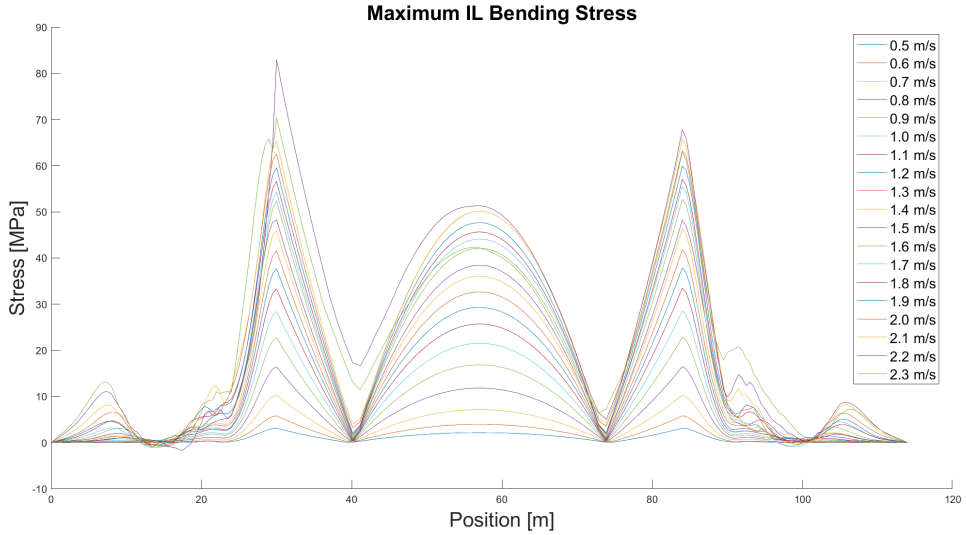

(a) IL - Maximum Bending Stress

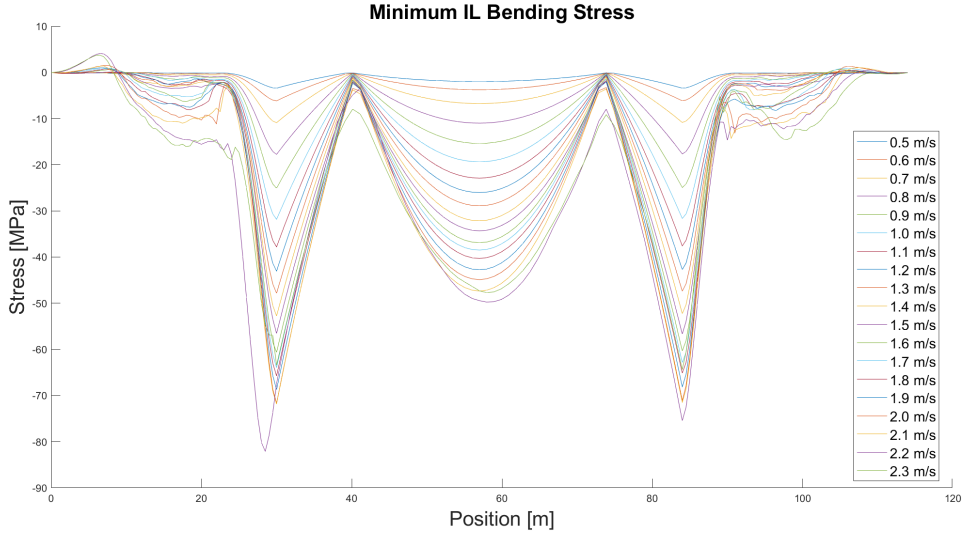

(b) IL - Minimum Bending Stress

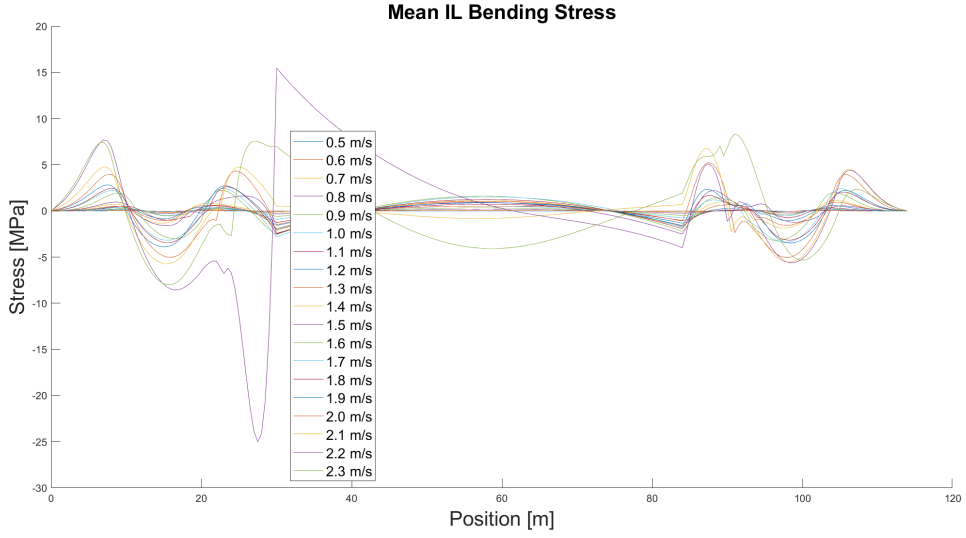

(c) IL - Mean Bending Stress

Figure 8.11: Plots of the calculated bending stress distribution in the IL direction for the Non-linear soil model and $\zeta_{soil} = 22\%$.

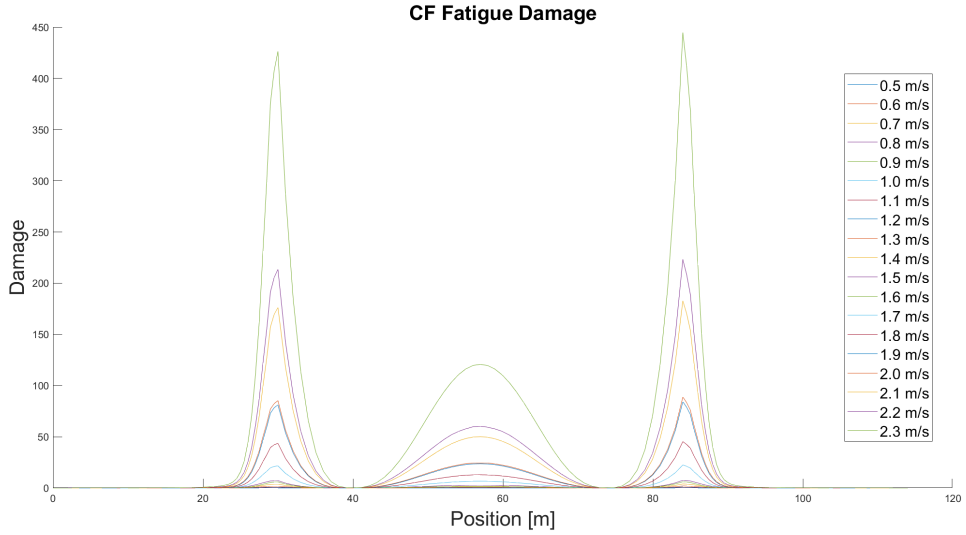

(a) CF - Fatigue Damage Accumulation

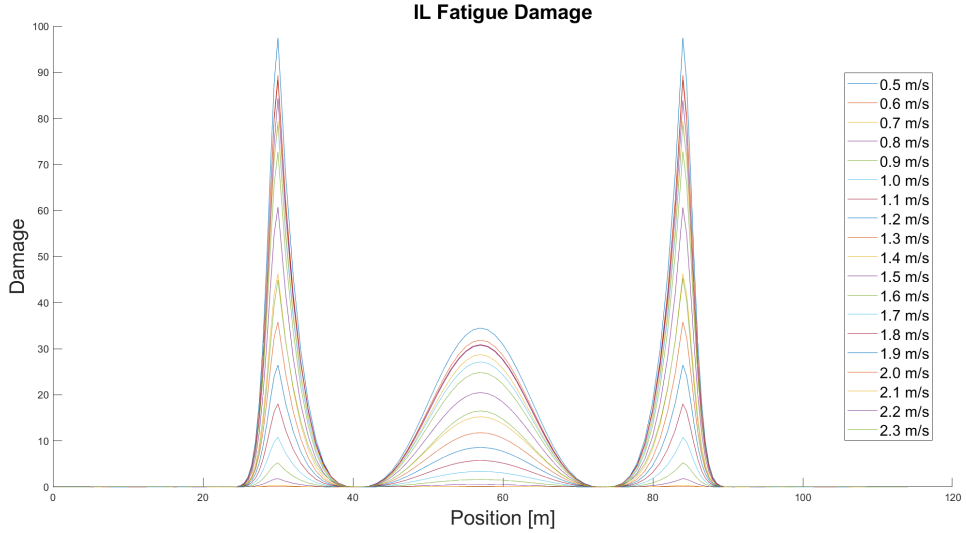

(b) IL - Fatigue Damage Accumulation

Figure 8.12: Plots of the calculated fatigue damage distribution in both directions for the Non-linear soil model and $\zeta_{soil} = 22\%$.

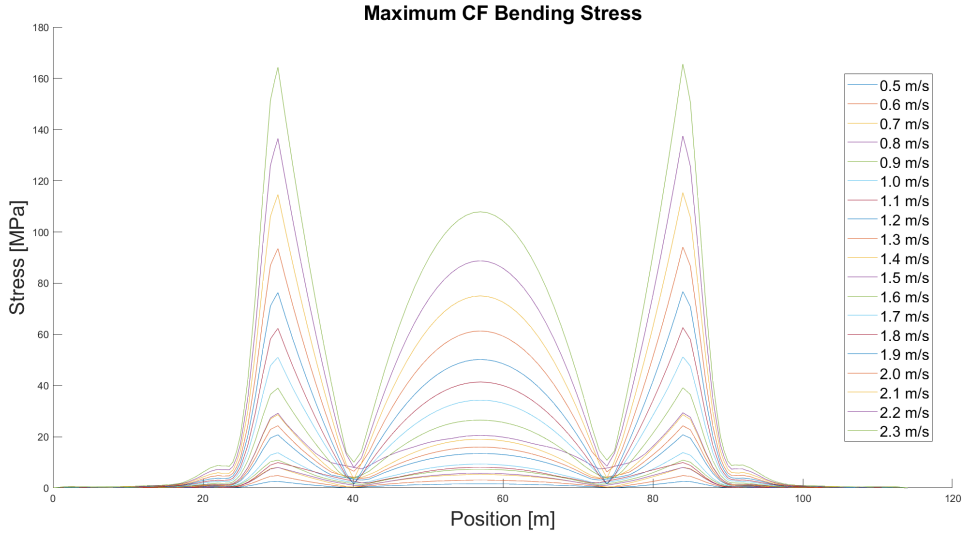

(a) CF - Maximum Bending Stress

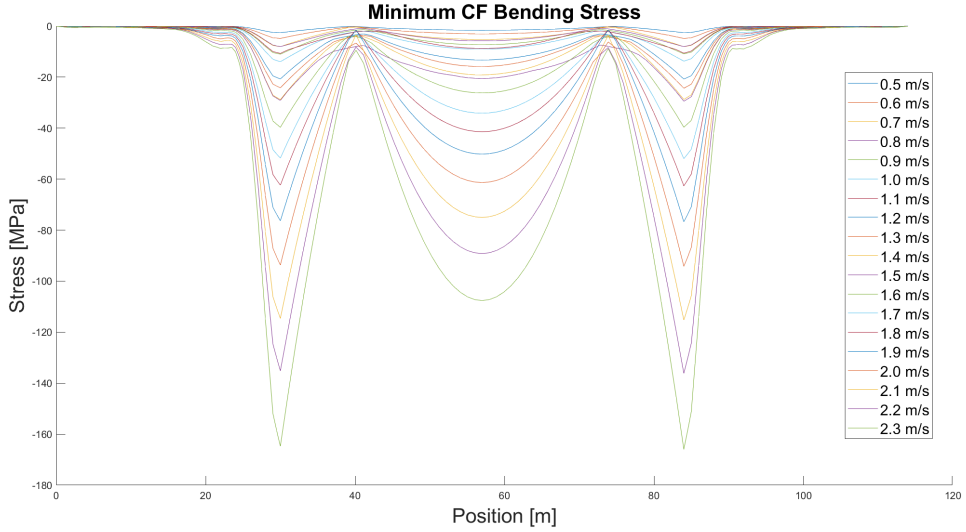

(b) CF - Minimum Bending Stress

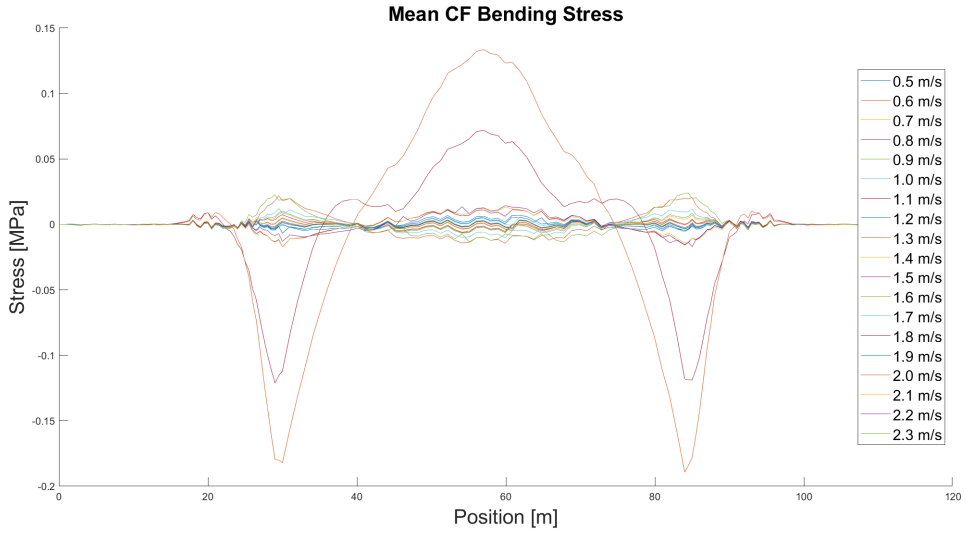

(c) CF - Mean Bending Stress

Figure 8.13: Plots of the calculated bending stress distribution in the CF direction for the Linear soil model and $\zeta_{soil} = 22\%$.

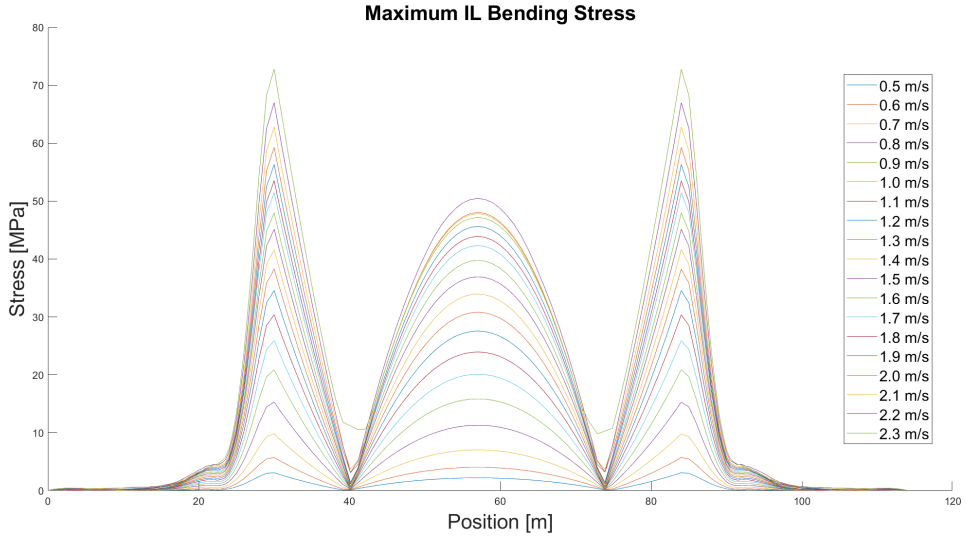

(a) IL - Maximum Bending Stress

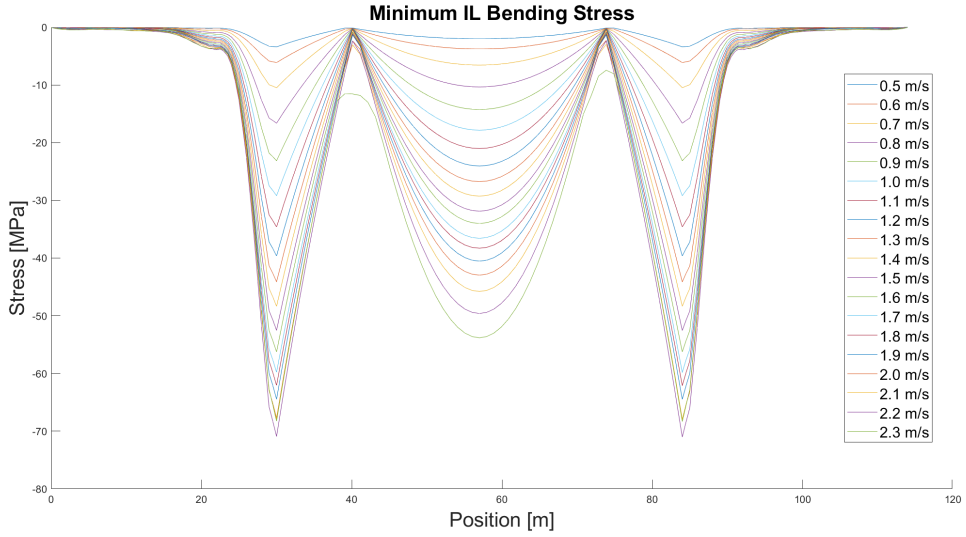

(b) IL - Minimum Bending Stress

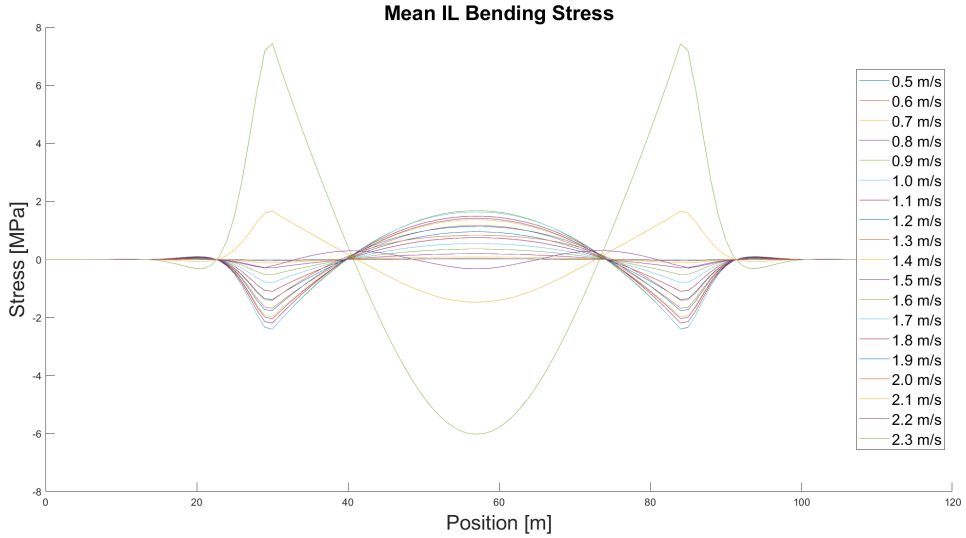

(c) IL - Mean Bending Stress

Figure 8.14: Plots of the calculated bending stress distribution in the IL direction for the Linear soil model and $\zeta_{soil} = 22\%$.

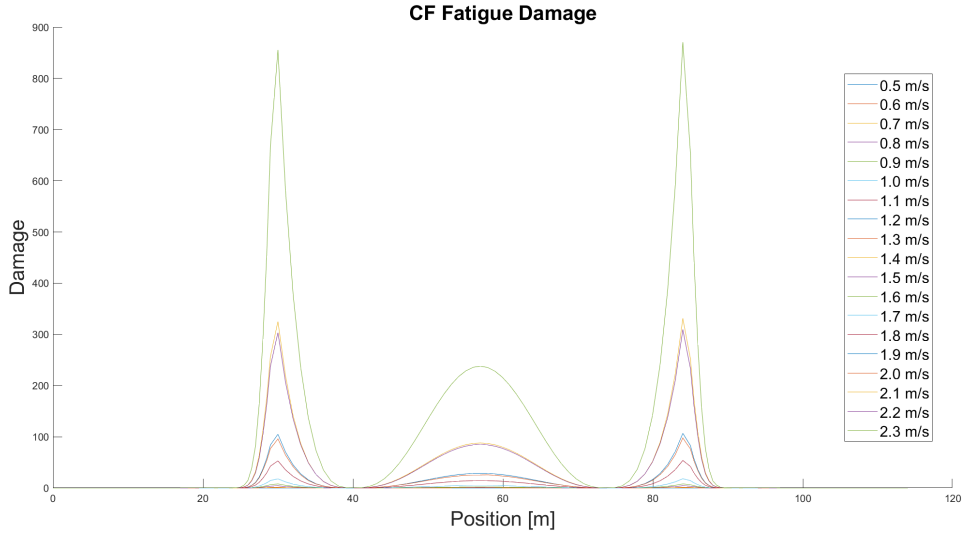

(a) CF - Fatigue Damage Accumulation

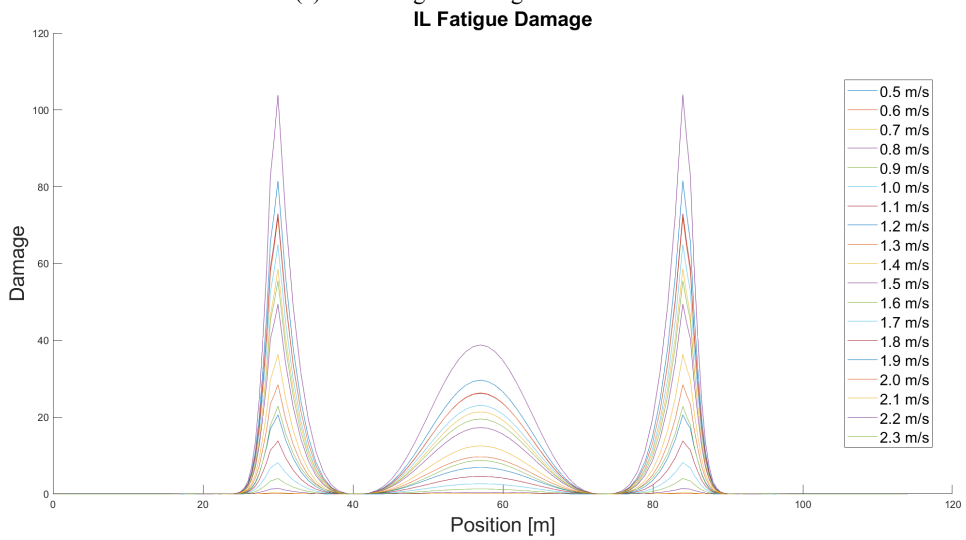

(b) IL - Fatigue Damage Accumulation

Figure 8.15: Plots of the calculated fatigue damage distribution in both directions for the Linear soil model and $\zeta_{soil} = 22\%$.

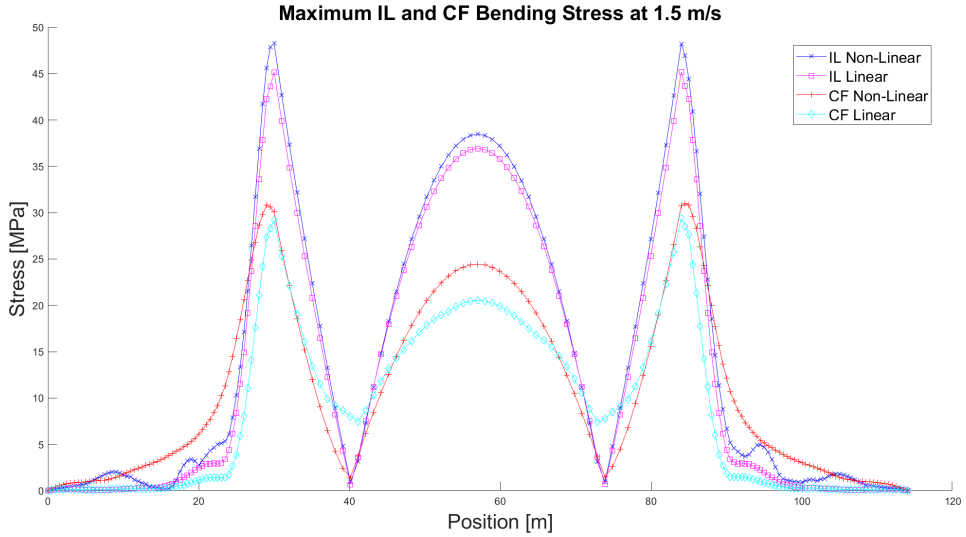

(a) CF and IL Maximum Bending Stress Distribution at 1.5 m/s

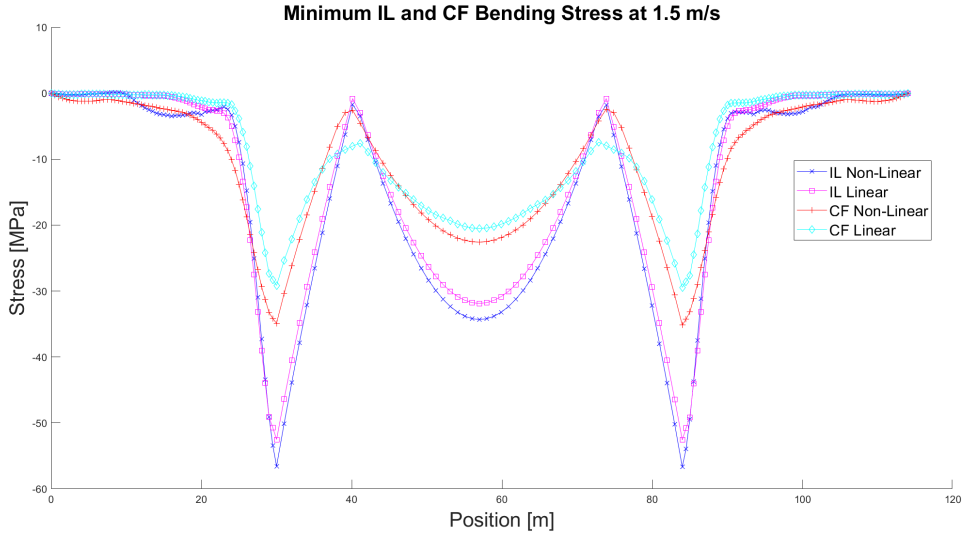

(b) CF and IL Minimum Bending Stress Distribution at 1.5 m/s

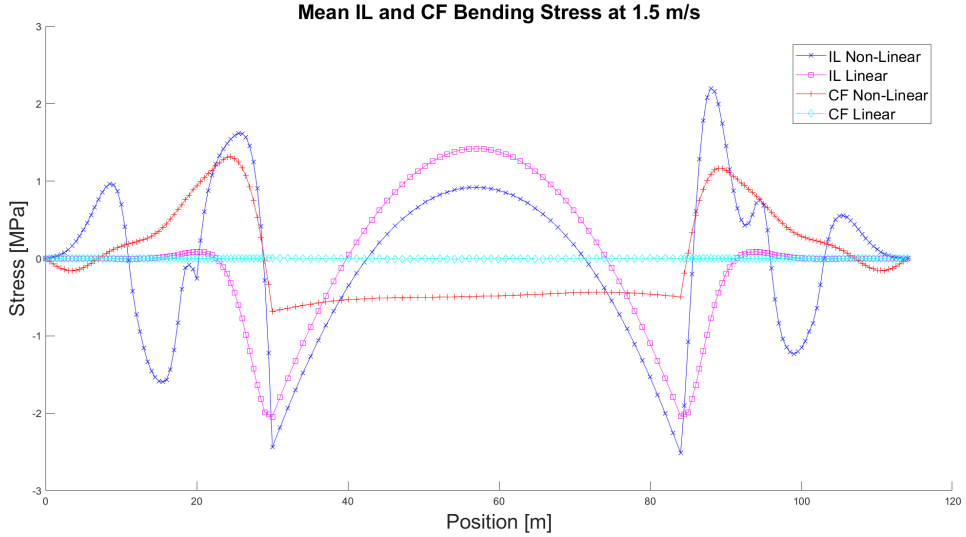

(c) CF and IL Mean Bending Stress Distribution at 1.5 m/s

Figure 8.16: Comparative plots of the calculated bending stress distribution for the two soil models and $\zeta_{soil} = 22\%$ at 1.5 m/s.

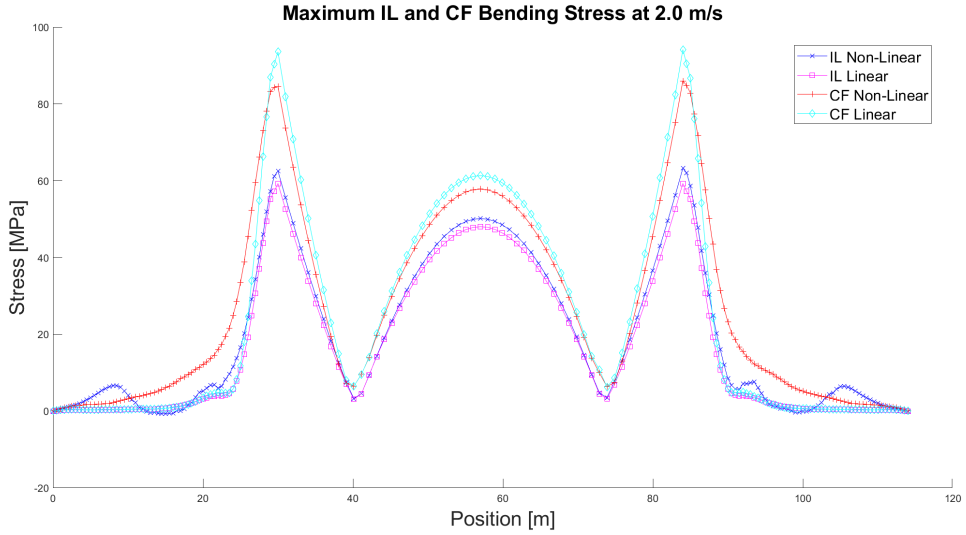

(a) CF and IL Maximum Bending Stress Distribution at 2.0 m/s

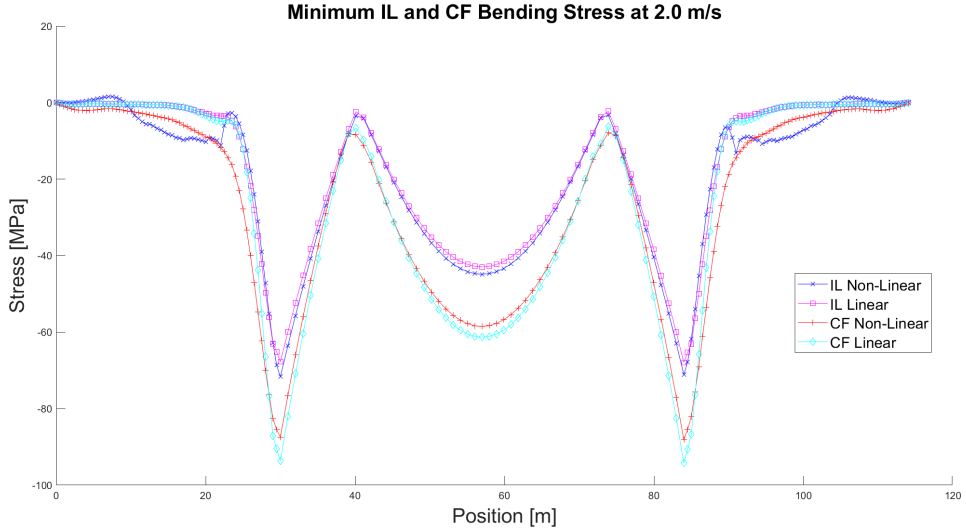

(b) CF and IL Minimum Bending Stress Distribution at 2.0 m/s

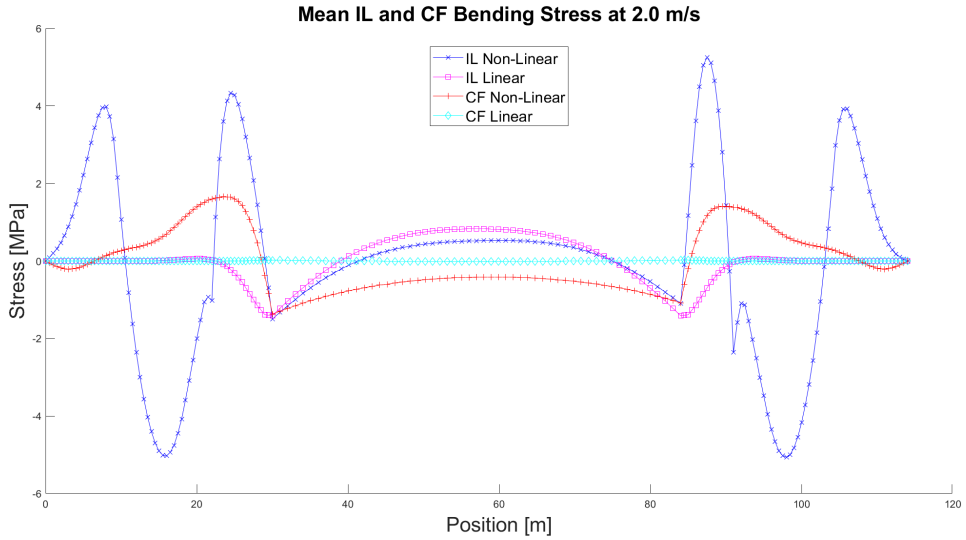

(c) CF and IL Mean Bending Stress Distribution at 2.0 m/s

Figure 8.17: Comparative plots of the calculated bending stress distribution for the two soil models and $\zeta_{soil} = 22\%$ at 2.0 m/s.

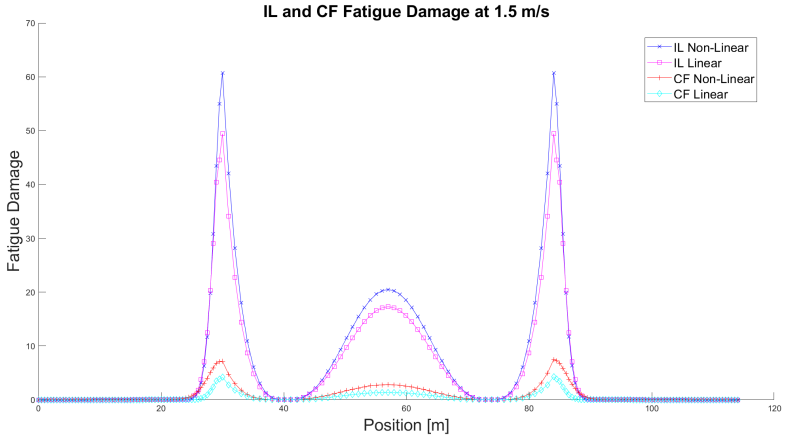

(a) CF and IL Fatigue Damage Accumulation at 1.5 m/s

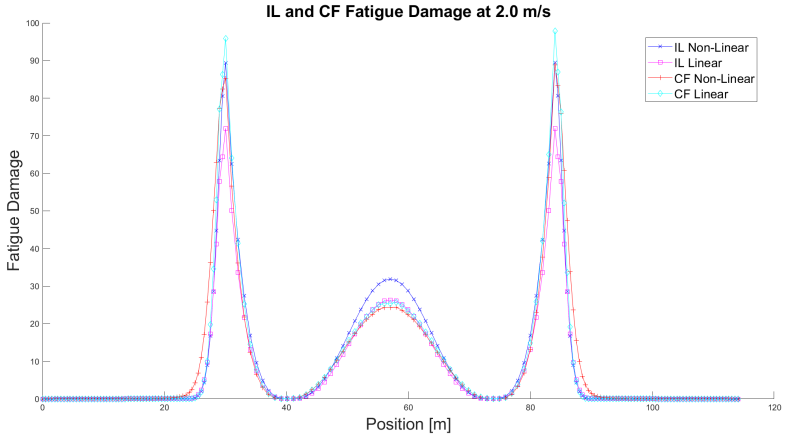

(b) CF and IL Fatigue Damage Accumulation at 2.0 m/s

Figure 8.18: Comparative plots of the calculated fatigue damage distribution for the two soil model and $\zeta_{soil} = 22\%$ at current velocities 1.5 and 2.0 m/s.

From Figures 8.10 - 8.18 it becomes apparent that as far as the two shoulders and the free span are concerned, the same trends can in general be observed for both examined soil models. However, some more profound deviations become clear in the soil supported part of the pipeline because of the differences of the two examined soil models and the more profound effect of the ”lift off” phenomenon there. To be more precise, both soil models predict that for all the examined current velocities, the bending stresses and the fatigue damage take their maximum values at the shoulders of the pipeline, while a lower peak can also be observed in the middle of the free span, something that is in total agreement with what is theoretically expected. Moreover, it becomes clear that in both directions, both the bending stresses and the fatigue damage generally increase with the current velocity. However, this is not true with regard to the computed IL bending stress and fatigue damage distribution for the highest velocity of 2.3 m/s. More specifically, the aforementioned increasing trend can be observed for velocities up to 2.2 m/s while for the velocity of 2.3 m/s somewhat smaller values were obtained. The difference from the respective curves corresponding to 2.2 m/s velocity, varies depending on the considered position along the length of the pipeline. These observations can again mainly be attributed to the pipeline curvature (see Figures B.20c and B.47c), which increases with the current velocity leading to the above mentioned issues and enhances the uncertainty of the results at high velocities. The fact that this is indeed the reason behind this different response becomes more easily understood with regard to the Linear model, since, due to the linearity and hence simplicity of this soil model, the observed

behaviour is not that random. To be more precise, from Figures 8.14a and 8.14b it becomes clear that the velocity of 2.3 m/s in fact gives the highest maximum (i.e. positive) stress at the shoulders and the highest minimum (i.e. negative) stress at the midspan. This behaviour is attributed to the extreme curvature of the pipeline and the consequent limitation of the dynamic response of the pipeline, which results in turn in much higher mean stresses for this velocity. These mean stresses have positive sign above the shoulders and negative sign at the midspan, as is shown clearly in Figure 8.14c. Moreover, this is also the reason why the velocity of 2.3 m/s does not give the highest IL fatigue damage, since these relatively high mean stresses do not contribute to the induced fatigue damage.

Furthermore, as far as the CF response is concerned, from Figures 8.10a and 8.10b, the effect of the ”lift off” phenomenon becomes evident, since a distribution of non-negligible stresses in a large segment of the soil-supported part of the pipeline can be observed. The existence of the ”lift off” phenomenon, which in turn results in a CF response that is not symmetric about the static configuration, is also proven in Figure 8.10c. In order to understand this, one has to take into account the fact that, as explained in section 7.2.5, the static curvature (and consequently the bending stress distribution because of the static configuration) had been removed from the curvature time series prior to this analysis. Therefore, the fact that there is a non-zero mean stress distribution along the pipeline proves that the CF response is indeed not symmetric. All the above observations with regard to the effects of the ”lift off” phenomenon become even more profound with regard to the distribution of the bending stresses in the IL direction. To be more precise, significant values of the bending stress, which seem to extend in almost the whole length of the soil-supported part of the pipeline, become clear in Figures 8.11a and 8.11b and a non-zero mean value is evident in Figure 8.11c. Moreover, the distribution of the IL bending stress above the seabed can be characterized as a bit chaotic and is definitely not as smooth as is observed with regard to the CF direction. This is something totally expected, since the rapid changes between ”contact” and ”no contact” conditions result in turn in repetitive alternations between having lateral springs and dampers corresponding to the dynamic soil properties and not having springs and dampers at all.

What is more, the fact that the ”lift off” phenomenon is not present when the Linear soil model is used becomes clear from Figures 8.13a - 8.13b and 8.14a - 8.14b with regard to the CF and IL directions respectively. More specifically, from these figures, it becomes apparent that there are no bending stresses induced in the part of the pipeline that is above the shoulders and is supported by the soil, apart from a very small region that extends 1-2 m beyond the free span. As already explained, the stresses that can be observed in these regions are a result of the fact that the soil properties are approximated by the utilization of springs and dampers and there is inevitably a small deformation of these springs due to the forces exerted on them by the motions of the pipeline. Nevertheless, the stresses that are induced in the pipeline at these regions are totally symmetric, as was also true with regard to the respective response of the structure. The latter becomes even more evident by the fact that the CF mean stress distribution is almost equal to zero along the whole length of the pipeline (i.e. both within the free span and within the soil-supported region). This is clearly illustrated in Figure 8.13c. Finally, all the above observations with regard to the two examined soil models are also verified in the comparative plots in Figures 8.16 - 8.18. Moreover, the existence of two touch-down points when the Non-Linear model is considered is clearly verified by the shape of the curves corresponding to the IL bending stress distribution within the soil-supported part of the pipeline in these Figures.

The next step of this analysis is to compare in more detail the results obtained using the two dif-

ferent soil models focusing on the deviations between them at the shoulders and at the midspan of the pipeline, where the maximum values for the induced bending stresses and fatigue damage were observed above. In Figure 8.19, the obtained results for the CF and IL Bending Stresses and Fatigue Damage induced at the left shoulder of the pipeline with regard to both examined soil models are presented. The exact same analysis was conducted for the right shoulder and the midspan of the pipeline too, but it was found the in general the same trends can be observed for all cases. For this reason it was preferred to present only the results corresponding to the left shoulder in the following. The respective findings for the rest of the examined cases can be found in Appendix B.3 (Figures B.96 - B.98).

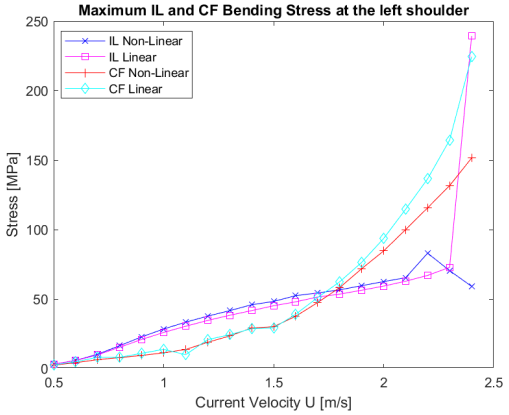

(a) Maximum Bending Stress at the left shoulder

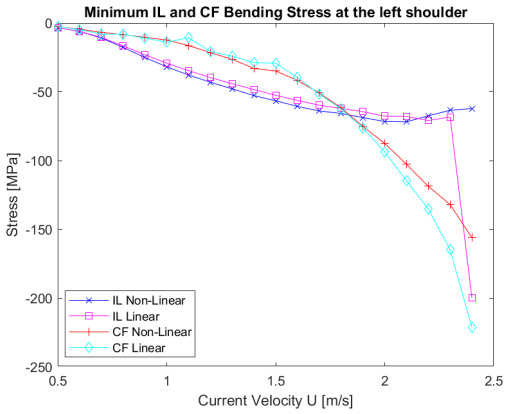

(b) Minimum Bending Stress at the left shoulder

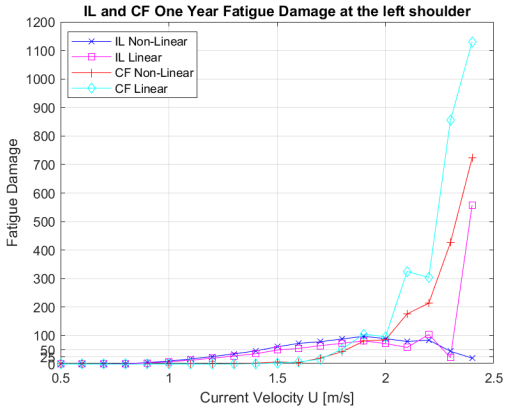

(c) Fatigue Damage Accumulation at the left shoulder

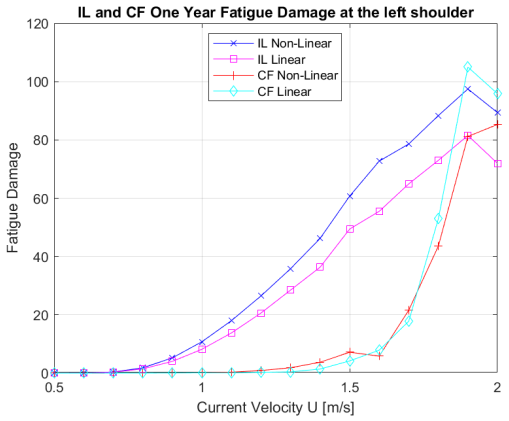

(d) Fatigue Damage Accumulation at the left shoulder (zoom at velocities up to 2.0 m/s)

Figure 8.19: Comparative plots of the calculated Bending Stress and Fatigue Damage at the left shoulder.

Neglecting again the results corresponding to the 2.4 m/s current velocity case, it becomes clear from Figures 8.19a and 8.19b that the maximum (positive) and minimum (negative) induced bending stresses at the left shoulder are almost symmetric and therefore the following analysis will be limited only to the maximum bending stress. At a first glance in Figure 8.19 it becomes evident that the two examined soil models seem to be in very good agreement. An interesting observation that becomes apparent from Figure 8.19a is the fact that the way that the bending stresses induced at the left shoulder increase as a function of the current velocity seems to be identical to the trends observed in Figure 8.1b with regard to the maximum response amplitude. More specifically, both models seem to give almost the same results for the IL bending stresses.

The Non-linear soil model gives somewhat higher values of the IL bending stress than the Linear model for the whole range of current velocities up to 2.1 m/s. The calculated deviations between the two models in this velocity range are quite small with the maximum discrepancy of 9.19% being observed at 1.4 m/s. The discrepancy between the two models is very small at the highest examined velocity of 2.3 m/s too, where the Linear model predicts a value of IL bending stress 3.39% higher than the Non-Linear model. Contrary to the aforementioned though, the difference between the results of the two models is much more profound at the velocity of 2.2 m/s where the maximum deviation of 19.28% can be observed.

As far as the CF bending stress is concerned, it becomes clear from Figure 8.19a that in general the Linear soil model constantly predicts higher CF bending stress for the whole range of the examined current velocities. The maximum deviation between the two models can be observed at the highest examined velocity of 2.3 m/s, where the Linear model gives 24.9% higher value than the Non-Linear one. There are only three velocities for which the opposite is true, at 1.1 m/s, 1.4 m/s and 1.5 m/s. For these three velocities, the Non-Linear model predicts 27.4%, 1.69% and 2.92% higher values of CF bending stress than the Linear model. As for the velocities of 1.4 and 1.5 m/s, it is clear that the deviation between the two soil models is almost negligible. Moreover, with regard to the velocity of 1.1 m/s, the observed discrepancy is not as significant as it appears to be, since the actual values of CF bending stress predicted by the Non-linear and the Linear models are 13.67 MPa and 9.92 MPa respectively. From these values it becomes obvious that, as explained previously, at such a low velocity the CF response is relatively small and without any practical importance.

As for the Fatigue Damage accumulation shown in Figure 8.19c, the same trends as for the induced bending stresses become apparent, something totally expected since, as explained previously based on the results of Figure 8.1a, there were no significant differences between the two soil models in terms of the calculated response frequency in both directions. In general, the results obtained using the two different soil models seem to be in good agreement. More specifically, from Figure 8.19c it becomes clear with regard to both examined soil models that the IL fatigue damage accumulation is much higher than the CF fatigue damage for the lower part of the examined velocities up to 1.9 m/s, where approximately the same contribution to the fatigue damage can be observed in the two directions. However, for higher velocities, the CF fatigue becomes the dominant cause of fatigue damage accumulation in the pipeline. As an illustrative example it is worth mentioning that for the highest examined velocity of 2.3 m/s, the Non-Linear and the Linear soil models predict about 10 and 20 times higher fatigue damage in the CF direction than in the IL direction respectively. This observation agrees well with the respective findings of Figure 8.1b with regard to the maximum response amplitude in the two directions, where it was found that the CF vibrations become more important and dominate the pipeline's response at a current velocity of about 1.8 m/s.

Moreover, as far as the IL fatigue damage is concerned, it becomes clear from Figures 8.19c and 8.19d that the Non-linear soil model constantly predicts approximately 20% higher values than the Linear model for the whole range of current velocities up to 2.1 m/s. The Non-Linear model gives higher fatigue damage accumulation for the highest examined velocity of 2.3 m/s too, and in fact the maximum discrepancy of 49% between the two models can be observed at this velocity. However, it should be noted that the actual fatigue damage predicted by both models for the velocity of 2.3 m/s is much smaller than the respective results for velocities between 1.5 and 2.2 m/s. Finally, the only velocity for which the Linear model gives a higher prediction than the Non-Linear one with respect to the IL fatigue damage is at 2.2 m/s and the respective deviation

between the two models is 23%. As for the CF direction, it becomes apparent that for the lower part of the considered velocity range up to 1.6 m/s, the CF fatigue damage can in general be regarded as negligible with regard to both soil models. For higher velocities, the contribution from the CF VIV to the fatigue damage accumulation increases rapidly. This growth is much more profound with respect to the Linear model, which seems to give much higher values than the Non-linear model. The maximum discrepancy between the two models can be observed at the highest velocity of 2.3 m/s and is equal to 100%, which means that the Linear model predicts two times higher fatigue damage than the Non-Linear one.

All the above observations both with regard to the bending stresses and the fatigue damage accumulation are totally expected and agree very well with the previous findings regarding the calculated dominant vibration frequency and the maximum response amplitude. More specifically, as far as the IL direction is concerned, the fact that the Non-Linear model gives higher predictions for the IL bending stress than the Linear one for the whole range of current velocities for which the IL response is of importance, is in agreement with the respective findings for the IL maximum response amplitude and can again be attributed to the effects of the ”lift off” phenomenon and the deactivation of the lateral soil springs and dampers in the Non-Linear model when there is not contact between the pipe and the seafloor. Moreover, the fact that the discrepancies between the two models are somewhat higher with regard to the IL bending stresses at the left shoulder compared to the respective results for the maximum response amplitude can be attributed to the previously mentioned fact that the effect of the ”lift off” phenomenon is more significant near the shoulder than it is in the vicinity of the midspan. Finally, as far as the IL fatigue damage accumulation at the left shoulder is concerned, as explained previously, it is governed by the respective bending stress and therefore the same trends become evident. The fact that the difference between the two soil models is higher in this case than what was observed above for the stresses, the response amplitude and the vibration frequency can be explained by the fact that all those three parameters together contribute to the level of the induced fatigue damage. Therefore, since the Non-Linear model gives slightly higher prediction for all three of these parameters ultimately results in an even higher deviation between the two models with regard to the IL fatigue damage accumulation.

Finally, as far as the CF direction is concerned, the fact that for the higher examined velocities for which the CF response is of interest, the Linear model gives considerably larger values of CF bending stress and fatigue damage accumulation at the left shoulder can be attributed to the ”lift off” phenomenon. To be more precise, the ability of the pipeline to detach and lift up above the seabed when the Non-Linear model is used results in a more smooth configuration of the pipeline in the vicinity of the shoulders. In other words, when the Non-Linear model is used there is not an abrupt change in curvature in the touch-down point as is the case for the Linear model, since the pipeline can lift up and reattach to the seafloor further away from the end of the initial free span resulting in a more smooth contact and thus in smaller change of curvature at the touch-down point. This reduced curvature change leads to an alleviation of the CF bending stresses induced at the shoulder and consequently to lower fatigue damage accumulation. This alleviation of stresses in the CF direction becomes clear if one analyzes the results presented in Figures 8.1a, 8.1b, 8.19a and 8.19d in combination. An illustrative example is regarding the velocity of 2.0 m/s. From Figures 8.1a and 8.1b it becomes apparent that both soil models give approximately the same response frequency and maximum amplitude at 2.0 m/s. However, a significant deviation between the CF bending stress and fatigue damage predicted by the two models can be observed in Figures 8.19a and 8.19d, which is a clear indication of the aforementioned stress alleviation in the Non-Linear model.

8.2 Comparative Study - Soil Damping Ratio 0.08

In this section, a comparative study between the most relevant of the results obtained using the Non-Linear and Linear soil models with regard to soil damping ratio $\zeta_{soil} = 8\%$ is conducted. The total set of findings with regard to soil damping ratio $\zeta_{soil} = 8\%$ (also including the results presented in this section) can be found in Appendices B.4, B.5 and B.6, where the results corresponding to the Non-Linear soil model alone, to the Linear soil model alone and to the comparative study between the two soil models are presented respectively. The main goal of this section is on the one hand to describe the observed trends in terms of how the characteristics of the VIV response change as a function of the examined current velocity and on the other hand to compare in detail the obtained results with respect to the two different soil models in order to identify the differences between the two soil models. In Figure 8.20, the dominant response frequencies and the maximum response amplitudes normalized by the pipe's diameter that were calculated by means of the time domain VIV analysis with regard to both examined soil models and considering the soil damping ratio $\zeta_{soil} = 8\%$ are illustrated.

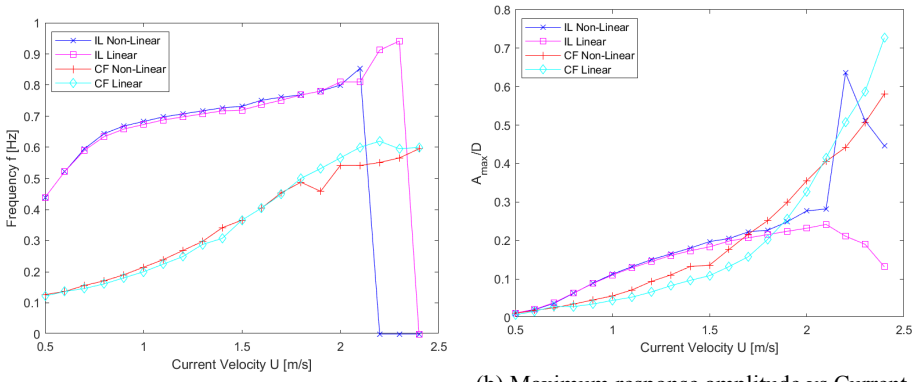

(a) Response Frequency vs Current Velocity

(b) Maximum response amplitude vs Current Velocity

Figure 8.20: Plots of the dominant response frequencies and the maximum response amplitudes for the Non-Linear and Linear soil models and $\zeta_{soil} = 8\%$.

At this point it is worth noting that, as becomes clear from Figure 8.20a, there are some problems observed when the higher current velocities are considered with regard to both examined soil models. More specifically, as far as the Linear model is concerned, the aforementioned issue of having extremely high pipeline curvature at the highest examined current velocity of 2.4 m/s is present in this case too. As was also observed and explained in detail in section 8.1, the high curvature results in increased tension and geometric stiffness in the system and eventually leads to unrealistic and chaotic bending stress and fatigue damage distribution in the IL direction, as can be seen clearly in Figures B.161 and B.162b with regard to the velocity of 2.4 m/s. As for the Non-Linear model, apart from the highest three examined current velocities (2.2-2.4 m/s), for which dominant vibration frequency equal to zero is predicted again for the IL direction, the analysis with regard to the velocity of 2.1 m/s is also problematic. However, contrary to the previous cases, the present problem does not have to do with the extreme curvature issue described above. In this case the problem is a result of the combination of using a smaller value of soil damping ratio and the fact that, as explained previously, the TD VIV model is applied to the whole length of the pipeline. To be more precise, the smaller damping ratio, as expected, results in higher response amplitudes all over the pipeline and hence to a more profound "lift off" effect at the shoulders. Moreover, apart from the increased contribution of the "lift off" phenomenon at the soil-supported part of the pipeline, the response of the pipeline in this region itself is higher due to the application of the TD VIV model there and also because of the use

of smaller soil damping ratio at the same time. The ultimate result is that a very small segment of the pipeline is in contact with the seafloor at each time instant. This fact, combined with the increased forces due to the higher pipeline response, leads eventually to a situation where the IL induced forces are higher than the vertical force exerted to the seabed times the friction coefficient $F_V \cdot \mu$ (although an extremely high value of μ is used). As a result, pipeline sliding occurred, as is clearly illustrated in Figures B.126 - B.129. The pipeline sliding leads in turn to chaotic bending stress and fatigue damage distribution in the IL direction, as shown in Figures B.134 and B.135b. For these reasons, the following analysis will focus only to current velocities up to 2.0 m/s, for which the obtained results were deemed reliable. The full set of the obtained results including the higher examined velocities can be found in Appendices B.4 - B.6.

From Figure 8.20, it becomes clear that in general the same trends, in terms of how the dominant vibration frequency and the maximum response amplitude in both the CF and IL directions change as a function of the current velocity, that became evident in Figure 8.1 in section 8.1 with regard to soil damping ratio $\zeta_{soil} = 22\%$, can be observed here too, at least for current velocities up to 2.0 m/s which are of interest. More specifically, from Figure 8.20a, it becomes apparent that for both the IL and CF responses, the dominant vibration frequency increases with the current velocity. This increase follows again an almost constant slope with regard to the CF direction. As for the IL response, the rate of increase of the corresponding curve is again much higher for the lower part of the considered velocities (up to 0.8 m/s), while for higher velocities an increasing trend is still apparent, but the slope of the curve is clearly smaller in this region. The only significant difference from Figure 8.1a can be observed in the CF direction, since the indentations, that were observed in the previous section for the upper half of the examined velocity range, are not present at all in the present case with regard to the Linear model, while only a small drop of the dominant CF frequency becomes evident for the Non-Linear model at 1.9 m/s. These small deviations also resulted in some minor changes in the obtained results for the ratio of the IL to the CF frequency, which is found for the lowest velocity equal to about 3.5-3.6 and increases slowly as the velocity becomes higher, taking its maximum value of $\frac{f_{IL}}{f_{CF}} \approx 4$ at 0.7 m/s. Subsequently, a gradual decrease with the current velocity can be observed until the value of about 1.45 is reached at 2.0 m/s. As far as the maximum response amplitudes are concerned, the trends illustrated in Figure 8.20b are almost identical to the respective findings of Figure 8.1b, since the CF response amplitude rises again at an increasing rate for higher current velocities, while the IL response amplitude rises with a slightly decreasing rate.

Based on the above presented findings of Figure 8.20, it becomes evident that there seems to be a very good agreement between the results of the two soil models especially as far as the IL response is concerned. However, more important deviations can be observed with regard to the CF direction. To be more precise, as far as the IL dominant vibration frequency is concerned, it becomes clear from Figure 8.20a that the Non-linear soil model seems to give slightly higher frequencies than the Linear model for current velocities up to 1.9 m/s, but the deviations are quite small, with the maximum discrepancy of 1.95% being observed at 1.6 m/s. Contrary to this, for the highest considered velocity of 2.0 m/s, the Linear model predicts 1.22% higher IL vibration frequency than the Non-Linear one. As for the CF vibration frequency, for the lower part of the examined current velocity range up to 1.7 m/s, the Non-linear soil model constantly predicts higher frequencies. The maximum discrepancy between the two models in this region becomes evident at 1.4 m/s and is equal to 10%. Furthermore, for the three highest considered velocities, the opposite trend is observed, with the Linear model giving higher CF response frequency than the Non-Linear model. The calculated deviations are 2.5% at 1.8 m/s, 15.96% at 1.9 m/s, which is the maximum overall discrepancy observed, and 4.5% at 2.0 m/s.

As far as the maximum response amplitudes are concerned, it becomes clear from Figure 8.20b that one of the most important deviations between the two models is that they predict that the CF vibrations will become more important and dominate the pipeline's response at different velocities. According to the Non-Linear model, the transition from an IL dominated response to a CF dominated response takes place at a current velocity between 1.6 and 1.7 m/s, while when the Linear model is considered, this transition occurs at a velocity between 1.8 and 1.9 m/s. Moreover, the Non-Linear model generally seems to give higher response amplitudes than the Linear model both in the IL and in the CF direction for the whole range of considered velocities up to 2.0 m/s, although for some of the lowest velocities up to 0.8 m/s, the opposite trend can also be observed. The deviation between the two models in general seems to be less significant with regard to the IL direction. More specifically, as far as the IL response amplitude is concerned, the difference between the two models seems to increase with the current velocity and thus the maximum discrepancy is observed at the highest velocity of 2.0 m/s and is equal to 16.25%. As for the CF response amplitude, the deviations are higher for velocities near the middle of the examined velocity range between 0.9 and 1.7 m/s. The discrepancies in this velocity range take values between 20.94% and 29.5% with the maximum deviation being observed at 1.2 m/s.

The above observations with regard to the IL response amplitude are totally expected and again can mainly be attributed to whether the "lift off" phenomenon takes place or not. More specifically, the fact that the deviation between the two models increases with the current velocity can be explained by the fact that as the velocity becomes higher the respective CF responses also increase and therefore the effect of the "lift off" phenomenon becomes more and more important. As for the predicted CF response amplitudes, it should be noted that contrary to what was observed with regard to the higher soil damping ratio that was examined previously, in the present case the Non-Linear model constantly predicts higher CF response than the Linear model. This observation can mainly be attributed to the fact that only velocities up to 2.0 m/s were considered in this case. For this velocity range it was found in the previous case too that the Non-Linear model gives either higher or comparable CF responses to the ones predicted by the Linear model. Moreover, taking a closer look at Figure 8.20b, it becomes apparent that for velocities above 2.0 m/s, the Linear model seems to give much higher CF responses than the Non-Linear one for the lower soil damping ratio too. Of course, these results are characterised by an increased level of uncertainty because of the aforementioned pipeline sliding that occurred when the Non-Linear model was used. However, it should be noted that on the one hand the results obtained using the Linear model are deemed valid for velocities up to 2.3 m/s and on the other hand the results of both soil models seem to agree well with the respective findings of the previous analyses with respect to the high soil damping ratio. Therefore, although the values presented in Figure 8.20b for velocities above 2.0 m/s cannot be used for a direct comparison between the two soil models, the observed trends can be utilized as an indication of the expected responses.

In Figures 8.21 - 8.24 comparative snapshots of the response predicted by the TD VIV model with respect to both the CF and the IL directions (subfigures (a) and (c) in the aforementioned Figures) are presented for four indicative current velocities along with zoomed images focusing on the details of the respective responses near the left shoulder of the pipeline (subfigures (b) and (d) in the aforementioned Figures). Moreover, additional snapshots corresponding to the timesteps for which the maximum (i.e. most positive) and minimum (i.e. most negative) responses for both directions were observed are illustrated in Figures 8.25 - 8.28 for the same four current velocities along with zoomed images focusing on the details of the respective responses near the left shoulder of the pipeline. Comparative snapshots for the whole range of the examined velocities can be found in Appendix B.6 (Figures B.164 - B.203).

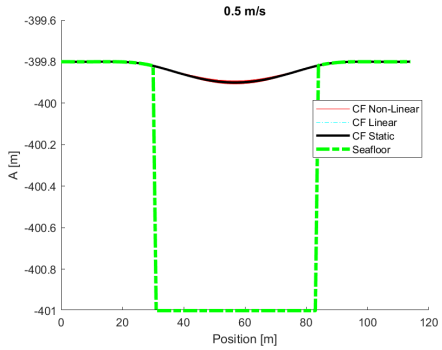

(a) CF - 0.5 m/s

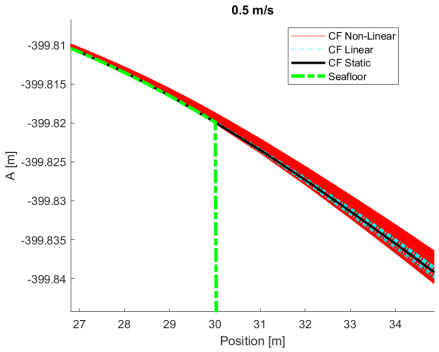

(b) CF - 0.5 m/s (zoom at the left shoulder)

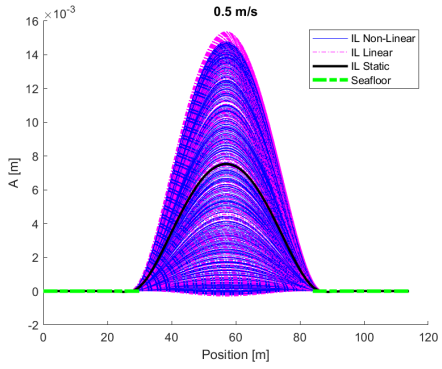

(c) IL - 0.5 m/s

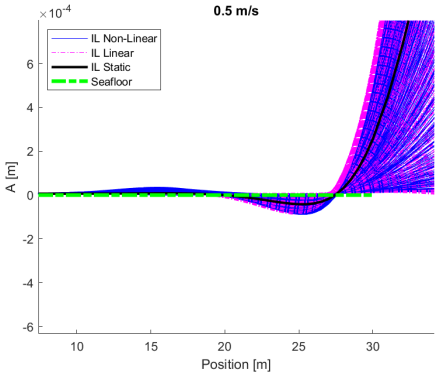

(d) IL - 0.5 m/s (zoom at the left shoulder)

Figure 8.21: Comparative snapshots of the calculated responses for the two soil models at 0.5 m/s.

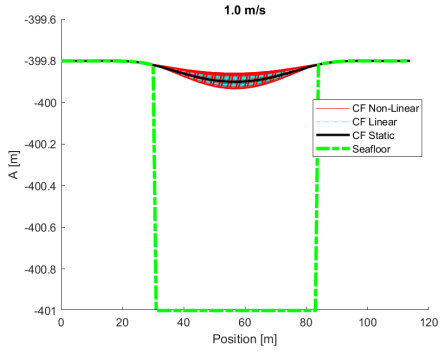

(a) CF - 1.0 m/s

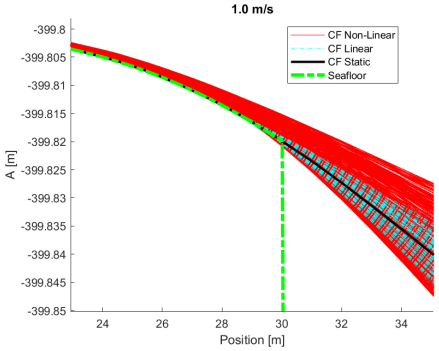

(b) CF - 1.0 m/s (zoom at the left shoulder)

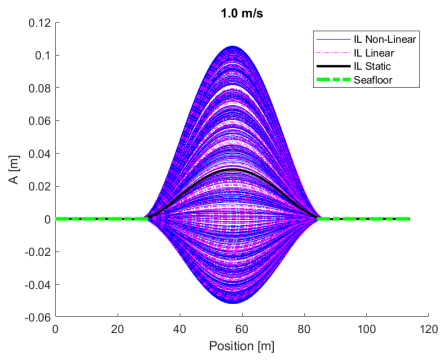

(c) IL - 1.0 m/s

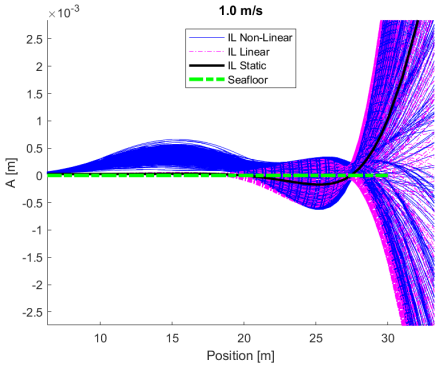

(d) IL - 1.0 m/s (zoom at the left shoulder)

Figure 8.22: Comparative snapshots of the calculated responses for the two soil models at 1.0 m/s.

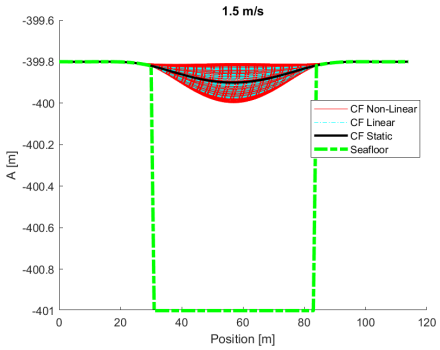

(a) CF - 1.5 m/s

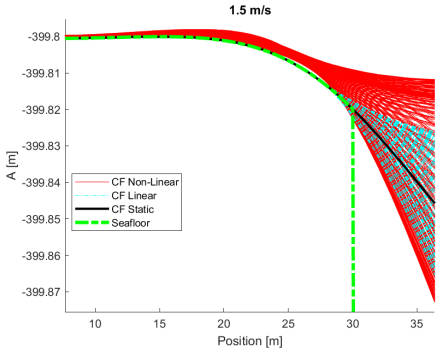

(b) CF - 1.5 m/s (zoom at the left shoulder)

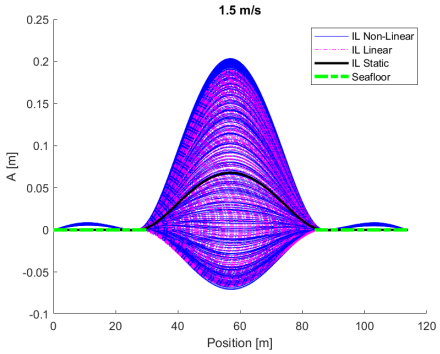

(c) IL - 1.5 m/s

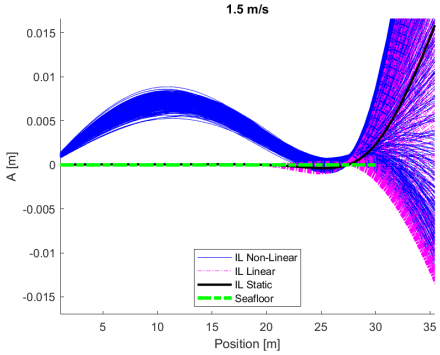

(d) IL - 1.5 m/s (zoom at the left shoulder)

Figure 8.23: Comparative snapshots of the calculated responses for the two soil models at 1.5 m/s.

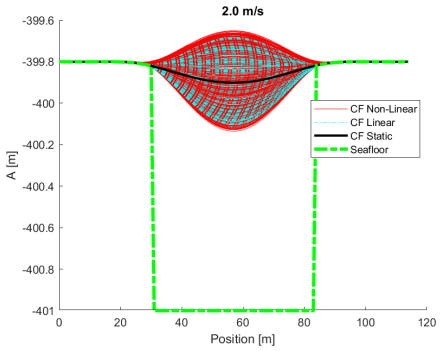

(a) CF - 2.0 m/s

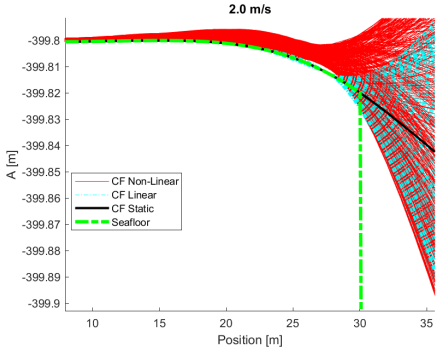

(b) CF - 2.0 m/s (zoom at the left shoulder)

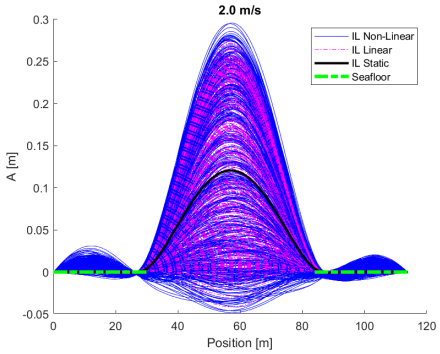

(c) IL - 2.0 m/s

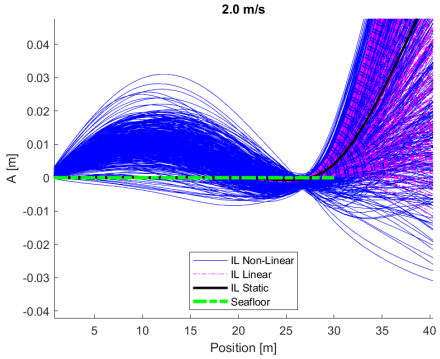

(d) IL - 2.0 m/s (zoom at the left shoulder)

Figure 8.24: Comparative snapshots of the calculated responses for the two soil models at 2.0 m/s.

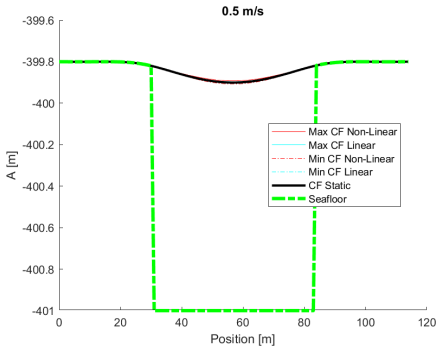

(a) CF - 0.5 m/s

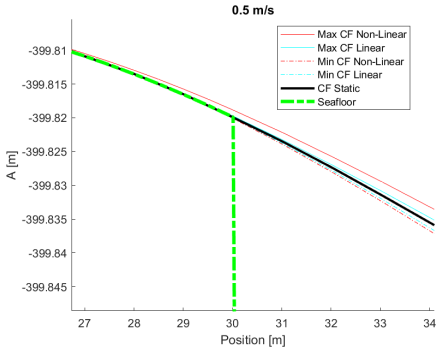

(b) CF - 0.5 m/s (zoom at the left shoulder)

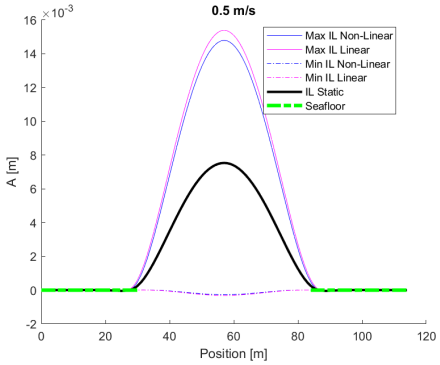

(c) IL - 0.5 m/s

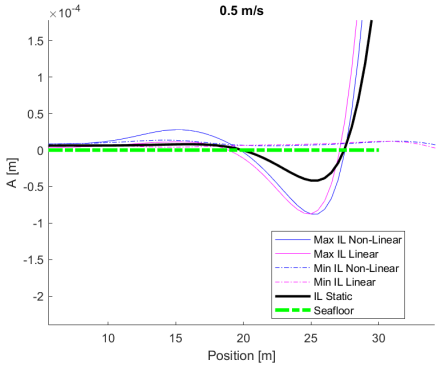

(d) IL - 0.5 m/s (zoom at the left shoulder)

Figure 8.25: Comparative snapshots of the max and min responses for the two soil models at 0.5 m/s.

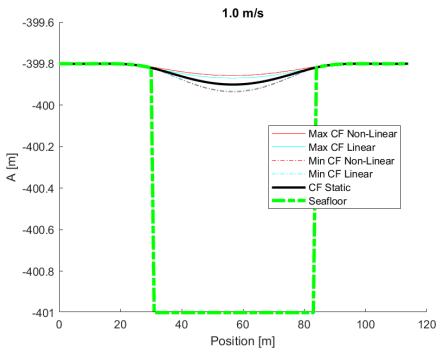

(a) CF - 1.0 m/s

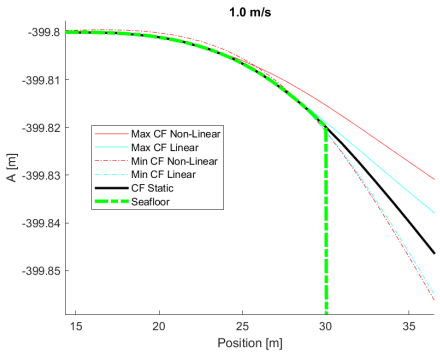

(b) CF - 1.0 m/s (zoom at the left shoulder)

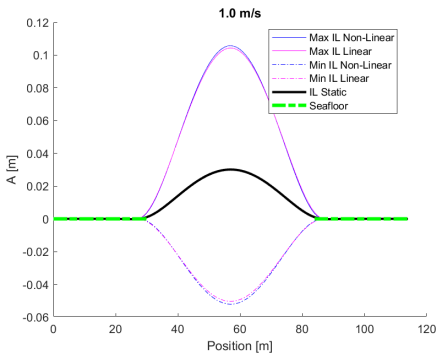

(c) IL - 1.0 m/s

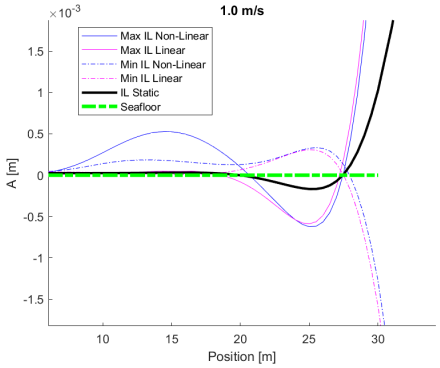

(d) IL - 1.0 m/s (zoom at the left shoulder)

Figure 8.26: Comparative snapshots of the max and min responses for the two soil models at 1.0 m/s.

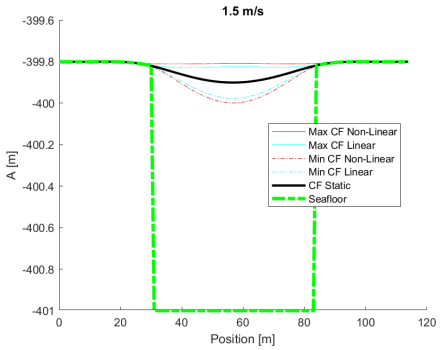

(a) CF - 1.5 m/s

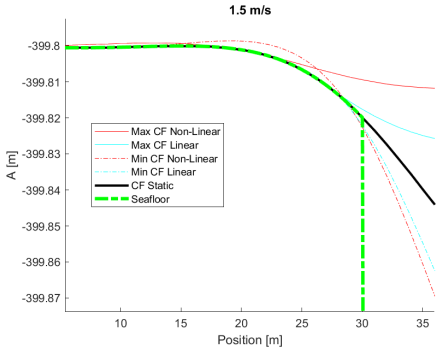

(b) CF - 1.5 m/s (zoom at the left shoulder)

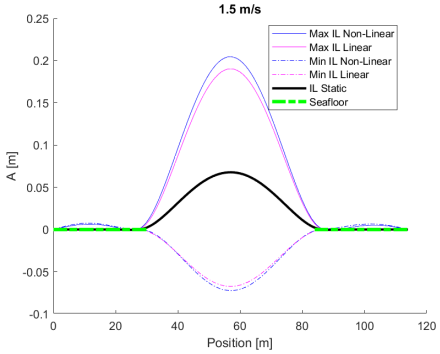

(c) IL - 1.5 m/s

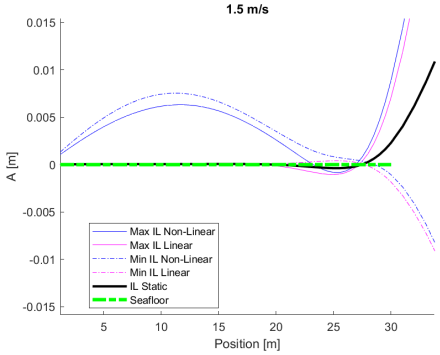

(d) IL - 1.5 m/s (zoom at the left shoulder)

Figure 8.27: Comparative snapshots of the max and min responses for the two soil models at 1.5 m/s.

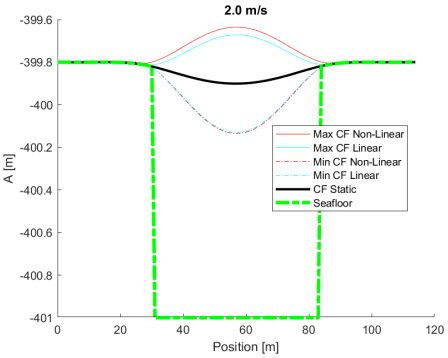

(a) CF - 2.0 m/s

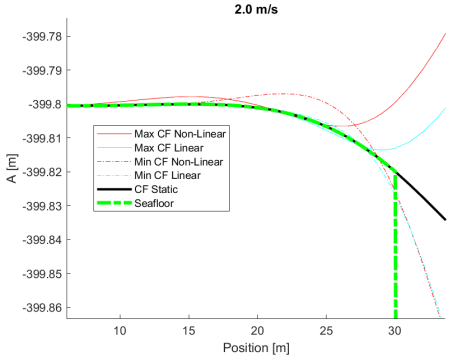

(b) CF - 2.0 m/s (zoom at the left shoulder)

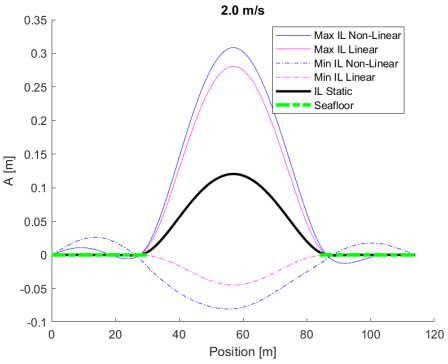

(c) IL - 2.0 m/s

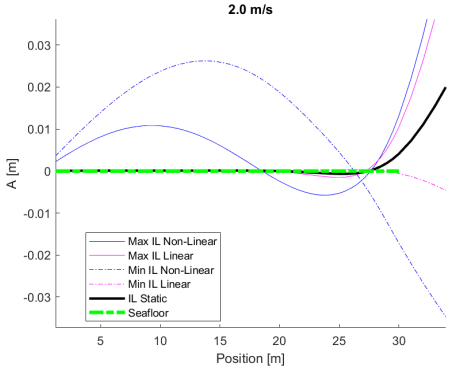

(d) IL - 2.0 m/s (zoom at the left shoulder)

Figure 8.28: Comparative snapshots of the max and min responses for the two soil models at 2.0 m/s.

Taking a closer look at Figures 8.21 - 8.24 the difference between the two soil models and the significant effect of the ”lift off” phenomenon becomes immediately apparent. At this point it is worth noting that the exact same phenomena, that were observed in section 8.1 with regard to the large value of soil damping ratio $\zeta_{soil} = 22\%$, become also evident for the present case and in fact they seem to be much more profound here. In short, as far as the CF response is concerned, from Figures 8.21b, 8.22b, 8.23b and 8.24b, it becomes again clear that the Linear model gives a perfectly symmetric response about the static configuration while the respective response predicted by the Non-Linear model is not symmetric. Moreover, this non-symmetric spreading of the CF response near the shoulder when the Non-Linear model is considered, seems again to be predominantly oriented upwards (i.e. to the positive CF direction), while the observed difference between the two models with regard to the predicted CF response in the negative CF direction is much smaller. Furthermore, it becomes obvious for the present case too, that there is an important CF response above the seafloor within the soil-supported part of the pipeline even far away from the free span when the Non-linear model is used, something that is again not true with regard to the Linear model. All the aforementioned findings verify clearly the existence of the ”lift off” phenomenon and the significant influence of it on the calculated VIV response.

As far as the IL response is concerned, it is again evident that there is a significant spreading of the IL response near the shoulder when the Non-Linear model is used. As was also observed for the high soil damping ratio case examined previously, in the present case the difference between the two models is much more important with regard to the the negative IL direction. This is shown more clearly in Figures 8.24c and 8.24d corresponding to the current velocity of 2.0 m/s than in the respective snapshots obtained at lower velocities (see Figures 8.21c - 8.23c) due to the more significant influence of the ”lift off” phenomenon on the obtained IL response at high velocities. Moreover, the fact that when the Non-Linear model is used, there are two touch-down points between the pipeline and the seabed both when the CF response is in the positive and in the negative directions becomes also evident for the present case, as is clearly illustrated in Figures 8.25b, 8.26b, 8.27b and 8.28b. This observation also explains the fact that in Figures 8.21c - 8.21d, 8.22c - 8.22d, 8.23c - 8.23d and 8.24c - 8.24d it becomes apparent for this low soil damping case too, that there is a considerable IL response above the seafloor that extends far away from the end of the free span when the Non-Linear model is used, something that is again not true with regard to the Linear model. Finally, in Figures 8.25b, 8.26b, 8.27b and 8.28b it is again evident that because of the ”lift off” phenomenon the first touch-down point in the Non-linear model is further away from the end of the initial free span than the contact point in the Linear model. At this point it should be noted that the explanation of all the above findings for the CF and IL responses and their connection to the ”lift off” phenomenon were described in detail in section 8.1 and therefore they will not be repeated here.

In Figures 8.29 - 8.31 the calculated distribution of the bending stresses and the respective fatigue damage accumulation along the pipeline both in the IL and the CF directions are illustrated with respect to the Non-Linear soil model and for soil damping ratio $\zeta_{soil} = 8\%$. The respective findings with regard to the Linear soil model are presented in Figures 8.32 - 8.34. These results are given here separately for the two soil models in order to observe the main trends with regard to the distribution of the bending stresses and the fatigue damage along the pipeline and also to describe the way these findings change as a function of the examined current velocity. Moreover, in Figures 8.35 - 8.37, comparative plots of the calculated distribution of the bending stresses and the respective fatigue damage accumulation are illustrated for two indicative current velocities for an easier identification of the main differences between the two examined soil models. The respective findings for other examined current velocities can be found in Appendix

B.6 (Figures B.207 - B.216).

At this point it should be noted that as was explained in detail in section 8.1, for soil damping ratio $\zeta_{soil} = 8\%$, the obtained distribution of the CF bending stresses and the respective fatigue damage accumulation, presents a somewhat more chaotic behavior for the current velocities of 1.5 m/s and 1.8 m/s compared to the rest of the velocities when the initial timestep is used for both examined soil models. For this reason the smaller timestep of 0.01 s was implemented again for the analysis of those two velocities. This phenomenon is in fact much more profound in this case in which a much smaller soil damping ratio is used, especially for the velocity of 1.8 m/s and becomes apparent in Figures B.133a - B.133b and B.160a - B.160b with regard to the Non-Linear and Linear soil models respectively.

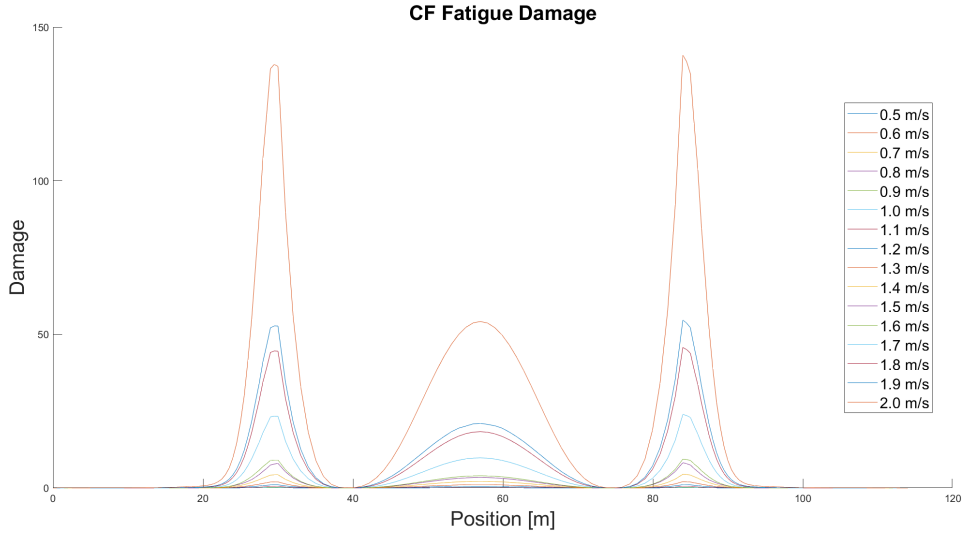

(a) CF - Fatigue Damage Accumulation

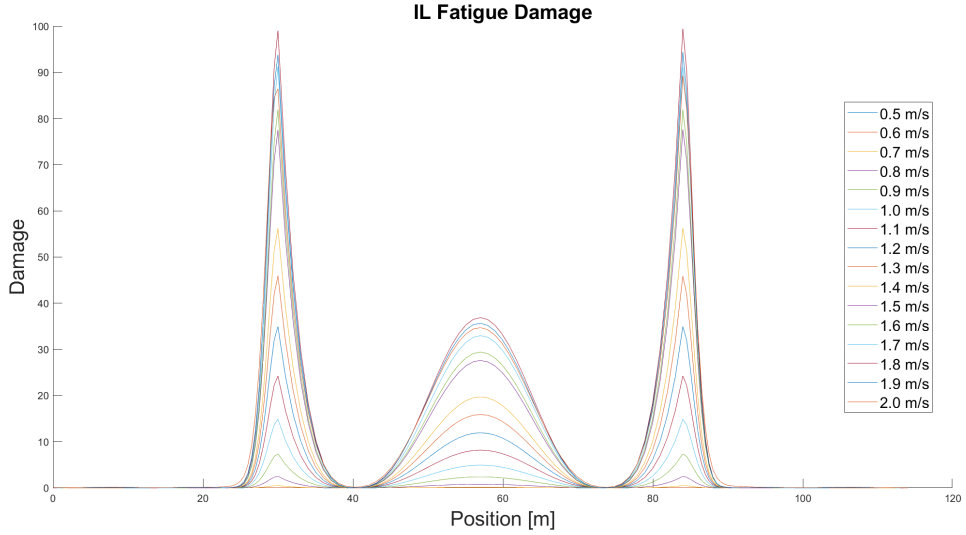

(b) IL - Fatigue Damage Accumulation

Figure 8.29: Plots of the calculated fatigue damage distribution in both directions for the Non-linear soil model and $\zeta_{soil} = 8\%$.

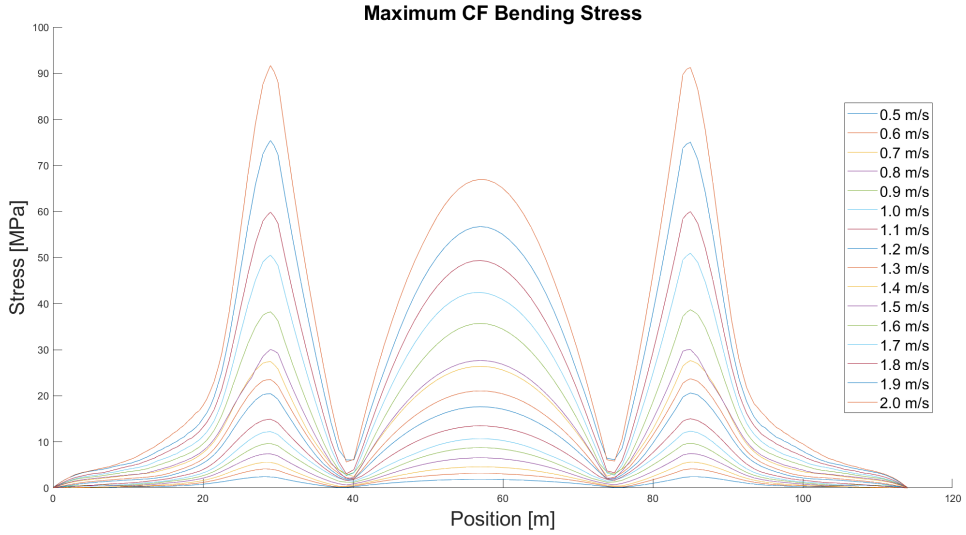

(a) CF - Maximum Bending Stress

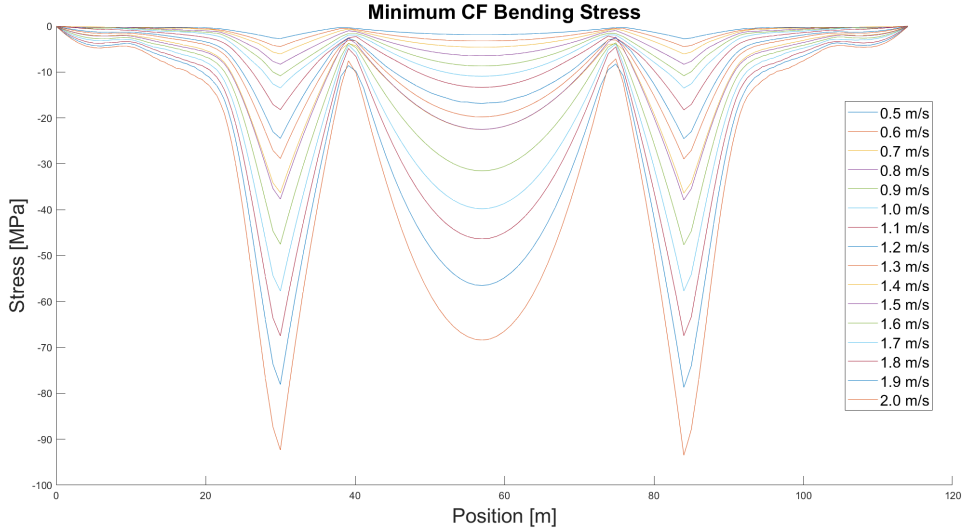

(b) CF - Minimum Bending Stress

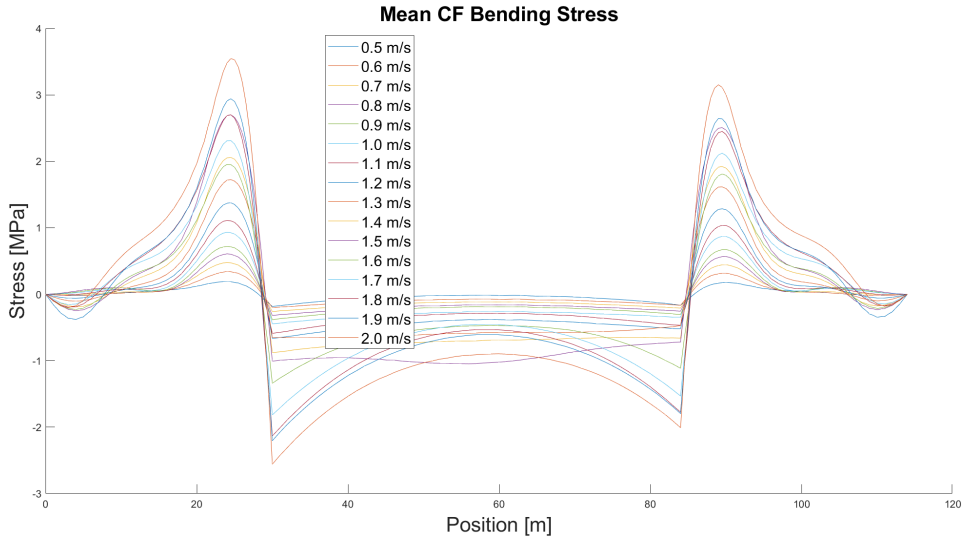

(c) CF - Mean Bending Stress

Figure 8.30: Plots of the calculated bending stress distribution in the CF direction for the Non-linear soil model and $\zeta_{soil} = 8\%$.

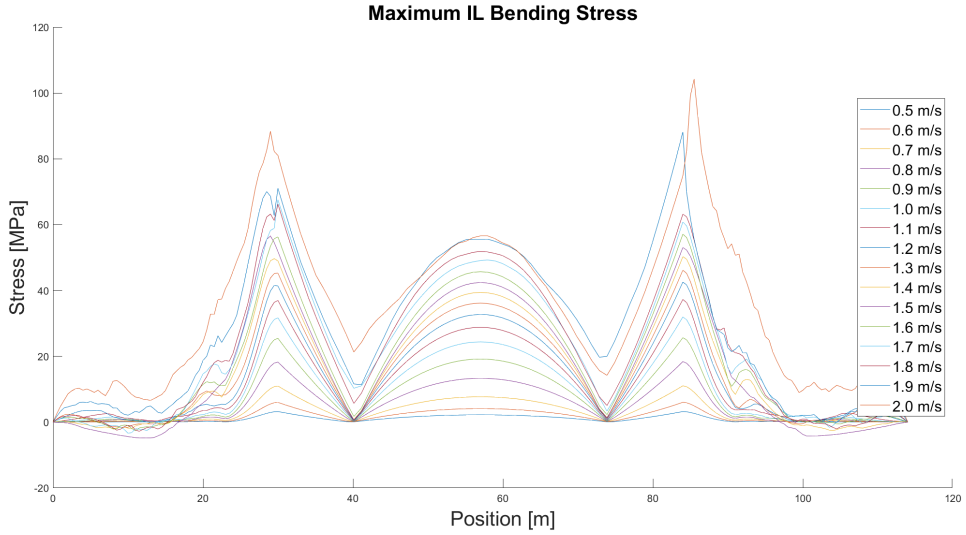

(a) IL - Maximum Bending Stress

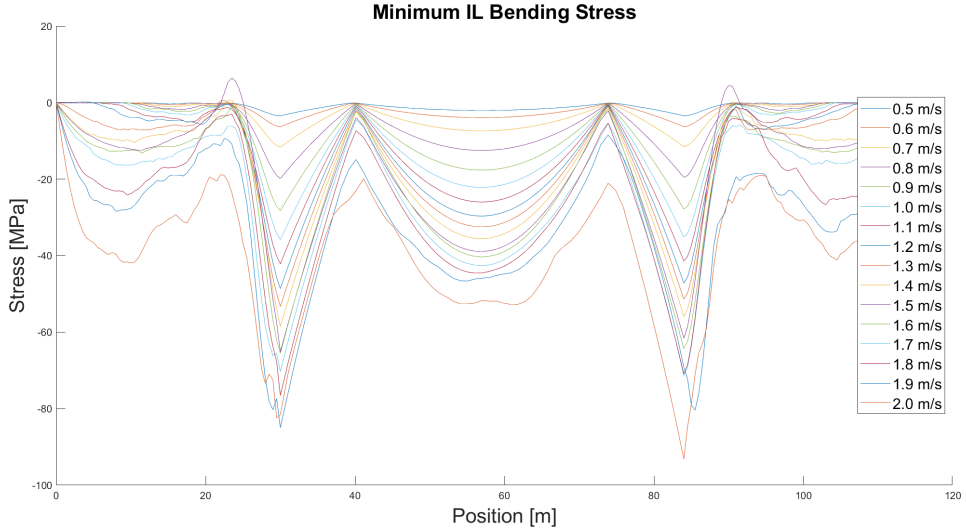

(b) IL - Minimum Bending Stress

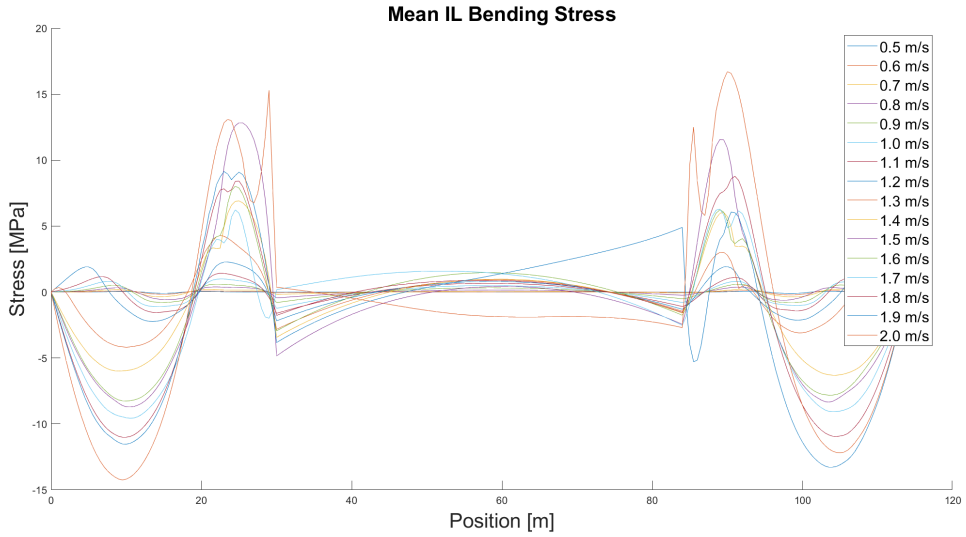

(c) IL - Mean Bending Stress

Figure 8.31: Plots of the calculated bending stress distribution in the IL direction for the Non-linear soil model and $\zeta_{soil} = 8\%$.

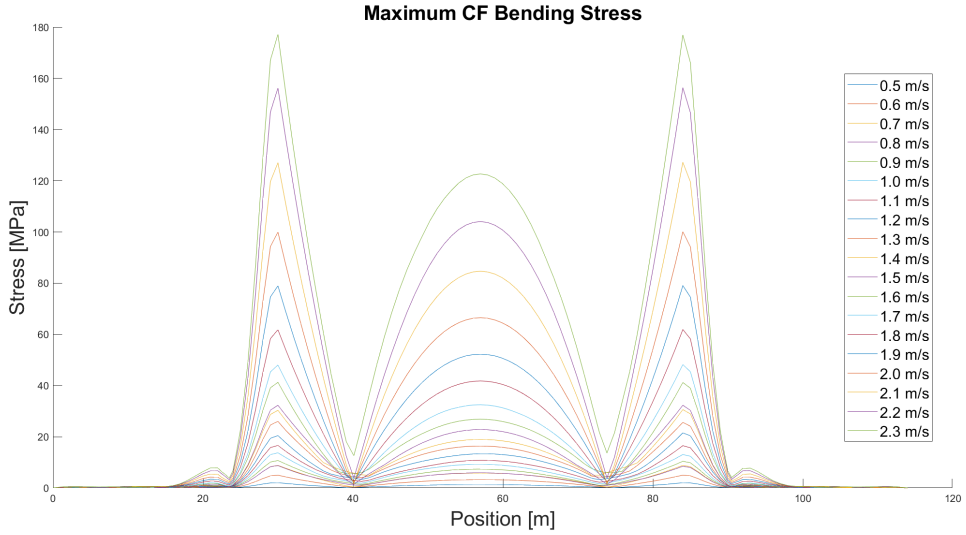

(a) CF - Maximum Bending Stress

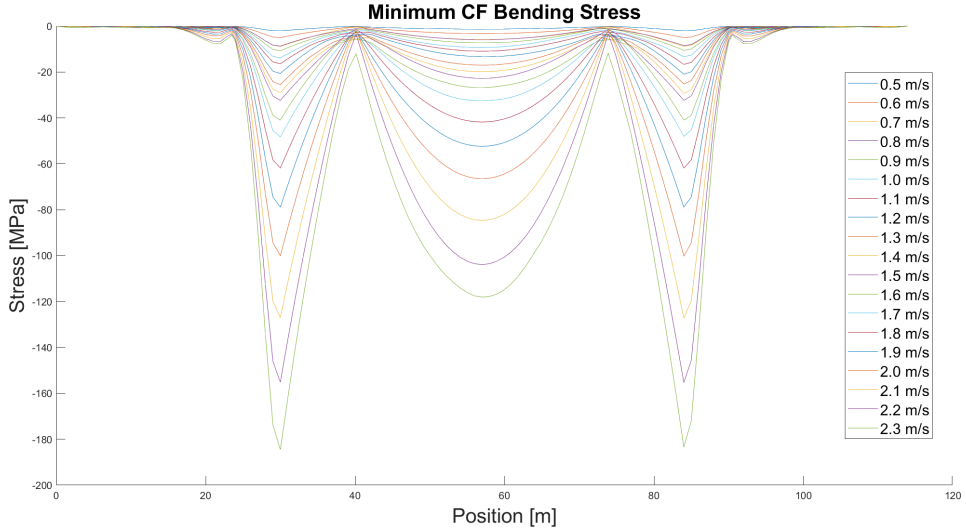

(b) CF - Minimum Bending Stress

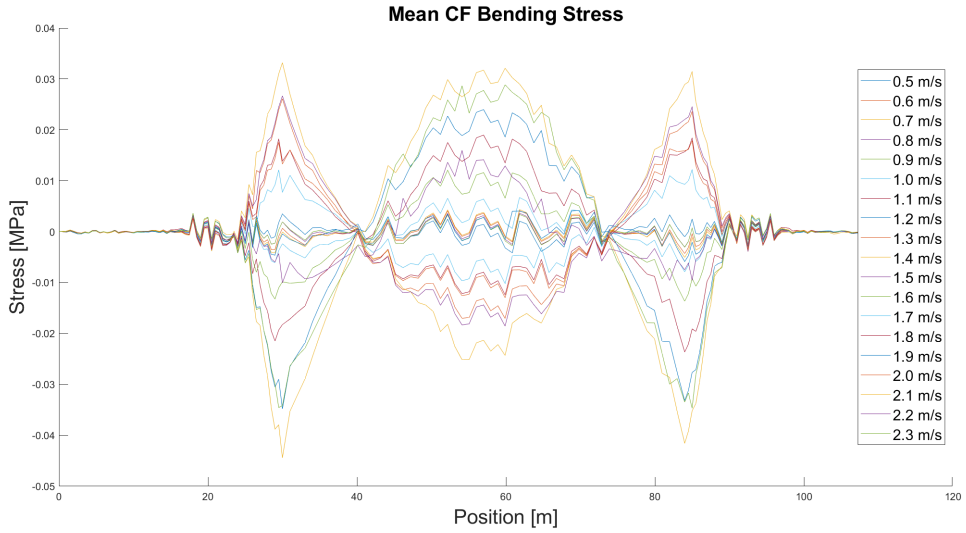

(c) CF - Mean Bending Stress

Figure 8.32: Plots of the calculated bending stress distribution in the CF direction for the Linear soil model and $\zeta_{soil} = 8\%$.

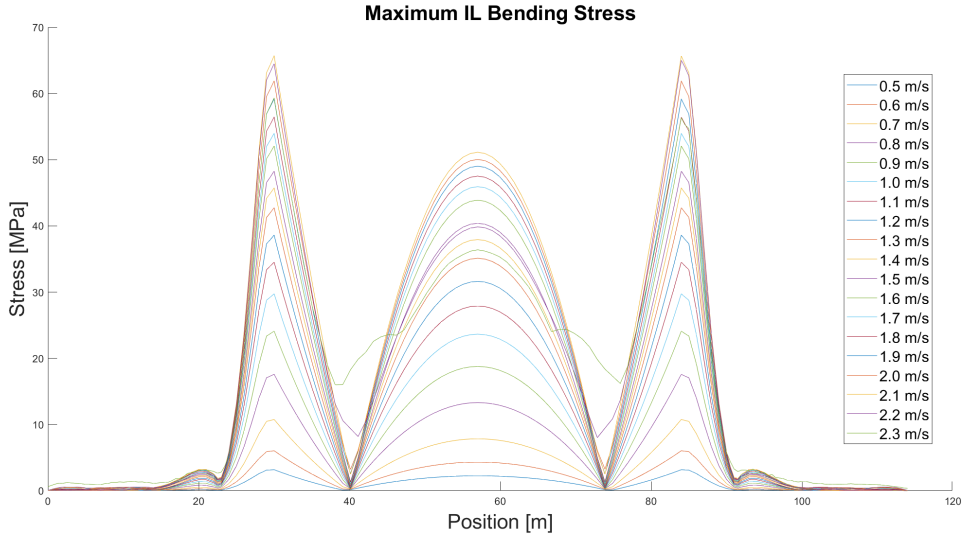

(a) IL - Maximum Bending Stress

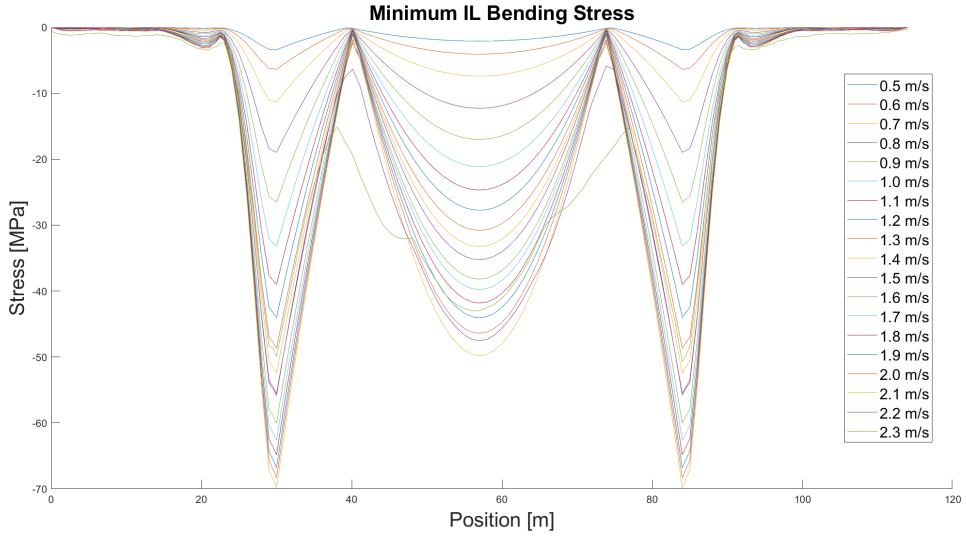

(b) IL - Minimum Bending Stress

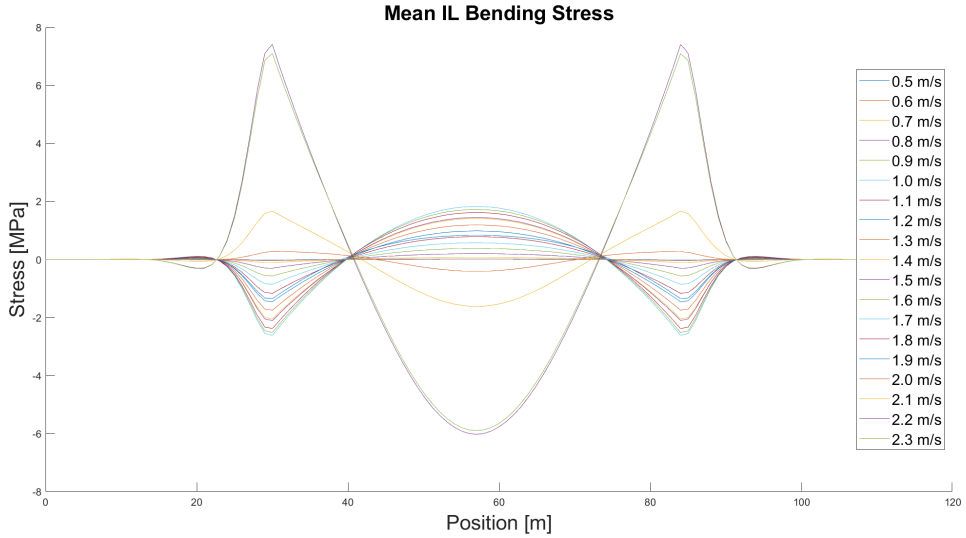

(c) IL - Mean Bending Stress

Figure 8.33: Plots of the calculated bending stress distribution in the IL direction for the Linear soil model and $\zeta_{soil} = 8\%$.

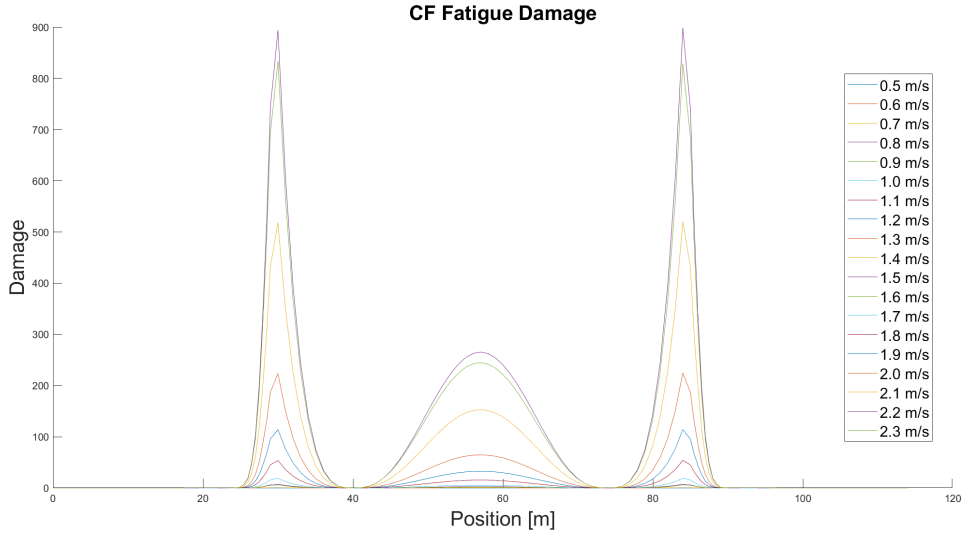

(a) CF - Fatigue Damage Accumulation

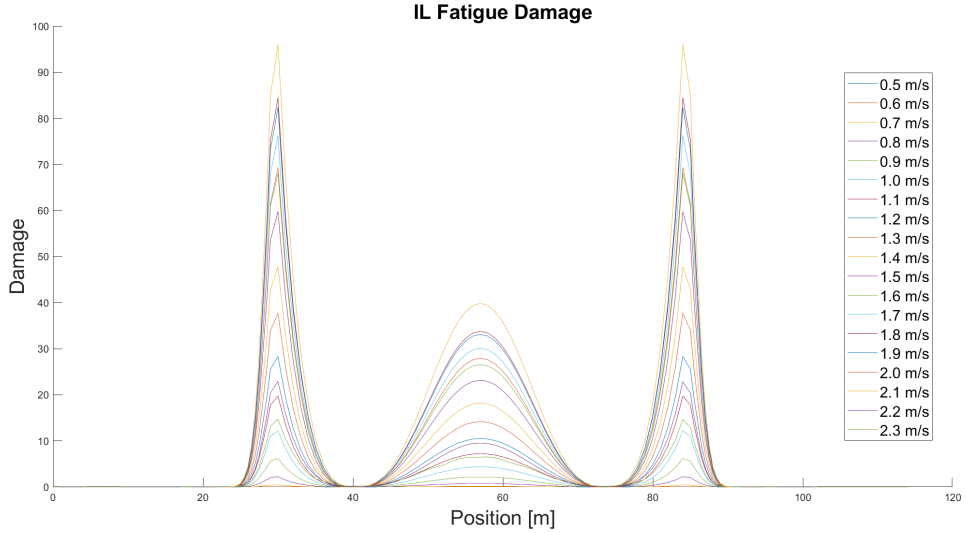

(b) IL - Fatigue Damage Accumulation

Figure 8.34: Plots of the calculated fatigue damage distribution in both directions for the Linear soil model and $\zeta_{soil} = 8\%$.

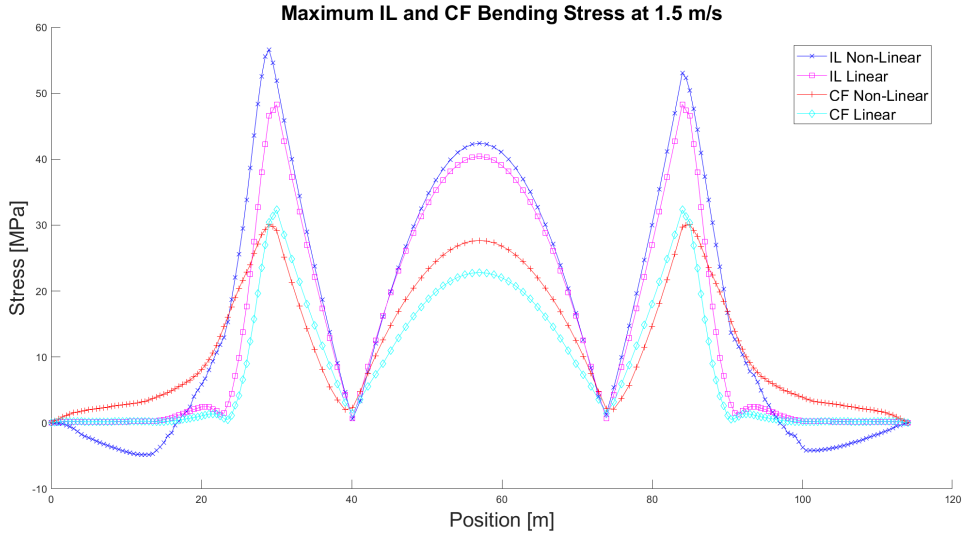

(a) CF and IL Maximum Bending Stress Distribution at 1.5 m/s

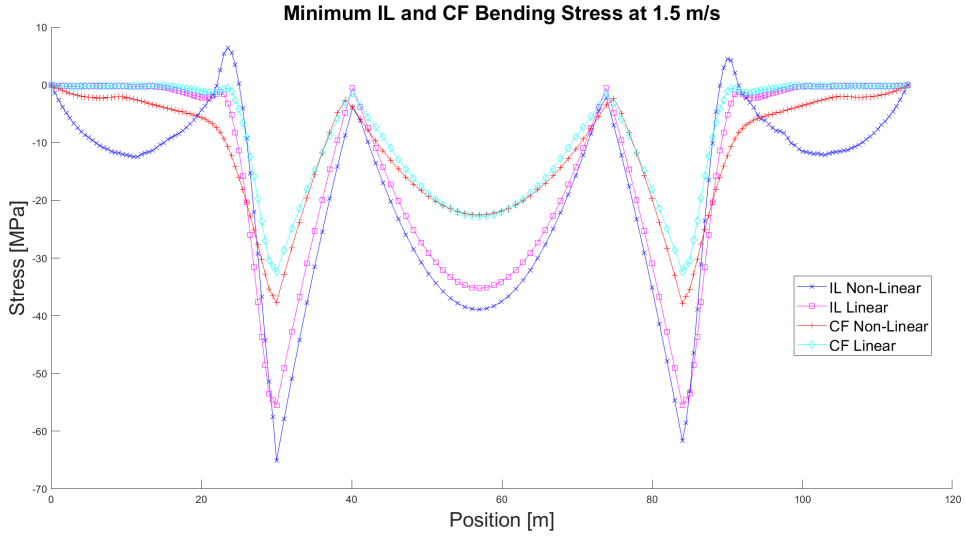

(b) CF and IL Minimum Bending Stress Distribution at 1.5 m/s

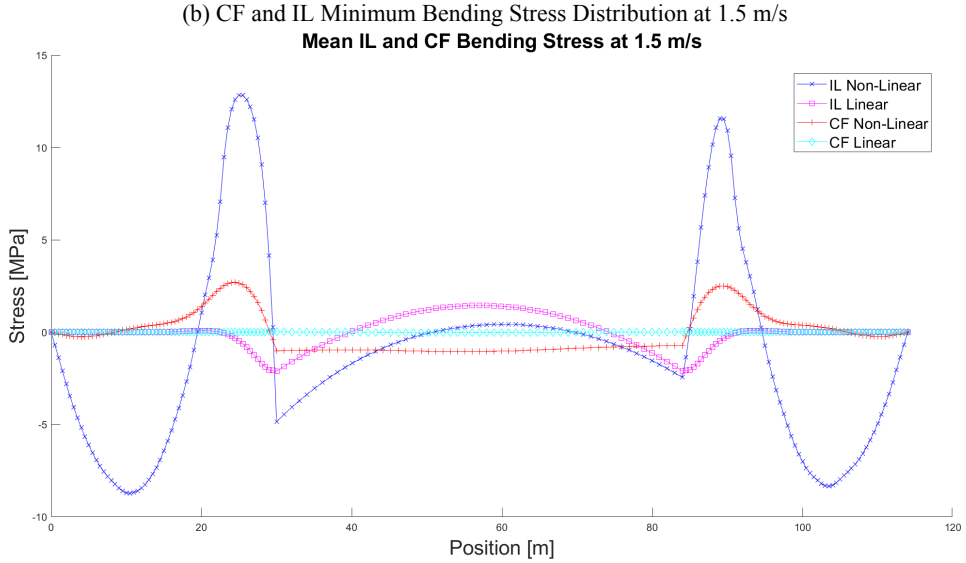

(c) CF and IL Mean Bending Stress Distribution at 1.5 m/s

Figure 8.35: Comparative plots of the calculated bending stress distribution for the two soil models and $\zeta_{soil} = 8\%$ at 1.5 m/s.

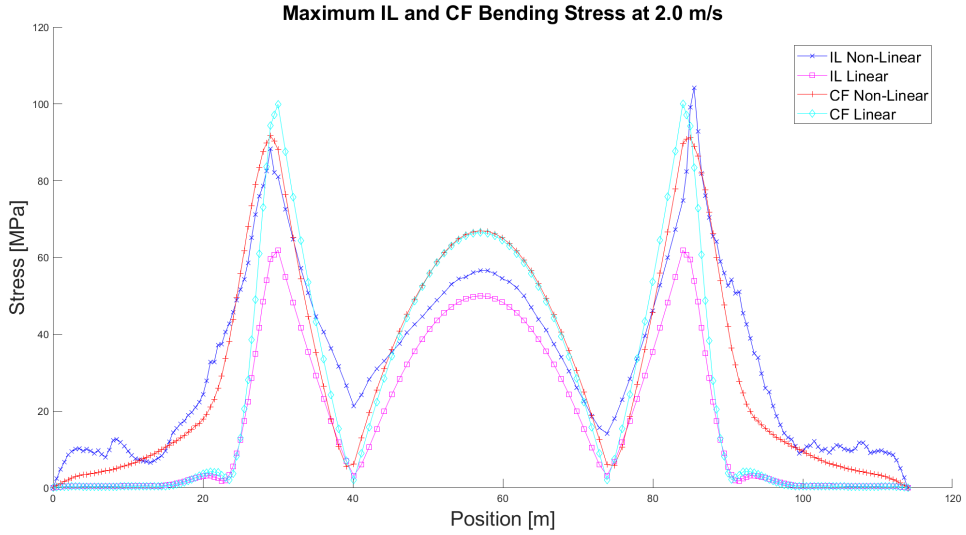

(a) CF and IL Maximum Bending Stress Distribution at 2.0 m/s

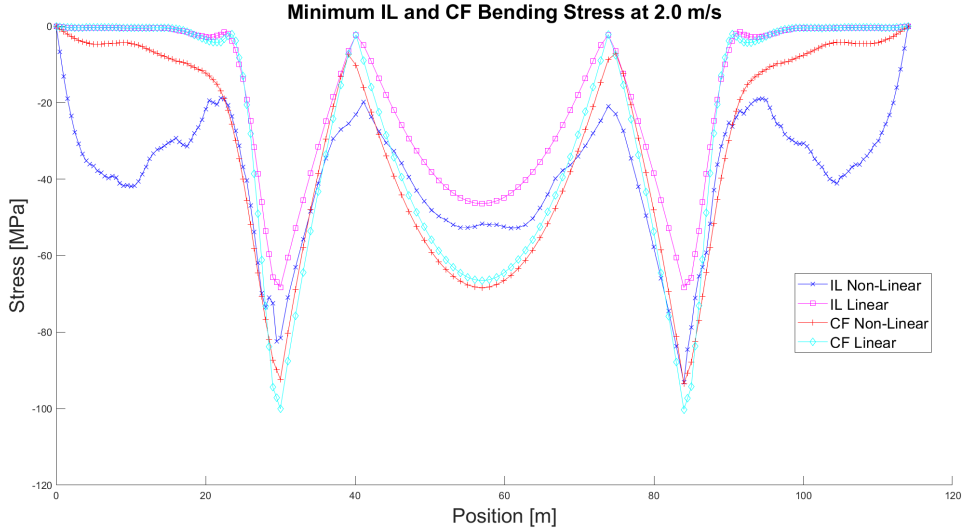

(b) CF and IL Minimum Bending Stress Distribution at 2.0 m/s

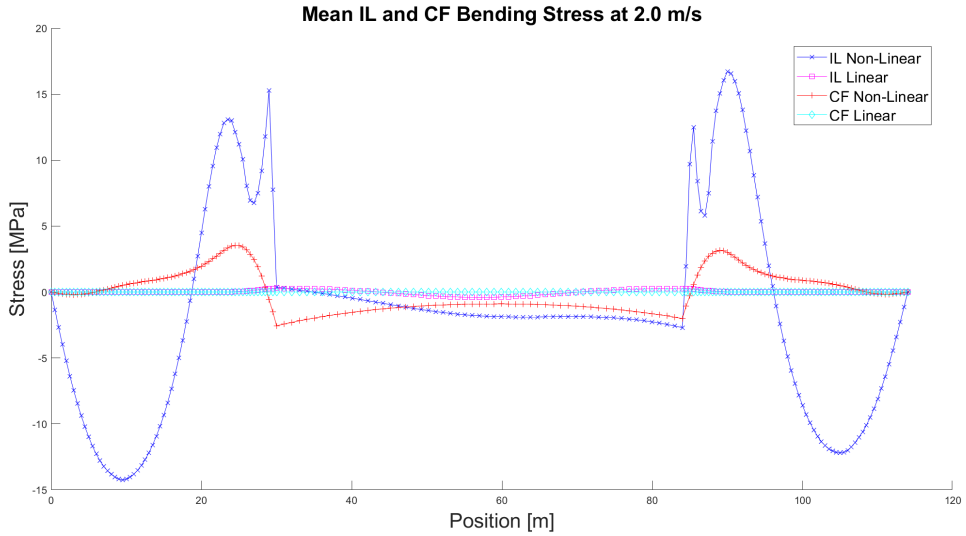

(c) CF and IL Mean Bending Stress Distribution at 2.0 m/s

Figure 8.36: Comparative plots of the calculated bending stress distribution for the two soil models and $\zeta_{soil} = 8\%$ at 2.0 m/s.

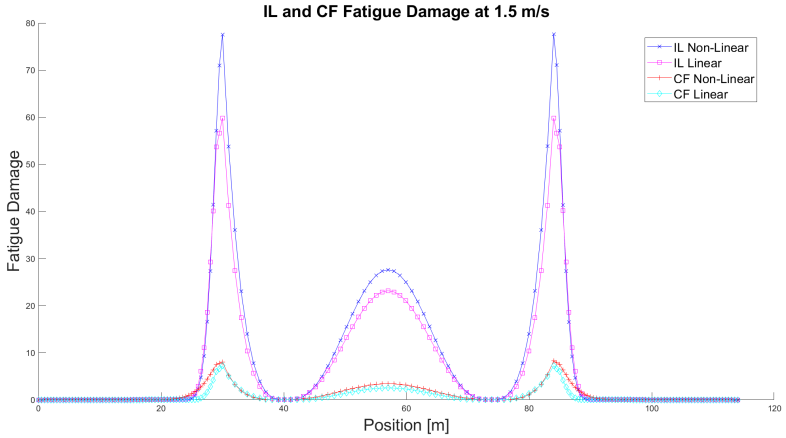

(a) CF and IL Fatigue Damage Accumulation at 1.5 m/s

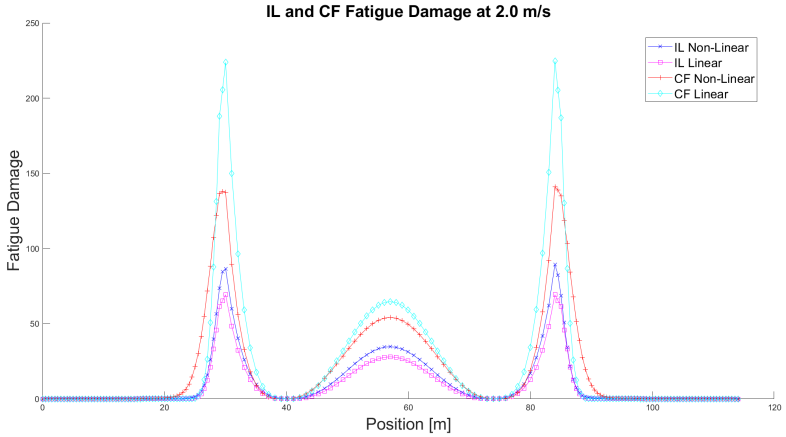

(b) CF and IL Fatigue Damage Accumulation at 2.0 m/s

Figure 8.37: Comparative plots of the calculated fatigue damage distribution for the two soil model and $\zeta_{soil} = 8\%$ at current velocities 1.5 and 2.0 m/s.

At a first glance, it becomes apparent that the trends that can be observed in Figures 8.29 - 8.31 and 8.32 - 8.34 are in general very similar to the findings of section 8.1 for both examined soil models. To begin with, it becomes again clear that the bending stresses and the fatigue damage accumulation with regard to both the IL and the CF directions generally increase as the current velocity becomes higher and that for all the examined current velocities, they take their maximum values at the shoulders of the pipeline. However, some differences from the previous cases become also evident with regard to the IL direction. As far as the Linear model is concerned, for which the results obtained for velocities up to 2.3 m/s can be regarded as reliable, the different behaviour that was observed in the previous cases with regard to the distribution of the IL bending stress and the fatigue damage accumulation at the highest velocity of 2.3 m/s, is in this case also observed at the second highest velocity of 2.2 m/s too. As a result, the highest values of IL bending stress and fatigue damage correspond to the velocity of 2.1 m/s and this is true throughout the whole length of the pipeline, contrary to what was observed in the previous cases, in which different velocities resulted in higher stresses at the shoulders and at the midspan. As for the Non-Linear model, the above mentioned increasing trend of the IL bending stress and fatigue damage can in this case be observed for the whole range of the examined velocities, since the higher velocities for which different behaviours were observed in the rest of the considered cases have already been neglected due to the aforementioned pipeline sliding issue. Moreover, the existence and the effects of the ”lift off” phenomenon on both directions when the

Non-Linear model is used, become clear in the aforementioned Figures for this low soil damping ratio case too. This can be easily understood by the fact that a distribution of considerable bending stresses allover the soil-supported part of the pipeline can be observed in Figures 8.30 - 8.31, while this is not true with regard to the Linear soil model with the exception of a really small region neighbouring the free span, as becomes apparent in Figures 8.32 - 8.33. Finally, in Figure 8.32 it is seen that the mean stress distribution in the CF direction is almost equal to zero along the whole length of the pipeline, proving in a very clear way that the pipeline's response is indeed symmetric, while the exact opposite behaviour becomes clear in Figure 8.30. These observation are also clearly verified in the comparative plots presented in Figures 8.35 - 8.37.

The next step of this analysis is to compare in more detail the results obtained using the two different soil models focusing on the deviations between them at the shoulders and at the midspan of the pipeline. In Figure 8.38, the obtained results for the CF and IL Bending Stresses and Fatigue Damage induced at the left shoulder with regard to both examined soil models are presented. The exact same analysis was conducted for the right shoulder and the midspan too, but it was found that in general the same trends can be observed for all cases. For this reason, it was preferred to present only the results corresponding to the left shoulder in the following. The respective findings for the rest of the examined cases can be found in Appendix B.6 (Figures B.204 - B.206).

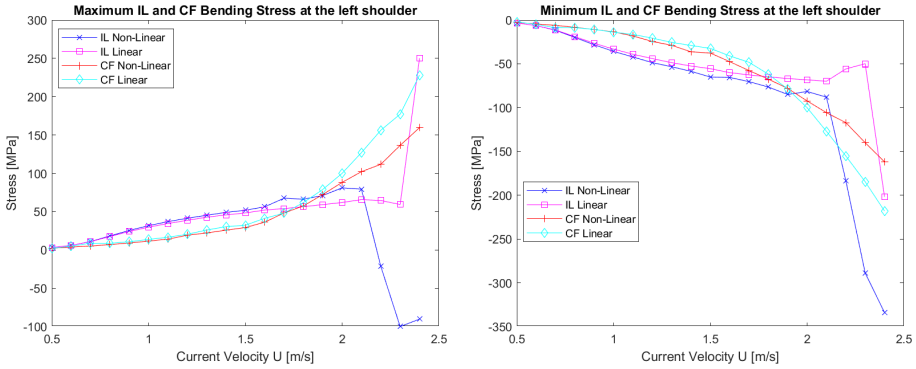

(a) Maximum Bending Stress at the left shoulder

(b) Minimum Bending Stress at the left shoulder

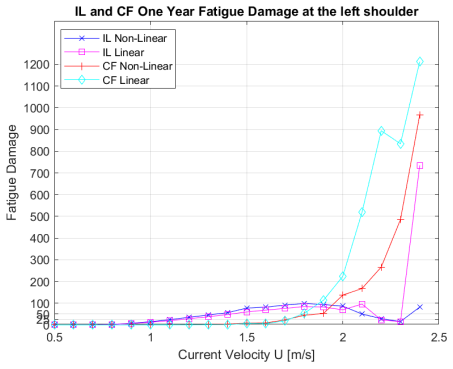

(c) Fatigue Damage Accumulation at the left shoulder

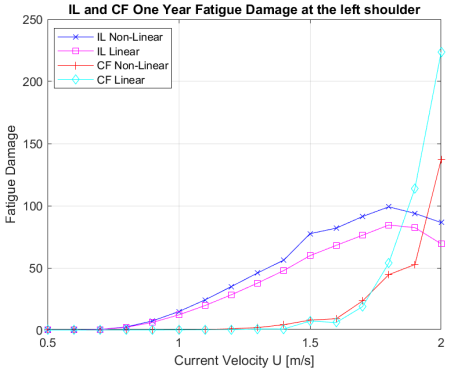

(d) Fatigue Damage Accumulation at the left shoulder (zoom at velocities up to 2.0 m/s)

Figure 8.38: Comparative plots of the Bending Stress and Fatigue Damage at the left shoulder.

Neglecting again the results corresponding to velocities above 2.0 m/s which were deemed unreliable with regard to the Non-Linear model, the symmetry between the obtained results for the maximum (positive) and minimum (negative) induced bending stresses at the left shoulder be-

comes again obvious from Figures 8.38a and 8.38b and hence only the maximum bending stress will be further analysed. As a general remark, from Figure 8.38 it becomes evident that the two examined soil models seem to be in very good agreement. More specifically, the Non-linear soil model constantly gives somewhat higher values of the IL bending stress than the Linear model for the whole range of current velocities up to 2.0 m/s. The calculated deviations between the two models in the lower part of this velocity range up to 1.6 m/s are quite small with the maximum discrepancy of 7.46% being observed at 1.6 m/s. For higher velocities, the difference between the two models becomes much more important and as a result the overall maximum deviation between the two models is observed at 2.0 m/s and is equal to 23.6%. What is more, as far as the CF bending stress is concerned it becomes clear from Figure 8.38a that in general the Linear soil model constantly predicts higher CF bending stress for the whole range of the examined current velocities, except for the lowest considered velocity for which it has already been explained in detail that the obtained CF response is negligible. Therefore, focusing in velocities above 1.3 m/s for which the CF response amplitude takes values above 0.1 D and is hence of practical importance, it is clear that the Linear model constantly predicts higher CF bending stress than the Non-Linear model, with the maximum discrepancy of 17.56% being observed at 1.4 m/s.

With regard to the Fatigue Damage accumulation, in Figure 8.38c the same trends as for the induced bending stresses become apparent, something totally expected considering that based on the results of Figure 8.20a, there were no significant differences between the two soil models in terms of the calculated response frequency in both directions. In general, the results obtained using the two different soil models seem to be in good agreement. However, some non-negligible differences can also be observed especially with regard to the CF direction. More specifically, from Figure 8.38c it becomes clear with regard to both examined soil models that the IL fatigue damage accumulation is much higher than the CF fatigue damage for the lower part of the examined velocities up to 1.8 m/s. Then, it becomes clear that for the velocity of 1.9 m/s the Linear model gives higher CF than IL fatigue damage, while the opposite is true with regard to the Non-Linear model. Finally, for the highest velocity of 2.0 m/s both models predict that the contribution of the CF response to the fatigue damage is higher than that of the IL response. The above observations seem to be in good agreement with the findings of the previous analysis with respect to the predicted maximum response amplitudes, where it was observed that the two soil models predict that the transition from the IL dominated response to the CF dominated response occurs at different velocities. Moreover, as far as the CF fatigue damage is concerned, it becomes apparent that for the lower part of the considered velocity range up to 1.7 m/s, the CF fatigue damage can in general be regarded as negligible with regard to both soil models. For higher velocities though, the contribution of the CF VIV in the fatigue damage accumulation increases rapidly and this growth is much more profound with respect to the Linear model, which seems to give much higher values than the Non-linear model. The maximum discrepancy between the two models can be observed at the velocity of 1.9 m/s and is equal to 116.22%, which means that the Linear model predicts more than two times higher fatigue damage than the Non-Linear one. As for the IL direction, it becomes obvious from Figures 8.38c and 8.38d that the Non-linear soil model constantly predicts higher values than the Linear model for the whole range of current velocities up to 2.0 m/s. For most velocities, the discrepancies between the two models take values in the range of $16\% - 23\%$, but it should be noted that for some velocities somewhat smaller deviations can be observed. From all the above findings, it becomes clear that the differences between the two examined soil models follow the same trends as were observed in section 8.1. The reasons behind these deviations, as well as the explanations for all the above presented general trends have already been analysed in detail in section 8.1 with regard to the higher soil damping ratio of $\zeta_{soil} = 22\%$, and therefore they will not be repeated here.

8.3 Overall Comparison

In this section, a comparative study of the previously presented results with regard to all four examined cases is conducted. The focus here is neither to describe the observed trends in terms of how the characteristics of the VIV response change as a function of the examined current velocity nor to directly compare the two considered soil models, since these comparisons were addressed in detail in the previous sections. The main goal of this analysis is to compare in more detail the obtained results with respect to the two different levels of soil damping that were examined. It should be noted that the following analysis will focus exclusively at current velocities up to 2.0 m/s, since for this range of current velocities the obtained results for all four cases were deemed valid. In Figure 8.39 and in Tables 8.1-8.4 the dominant response frequencies and the maximum response amplitudes normalized by the pipe's diameter that were calculated by means of the time domain VIV analysis with regard to all for examined cases are illustrated.

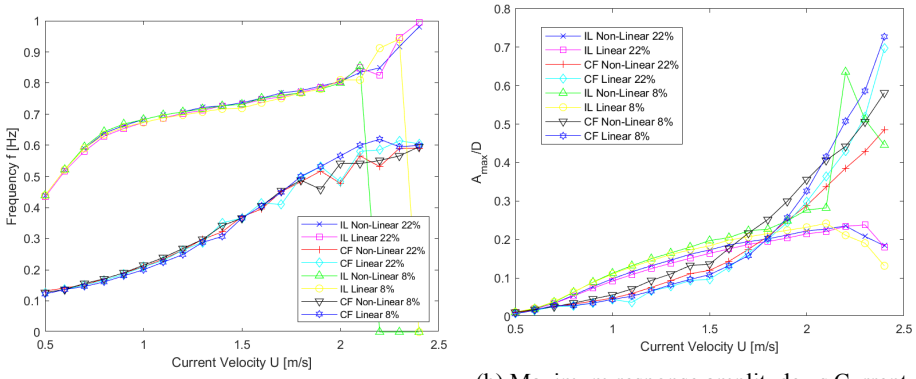

(a) Response Frequency vs Current Velocity

(b) Maximum response amplitude vs Current Velocity

Figure 8.39: Comparative plots of the dominant response frequencies and the maximum response amplitudes for all the examined cases.

Table 8.1: Dominant Response Frequency for all four examined cases

	Non-Linear Model - Dominant Frequency [Hz]				Linear Model - Dominant Frequency [Hz]			
Velocity [m/s]	CF 8%	CF 22%	IL 8%	IL 22%	CF 8%	CF 22%	IL 8%	IL 22%
0.5	0.13	0.13	0.44	0.44	0.12	0.13	0.44	0.43
0.6	0.14	0.14	0.52	0.52	0.14	0.14	0.52	0.52
0.7	0.16	0.15	0.60	0.59	0.15	0.15	0.59	0.58
0.8	0.17	0.17	0.64	0.64	0.16	0.17	0.63	0.63
0.9	0.19	0.19	0.67	0.66	0.18	0.19	0.66	0.65
1.0	0.21	0.21	0.68	0.68	0.20	0.21	0.67	0.67
1.1	0.24	0.23	0.70	0.70	0.22	0.23	0.69	0.69
1.2	0.27	0.26	0.71	0.71	0.25	0.26	0.70	0.70
1.3	0.30	0.30	0.72	0.72	0.29	0.29	0.71	0.71
1.4	0.34	0.32	0.73	0.73	0.31	0.35	0.72	0.73
1.5	0.37	0.37	0.73	0.74	0.37	0.37	0.72	0.73
1.6	0.40	0.40	0.75	0.75	0.40	0.41	0.74	0.75
1.7	0.45	0.45	0.76	0.77	0.45	0.41	0.75	0.76
1.8	0.49	0.48	0.77	0.78	0.50	0.50	0.77	0.77
1.9	0.46	0.52	0.78	0.79	0.53	0.53	0.78	0.79
2.0	0.54	0.48	0.80	0.80	0.57	0.48	0.81	0.80

Table 8.2: The effect of the reduction in the soil damping ratio from 22% to 8% on the Dominant Response Frequency

	Non-Linear Model - % Change in Frequency		Linear Model - % Change in Frequency	
Velocity [m/s]	CF	IL	CF	IL
0.50	−3.70	0.00	−3.85	1.12
0.60	−3.45	0.00	0.00	0.94
0.70	3.23	0.83	−3.23	1.68
0.80	0.00	0.76	−2.94	0.78
0.90	0.00	0.74	−2.63	0.75
1.00	2.33	0.00	−4.65	0.00
1.10	2.08	0.00	−2.13	0.00
1.20	1.85	0.00	−5.56	−0.69
1.30	0.00	−0.68	0.00	−0.68
1.40	6.06	0.00	−12.50	−1.34
1.50	−1.32	−0.66	0.00	−1.67
1.60	2.47	0.00	−2.35	−1.31
1.70	0.54	−0.95	9.52	−0.65
1.80	1.01	−0.94	0.49	−0.32
1.90	−11.32	−1.23	0.00	−0.62
2.00	13.27	−0.61	17.17	0.61

Table 8.3: Maximum Response Amplitude normalized by the pipe's diameter for all four examined cases

	Non-Linear Model - A_{max}/D [-]				Linear Model - A_{max}/D [-]			
Velocity [m/s]	CF 8%	CF 22%	IL 8%	IL 22%	CF 8%	CF 22%	IL 8%	IL 22%
0.5	0.01	0.01	0.01	0.01	0.01	0.01	0.01	0.01
0.6	0.02	0.02	0.02	0.02	0.02	0.02	0.02	0.02
0.7	0.03	0.03	0.04	0.03	0.03	0.03	0.04	0.03
0.8	0.03	0.03	0.06	0.06	0.03	0.03	0.06	0.05
0.9	0.05	0.04	0.09	0.08	0.03	0.04	0.09	0.07
1.0	0.06	0.05	0.11	0.10	0.04	0.04	0.11	0.09
1.1	0.07	0.06	0.13	0.12	0.05	0.04	0.13	0.11
1.2	0.09	0.08	0.15	0.13	0.07	0.07	0.15	0.12
1.3	0.11	0.09	0.17	0.15	0.08	0.08	0.16	0.14
1.4	0.13	0.11	0.18	0.16	0.10	0.09	0.17	0.15
1.5	0.14	0.12	0.20	0.17	0.11	0.10	0.18	0.16
1.6	0.18	0.14	0.21	0.19	0.13	0.13	0.20	0.18
1.7	0.22	0.17	0.22	0.19	0.16	0.17	0.21	0.19
1.8	0.25	0.21	0.23	0.20	0.20	0.20	0.22	0.19
1.9	0.30	0.25	0.25	0.21	0.26	0.24	0.22	0.20
2.0	0.36	0.29	0.28	0.22	0.33	0.30	0.23	0.21

Table 8.4: The effect of the reduction in the soil damping ratio from 22% to 8% on the Maximum Response Amplitude

	Non-Linear Model - % Change in A_{max}/D		Linear Model - % Change in A_{max}/D	
Velocity [m/s]	CF	IL	CF	IL
0.50	10.60	2.92	−19.41	3.91
0.60	9.03	4.53	5.99	8.40
0.70	0.17	9.09	11.66	13.45
0.80	7.96	14.03	4.43	19.80
0.90	14.80	15.02	−0.74	20.61
1.00	17.53	14.78	−0.15	19.80
1.10	20.28	13.71	43.86	18.78
1.20	23.80	13.92	−0.30	16.96
1.30	19.06	12.93	6.15	16.54
1.40	19.31	11.60	3.43	14.61
1.50	13.47	14.02	12.16	11.86
1.60	23.22	10.20	3.35	13.23
1.70	24.11	14.59	−4.56	10.56
1.80	21.13	12.54	1.33	10.61
1.90	19.94	17.49	5.36	9.94
2.00	23.26	24.53	9.58	7.94

To begin with, as far as the IL dominant frequency is concerned, it becomes apparent from Figure 8.39a that the effect of the soil damping ratio is almost negligible and the obtained results for all four examined cases are almost identical. In Table 8.2 it is seen that the biggest change in the predicted IL dominant frequency due to the reduction of the soil damping ratio from 22% to 8% is observed with regard to the Linear soil model at the velocity of 1.5 m/s and is found equal to only 1.67%. However, some small effects become evident with respect to the predicted CF dominant frequencies especially for the higher examined current velocities. For both soil models, the reduction of the soil damping ratio brought about the biggest change in the predicted CF dominant frequency at the velocity of 2.0 m/s which is found equal to 13.27% for the Non-Linear model and to 17.17% for the Linear model. However, for both soil models, the change in the predicted CF dominant frequency as a function of the soil damping ratio does not seem to follow a specific trend (increasing or decreasing) but instead it seems to be random.

What is more, from Figure 8.39b it becomes clear that the effect of the level of soil damping on the obtained results for the maximum response amplitude is much more profound. For both examined soil models and for both IL and CF directions, the reduction of the soil damping ratio seems to result in a significant increase in the response amplitudes. As far as the Non-Linear model is concerned, it becomes clear from Table 8.4 that the effect of the soil damping ratio on the IL response amplitude seems to increase with the current velocity up to the velocity of 0.9 m/s, for which an increase of 15.02% in the IL response amplitude is found. For the current velocity range between 1.0 and 1.8 m/s, an almost constant increase of $10\% - 14\%$ is observed, while for even higher velocities, the effect of the soil damping ratio seems to be more important and the maximum increase of 24.53% is found at the highest examined velocity of 2.0 m/s. As for the CF direction, the effect of the soil damping on the response amplitude seems to increase as the current velocity becomes higher up to the velocity of 1.2 m/s, for which an increase of 23.8% is observed. Subsequently, for even higher current velocities, the effect of soil damping on the CF vibration amplitude seems to be almost constant, since an increase of about $19\% - 24\%$ can be observed. The maximum increase of 24.11% is found at 1.7 m/s.

Moreover, as far as the Linear model is concerned, the effect of the soil damping ratio on the IL response amplitude increases with the current velocity for the lower part of the examined velocity range up to the velocity of 0.9 m/s, for which the maximum increase of 20.61% is observed. However, for higher velocities, a constantly decreasing trend becomes evident resulting in a much smaller increase of 7.94% in the IL vibration amplitude at the highest current velocity of 2.0 m/s. Contrary to all the above findings though, the effect of the examined level of soil damping in the CF response amplitude when the Linear soil model is used seems to be much smaller and in general more random than in all the other cases. More specifically, for the lower part of the examined current velocity range up to 1.3 m/s, the change in the predicted CF response amplitudes as a function of the soil damping ratio does not seem to follow a specific trend, since for some velocities an increase in the CF response becomes evident, while for other velocities the opposite behaviour is observed. However, as already explained in detail, for such low velocities the CF response is relatively small or even negligible in practice. As for the higher examined velocities, in general the reduction of the soil damping level seems to result in a relatively small increase in the CF response, which takes its maximum value of 12.16% at 1.5 m/s. At this point, it should be noted that the observed increase is in general much smaller for the rest of the velocities and in fact a small decrease of 4.56% is also observed at 1.7 m/s.

Finally, as far as the effect of the considered levels of soil damping on the deviations between the two soil models is concerned, from Figure 8.39b it becomes evident that in general the reduction of the soil damping ratio from 22% to 8% results in higher discrepancies in the results obtained using the two different soil models. This observation agrees very well with the findings of sections 8.1 and 8.2. To be more precise, as far as the IL response amplitudes are concerned, it was found in section 8.1 that when the higher soil damping ratio of 22% is used, the deviations between the two soil models are generally very small with the maximum discrepancy of 6.4% being observed at 1.1 and 1.4 m/s. Contrary to this, in section 8.2 it was found with regard to the lower value of the soil damping ratio that the difference between the two soil models increases with the current velocity and the maximum discrepancy was observed at the highest velocity of 2.0 m/s and was found equal to the much higher value of 16.25%. As for the CF response amplitude, it was found in section 8.1 regarding $\zeta_{soil} = 22\%$ that for current velocities above 1.3 m/s, for which the CF response predicted for this soil damping level is of practical importance, the Non-linear model predicts higher CF response than the Linear model with the maximum deviation of 19% being observed at 1.5 m/s and becoming smaller for higher velocities. As for the smaller value of soil damping ratio, in section 8.2 it was found that the deviations between the two soil models in general take somewhat higher values and especially for velocities near the middle of the examined velocity range between 0.9 m/s and 1.7 m/s. The discrepancies in this velocity range take values between 20.94% and 29.5% with the maximum deviation being observed at the velocity of 1.2 m/s.

To sum up, from all the above findings and focusing mainly on the range of current velocities between 0.9 m/s and 2.0 m/s for which on the one hand the VIV response in both directions is large enough to be regarded as important for most practical applications and on the other hand the obtained results for all four cases are regarded valid, it becomes apparent that the reduction of the soil damping level results in an increase in the response amplitude in both directions. However, the most interesting finding is the fact that this increase seems to be much more profound when the Non-Linear model is used. This observation also explains the above findings with regard to the effect that the considered levels of soil damping have on the deviations between the two soil models. To be more precise, for both examined levels of soil damping, it was found that for the above velocity range the Non-Linear model predicts higher response amplitudes than the Linear

model both in the IL and the CF directions. Moreover, taking into account that the reduction of the soil damping ratio leads in an increase in the response amplitudes and that this increase is more profound when the Non-Linear model is used, it is totally reasonable that indeed the reduction of the soil damping ratio also results in a higher deviation between the results obtained by the two soil models. As far as the IL direction is concerned, this observation can mainly be attributed to the fact that, although the reduced damping results in a higher IL response for the Linear model too, when the Non-Linear model is used, apart from the increased IL response due to the reduced damping in the IL direction, at the same time the higher CF response also leads in a more important ”lift off” effect. Therefore, a smaller part of the pipeline is in contact with the seabed at each time instance, ultimately resulting in a much higher IL response. Contrary to this, the explanation of the above findings with regard to the CF response amplitude is much more complicated, since the observed behaviour is the opposite of what is theoretically expected. That is, typically it would be expected that the reduction of the soil damping ratio would have a more significant influence on the Linear model. The reason for this is that the dampers are always active in this model and hence a change of the damping level should be of paramount importance. Instead, in the Non-Linear model the dampers are active only when there is contact between the pipe and the seafloor. So when the pipeline during its vibrations is moving upwards and detaches from the seabed the damping forces are equal to zero and thus in such a case the change in the considered damping level does not affect the VIV response at all. In order to explain the above presented results, one has to keep in mind that contrary to the Linear model for which the soil forces are constantly active and only their magnitude and direction change in time, when the Non-Linear model is used, due to the ”lift off” and the resulting repetitive activation and deactivation of the soil springs and dampers, the application of the soil forces is in fact a dynamic phenomenon which is characterised by a frequency corresponding to the frequency of alternation between ”contact” and ”no contact” conditions. Therefore, if this frequency of the soil forces becomes close to one of the systems eigenfrequencies an additional resonant phenomenon could occur which could lead in turn in a significant amplification of the response. The effect of this additional resonance and the resulting amplification of the response will be much higher when the level of damping in the system is smaller, something that explains why the reduction of the soil damping ratio has a more profound effect when the Non-Linear model is used.

In Figure 8.40 and in Tables 8.5 - 8.8 the obtained results for the CF and IL Bending Stresses and Fatigue Damage induced at the left shoulder of the pipeline with regard to all four examined cases are presented. Only the results corresponding to the left shoulder are presented in the following, since the respective findings for the right shoulder and the midspan of the pipeline were found to be almost identical. Moreover, comparative plots of the calculated distribution of the bending stresses and the respective fatigue damage accumulation along the pipeline both in the IL and the CF directions were created for five indicative current velocities. However, such plots are not suitable so as to reach conclusions about the effect of the soil damping level on the VIV responses and in addition such plots and the observed trends have already been described in detail separately for each soil damping ratio in sections 8.1 and 8.2. Therefore it was decided to not present these plots in the following. The total set of results corresponding to this comparative study for all four examined cases can be found in Appendix B.7 (Figures B.217 - B.230).

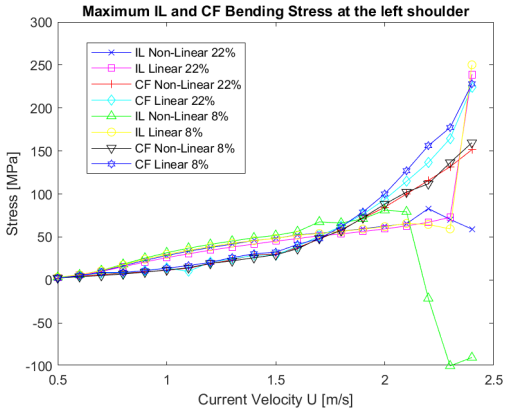

(a) Maximum Bending Stress at the left shoulder

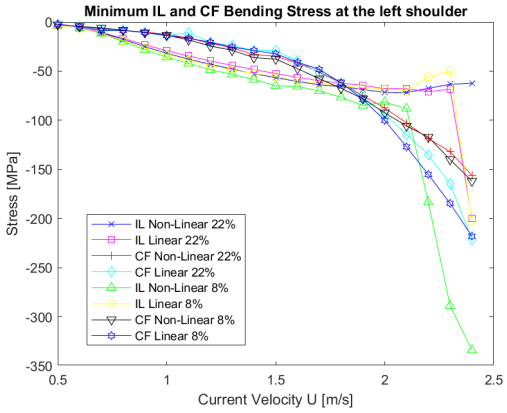

(b) Minimum Bending Stress at the left shoulder

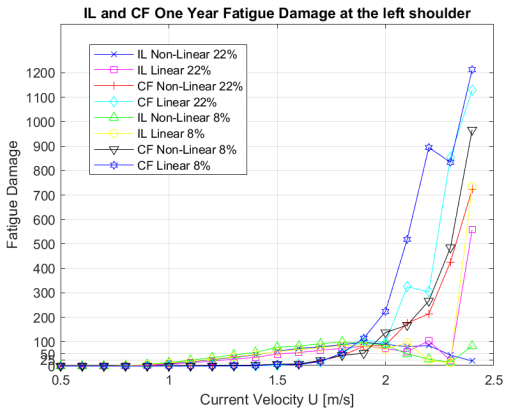

(c) Fatigue Damage Accumulation at the left shoulder

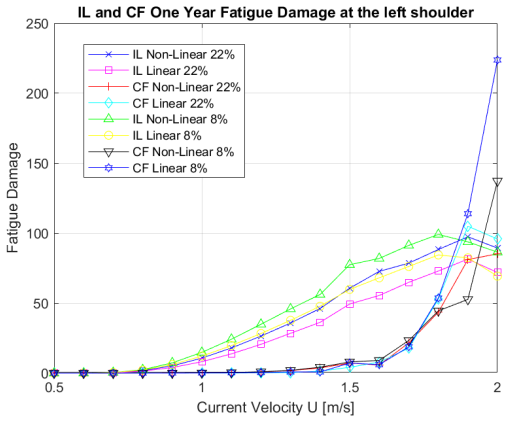

(d) Fatigue Damage Accumulation at the left shoulder (zoom at velocities up to 2.0 m/s)

Figure 8.40: Comparative plots of the calculated Bending Stress and Fatigue Damage at the left shoulder for all the examined cases.

Table 8.5: Maximum Bending Stress at the left shoulder of the pipeline for all four examined cases

	Non-Linear Model - Bending Stress [MPa]				Linear Model - Bending Stress [MPa]			
Velocity [m/s]	CF 8%	CF 22%	IL 8%	IL 22%	CF 8%	CF 22%	IL 8%	IL 22%
0.5	2.21	2.42	3.22	3.14	2.07	2.60	3.18	3.11
0.6	3.80	4.16	6.00	5.82	4.98	4.84	6.04	5.74
0.7	5.17	6.38	10.97	10.26	8.83	8.08	10.77	9.83
0.8	6.94	7.81	18.26	16.43	8.75	8.03	17.59	15.31
0.9	9.14	9.39	25.47	22.76	10.72	10.92	24.11	20.89
1.0	11.57	11.29	31.70	28.43	13.75	13.79	29.74	25.96
1.1	14.14	13.67	36.98	33.36	16.62	9.92	34.53	30.41
1.2	19.22	18.85	41.38	37.70	20.47	20.77	38.61	34.59
1.3	22.19	23.41	45.29	41.61	26.02	24.31	42.76	38.29
1.4	25.83	29.14	48.99	45.89	30.36	28.65	45.73	41.67
1.5	29.22	30.07	51.85	48.27	32.32	29.19	48.28	45.17
1.6	36.25	37.57	56.28	52.43	41.28	39.01	52.08	47.99
1.7	48.29	47.47	67.55	54.39	48.05	51.08	53.99	51.47
1.8	57.43	58.20	66.27	56.60	61.83	62.38	56.46	53.52
1.9	72.36	71.81	71.05	59.61	78.97	76.36	59.19	56.35
2.0	88.15	84.61	81.05	62.55	99.97	93.58	61.92	59.31

Table 8.6: The effect of the reduction in the soil damping ratio from 22% to 8% on the Maximum Induced Bending Stress at the left shoulder of the pipeline

	Non-Linear Model - % Change in Stress		Linear Model - % Change in Stress	
Velocity [m/s]	CF	IL	CF	IL
0.50	−8.44	2.50	−20.61	2.21
0.60	−8.62	3.01	2.99	5.20
0.70	−19.03	6.94	9.36	9.51
0.80	−11.16	11.10	8.86	14.87
0.90	−2.65	11.90	−1.87	15.43
1.00	2.48	11.53	−0.25	14.58
1.10	3.43	10.84	67.43	13.57
1.20	1.97	9.75	−1.46	11.63
1.30	−5.20	8.85	7.03	11.65
1.40	−11.37	6.77	5.98	9.75
1.50	−2.82	7.41	10.70	6.89
1.60	−3.50	7.35	5.82	8.53
1.70	1.72	24.20	−5.94	4.90
1.80	−1.33	17.10	−0.87	5.48
1.90	0.77	19.18	3.42	5.04
2.00	4.19	29.58	6.83	4.40

Table 8.7: Fatigue Damage Accumulation at the left shoulder of the pipeline for all four examined cases

	Non-Linear Model - Fatigue Damage [-]				Linear Model - Fatigue Damage [-]			
Velocity [m/s]	CF 8%	CF 22%	IL 8%	IL 22%	CF 8%	CF 22%	IL 8%	IL 22%
0.5	0.00	0.00	0.01	0.01	0.00	0.00	0.01	0.01
0.6	0.01	0.01	0.07	0.06	0.01	0.01	0.07	0.06
0.7	0.01	0.02	0.49	0.40	0.07	0.05	0.45	0.35
0.8	0.04	0.05	2.51	1.83	0.04	0.03	2.23	1.48
0.9	0.08	0.09	7.39	5.24	0.07	0.07	6.19	4.05
1.0	0.21	0.17	14.87	10.76	0.13	0.12	12.19	8.18
1.1	0.45	0.36	24.27	18.02	0.23	0.11	19.73	13.81
1.2	1.03	0.90	34.95	26.49	0.43	0.30	28.36	20.62
1.3	1.99	1.87	45.91	35.82	0.91	0.45	37.78	28.50
1.4	4.30	3.74	56.25	46.23	0.89	1.42	47.86	36.35
1.5	8.02	7.19	77.51	60.72	7.23	4.22	59.84	49.44
1.6	9.12	5.86	81.98	72.73	6.08	7.88	68.15	55.51
1.7	23.37	21.63	91.32	78.62	18.81	17.84	76.26	64.94
1.8	44.52	43.58	99.11	88.35	53.75	52.95	84.50	72.99
1.9	52.72	81.18	93.83	97.47	113.99	104.99	82.39	81.53
2.0	137.28	85.30	86.48	89.39	223.80	95.87	69.33	71.97

Table 8.8: The effect of the reduction in the soil damping ratio from 22% to 8% on the Fatigue Damage Accumulation at the left shoulder of the pipeline

	Non-Linear Model - % Change in Fatigue		Linear Model - % Change in Fatigue	
Velocity [m/s]	CF	IL	CF	IL
0.50	−9.15	2.34	−64.65	3.28
0.60	−11.69	6.96	7.47	14.02
0.70	−39.42	22.66	58.33	29.97
0.80	−23.12	37.45	26.99	50.88
0.90	−10.42	40.93	3.84	52.99
1.00	22.16	38.21	7.49	48.95
1.10	25.38	34.66	111.86	42.90
1.20	13.85	31.94	44.40	37.53
1.30	6.43	28.17	103.22	32.56
1.40	14.78	21.67	−37.05	31.69
1.50	11.61	27.64	71.51	21.05
1.60	55.70	12.72	−22.87	22.76
1.70	8.07	16.15	5.42	17.43
1.80	2.17	12.17	1.51	15.76
1.90	−35.06	−3.74	8.58	1.06
2.00	60.94	−3.25	133.43	3.66

To begin with, as far as the induced bending stresses in the IL direction are concerned, it becomes apparent from Figures 8.40a and 8.40b that the reduction of the soil damping ratio results in a significant increase in the induced IL bending stresses for both examined soil models. More specifically, from Table 8.6 it becomes clear for the Non-Linear model, that the effect of the soil damping level seems to increase with the current velocity for the lower part of the examined velocity range up to 0.9 m/s, where an increase of 11.9% in the measured IL bending stress is observed. Subsequently, for velocities ranging between 1.0 m/s and 1.6 m/s, a slowly decreasing trend becomes evident leading to a smaller increase of 7.35% at 1.6 m/s. However, for even higher velocities, the reduction of the soil damping ratio seems to have a dominant effect in the IL bending stress, leading to the maximum increase of 29.58% being observed at the highest velocity of 2.0 m/s. As for the Linear model, a similar behaviour becomes evident with regard to the lower examined velocities up to 0.9 m/s. That is, the effect of the soil damping level seems to grow as the current velocity becomes higher, giving the maximum observed increase of 15.43% in the IL bending stress at 0.9 m/s. However, contrary to what was observed previously, a constantly decreasing effect becomes obvious for all the considered higher velocities, ultimately resulting in the prediction of a very small increase of 4.4% at the highest velocity of 2.0 m/s. The fact that the reduction of the soil damping ratio for both soil models leads to an important growth in the estimated IL bending stresses is totally expected, since the smaller level of damping in the system results in higher responses and consequently in increased curvature in the pipeline. Moreover, the way the decrease in the soil damping ratio influences the results for the IL bending stresses seems to follow exactly the trends that were identified previously with regard to the maximum IL response amplitudes, something that is again totally reasonable.

What is more, as far as the Induced bending stresses in the CF direction are concerned and considering only velocities above 1.3 m/s for which the CF response is more significant, it becomes evident from Figures 8.40a and 8.40b that the change in the predicted CF bending stress as a function of the soil damping ratio does not seem to follow a specific trend but instead it seems

to be random. This is particularly obvious with regard to the Non-Linear model for which the reduction of the soil damping ratio results in an increase in the measured CF bending stresses for some current velocities, while the opposite is true for other velocities. As shown in Table 8.6, the maximum increase is observed at 2.0 m/s and is equal to 4.19%, while the maximum reduction of 11.37% is found at 1.4 m/s. Contrary to this, when the Linear model is used, a considerable increase up to 10.7% in the estimated CF bending stress becomes clear for velocities above 1.3 m/s, apart from two cases corresponding to 1.7 and 1.8 m/s, for which a small reduction of 5.94% and 0.87% is observed respectively. This increase in the CF bending stress is totally expected, since again the higher obtained CF response due to the smaller damping level leads in turn to higher curvature in the pipeline and thus increased stresses. As for the two velocities for which a reduction in the CF bending stress is observed instead, a possible explanation could be the aforementioned complex interaction between the VIV responses in the CF and IL directions for this specific velocity range for which the amplitude of those two responses is of the same magnitude. Finally, the above findings with regard to the Non-Linear soil model could mainly be attributed to a combination of the effects of the increased CF response and the occurrence of the ”lift off” phenomenon. To be more precise, when the Non-Linear model is used, an alleviation of stresses takes place near the shoulders of the pipeline as a result of the smoother and less abrupt change in curvature in the touch-down point, as was explained in detail in section 8.1. So, the increase in the bending stress due to the higher response amplitude is combined with the alleviation of stresses near the shoulders and this ultimately results in some cases in an increase and in some cases in a reduction in the total value of the induced bending stress at the left shoulder.

What is more, from Figures 8.40c and 8.40d it becomes clear that for both soil models, the reduction of the soil damping ratio leads to a considerable increase in the IL fatigue damage accumulation at the left shoulder of the pipeline for the whole range of examined velocities, except for the two highest velocities of 1.9 and 2.0 m/s, for which approximately the same results were obtained for both examined levels of soil damping. Moreover, from Table 8.8 it becomes clear that for both soil models, the maximum increase in the IL fatigue damage is observed at the velocity of 0.9 m/s and is equal to 40.93% with respect to the Non-Linear model and to 52.99% for the Linear model. This considerable increase in the IL fatigue damage accumulation is totally expected, since a significant growth in the IL bending stress was also observed previously and at the same time it was found that the effect of the soil damping in the IL response frequency is in general negligible. As for the CF fatigue damage accumulation, it becomes again apparent that for both soil models, the reduction of the soil damping ratio leads into an important increase in the CF fatigue damage accumulation at the left shoulder of the pipeline for the whole range of examined velocities above 1.6 m/s, for which there is a significant contribution of the CF response to the fatigue damage. The maximum increase in the CF fatigue damage is observed for both soil models at the highest considered velocity of 2.0 m/s and is equal to 60.94% with respect to the Non-Linear model and to 133.43% for the Linear model. However, it should also be noted that there is one specific velocity for which the Non-Linear model gives a significant drop in the CF fatigue damage due to the reduction of the soil damping ratio. That is clearly illustrated for the velocity of 1.9 m/s, for which a reduction of 35.05% is found when the Non-Linear model is used. This observation is in total agreement with the previous findings regarding the CF response at this velocity. More specifically, it was found above that the reduction in the level of soil damping results in a severe drop of 11.32% in the CF dominant frequency predicted by the Non-Linear model for the velocity of 1.9 m/s, while at the same time the change of the soil damping was found to have no influence at all in the obtained results for the induced CF bending stress at this velocity. So ultimately this significantly smaller CF vibration frequency led to an important drop in the resulting fatigue damage accumulation.

9 Conclusions and Recommendations for further work

9.1 Summary and Conclusions

The first objective of the present work was to validate and calibrate the TD VIV prediction tool focusing on both the pure IL and the combined IL and CF VIV in free spanning pipelines. The aim of the followed calibration procedure was to find one single set of empirical hydrodynamic coefficients that give results in good agreement with the reference data and at the same time to use a sufficiently wide synchronization range in the IL synchronization model in order to be able to account for both pure IL and CF-induced IL vibrations simultaneously. For this reason, it was decided to keep the lower and upper limits of the synchronization ranges both in the IL and the CF directions fixed and to vary only the values of the non-dimensional frequency of maximum energy transfer in the two directions, $\hat{f}_{0,x}$ and $\hat{f}_{0,y}$ respectively. As a general remark it was found that the reduction of the values of $\hat{f}_{0,x}$ and $\hat{f}_{0,y}$ resulted on the one hand in the prediction of smaller values for the dominant vibration frequencies in both directions and on the other hand in a small increase in the obtained results for the response amplitudes. Moreover, it was also found that in general reducing the values of $\hat{f}_{0,x}$ and $\hat{f}_{0,y}$ leads to the prediction of the transition from the pure IL to the combined CF and IL phenomenon at slightly higher current velocities.

The most relevant data regarding three series of laboratory experiments and the results of an earlier frequency domain analysis of these model tests were used as a benchmark for the calibration of the TD VIV model. As a first step, a preliminary comparative study between the results of the TD VIV model for the different examined parameter sets and the reference data was conducted. On the basis of this comparative study, although several parameter sets were found to be able to give quite accurate results, it was ultimately concluded that from the engineering point of view, Parameter Sets No. 8 is the overall optimum parameter set with regard to all three investigated Test Series, since it was demonstrated that it is able to either predict the experimentally captured VIV response very accurately or to give slightly more conservative results. Subsequently, an in depth comparison between the results of the optimum parameter set and the experimental data was conducted. Based on this detailed comparative study, it was proven that, even for the velocities for which some non-negligible deviations from the experimental data were observed during the aforementioned preliminary comparative study, the results of the TD VIV model are in fact in very good agreement with the actual response of the pipeline. The most important finding was the fact that the TD VIV model was found to give improved results compared to the modal analysis and the frequency domain analysis. The latter are simplified methods based on the linearization of complex non-linear dynamic phenomena like VIV. Consequently, unreliable and even unreasonable results can often be obtained using these methods, especially when relatively high flow velocities are considered, since the increased velocities lead to higher response frequencies and enhance the non-linearities of the examined phenomena. This issue can be avoided by utilizing the more complicated but more accurate time domain analysis. Therefore, it can be concluded that frequency domain methods, like modal analysis, should not be applied for the analysis of complex dynamic phenomena and experimental data when high velocities are examined, and time domain methods should be preferred instead.

Subsequently, the above identified optimum parameter set was implemented in order to investigate a realistic case of VIV in a free spanning pipeline. The main focus of this analysis was on the investigation of the effects from damping due to soil-pipe interaction and the effect of the non-linear boundary conditions on the induced stresses and the accumulation fatigue damage. For this reason, two different soil models, one Linear and one Non-Linear, were developed and two different values of soil damping ratio, $\zeta_{soil} = 8\%$ and $\zeta_{soil} = 22\%$, were examined.

By comparing the results of the two examined soil models, it was found that in general the two models give almost identical results for the predicted dominant vibration frequencies both in the IL and the CF directions. However, some relatively small deviations between the two soil models were observed with regard to the maximum response amplitudes. More specifically, the maximum response amplitudes correspond to the free span of the pipeline, where it was found with regard to the IL direction that the Non-Linear model constantly predicts somewhat higher IL response than the Linear model. As for the CF direction, it was found that the Non-Linear model slightly overestimates the CF response for current velocities below 2.0 m/s, while the exact opposite behaviour was observed for higher velocities. Contrary to this, considerable differences between the two soil models and the significant effect of the ”lift off” phenomenon became apparent with regard to the predicted responses in the vicinity of the shoulders and above the soil-supported part of the pipeline. More specifically, the Non-Linear model predicted a non-symmetric response since a significant spreading of the response near the shoulder was observed in both directions due to the non-linear contact between the pipe and the seafloor as a result of the ”lift off” phenomenon. Moreover, when the Non-Linear model was examined, considerable responses above the seafloor within the soil-supported part of the pipeline were predicted in both directions and in fact this phenomenon was found to extend far away from the end of the free span, something that was not observed with regard to the Linear model.

Furthermore, it was found that the results of the two soil models, in terms of the way the induced bending stresses and the respective fatigue damage change as a function of the examined current velocity, are in general in good agreement. However, some non-negligible differences in the values of the bending stress and the fatigue damage predicted by the two models were also observed. More specifically, it was found that both at the shoulders and at the midspan of the pipeline the Non-Linear model constantly gives higher induced bending stresses in the IL direction, while the exact opposite behaviour was observed with regard to the CF direction. The same findings were also observed for the fatigue damage accumulation along the pipeline and in fact the deviation between the two models was found to be much more significant. These differences between the two soil models were found to be much more profound within the soil-supported part of the pipeline, where the ability of the pipeline to lift up and detach from the seafloor when the Non-Linear model was used, led to a significant distribution of bending stresses above the seabed in both directions, while the Linear model predicted zero stresses induced in this region. Moreover, as far as the effect of the different levels of soil damping on the predicted VIV responses is concerned, it was found for both examined soil models and for both directions that the reduction of the soil damping ratio from $\zeta_{soil} = 22\%$ to $\zeta_{soil} = 8\%$ did not influence the predicted vibration frequencies at all, while it resulted in a considerable increase in the predicted response amplitudes. In fact this increase was found to be much more profound with regard to the Non-Linear model. An increase was also observed with regard to the induced fatigue damage along the pipeline, but in this case the Linear model was influenced to a greater extent than the Non-Linear model. Finally, it was found that the reduction of the level of soil damping ultimately amplified the discrepancies between the two soil models.

To sum up, it can be concluded that, since the deviations between the two soil models are reasonably small within the free span of the pipeline and especially in terms of the predicted vibration frequencies and amplitudes, the simpler and computationally faster Linear model seems to be a reasonable choice when only the global response of the pipeline is of interest. On the contrary, in case the the response of the pipeline locally in the vicinity of the shoulders is also of interest and especially in case the focus of the investigation is mainly on the induced bending stresses and fatigue damage, then the Non-Linear soil model should be considered instead.

9.2 Recommendations for further work

In the previous section it was concluded that the TD VIV model developed and calibrated in the context of the present thesis is indeed able to capture quite accurately the VIV responses observed during the model tests with regard to all three examined Test Series and additionally it was found that in fact the TD VIV model gives improved results compared to other typically used methods of analysis including the VIVANA-FD model and modal analysis. However, in the present thesis only uniform incident fluid flows were investigated. So another interesting study subject would be the effect that a space-varying flow like a sheared current would have on the considered pipelines. At this point it should be noted that, although the pipes were initially assumed to be horizontal, in reality there is a non-negligible sag present in the middle of the pipe both in the CF and in the IL directions due to the weight of the pipe and the incident current respectively. Therefore, different cross-sections along the pipe's length will see different onset flow velocities when a sheared current is considered. This could result in the excitation of multiple response frequencies along the pipe and thus enhance the above observed multi-frequency response phenomena, which were shown to influence considerably the predicted VIV responses.

Moreover, it was also concluded with regard to the Realistic Free Span Scenario that, although the results obtained using the two different soil models in general followed the same trends, some considerable deviations between the two soil models became also evident especially in the vicinity of the shoulders and within the soil-supported part of the pipeline. So, keeping in mind that comprehensive studies about the effect of the pipe-soil interaction and more specifically of the non-linear boundary conditions and the application of non-linear soil damping on the predicted VIV responses are limited in literature, it becomes apparent that there are many possibilities for further work. More case studies can be conducted, increasing the understanding of the effect of the inherent non-linear pipe-soil interaction on the pipeline's response. For example, other pipelines with different structural properties could be examined and in this way the investigation of higher velocities might be possible in case the aforementioned issue of the extremely high pipeline curvature is avoided. Furthermore, different seabed configurations and even soil properties could also be considered such as using clay instead of sand to model the seabed.

What is more, taking into account that several difficulties and issues had to be overcome during the present work in order to implement the two soil models and especially the Non-Linear one into RIFLEX, and also considering that because of these issues several simplifications had to be adopted, another area of further work could be the improvement of the existing software like RIFLEX so that they are able to model more accurately and more easily the pipe-soil interaction. For example, one major difficulty that had to be dealt with in the present work is that in RIFLEX's "Seafloor Spring Contact" component only one set of soil properties can be given as input and thus it was used only for modelling the Vertical Static Soil Stiffness while the Vertical Dynamic Soil Stiffness had to be modelled separately using bi-linear global springs. Furthermore, another difficulty had to do with the fact that there is no coupling between the global springs applied to the CF and IL directions in RIFLEX. For this reason, the "Seafloor Spring Contact" component was used to model the Lateral Dynamic Soil Stiffness too, because separate bi-linear springs could not be utilized for this purpose, since having contact or not could not be related to the springs being in tension or in compression as was the case in the vertical direction. However, within the "Seafloor Spring Contact" component the Coulomb friction model is also implemented in the lateral direction and as a result, pipeline sliding was observed in the IL direction for velocities above 1.0 m/s even when only the static loads were considered (i.e.

only the current loads and not the additional VIV forces). So, in order to examine higher current velocities, an extremely high value had to be used for the friction coefficient and even in this way pipeline sliding was still observed at velocities above 2.0 m/s within the dynamic analysis. Therefore, in case there was coupling between the global springs in the two directions, the ”lift off” phenomenon could have been captured using only the global springs and thus without considering the Coulomb friction model at all and thus the above problem could have been avoided.

Furthermore, at the moment one new module of RIFLEX is under development, in which Linear analysis will be utilized for carrying out TD VIV analyses. The main difference of this module is that linear time integration will be used instead of the non-linear one used in the present version. So when this new module is fully developed, another interesting case study would be to repeat all the analyses presented in the present thesis using this new module. So, in case it is found that the differences between the results presented above and the respective finding of the new module are relatively small, the new Linear module could be used instead as the default module for carrying out TD VIV analyses, reducing in this way considerably the required computational effort.

Finally, it should be noted that in the present work only cases regarding single span pipelines were addressed. Therefore, another interesting study would be to also examine multi-span pipelines in order to investigate the way the adjacent spans interact with each other.

References

[1] J. Lienard. *Synopsis of Lift, Drag and Vortex Frequency Data for Rigid Circular Cylinders*. Washington State University, College of Engineering, 1966.

[2] O. M. Faltinsen. *Sea loads on ships and offshore structures*. Cambridge University Press, 1990.

[3] P. E. Voie, C. M. Larsen, J. Wu, and T. Resvanis. *VIV Best Practice: Guideline on analysis of vortex-induced vibrations in risers and umbilicals*. Det Norske Veritas AS, 2016.

[4] C. M. Larsen. *Vortex Induced Vibrations VIV*. Department Of Marine Technology, NTNU, Trondheim, 2011.

[5] K. H. Aronsen. *An experimental investigation of in-line and combined in-line and cross-flow vortex induced vibrations.* PhD thesis, Norwegian University of Science and Technology, 2007.

[6] D. N. Veritas. *Recommended Practice: Pipe-soil interaction for submarine pipelines*. DNVGL-RP-F114, 2017.

[7] E. Passano, J. Wu, and C.M. Larsen. *VIV of free spanning pipelines: Comparison of response from semi-empirical code to model tests*. In proceedings of the ASME 2010 29_{th} International Conference on Ocean, Offshore and Arctic Engineering, OMAE2010-20330, June 6-11, 2010, Shanghai, China, 2010.

[8] O. Øritsland. *MARINTEK Report MT51 F03-260.* MARINTEK, Trondheim, Norway, 2004.

[9] F. Solaas. *MARINTEK Report MT51 F01-131.* MARINTEK, Trondheim, Norway, 2001.

[10] V. Shinde, J. Jha, A. Tewari, and S. Miashra. *Modified Rainflow Counting Algorithm for Fatigue Life Calculation.* Proceedings of Fatigue, Durability and Fracture Mechanics, pages 381–387, 2018.

[11] J. Wu, D. Yin, E. Passano, H. Lie, R. Peek, O. E. Sequeiros, S. Y. Ang, C. Bernardo, and M. Atienza. *Forced Vibration Tests for In-Line VIV to Assess Partially Strake-Covered Pipeline Spans.* Journal of Offshore Mechanics and Arctic Engineering, 2019.

[12] J. Wu, D. Yin, E. Passano, H. Lie, R. Peek, O. E. Sequeiros, S. Y. Ang, C. Bernardo, and M. Atienza. *Forced Vibration Tests for In-Line VIV to Assess Partially Strake-Covered Pipeline Spans.* Proceedings of the ASME 2019 38th International Conference on Ocean, Offshore and Arctic Engineering, OMAE2019, June 9-14, 2019, Glasgow, Scotland, 2019.

[13] R. D. Blevins. *Flow-Induced Vibration*. Van Nostrand Reinhold, New York, 2^{nd} edition, 1990.

[14] J. Dahl, F. Hover, and M. Triantafyllou. *Two-degree-of-freedom vortex-induced vibrations using a force assisted apparatus*. Journal of Fluids and Structures, 22(6):807–818, 2006.

[15] J. K. Vandiver, S. B. Swithenbank, V. Jaiswal, and V. Jhingran. *Fatigue damage from high mode number vortex-induced vibration*. 25^{th} OMAE Conf., 2006.

[16] M. Triantafyllou, G. Triantafyllou, Y. D. Tein, and B. D. Ambrose. *Pragmatic riser VIV analysis*. In Proceedings of the Offshore Technology Conference, Houston, TX, USA, 3–6 May 1999; Number OTC-10931-MS, 1999.

[17] J. K. Vandiver and L. Li. *Shear7 v4.5 Program Theoretical Manual*. Massachusetts Institute of Technology: Cambridge, MA, USA, 2007.

[18] C.M. Larsen, H. Lie, E. Passano, R. Yttervik, J. Wu, and G. Baarholm. *VIVANA—Theory Manual Version 4.20.2*. Sintef Ocean: Trondheim, Norway, 2021.

[19] R. Langen and R. Sigbjörnsson. *Dynamic Analysis of Constructions (Dynamisk Analyse av Konstruksjoner)*. Tapir Academic Press, Trondheim, 1979.

[20] D. Fergestad and S. A. Løtveit. *Handbook on Design and operation of flexible pipes*. Joint Industry Project: "Safe and Cost Effective Operation of Flexible Pipes", NTNU, 4Subsea, SINTEF Ocean, Otto Nielsens veg 10, Trondheim, Norway, 2017.

[21] D. N. Veritas. *Recommended Practice: Free spanning pipelines*. DNVGL-RP-F105, 2017.

[22] M. J. Thorsen, S. Sævik, and C. M. Larsen. *A simplified method for time domain simulation of cross-flow vortex-induced vibrations*. Journal of Fluids and Structures, 49:135–148, 2014.

[23] M. J. Thorsen, S. Sævik, and C. M. Larsen. *Fatigue damage from time domain simulation of combined in-line and cross-flow vortex-induced vibrations*. Marine Structures, 41:200–222, 2015.

[24] M. J. Thorsen, S. Sævik, and C. M. Larsen. *Time domain simulation of vortex-induced vibrations based on phase-coupled oscillator synchronization*. OMAE2015-41881, V002T08A029, 2015.

[25] M. J. Thorsen. *Time Domain Analysis of Vortex-Induced Vibrations*. PhD thesis, Norwegian University of Science and Technology, 2016.

[26] J. V. Ulveseter. *Advances in semi-empirical time domain modelling of vortex-induced vibrations*. PhD thesis, Norwegian University of Science and Technology, 2018.

[27] M. J. Thorsen, S. Sævik, and C. M. Larsen. *Time domain simulation of vortex-induced vibrations in stationary and oscillating flows*. Journal of Fluids and Structures, 61:1–19, 2016.

[28] J. V. Ulveseter, M. J. Thorsen, S. Sævik, and C. M. Larsen. *Time domain simulation of riser viv in current and irregular waves*. Marine Structures, 60:241–260, 2018.

[29] B. M. Sumer and J. Fredsøe. *Hydrodynamics around cylindrical structures*. vol. 12. World Scientific Publishing Company, 1997.

[30] M. Greco. *TMR 4215: Sea Loads - Lecture Notes*. Department Of Marine Technology, NTNU, Trondheim, 2021.

[31] J. D. Anderson. *Introduction to flight*. The McGraw-Hill Companies, Inc., Avenue of the Americas, New York, 5th edition, 2005.

[32] L. J. Clancy. *Aerodynamics*. New York : Wiley, 1975.

[33] G. S. Baarholm, C. M. Larsen, and H. Lie. *On fatigue damage accumulation from in-line and cross-flow vortex-induced vibrations in risers.* Journal of Fluids and Structures, 1(22):109–127, 2006.

[34] M. Triantafyllou, F. Hover, A. Techet, and D. Yue. *Vortex-induced vibrations of slender structures in shear flow.* I: IUTAM Symposium on Integrated Modeling of Fully Coupled Fluid Structure Interactions Using Analysis, Computations and Experiments., pages 313–327, 2003.

[35] A. D. Trim, H. Braaten, and M. A. Tognarelli. *Experimental investigation of vortex-induced vibration of long marine risers.* Journal of Fluids and Structures, 21(3):335–361, 2005.

[36] J. Wu, D. Yin, H. Lie, C. M. Larsen, R. J. Baarholm, V. Jhingran, and S. Liapis. *On the occurrence of higher harmonics in the VIV response.* Proceedings of the ASME 2015 34th International Conference on Ocean, Offshore and Arctic Engineering, 2015.

[37] J. Wu, D. Yin, H. Lie, C. M. Larsen, R. J. Baarholm, V. Jhingran, and S. Liapis. *On the significance of the higher order stress in riser vortex-induced vibrations responses.* Journal of Offshore Mechanics and Arctic Engineering, 141, 2017.

[38] E. H. Zarantonello and G. Brikhoff. *Jets, Wakes, and Cavities.* Academic Press Inc., New York, 1957.

[39] L. Finn, K. Lambrakos, and J. Maher. *Time domain prediction of riser viv.* 4th International Conference on Advances in Riser Technologies, 1999.

[40] P. Maincon and C. M. Larsen. *Towards a time-domain finite element analysis of vortex induced vibrations.* In: Proceedings of the ASME 2011 30th International Conference on Ocean, Offshore and Arctic Engineering OMAE2011, 2011.

[41] M. J. Thorsen, S. Sævik, and C. M. Larsen. *Non-linear time domain analysis of cross-flow vortex-induced vibrations*. Marine Structures, 51:134–151, 2017.

[42] J. V. Ulveseter, S. Sævik, and C. M. Larsen. *Time domain model for calculation of pure in-line vortex-induced vibrations*. Journal of Fluids and Structures, 68:158–173, 2017.

[43] S. W. Kim, S. Sævik, J. Wu, and B. J. Leira. *Prediction of deepwater riser VIV with an improved time domain model including non-linear structural behavior.* Journal of Ocean Engineering, 236:1–17, 2021.

[44] X. J. Zhang and M. S. Aggour. *Damping determination of sands under different loadings.* Eleventh World Conference on Earthquake Engineering, (364), 1996.

[45] S. Chong. *Theoretical Framework for Characterizing Strain-Dependent Dynamic Soil Properties.* Multidisciplinary Digital Publishing Institute, 2019.

[46] E. Delfosse-Ribay, I. Djeran-Maigre, R. Cabrillac, and D. Gouvenot. *Shear modulus and damping ratio of grouted sand.* Journal of Soil Dynamics and Earthquake Engineering, 24:461–471, 2004.

[47] E. Huse. *MARINTEK Report MT51-F01.040.* MARINTEK, Trondheim, Norway, 2001.

[48] K. Mo and F. Solaas. *MARINTEK Report MT51 F02-038.* MARINTEK, Trondheim, Norway, 2002.

[49] T. Sarpkaya. *Force on a circular cylinder in viscous oscillatory flow at low keulegan-carpenter numbers.* Journal of Fluid Mechanics, 165:61–71, 1986.

[50] SINTEF Ocean. *RIFLEX—User Guide Version 4.20.2*. SINTEF Ocean, 2021.

[51] SINTEF Ocean. *RIFLEX—Theory Manual Version 4.20.2*. SINTEF Ocean, 2021.

[52] S. K. Ås and S. Berge. *TMR 4200: Fatigue and Fracture of Marine Structures - Compendium*. Department Of Marine Technology, NTNU, Trondheim, 2017.

[53] L. Sieber. *VIV fatigue of rigid spool for subsea template by a time domain model*. Master's thesis, Norwegian University of Science and Technology, 2020.

[54] H. Drengsrud. *Systematic Evaluation of VIV Prediction for Riser with Partial Strake Coverage*. Master's thesis, Norwegian University of Science and Technology, 2019.

[55] M. Matsuishi and T. Endo. *Fatigue of metals subjected to varying stress.* Japan Society of Mechanical Engineers, 1968.

[56] B. Ligaj. *An analysis of the influence of cycle counting methods on fatigue life calculations of steel.* Scientific Problems of Machines Operation and Maintenance, 4(168):25–43, 2011.

[57] N. Hong. *A modified rainflow counting method.* International journal of fatigue, 13(6):465–469, 1991.

[58] L. L. Schulter and H. J. Sutherland. *User's guide for life2's rainflow counting algorithm.* New Mexico and Livermore, California: Sandia National Laboratories, pages 1–37, 1991.

[59] ASTM. *Standard practices for cycle counting in fatigue analysis.* Annual book of ASTM standards, 3(01):614–620, 2005.

Appendices

A Total sets of results of the calibration procedure

A.1 Test Series 10 - Total set of results

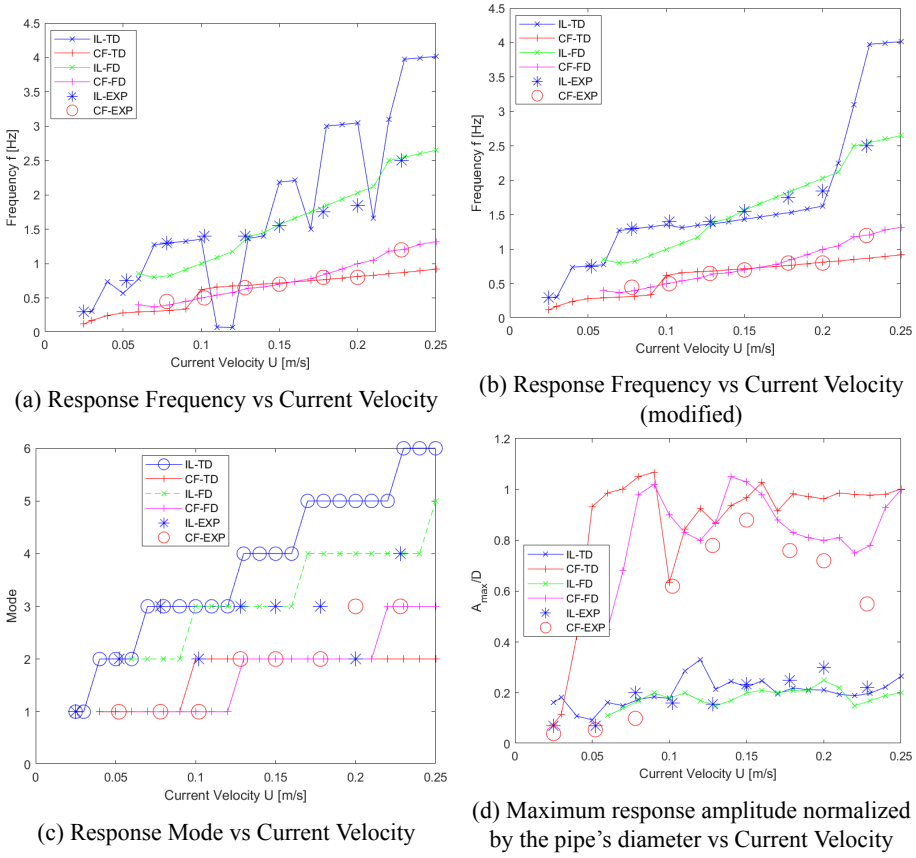

(a) Response Frequency vs Current Velocity

(b) Response Frequency vs Current Velocity (modified)

(c) Response Mode vs Current Velocity

(d) Maximum response amplitude normalized by the pipe's diameter vs Current Velocity

Figure A.1: Comparative plots of the fundamental experimental results and the respective findings of the frequency domain analysis and the time domain analysis conducted in the context of the Project Thesis.

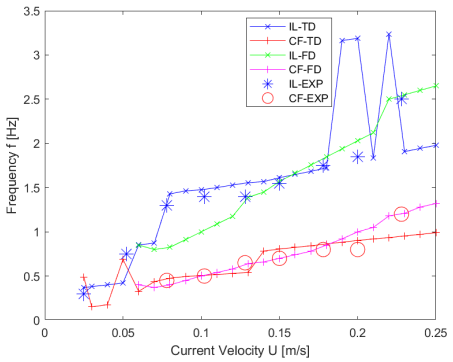

(a) Response Frequency vs Current Velocity

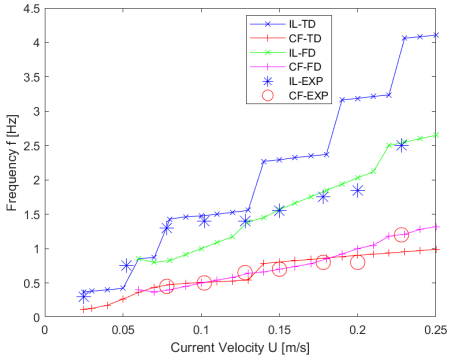

(b) Response Frequency vs Current Velocity (modified)

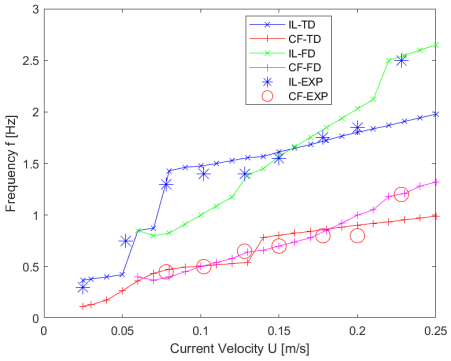

(c) Response Frequency vs Current Velocity (modified)

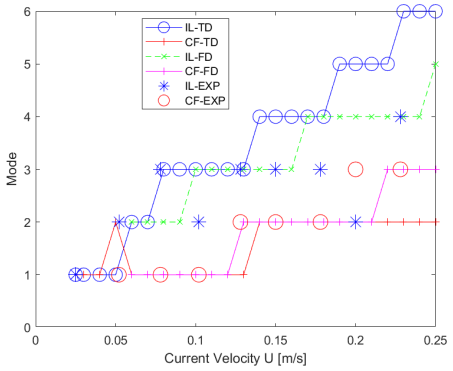

(d) Response Mode vs Current Velocity

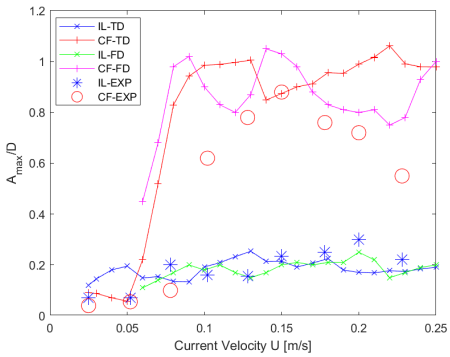

(e) Maximum response amplitude normalized by the pipe's diameter vs Current Velocity

Figure A.2: Comparative plots of the fundamental experimental results and the respective findings of the frequency domain analysis and the time domain analysis for Parameter Set No. 1.

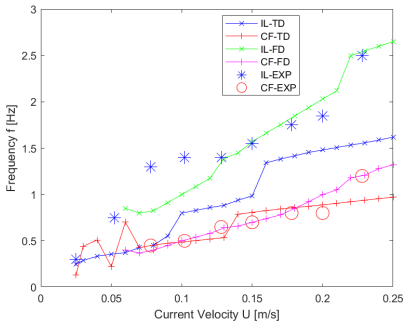

(a) Response Frequency vs Current Velocity

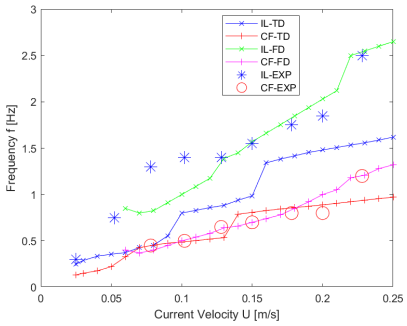

(b) Response Frequency vs Current Velocity (modified)

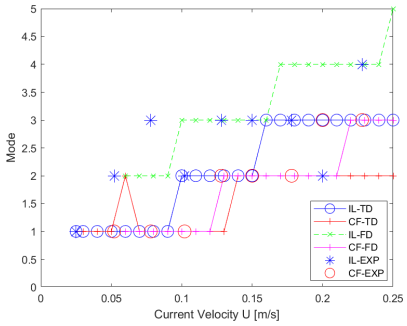

(c) Response Mode vs Current Velocity

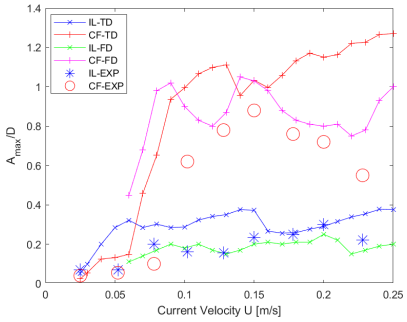

(d) Maximum response amplitude normalized by the pipe's diameter vs Current Velocity

Figure A.3: Comparative plots of the fundamental results for Parameter Set No. 2.

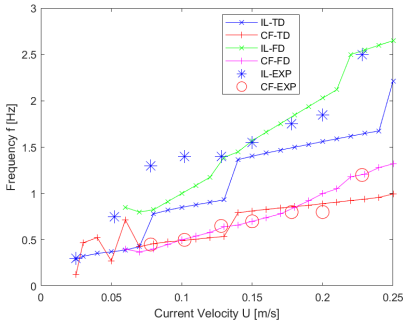

(a) Response Frequency vs Current Velocity

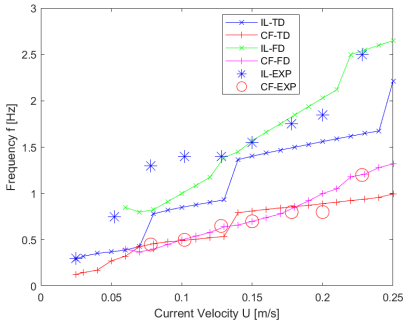

(b) Response Frequency vs Current Velocity (modified)

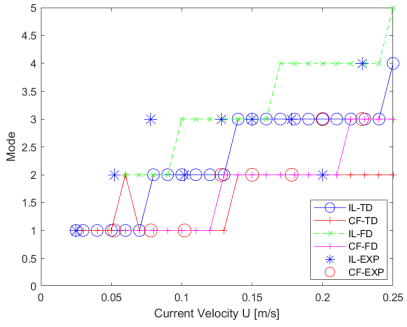

(c) Response Mode vs Current Velocity

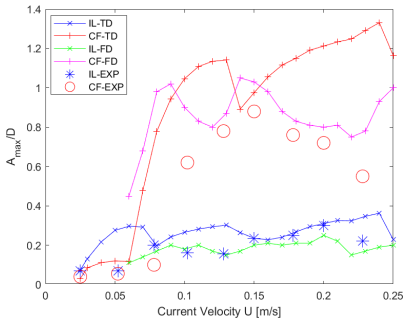

(d) Maximum response amplitude normalized by the pipe's diameter vs Current Velocity

Figure A.4: Comparative plots of the fundamental results for Parameter Set No. 3.

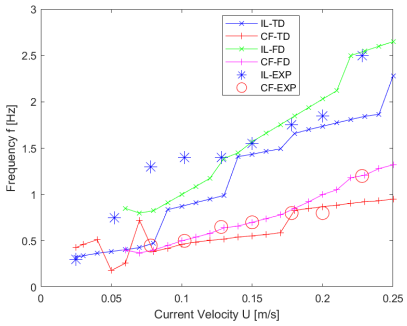

(a) Response Frequency vs Current Velocity

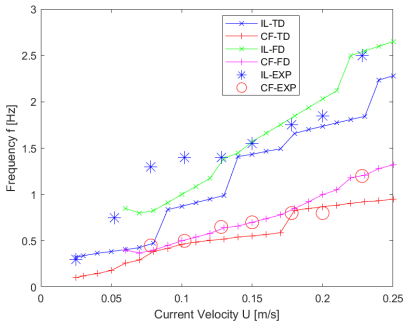

(b) Response Frequency vs Current Velocity (modified)

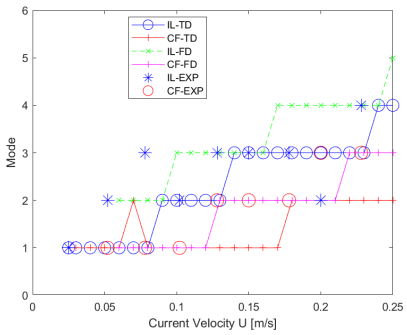

(c) Response Mode vs Current Velocity

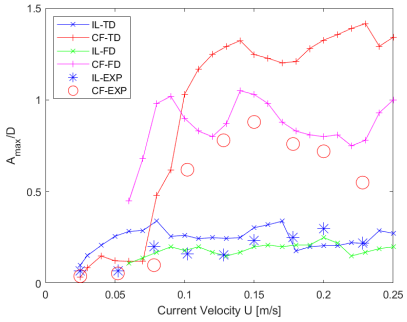

(d) Maximum response amplitude normalized by the pipe's diameter vs Current Velocity

Figure A.5: Comparative plots of the fundamental results for Parameter Set No. 4.

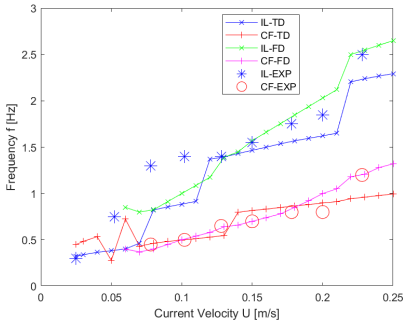

(a) Response Frequency vs Current Velocity

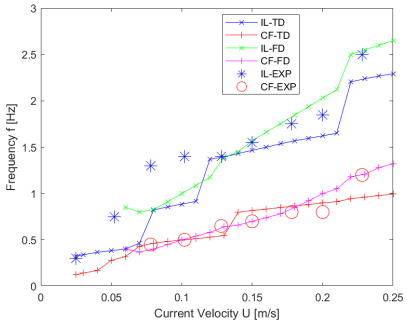

(b) Response Frequency vs Current Velocity (modified)

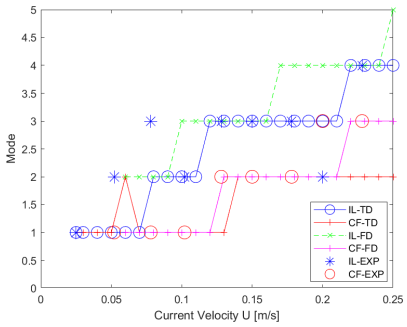

(c) Response Mode vs Current Velocity

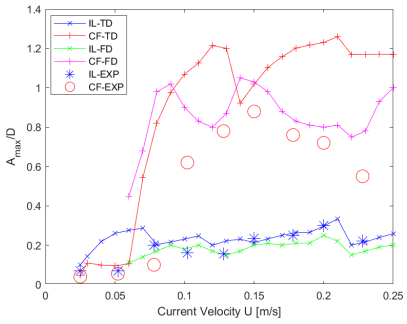

(d) Maximum response amplitude normalized by the pipe's diameter vs Current Velocity

Figure A.6: Comparative plots of the fundamental results for Parameter Set No. 5.

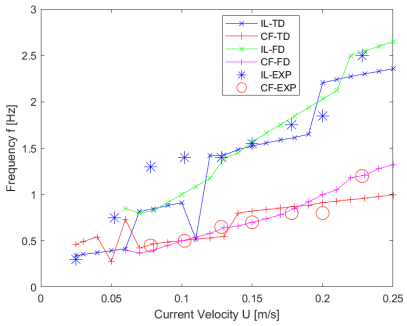

(a) Response Frequency vs Current Velocity

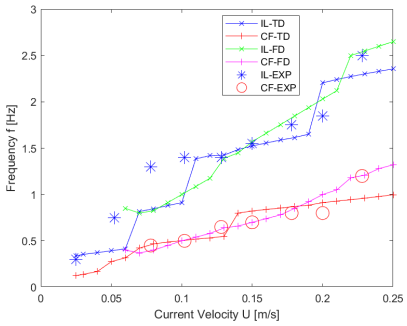

(b) Response Frequency vs Current Velocity (modified)

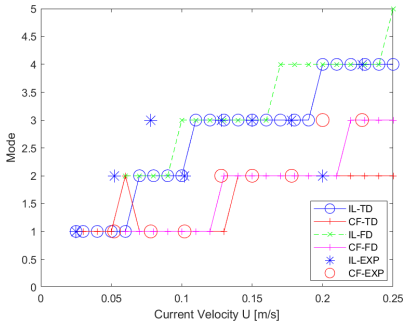

(c) Response Mode vs Current Velocity

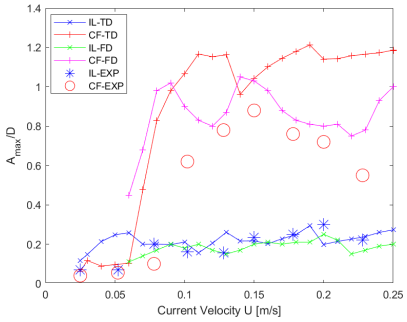

(d) Maximum response amplitude normalized by the pipe's diameter vs Current Velocity

Figure A.7: Comparative plots of the fundamental results for Parameter Set No. 6.

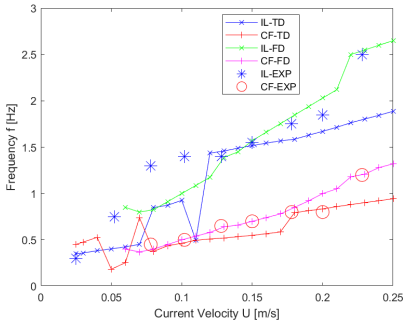

(a) Response Frequency vs Current Velocity

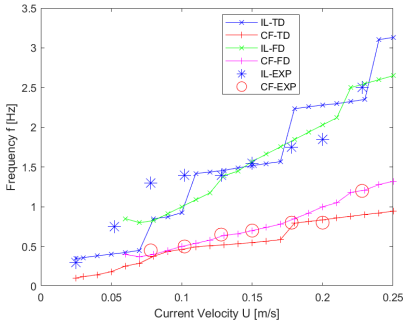

(b) Response Frequency vs Current Velocity (modified)

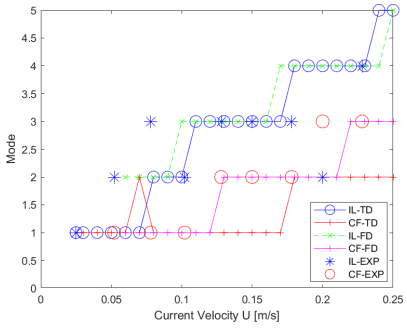

(c) Response Mode vs Current Velocity

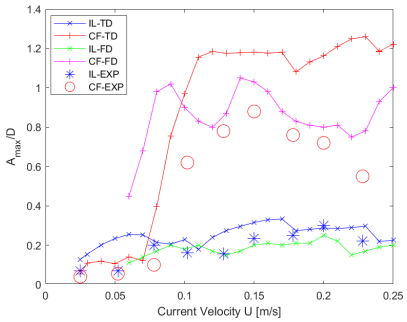

(d) Maximum response amplitude normalized by the pipe's diameter vs Current Velocity

Figure A.8: Comparative plots of the fundamental results for Parameter Set No. 7.

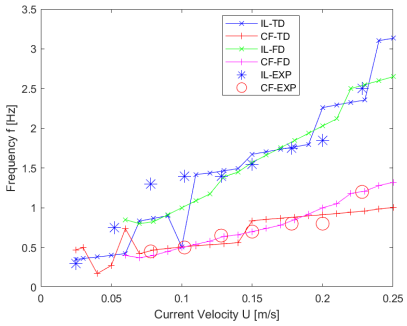

(a) Response Frequency vs Current Velocity

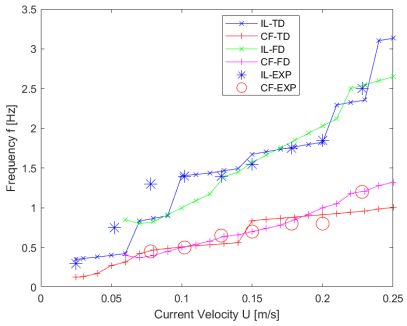

(b) Response Frequency vs Current Velocity (modified)

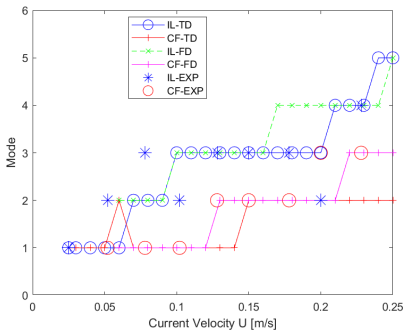

(c) Response Mode vs Current Velocity

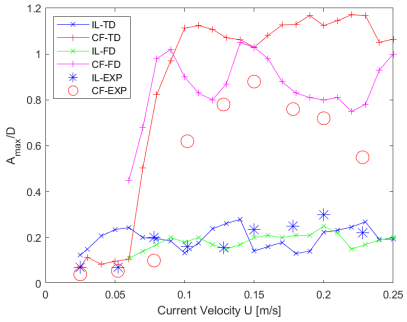

(d) Maximum response amplitude normalized by the pipe's diameter vs Current Velocity

Figure A.9: Comparative plots of the fundamental results for Parameter Set No. 8.

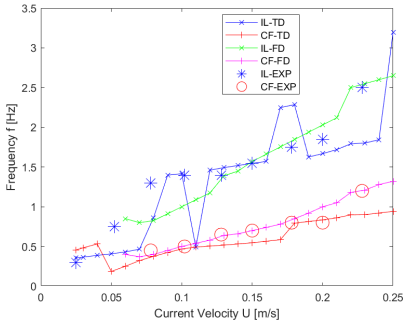

(a) Response Frequency vs Current Velocity

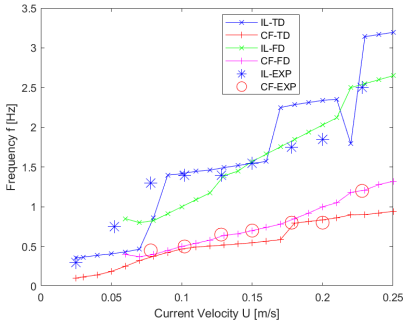

(b) Response Frequency vs Current Velocity (modified)

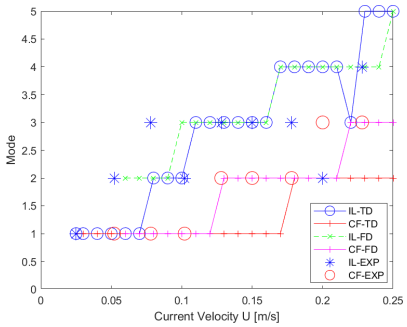

(c) Response Mode vs Current Velocity

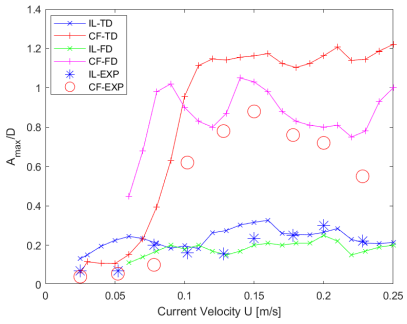

(d) Maximum response amplitude normalized by the pipe's diameter vs Current Velocity

Figure A.10: Comparative plots of the fundamental results for Parameter Set No. 9.

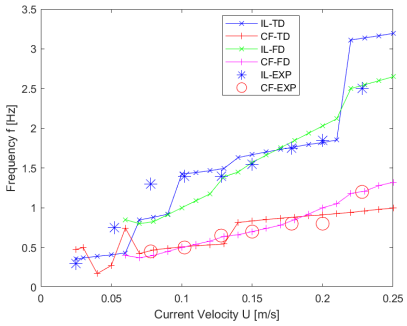

(a) Response Frequency vs Current Velocity

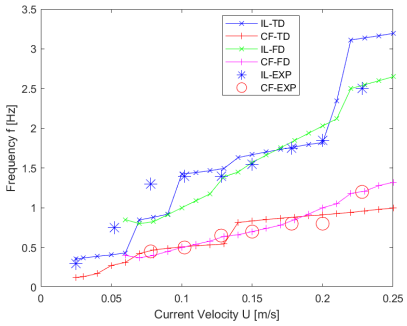

(b) Response Frequency vs Current Velocity (modified)

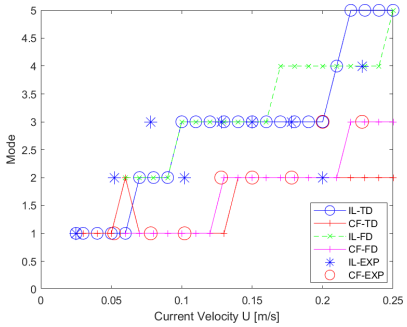

(c) Response Mode vs Current Velocity

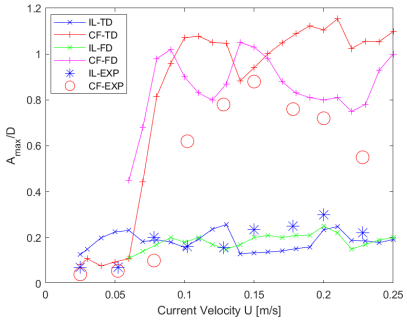

(d) Maximum response amplitude normalized by the pipe's diameter vs Current Velocity

Figure A.11: Comparative plots of the fundamental results for Parameter Set No. 10.

A.2 Test Series 42 - Total set of results

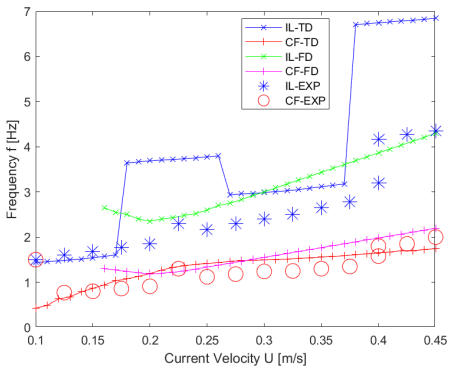

(a) Response Frequency vs Current Velocity

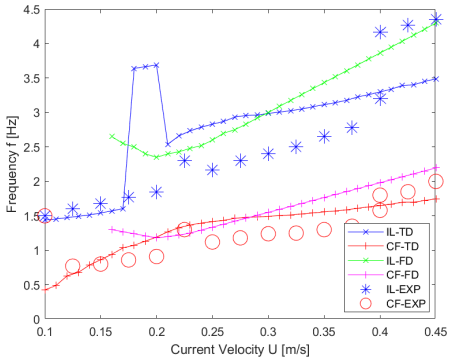

(b) Response Frequency vs Current Velocity (modified)

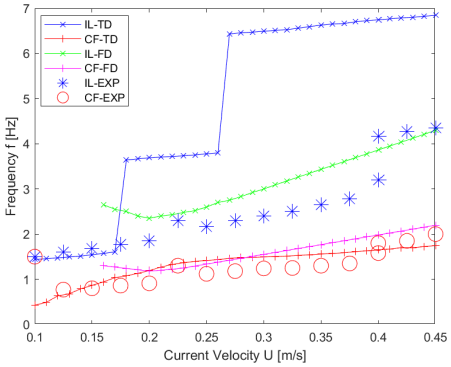

(c) Response Frequency vs Current Velocity (modified)

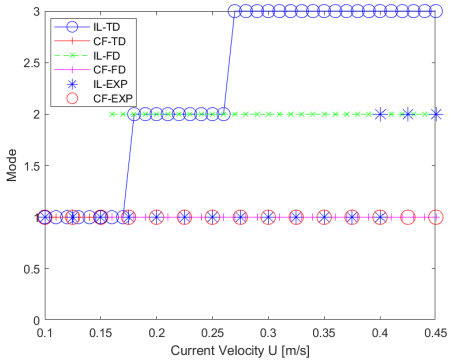

(d) Response Mode vs Current Velocity

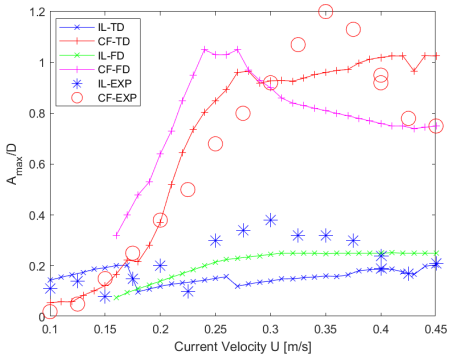

(e) Maximum response amplitude normalized by the pipe's diameter vs Current Velocity

Figure A.12: Comparative plots of the fundamental experimental results and the respective findings of the frequency domain analysis and the time domain analysis for Parameter Set No. 1.

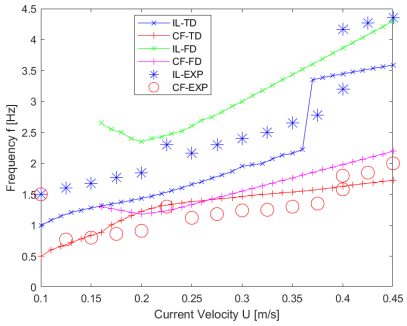

(a) Response Frequency vs Current Velocity

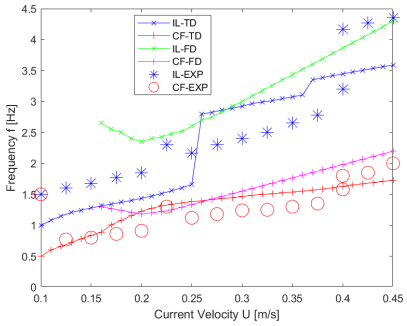

(b) Response Frequency vs Current Velocity (modified)

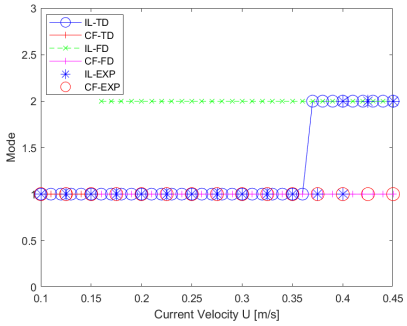

(c) Response Mode vs Current Velocity

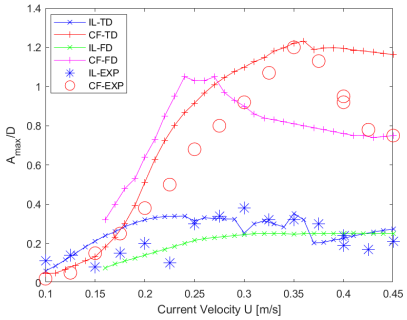

(d) Maximum response amplitude normalized by the pipe's diameter vs Current Velocity

Figure A.13: Comparative plots of the fundamental results for Parameter Set No. 2.

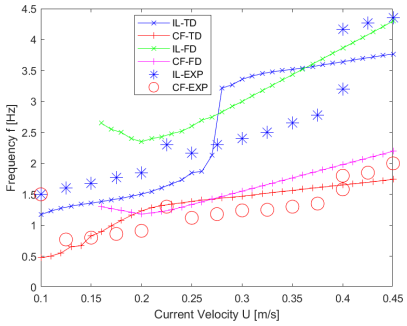

(a) Response Frequency vs Current Velocity

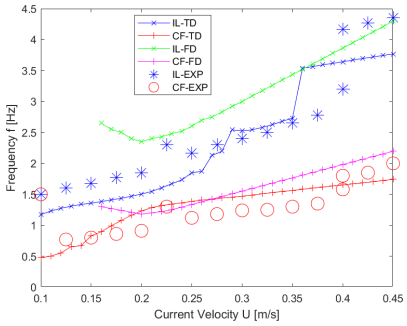

(b) Response Frequency vs Current Velocity (modified)

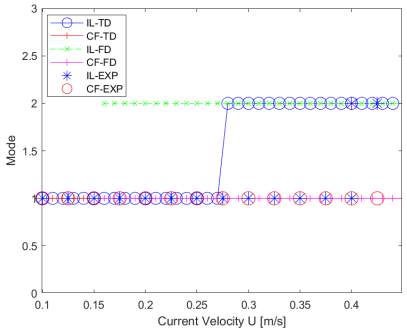

(c) Response Mode vs Current Velocity

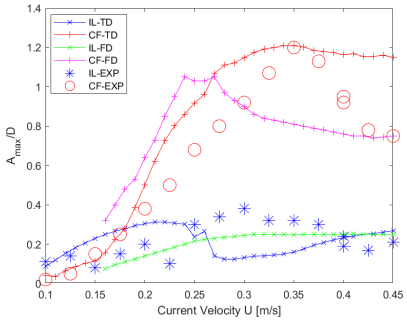

(d) Maximum response amplitude normalized by the pipe's diameter vs Current Velocity

Figure A.14: Comparative plots of the fundamental results for Parameter Set No. 3.

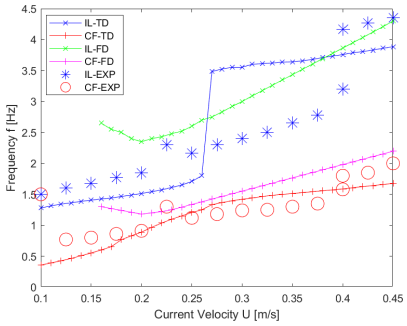

(a) Response Frequency vs Current Velocity

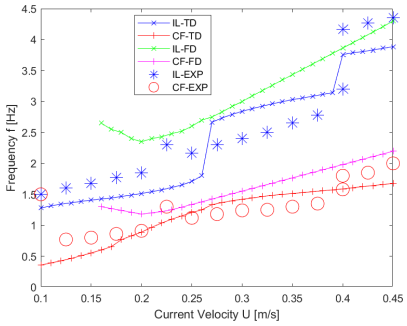

(b) Response Frequency vs Current Velocity (modified)

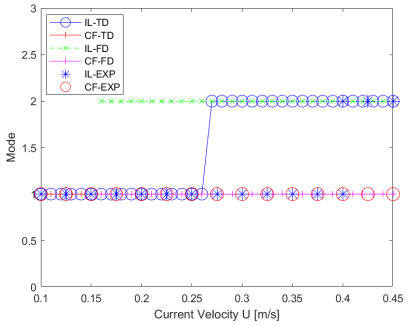

(c) Response Mode vs Current Velocity

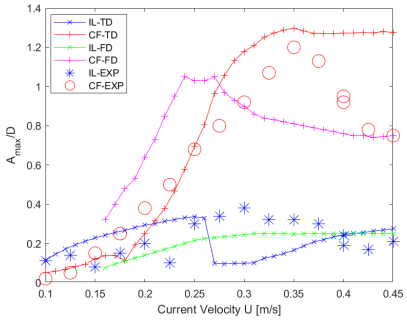

(d) Maximum response amplitude normalized by the pipe's diameter vs Current Velocity

Figure A.15: Comparative plots of the fundamental results for Parameter Set No. 4.

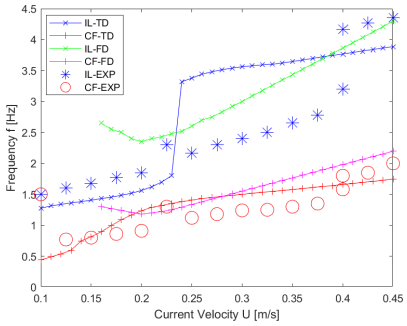

(a) Response Frequency vs Current Velocity

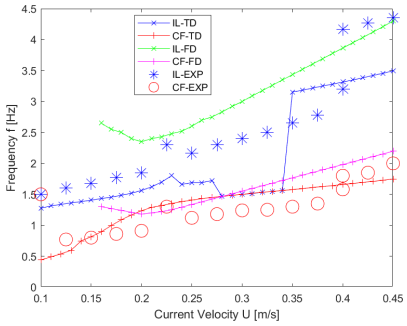

(b) Response Frequency vs Current Velocity (modified)

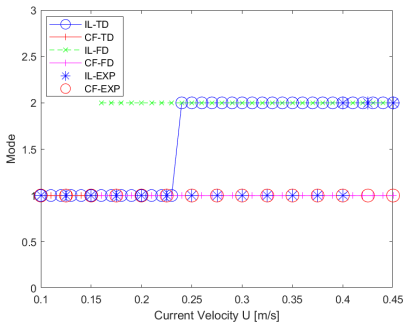

(c) Response Mode vs Current Velocity

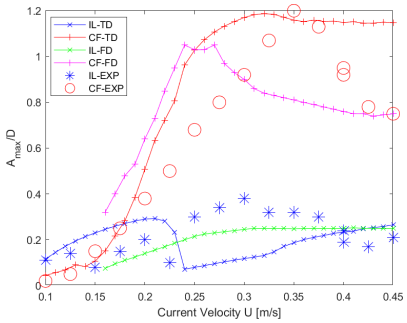

(d) Maximum response amplitude normalized by the pipe's diameter vs Current Velocity

Figure A.16: Comparative plots of the fundamental results for Parameter Set No. 5.

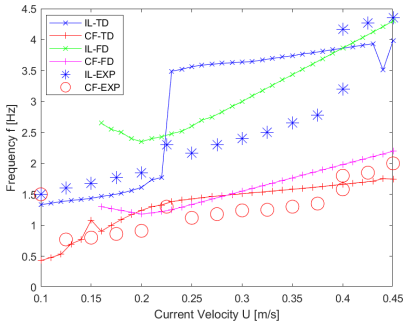

(a) Response Frequency vs Current Velocity

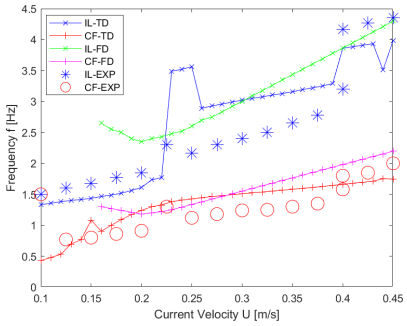

(b) Response Frequency vs Current Velocity (modified)

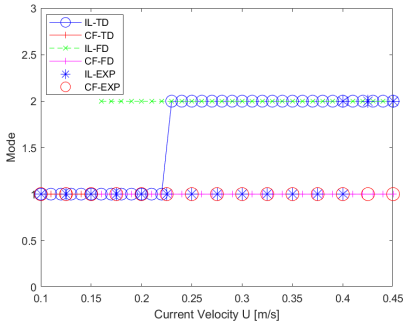

(c) Response Mode vs Current Velocity

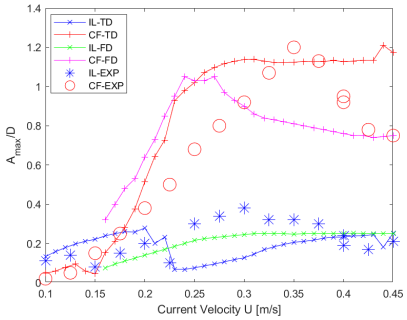

(d) Maximum response amplitude normalized by the pipe's diameter vs Current Velocity

Figure A.17: Comparative plots of the fundamental results for Parameter Set No. 6.

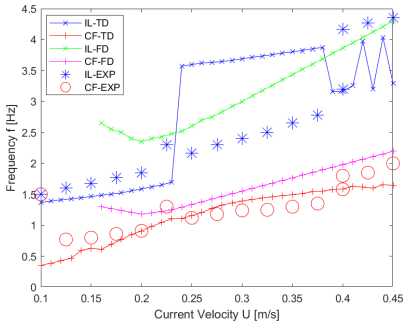

(a) Response Frequency vs Current Velocity

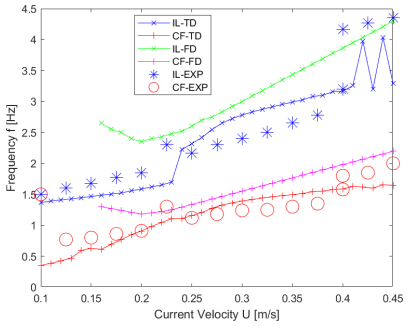

(b) Response Frequency vs Current Velocity (modified)

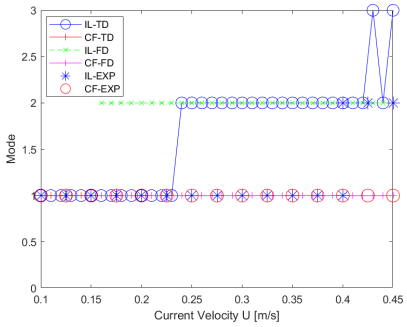

(c) Response Mode vs Current Velocity

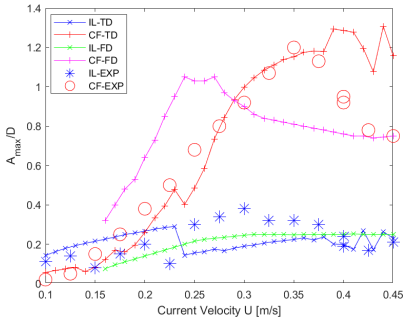

(d) Maximum response amplitude normalized by the pipe's diameter vs Current Velocity

Figure A.18: Comparative plots of the fundamental results for Parameter Set No. 7.

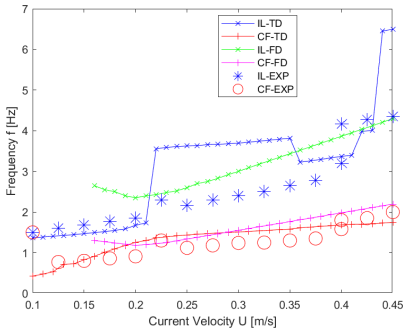

(a) Response Frequency vs Current Velocity

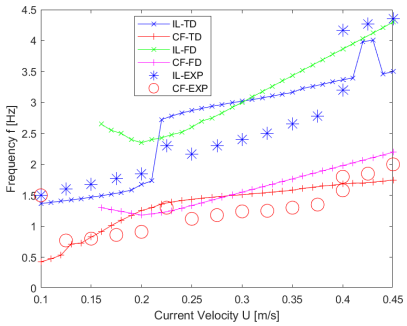

(b) Response Frequency vs Current Velocity (modified)

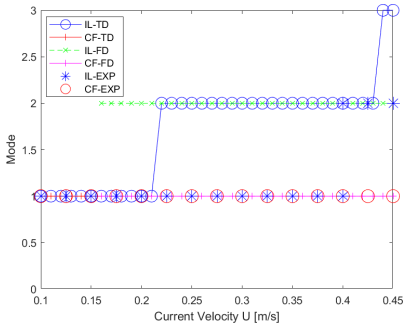

(c) Response Mode vs Current Velocity

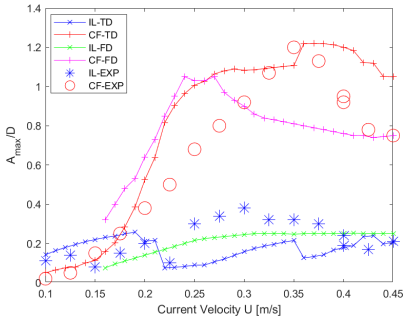

(d) Maximum response amplitude normalized by the pipe's diameter vs Current Velocity

Figure A.19: Comparative plots of the fundamental results for Parameter Set No. 8.

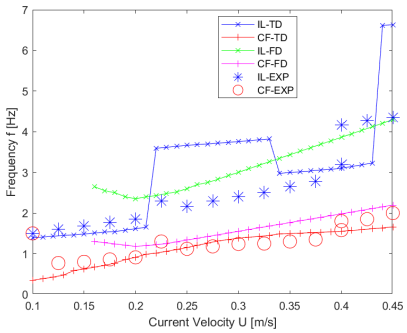

(a) Response Frequency vs Current Velocity

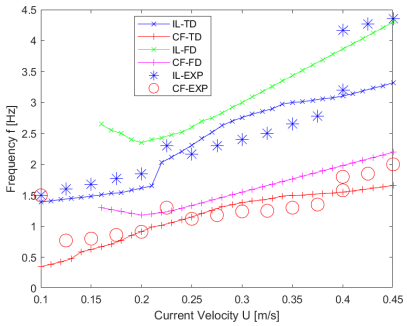

(b) Response Frequency vs Current Velocity (modified)

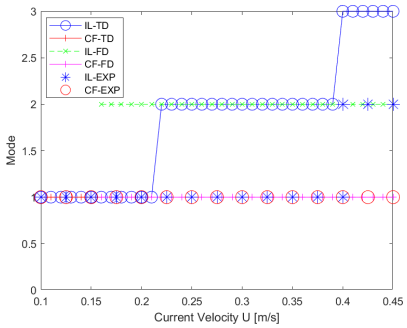

(c) Response Mode vs Current Velocity

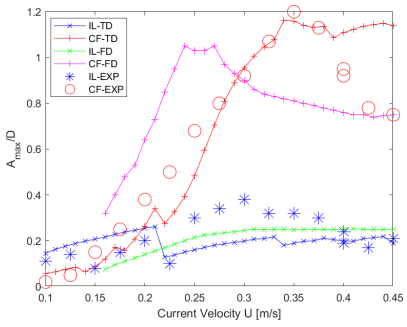

(d) Maximum response amplitude normalized by the pipe's diameter vs Current Velocity

Figure A.20: Comparative plots of the fundamental results for Parameter Set No. 9.

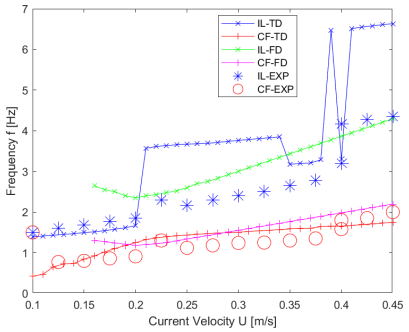

(a) Response Frequency vs Current Velocity

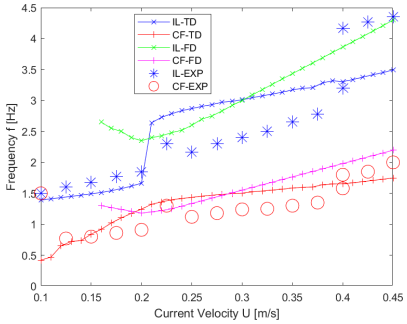

(b) Response Frequency vs Current Velocity (modified)

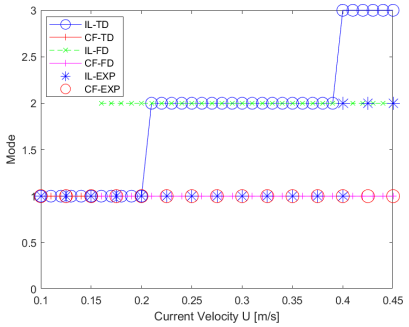

(c) Response Mode vs Current Velocity

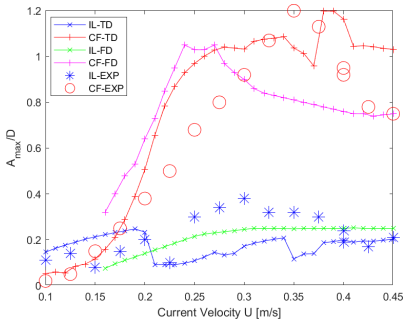

(d) Maximum response amplitude normalized by the pipe's diameter vs Current Velocity

Figure A.21: Comparative plots of the fundamental results for Parameter Set No. 10.

A.3 Test Series 75 - Total set of results

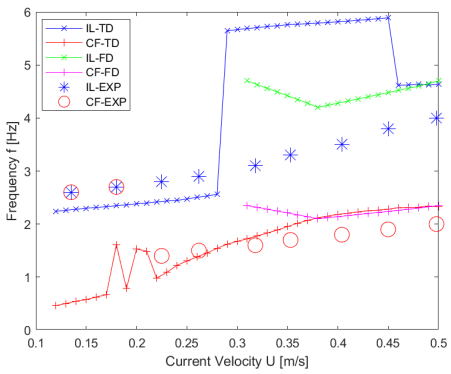

(a) Response Frequency vs Current Velocity

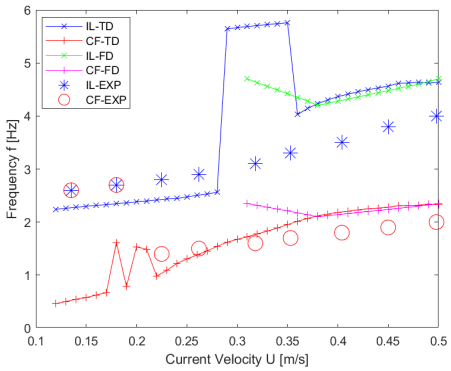

(b) Response Frequency vs Current Velocity (modified)

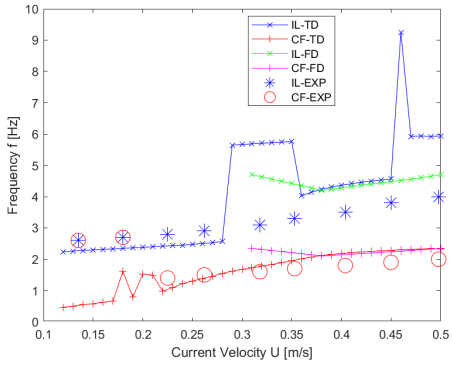

(c) Response Frequency vs Current Velocity (modified)

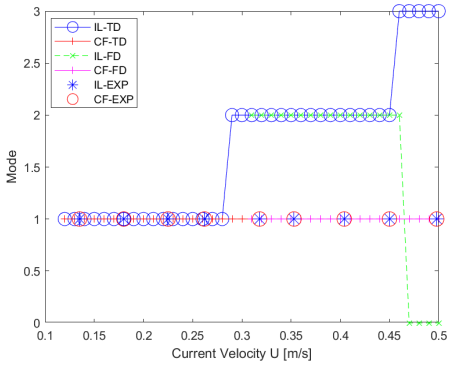

(d) Response Mode vs Current Velocity

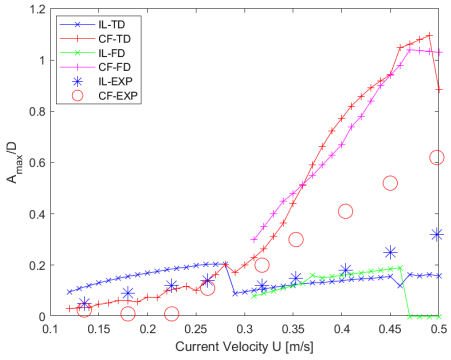

(e) Maximum response amplitude normalized by the pipe's diameter vs Current Velocity

Figure A.22: Comparative plots of the fundamental experimental results and the respective findings of the frequency domain analysis and the time domain analysis for Parameter Set No. 1.

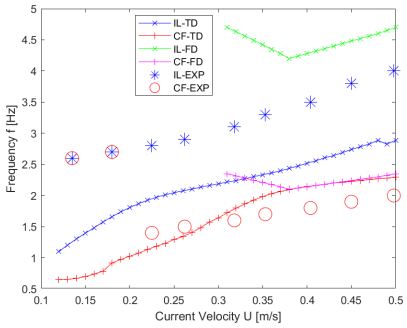

(a) Response Frequency vs Current Velocity

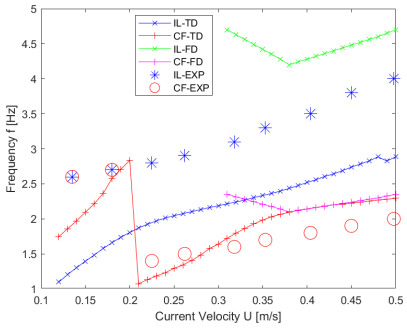

(b) Response Frequency vs Current Velocity (modified)

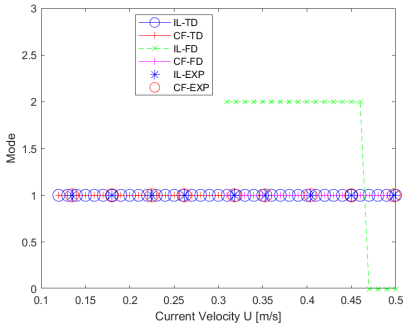

(c) Response Mode vs Current Velocity

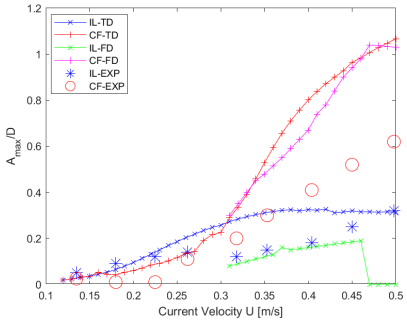

(d) Maximum response amplitude normalized by the pipe's diameter vs Current Velocity

Figure A.23: Comparative plots of the fundamental results for Parameter Set No. 2.

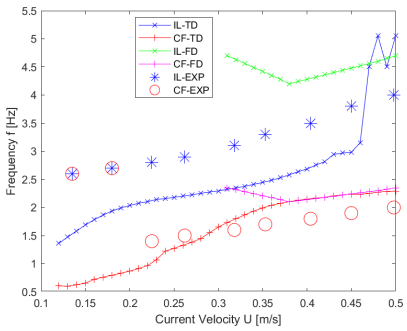

(a) Response Frequency vs Current Velocity

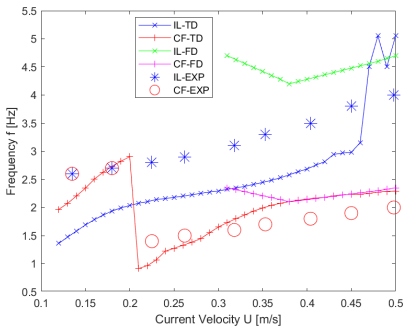

(b) Response Frequency vs Current Velocity (modified)

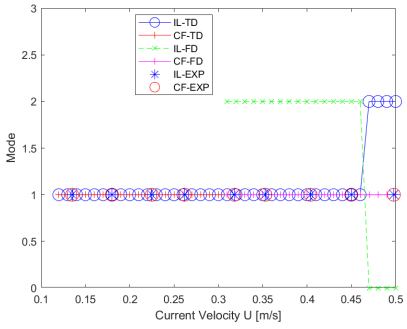

(c) Response Mode vs Current Velocity

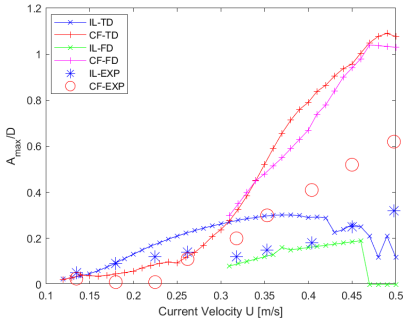

(d) Maximum response amplitude normalized by the pipe's diameter vs Current Velocity

Figure A.24: Comparative plots of the fundamental results for Parameter Set No. 3.

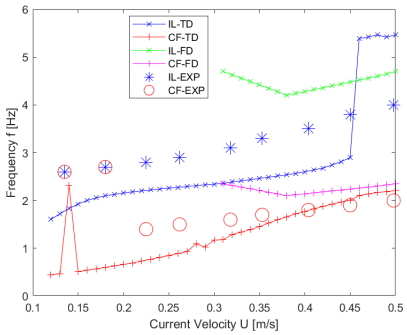

(a) Response Frequency vs Current Velocity

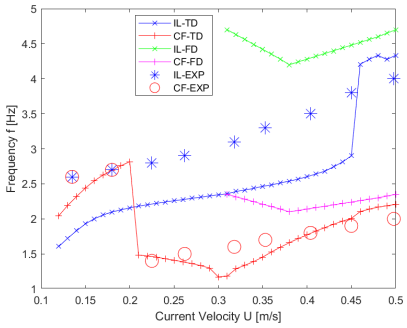

(b) Response Frequency vs Current Velocity (modified)

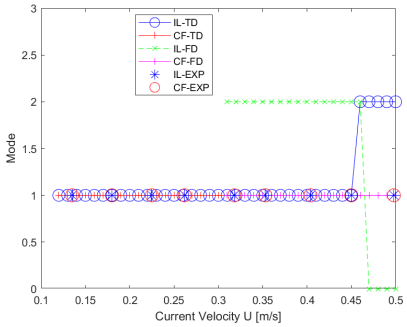

(c) Response Mode vs Current Velocity

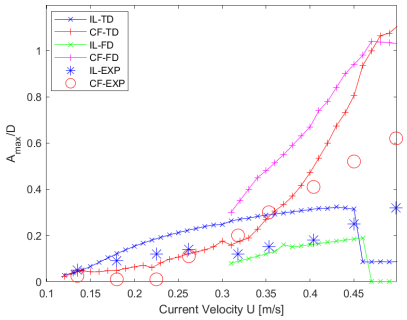

(d) Maximum response amplitude normalized by the pipe's diameter vs Current Velocity

Figure A.25: Comparative plots of the fundamental results for Parameter Set No. 4.

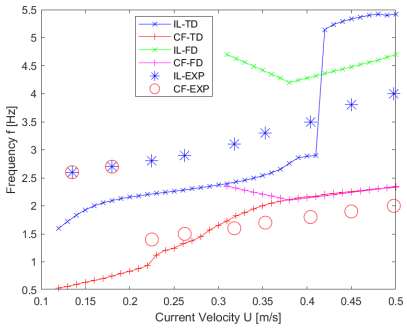

(a) Response Frequency vs Current Velocity

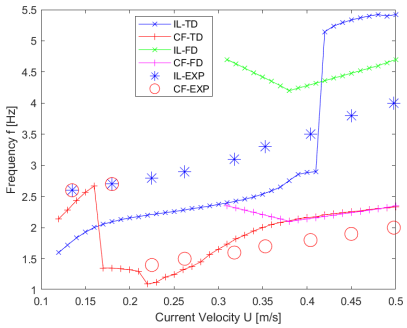

(b) Response Frequency vs Current Velocity (modified)

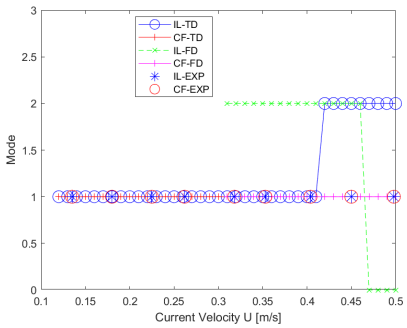

(c) Response Mode vs Current Velocity

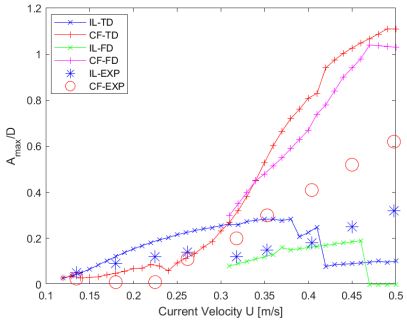

(d) Maximum response amplitude normalized by the pipe's diameter vs Current Velocity

Figure A.26: Comparative plots of the fundamental results for Parameter Set No. 5.

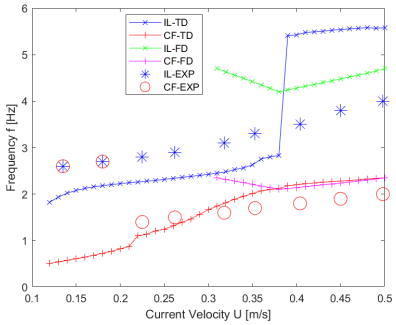

(a) Response Frequency vs Current Velocity

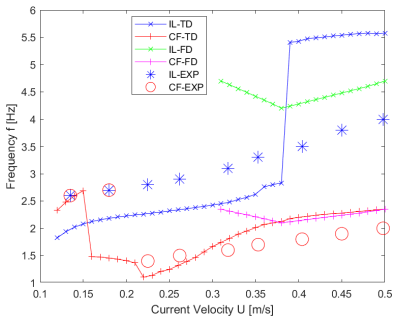

(b) Response Frequency vs Current Velocity (modified)

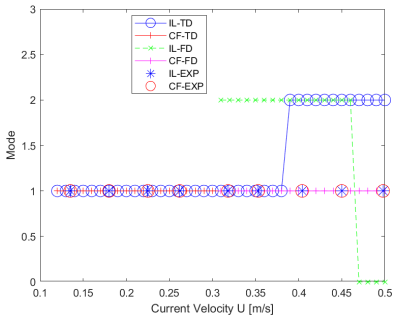

(c) Response Mode vs Current Velocity

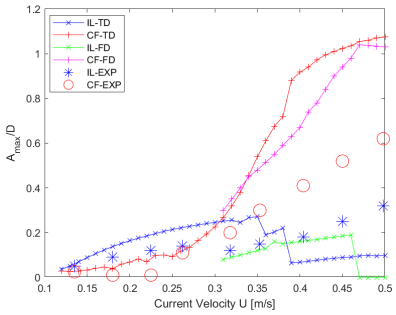

(d) Maximum response amplitude normalized by the pipe's diameter vs Current Velocity

Figure A.27: Comparative plots of the fundamental results for Parameter Set No. 6.

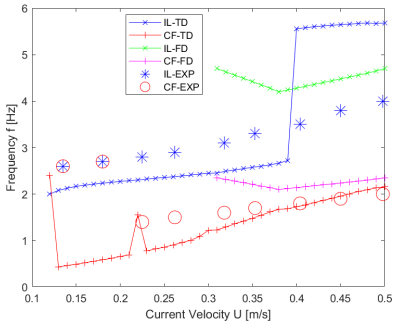

(a) Response Frequency vs Current Velocity

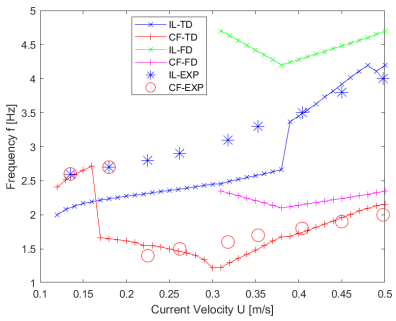

(b) Response Frequency vs Current Velocity (modified)

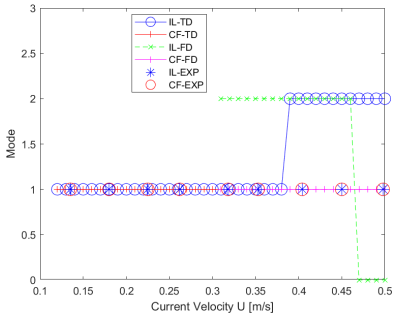

(c) Response Mode vs Current Velocity

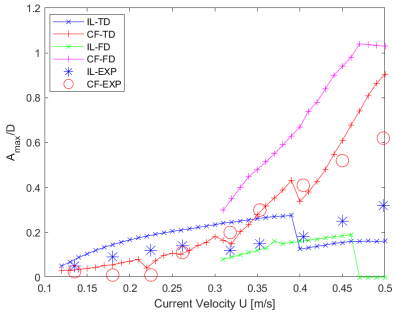

(d) Maximum response amplitude normalized by the pipe's diameter vs Current Velocity

Figure A.28: Comparative plots of the fundamental results for Parameter Set No. 7.

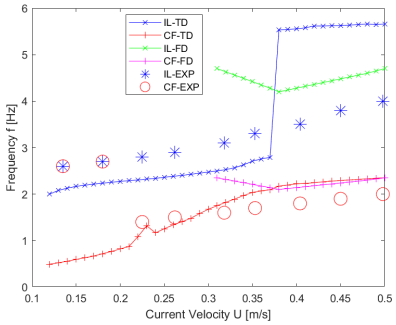

(a) Response Frequency vs Current Velocity

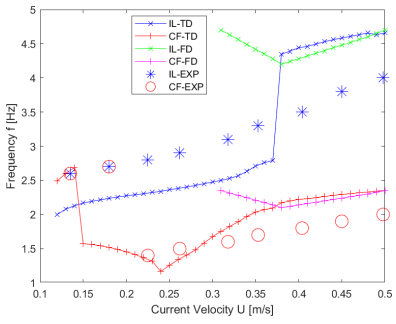

(b) Response Frequency vs Current Velocity (modified)

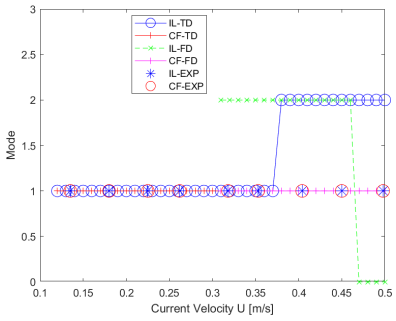

(c) Response Mode vs Current Velocity

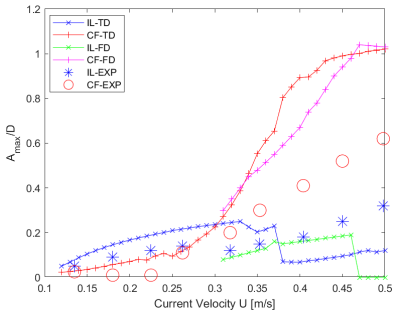

(d) Maximum response amplitude normalized by the pipe's diameter vs Current Velocity

Figure A.29: Comparative plots of the fundamental results for Parameter Set No. 8.

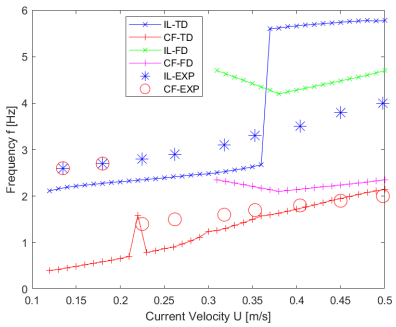

(a) Response Frequency vs Current Velocity

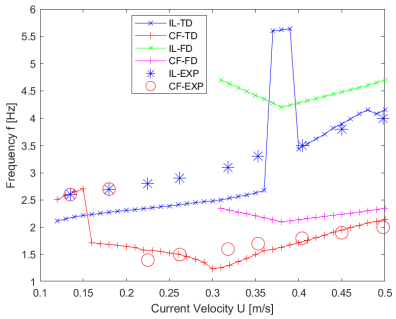

(b) Response Frequency vs Current Velocity (modified)

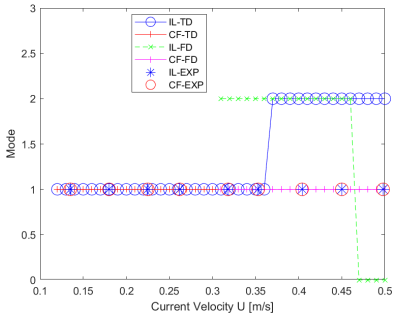

(c) Response Mode vs Current Velocity

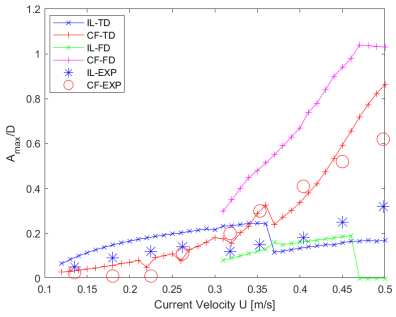

(d) Maximum response amplitude normalized by the pipe's diameter vs Current Velocity

Figure A.30: Comparative plots of the fundamental results for Parameter Set No. 9.

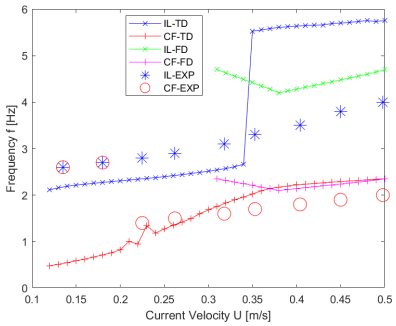

(a) Response Frequency vs Current Velocity

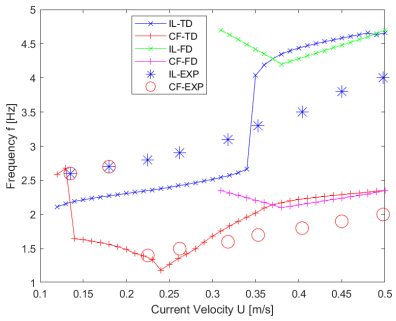

(b) Response Frequency vs Current Velocity (modified)

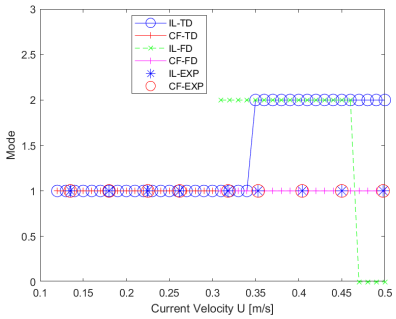

(c) Response Mode vs Current Velocity

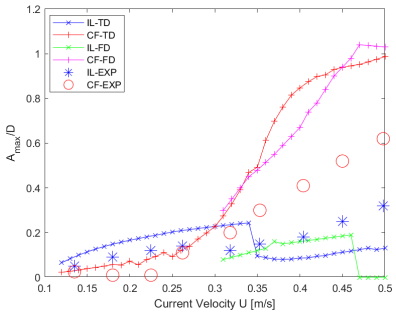

(d) Maximum response amplitude normalized by the pipe's diameter vs Current Velocity

Figure A.31: Comparative plots of the fundamental results for Parameter Set No. 10.

A.4 In depth comparison between the overall optimum parameter set and the experimental data - Additional Results

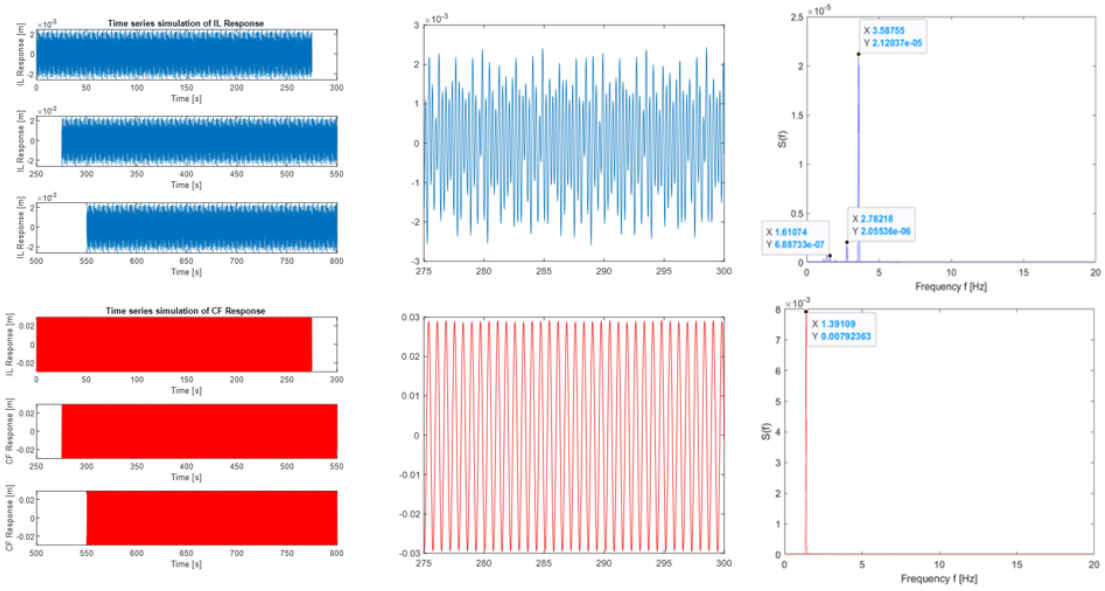

(a) Response Time Series and Spectra

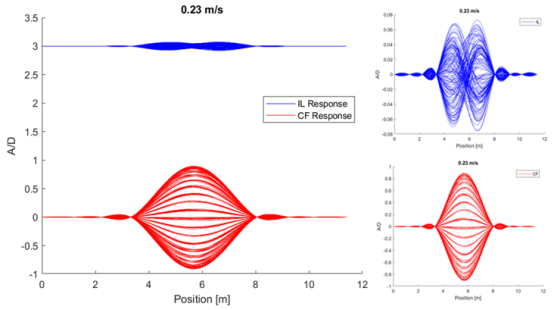

(b) Response Snapshots

Figure A.32: Summary of the time domain analysis results for Test Series 42 at 0.23 m/s

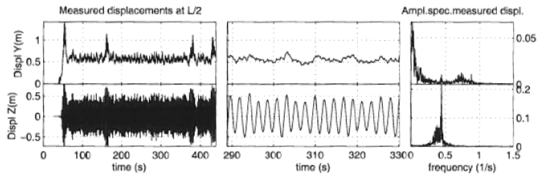

(a) Response Time Series and Spectra

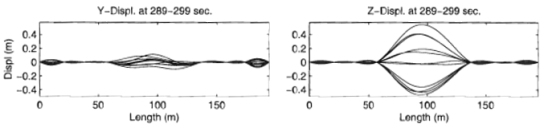

(b) Response Snapshots

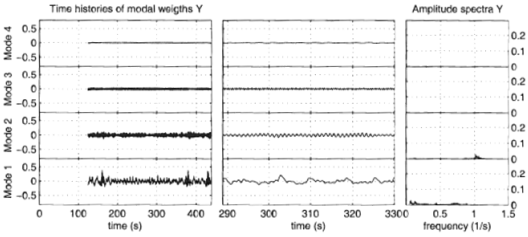

(c) IL - Modal Weights Time Series and Spectra

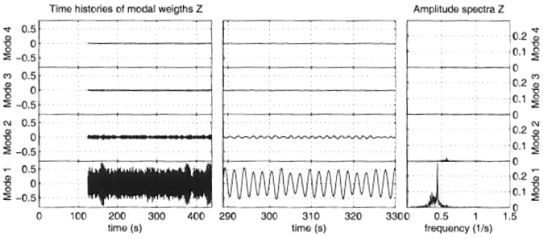

(d) CF - Modal Weights Time Series and Spectra

Figure A.33: Summary of the experimental results for Test Series 42 at 0.4 m/s (second trial)

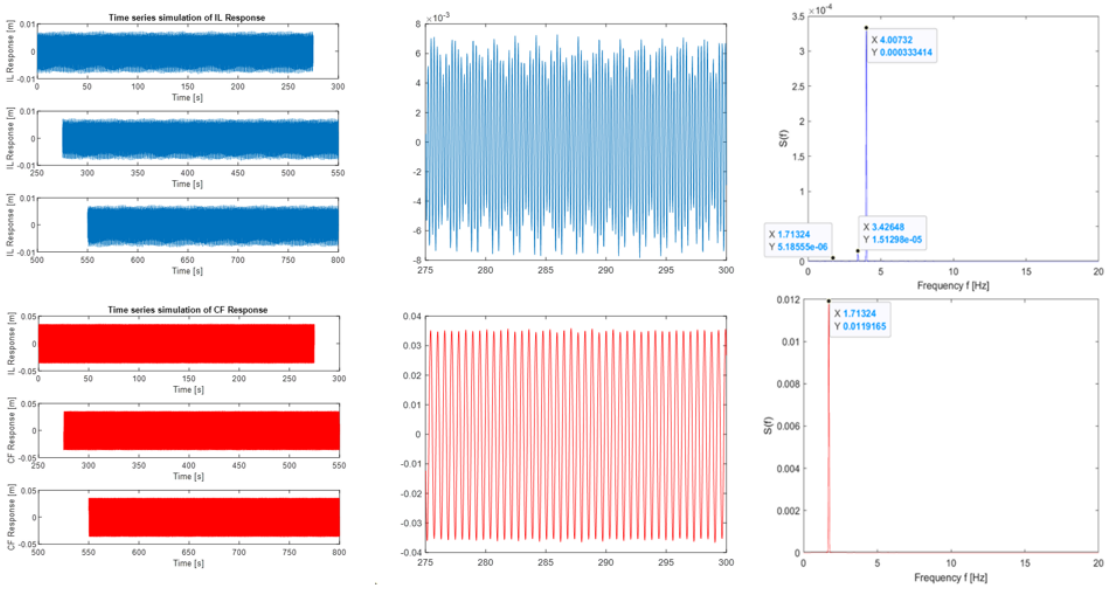

(a) Response Time Series and Spectra

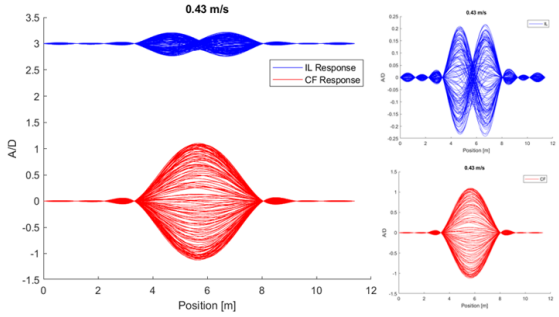

(b) Response Snapshots

Figure A.34: Summary of the time domain analysis results for Test Series 42 at 0.43 m/s

B Total sets of results for the Realistic Free Span Scenario

B.1 Non-Linear Soil Model - Soil Damping Ratio 0.22 - Total set of results

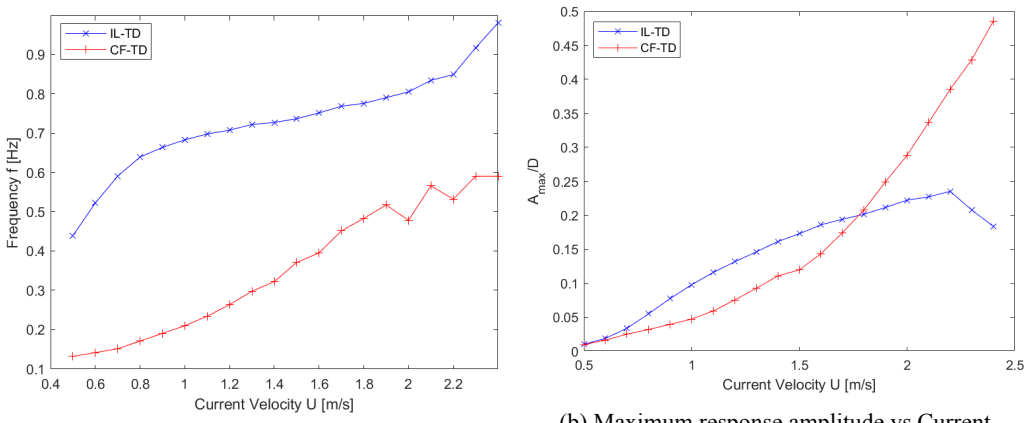

(a) Response Frequency vs Current Velocity

(b) Maximum response amplitude vs Current Velocity

Figure B.1: Plots of the dominant response frequencies and the maximum response amplitudes for the Non-linear soil model and $\zeta_{soil} = 22\%$.

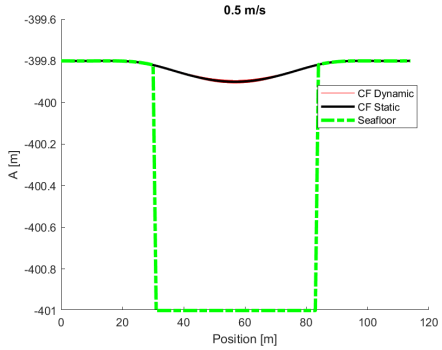

(a) CF - 0.5 m/s

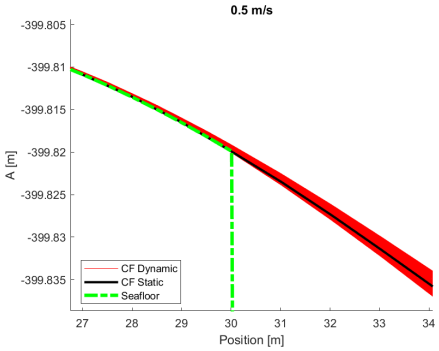

(b) CF - 0.5 m/s (zoom at the left shoulder)

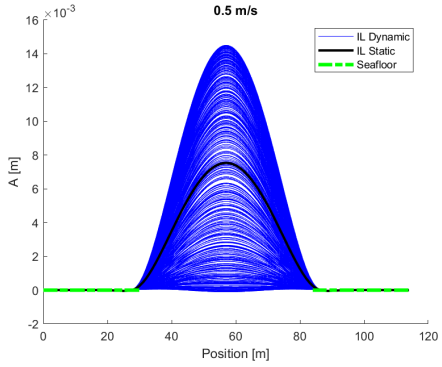

(c) IL - 0.5 m/s

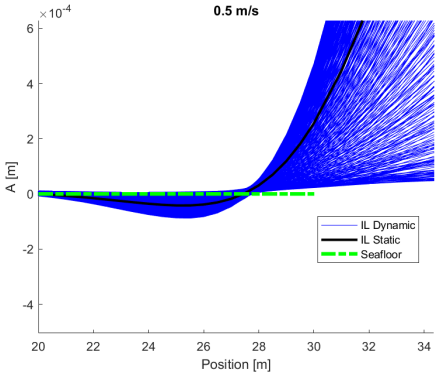

(d) IL - 0.5 m/s (zoom at the left shoulder)

Figure B.2: Snapshots of the calculated response at 0.5 m/s.

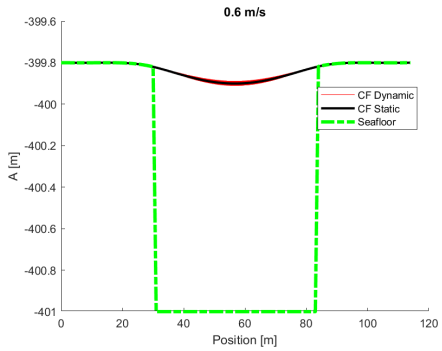

(a) CF - 0.6 m/s

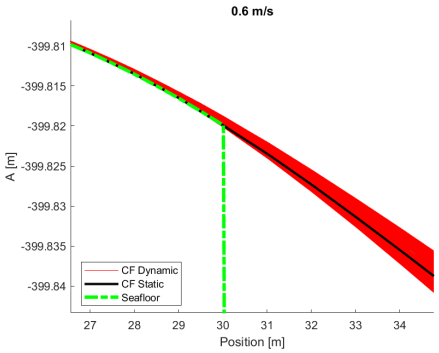

(b) CF - 0.6 m/s (zoom at the left shoulder)

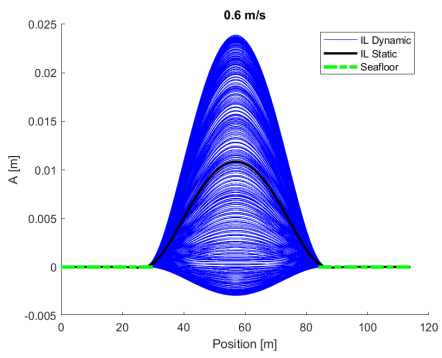

(c) IL - 0.6 m/s

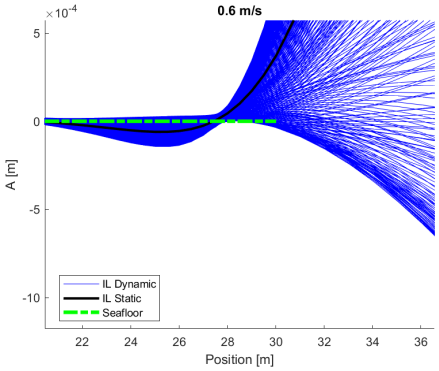

(d) IL - 0.6 m/s (zoom at the left shoulder)

Figure B.3: Snapshots of the calculated response at 0.6 m/s.

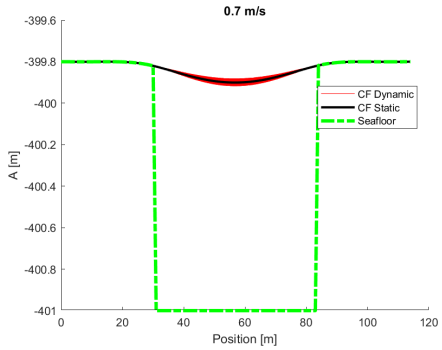

(a) CF - 0.7 m/s

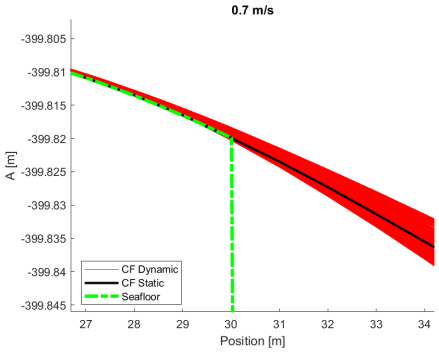

(b) CF - 0.7 m/s (zoom at the left shoulder)

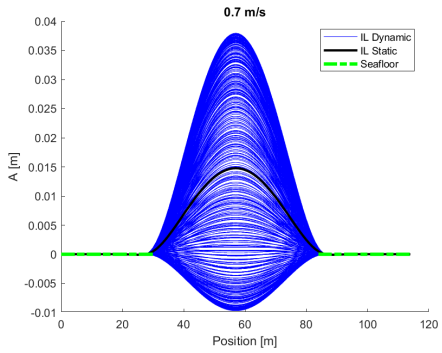

(c) IL - 0.7 m/s

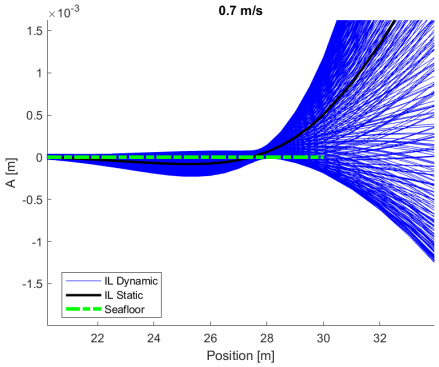

(d) IL - 0.7 m/s (zoom at the left shoulder)

Figure B.4: Snapshots of the calculated response at 0.7 m/s.

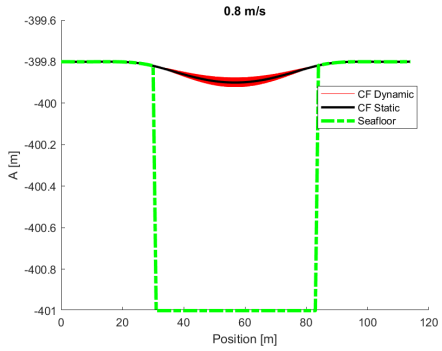

(a) CF - 0.8 m/s

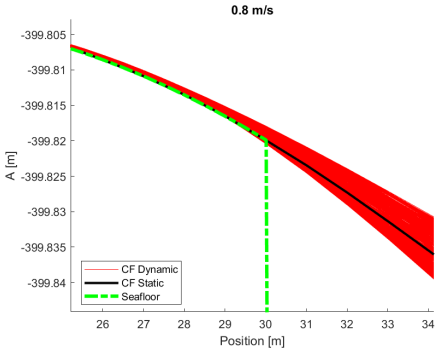

(b) CF - 0.8 m/s (zoom at the left shoulder)

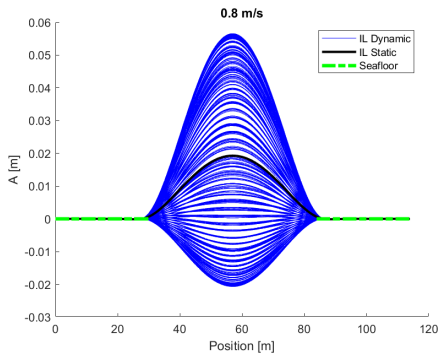

(c) IL - 0.8 m/s

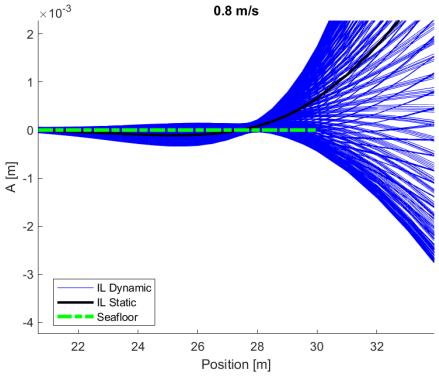

(d) IL - 0.8 m/s (zoom at the left shoulder)

Figure B.5: Snapshots of the calculated response at 0.8 m/s.

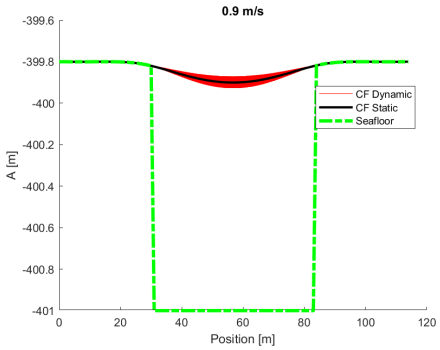

(a) CF - 0.9 m/s

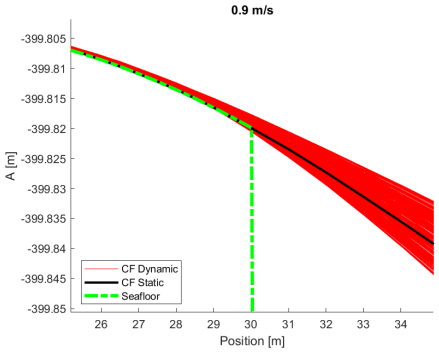

(b) CF - 0.9 m/s (zoom at the left shoulder)

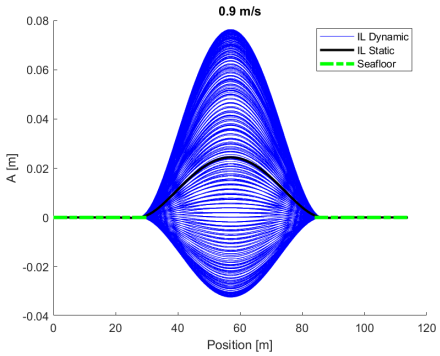

(c) IL - 0.9 m/s

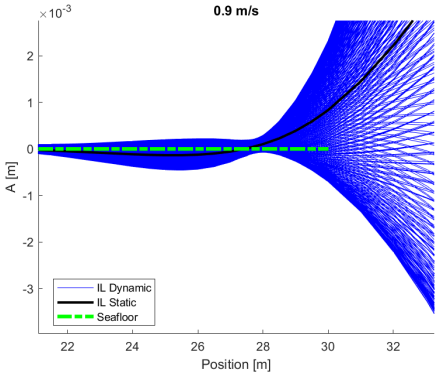

(d) IL - 0.9 m/s (zoom at the left shoulder)

Figure B.6: Snapshots of the calculated response at 0.9 m/s.

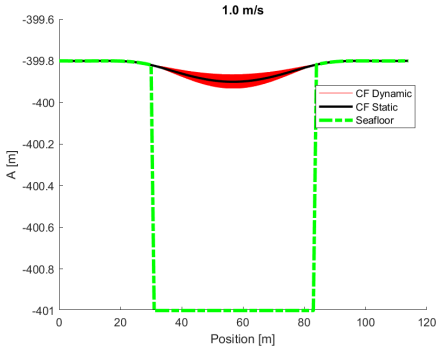

(a) CF - 1.0 m/s

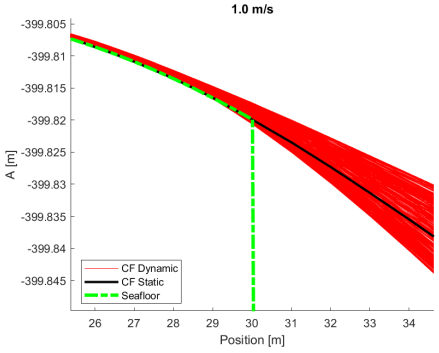

(b) CF - 1.0 m/s (zoom at the left shoulder)

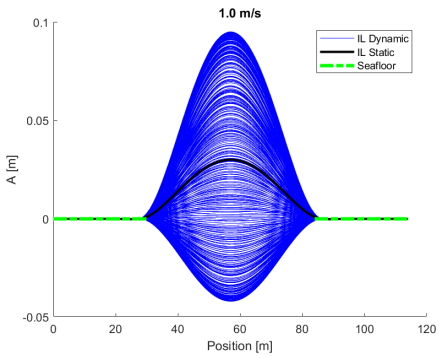

(c) IL - 1.0 m/s

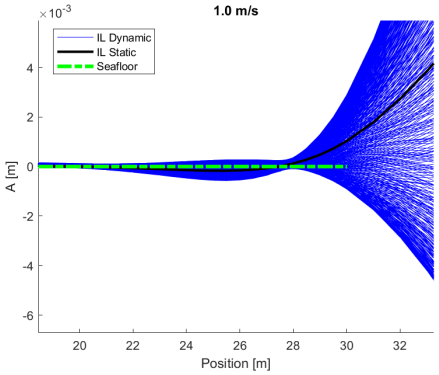

(d) IL - 1.0 m/s (zoom at the left shoulder)

Figure B.7: Snapshots of the calculated response at 1.0 m/s.

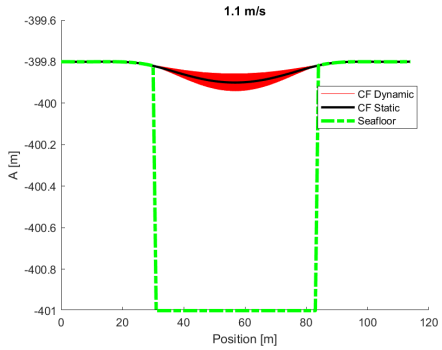

(a) CF - 1.1 m/s

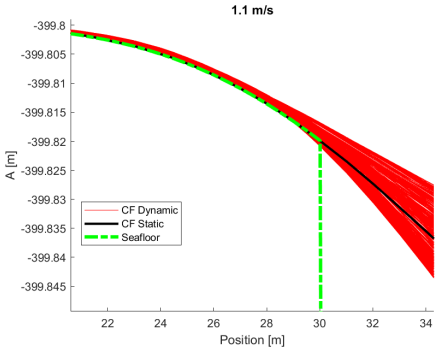

(b) CF - 1.1 m/s (zoom at the left shoulder)

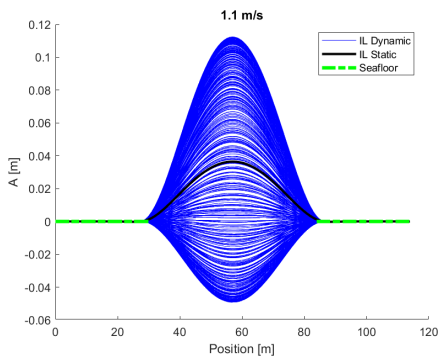

(c) IL - 1.1 m/s

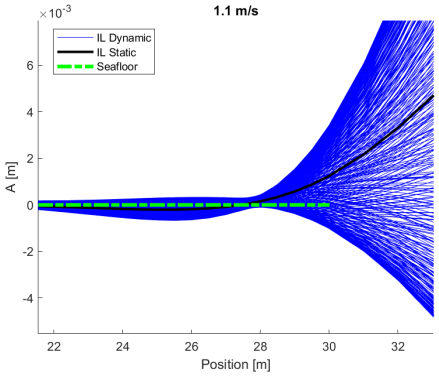

(d) IL - 1.1 m/s (zoom at the left shoulder)

Figure B.8: Snapshots of the calculated response at 1.1 m/s.

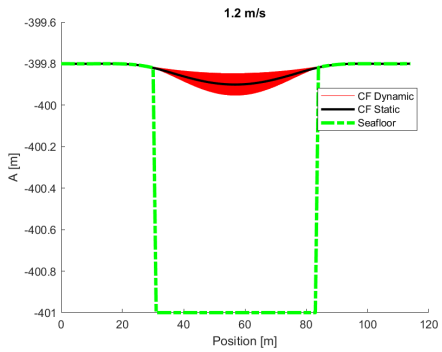

(a) CF - 1.2 m/s

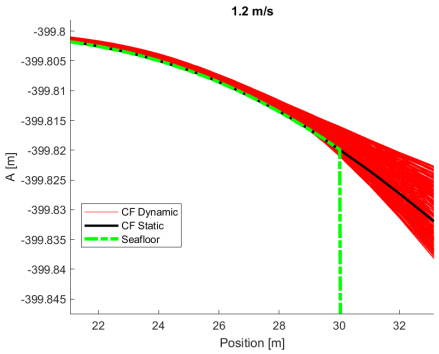

(b) CF - 1.2 m/s (zoom at the left shoulder)

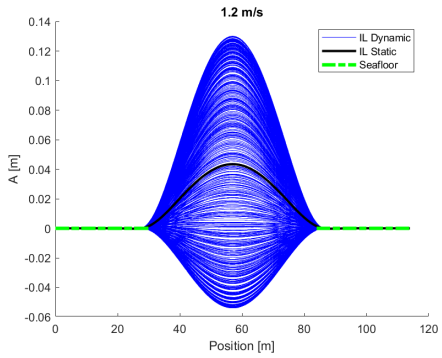

(c) IL - 1.2 m/s

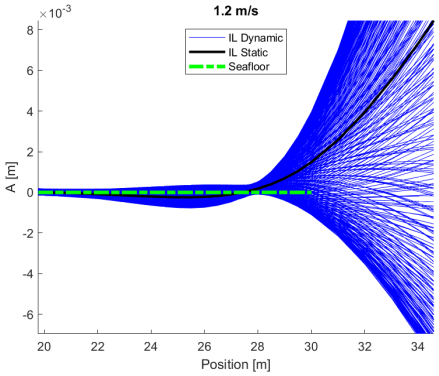

(d) IL - 1.2 m/s (zoom at the left shoulder)

Figure B.9: Snapshots of the calculated response at 1.2 m/s.

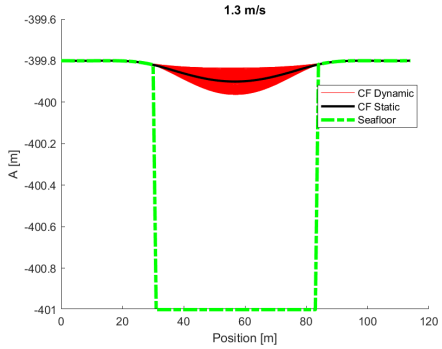

(a) CF - 1.3 m/s

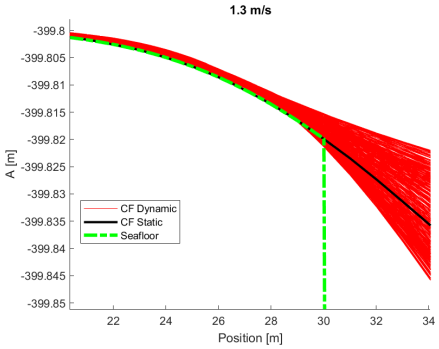

(b) CF - 1.3 m/s (zoom at the left shoulder)

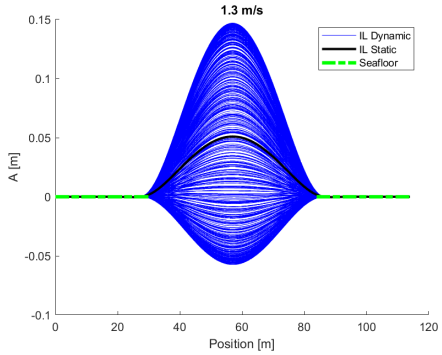

(c) IL - 1.3 m/s

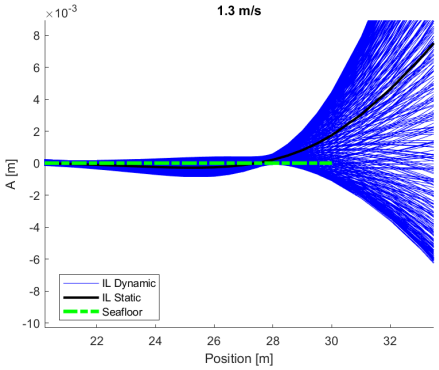

(d) IL - 1.3 m/s (zoom at the left shoulder)

Figure B.10: Snapshots of the calculated response at 1.3 m/s.

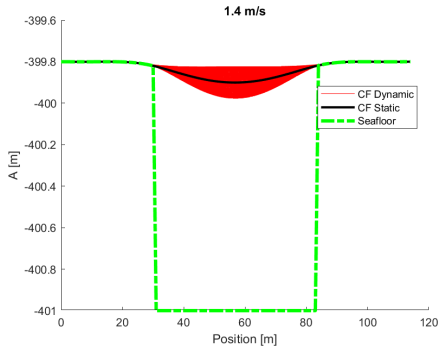

(a) CF - 1.4 m/s

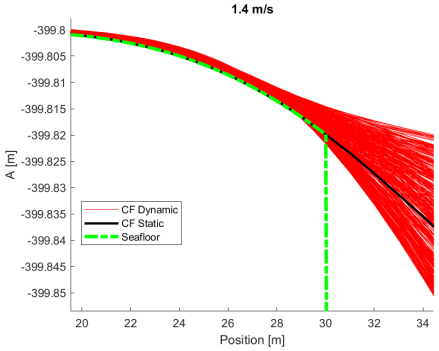

(b) CF - 1.4 m/s (zoom at the left shoulder)

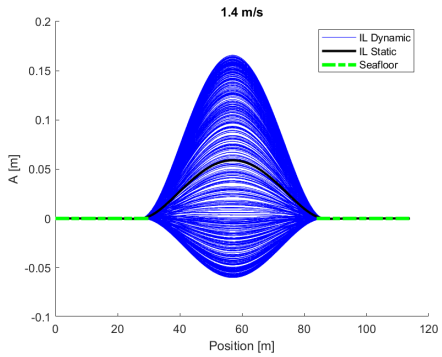

(c) IL - 1.4 m/s

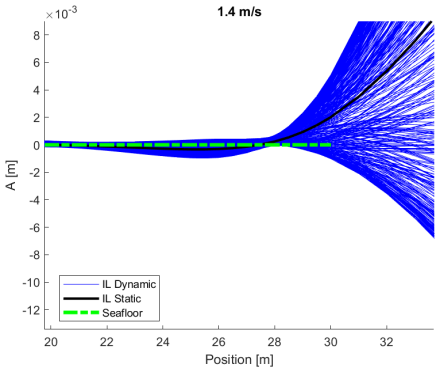

(d) IL - 1.4 m/s (zoom at the left shoulder)

Figure B.11: Snapshots of the calculated response at 1.4 m/s.

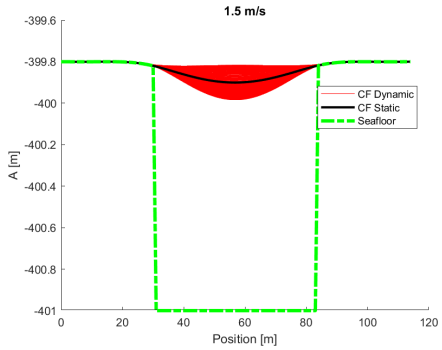

(a) CF - 1.5 m/s

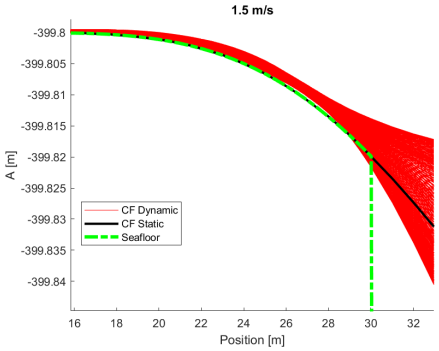

(b) CF - 1.5 m/s (zoom at the left shoulder)

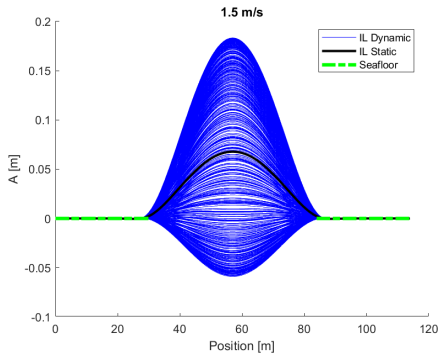

(c) IL - 1.5 m/s

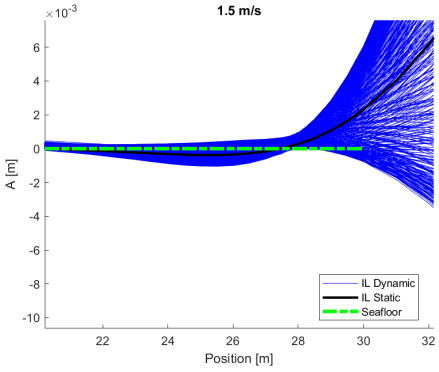

(d) IL - 1.5 m/s (zoom at the left shoulder)

Figure B.12: Snapshots of the calculated response at 1.5 m/s.

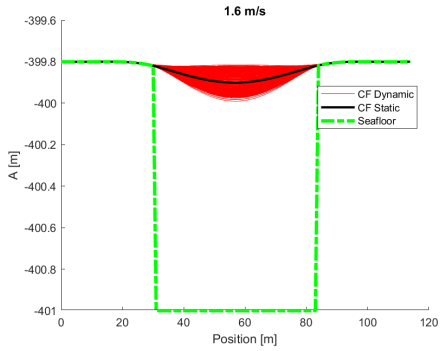

(a) CF - 1.6 m/s

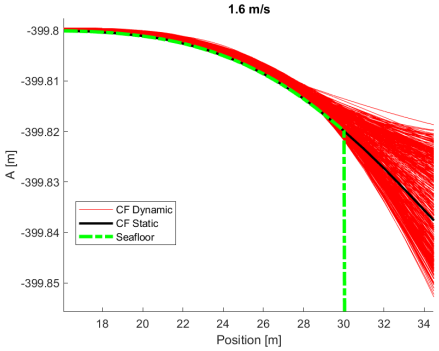

(b) CF - 1.6 m/s (zoom at the left shoulder)

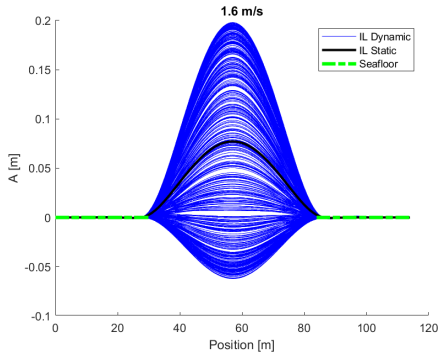

(c) IL - 1.6 m/s

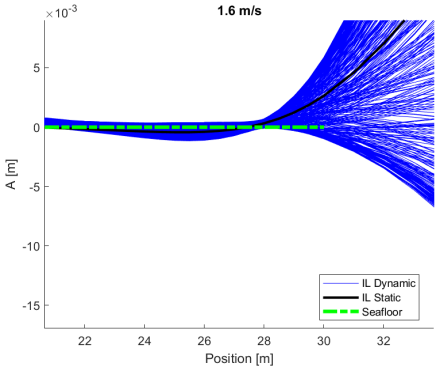

(d) IL - 1.6 m/s (zoom at the left shoulder)

Figure B.13: Snapshots of the calculated response at 1.6 m/s.

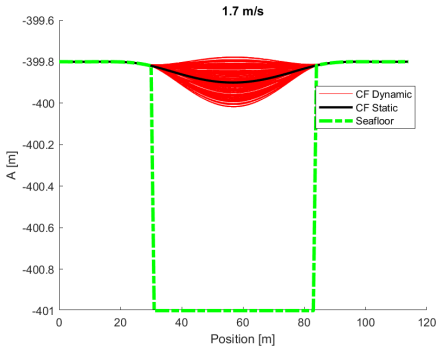

(a) CF - 1.7 m/s

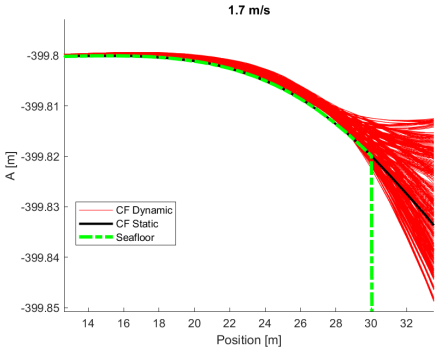

(b) CF - 1.7 m/s (zoom at the left shoulder)

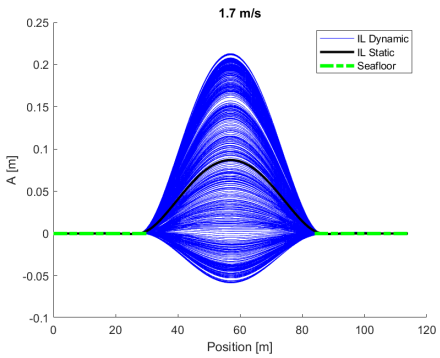

(c) IL - 1.7 m/s

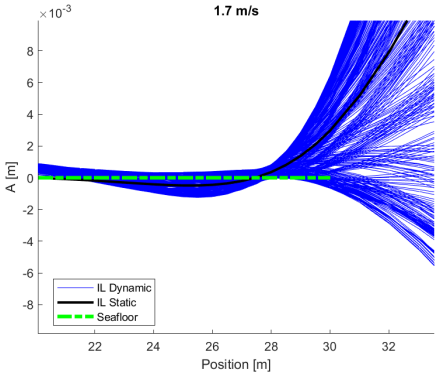

(d) IL - 1.7 m/s (zoom at the left shoulder)

Figure B.14: Snapshots of the calculated response at 1.7 m/s.

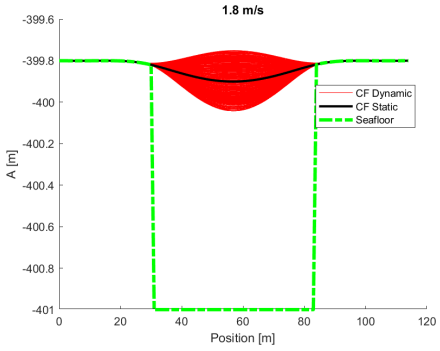

(a) CF - 1.8 m/s

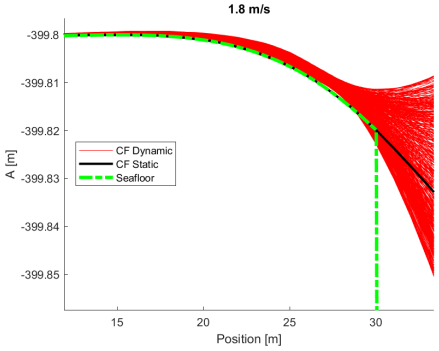

(b) CF - 1.8 m/s (zoom at the left shoulder)

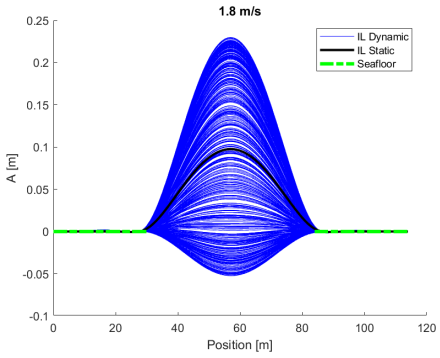

(c) IL - 1.8 m/s

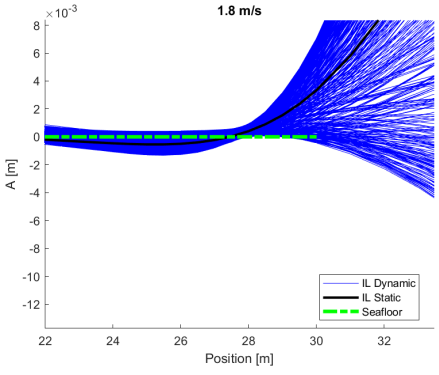

(d) IL - 1.8 m/s (zoom at the left shoulder)

Figure B.15: Snapshots of the calculated response at 1.8 m/s.

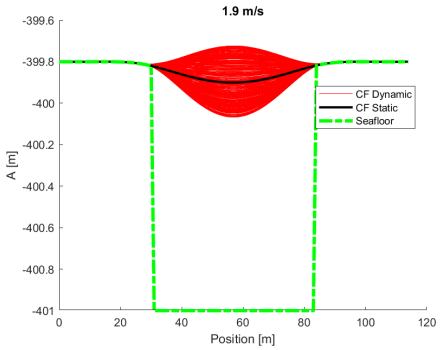

(a) CF - 1.9 m/s

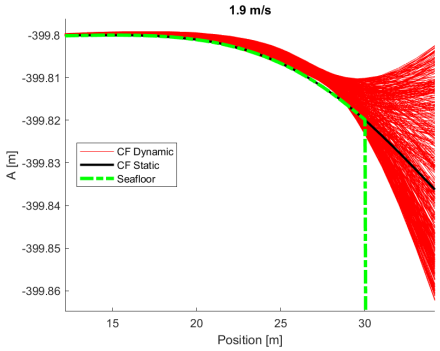

(b) CF - 1.9 m/s (zoom at the left shoulder)

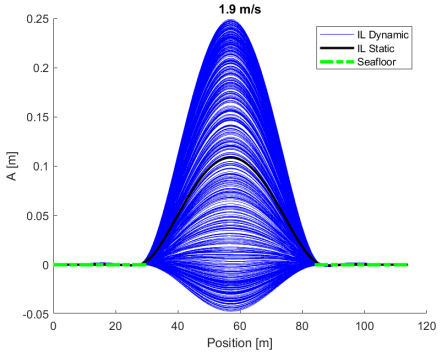

(c) IL - 1.9 m/s

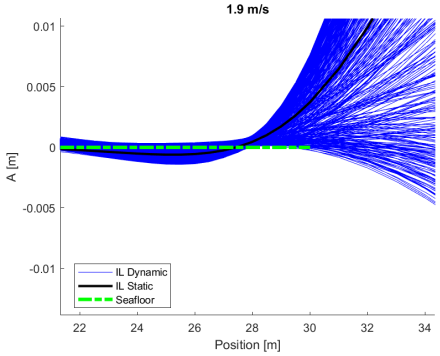

(d) IL - 1.9 m/s (zoom at the left shoulder)

Figure B.16: Snapshots of the calculated response at 1.9 m/s.

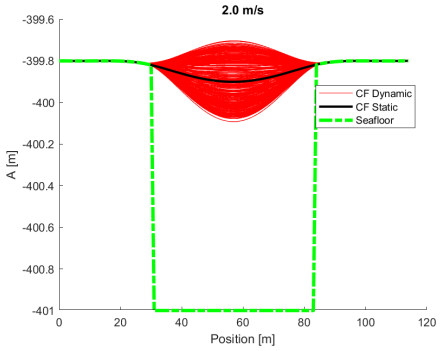

(a) CF - 2.0 m/s

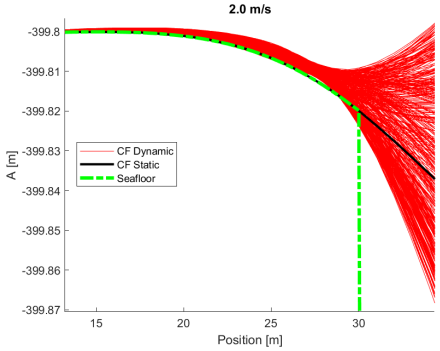

(b) CF - 2.0 m/s (zoom at the left shoulder)

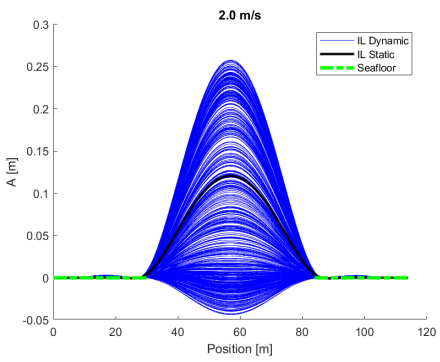

(c) IL - 2.0 m/s

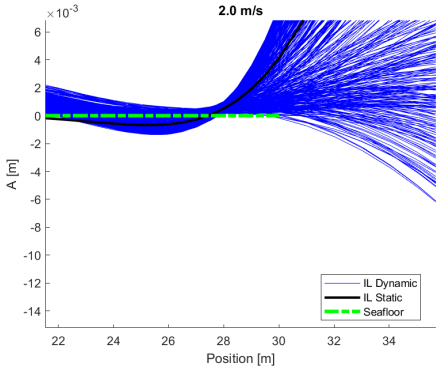

(d) IL - 2.0 m/s (zoom at the left shoulder)

Figure B.17: Snapshots of the calculated response at 2.0 m/s.

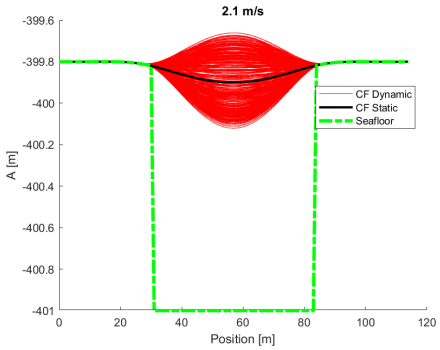

(a) CF - 2.1 m/s

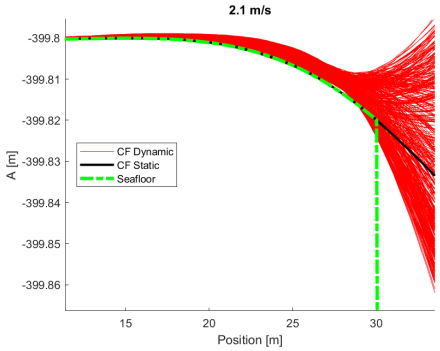

(b) CF - 2.1 m/s (zoom at the left shoulder)

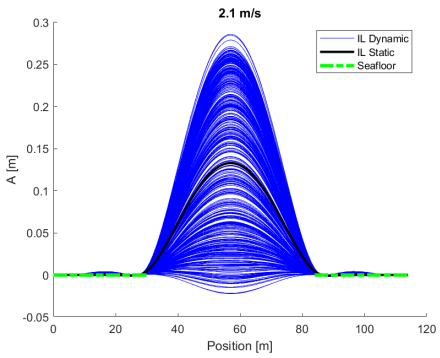

(c) IL - 2.1 m/s

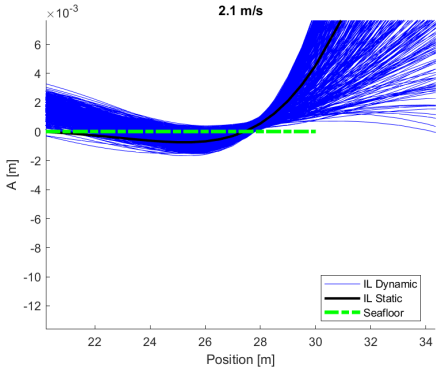

(d) IL - 2.1 m/s (zoom at the left shoulder)

Figure B.18: Snapshots of the calculated response at 2.1 m/s.

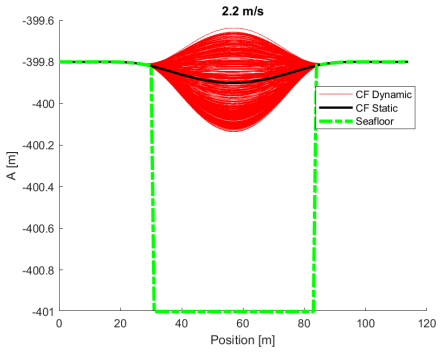

(a) CF - 2.2 m/s

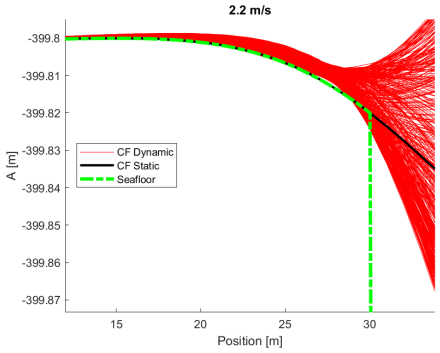

(b) CF - 2.2 m/s (zoom at the left shoulder)

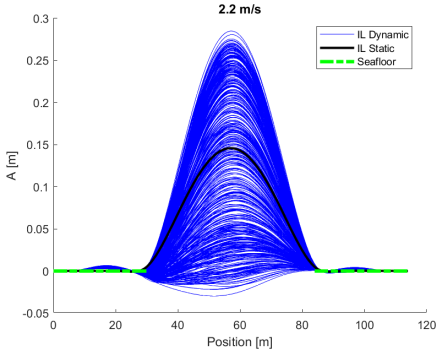

(c) IL - 2.2 m/s

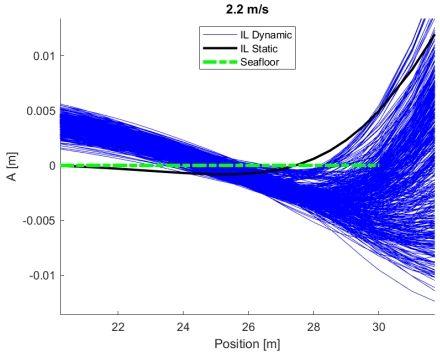

(d) IL - 2.2 m/s (zoom at the left shoulder)

Figure B.19: Snapshots of the calculated response at 2.2 m/s.

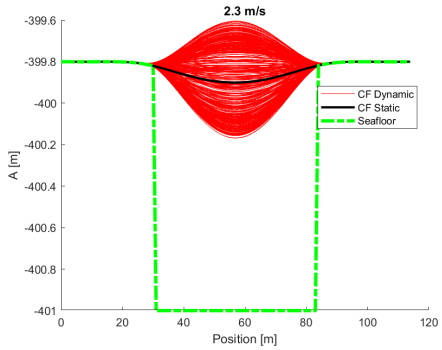

(a) CF - 2.3 m/s

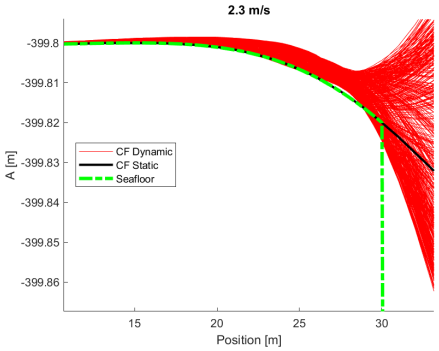

(b) CF - 2.3 m/s (zoom at the left shoulder)

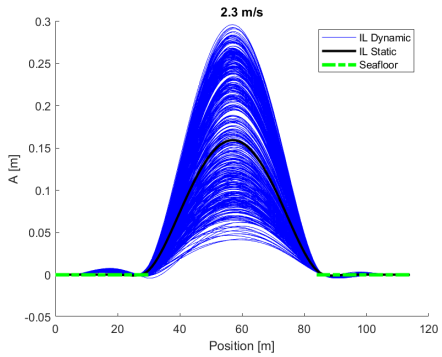

(c) IL - 2.3 m/s

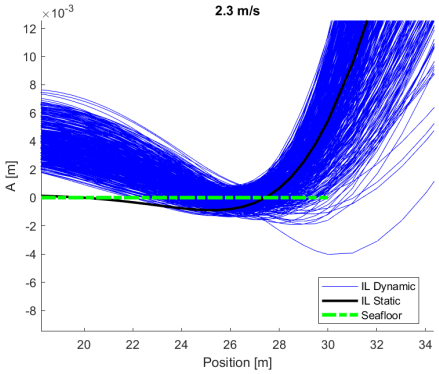

(d) IL - 2.3 m/s (zoom at the left shoulder)

Figure B.20: Snapshots of the calculated response at 2.3 m/s.

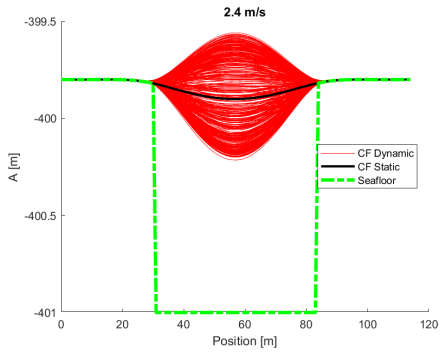

(a) CF - 2.4 m/s

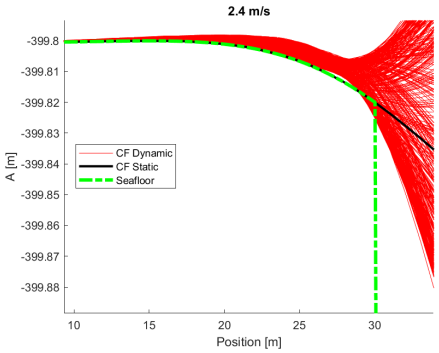

(b) CF - 2.4 m/s (zoom at the left shoulder)

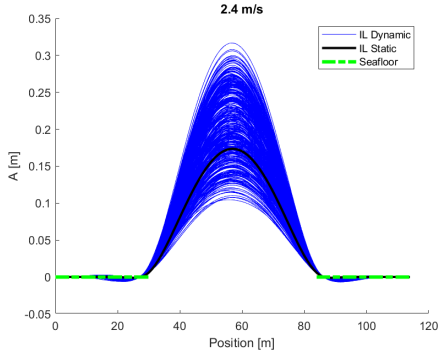

(c) IL - 2.4 m/s

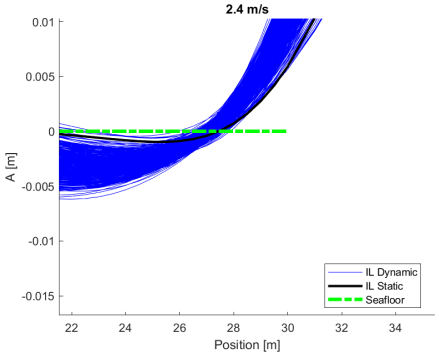

(d) IL - 2.4 m/s (zoom at the left shoulder)

Figure B.21: Snapshots of the calculated response at 2.4 m/s.

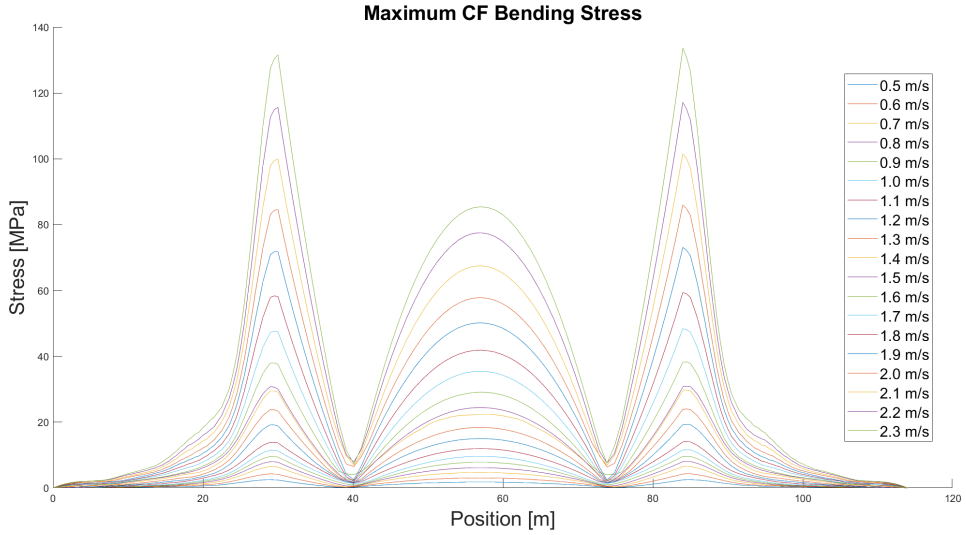

(a) CF - Maximum Bending Stress

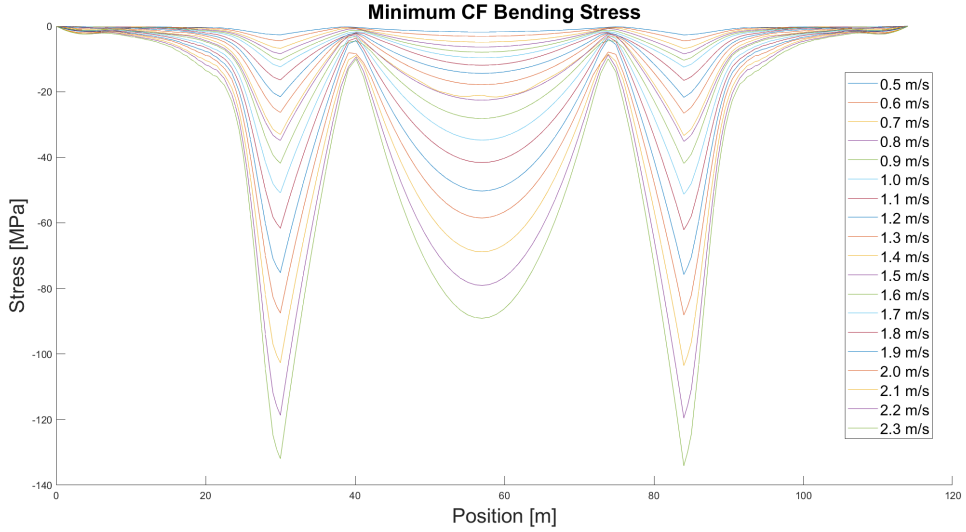

(b) CF - Minimum Bending Stress

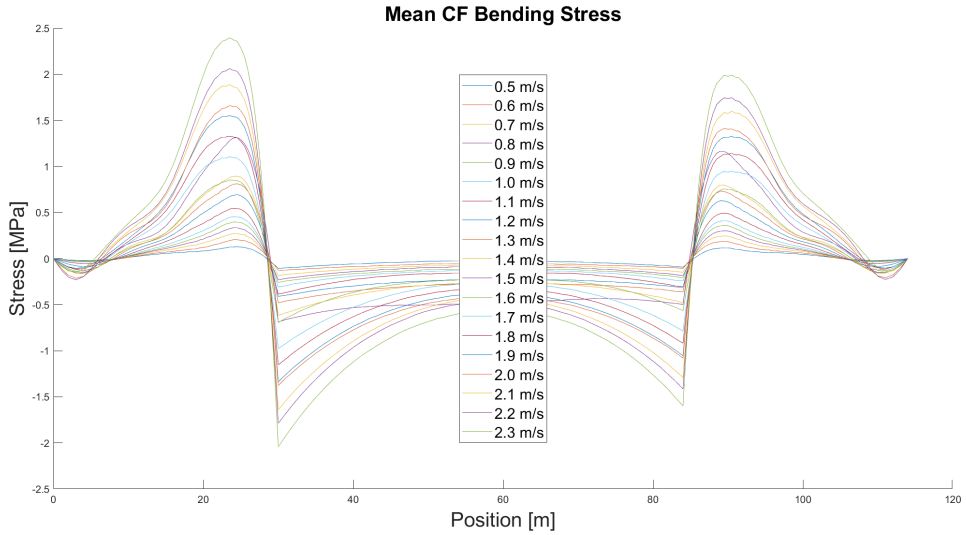

(c) CF - Mean Bending Stress

Figure B.22: Plots of the calculated bending stress distribution in the CF direction for the Non-linear soil model and $\zeta_{soil} = 22\%$.

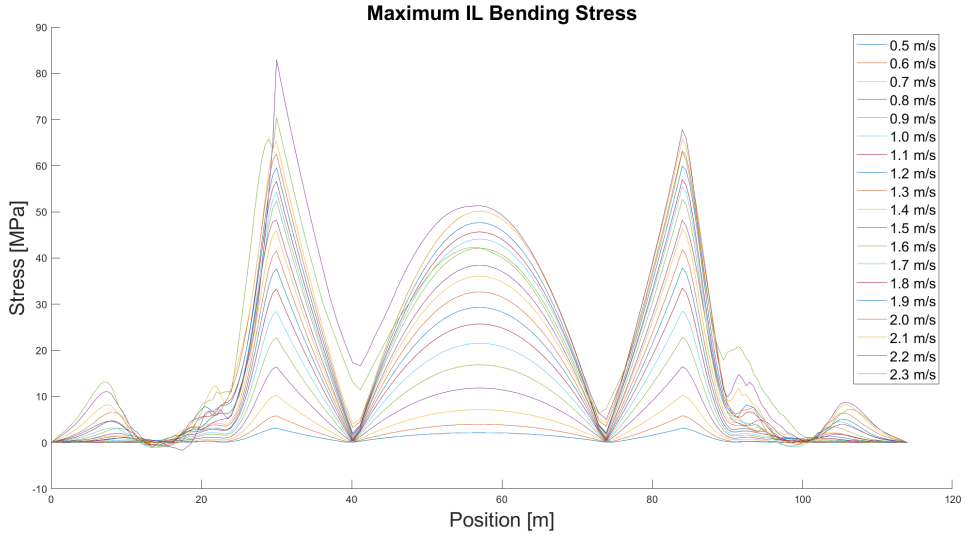

(a) IL - Maximum Bending Stress

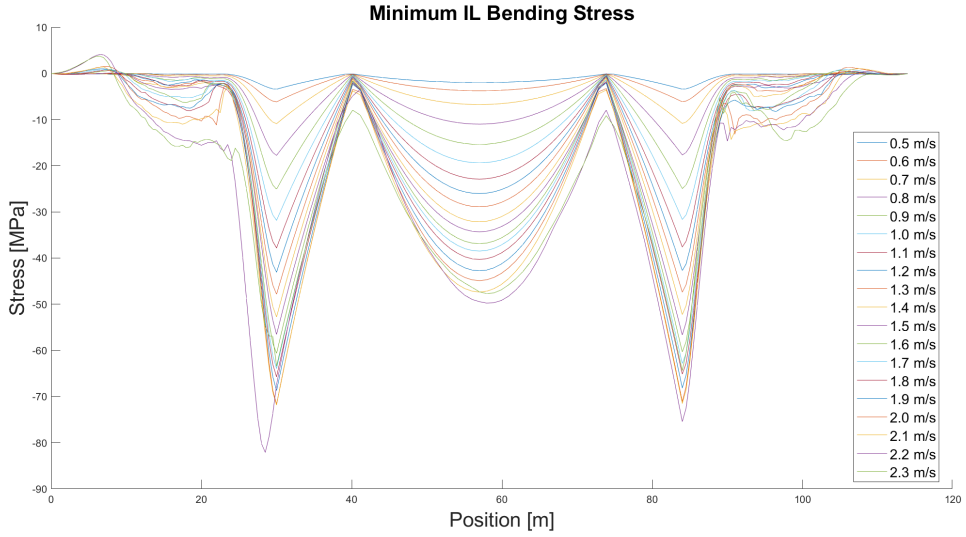

(b) IL - Minimum Bending Stress

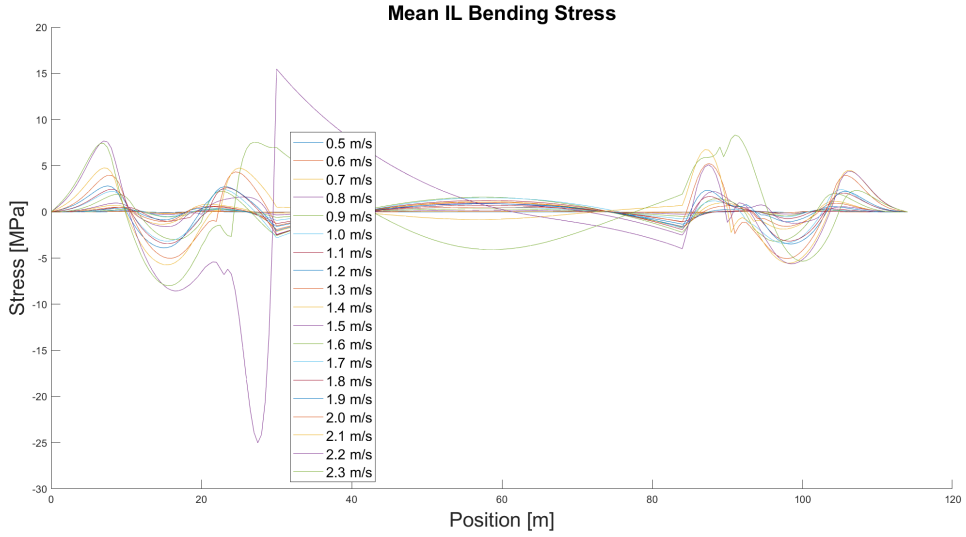

(c) IL - Mean Bending Stress

Figure B.23: Plots of the calculated bending stress distribution in the IL direction for the Non-linear soil model and $\zeta_{soil} = 22\%$.

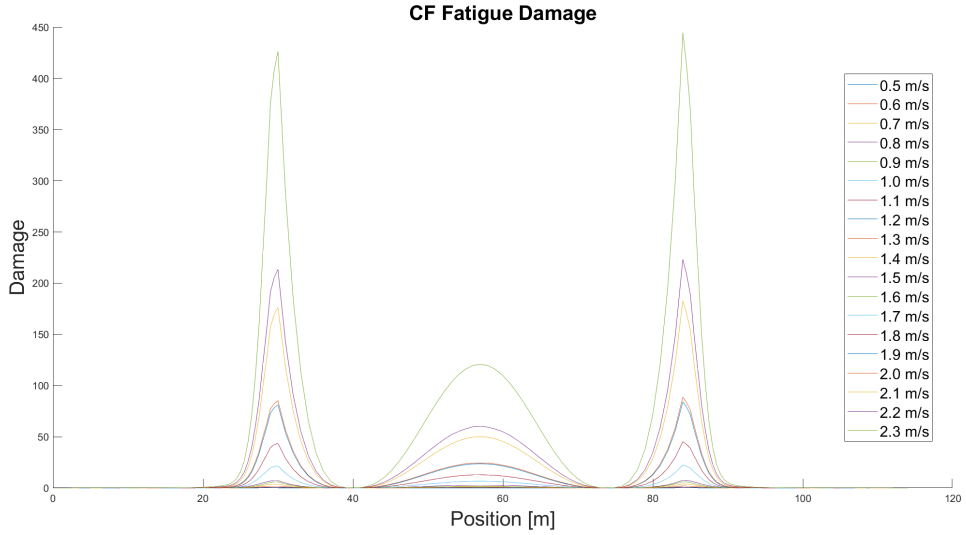

(a) CF - Fatigue Damage Accumulation

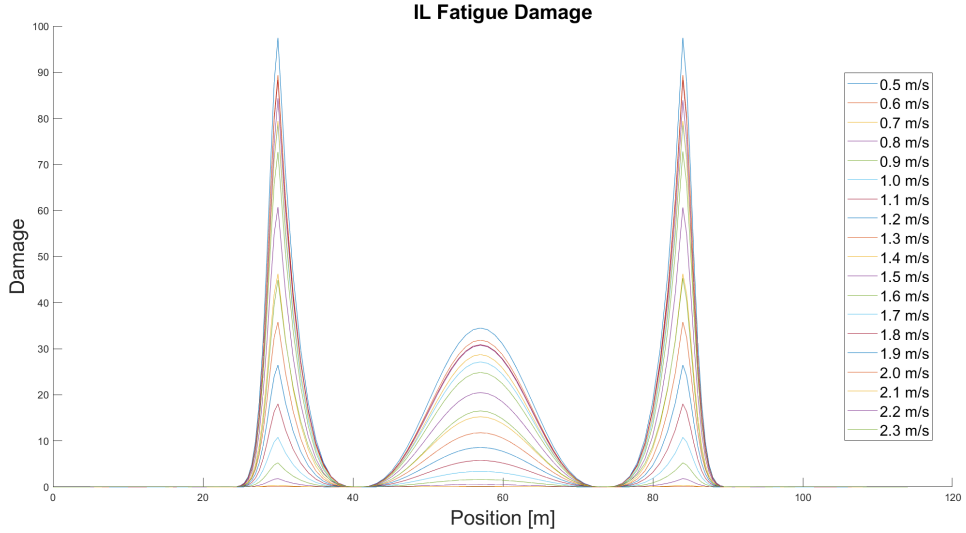

(b) IL - Fatigue Damage Accumulation

Figure B.24: Plots of the calculated fatigue damage distribution in both directions for the Non-linear soil model and $\zeta_{soil} = 22\%$.

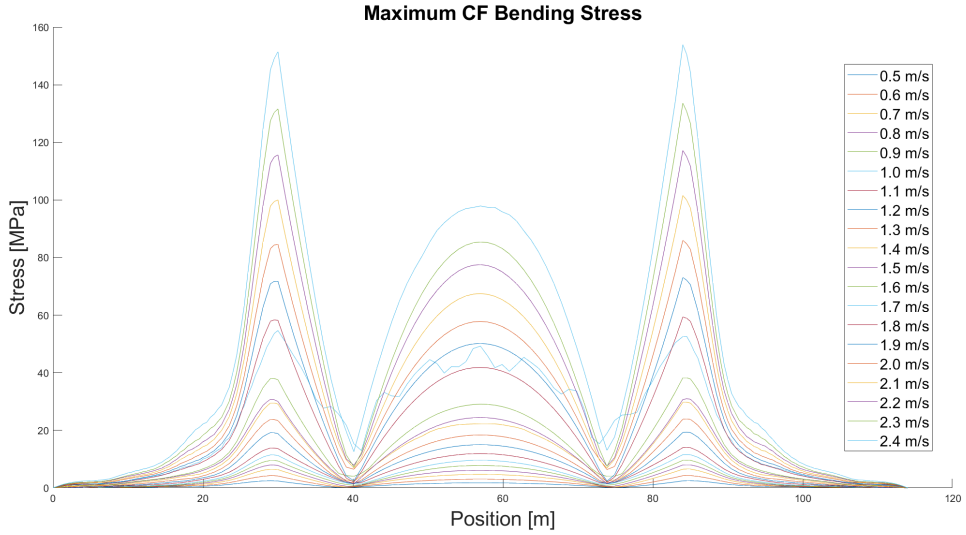

(a) CF - Maximum Bending Stress

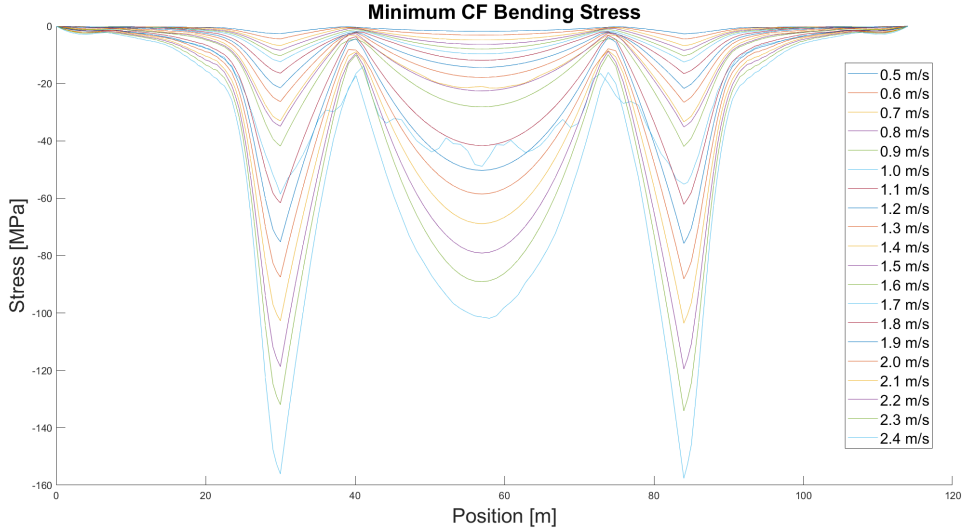

(b) CF - Minimum Bending Stress

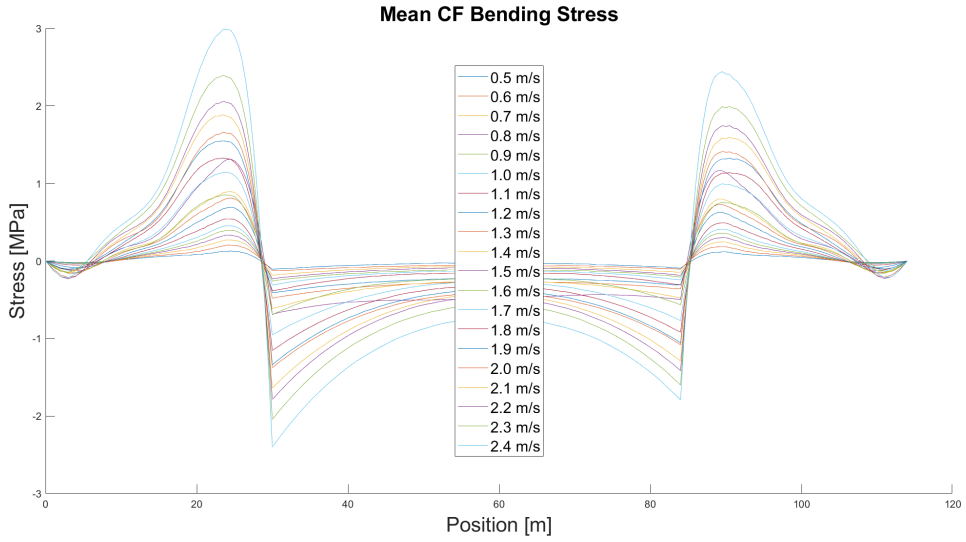

(c) CF - Mean Bending Stress

Figure B.25: Plots of the calculated bending stress distribution in the CF direction for the Non-linear soil model and $\zeta_{soil} = 22\%$ including the velocity of 2.4 m/s and the results obtained for the velocity of 1.7 m/s when the initial timestep was used.

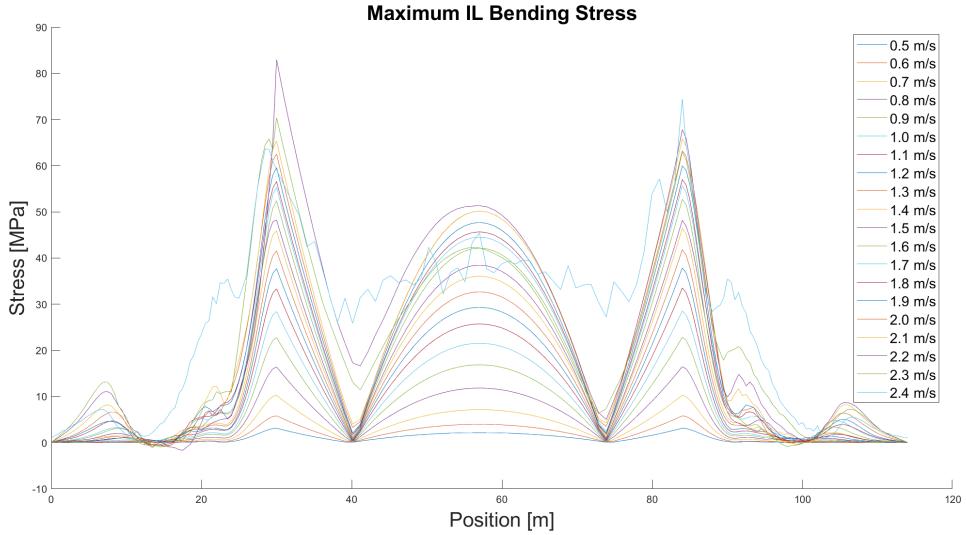

(a) IL - Maximum Bending Stress

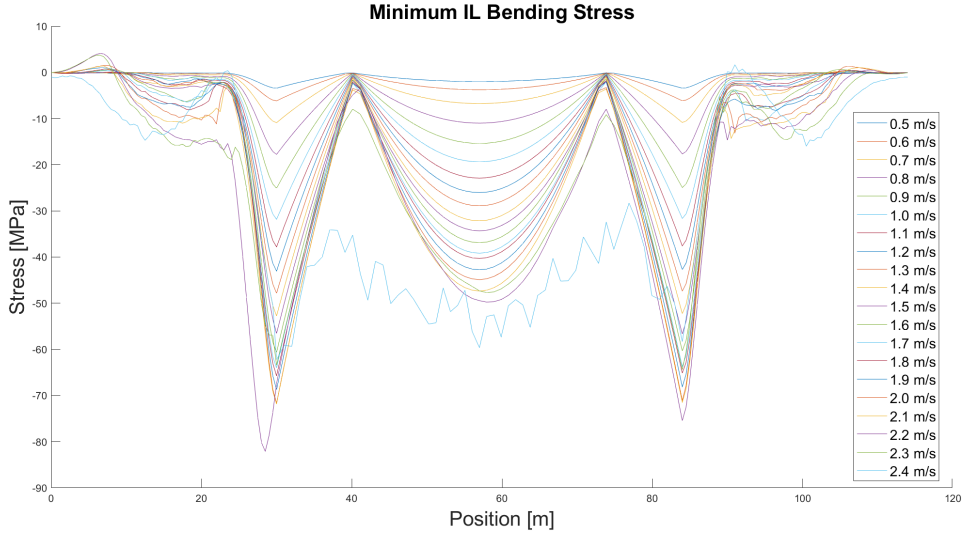

(b) IL - Minimum Bending Stress

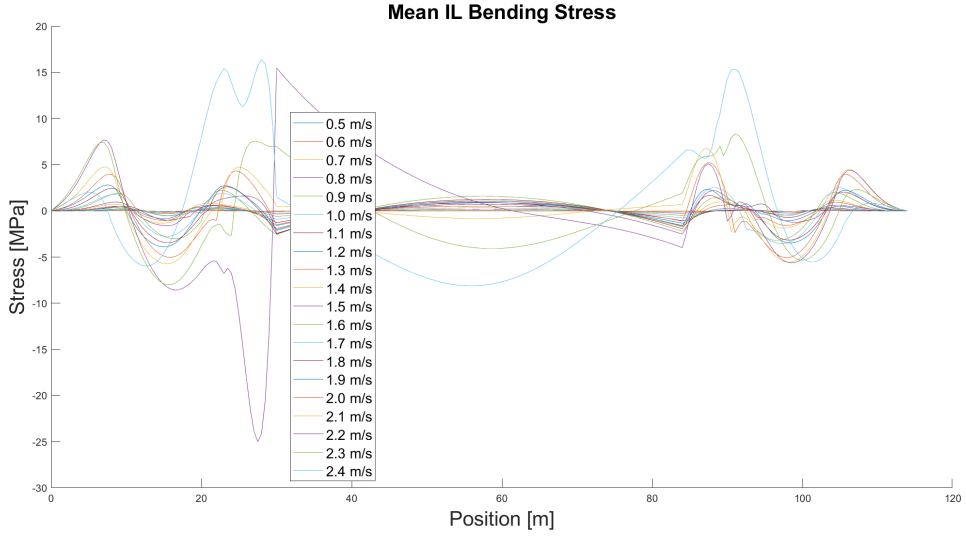

(c) IL - Mean Bending Stress

Figure B.26: Plots of the calculated bending stress distribution in the IL direction for the Non-linear soil model and $\zeta_{soil} = 22\%$ including the velocity of 2.4 m/s and the results obtained for the velocity of 1.7 m/s when the initial timestep was used.

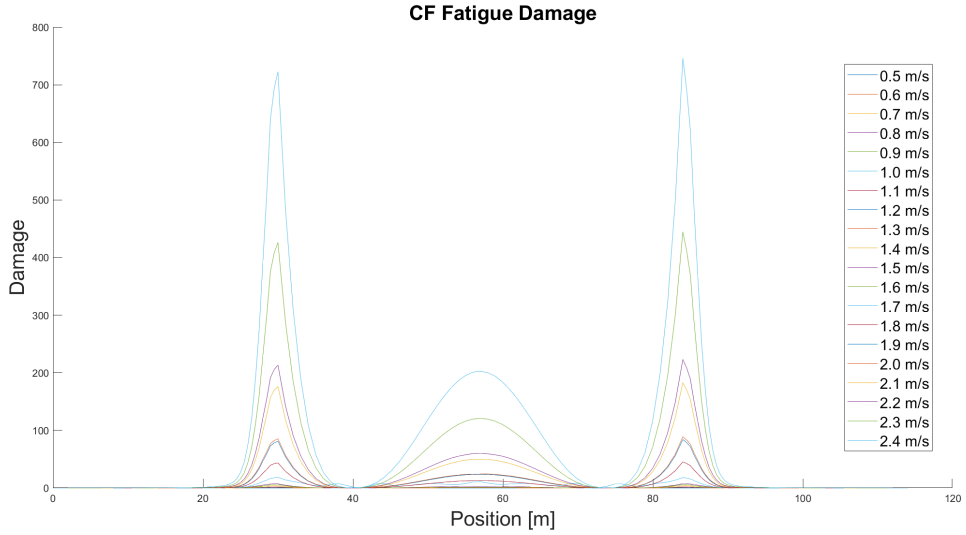

(a) CF - Fatigue Damage Accumulation

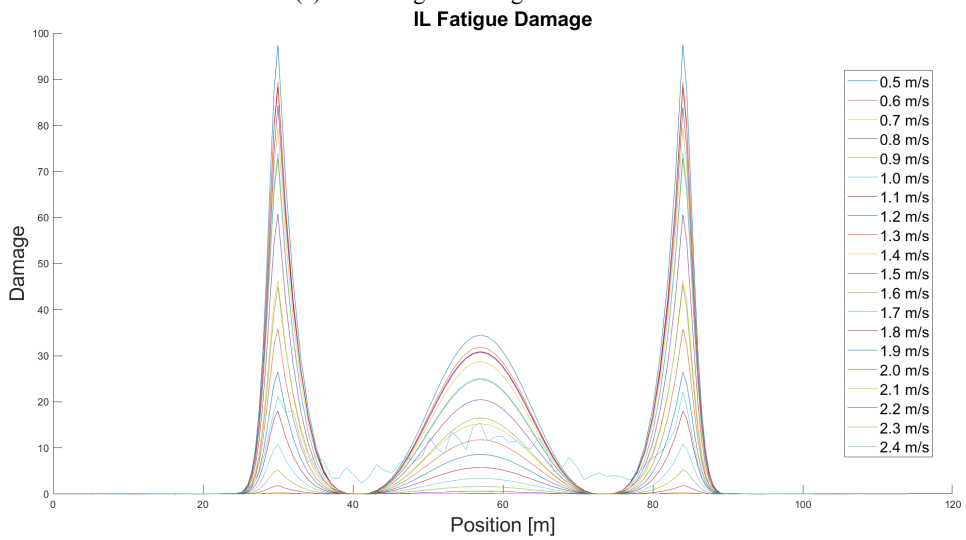

(b) IL - Fatigue Damage Accumulation

Figure B.27: Plots of the calculated fatigue damage distribution in both directions for the Non-linear soil model and $\zeta_{soil} = 22\%$ including the velocity of 2.4 m/s and the results obtained for the velocity of 1.7 m/s when the initial timestep was used.

B.2 Linear Soil Model - Soil Damping Ratio 0.22 - Total set of results

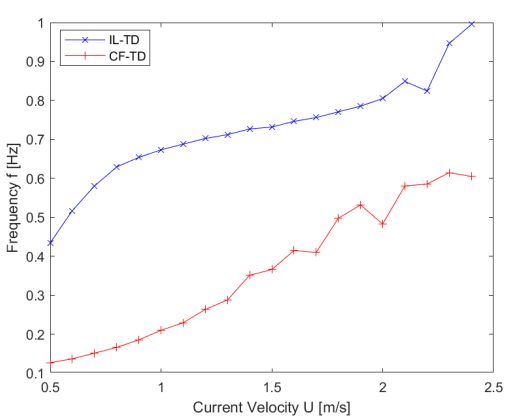

(a) Response Frequency vs Current Velocity

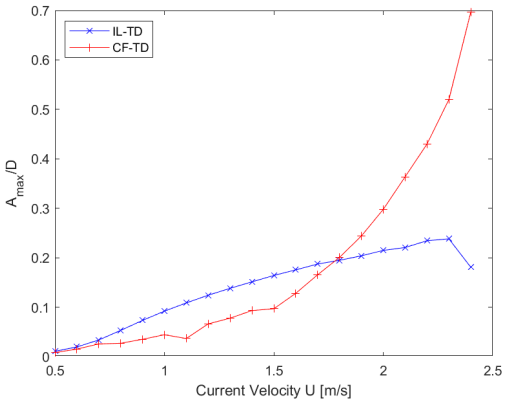

(b) Maximum response amplitude vs Current Velocity

Figure B.28: Plots of the dominant response frequencies and the maximum response amplitudes for the Linear soil model and $\zeta_{soil} = 22\%$.

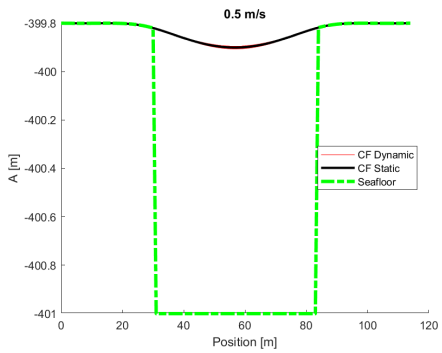

(a) CF - 0.5 m/s

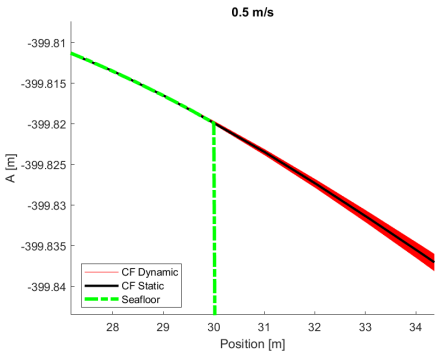

(b) CF - 0.5 m/s (zoom at the left shoulder)

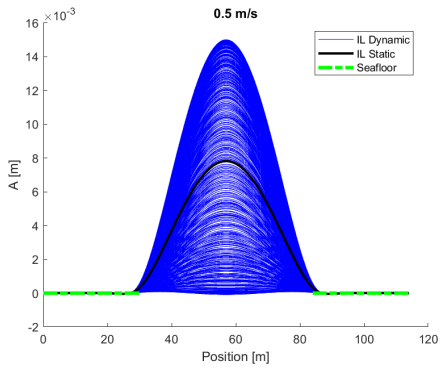

(c) IL - 0.5 m/s

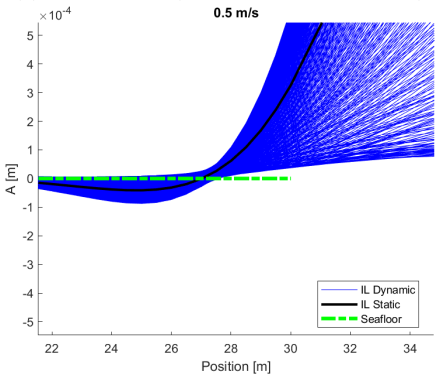

(d) IL - 0.5 m/s (zoom at the left shoulder)

Figure B.29: Snapshots of the calculated response at 0.5 m/s.

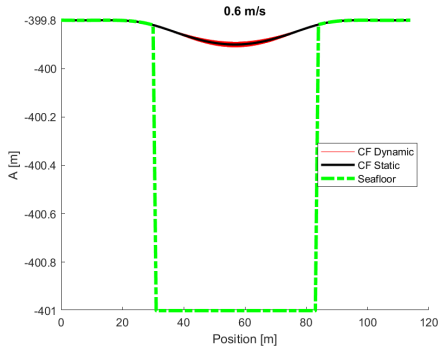

(a) CF - 0.6 m/s

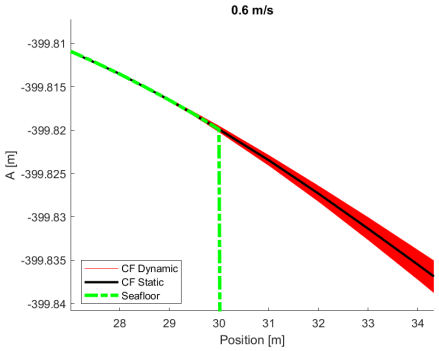

(b) CF - 0.6 m/s (zoom at the left shoulder)

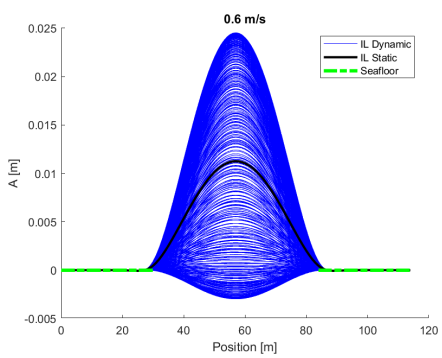

(c) IL - 0.6 m/s

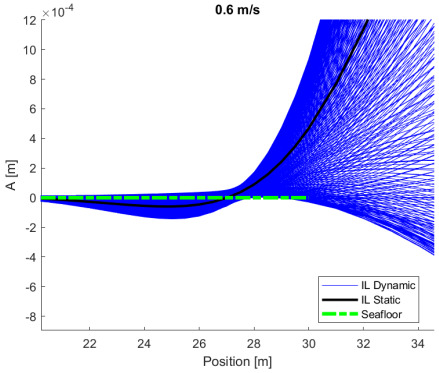

(d) IL - 0.6 m/s (zoom at the left shoulder)

Figure B.30: Snapshots of the calculated response at 0.6 m/s.

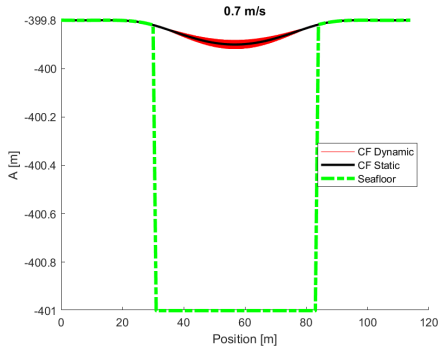

(a) CF - 0.7 m/s

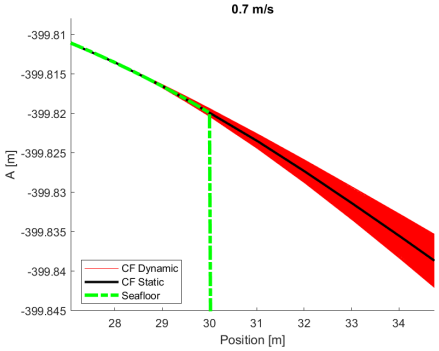

(b) CF - 0.7 m/s (zoom at the left shoulder)

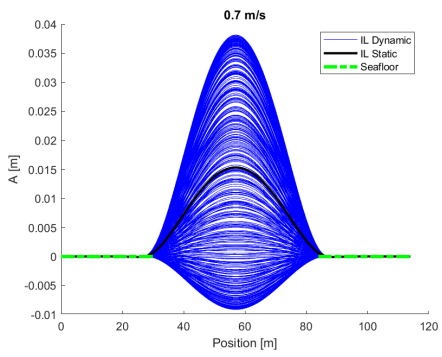

(c) IL - 0.7 m/s

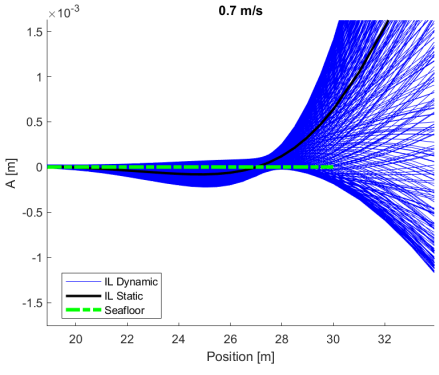

(d) IL - 0.7 m/s (zoom at the left shoulder)

Figure B.31: Snapshots of the calculated response at 0.7 m/s.

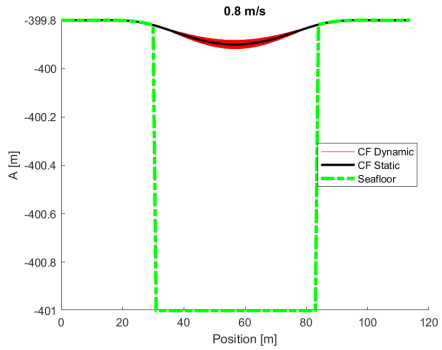

(a) CF - 0.8 m/s

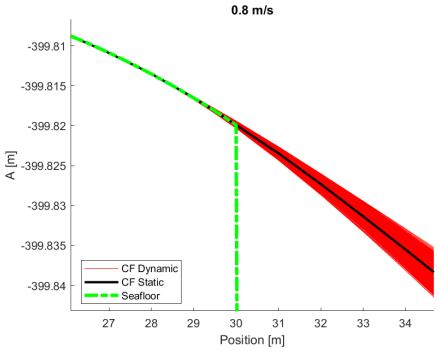

(b) CF - 0.8 m/s (zoom at the left shoulder)

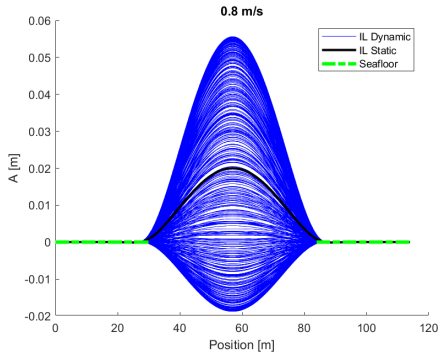

(c) IL - 0.8 m/s

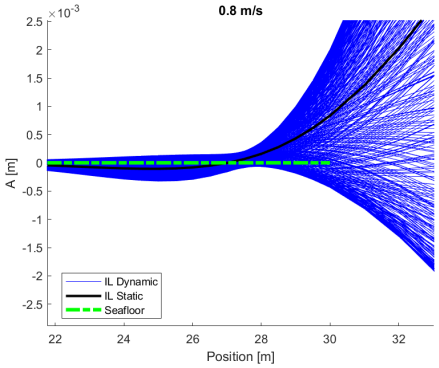

(d) IL - 0.8 m/s (zoom at the left shoulder)

Figure B.32: Snapshots of the calculated response at 0.8 m/s.

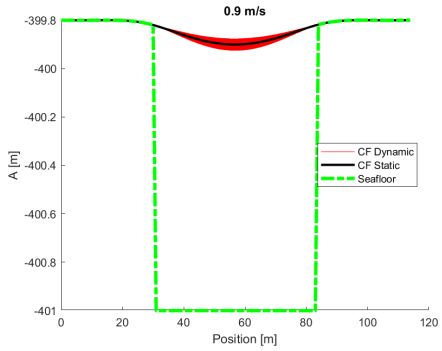

(a) CF - 0.9 m/s

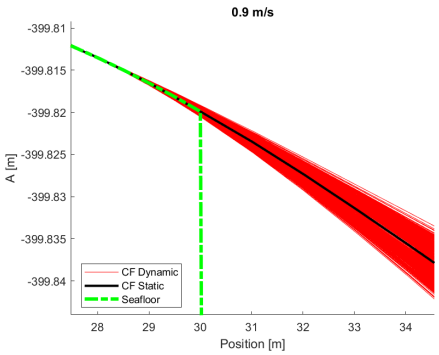

(b) CF - 0.9 m/s (zoom at the left shoulder)

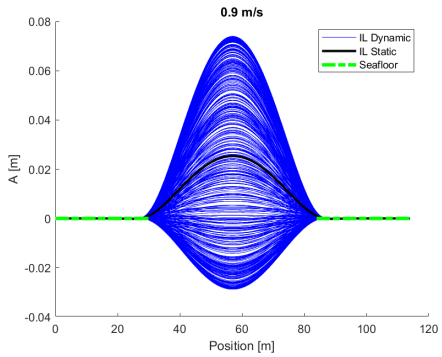

(c) IL - 0.9 m/s

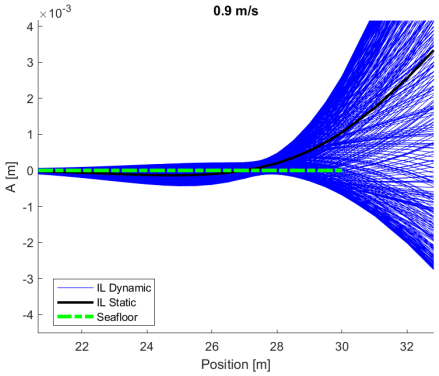

(d) IL - 0.9 m/s (zoom at the left shoulder)

Figure B.33: Snapshots of the calculated response at 0.9 m/s.

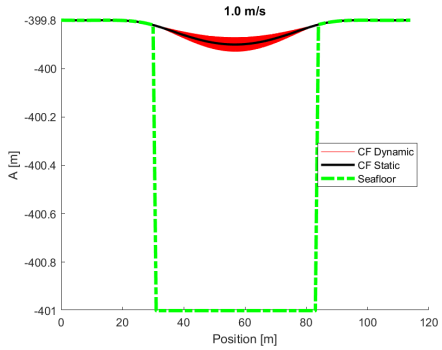

(a) CF - 1.0 m/s

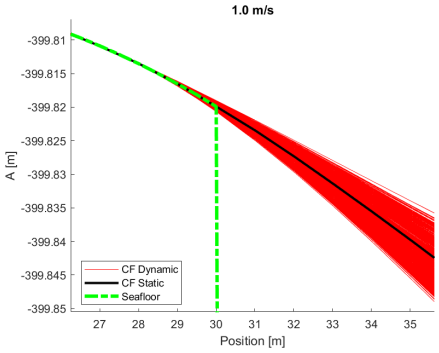

(b) CF - 1.0 m/s (zoom at the left shoulder)

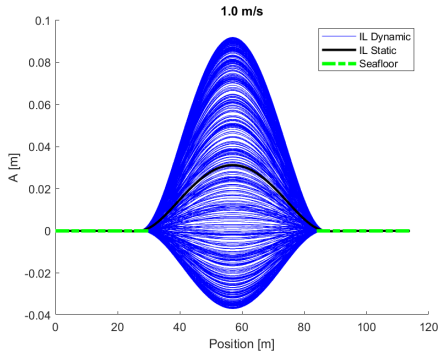

(c) IL - 1.0 m/s

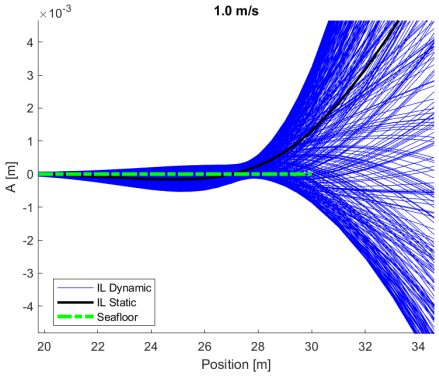

(d) IL - 1.0 m/s (zoom at the left shoulder)

Figure B.34: Snapshots of the calculated response at 1.0 m/s.

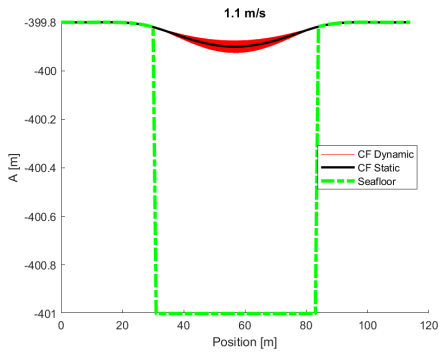

(a) CF - 1.1 m/s

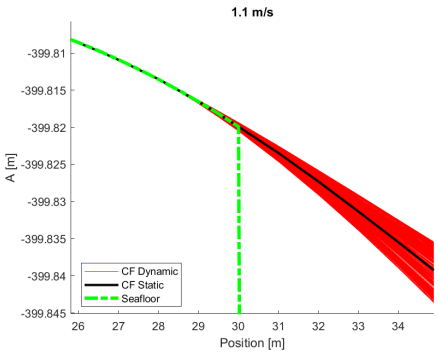

(b) CF - 1.1 m/s (zoom at the left shoulder)

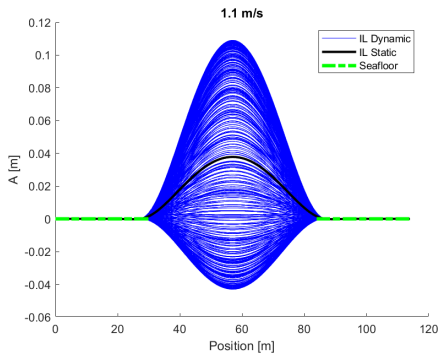

(c) IL - 1.1 m/s

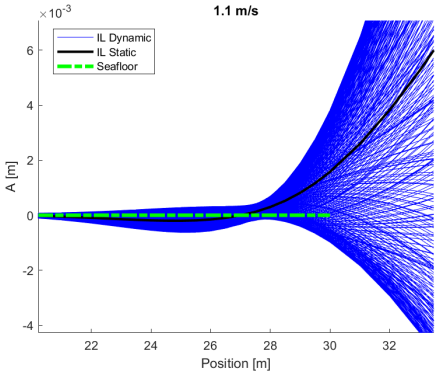

(d) IL - 1.1 m/s (zoom at the left shoulder)

Figure B.35: Snapshots of the calculated response at 1.1 m/s.

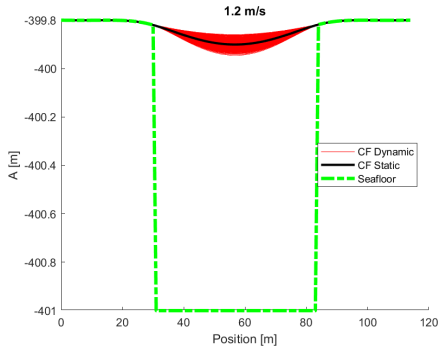

(a) CF - 1.2 m/s

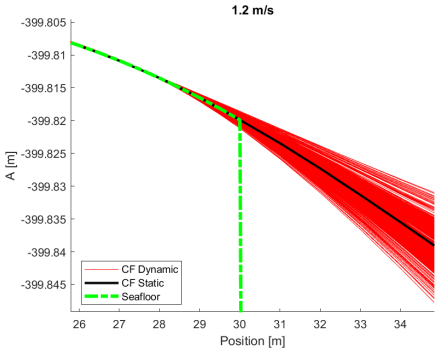

(b) CF - 1.2 m/s (zoom at the left shoulder)

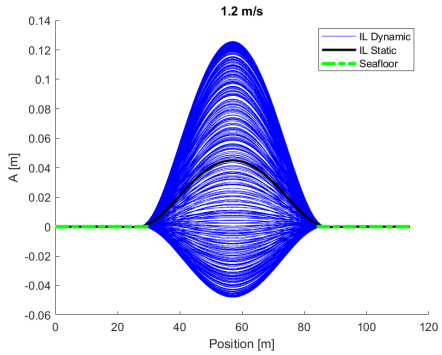

(c) IL - 1.2 m/s

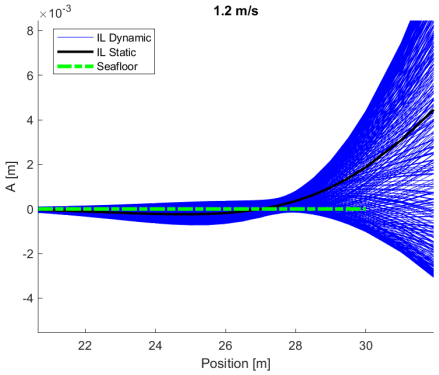

(d) IL - 1.2 m/s (zoom at the left shoulder)

Figure B.36: Snapshots of the calculated response at 1.2 m/s.

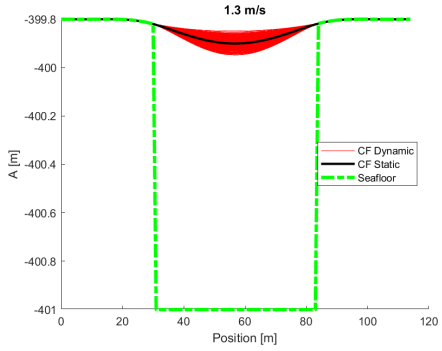

(a) CF - 1.3 m/s

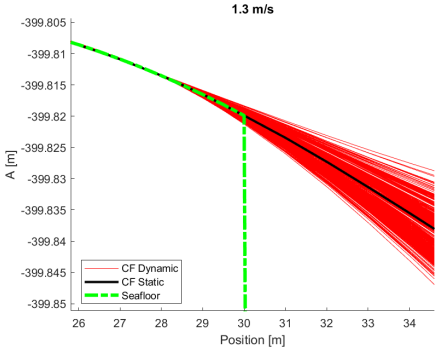

(b) CF - 1.3 m/s (zoom at the left shoulder)

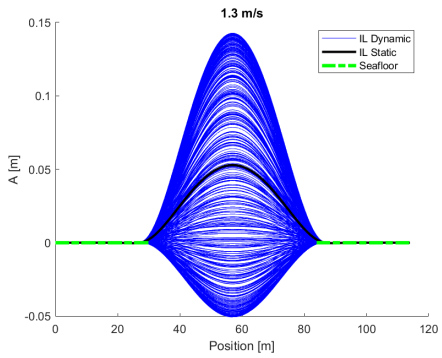

(c) IL - 1.3 m/s

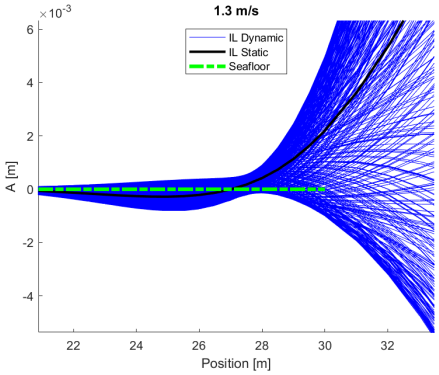

(d) IL - 1.3 m/s (zoom at the left shoulder)

Figure B.37: Snapshots of the calculated response at 1.3 m/s.

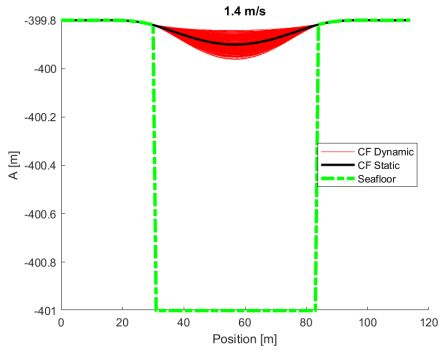

(a) CF - 1.4 m/s

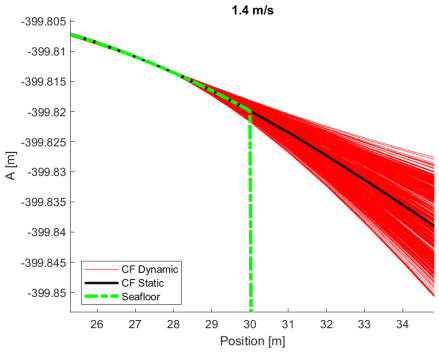

(b) CF - 1.4 m/s (zoom at the left shoulder)

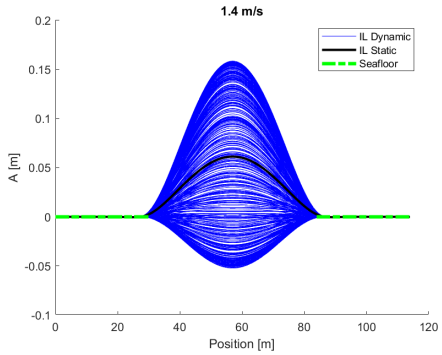

(c) IL - 1.4 m/s

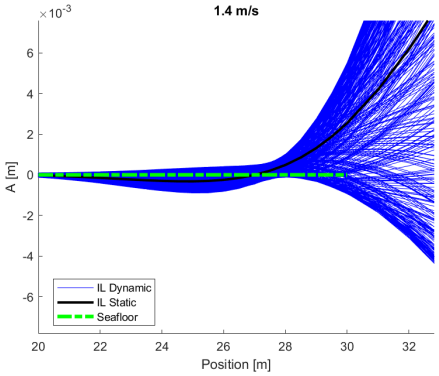

(d) IL - 1.4 m/s (zoom at the left shoulder)

Figure B.38: Snapshots of the calculated response at 1.4 m/s.

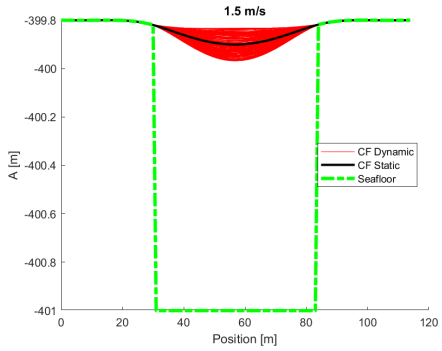

(a) CF - 1.5 m/s

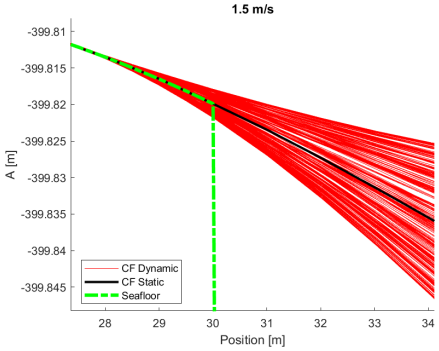

(b) CF - 1.5 m/s (zoom at the left shoulder)

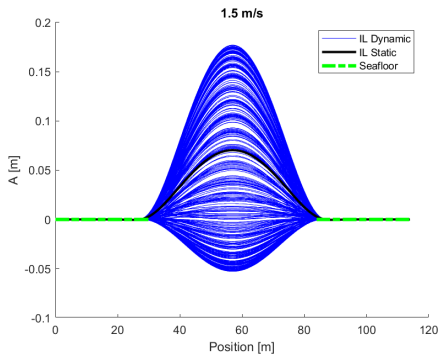

(c) IL - 1.5 m/s

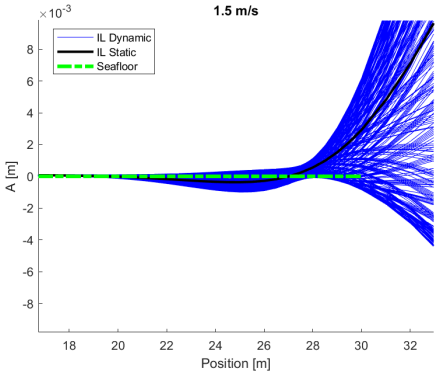

(d) IL - 1.5 m/s (zoom at the left shoulder)

Figure B.39: Snapshots of the calculated response at 1.5 m/s.

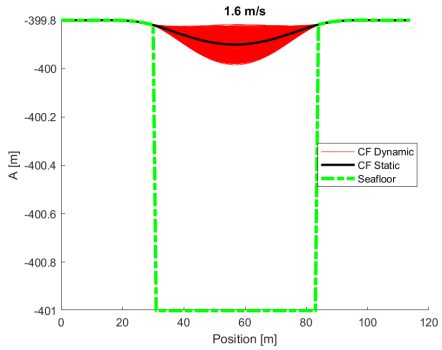

(a) CF - 1.6 m/s

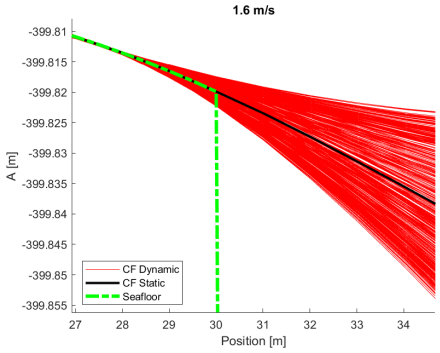

(b) CF - 1.6 m/s (zoom at the left shoulder)

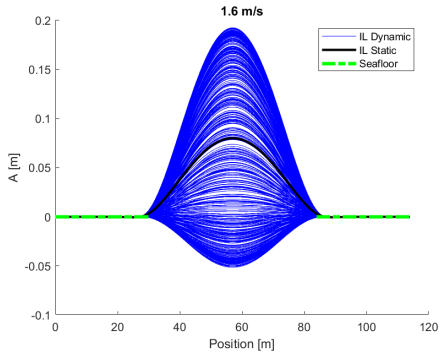

(c) IL - 1.6 m/s

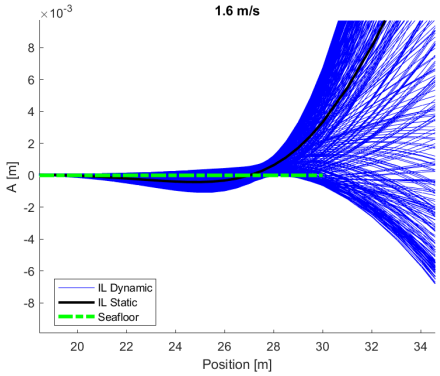

(d) IL - 1.6 m/s (zoom at the left shoulder)

Figure B.40: Snapshots of the calculated response at 1.6 m/s.

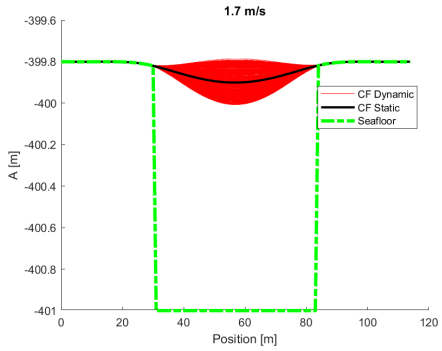

(a) CF - 1.7 m/s

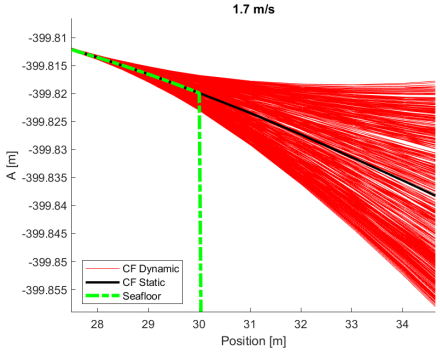

(b) CF - 1.7 m/s (zoom at the left shoulder)

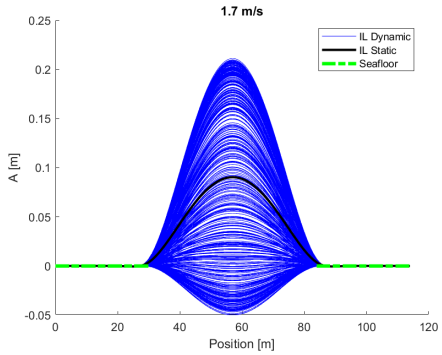

(c) IL - 1.7 m/s

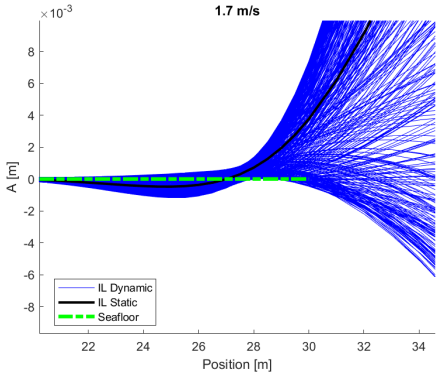

(d) IL - 1.7 m/s (zoom at the left shoulder)

Figure B.41: Snapshots of the calculated response at 1.7 m/s.

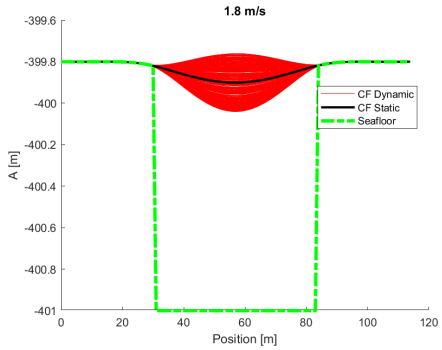

(a) CF - 1.8 m/s

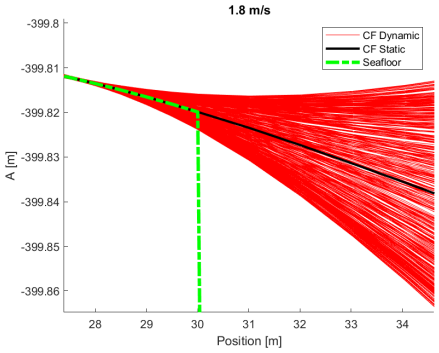

(b) CF - 1.8 m/s (zoom at the left shoulder)

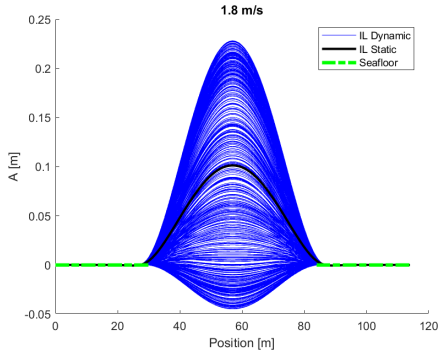

(c) IL - 1.8 m/s

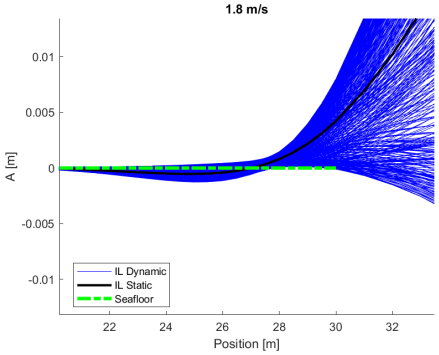

(d) IL - 1.8 m/s (zoom at the left shoulder)

Figure B.42: Snapshots of the calculated response at 1.8 m/s.

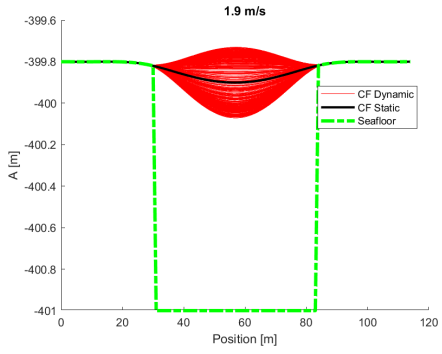

(a) CF - 1.9 m/s

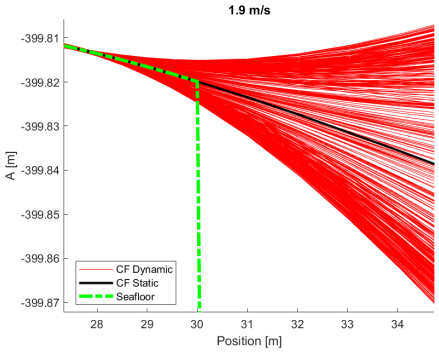

(b) CF - 1.9 m/s (zoom at the left shoulder)

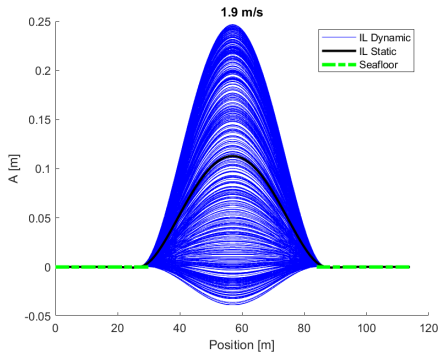

(c) IL - 1.9 m/s

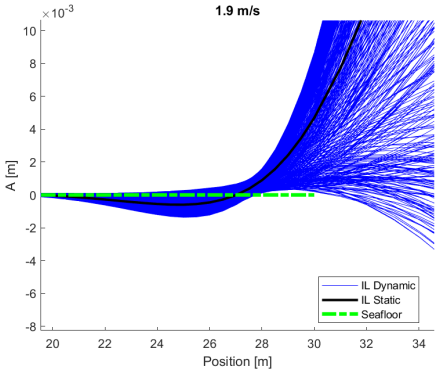

(d) IL - 1.9 m/s (zoom at the left shoulder)

Figure B.43: Snapshots of the calculated response at 1.9 m/s.

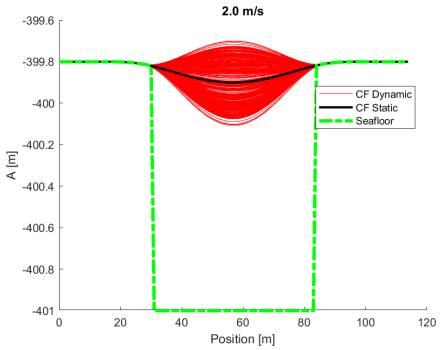

(a) CF - 2.0 m/s

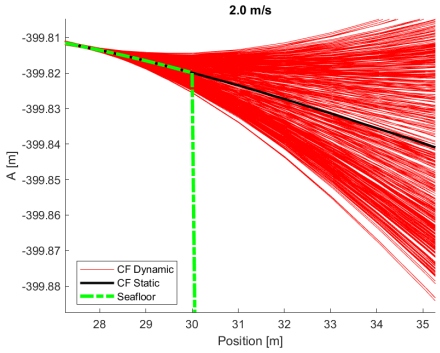

(b) CF - 2.0 m/s (zoom at the left shoulder)

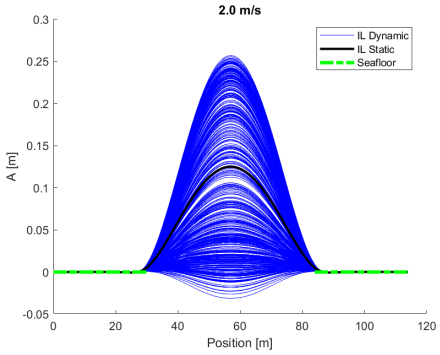

(c) IL - 2.0 m/s

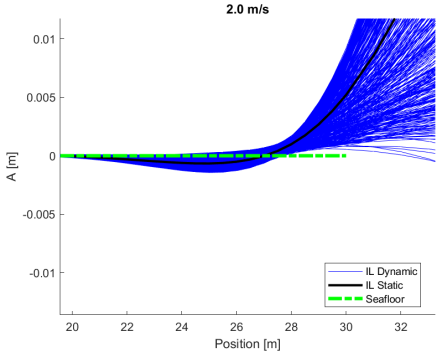

(d) IL - 2.0 m/s (zoom at the left shoulder)

Figure B.44: Snapshots of the calculated response at 2.0 m/s.

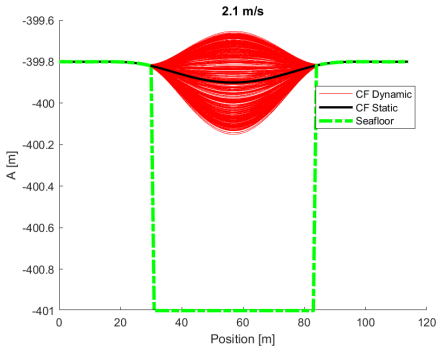

(a) CF - 2.1 m/s

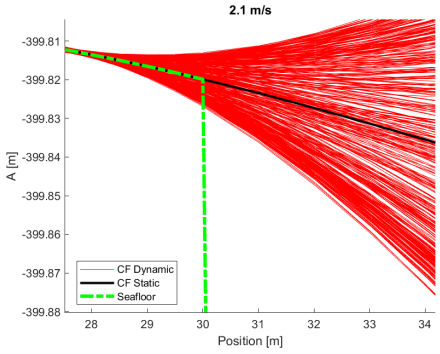

(b) CF - 2.1 m/s (zoom at the left shoulder)

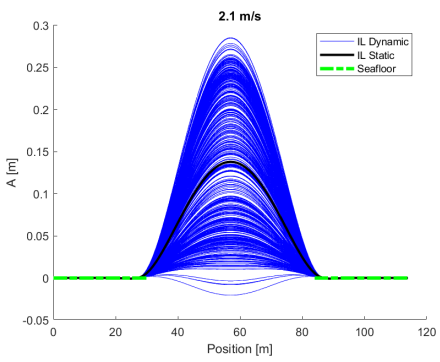

(c) IL - 2.1 m/s

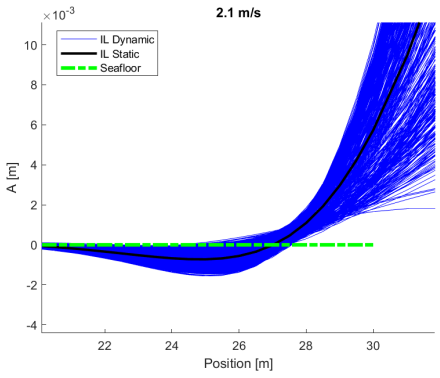

(d) IL - 2.1 m/s (zoom at the left shoulder)

Figure B.45: Snapshots of the calculated response at 2.1 m/s.

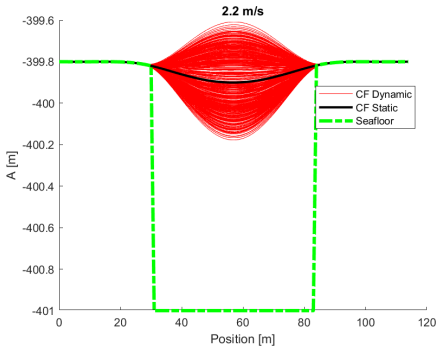

(a) CF - 2.2 m/s

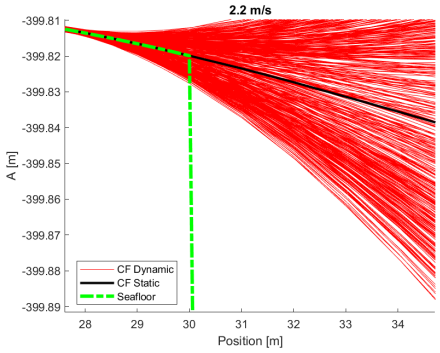

(b) CF - 2.2 m/s (zoom at the left shoulder)

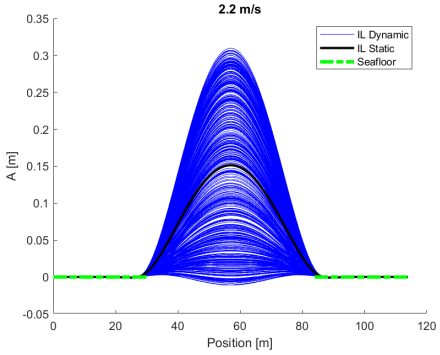

(c) IL - 2.2 m/s

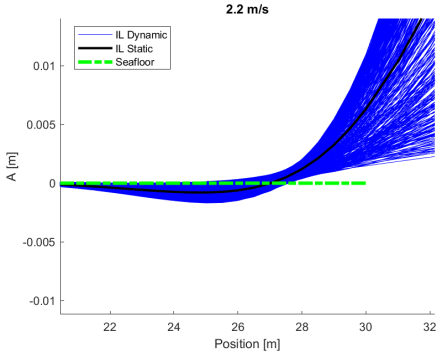

(d) IL - 2.2 m/s (zoom at the left shoulder)

Figure B.46: Snapshots of the calculated response at 2.2 m/s.

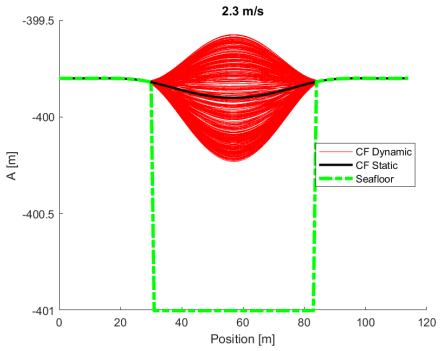

(a) CF - 2.3 m/s

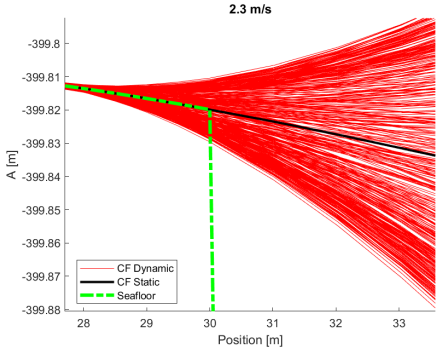

(b) CF - 2.3 m/s (zoom at the left shoulder)

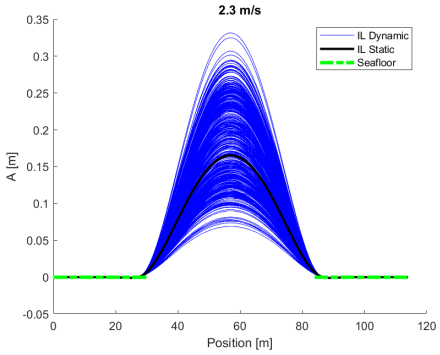

(c) IL - 2.3 m/s

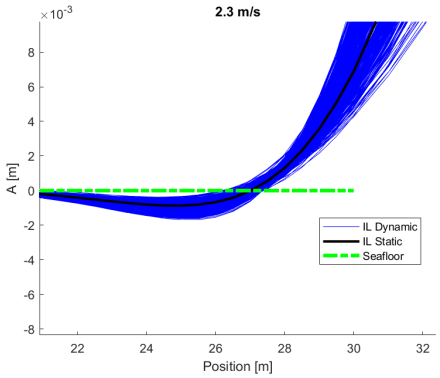

(d) IL - 2.3 m/s (zoom at the left shoulder)

Figure B.47: Snapshots of the calculated response at 2.3 m/s.

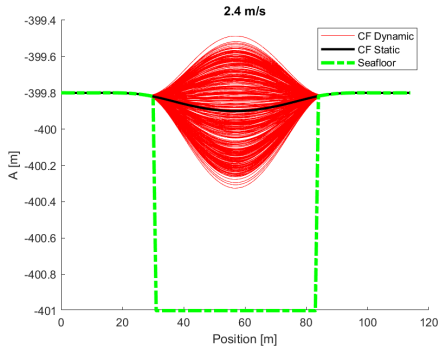

(a) CF - 2.4 m/s

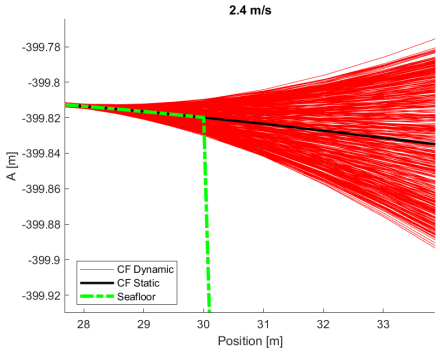

(b) CF - 2.4 m/s (zoom at the left shoulder)

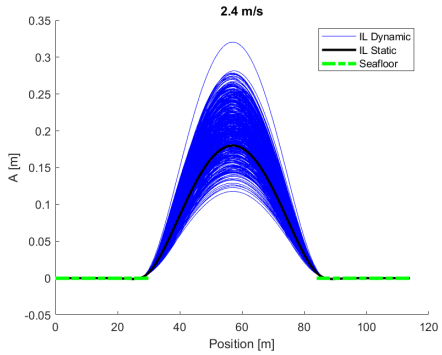

(c) IL - 2.4 m/s

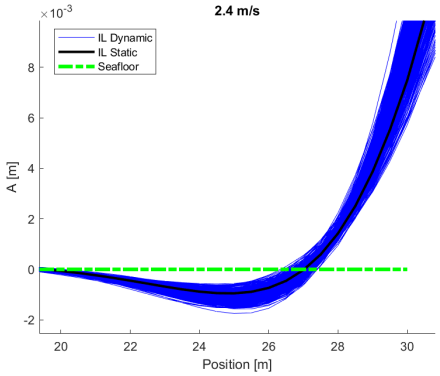

(d) IL - 2.4 m/s (zoom at the left shoulder)

Figure B.48: Snapshots of the calculated response at 2.4 m/s.

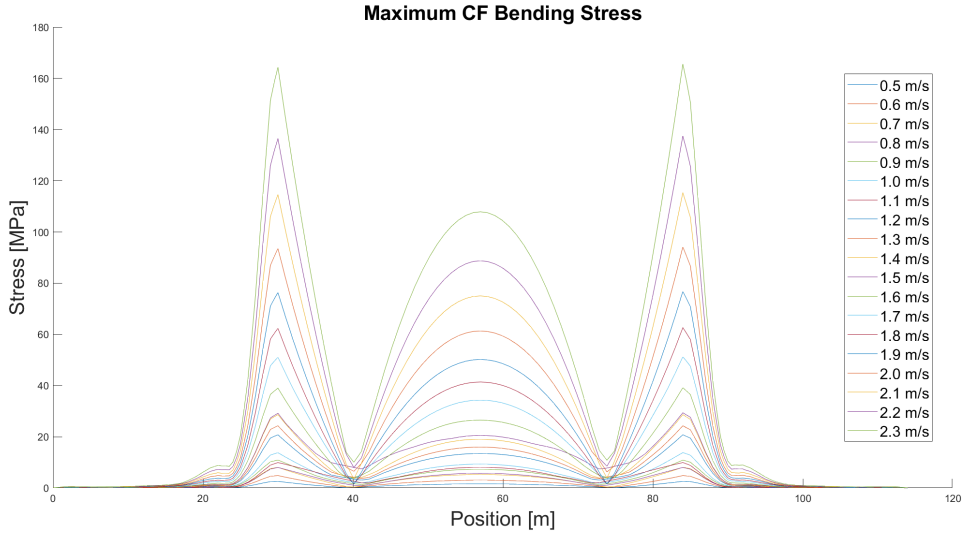

(a) CF - Maximum Bending Stress

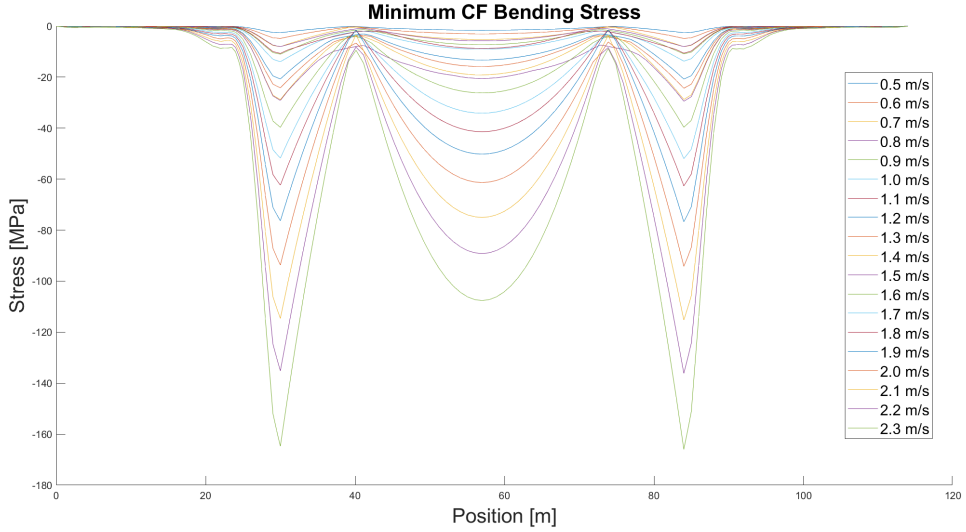

(b) CF - Minimum Bending Stress

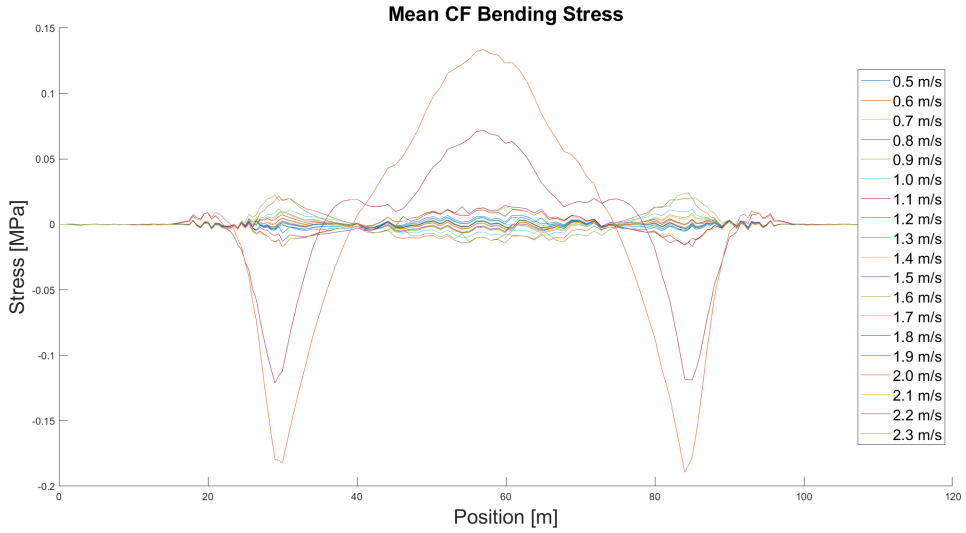

(c) CF - Mean Bending Stress

Figure B.49: Plots of the calculated bending stress distribution in the CF direction for the Linear soil model and $\zeta_{soil} = 22\%$.

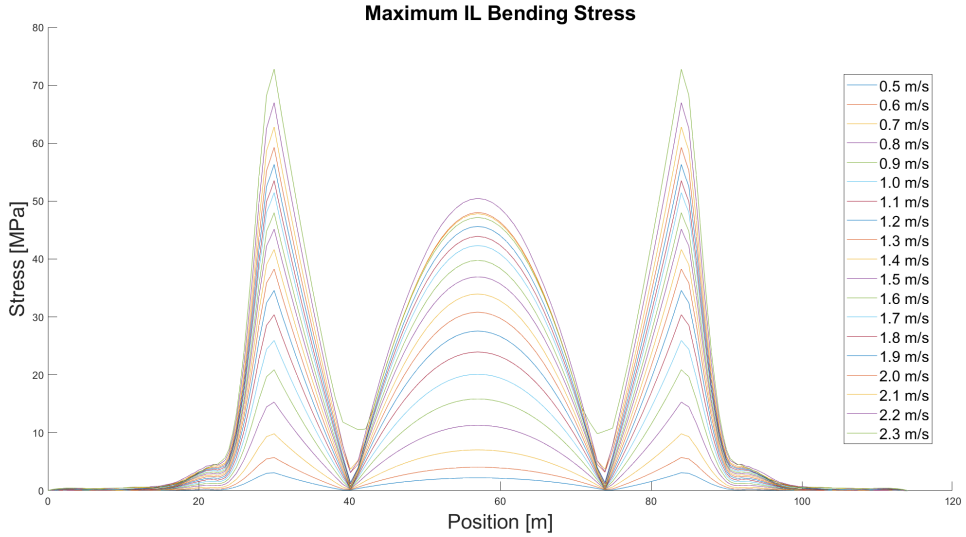

(a) IL - Maximum Bending Stress

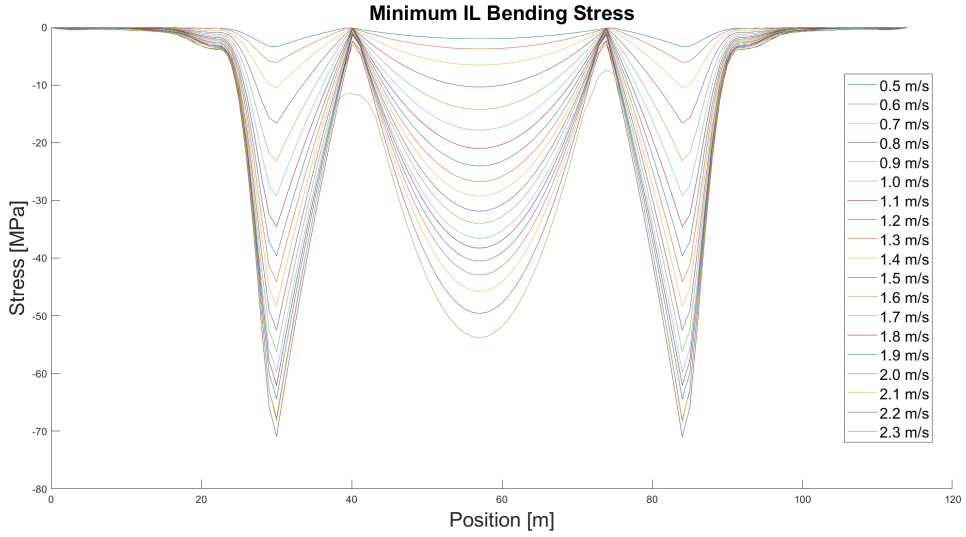

(b) IL - Minimum Bending Stress

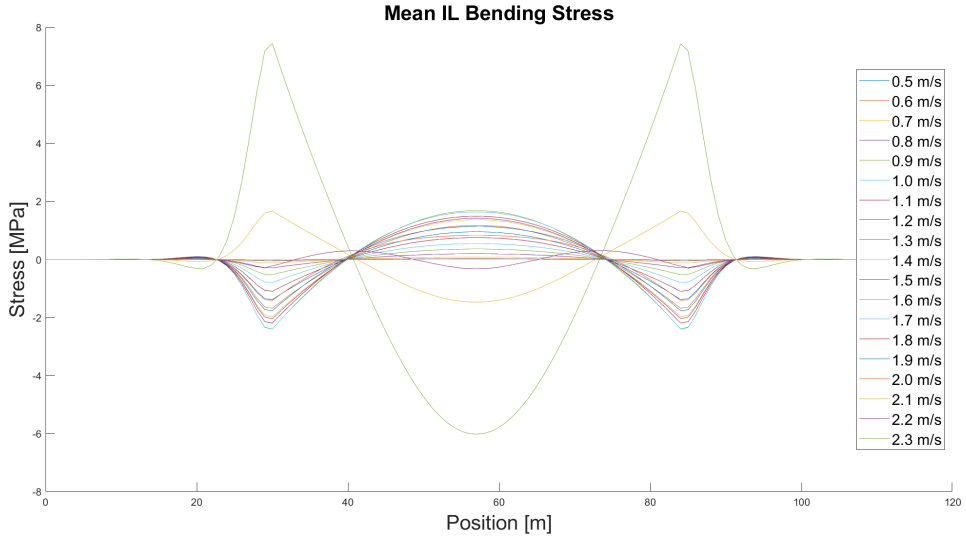

(c) IL - Mean Bending Stress

Figure B.50: Plots of the calculated bending stress distribution in the IL direction for the Linear soil model and $\zeta_{soil} = 22\%$.

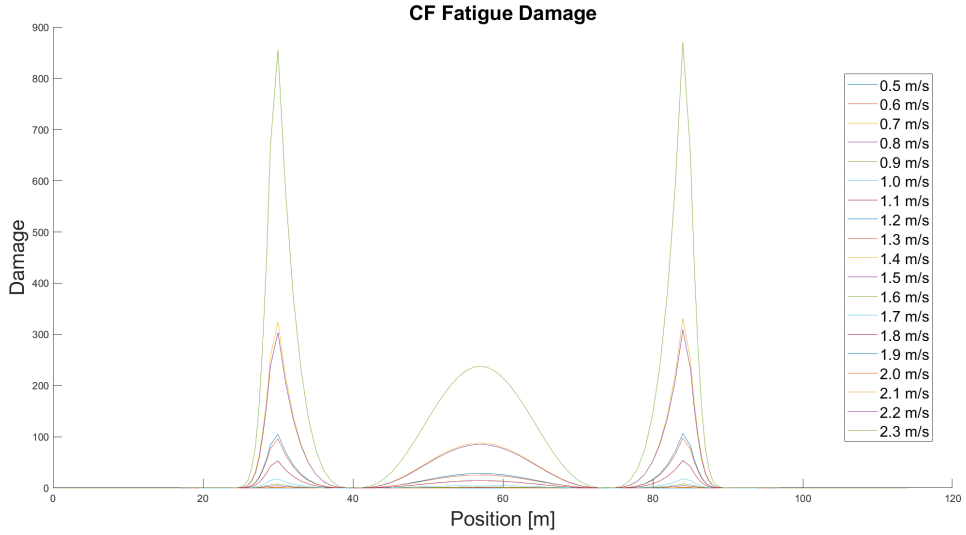

(a) CF - Fatigue Damage Accumulation

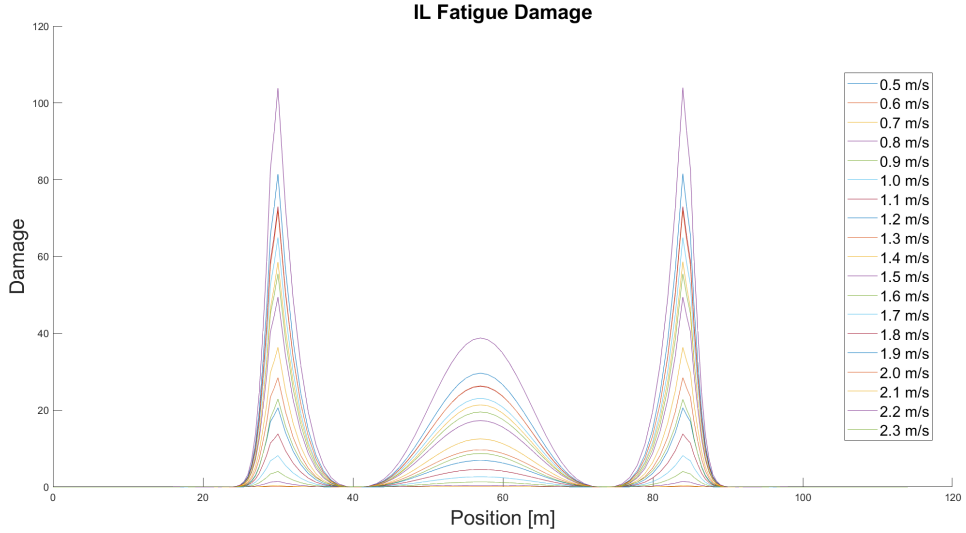

(b) IL - Fatigue Damage Accumulation

Figure B.51: Plots of the calculated fatigue damage distribution in both directions for the Linear soil model and $\zeta_{soil} = 22\%$.

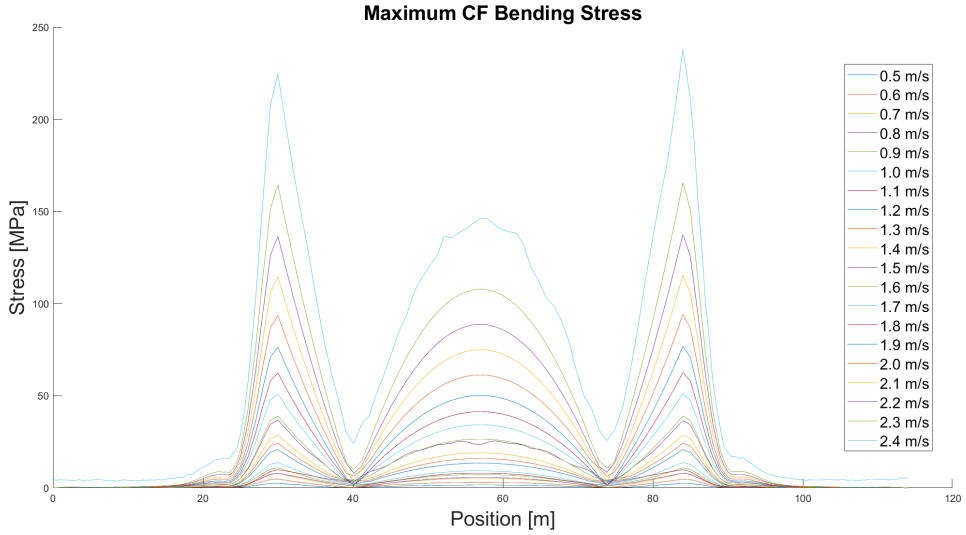

(a) CF - Maximum Bending Stress

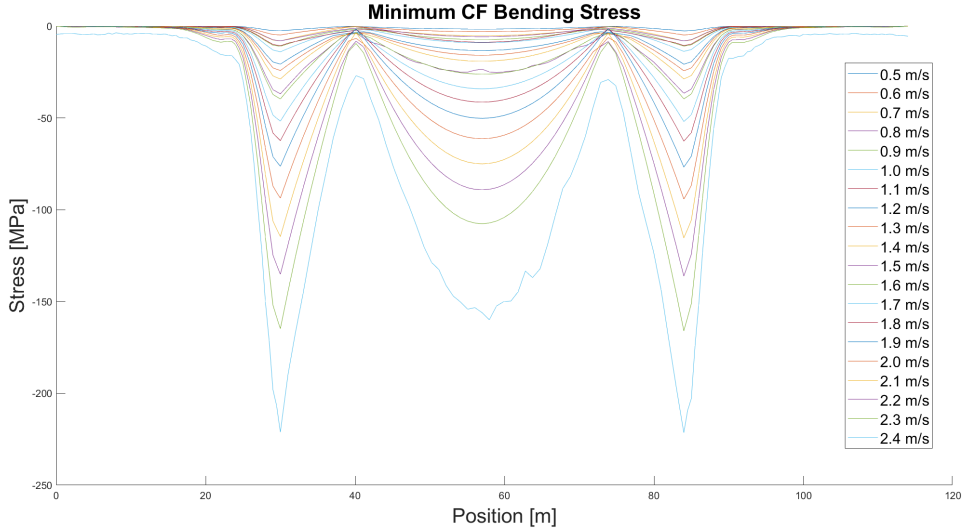

(b) CF - Minimum Bending Stress

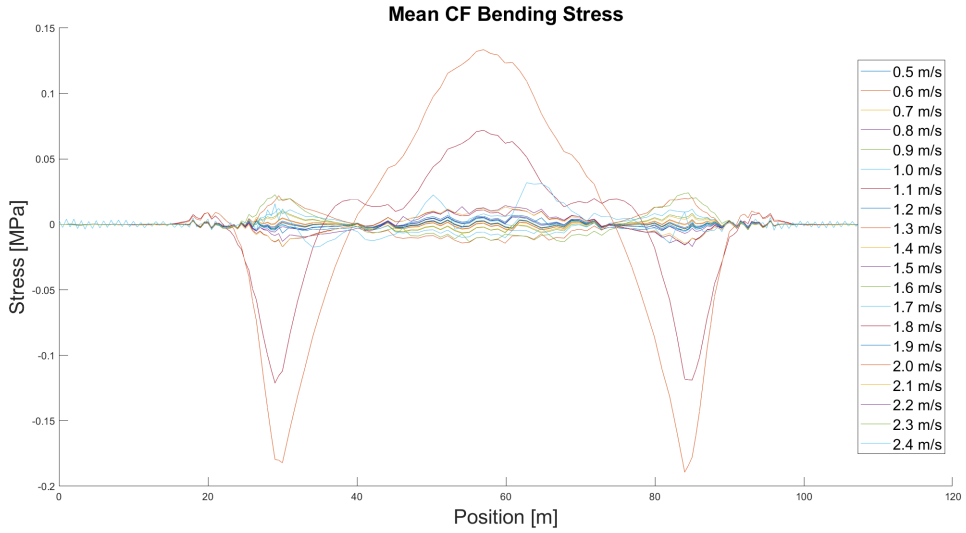

(c) CF - Mean Bending Stress

Figure B.52: Plots of the calculated bending stress distribution in the CF direction for the Linear soil model and $\zeta_{soil} = 22\%$ including the velocity of 2.4 m/s and the results obtained for the velocity of 1.5 m/s when the initial timestep was used.

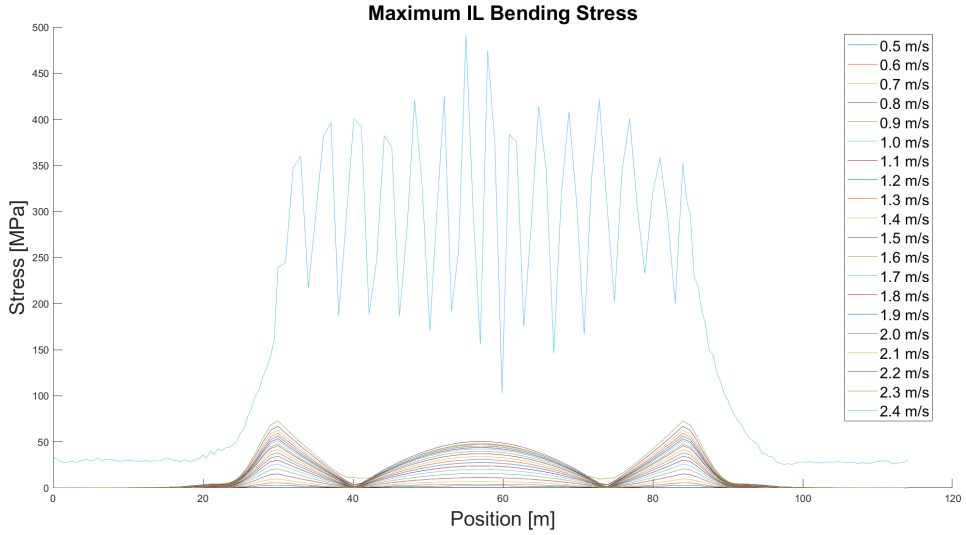

(a) IL - Maximum Bending Stress

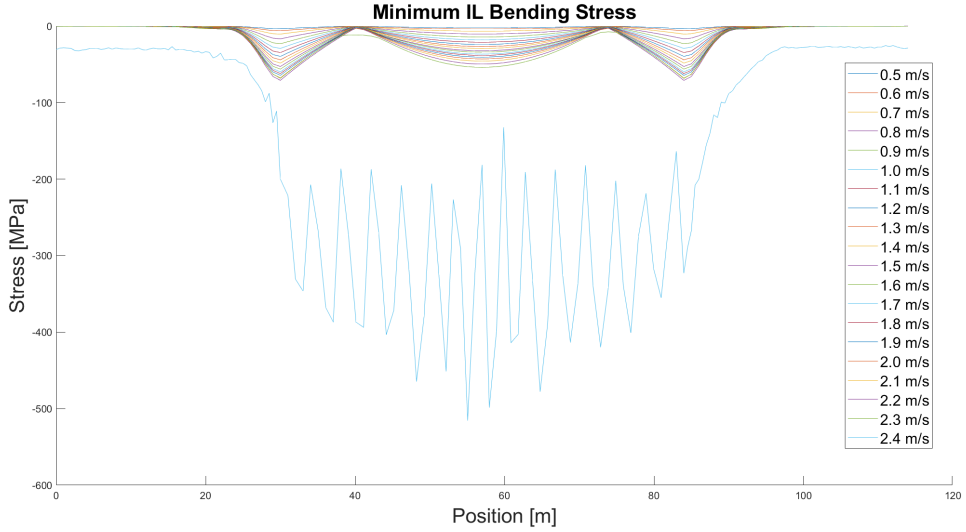

(b) IL - Minimum Bending Stress

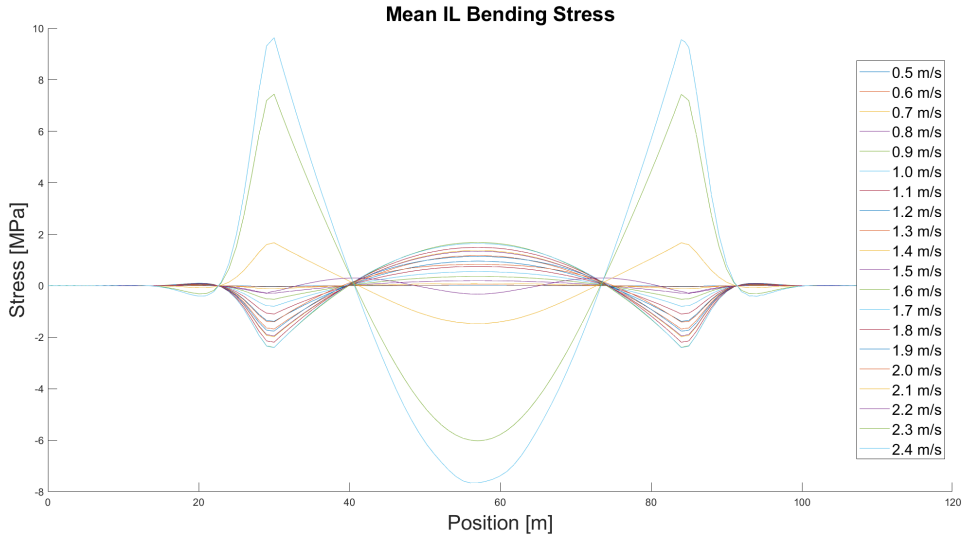

(c) IL - Mean Bending Stress

Figure B.53: Plots of the calculated bending stress distribution in the IL direction for the Linear soil model and $\zeta_{soil} = 22\%$ including the velocity of 2.4 m/s and the results obtained for the velocity of 1.5 m/s when the initial timestep was used.

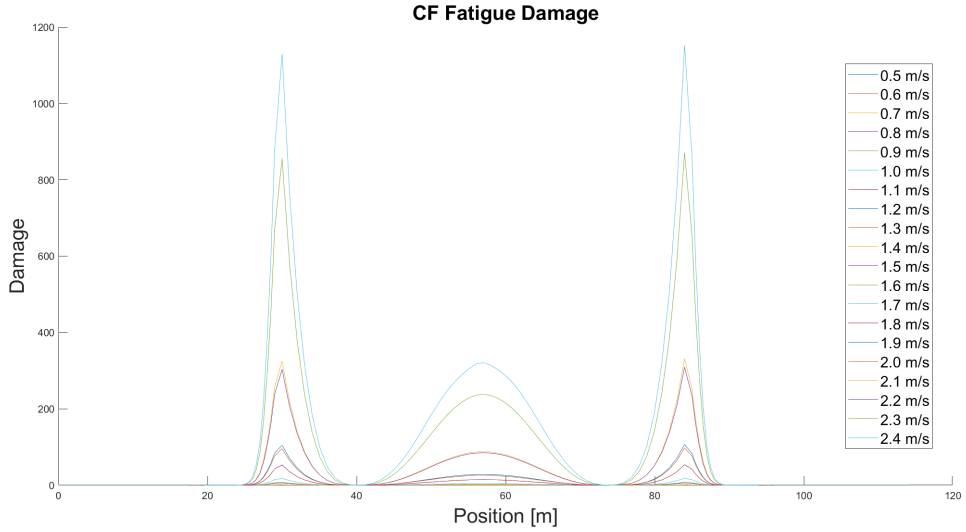

(a) CF - Fatigue Damage Accumulation

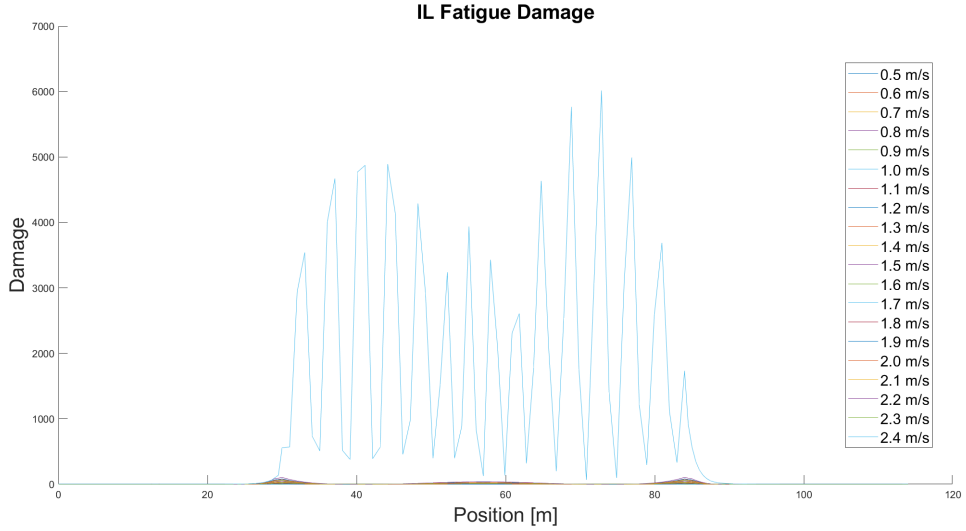

(b) IL - Fatigue Damage Accumulation

Figure B.54: Plots of the calculated fatigue damage distribution in both directions for the Linear soil model and $\zeta_{soil} = 22\%$ including the velocity of 2.4 m/s and the results obtained for the velocity of 1.5 m/s when the initial timestep was used.

B.3 Comparative Study - Soil Damping Ratio 0.22 - Total set of results

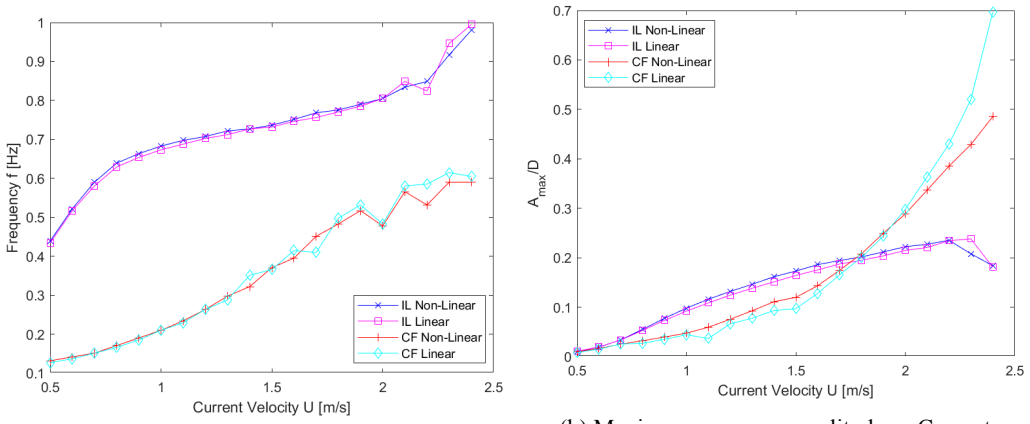

(a) Response Frequency vs Current Velocity

(b) Maximum response amplitude vs Current Velocity

Figure B.55: Plots of the dominant response frequencies and the maximum response amplitudes for the Non-Linear and Linear soil models and $\zeta_{soil} = 22\%$.

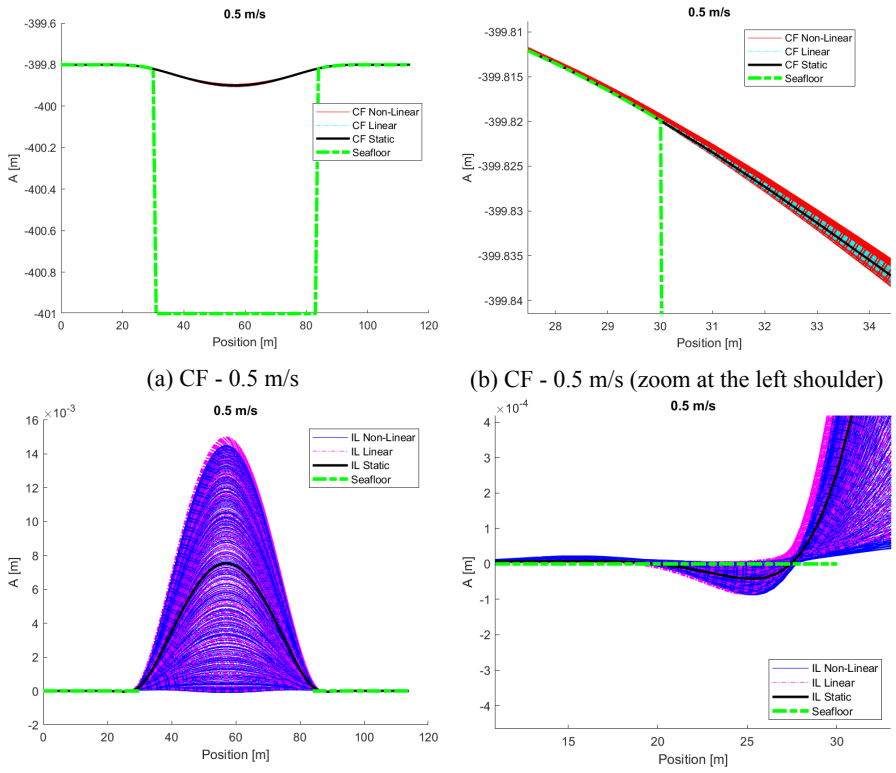

(a) CF - 0.5 m/s

(b) CF - 0.5 m/s (zoom at the left shoulder)

(c) IL - 0.5 m/s

(d) IL - 0.5 m/s (zoom at the left shoulder)

Figure B.56: Comparative snapshots of the calculated responses for the two soil models at 0.5 m/s.

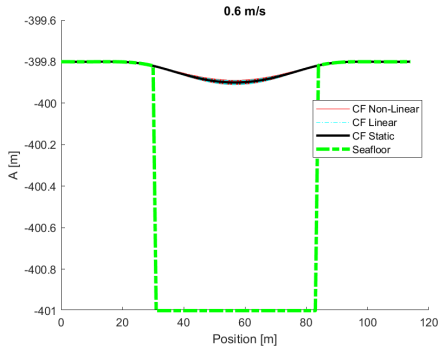

(a) CF - 0.6 m/s

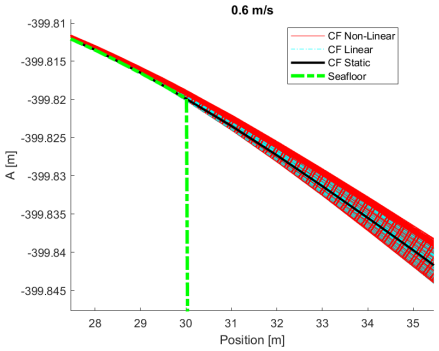

(b) CF - 0.6 m/s (zoom at the left shoulder)

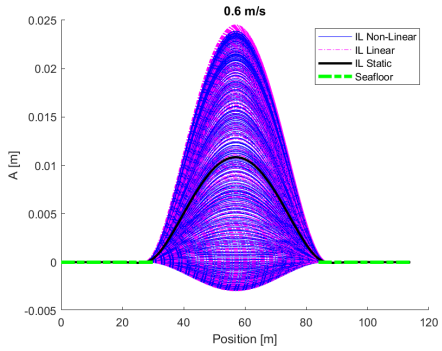

(c) IL - 0.6 m/s

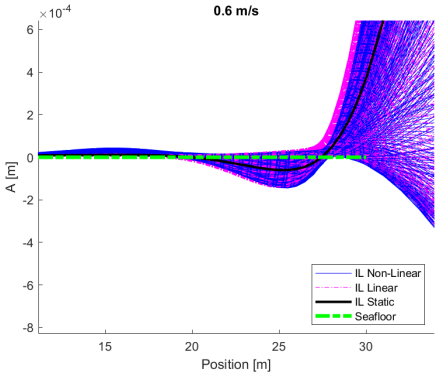

(d) IL - 0.6 m/s (zoom at the left shoulder)

Figure B.57: Comparative snapshots of the calculated responses for the two soil models at 0.6 m/s.

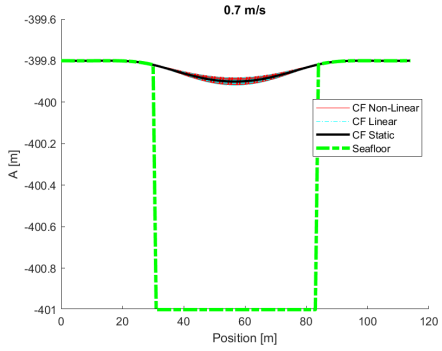

(a) CF - 0.7 m/s

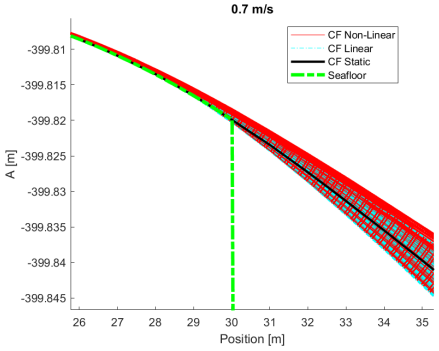

(b) CF - 0.7 m/s (zoom at the left shoulder)

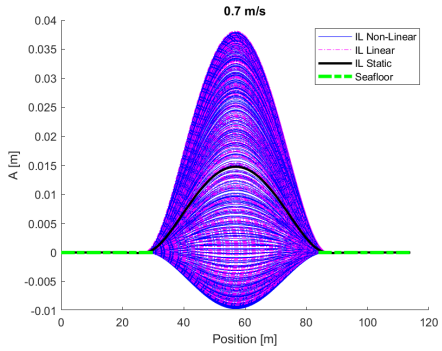

(c) IL - 0.7 m/s

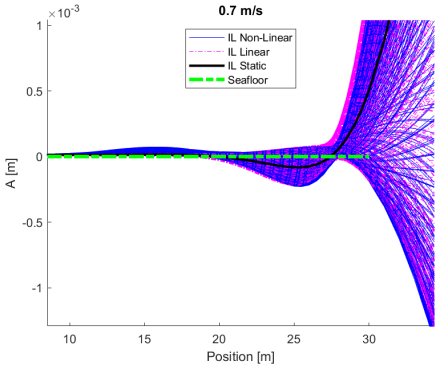

(d) IL - 0.7 m/s (zoom at the left shoulder)

Figure B.58: Comparative snapshots of the calculated responses for the two soil models at 0.7 m/s.

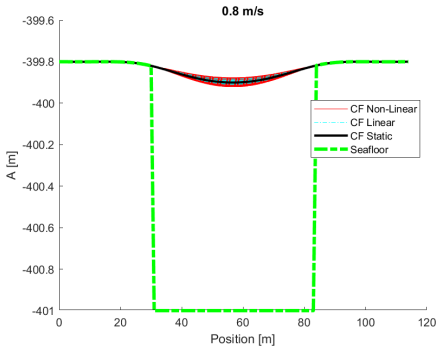

(a) CF - 0.8 m/s

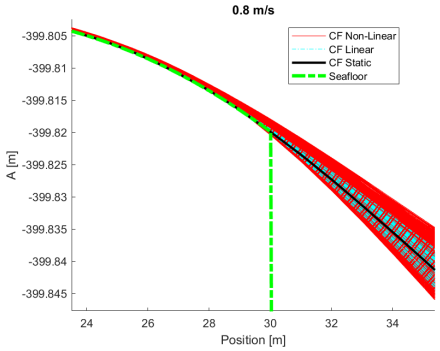

(b) CF - 0.8 m/s (zoom at the left shoulder)

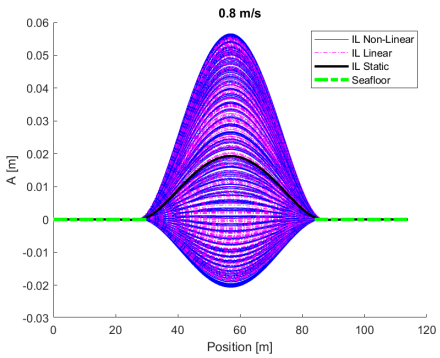

(c) IL - 0.8 m/s

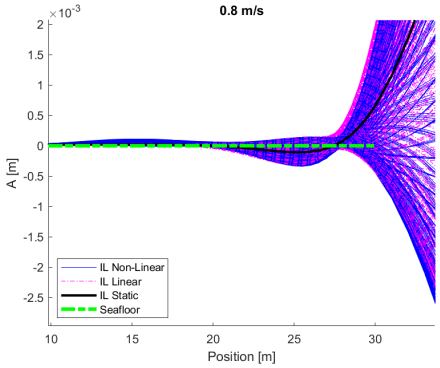

(d) IL - 0.8 m/s (zoom at the left shoulder)

Figure B.59: Comparative snapshots of the calculated responses for the two soil models at 0.8 m/s.

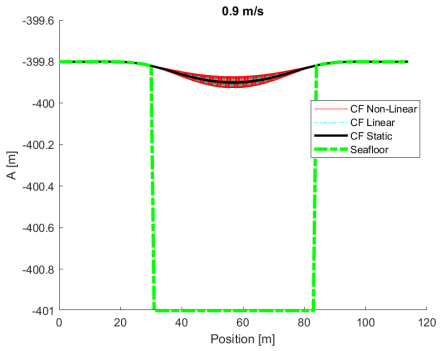

(a) CF - 0.9 m/s

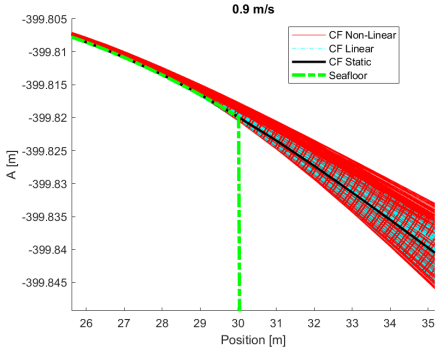

(b) CF - 0.9 m/s (zoom at the left shoulder)

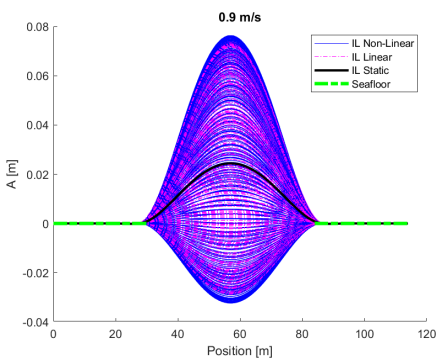

(c) IL - 0.9 m/s

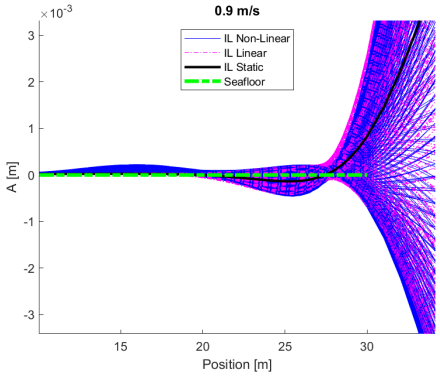

(d) IL - 0.9 m/s (zoom at the left shoulder)

Figure B.60: Comparative snapshots of the calculated responses for the two soil models at 0.9 m/s.

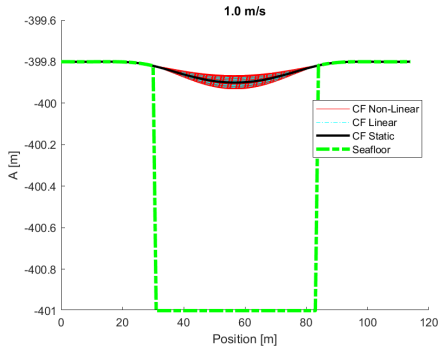

(a) CF - 1.0 m/s

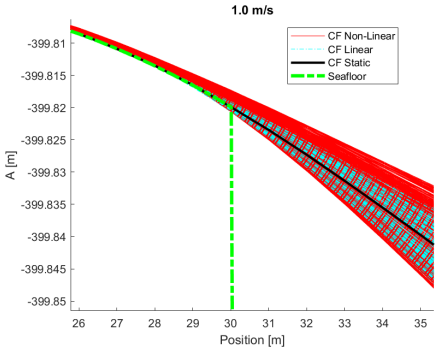

(b) CF - 1.0 m/s (zoom at the left shoulder)

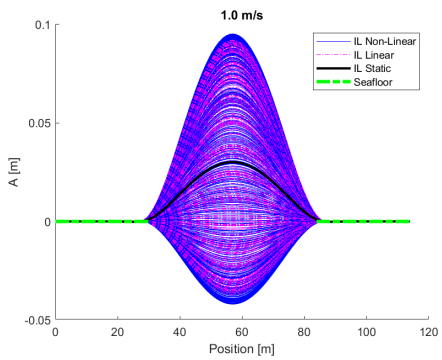

(c) IL - 1.0 m/s

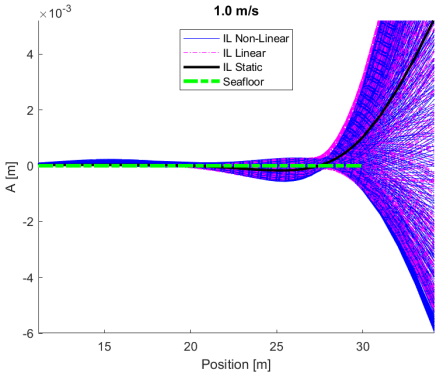

(d) IL - 1.0 m/s (zoom at the left shoulder)

Figure B.61: Comparative snapshots of the calculated responses for the two soil models at 1.0 m/s.

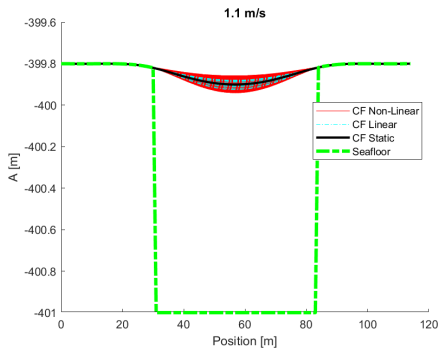

(a) CF - 1.1 m/s

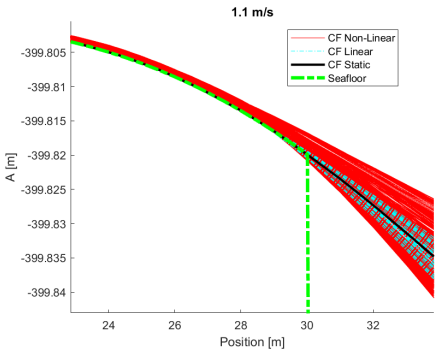

(b) CF - 1.1 m/s (zoom at the left shoulder)

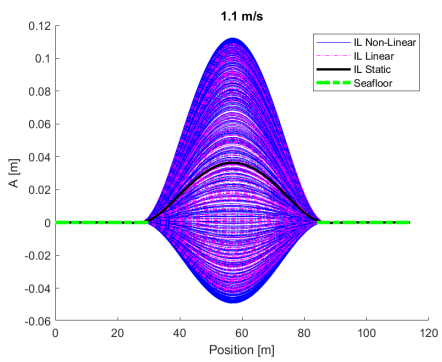

(c) IL - 1.1 m/s

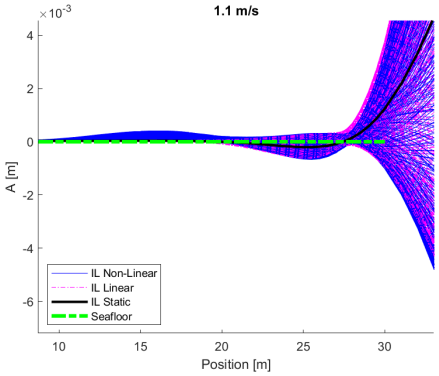

(d) IL - 1.1 m/s (zoom at the left shoulder)

Figure B.62: Comparative snapshots of the calculated responses for the two soil models at 1.1 m/s.

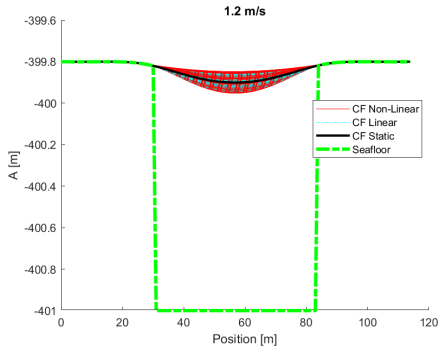

(a) CF - 1.2 m/s

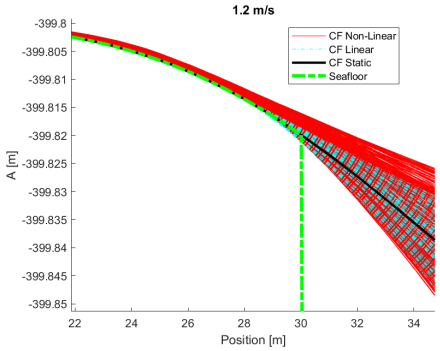

(b) CF - 1.2 m/s (zoom at the left shoulder)

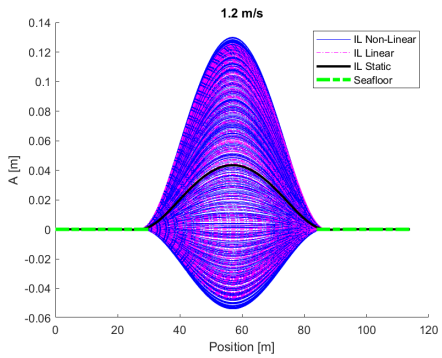

(c) IL - 1.2 m/s

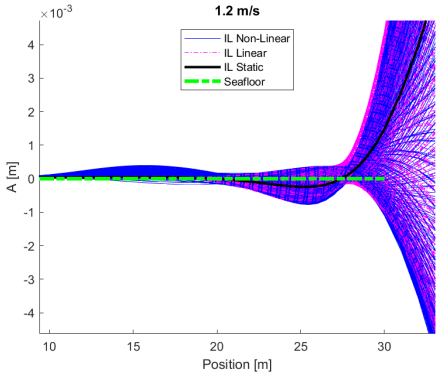

(d) IL - 1.2 m/s (zoom at the left shoulder)

Figure B.63: Comparative snapshots of the calculated responses for the two soil models at 1.2 m/s.

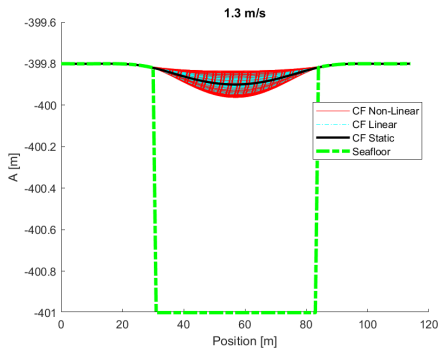

(a) CF - 1.3 m/s

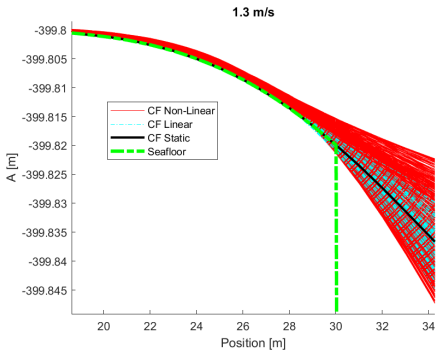

(b) CF - 1.3 m/s (zoom at the left shoulder)

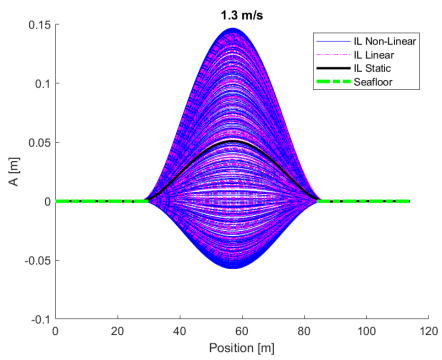

(c) IL - 1.3 m/s

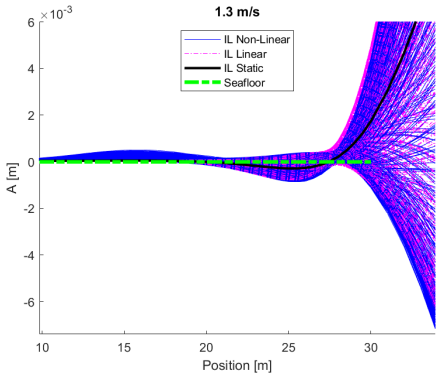

(d) IL - 1.3 m/s (zoom at the left shoulder)

Figure B.64: Comparative snapshots of the calculated responses for the two soil models at 1.3 m/s.

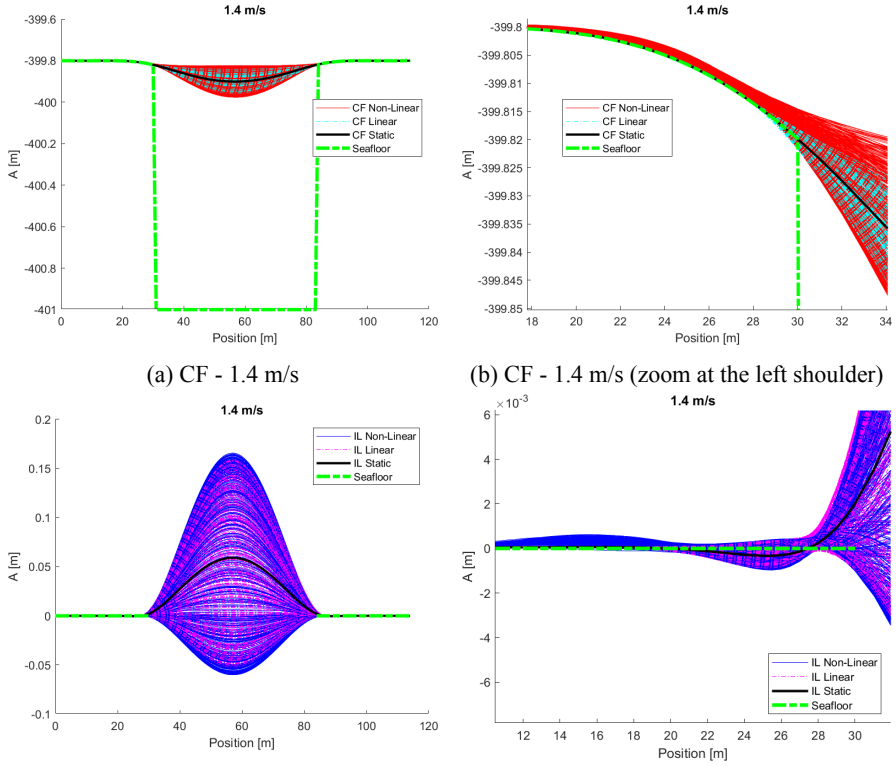

(a) CF - 1.4 m/s

(b) CF - 1.4 m/s (zoom at the left shoulder)

(c) IL - 1.4 m/s

(d) IL - 1.4 m/s (zoom at the left shoulder)

Figure B.65: Comparative snapshots of the calculated responses for the two soil models at 1.4 m/s.

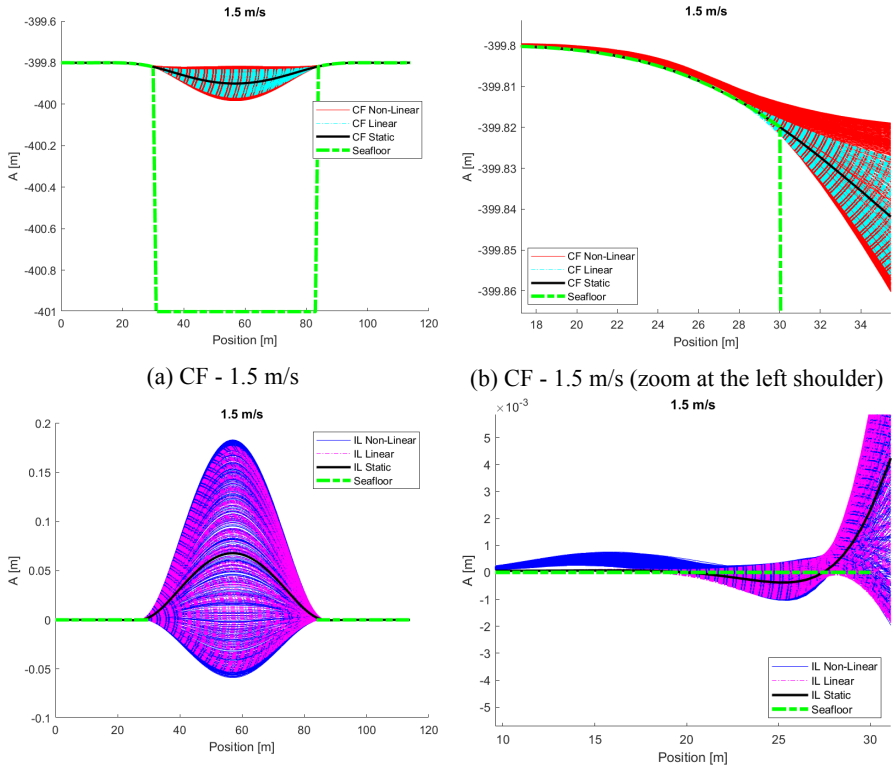

(a) CF - 1.5 m/s

(b) CF - 1.5 m/s (zoom at the left shoulder)

(c) IL - 1.5 m/s

(d) IL - 1.5 m/s (zoom at the left shoulder)

Figure B.66: Comparative snapshots of the calculated responses for the two soil models at 1.5 m/s.

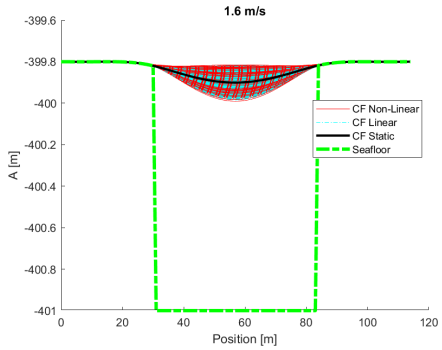

(a) CF - 1.6 m/s

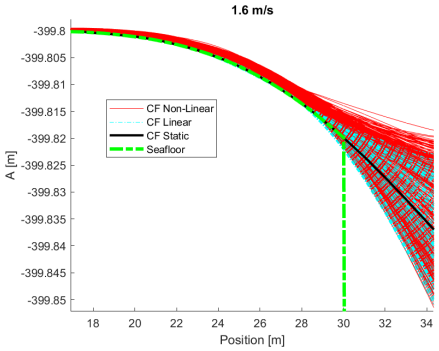

(b) CF - 1.6 m/s (zoom at the left shoulder)

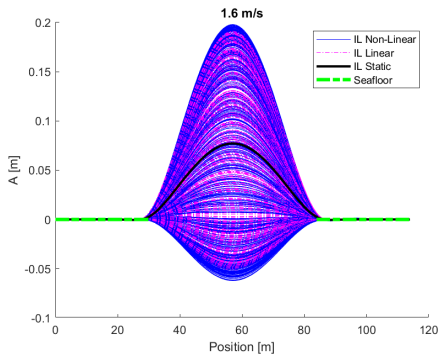

(c) IL - 1.6 m/s

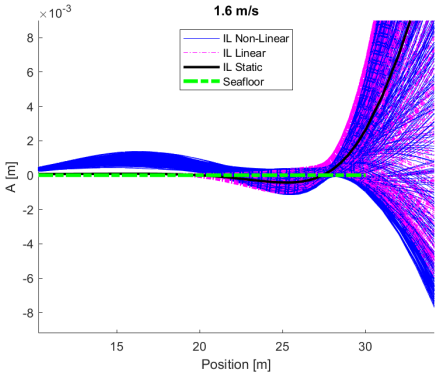

(d) IL - 1.6 m/s (zoom at the left shoulder)

Figure B.67: Comparative snapshots of the calculated responses for the two soil models at 1.6 m/s.

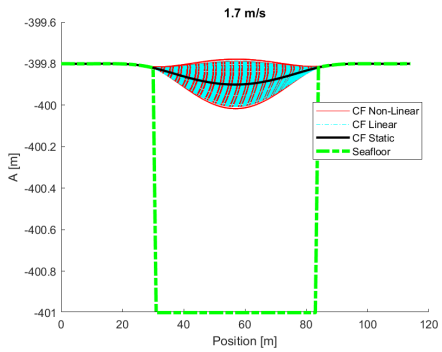

(a) CF - 1.7 m/s

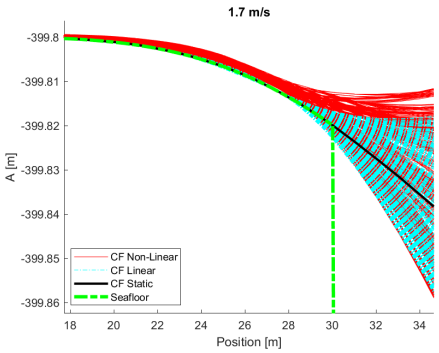

(b) CF - 1.7 m/s (zoom at the left shoulder)

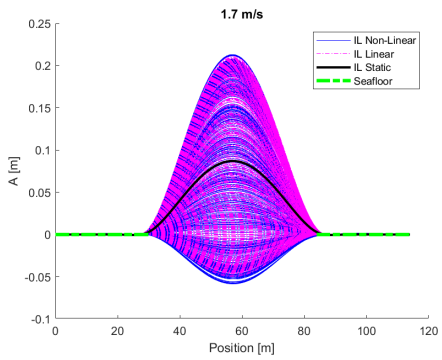

(c) IL - 1.7 m/s

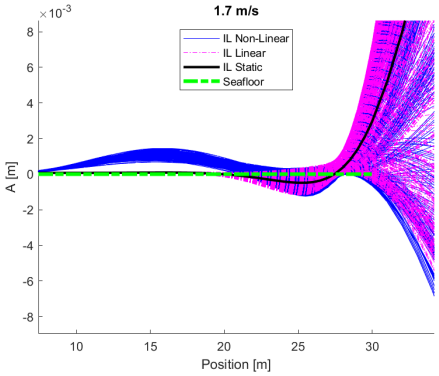

(d) IL - 1.7 m/s (zoom at the left shoulder)

Figure B.68: Comparative snapshots of the calculated responses for the two soil models at 1.7 m/s.

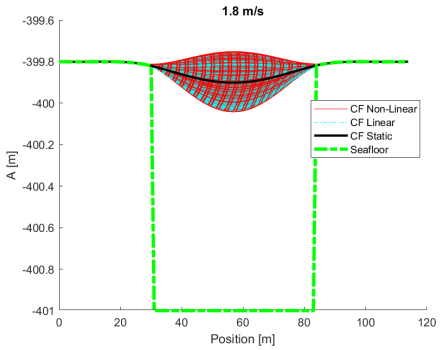

(a) CF - 1.8 m/s

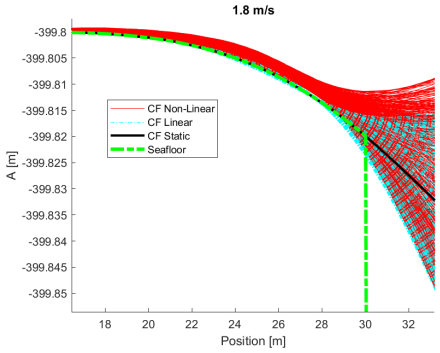

(b) CF - 1.8 m/s (zoom at the left shoulder)

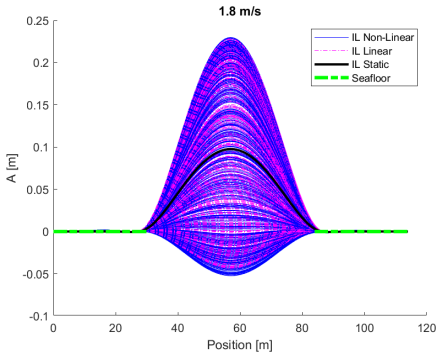

(c) IL - 1.8 m/s

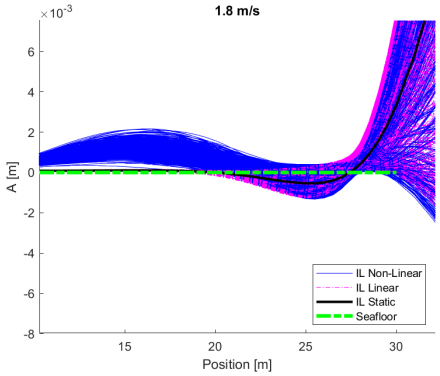

(d) IL - 1.8 m/s (zoom at the left shoulder)

Figure B.69: Comparative snapshots of the calculated responses for the two soil models at 1.8 m/s.

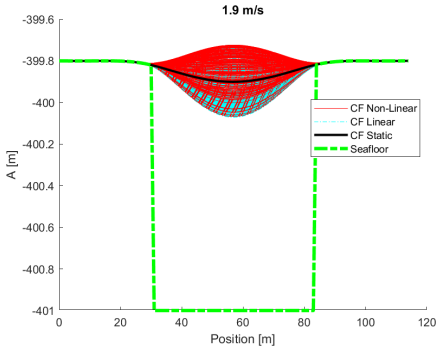

(a) CF - 1.9 m/s

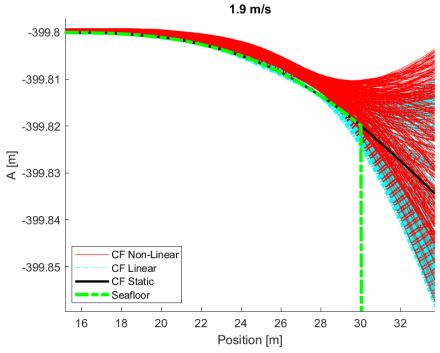

(b) CF - 1.9 m/s (zoom at the left shoulder)

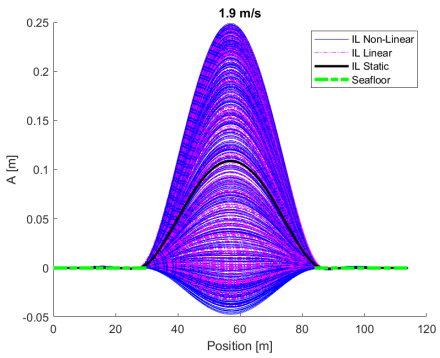

(c) IL - 1.9 m/s

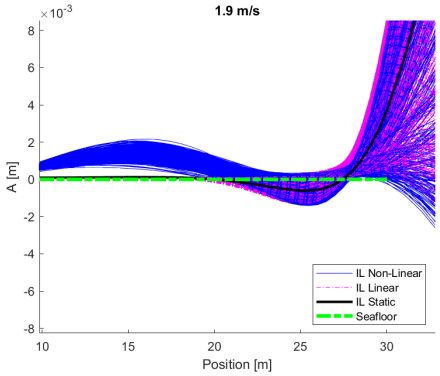

(d) IL - 1.9 m/s (zoom at the left shoulder)

Figure B.70: Comparative snapshots of the calculated responses for the two soil models at 1.9 m/s.

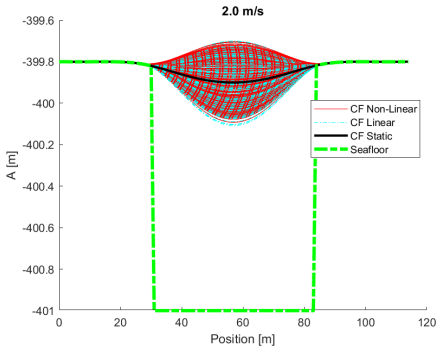

(a) CF - 2.0 m/s

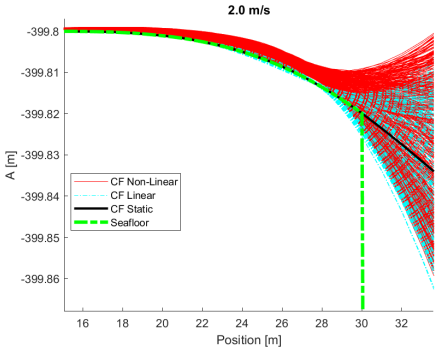

(b) CF - 2.0 m/s (zoom at the left shoulder)

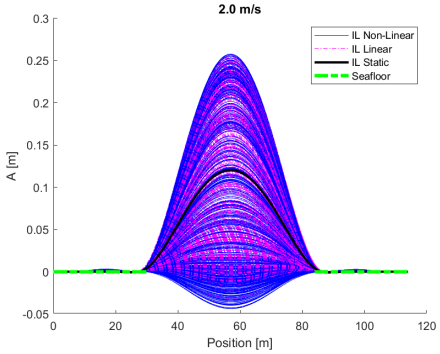

(c) IL - 2.0 m/s

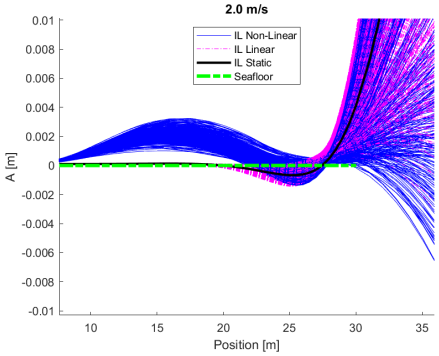

(d) IL - 2.0 m/s (zoom at the left shoulder)

Figure B.71: Comparative snapshots of the calculated responses for the two soil models at 2.0 m/s.

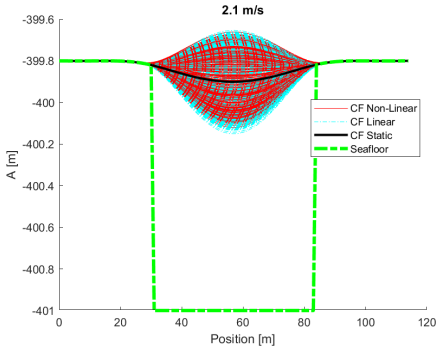

(a) CF - 2.1 m/s

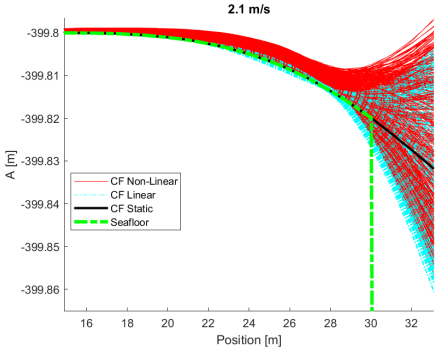

(b) CF - 2.1 m/s (zoom at the left shoulder)

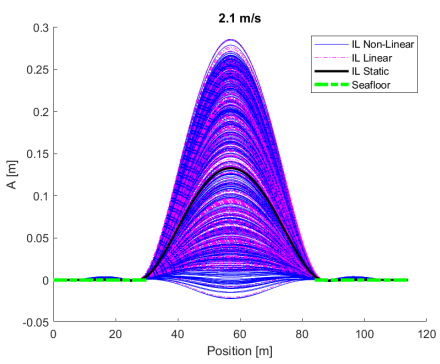

(c) IL - 2.1 m/s

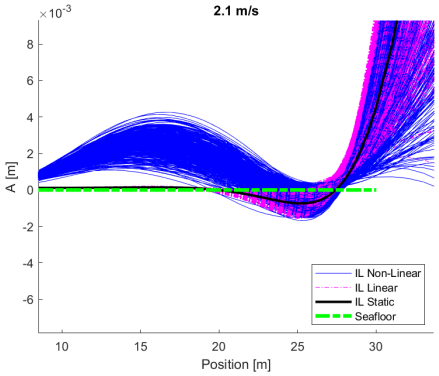

(d) IL - 2.1 m/s (zoom at the left shoulder)

Figure B.72: Comparative snapshots of the calculated responses for the two soil models at 2.1 m/s.

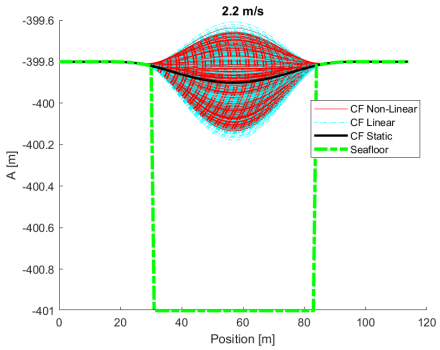

(a) CF - 2.2 m/s

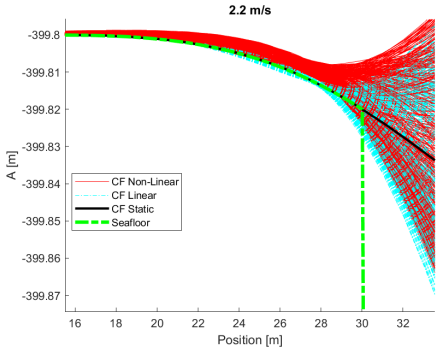

(b) CF - 2.2 m/s (zoom at the left shoulder)

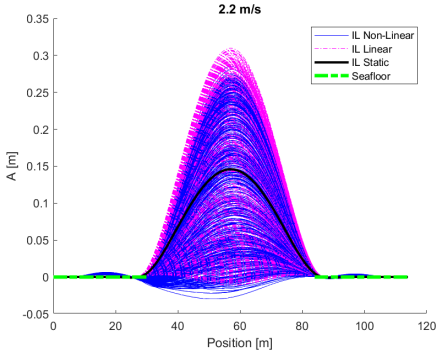

(c) IL - 2.2 m/s

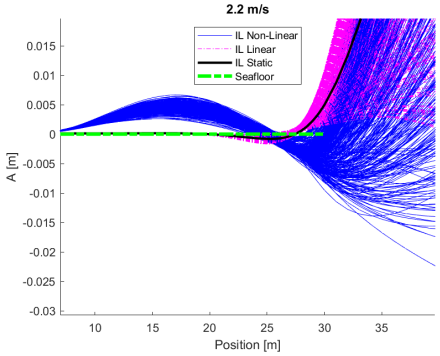

(d) IL - 2.2 m/s (zoom at the left shoulder)

Figure B.73: Comparative snapshots of the calculated responses for the two soil models at 2.2 m/s.

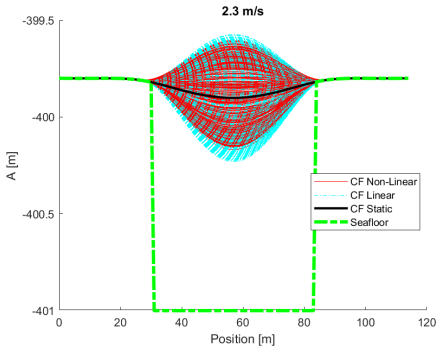

(a) CF - 2.3 m/s

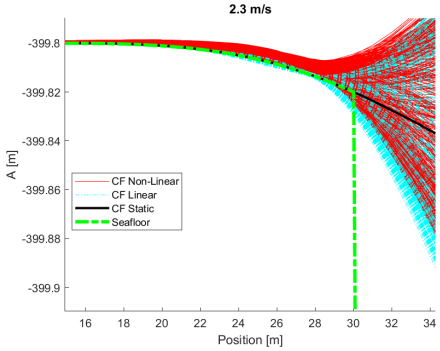

(b) CF - 2.3 m/s (zoom at the left shoulder)

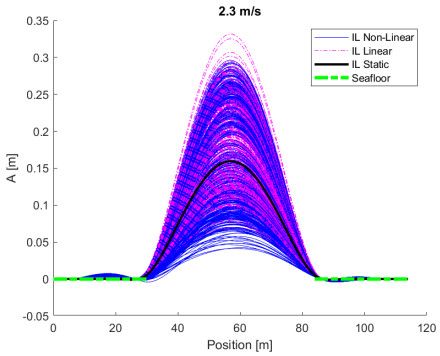

(c) IL - 2.3 m/s

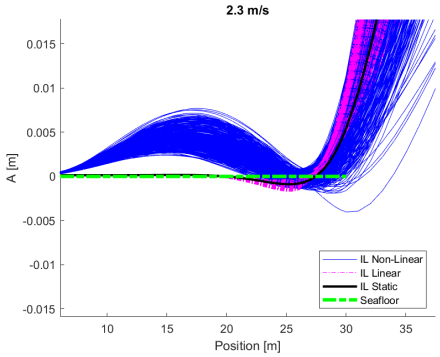

(d) IL - 2.3 m/s (zoom at the left shoulder)

Figure B.74: Comparative snapshots of the calculated responses for the two soil models at 2.3 m/s.

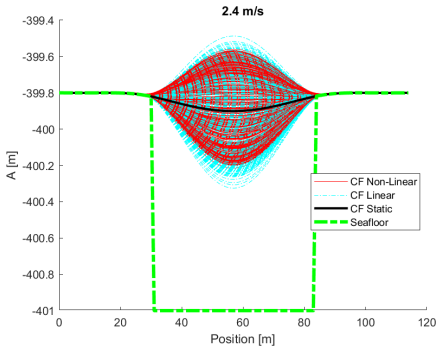

(a) CF - 2.4 m/s

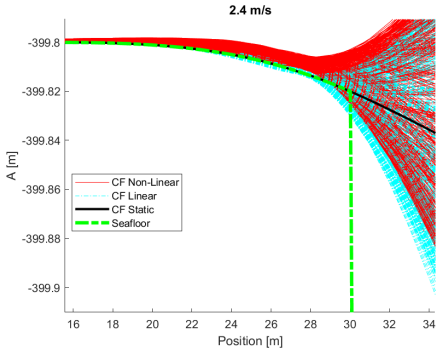

(b) CF - 2.4 m/s (zoom at the left shoulder)

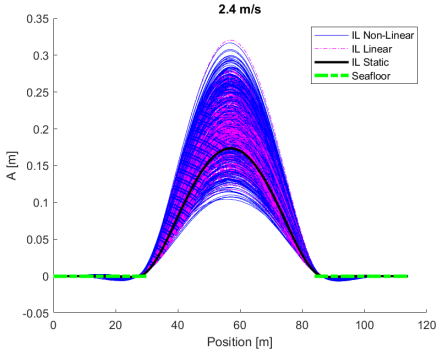

(c) IL - 2.4 m/s

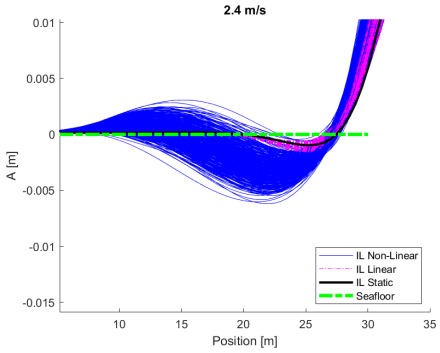

(d) IL - 2.4 m/s (zoom at the left shoulder)

Figure B.75: Comparative snapshots of the calculated responses for the two soil models at 2.4 m/s.

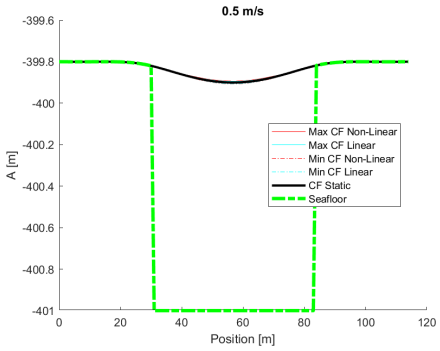

(a) CF - 0.5 m/s

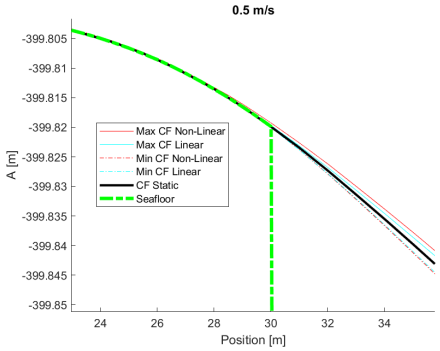

(b) CF - 0.5 m/s (zoom at the left shoulder)

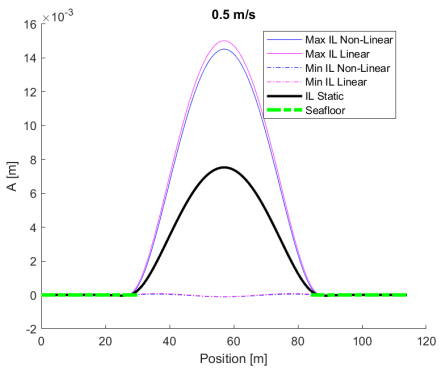

(c) IL - 0.5 m/s

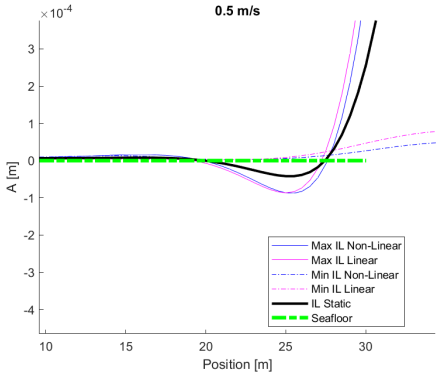

(d) IL - 0.5 m/s (zoom at the left shoulder)

Figure B.76: Comparative snapshots of the max and min responses for the two soil models at 0.5 m/s.

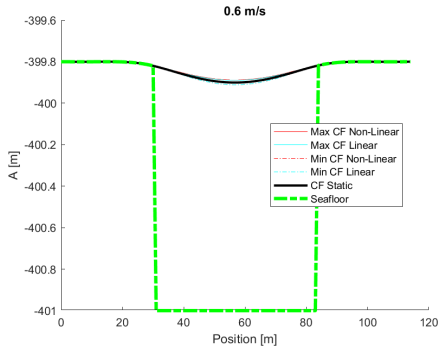

(a) CF - 0.6 m/s

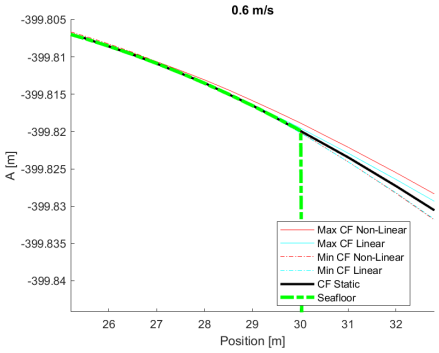

(b) CF - 0.6 m/s (zoom at the left shoulder)

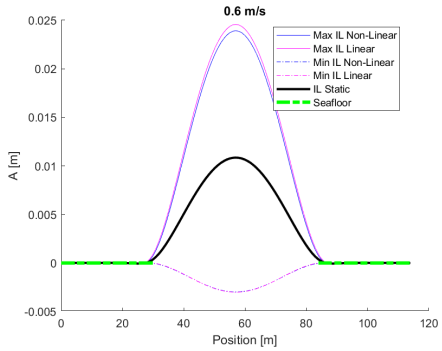

(c) IL - 0.6 m/s

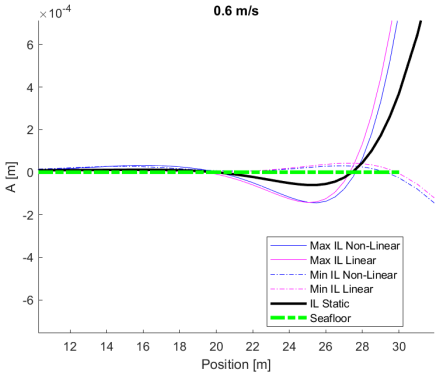

(d) IL - 0.6 m/s (zoom at the left shoulder)

Figure B.77: Comparative snapshots of the max and min responses for the two soil models at 0.6 m/s.

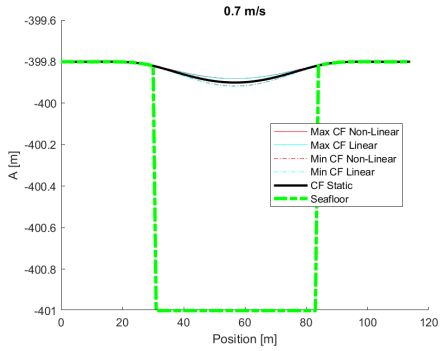

(a) CF - 0.7 m/s

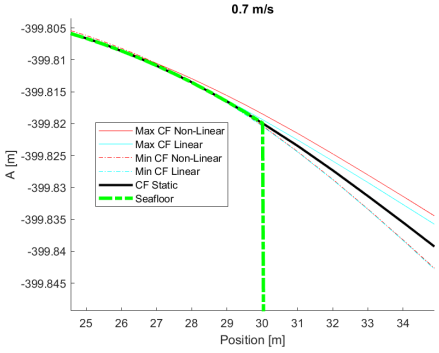

(b) CF - 0.7 m/s (zoom at the left shoulder)

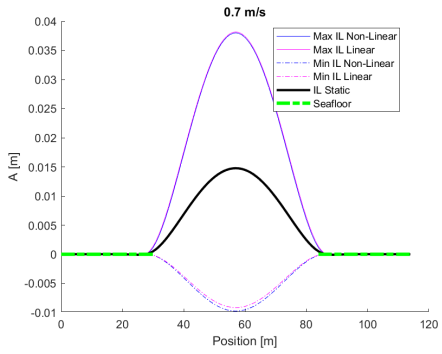

(c) IL - 0.7 m/s

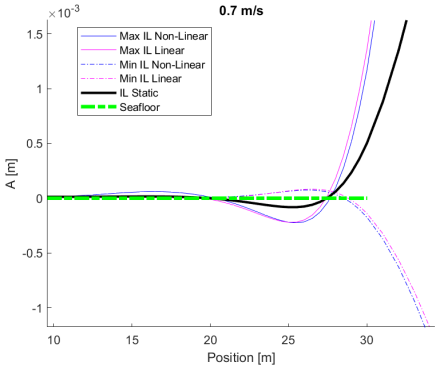

(d) IL - 0.7 m/s (zoom at the left shoulder)

Figure B.78: Comparative snapshots of the max and min responses for the two soil models at 0.7 m/s.

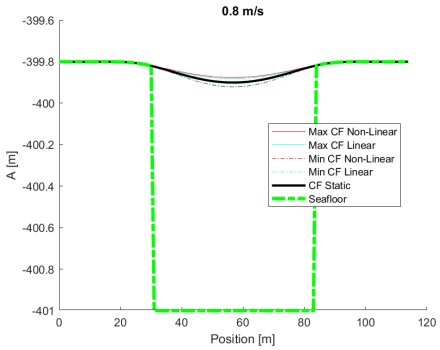

(a) CF - 0.8 m/s

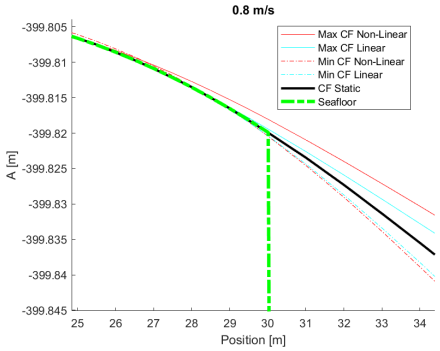

(b) CF - 0.8 m/s (zoom at the left shoulder)

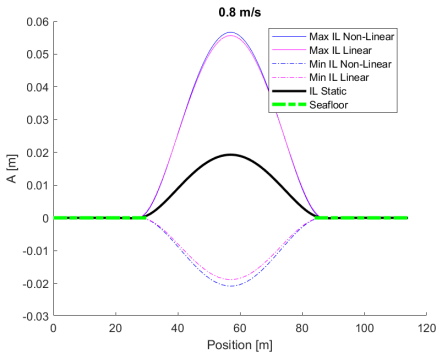

(c) IL - 0.8 m/s

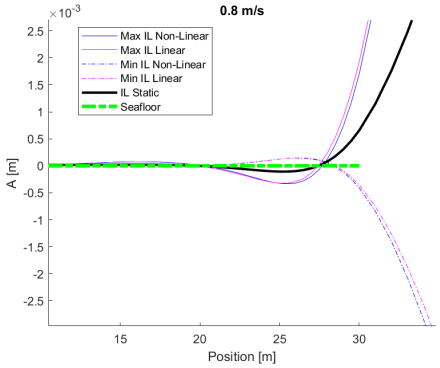

(d) IL - 0.8 m/s (zoom at the left shoulder)

Figure B.79: Comparative snapshots of the max and min responses for the two soil models at 0.8 m/s.

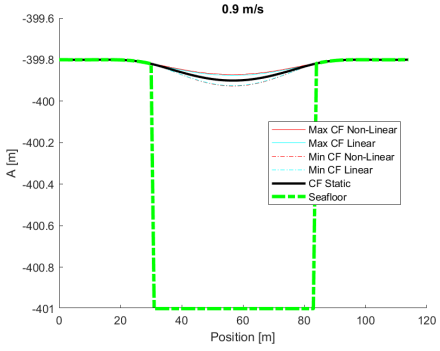

(a) CF - 0.9 m/s

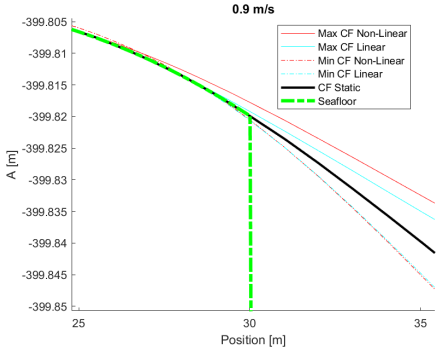

(b) CF - 0.9 m/s (zoom at the left shoulder)

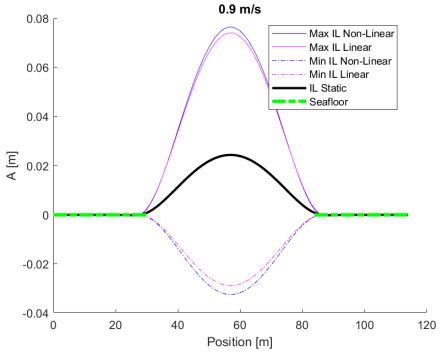

(c) IL - 0.9 m/s

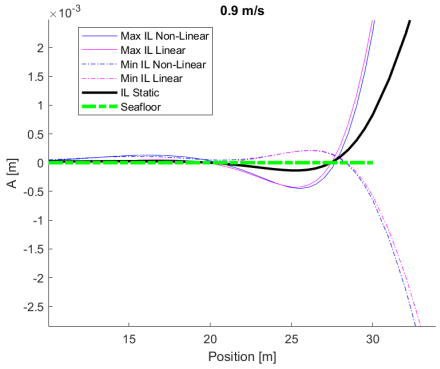

(d) IL - 0.9 m/s (zoom at the left shoulder)

Figure B.80: Comparative snapshots of the max and min responses for the two soil models at 0.9 m/s.

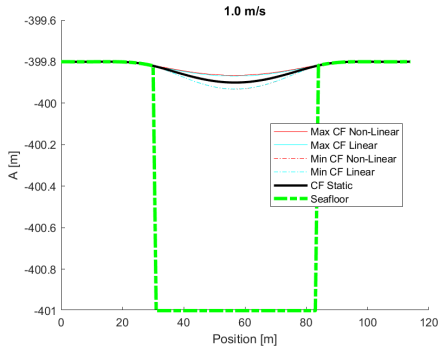

(a) CF - 1.0 m/s

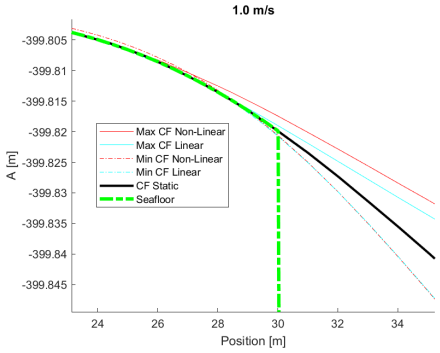

(b) CF - 1.0 m/s (zoom at the left shoulder)

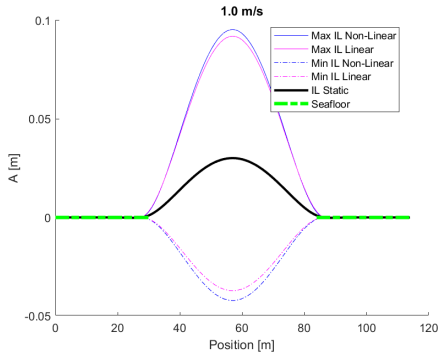

(c) IL - 1.0 m/s

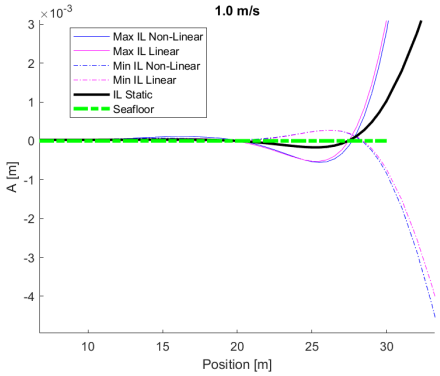

(d) IL - 1.0 m/s (zoom at the left shoulder)

Figure B.81: Comparative snapshots of the max and min responses for the two soil models at 1.0 m/s.

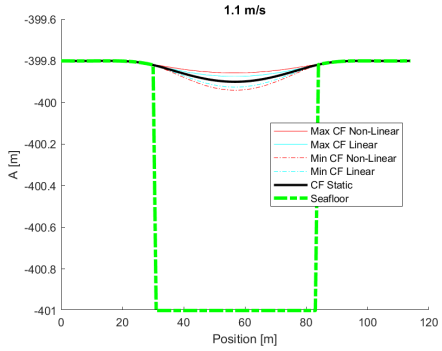

(a) CF - 1.1 m/s

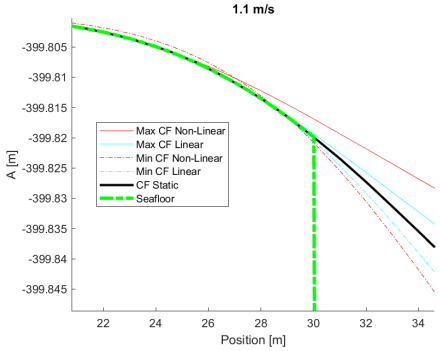

(b) CF - 1.1 m/s (zoom at the left shoulder)

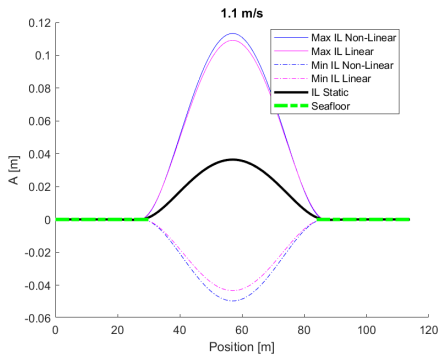

(c) IL - 1.1 m/s

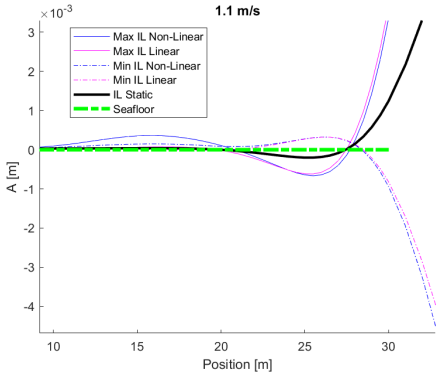

(d) IL - 1.1 m/s (zoom at the left shoulder)

Figure B.82: Comparative snapshots of the max and min responses for the two soil models at 1.1 m/s.

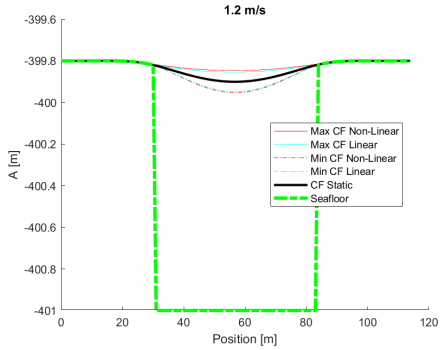

(a) CF - 1.2 m/s

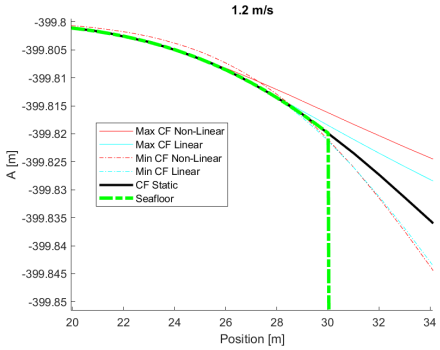

(b) CF - 1.2 m/s (zoom at the left shoulder)

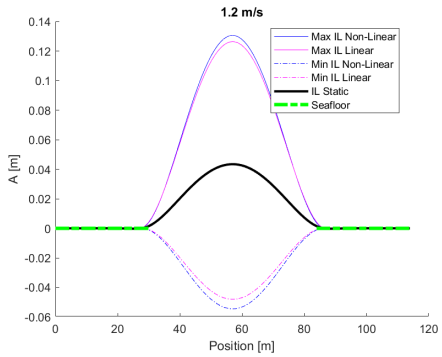

(c) IL - 1.2 m/s

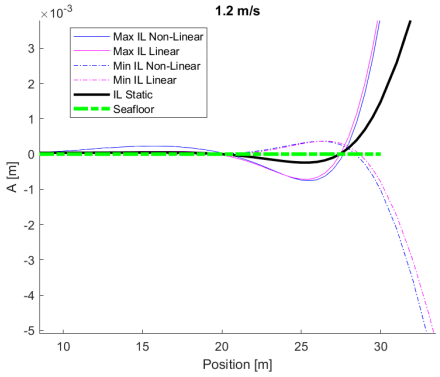

(d) IL - 1.2 m/s (zoom at the left shoulder)

Figure B.83: Comparative snapshots of the max and min responses for the two soil models at 1.2 m/s.

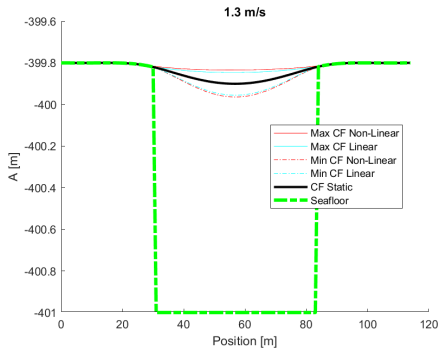

(a) CF - 1.3 m/s

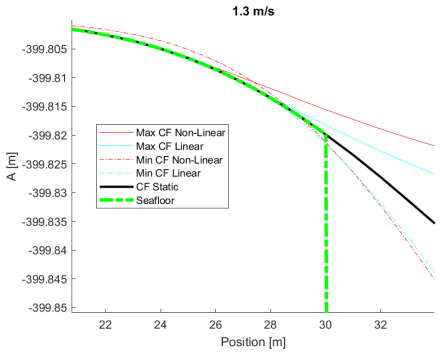

(b) CF - 1.3 m/s (zoom at the left shoulder)

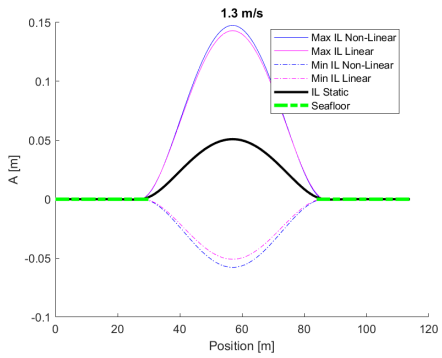

(c) IL - 1.3 m/s

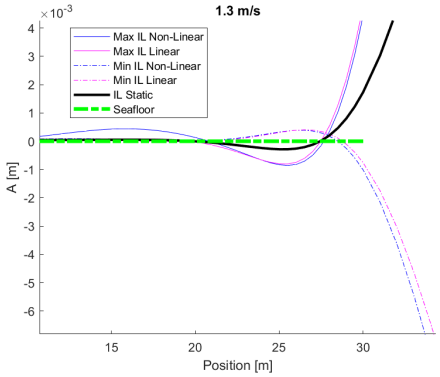

(d) IL - 1.3 m/s (zoom at the left shoulder)

Figure B.84: Comparative snapshots of the max and min responses for the two soil models at 1.3 m/s.

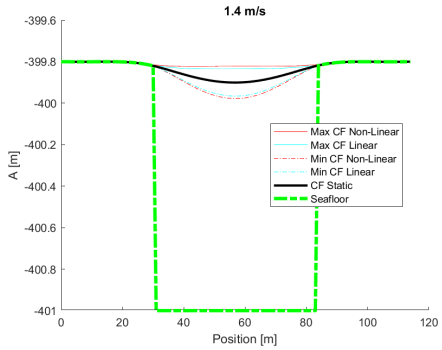

(a) CF - 1.4 m/s

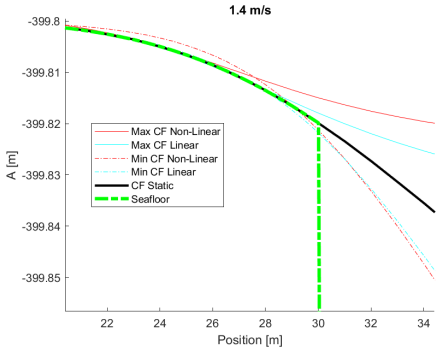

(b) CF - 1.4 m/s (zoom at the left shoulder)

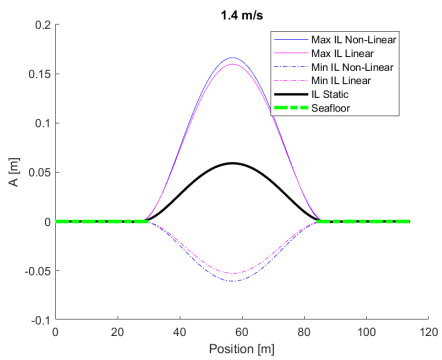

(c) IL - 1.4 m/s

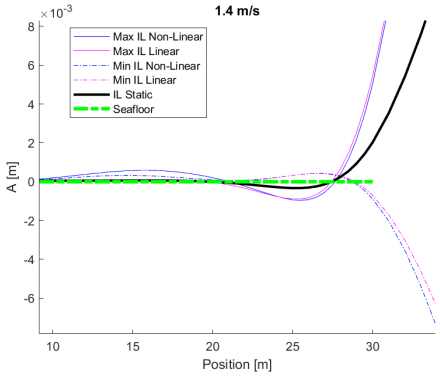

(d) IL - 1.4 m/s (zoom at the left shoulder)

Figure B.85: Comparative snapshots of the max and min responses for the two soil models at 1.4 m/s.

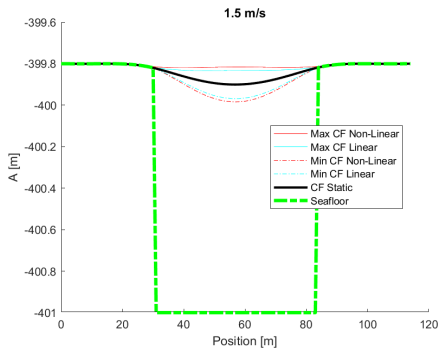

(a) CF - 1.5 m/s

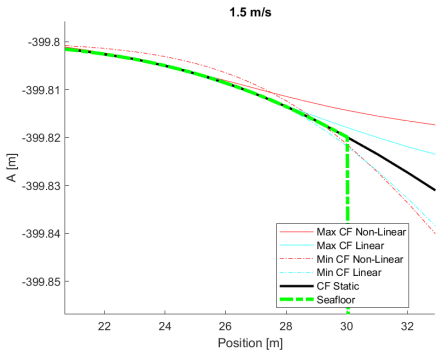

(b) CF - 1.5 m/s (zoom at the left shoulder)

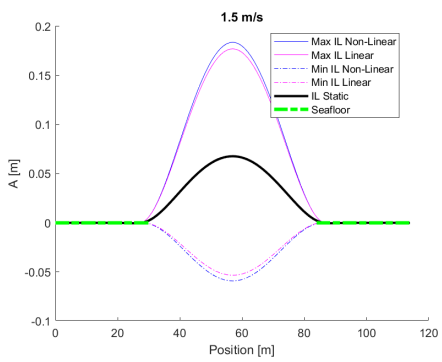

(c) IL - 1.5 m/s

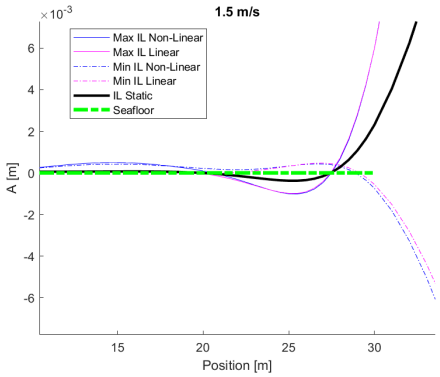

(d) IL - 1.5 m/s (zoom at the left shoulder)

Figure B.86: Comparative snapshots of the max and min responses for the two soil models at 1.5 m/s.

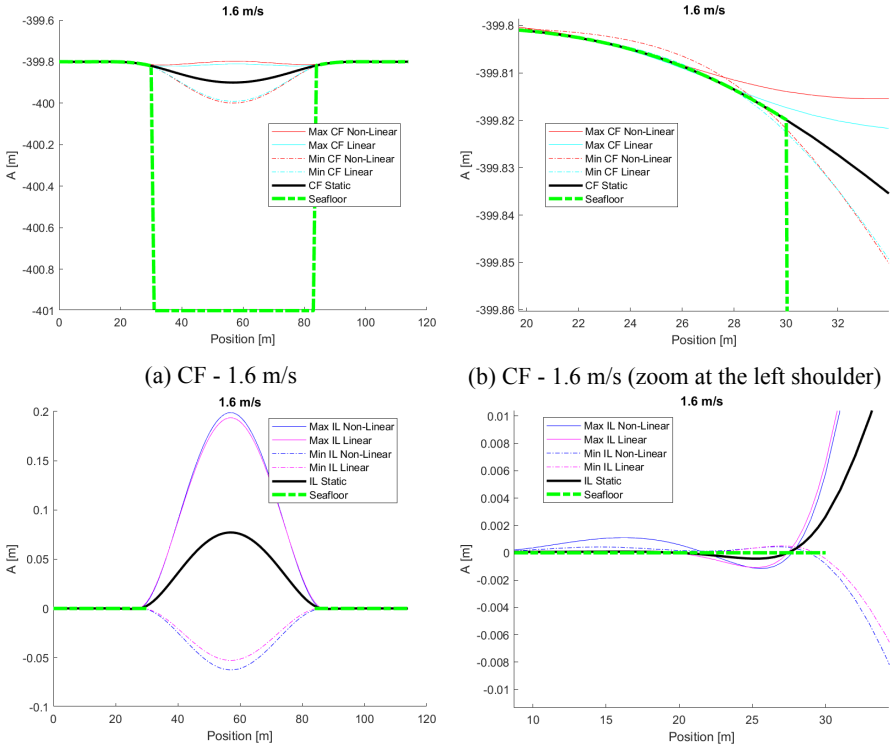

(a) CF - 1.6 m/s (b) CF - 1.6 m/s (zoom at the left shoulder)

(c) IL - 1.6 m/s (d) IL - 1.6 m/s (zoom at the left shoulder)

Figure B.87: Comparative snapshots of the max and min responses for the two soil models at 1.6 m/s.

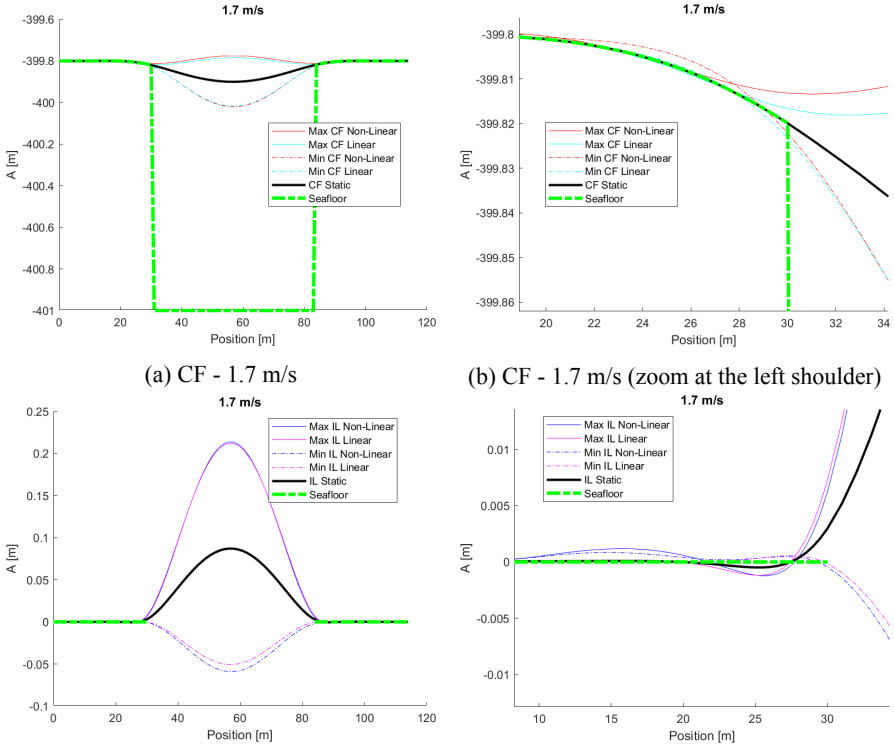

(a) CF - 1.7 m/s (b) CF - 1.7 m/s (zoom at the left shoulder)

(c) IL - 1.7 m/s (d) IL - 1.7 m/s (zoom at the left shoulder)

Figure B.88: Comparative snapshots of the max and min responses for the two soil models at 1.7 m/s.

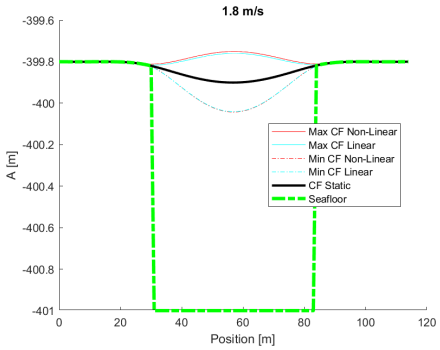

(a) CF - 1.8 m/s

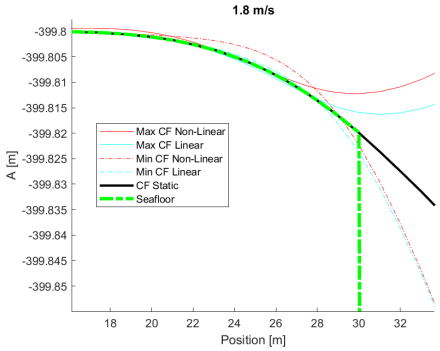

(b) CF - 1.8 m/s (zoom at the left shoulder)

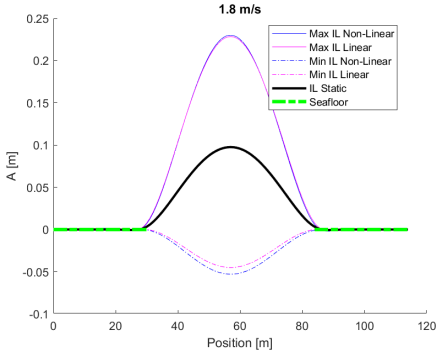

(c) IL - 1.8 m/s

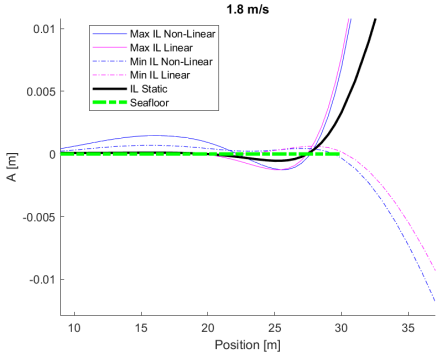

(d) IL - 1.8 m/s (zoom at the left shoulder)

Figure B.89: Comparative snapshots of the max and min responses for the two soil models at 1.8 m/s.

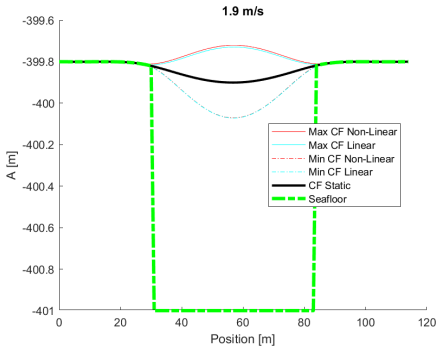

(a) CF - 1.9 m/s

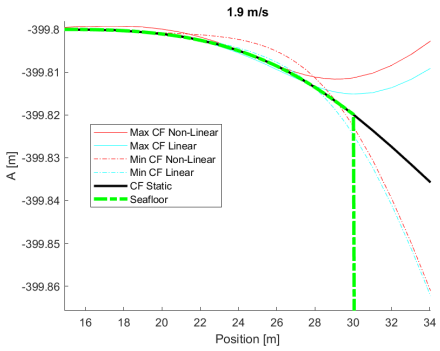

(b) CF - 1.9 m/s (zoom at the left shoulder)

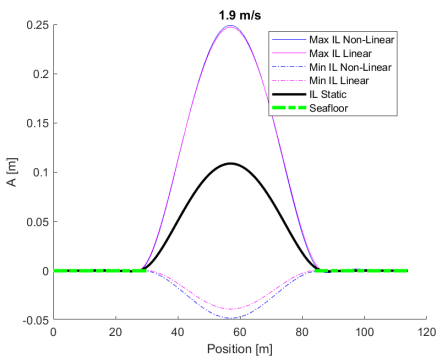

(c) IL - 1.9 m/s

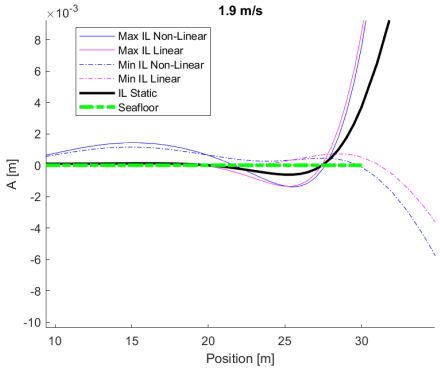

(d) IL - 1.9 m/s (zoom at the left shoulder)

Figure B.90: Comparative snapshots of the max and min responses for the two soil models at 1.9 m/s.

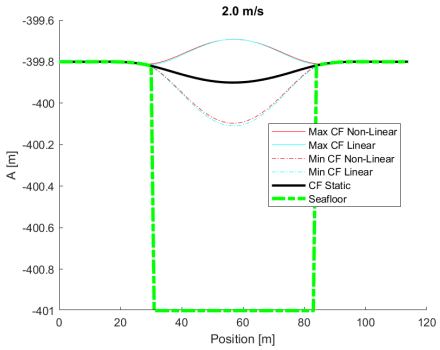

(a) CF - 2.0 m/s

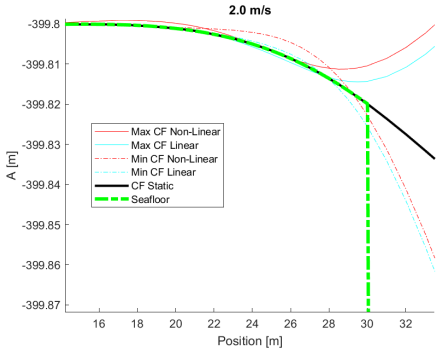

(b) CF - 2.0 m/s (zoom at the left shoulder)

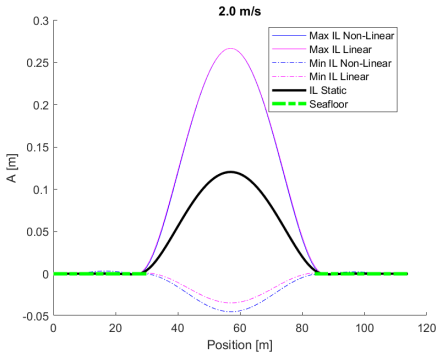

(c) IL - 2.0 m/s

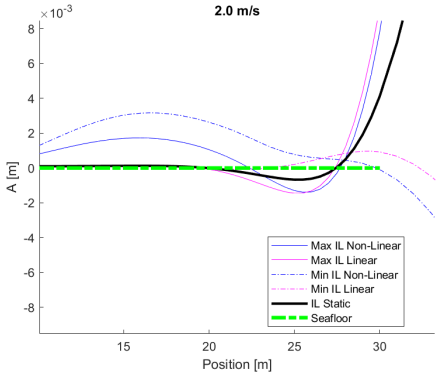

(d) IL - 2.0 m/s (zoom at the left shoulder)

Figure B.91: Comparative snapshots of the max and min responses for the two soil models at 2.0 m/s.

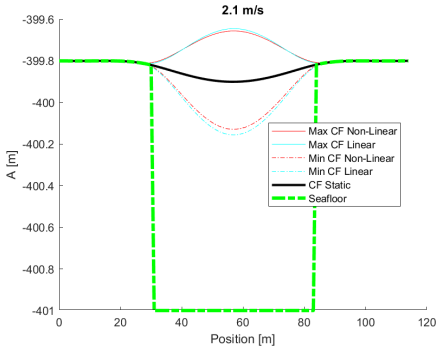

(a) CF - 2.1 m/s

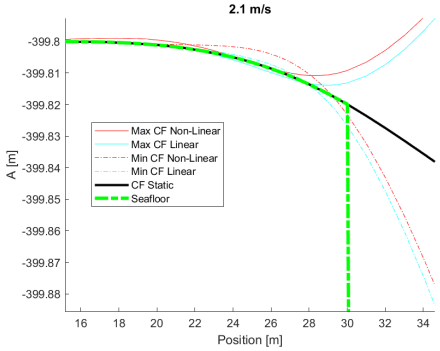

(b) CF - 2.1 m/s (zoom at the left shoulder)

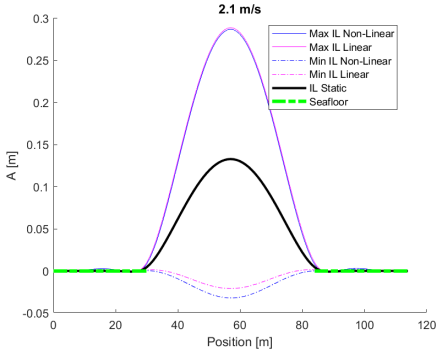

(c) IL - 2.1 m/s

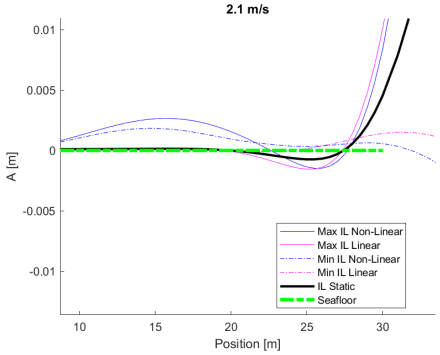

(d) IL - 2.1 m/s (zoom at the left shoulder)

Figure B.92: Comparative snapshots of the max and min responses for the two soil models at 2.1 m/s.

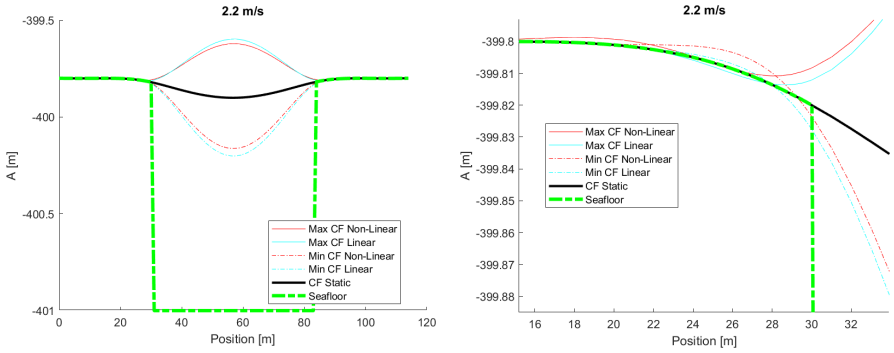

(a) CF - 2.2 m/s

(b) CF - 2.2 m/s (zoom at the left shoulder)

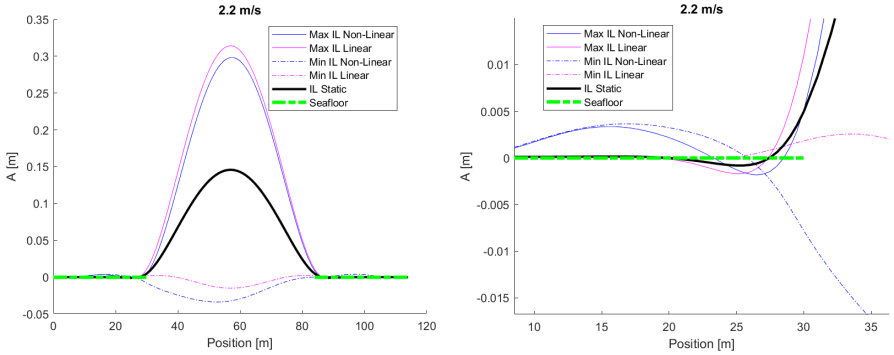

(c) IL - 2.2 m/s

(d) IL - 2.2 m/s (zoom at the left shoulder)

Figure B.93: Comparative snapshots of the max and min responses for the two soil models at 2.2 m/s.

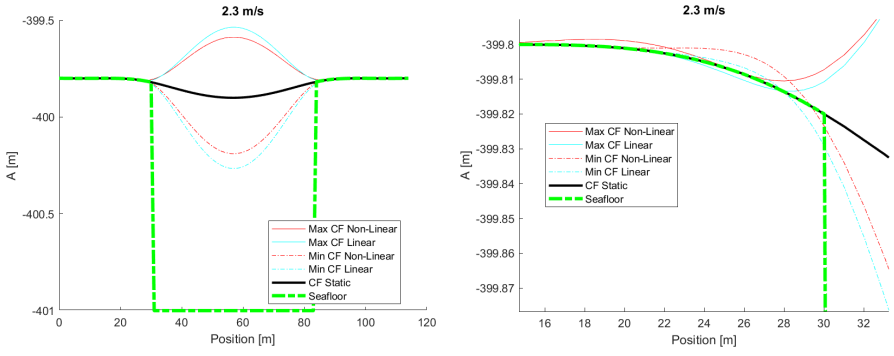

(a) CF - 2.3 m/s

(b) CF - 2.3 m/s (zoom at the left shoulder)

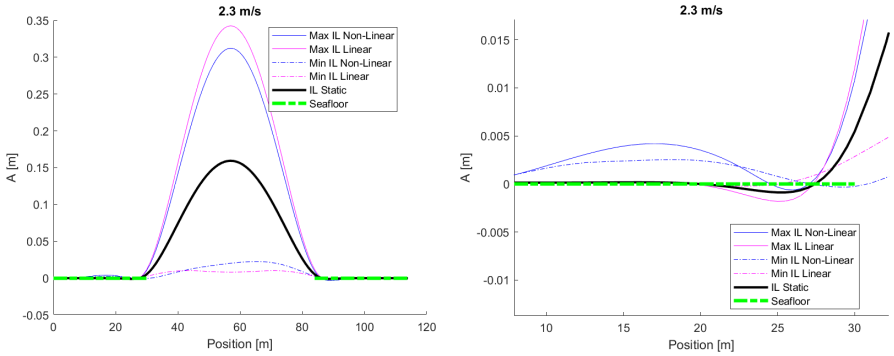

(c) IL - 2.3 m/s

(d) IL - 2.3 m/s (zoom at the left shoulder)

Figure B.94: Comparative snapshots of the max and min responses for the two soil models at 2.3 m/s.

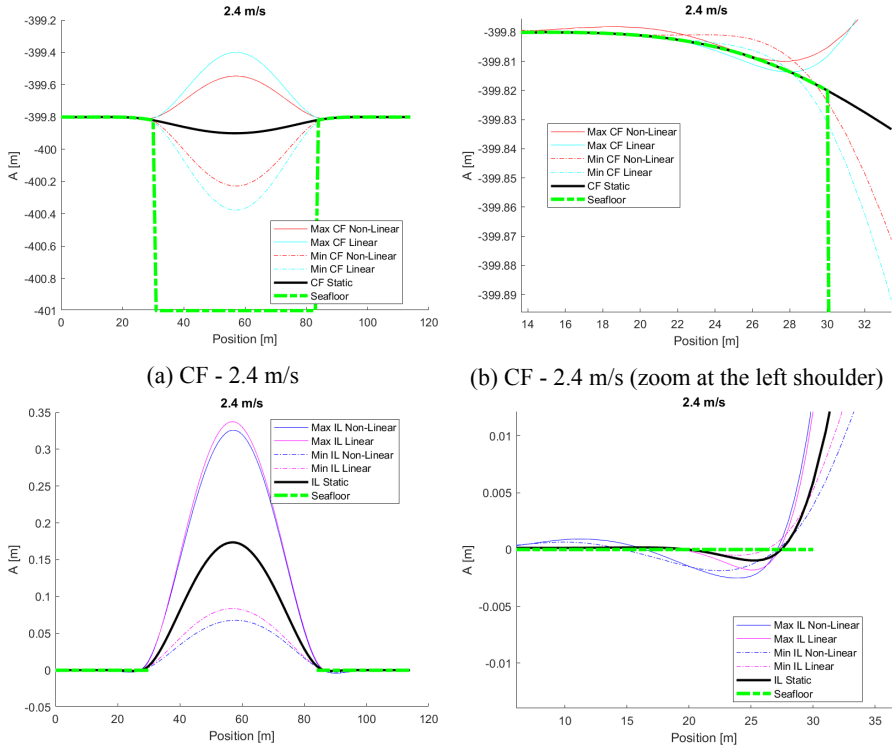

(a) CF - 2.4 m/s

(b) CF - 2.4 m/s (zoom at the left shoulder)

(c) IL - 2.4 m/s

(d) IL - 2.4 m/s (zoom at the left shoulder)

Figure B.95: Comparative snapshots of the max and min responses for the two soil models at 2.4 m/s.

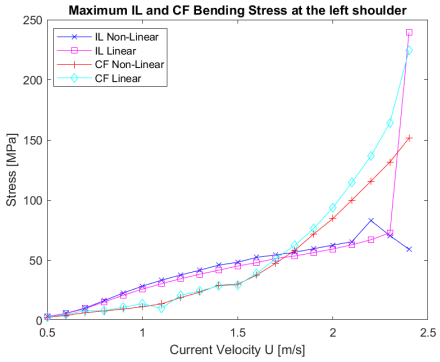

(a) Maximum Bending Stress at the left shoulder

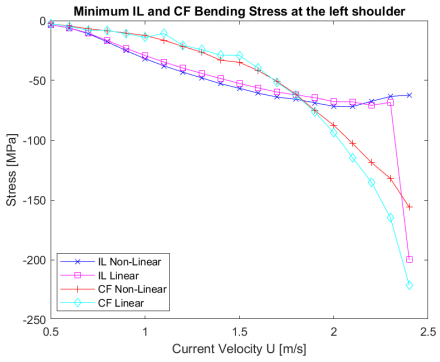

(b) Minimum Bending Stress at the left shoulder

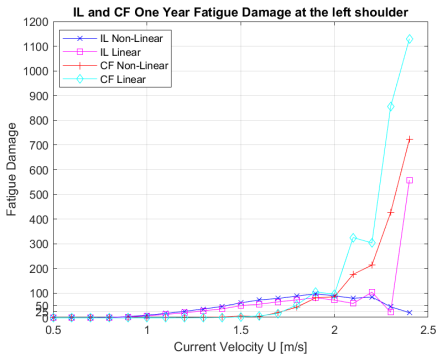

(c) Fatigue Damage Accumulation at the left shoulder

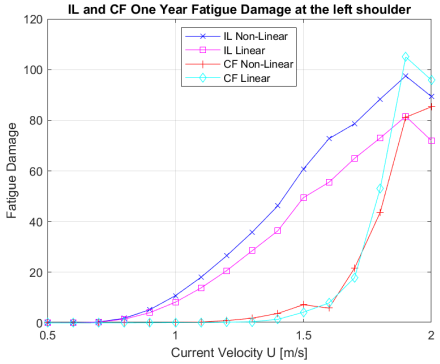

(d) Fatigue Damage Accumulation at the left shoulder (zoom at velocities up to 2.0 m/s)

Figure B.96: Comparative plots of the calculated Bending Stress and Fatigue Damage at the left shoulder.

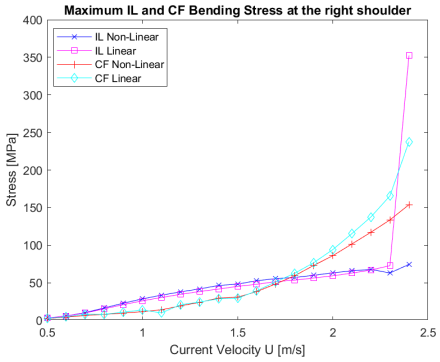

(a) Maximum Bending Stress at the right shoulder

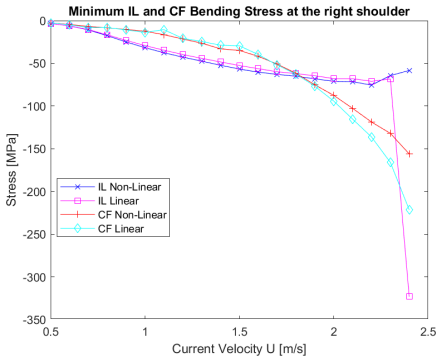

(b) Minimum Bending Stress at the right shoulder

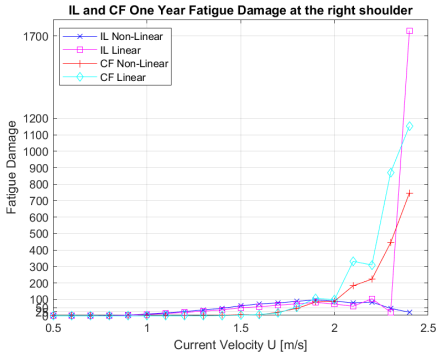

(c) Fatigue Damage Accumulation at the right shoulder

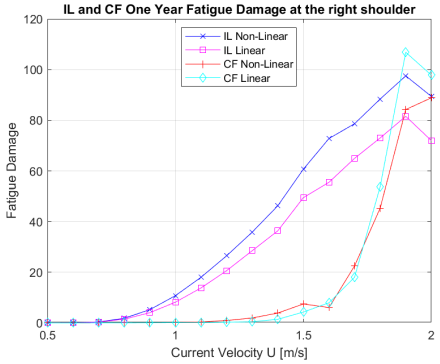

(d) Fatigue Damage Accumulation at the right shoulder (zoom at velocities up to 2.0 m/s)

Figure B.97: Comparative plots of the calculated Bending Stress and Fatigue Damage at the right shoulder.

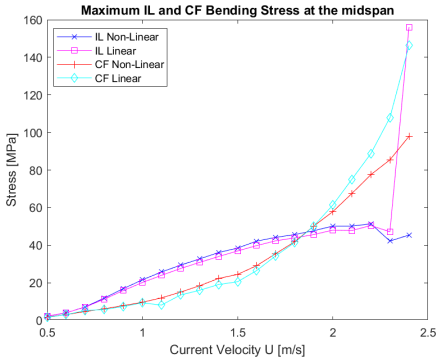

(a) Maximum Bending Stress at the midspan

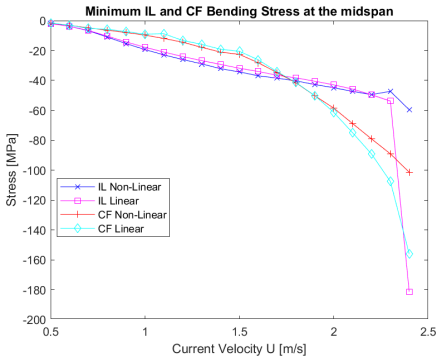

(b) Minimum Bending Stress at the midspan

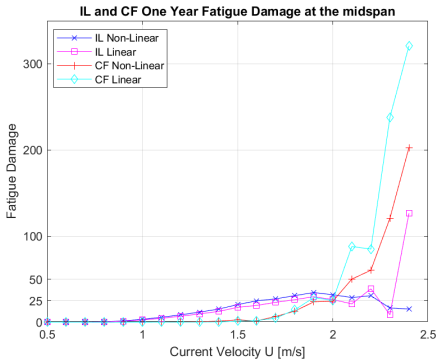

(c) Fatigue Damage Accumulation at the midspan

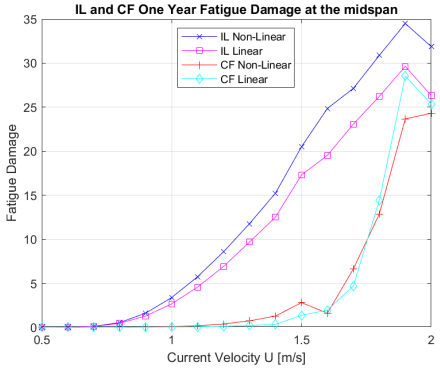

(d) Fatigue Damage Accumulation at the midspan (zoom at velocities up to 2.0 m/s)

Figure B.98: Comparative plots of the calculated Bending Stress and Fatigue Damage at the midspan.

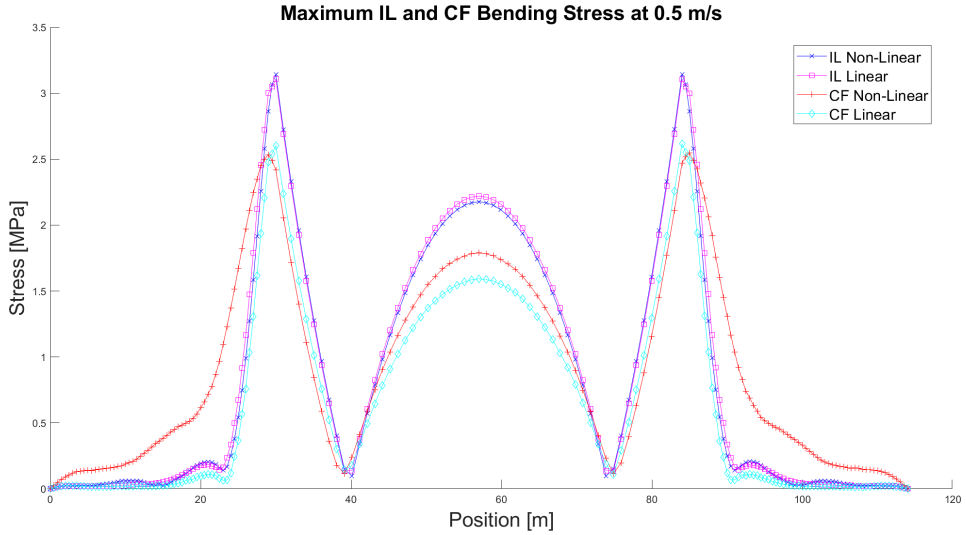

(a) CF and IL Maximum Bending Stress Distribution at 0.5 m/s

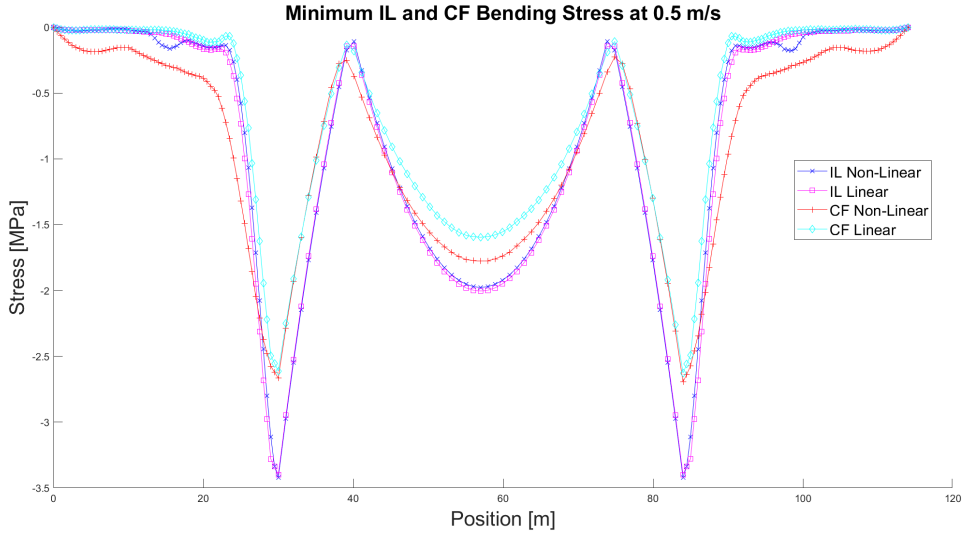

(b) CF and IL Minimum Bending Stress Distribution at 0.5 m/s

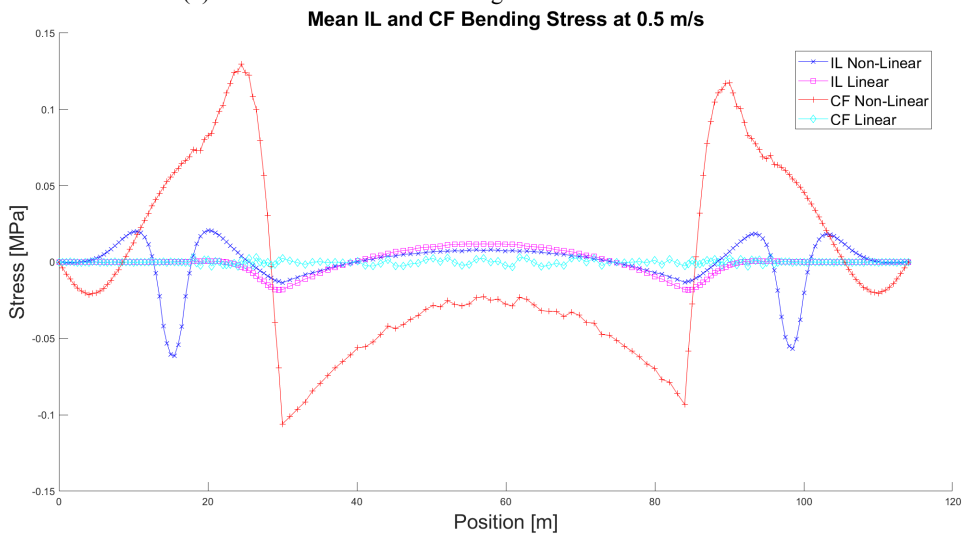

(c) CF and IL Mean Bending Stress Distribution at 0.5 m/s

Figure B.99: Comparative plots of the calculated bending stress distribution for the two soil models and $\zeta_{soil} = 22\%$ at 0.5 m/s.

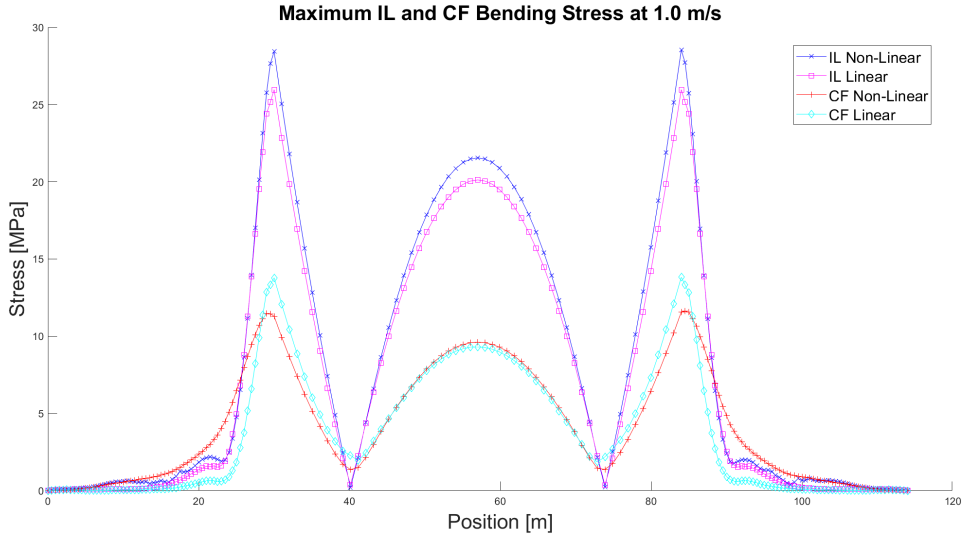

(a) CF and IL Maximum Bending Stress Distribution at 1.0 m/s

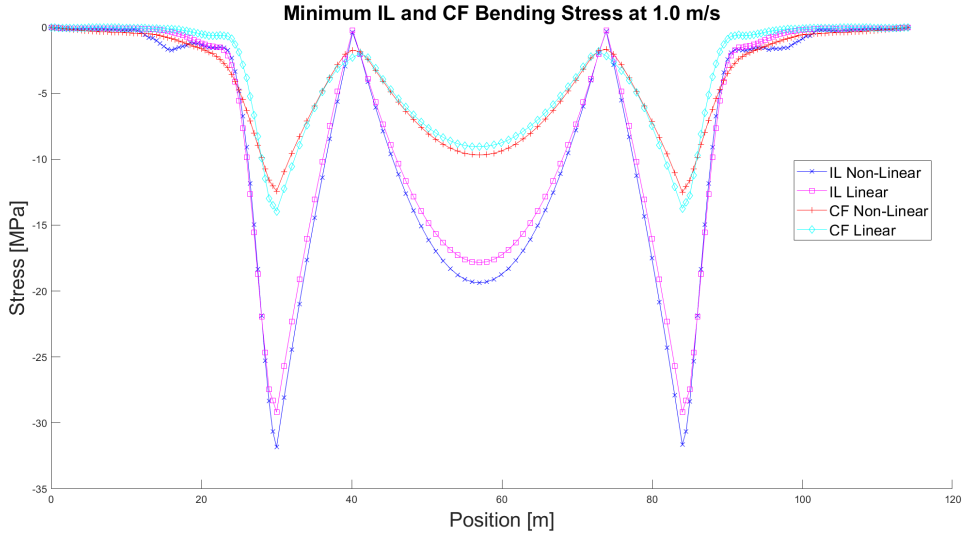

(b) CF and IL Minimum Bending Stress Distribution at 1.0 m/s

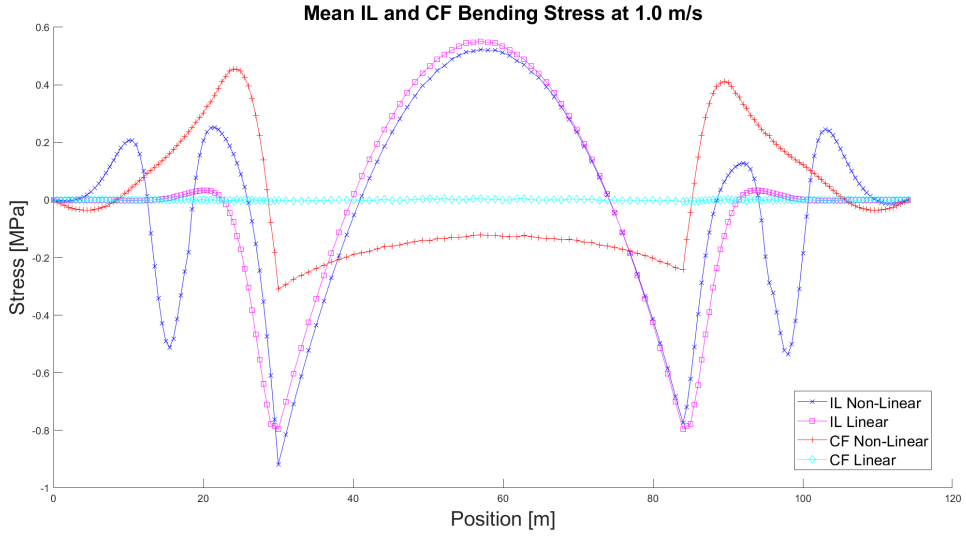

(c) CF and IL Mean Bending Stress Distribution at 1.0 m/s

Figure B.100: Comparative plots of the calculated bending stress distribution for the two soil models and $\zeta_{soil} = 22\%$ at 1.0 m/s.

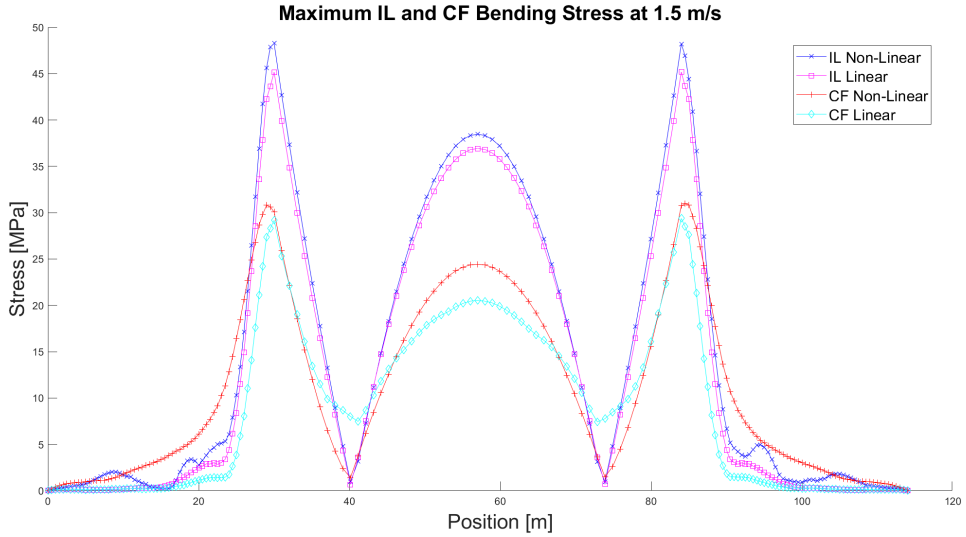

(a) CF and IL Maximum Bending Stress Distribution at 1.5 m/s

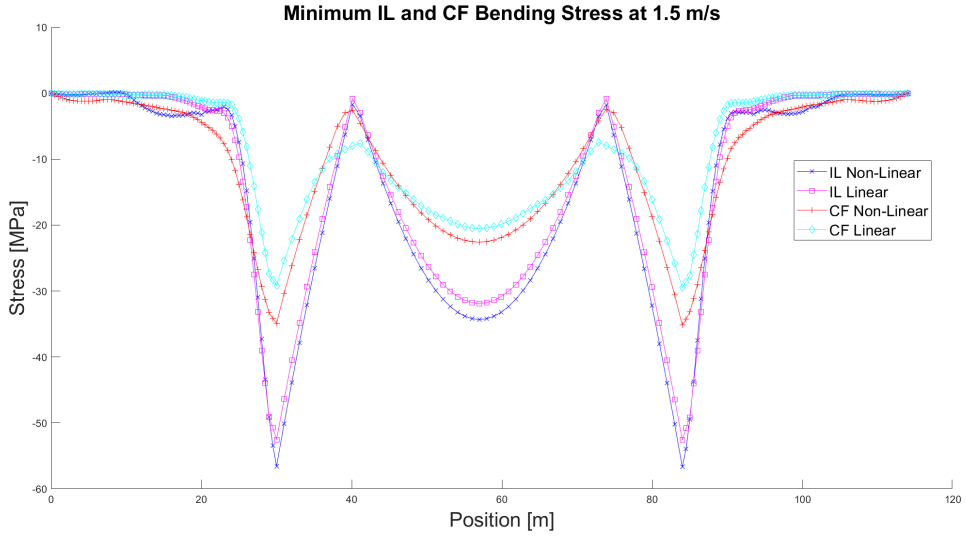

(b) CF and IL Minimum Bending Stress Distribution at 1.5 m/s

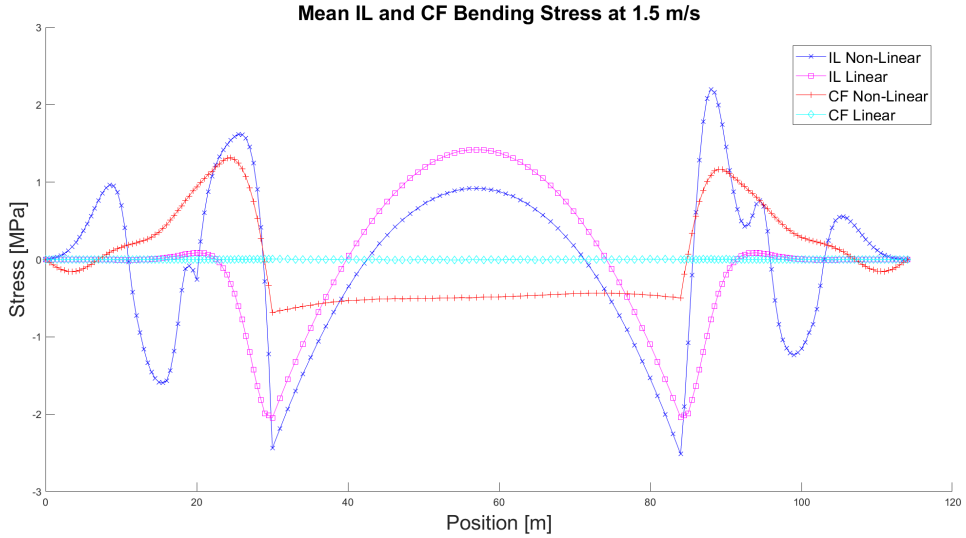

(c) CF and IL Mean Bending Stress Distribution at 1.5 m/s

Figure B.101: Comparative plots of the calculated bending stress distribution for the two soil models and $\zeta_{soil} = 22\%$ at 1.5 m/s.

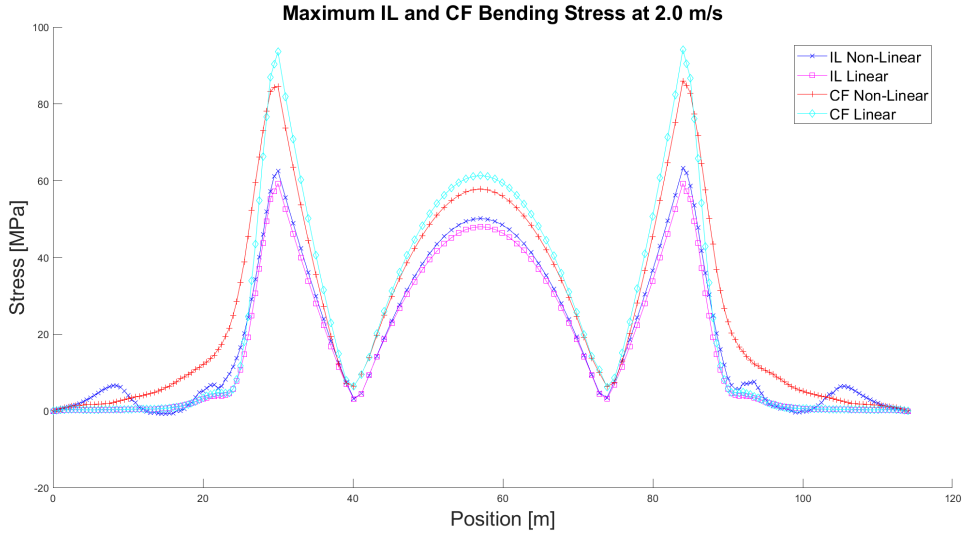

(a) CF and IL Maximum Bending Stress Distribution at 2.0 m/s

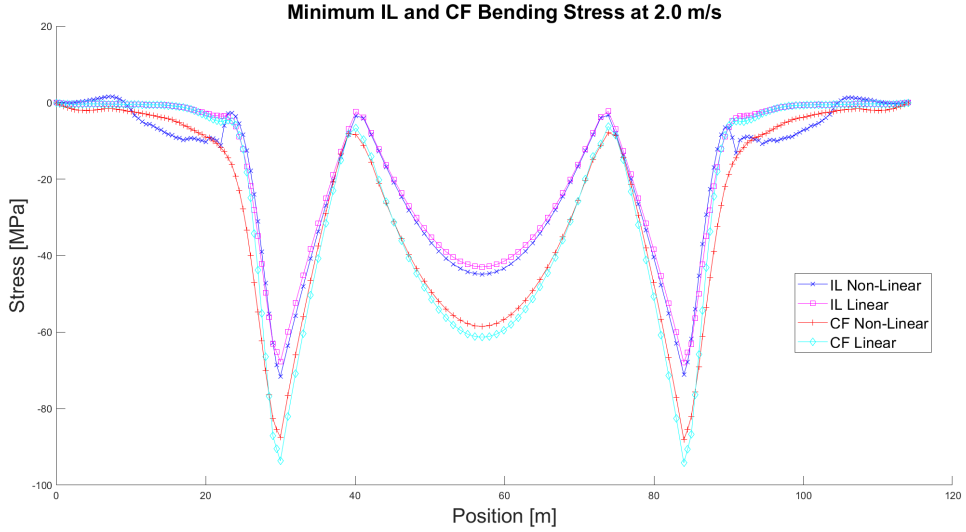

(b) CF and IL Minimum Bending Stress Distribution at 2.0 m/s

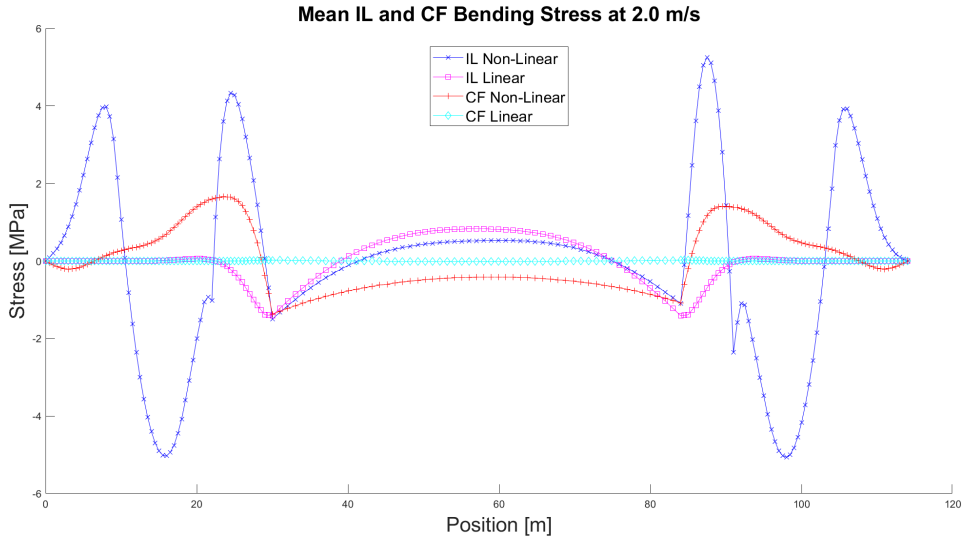

(c) CF and IL Mean Bending Stress Distribution at 2.0 m/s

Figure B.102: Comparative plots of the calculated bending stress distribution for the two soil models and $\zeta_{soil} = 22\%$ at 2.0 m/s.

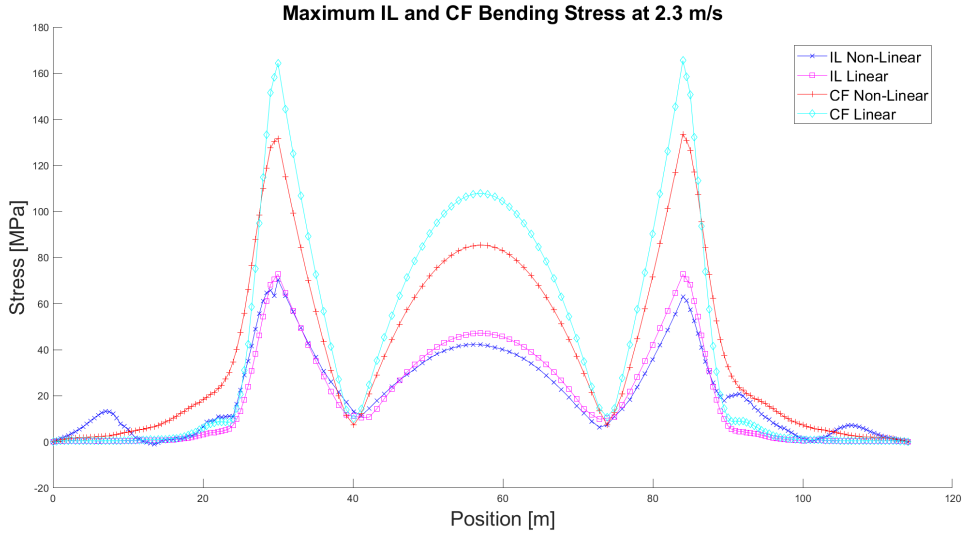

(a) CF and IL Maximum Bending Stress Distribution at 2.3 m/s

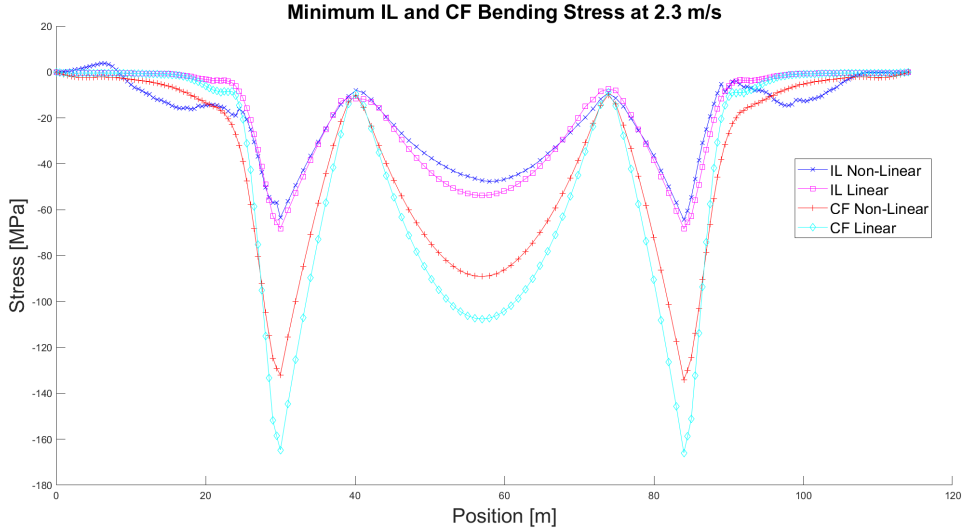

(b) CF and IL Minimum Bending Stress Distribution at 2.3 m/s

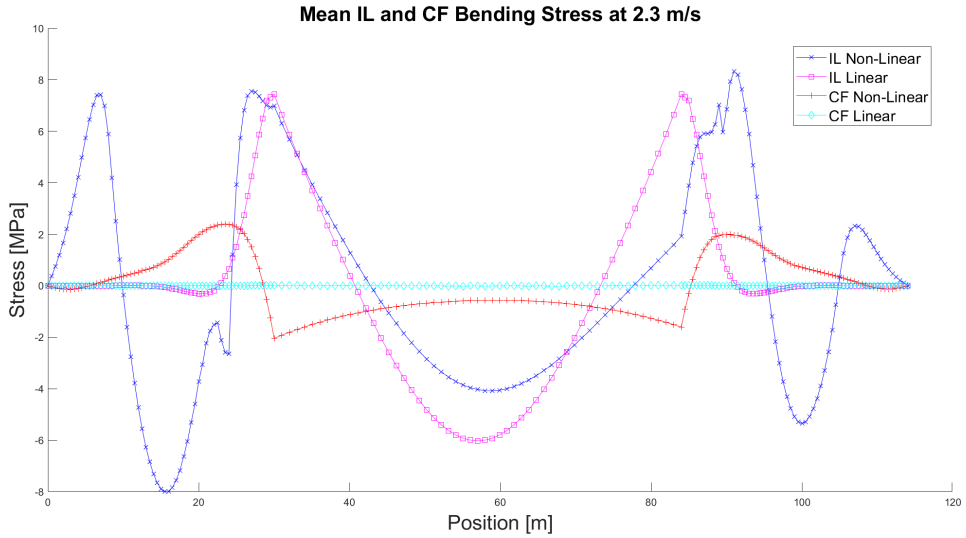

(c) CF and IL Mean Bending Stress Distribution at 2.3 m/s

Figure B.103: Comparative plots of the calculated bending stress distribution for the two soil models and $\zeta_{soil} = 22\%$ at 2.3 m/s.

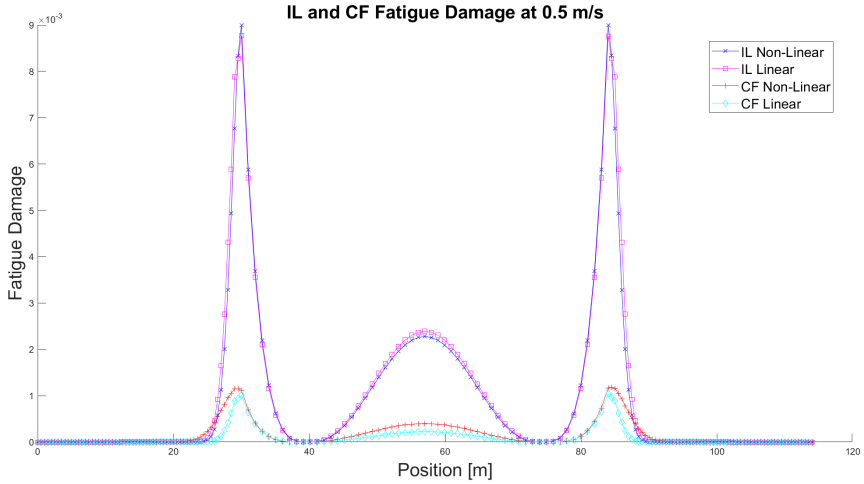

Figure B.104: Comparative plots of the calculated fatigue damage distribution for the two soil model and $\zeta_{soil} = 22\%$ at current velocity 0.5 m/s.

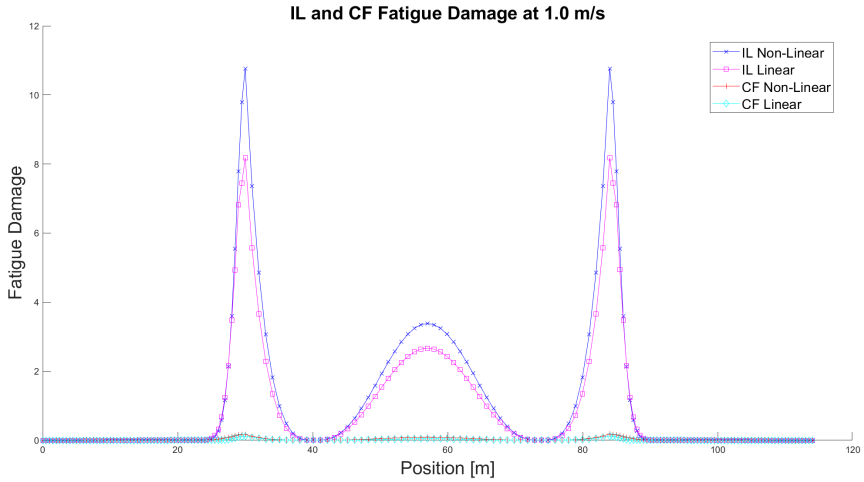

Figure B.105: Comparative plots of the calculated fatigue damage distribution for the two soil model and $\zeta_{soil} = 22\%$ at current velocity 1.0 m/s.

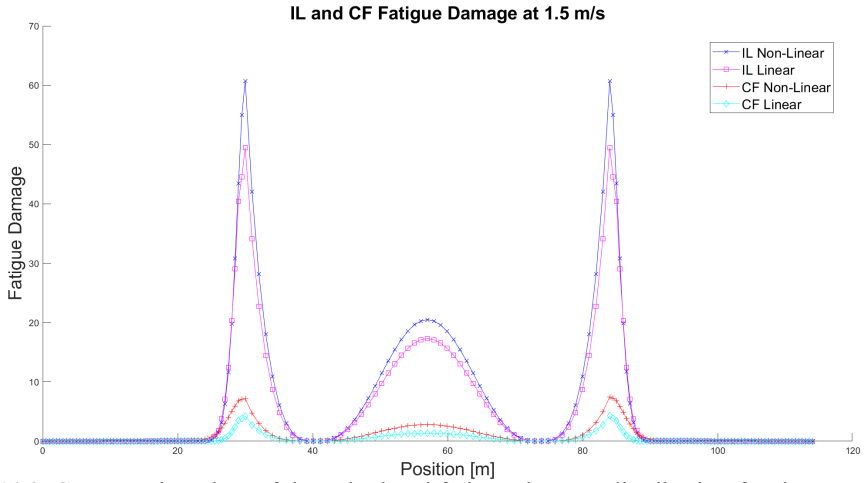

Figure B.106: Comparative plots of the calculated fatigue damage distribution for the two soil model and $\zeta_{soil} = 22\%$ at current velocity 1.5 m/s.

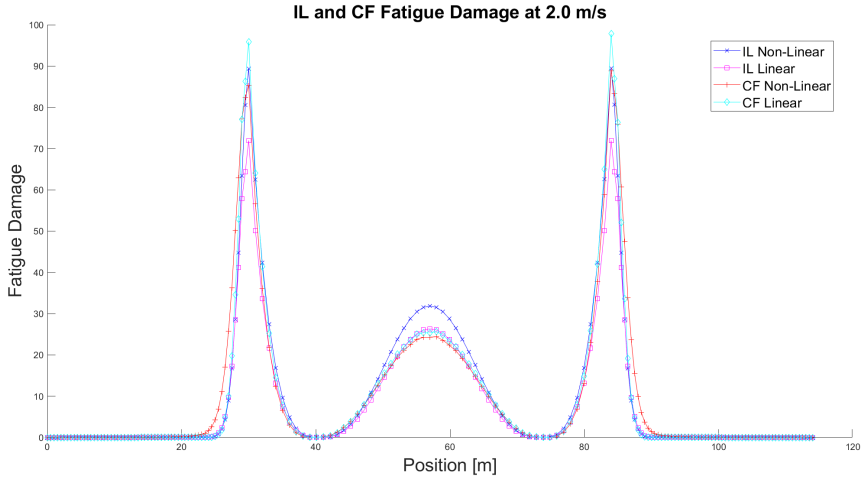

Figure B.107: Comparative plots of the calculated fatigue damage distribution for the two soil model and $\zeta_{soil} = 22\%$ at current velocity 2.0 m/s.

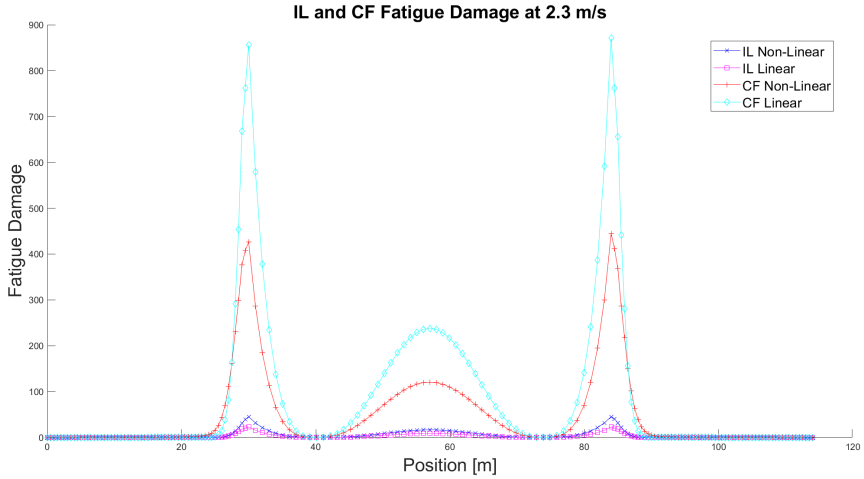

Figure B.108: Comparative plots of the calculated fatigue damage distribution for the two soil model and $\zeta_{soil} = 22\%$ at current velocity 2.3 m/s.

B.4 Non-Linear Soil Model - Soil Damping Ratio 0.08 - Total set of results

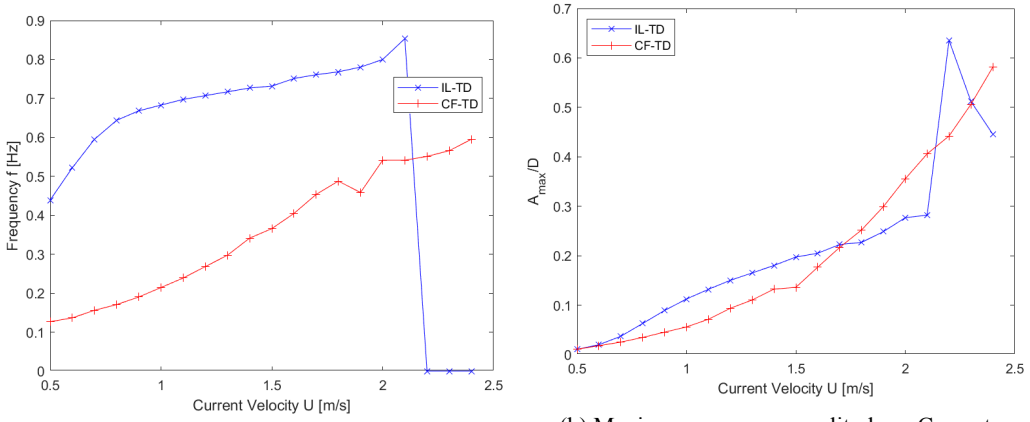

(a) Response Frequency vs Current Velocity

(b) Maximum response amplitude vs Current Velocity

Figure B.109: Plots of the dominant response frequencies and the maximum response amplitudes for the Non-linear soil model and $\zeta_{soil} = 8\%$.

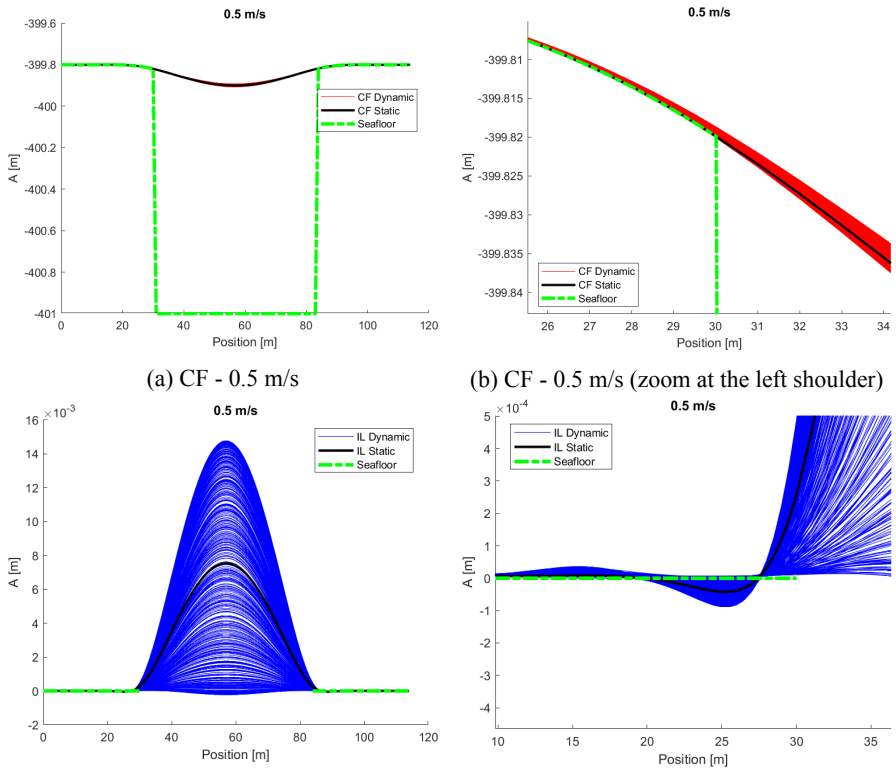

(a) CF - 0.5 m/s

(b) CF - 0.5 m/s (zoom at the left shoulder)

(c) IL - 0.5 m/s

(d) IL - 0.5 m/s (zoom at the left shoulder)

Figure B.110: Snapshots of the calculated response at 0.5 m/s.

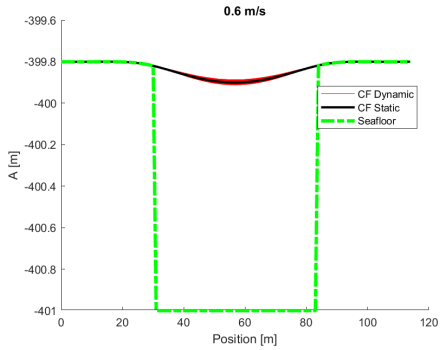

(a) CF - 0.6 m/s

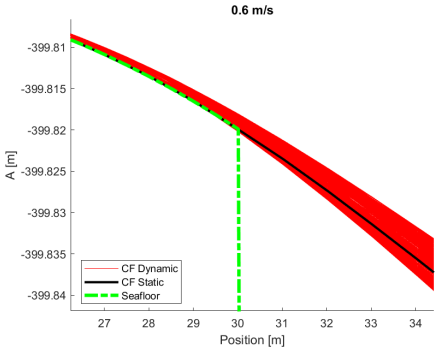

(b) CF - 0.6 m/s (zoom at the left shoulder)

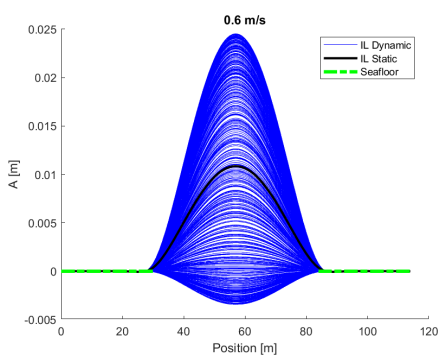

(c) IL - 0.6 m/s

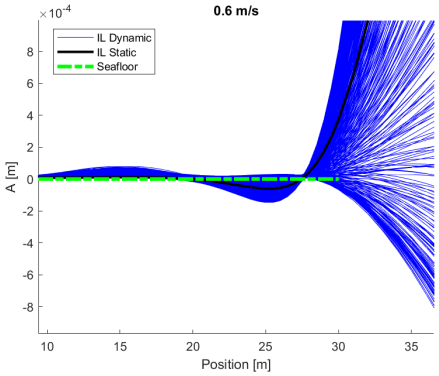

(d) IL - 0.6 m/s (zoom at the left shoulder)

Figure B.111: Snapshots of the calculated response at 0.6 m/s.

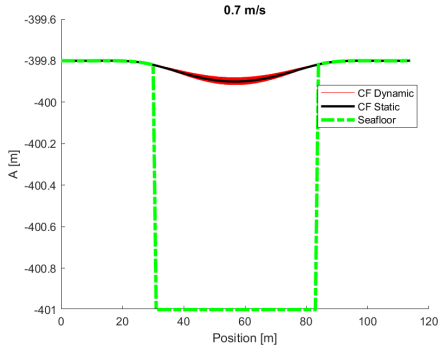

(a) CF - 0.7 m/s

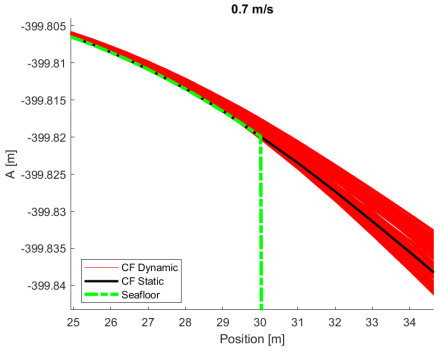

(b) CF - 0.7 m/s (zoom at the left shoulder)

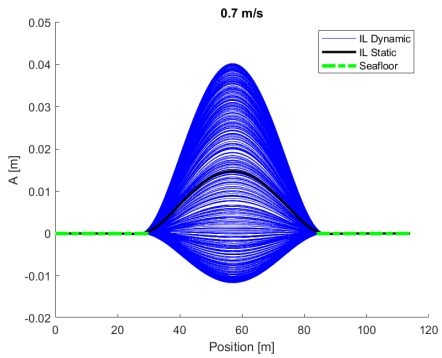

(c) IL - 0.7 m/s

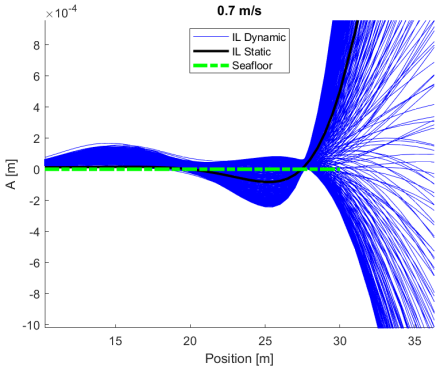

(d) IL - 0.7 m/s (zoom at the left shoulder)

Figure B.112: Snapshots of the calculated response at 0.7 m/s.

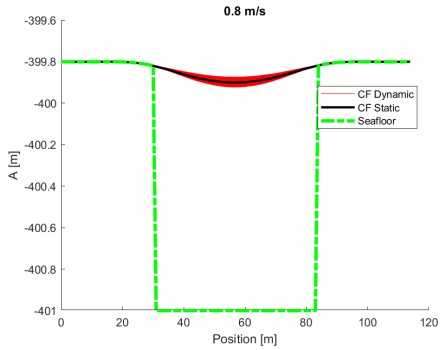

(a) CF - 0.8 m/s

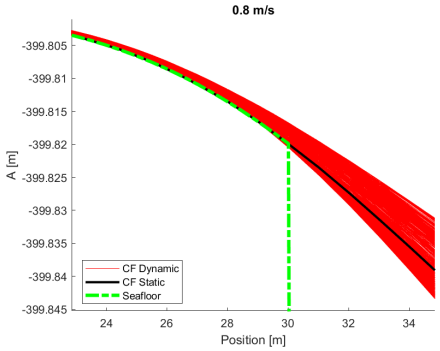

(b) CF - 0.8 m/s (zoom at the left shoulder)

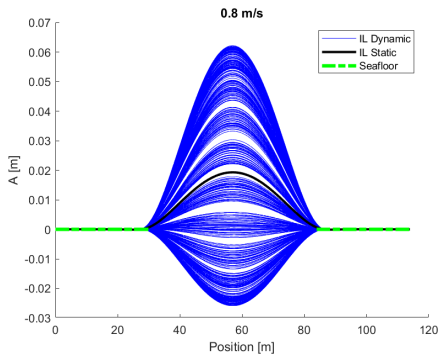

(c) IL - 0.8 m/s

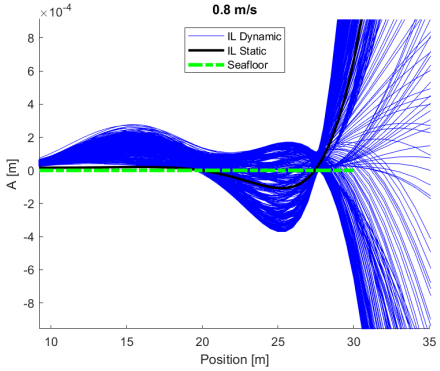

(d) IL - 0.8 m/s (zoom at the left shoulder)

Figure B.113: Snapshots of the calculated response at 0.8 m/s.

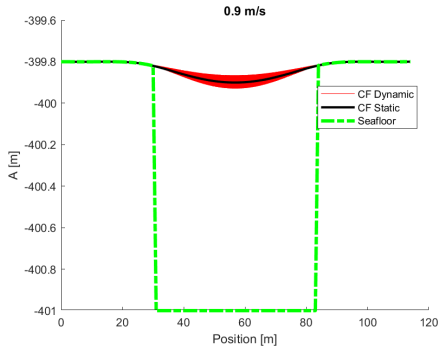

(a) CF - 0.9 m/s

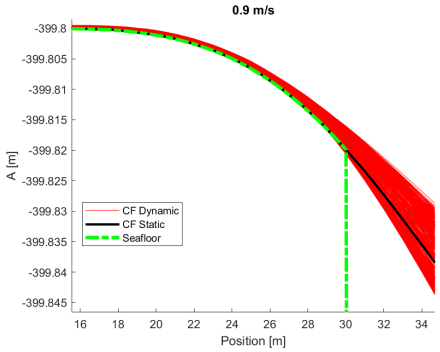

(b) CF - 0.9 m/s (zoom at the left shoulder)

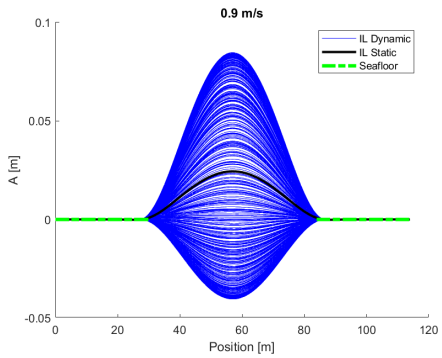

(c) IL - 0.9 m/s

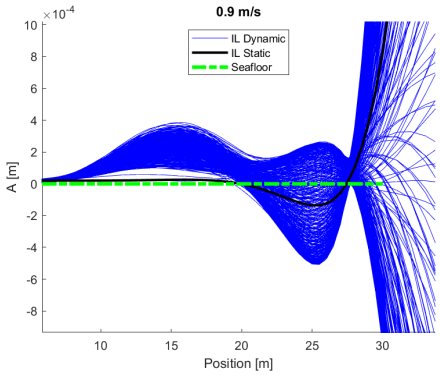

(d) IL - 0.9 m/s (zoom at the left shoulder)

Figure B.114: Snapshots of the calculated response at 0.9 m/s.

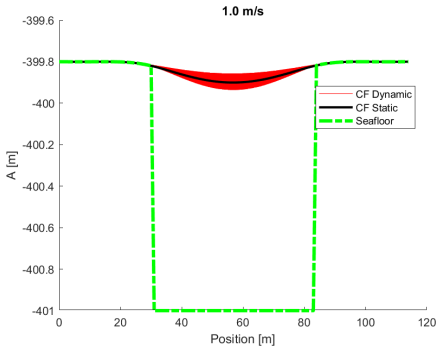

(a) CF - 1.0 m/s

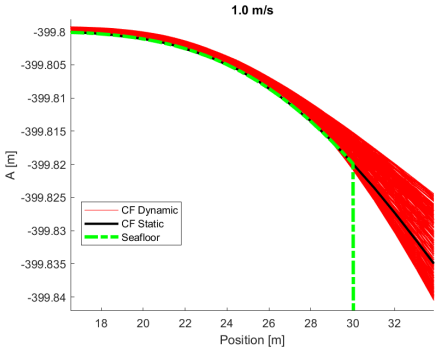

(b) CF - 1.0 m/s (zoom at the left shoulder)

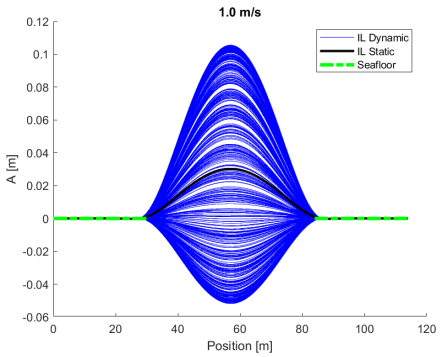

(c) IL - 1.0 m/s

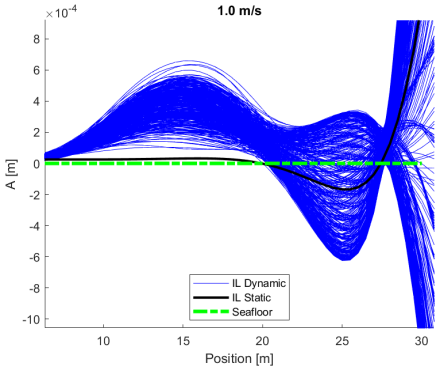

(d) IL - 1.0 m/s (zoom at the left shoulder)

Figure B.115: Snapshots of the calculated response at 1.0 m/s.

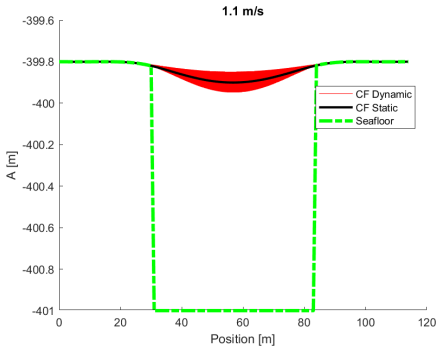

(a) CF - 1.1 m/s

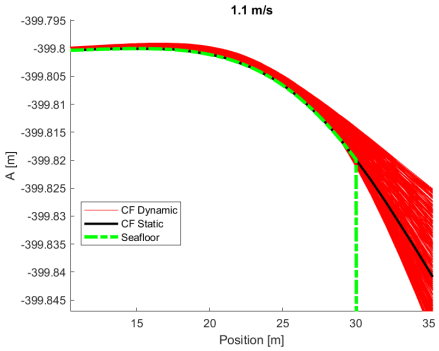

(b) CF - 1.1 m/s (zoom at the left shoulder)

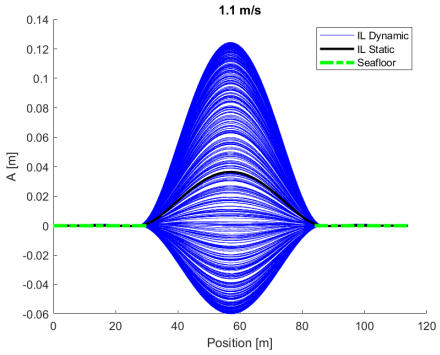

(c) IL - 1.1 m/s

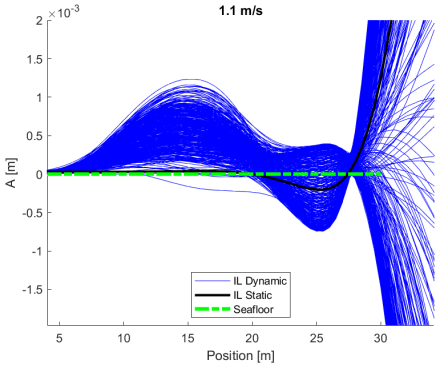

(d) IL - 1.1 m/s (zoom at the left shoulder)

Figure B.116: Snapshots of the calculated response at 1.1 m/s.

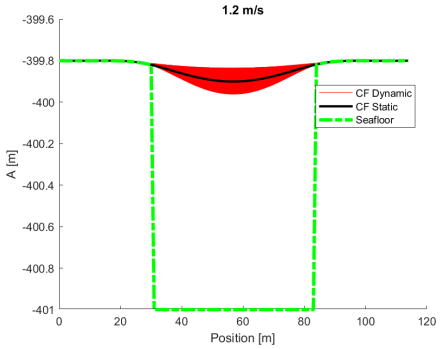

(a) CF - 1.2 m/s

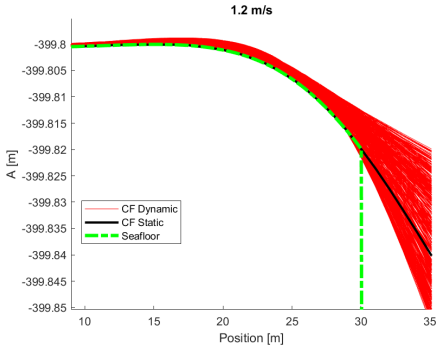

(b) CF - 1.2 m/s (zoom at the left shoulder)

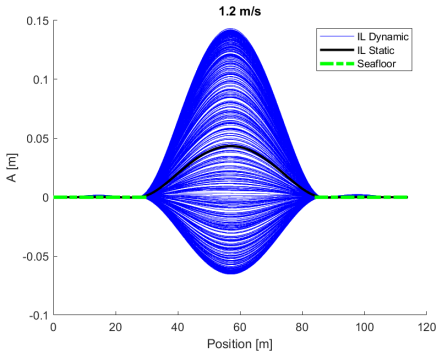

(c) IL - 1.2 m/s

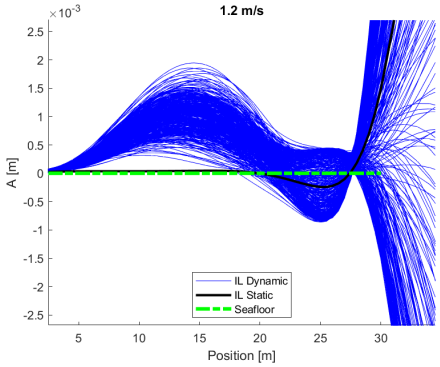

(d) IL - 1.2 m/s (zoom at the left shoulder)

Figure B.117: Snapshots of the calculated response at 1.2 m/s.

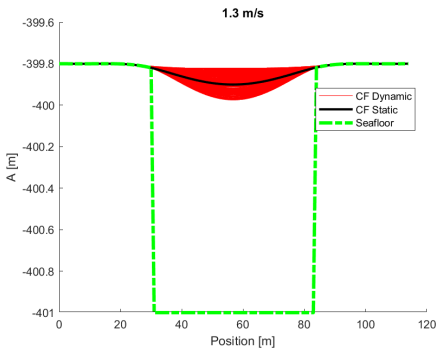

(a) CF - 1.3 m/s

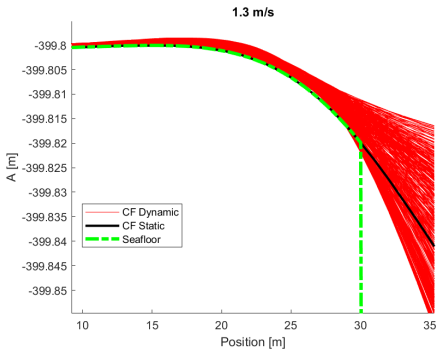

(b) CF - 1.3 m/s (zoom at the left shoulder)

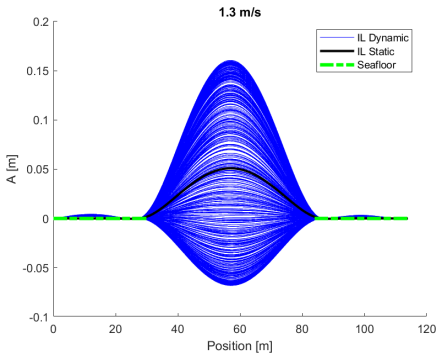

(c) IL - 1.3 m/s

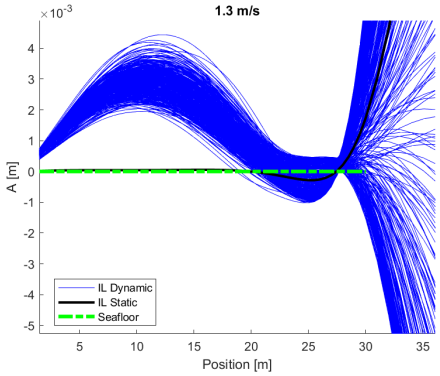

(d) IL - 1.3 m/s (zoom at the left shoulder)

Figure B.118: Snapshots of the calculated response at 1.3 m/s.

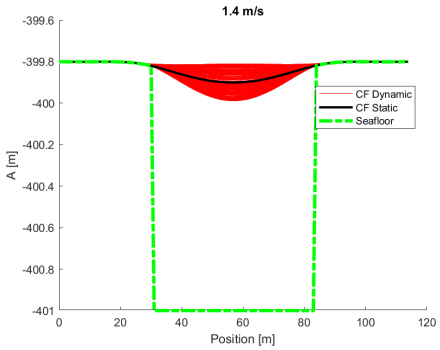

(a) CF - 1.4 m/s

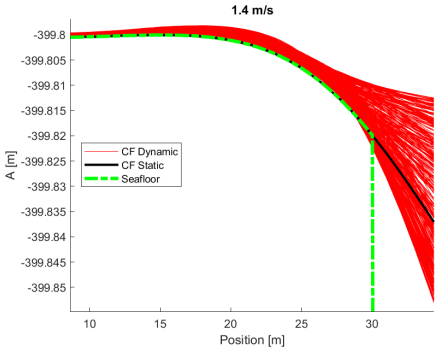

(b) CF - 1.4 m/s (zoom at the left shoulder)

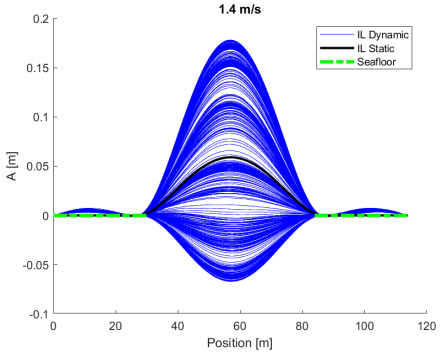

(c) IL - 1.4 m/s

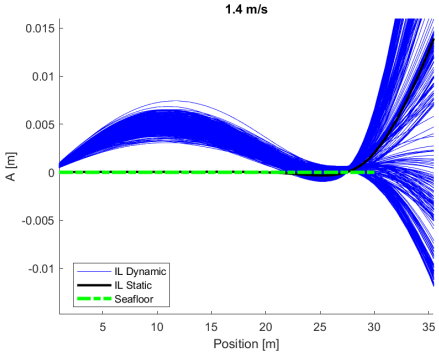

(d) IL - 1.4 m/s (zoom at the left shoulder)

Figure B.119: Snapshots of the calculated response at 1.4 m/s.

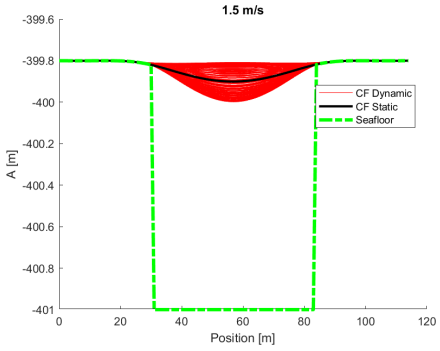

(a) CF - 1.5 m/s

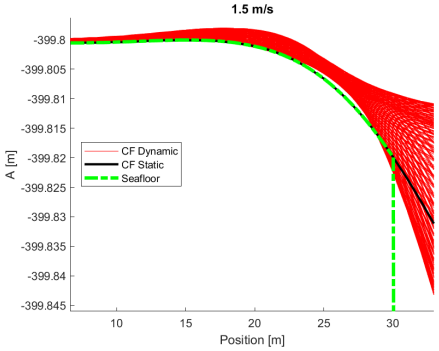

(b) CF - 1.5 m/s (zoom at the left shoulder)

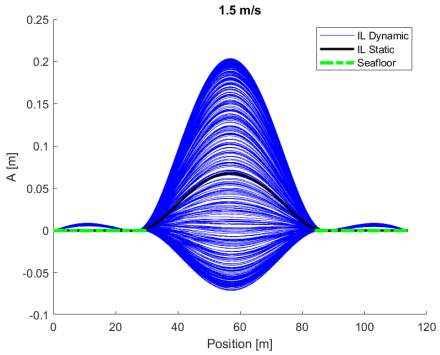

(c) IL - 1.5 m/s

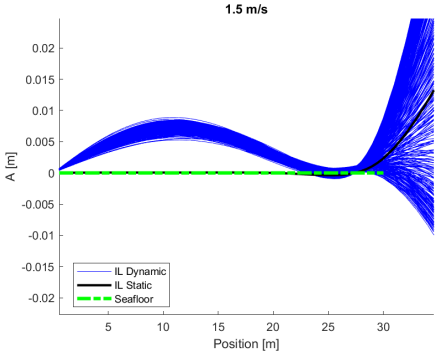

(d) IL - 1.5 m/s (zoom at the left shoulder)

Figure B.120: Snapshots of the calculated response at 1.5 m/s.

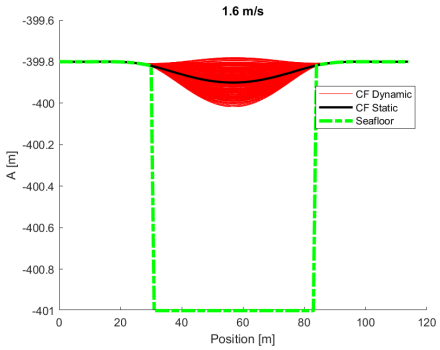

(a) CF - 1.6 m/s

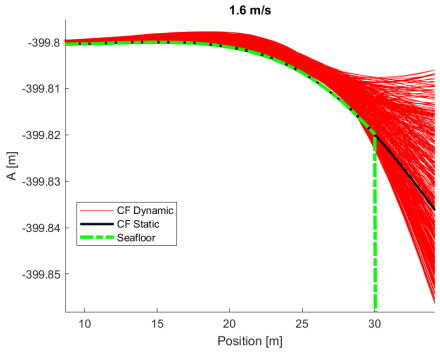

(b) CF - 1.6 m/s (zoom at the left shoulder)

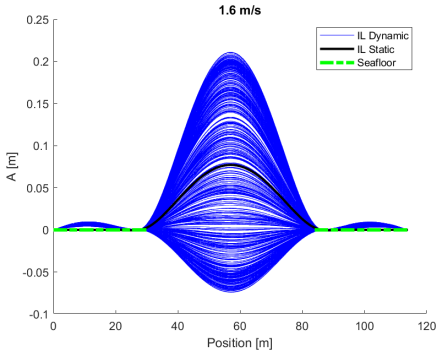

(c) IL - 1.6 m/s

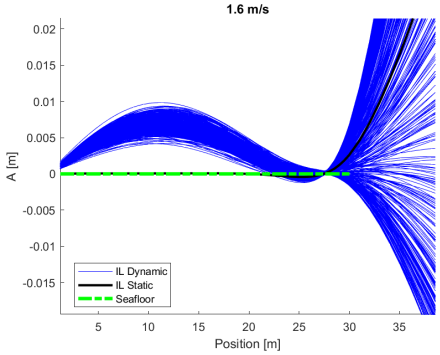

(d) IL - 1.6 m/s (zoom at the left shoulder)

Figure B.121: Snapshots of the calculated response at 1.6 m/s.

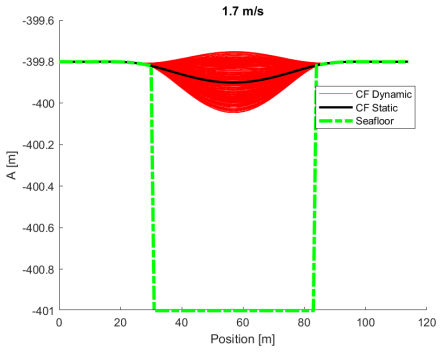

(a) CF - 1.7 m/s

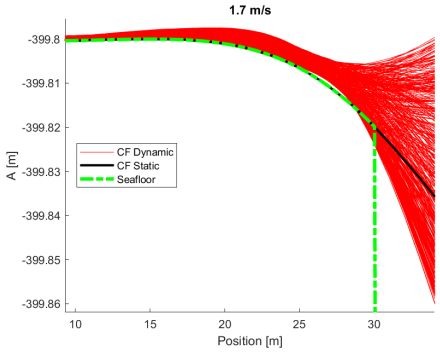

(b) CF - 1.7 m/s (zoom at the left shoulder)

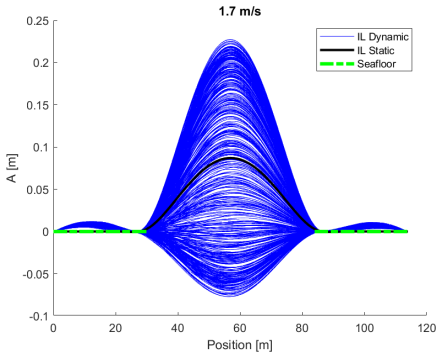

(c) IL - 1.7 m/s

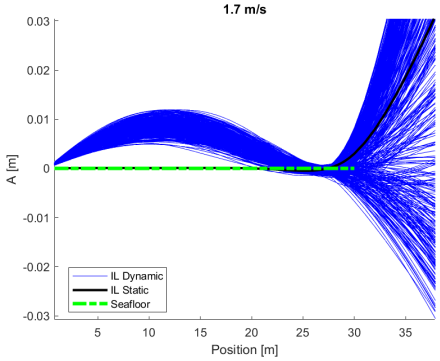

(d) IL - 1.7 m/s (zoom at the left shoulder)

Figure B.122: Snapshots of the calculated response at 1.7 m/s.

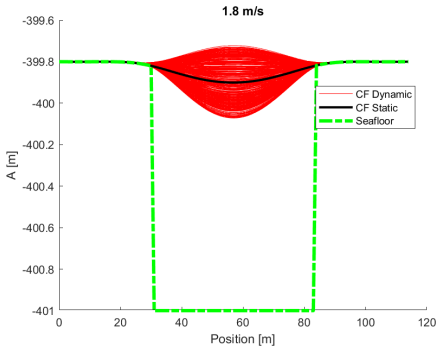

(a) CF - 1.8 m/s

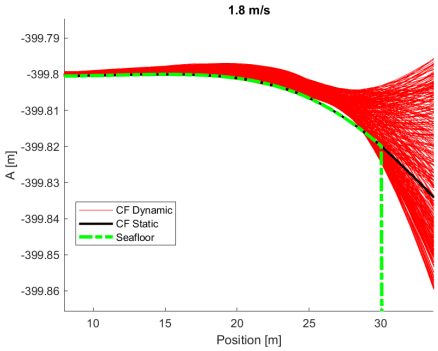

(b) CF - 1.8 m/s (zoom at the left shoulder)

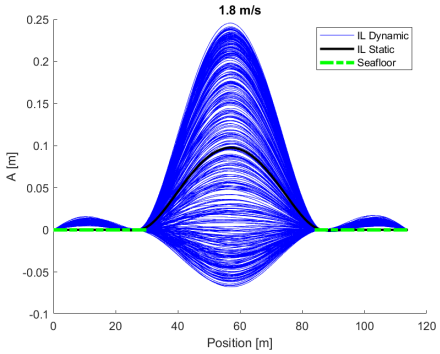

(c) IL - 1.8 m/s

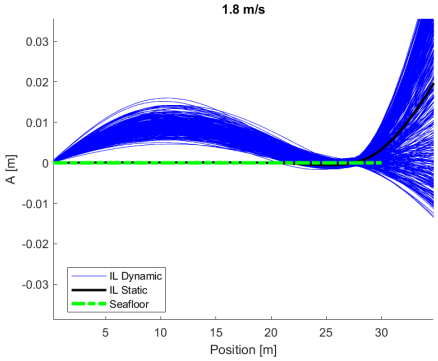

(d) IL - 1.8 m/s (zoom at the left shoulder)

Figure B.123: Snapshots of the calculated response at 1.8 m/s.

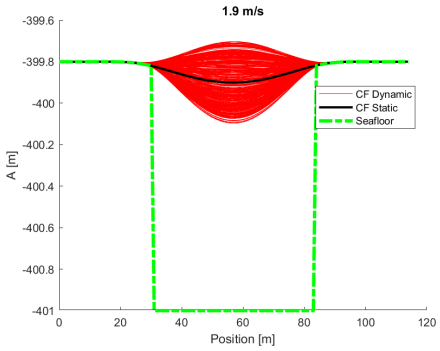

(a) CF - 1.9 m/s

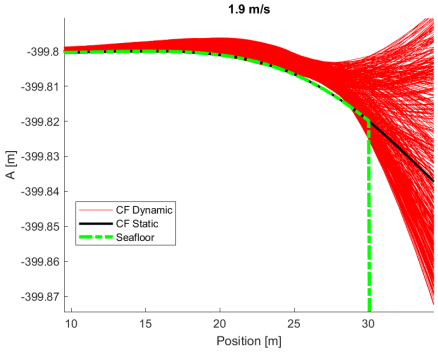

(b) CF - 1.9 m/s (zoom at the left shoulder)

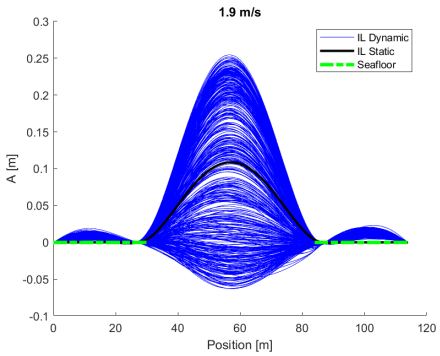

(c) IL - 1.9 m/s

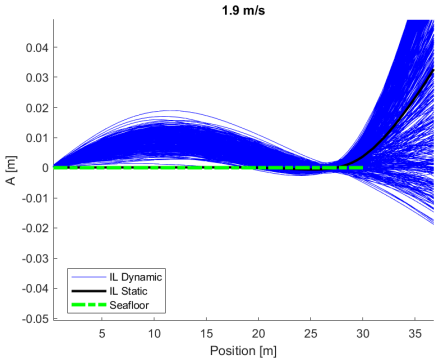

(d) IL - 1.9 m/s (zoom at the left shoulder)

Figure B.124: Snapshots of the calculated response at 1.9 m/s.

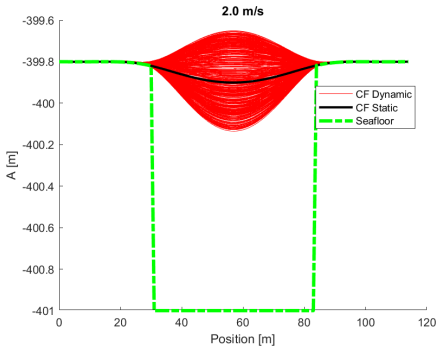

(a) CF - 2.0 m/s

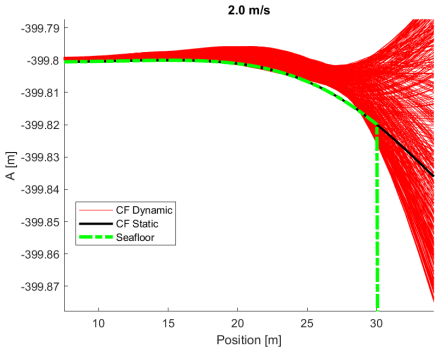

(b) CF - 2.0 m/s (zoom at the left shoulder)

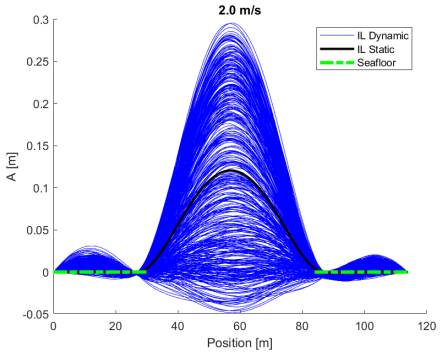

(c) IL - 2.0 m/s

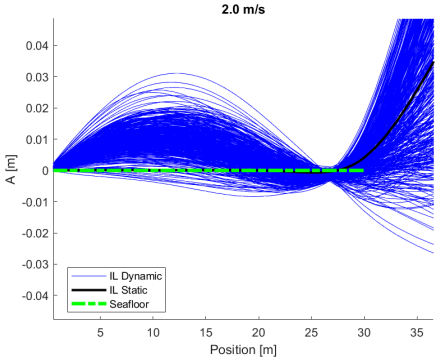

(d) IL - 2.0 m/s (zoom at the left shoulder)

Figure B.125: Snapshots of the calculated response at 2.0 m/s.

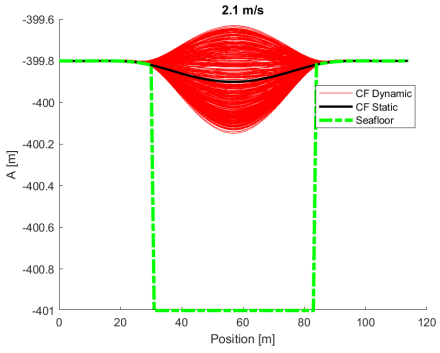

(a) CF - 2.1 m/s

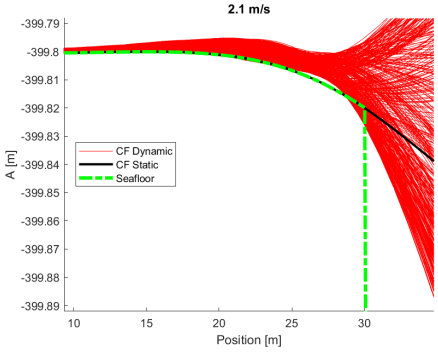

(b) CF - 2.1 m/s (zoom at the left shoulder)

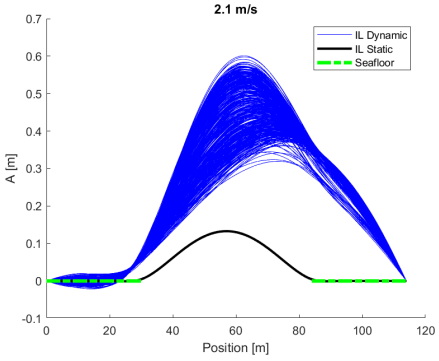

(c) IL - 2.1 m/s

Figure B.126: Snapshots of the calculated response at 2.1 m/s.

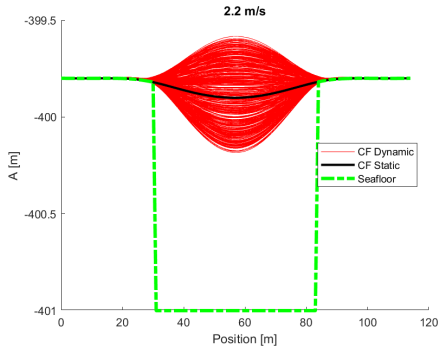

(a) CF - 2.2 m/s

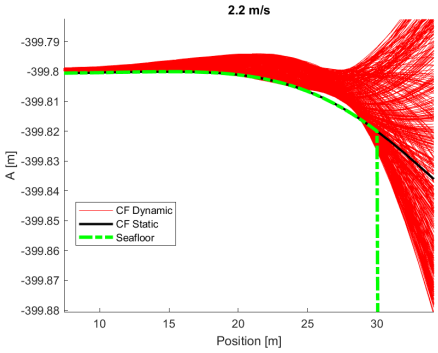

(b) CF - 2.2 m/s (zoom at the left shoulder)

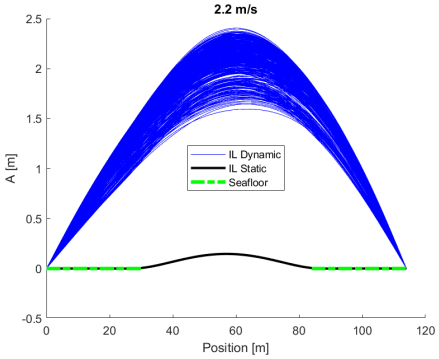

(c) IL - 2.2 m/s

Figure B.127: Snapshots of the calculated response at 2.2 m/s.

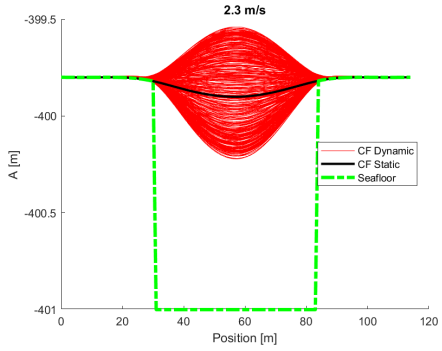

(a) CF - 2.3 m/s

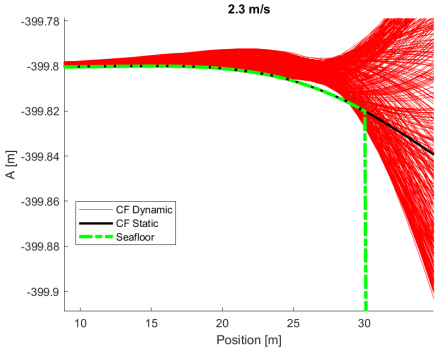

(b) CF - 2.3 m/s (zoom at the left shoulder)

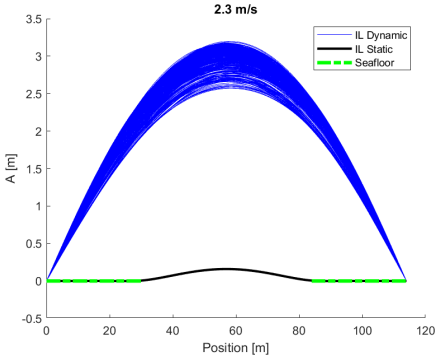

(c) IL - 2.3 m/s

Figure B.128: Snapshots of the calculated response at 2.3 m/s.

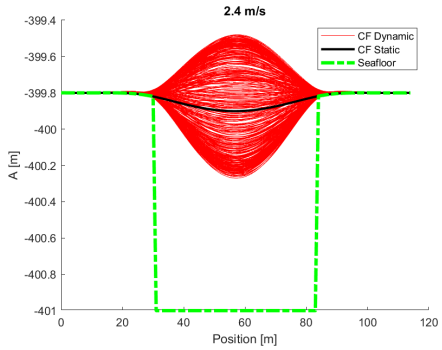

(a) CF - 2.4 m/s

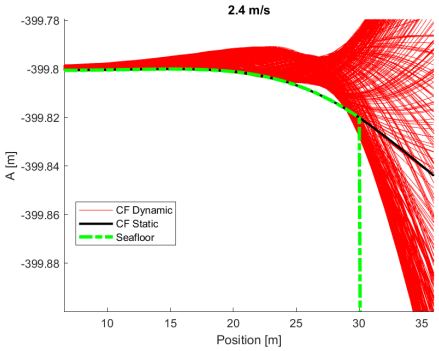

(b) CF - 2.4 m/s (zoom at the left shoulder)

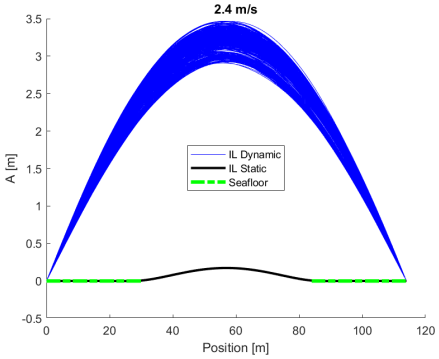

(c) IL - 2.4 m/s

Figure B.129: Snapshots of the calculated response at 2.4 m/s.

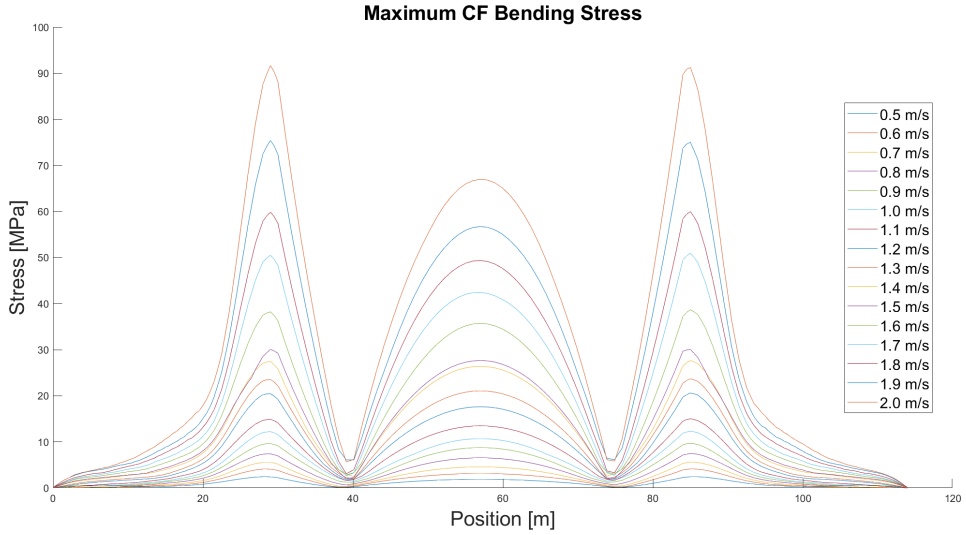

(a) CF - Maximum Bending Stress

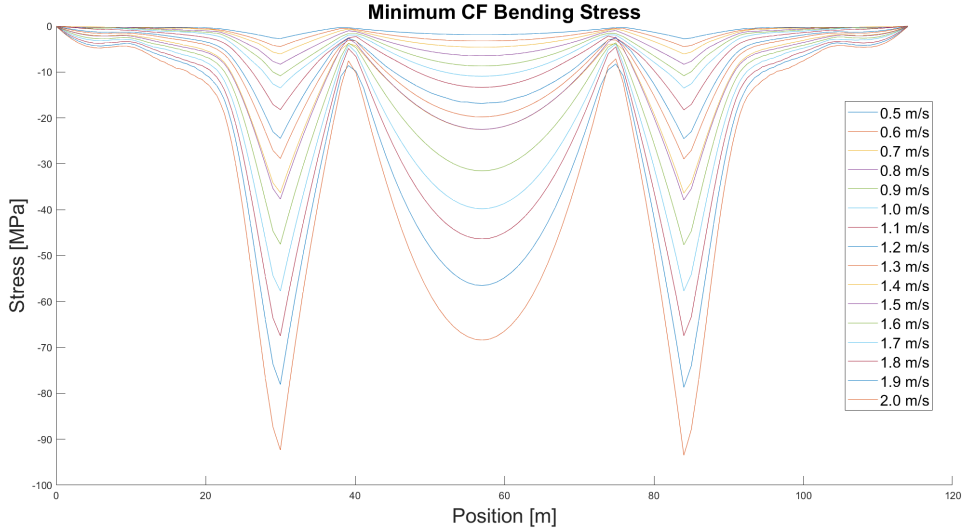

(b) CF - Minimum Bending Stress

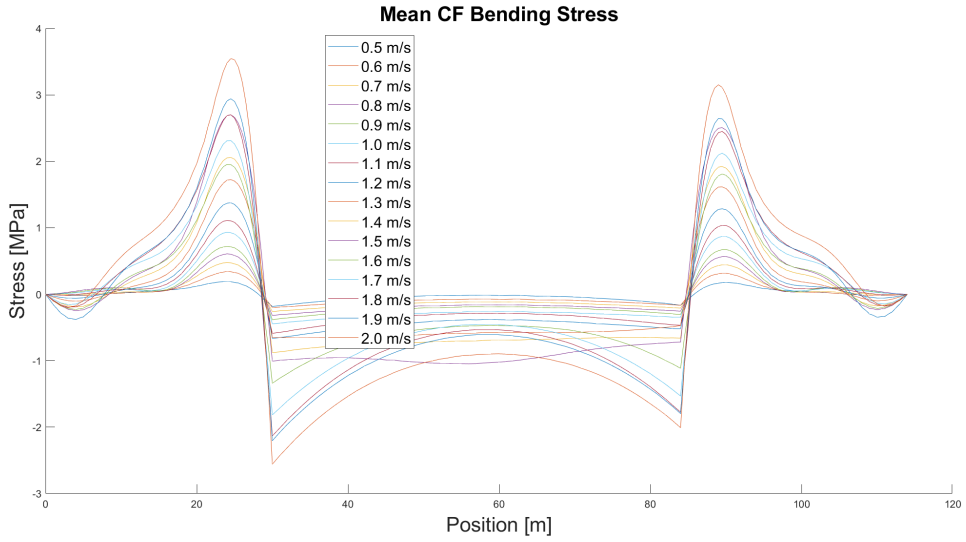

(c) CF - Mean Bending Stress

Figure B.130: Plots of the calculated bending stress distribution in the CF direction for the Non-linear soil model and $\zeta_{soil} = 8\%$.

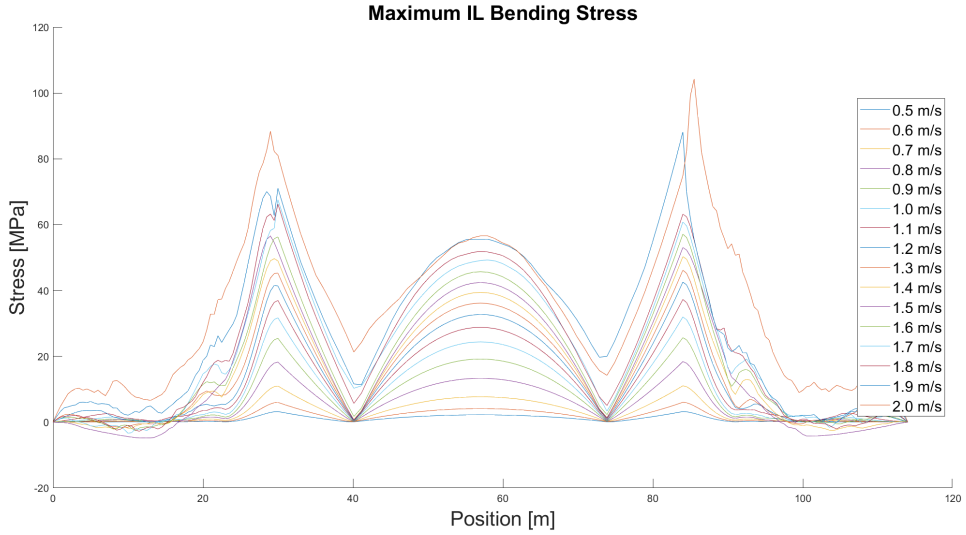

(a) IL - Maximum Bending Stress

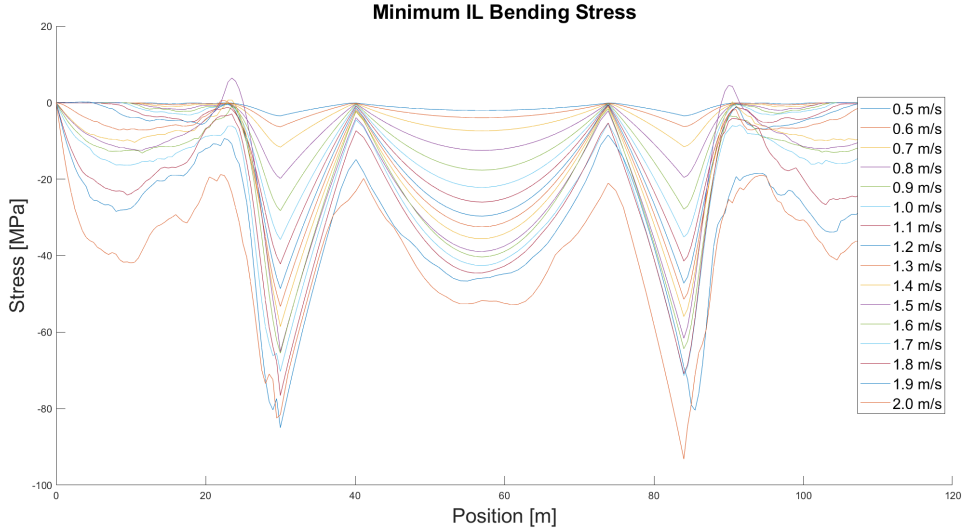

(b) IL - Minimum Bending Stress

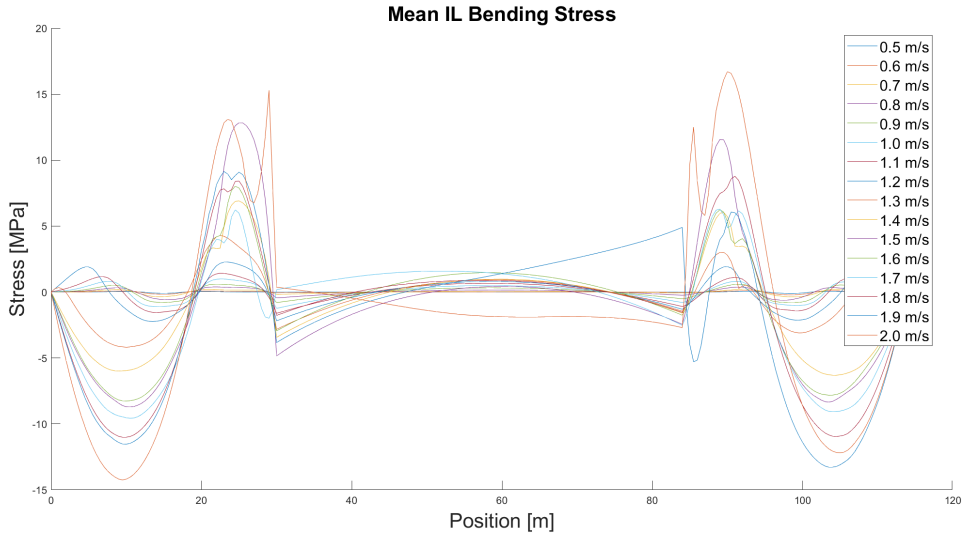

(c) IL - Mean Bending Stress

Figure B.131: Plots of the calculated bending stress distribution in the IL direction for the Non-linear soil model and $\zeta_{soil} = 8\%$.

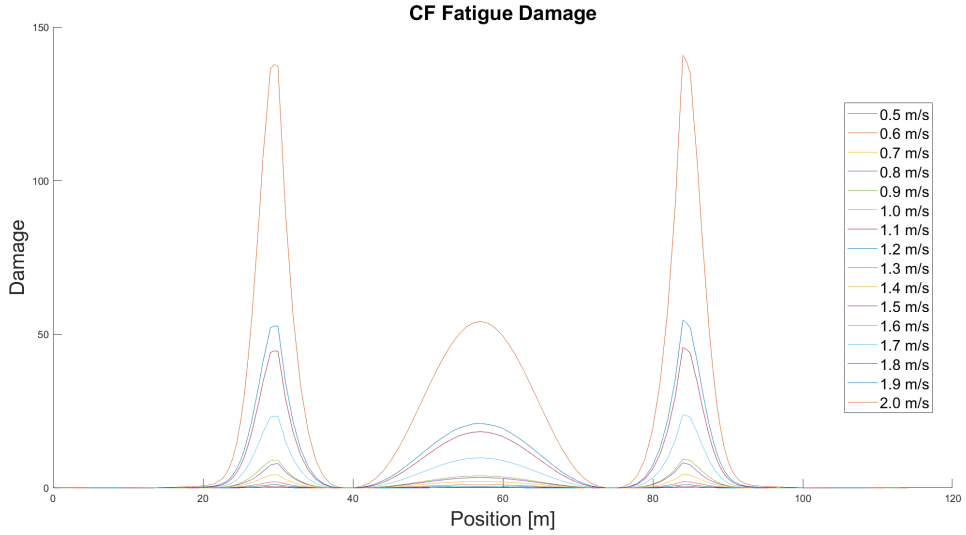

(a) CF - Fatigue Damage Accumulation

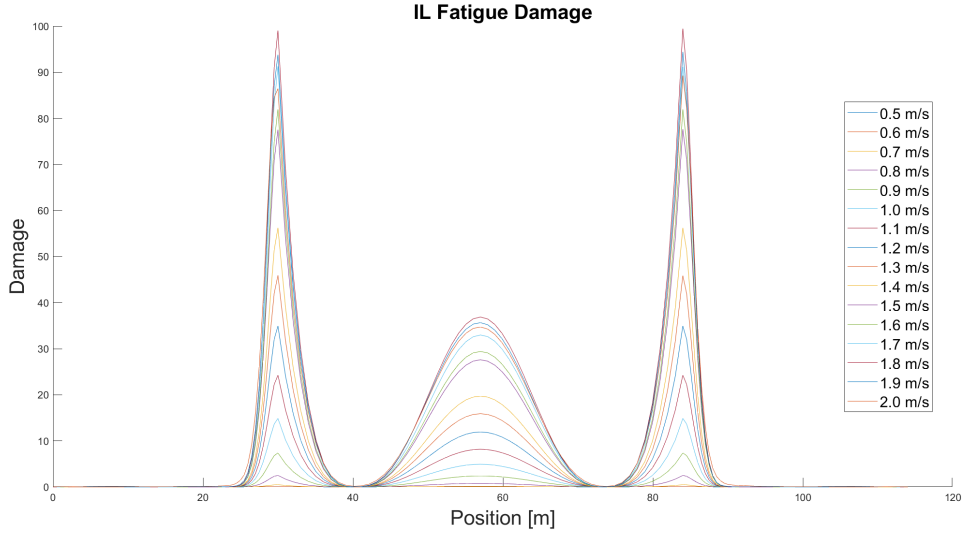

(b) IL - Fatigue Damage Accumulation

Figure B.132: Plots of the calculated fatigue damage distribution in both directions for the Non-linear soil model and $\zeta_{soil} = 8\%$.

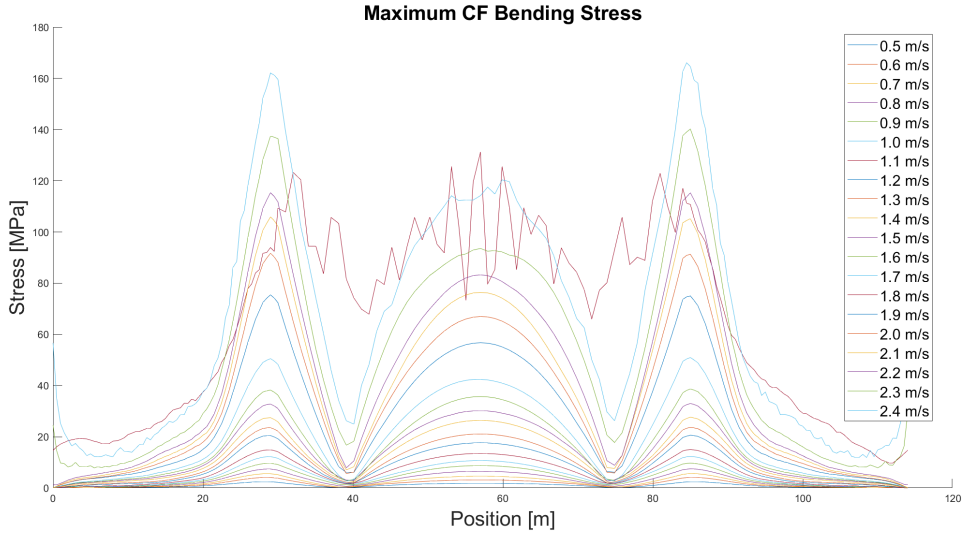

(a) CF - Maximum Bending Stress

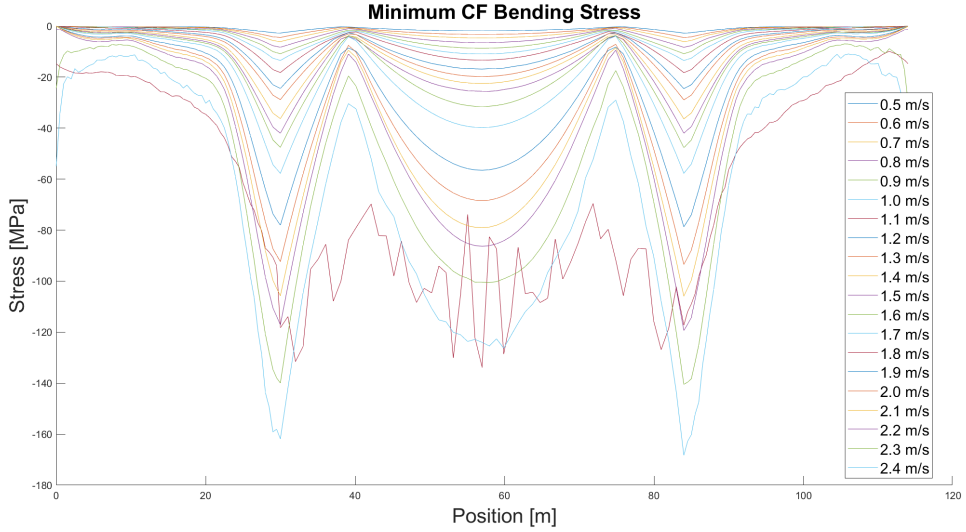

(b) CF - Minimum Bending Stress

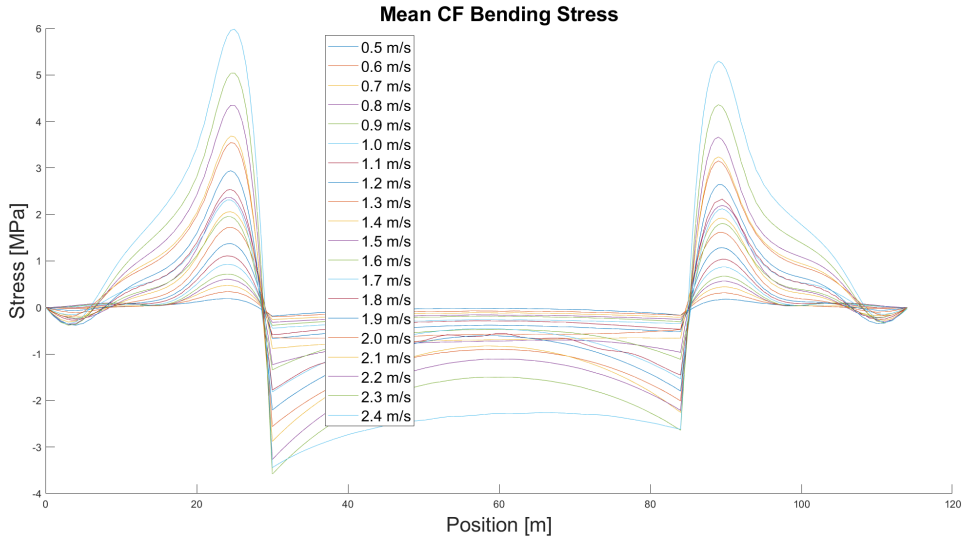

(c) CF - Mean Bending Stress

Figure B.133: Plots of the calculated bending stress distribution in the CF direction for the Non-linear soil model and $\zeta_{soil} = 8\%$ including the higher current velocities of 2.1-2.4 m/s.

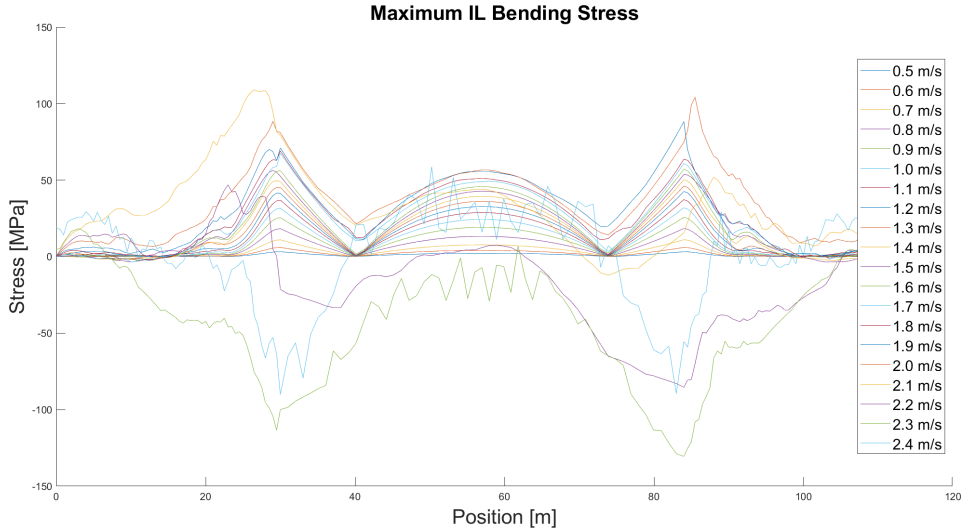

(a) IL - Maximum Bending Stress

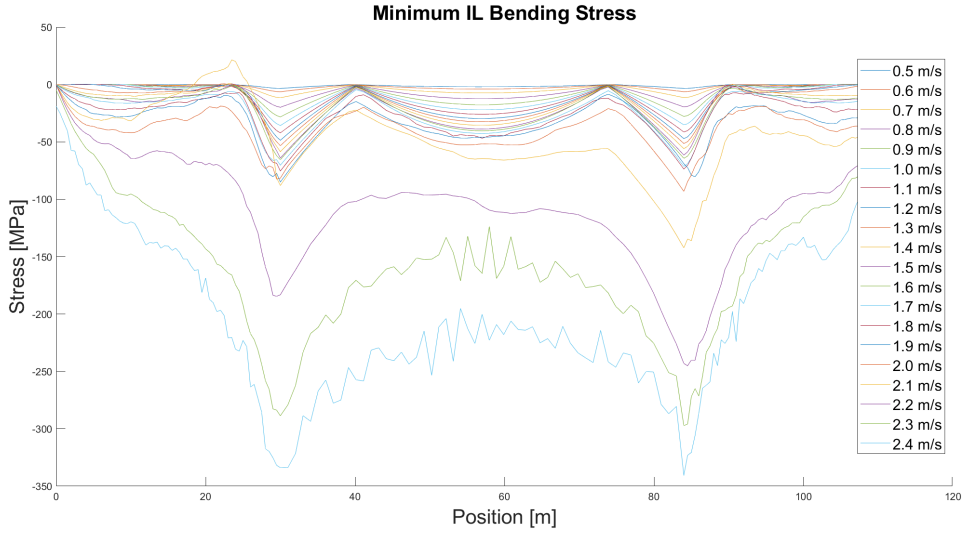

(b) IL - Minimum Bending Stress

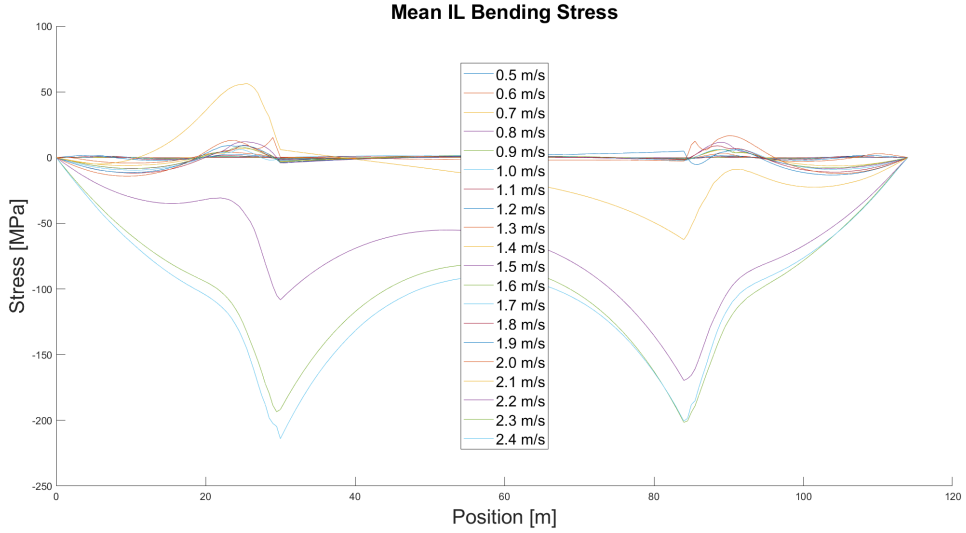

(c) IL - Mean Bending Stress

Figure B.134: Plots of the calculated bending stress distribution in the IL direction for the Non-linear soil model and $\zeta_{soil} = 8\%$ including the higher current velocities of 2.1-2.4 m/s.

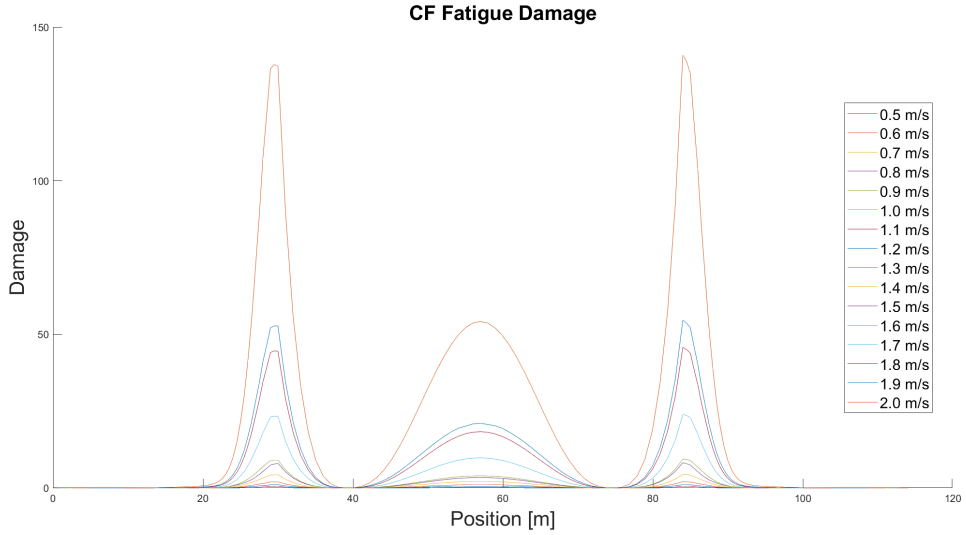

(a) CF - Fatigue Damage Accumulation

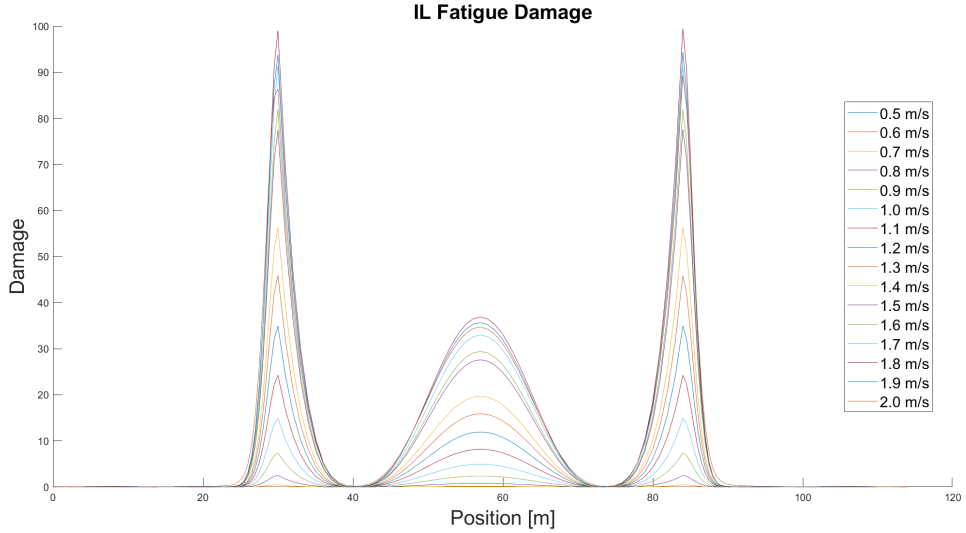

(b) IL - Fatigue Damage Accumulation

Figure B.135: Plots of the calculated fatigue damage distribution in both directions for the Non-linear soil model and $\zeta_{soil} = 8\%$ including the higher current velocities of 2.1-2.4 m/s.

B.5 Linear Soil Model - Soil Damping Ratio 0.08 - Total set of results

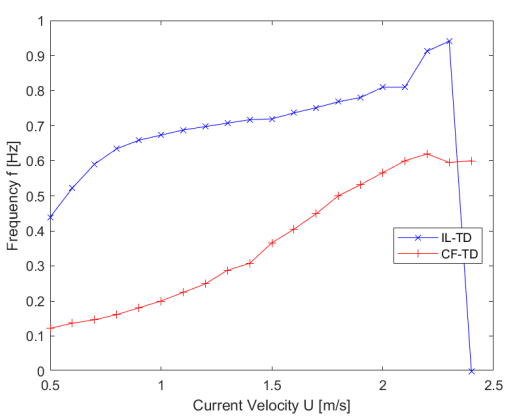

(a) Response Frequency vs Current Velocity

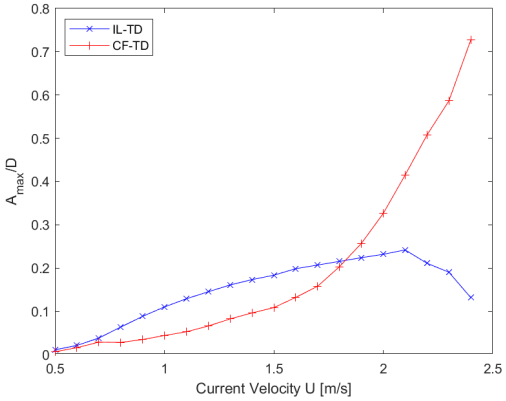

(b) Maximum response amplitude vs Current Velocity

Figure B.136: Plots of the dominant response frequencies and the maximum response amplitudes for the Linear soil model and $\zeta_{soil} = 8\%$.

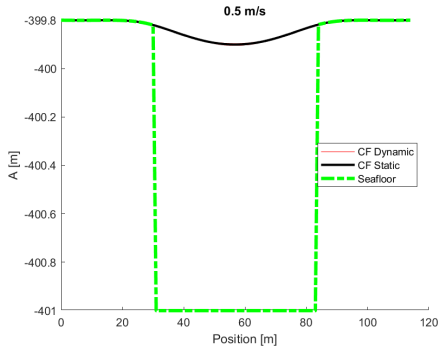

(a) CF - 0.5 m/s

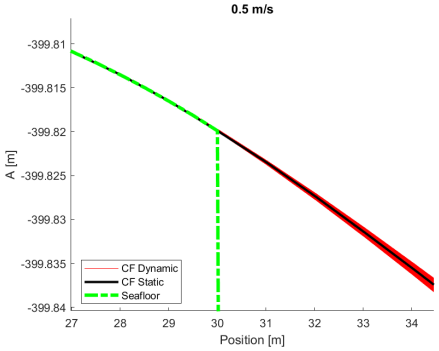

(b) CF - 0.5 m/s (zoom at the left shoulder)

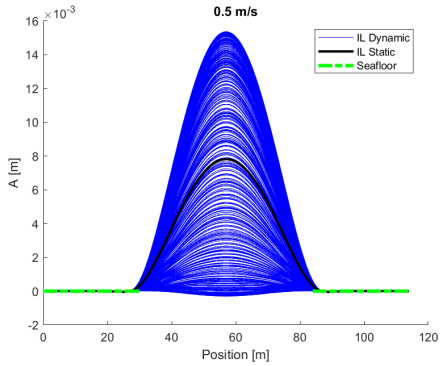

(c) IL - 0.5 m/s

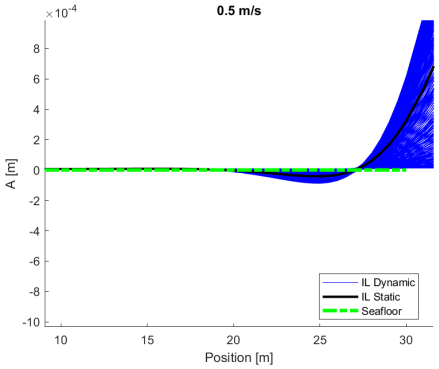

(d) IL - 0.5 m/s (zoom at the left shoulder)

Figure B.137: Snapshots of the calculated response at 0.5 m/s.

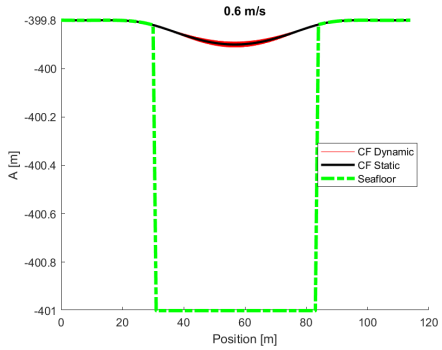

(a) CF - 0.6 m/s

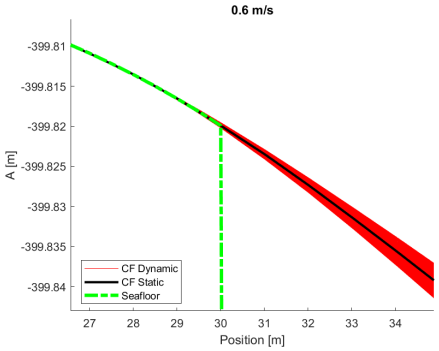

(b) CF - 0.6 m/s (zoom at the left shoulder)

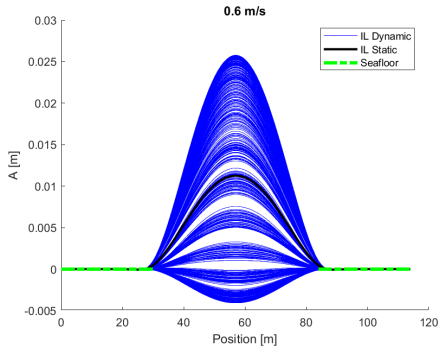

(c) IL - 0.6 m/s

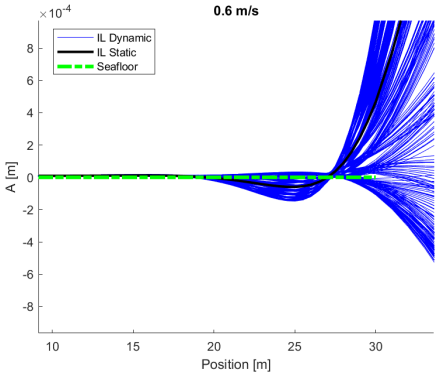

(d) IL - 0.6 m/s (zoom at the left shoulder)

Figure B.138: Snapshots of the calculated response at 0.6 m/s.

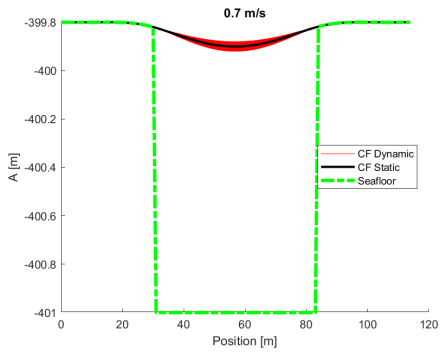

(a) CF - 0.7 m/s

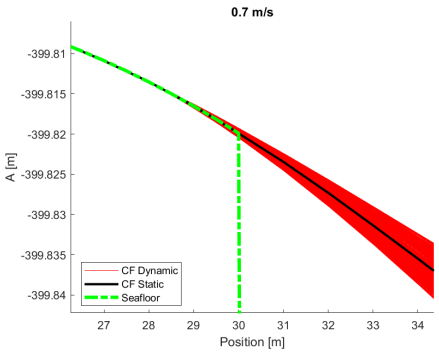

(b) CF - 0.7 m/s (zoom at the left shoulder)

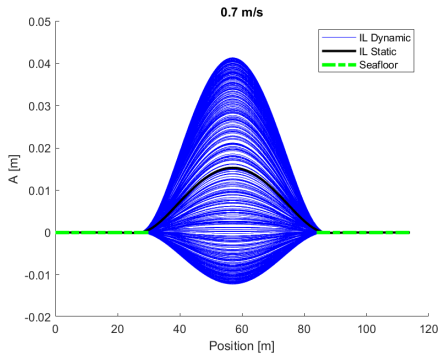

(c) IL - 0.7 m/s

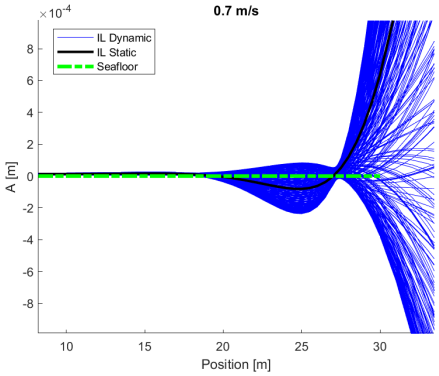

(d) IL - 0.7 m/s (zoom at the left shoulder)

Figure B.139: Snapshots of the calculated response at 0.7 m/s.

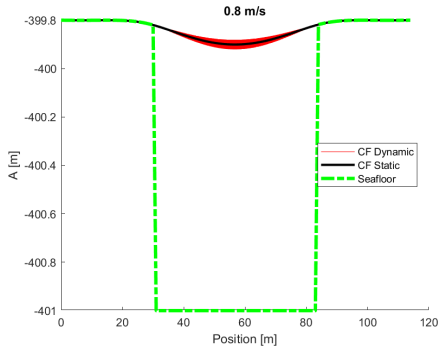

(a) CF - 0.8 m/s

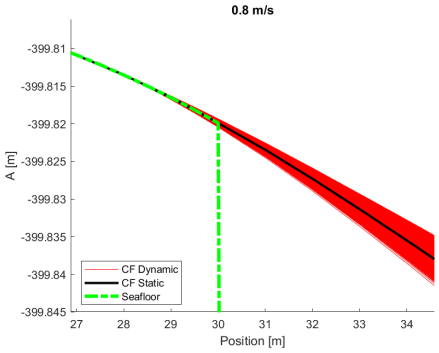

(b) CF - 0.8 m/s (zoom at the left shoulder)

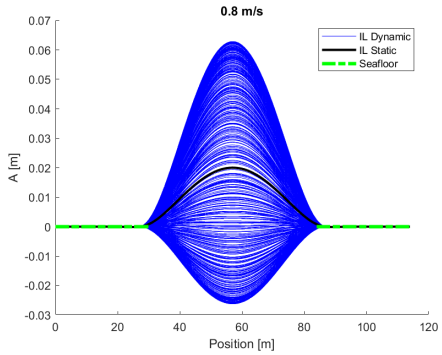

(c) IL - 0.8 m/s

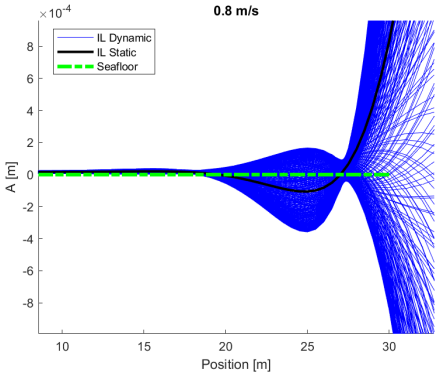

(d) IL - 0.8 m/s (zoom at the left shoulder)

Figure B.140: Snapshots of the calculated response at 0.8 m/s.

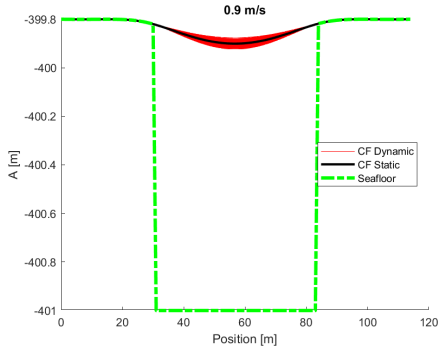

(a) CF - 0.9 m/s

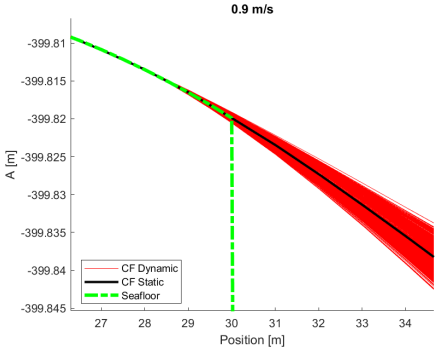

(b) CF - 0.9 m/s (zoom at the left shoulder)

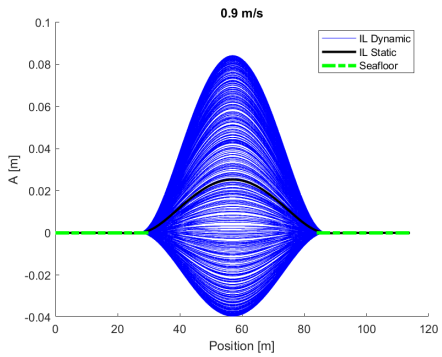

(c) IL - 0.9 m/s

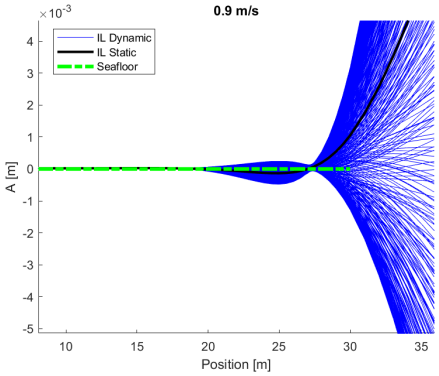

(d) IL - 0.9 m/s (zoom at the left shoulder)

Figure B.141: Snapshots of the calculated response at 0.9 m/s.

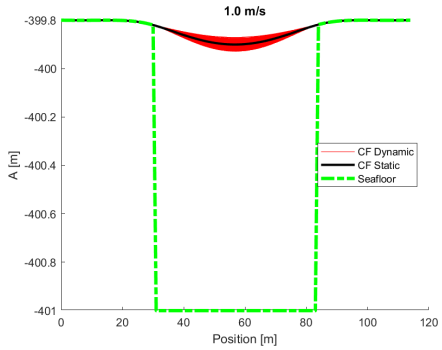

(a) CF - 1.0 m/s

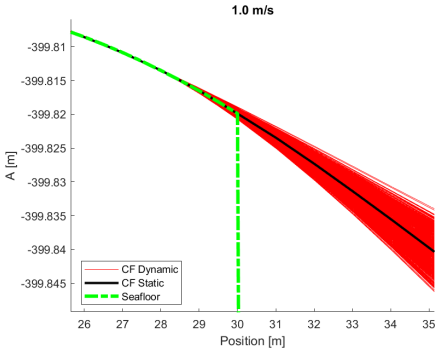

(b) CF - 1.0 m/s (zoom at the left shoulder)

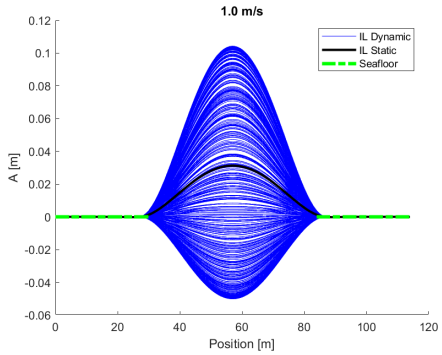

(c) IL - 1.0 m/s

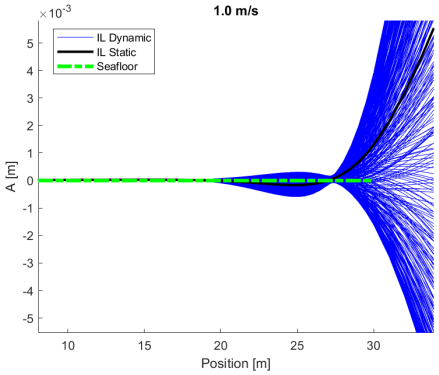

(d) IL - 1.0 m/s (zoom at the left shoulder)

Figure B.142: Snapshots of the calculated response at 1.0 m/s.

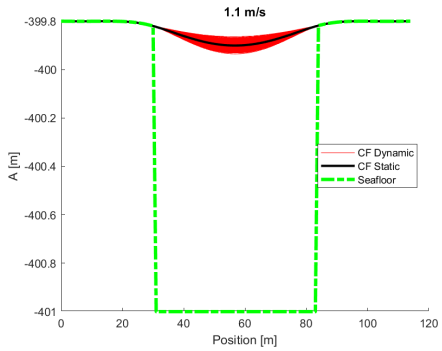

(a) CF - 1.1 m/s

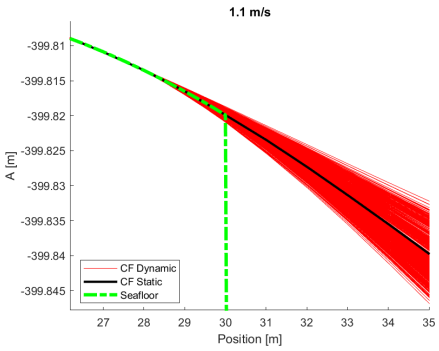

(b) CF - 1.1 m/s (zoom at the left shoulder)

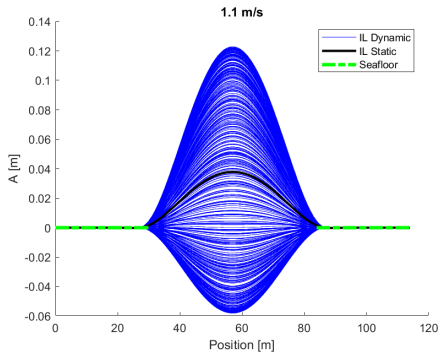

(c) IL - 1.1 m/s

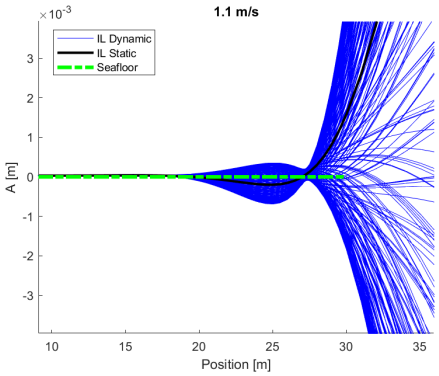

(d) IL - 1.1 m/s (zoom at the left shoulder)

Figure B.143: Snapshots of the calculated response at 1.1 m/s.

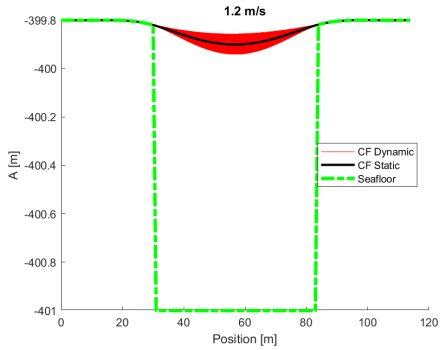

(a) CF - 1.2 m/s

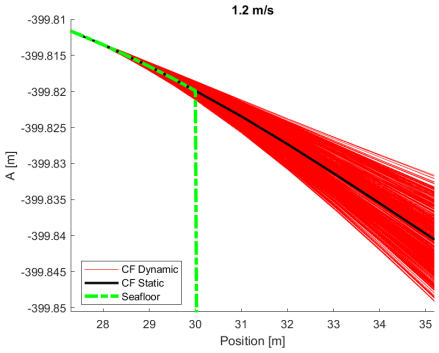

(b) CF - 1.2 m/s (zoom at the left shoulder)

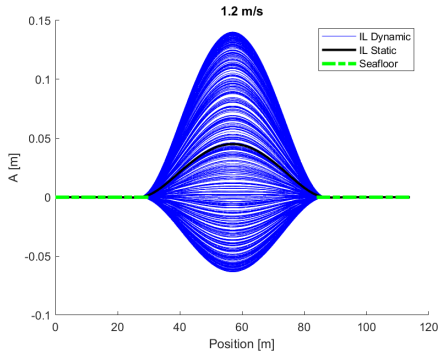

(c) IL - 1.2 m/s

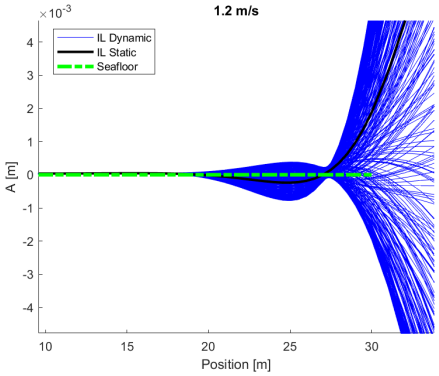

(d) IL - 1.2 m/s (zoom at the left shoulder)

Figure B.144: Snapshots of the calculated response at 1.2 m/s.

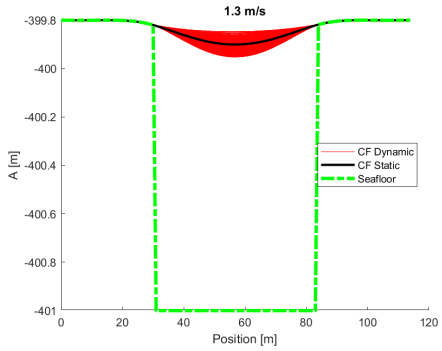

(a) CF - 1.3 m/s

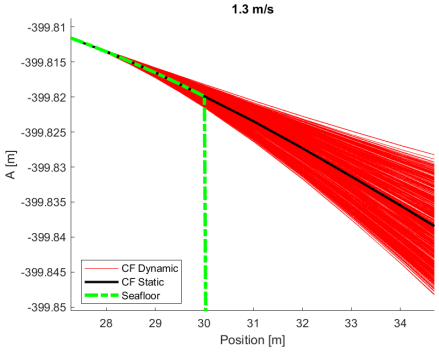

(b) CF - 1.3 m/s (zoom at the left shoulder)

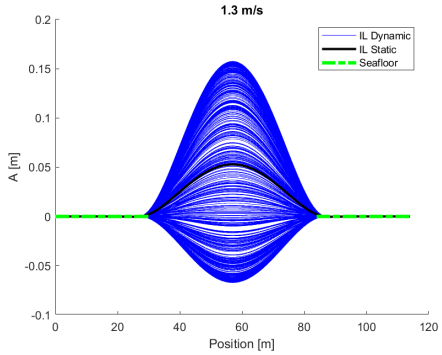

(c) IL - 1.3 m/s

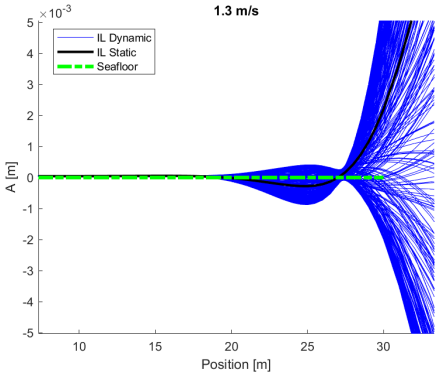

(d) IL - 1.3 m/s (zoom at the left shoulder)

Figure B.145: Snapshots of the calculated response at 1.3 m/s.

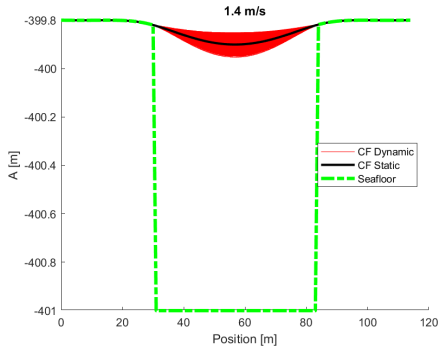

(a) CF - 1.4 m/s

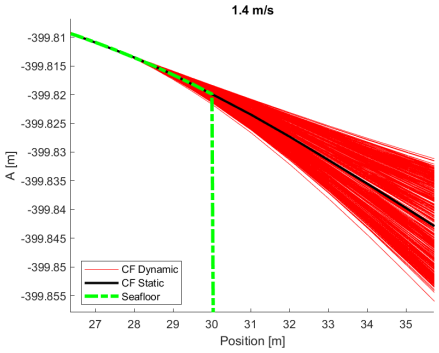

(b) CF - 1.4 m/s (zoom at the left shoulder)

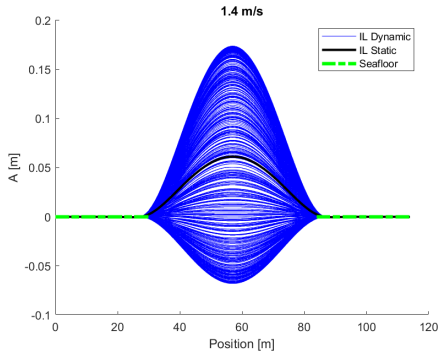

(c) IL - 1.4 m/s

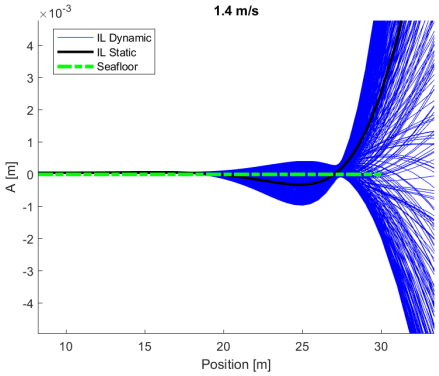

(d) IL - 1.4 m/s (zoom at the left shoulder)

Figure B.146: Snapshots of the calculated response at 1.4 m/s.

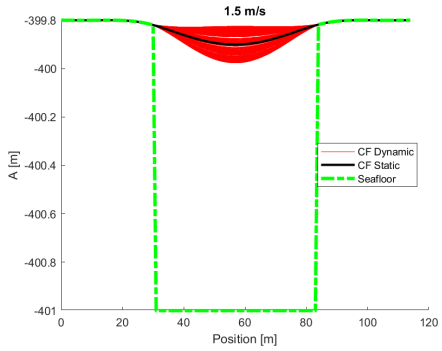

(a) CF - 1.5 m/s

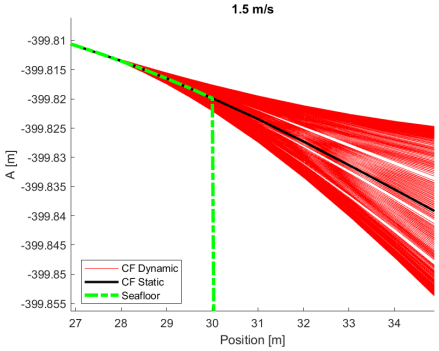

(b) CF - 1.5 m/s (zoom at the left shoulder)

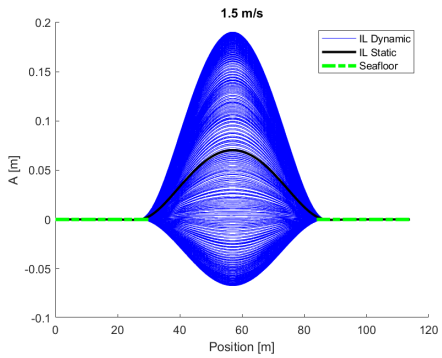

(c) IL - 1.5 m/s

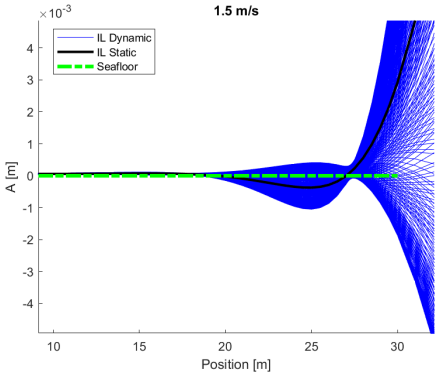

(d) IL - 1.5 m/s (zoom at the left shoulder)

Figure B.147: Snapshots of the calculated response at 1.5 m/s.

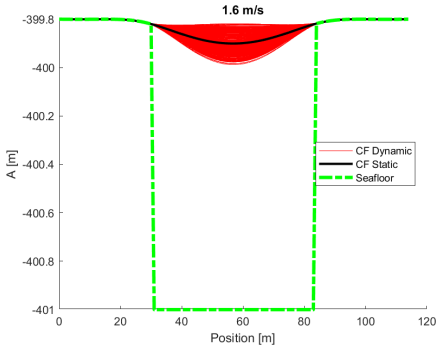

(a) CF - 1.6 m/s

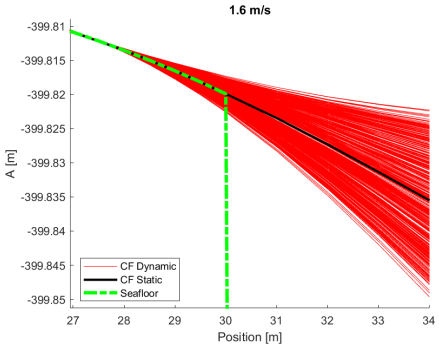

(b) CF - 1.6 m/s (zoom at the left shoulder)

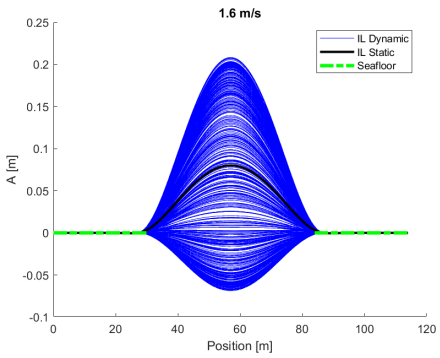

(c) IL - 1.6 m/s

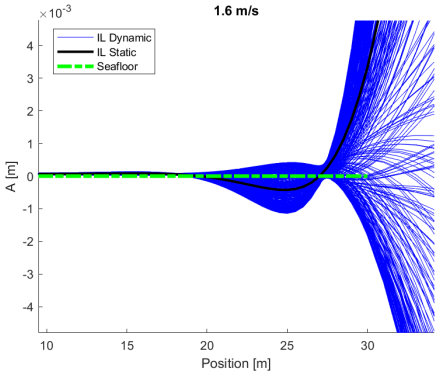

(d) IL - 1.6 m/s (zoom at the left shoulder)

Figure B.148: Snapshots of the calculated response at 1.6 m/s.

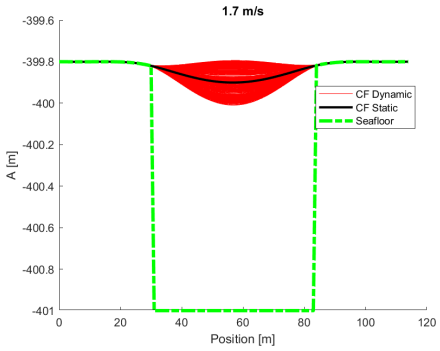

(a) CF - 1.7 m/s

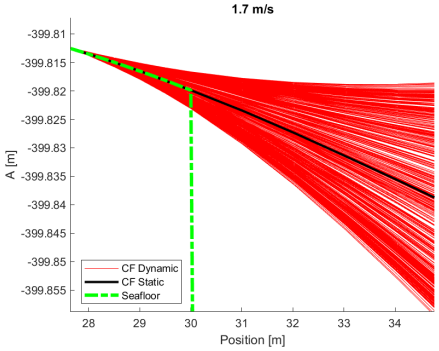

(b) CF - 1.7 m/s (zoom at the left shoulder)

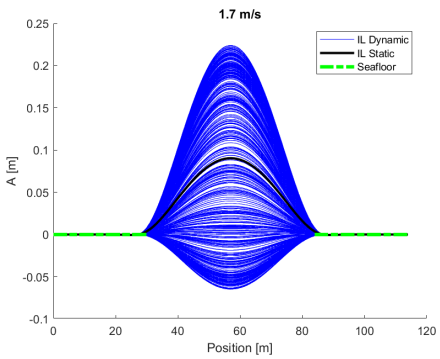

(c) IL - 1.7 m/s

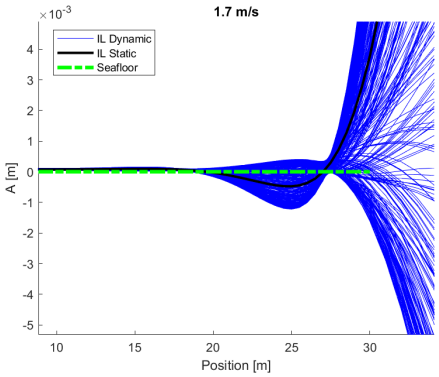

(d) IL - 1.7 m/s (zoom at the left shoulder)

Figure B.149: Snapshots of the calculated response at 1.7 m/s.

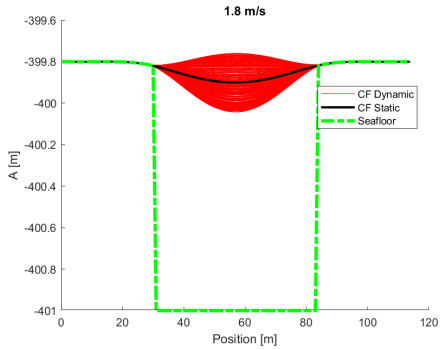

(a) CF - 1.8 m/s

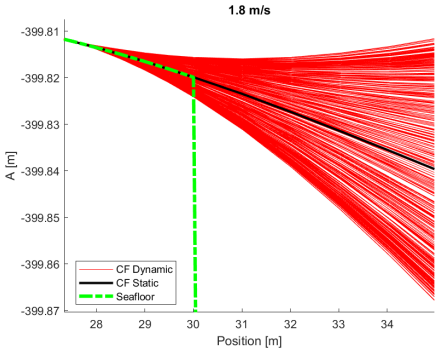

(b) CF - 1.8 m/s (zoom at the left shoulder)

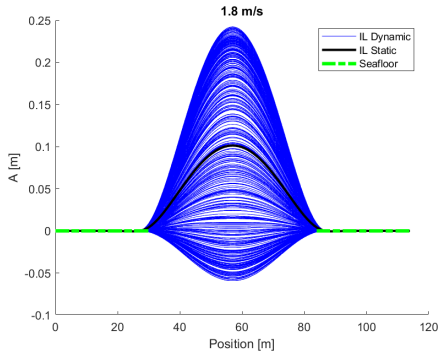

(c) IL - 1.8 m/s

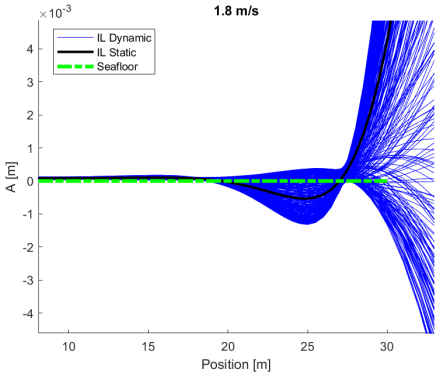

(d) IL - 1.8 m/s (zoom at the left shoulder)

Figure B.150: Snapshots of the calculated response at 1.8 m/s.

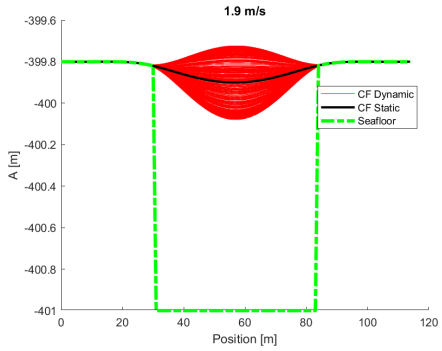

(a) CF - 1.9 m/s

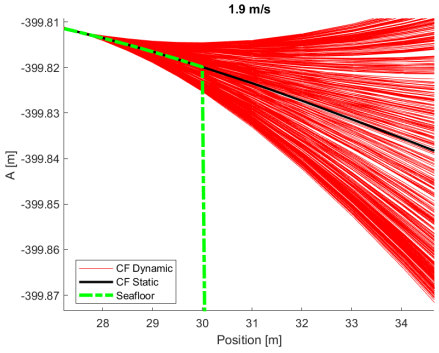

(b) CF - 1.9 m/s (zoom at the left shoulder)

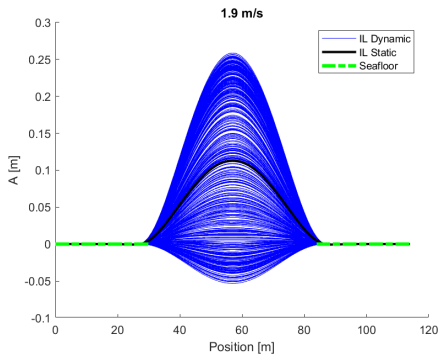

(c) IL - 1.9 m/s

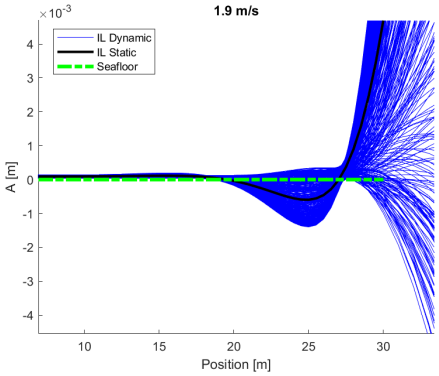

(d) IL - 1.9 m/s (zoom at the left shoulder)

Figure B.151: Snapshots of the calculated response at 1.9 m/s.

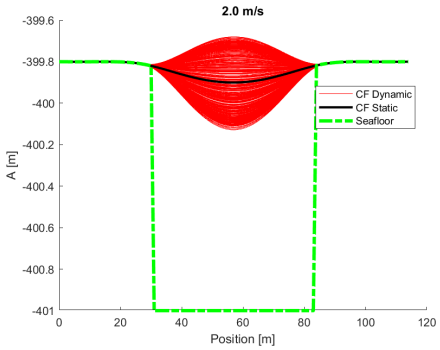

(a) CF - 2.0 m/s

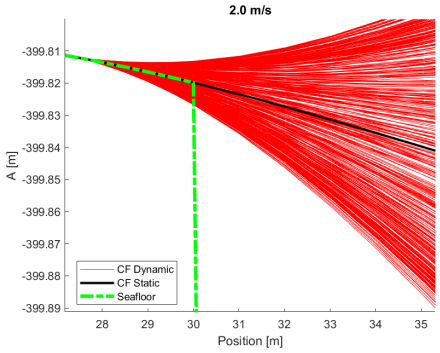

(b) CF - 2.0 m/s (zoom at the left shoulder)

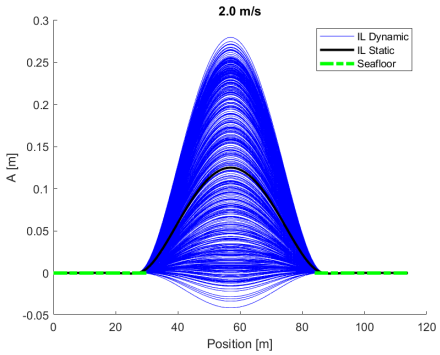

(c) IL - 2.0 m/s

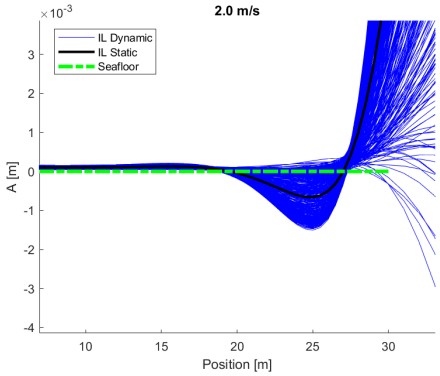

(d) IL - 2.0 m/s (zoom at the left shoulder)

Figure B.152: Snapshots of the calculated response at 2.0 m/s.

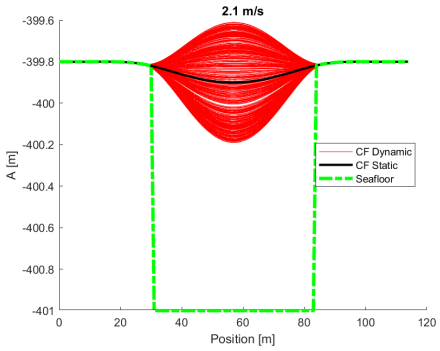

(a) CF - 2.1 m/s

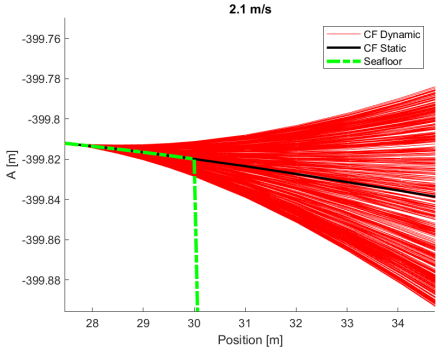

(b) CF - 2.1 m/s (zoom at the left shoulder)

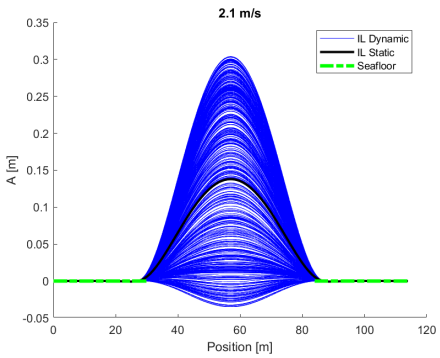

(c) IL - 2.1 m/s

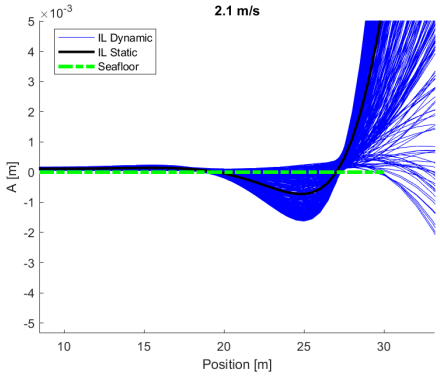

(d) IL - 2.1 m/s (zoom at the left shoulder)

Figure B.153: Snapshots of the calculated response at 2.1 m/s.

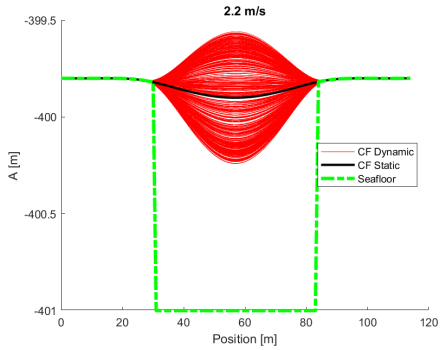

(a) CF - 2.2 m/s

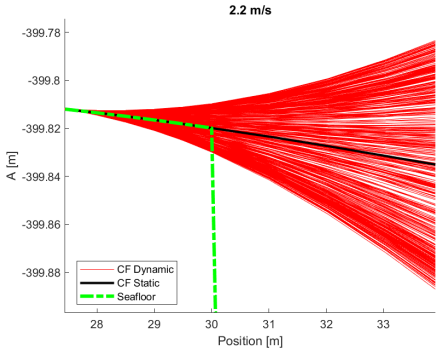

(b) CF - 2.2 m/s (zoom at the left shoulder)

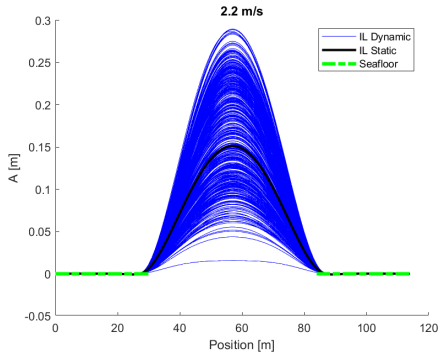

(c) IL - 2.2 m/s

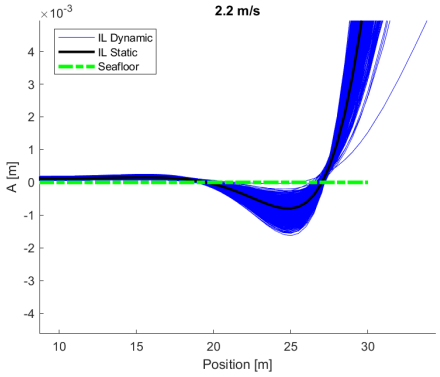

(d) IL - 2.2 m/s (zoom at the left shoulder)

Figure B.154: Snapshots of the calculated response at 2.2 m/s.

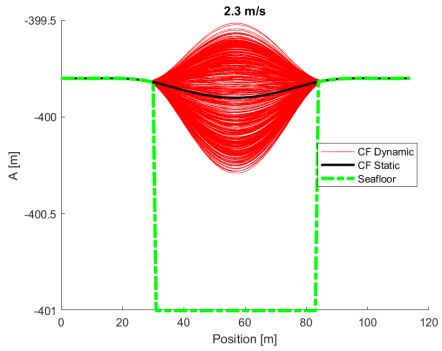

(a) CF - 2.3 m/s

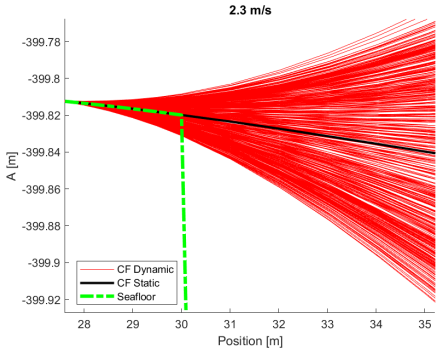

(b) CF - 2.3 m/s (zoom at the left shoulder)

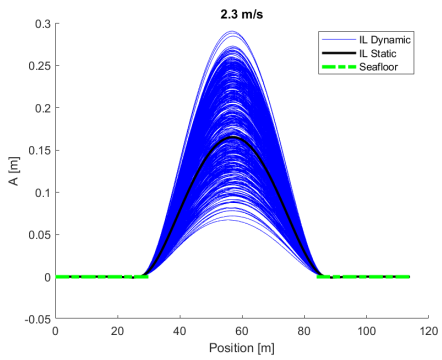

(c) IL - 2.3 m/s

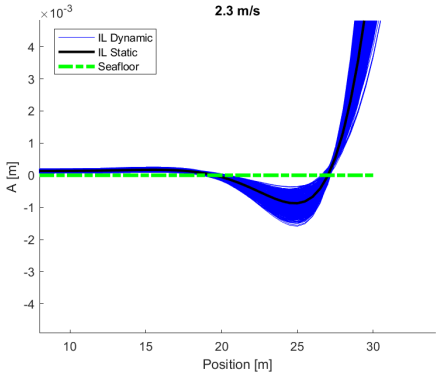

(d) IL - 2.3 m/s (zoom at the left shoulder)

Figure B.155: Snapshots of the calculated response at 2.3 m/s.

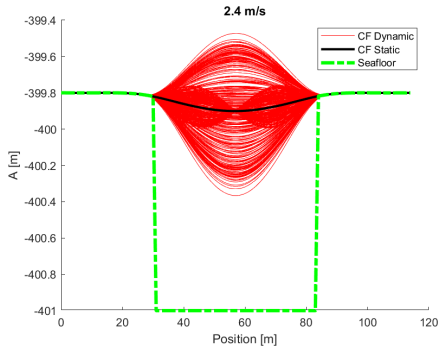

(a) CF - 2.4 m/s

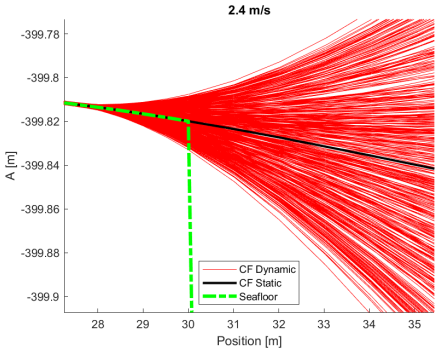

(b) CF - 2.4 m/s (zoom at the left shoulder)

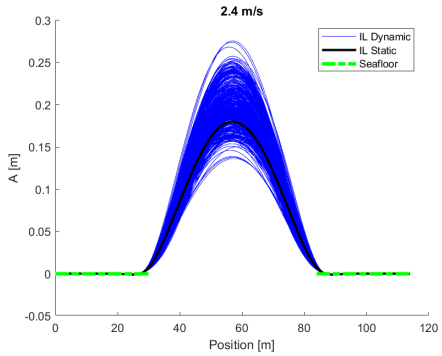

(c) IL - 2.4 m/s

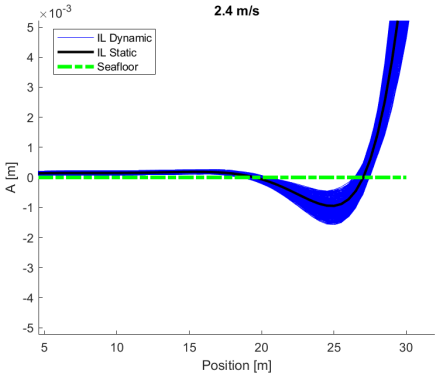

(d) IL - 2.4 m/s (zoom at the left shoulder)

Figure B.156: Snapshots of the calculated response at 2.4 m/s.

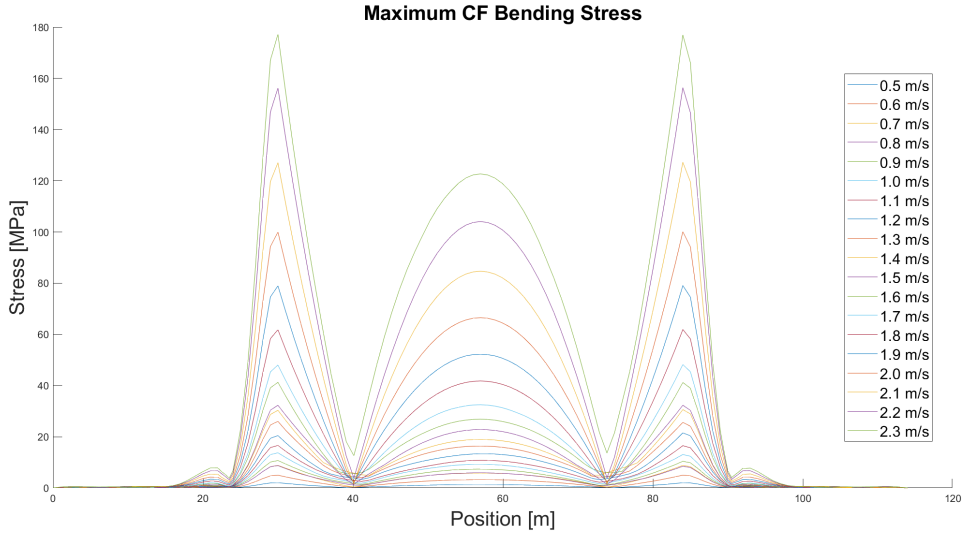

(a) CF - Maximum Bending Stress

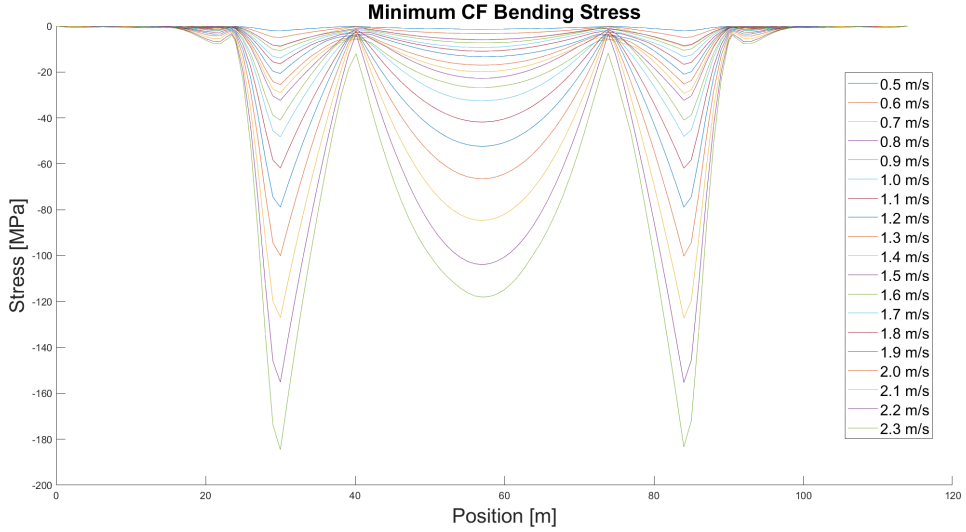

(b) CF - Minimum Bending Stress

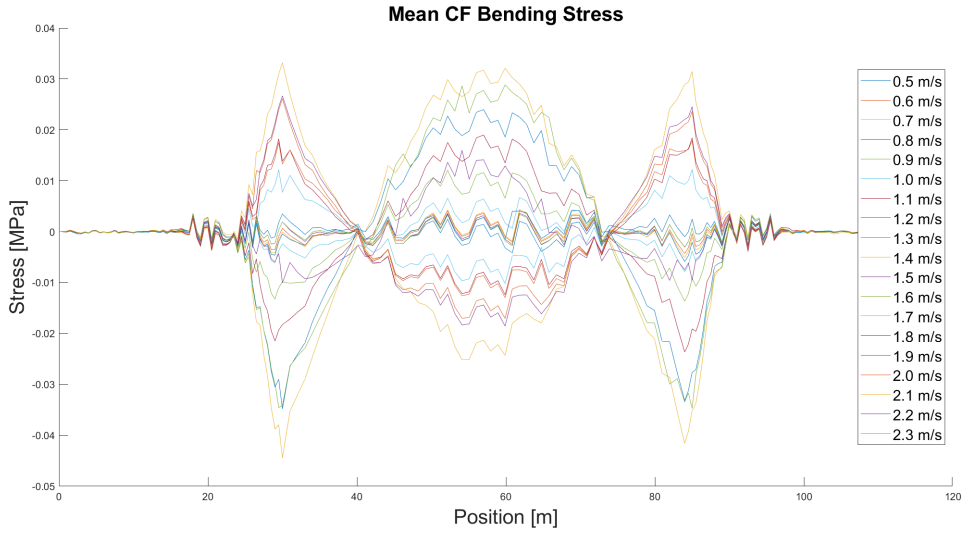

(c) CF - Mean Bending Stress

Figure B.157: Plots of the calculated bending stress distribution in the CF direction for the Linear soil model and $\zeta_{soil} = 8\%$.

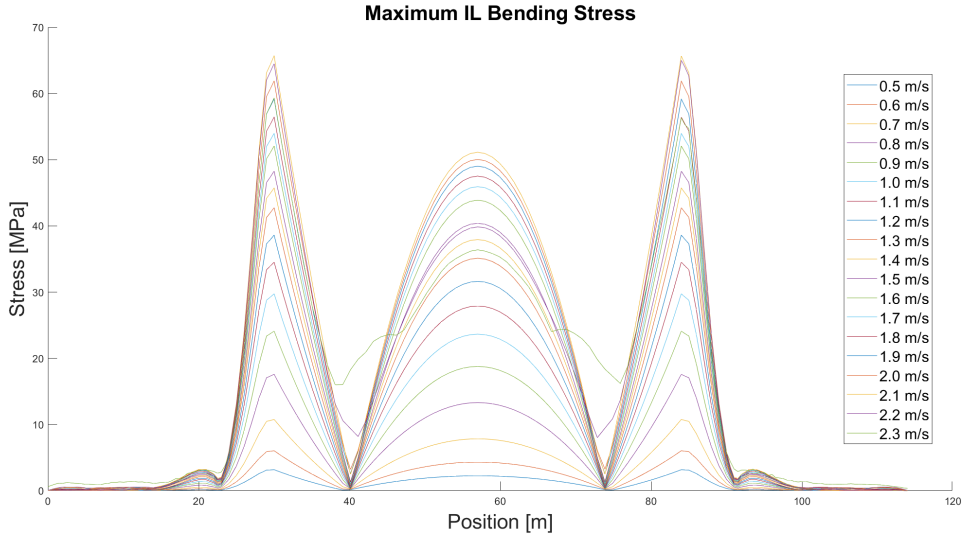

(a) IL - Maximum Bending Stress

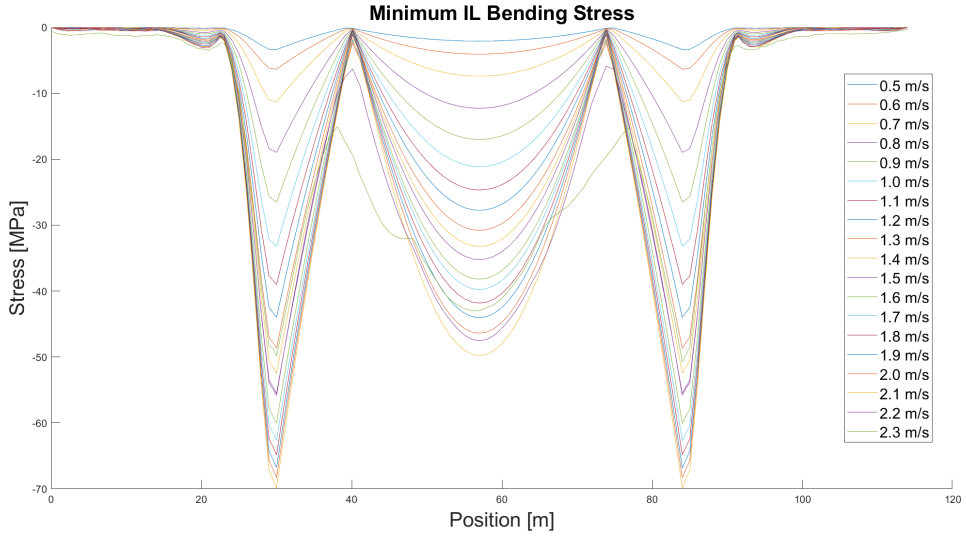

(b) IL - Minimum Bending Stress

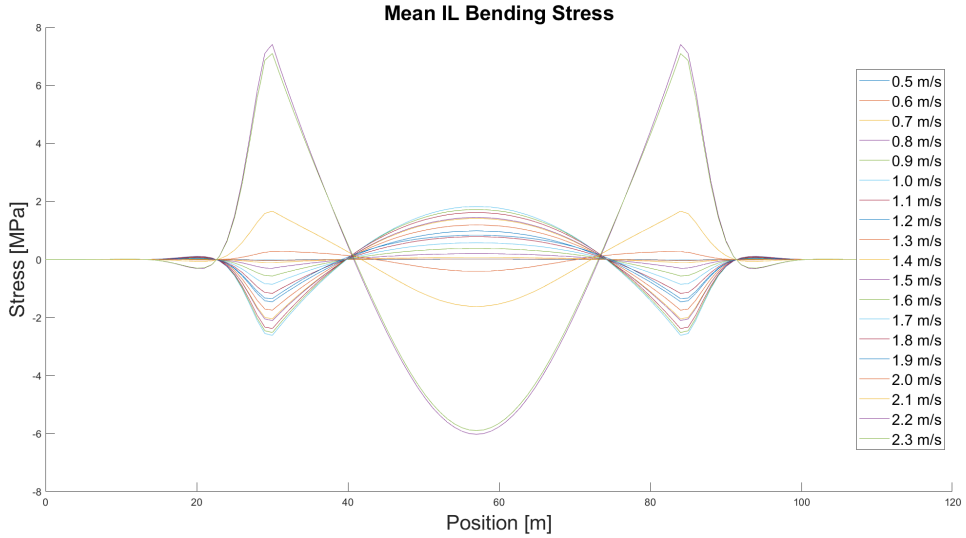

(c) IL - Mean Bending Stress

Figure B.158: Plots of the calculated bending stress distribution in the IL direction for the Linear soil model and $\zeta_{soil} = 8\%$.

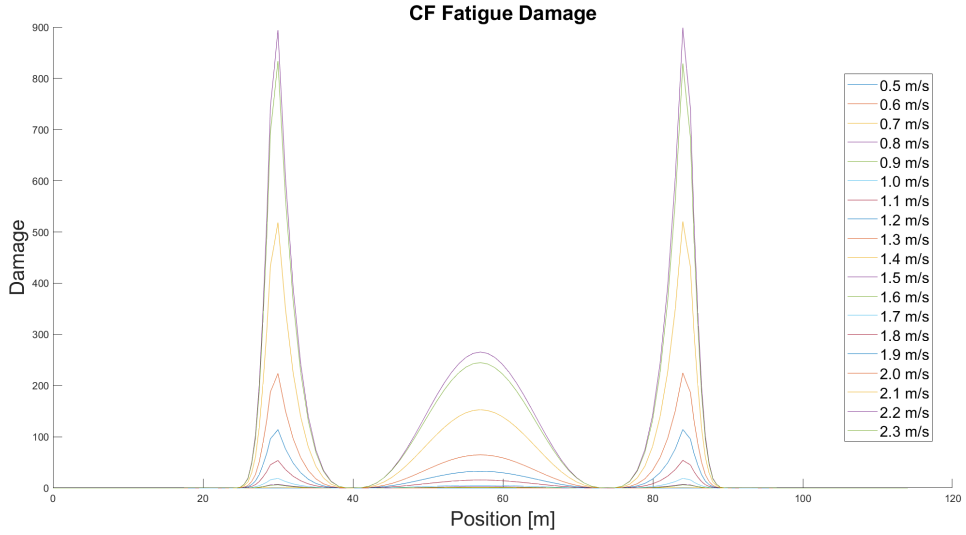

(a) CF - Fatigue Damage Accumulation

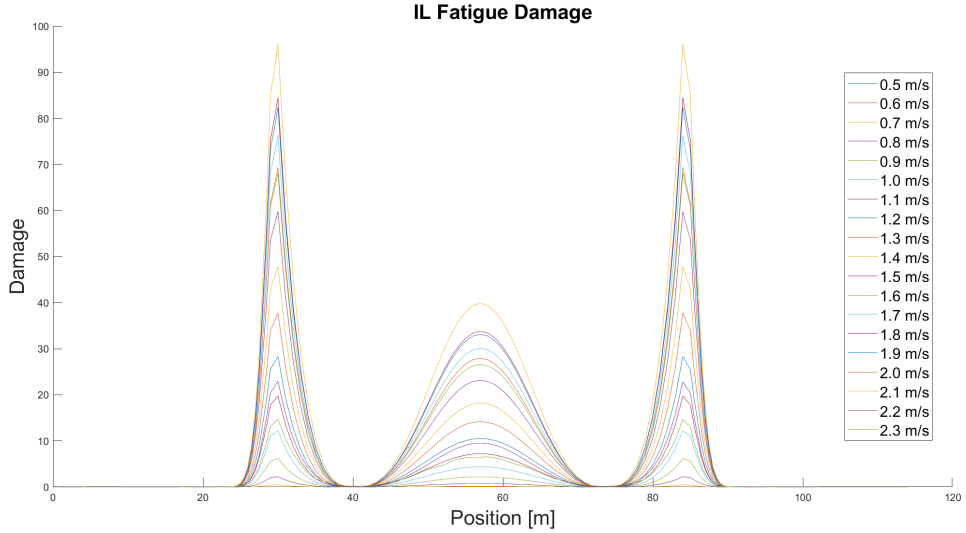

(b) IL - Fatigue Damage Accumulation

Figure B.159: Plots of the calculated fatigue damage distribution in both directions for the Linear soil model and $\zeta_{soil} = 8\%$.

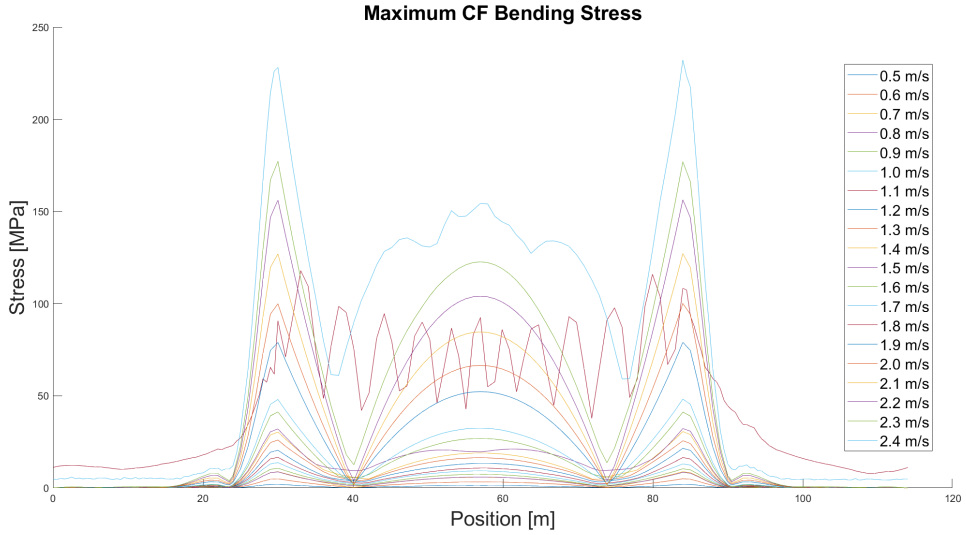

(a) CF - Maximum Bending Stress

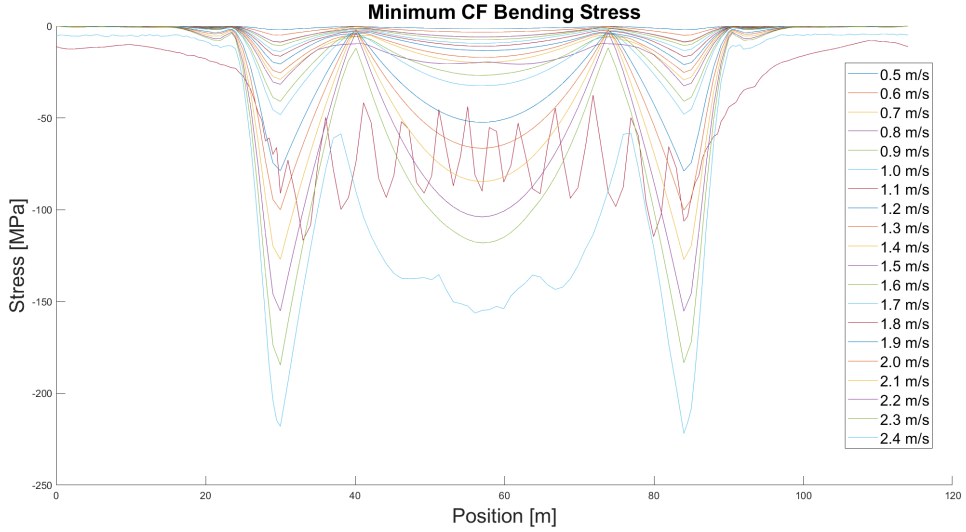

(b) CF - Minimum Bending Stress

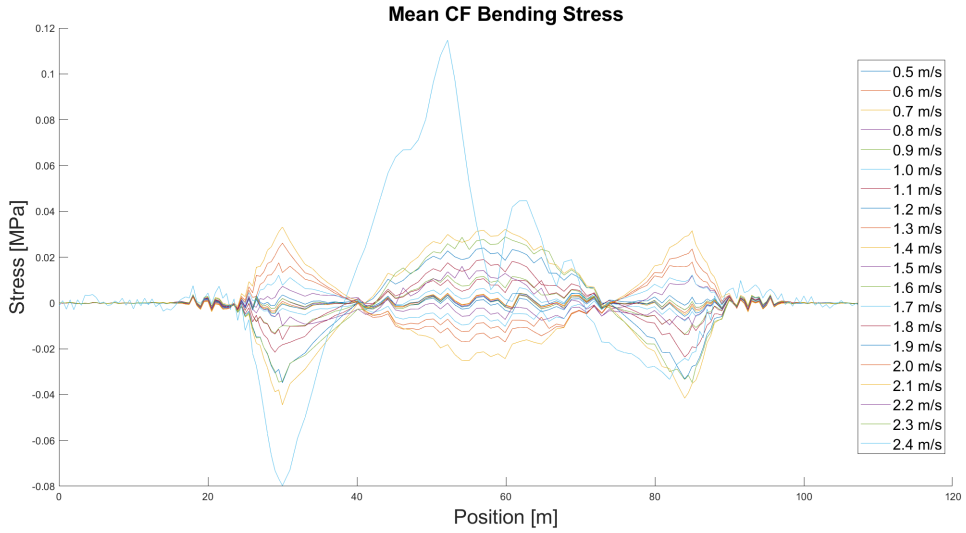

(c) CF - Mean Bending Stress

Figure B.160: Plots of the calculated bending stress distribution in the CF direction for the Linear soil model and $\zeta_{soil} = 8\%$ including the velocity of 2.4 m/s.

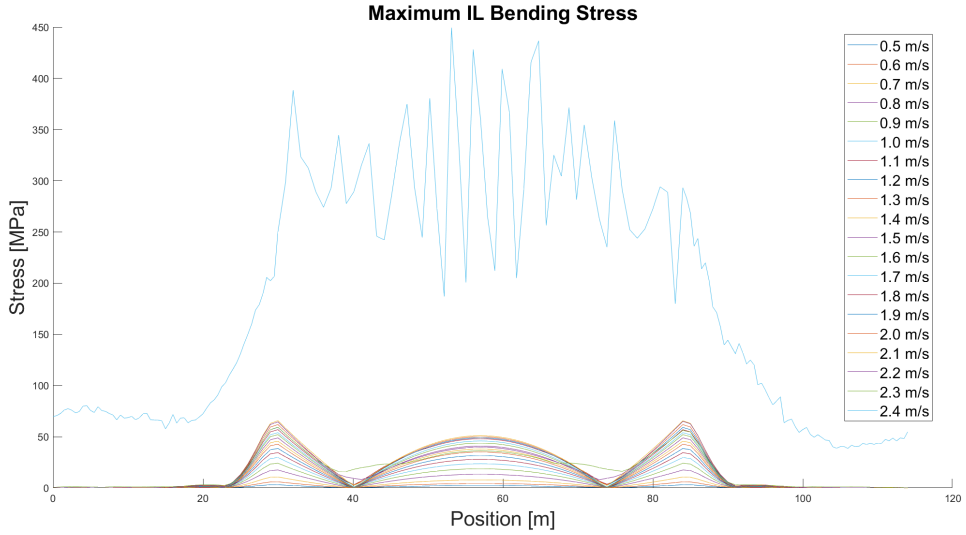

(a) IL - Maximum Bending Stress

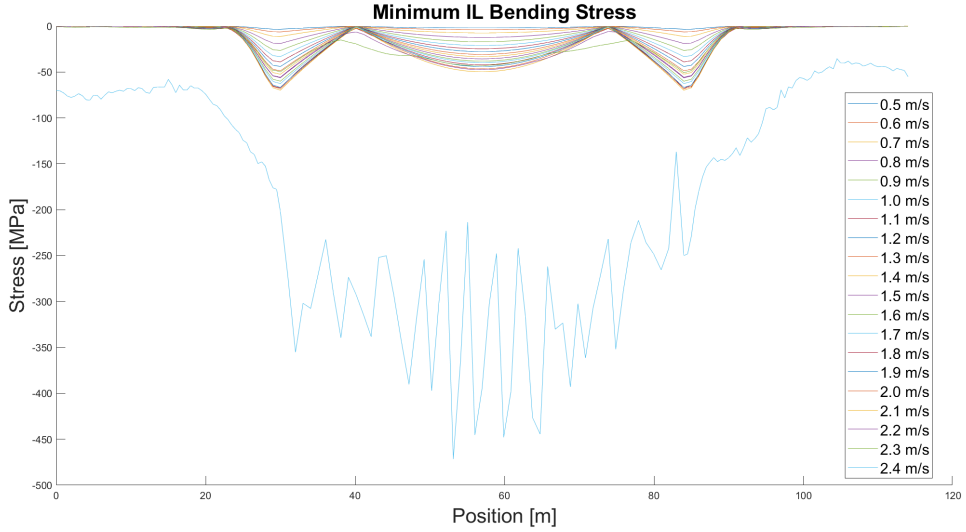

(b) IL - Minimum Bending Stress

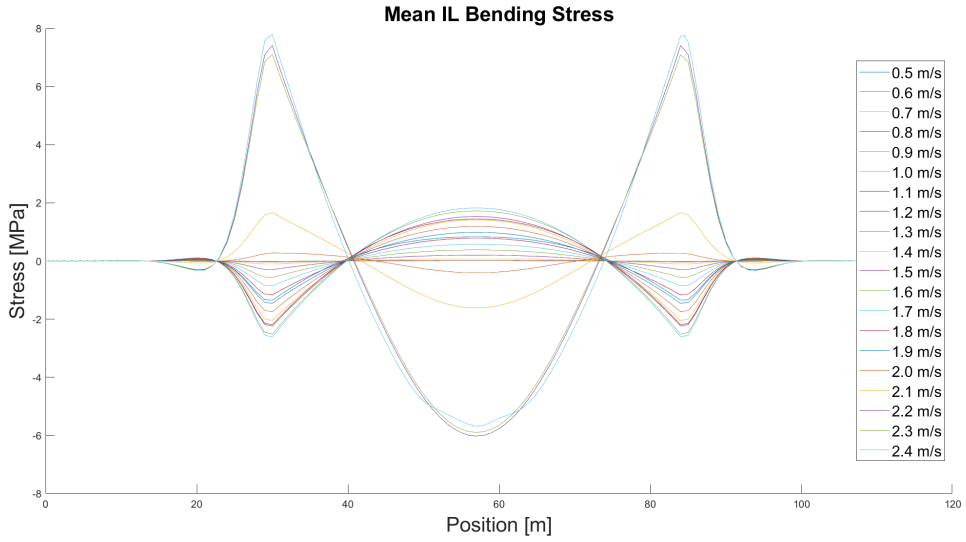

(c) IL - Mean Bending Stress

Figure B.161: Plots of the calculated bending stress distribution in the IL direction for the Linear soil model and $\zeta_{soil} = 8\%$ including the velocity of 2.4 m/s.

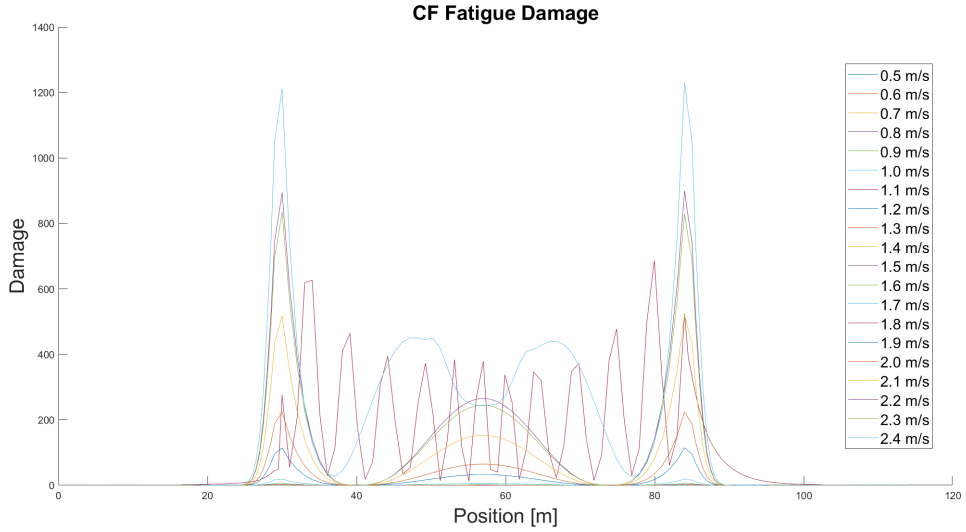

(a) CF - Fatigue Damage Accumulation

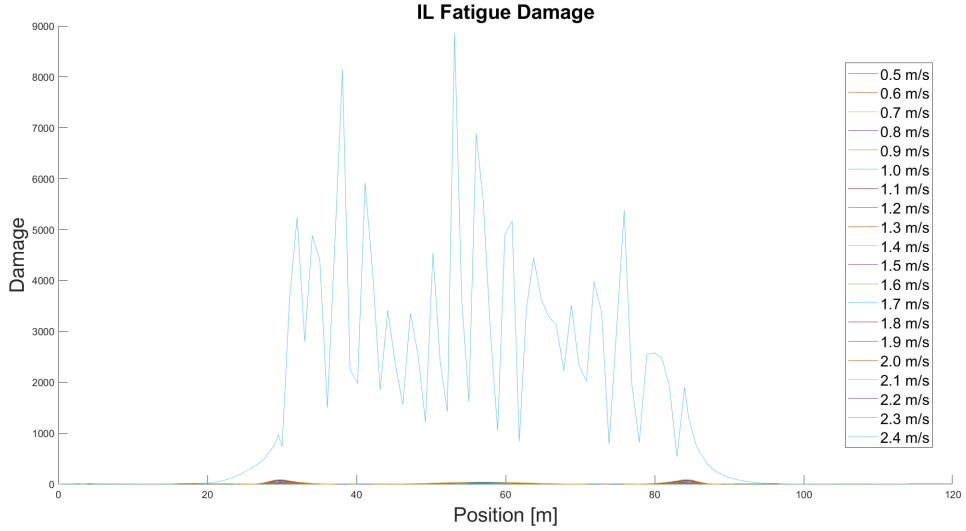

(b) IL - Fatigue Damage Accumulation

Figure B.162: Plots of the calculated fatigue damage distribution in both directions for the Linear soil model and $\zeta_{soil} = 8\%$ including the velocity of 2.4 m/s.

B.6 Comparative Study - Soil Damping Ratio 0.08 - Total set of results

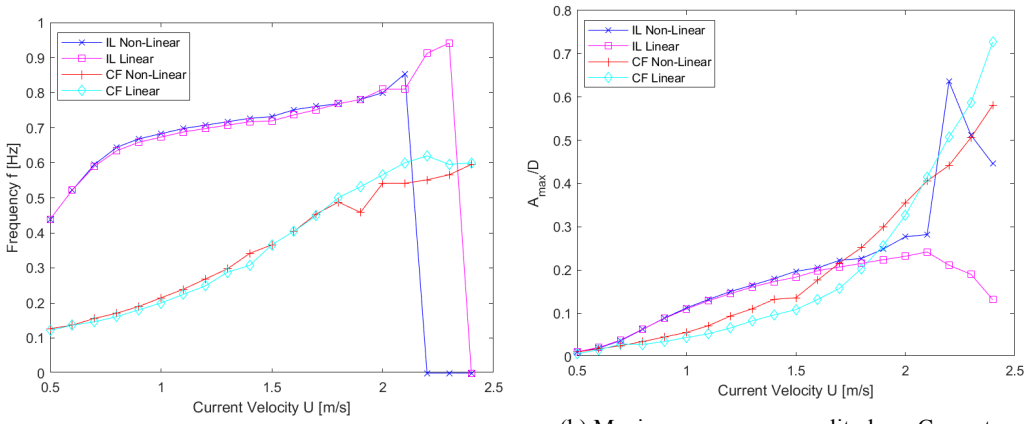

(a) Response Frequency vs Current Velocity

(b) Maximum response amplitude vs Current Velocity

Figure B.163: Plots of the dominant response frequencies and the maximum response amplitudes for the Non-Linear and Linear soil models and $\zeta_{soil} = 8\%$.

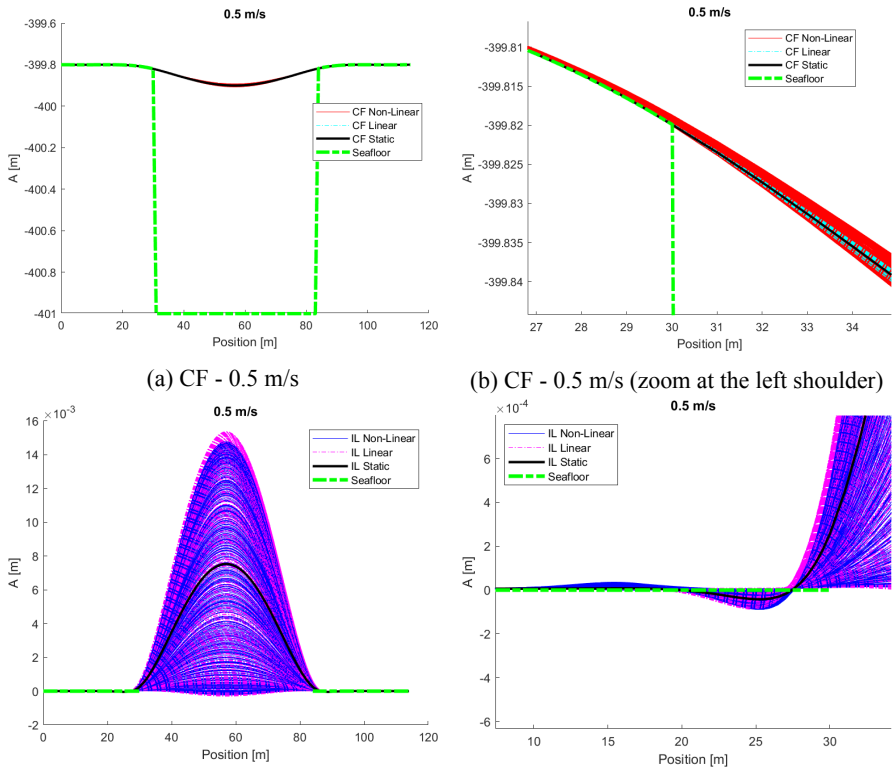

(a) CF - 0.5 m/s

(b) CF - 0.5 m/s (zoom at the left shoulder)

(c) IL - 0.5 m/s

(d) IL - 0.5 m/s (zoom at the left shoulder)

Figure B.164: Comparative snapshots of the calculated responses for the two soil models at 0.5 m/s.

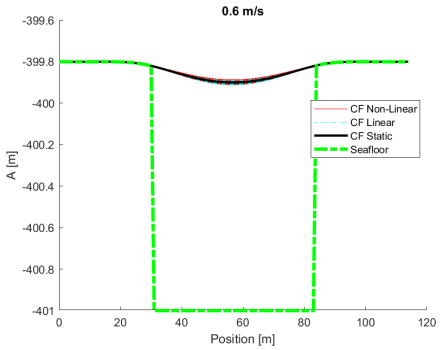

(a) CF - 0.6 m/s

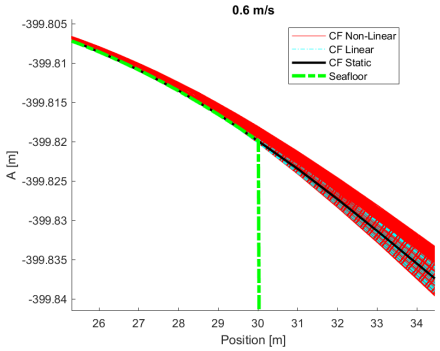

(b) CF - 0.6 m/s (zoom at the left shoulder)

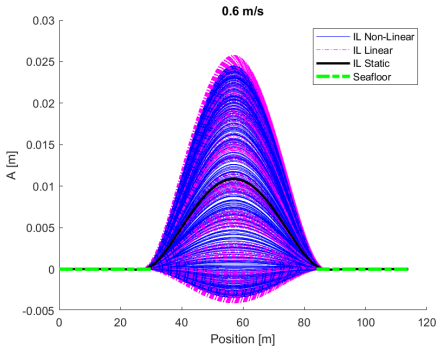

(c) IL - 0.6 m/s

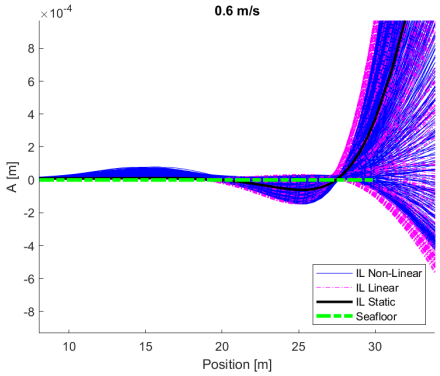

(d) IL - 0.6 m/s (zoom at the left shoulder)

Figure B.165: Comparative snapshots of the calculated responses for the two soil models at 0.6 m/s.

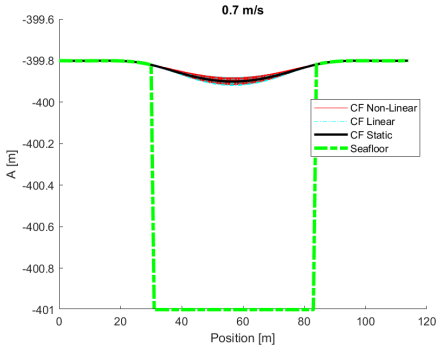

(a) CF - 0.7 m/s

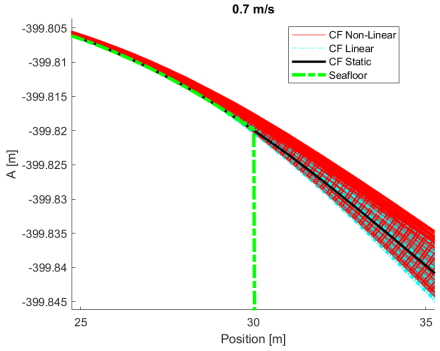

(b) CF - 0.7 m/s (zoom at the left shoulder)

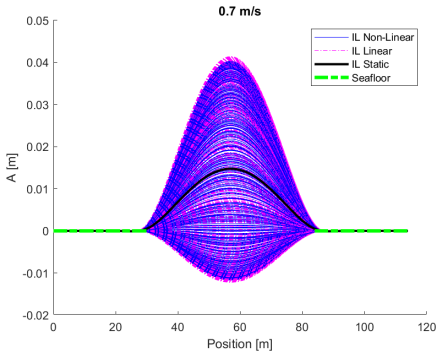

(c) IL - 0.7 m/s

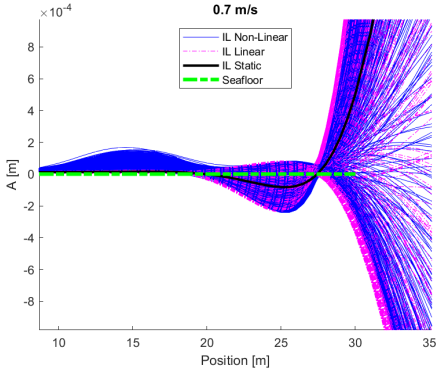

(d) IL - 0.7 m/s (zoom at the left shoulder)

Figure B.166: Comparative snapshots of the calculated responses for the two soil models at 0.7 m/s.

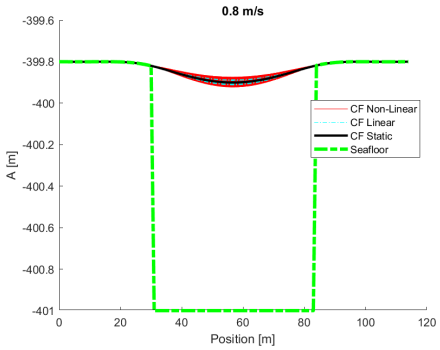

(a) CF - 0.8 m/s

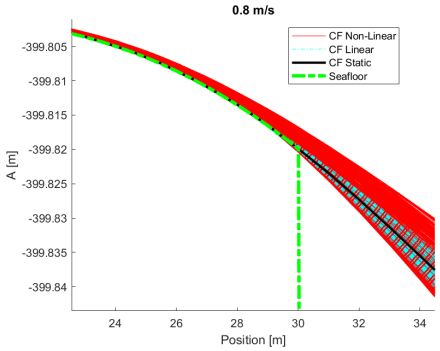

(b) CF - 0.8 m/s (zoom at the left shoulder)

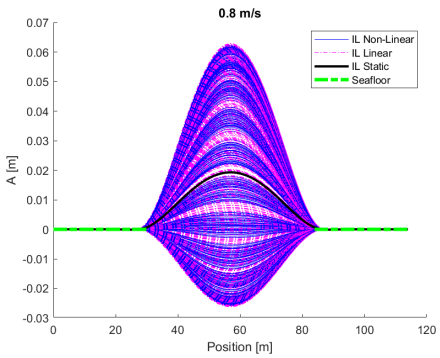

(c) IL - 0.8 m/s

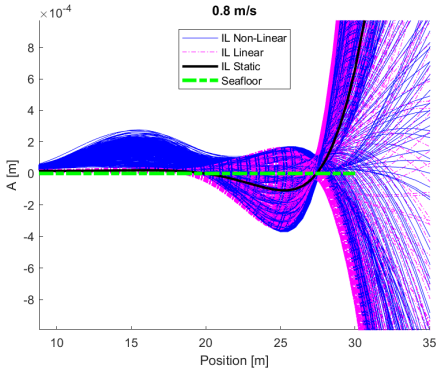

(d) IL - 0.8 m/s (zoom at the left shoulder)

Figure B.167: Comparative snapshots of the calculated responses for the two soil models at 0.8 m/s.

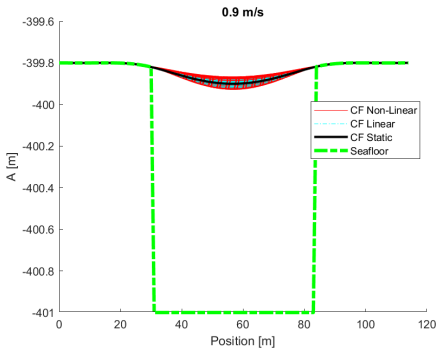

(a) CF - 0.9 m/s

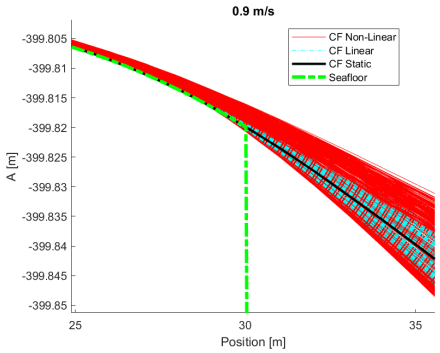

(b) CF - 0.9 m/s (zoom at the left shoulder)

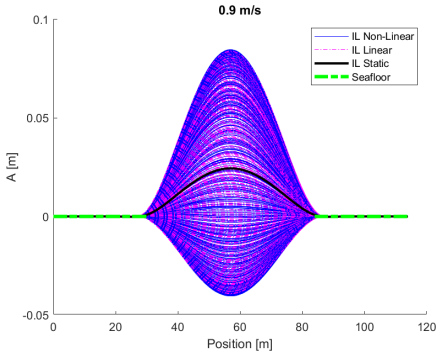

(c) IL - 0.9 m/s

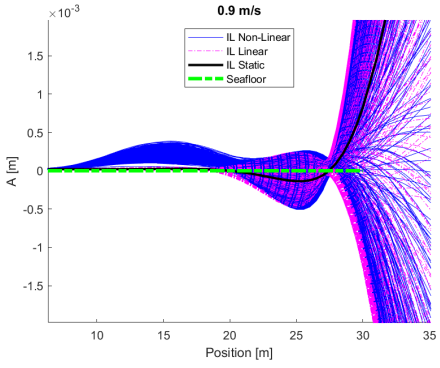

(d) IL - 0.9 m/s (zoom at the left shoulder)

Figure B.168: Comparative snapshots of the calculated responses for the two soil models at 0.9 m/s.

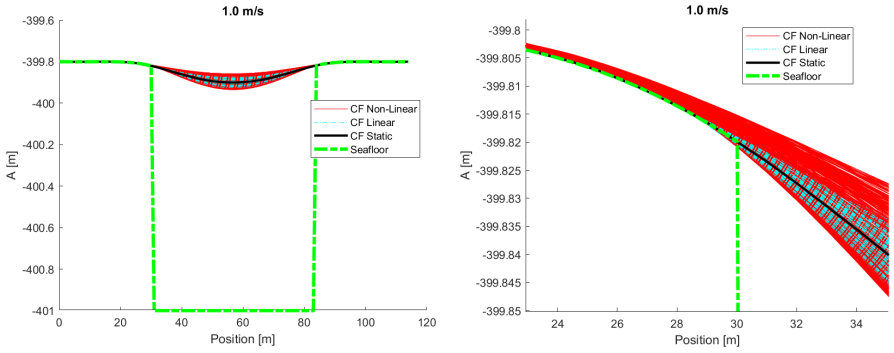

(a) CF - 1.0 m/s

(b) CF - 1.0 m/s (zoom at the left shoulder)

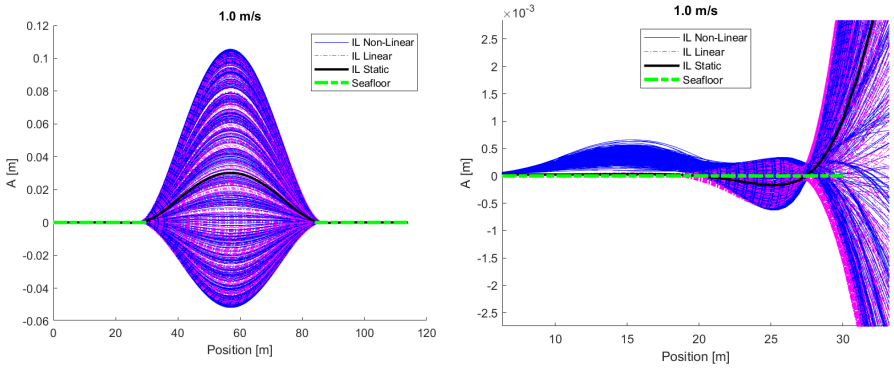

(c) IL - 1.0 m/s

(d) IL - 1.0 m/s (zoom at the left shoulder)

Figure B.169: Comparative snapshots of the calculated responses for the two soil models at 1.0 m/s.

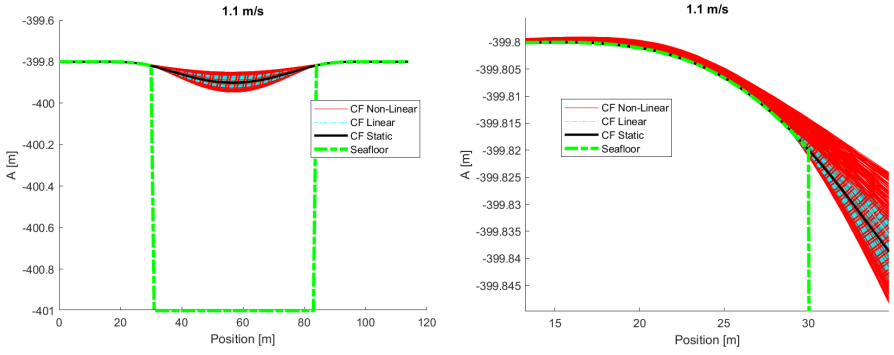

(a) CF - 1.1 m/s

(b) CF - 1.1 m/s (zoom at the left shoulder)

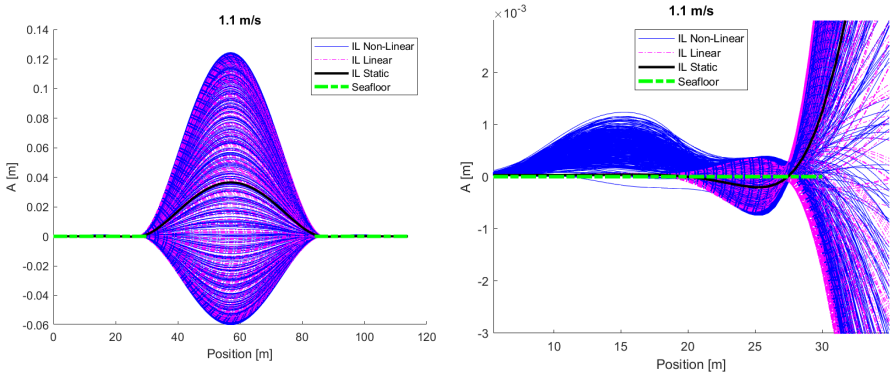

(c) IL - 1.1 m/s

(d) IL - 1.1 m/s (zoom at the left shoulder)

Figure B.170: Comparative snapshots of the calculated responses for the two soil models at 1.1 m/s.

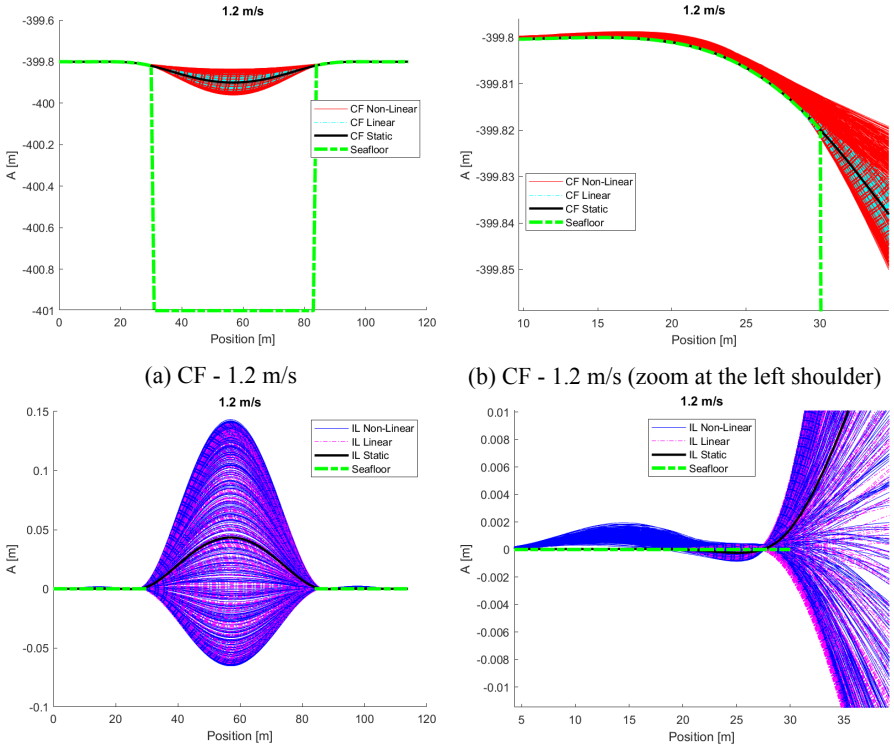

(a) CF - 1.2 m/s (b) CF - 1.2 m/s (zoom at the left shoulder)

(c) IL - 1.2 m/s (d) IL - 1.2 m/s (zoom at the left shoulder)

Figure B.171: Comparative snapshots of the calculated responses for the two soil models at 1.2 m/s.

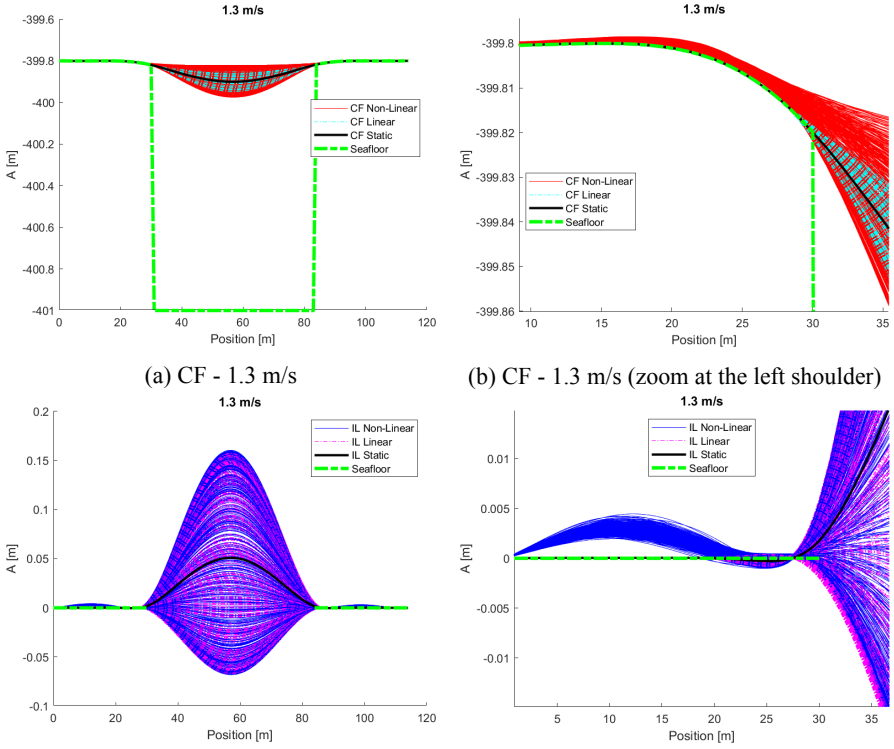

(a) CF - 1.3 m/s (b) CF - 1.3 m/s (zoom at the left shoulder)

(c) IL - 1.3 m/s (d) IL - 1.3 m/s (zoom at the left shoulder)

Figure B.172: Comparative snapshots of the calculated responses for the two soil models at 1.3 m/s.

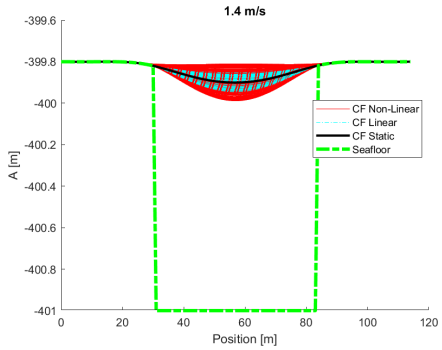

(a) CF - 1.4 m/s

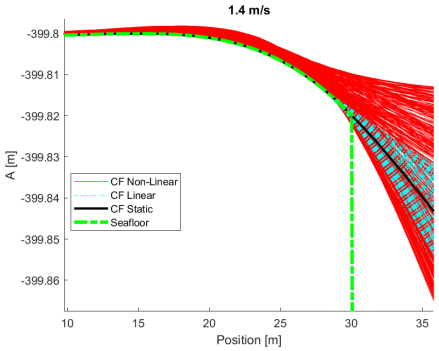

(b) CF - 1.4 m/s (zoom at the left shoulder)

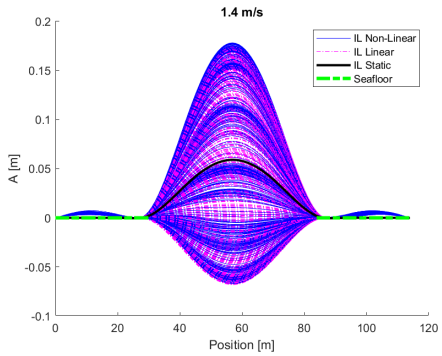

(c) IL - 1.4 m/s

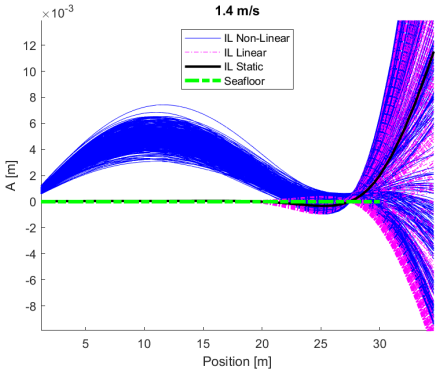

(d) IL - 1.4 m/s (zoom at the left shoulder)

Figure B.173: Comparative snapshots of the calculated responses for the two soil models at 1.4 m/s.

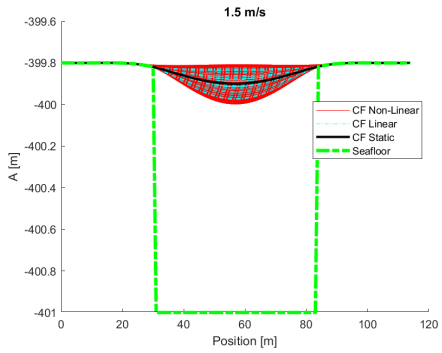

(a) CF - 1.5 m/s

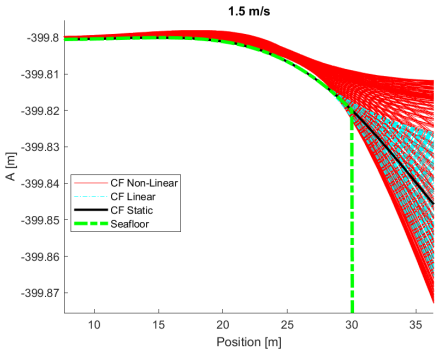

(b) CF - 1.5 m/s (zoom at the left shoulder)

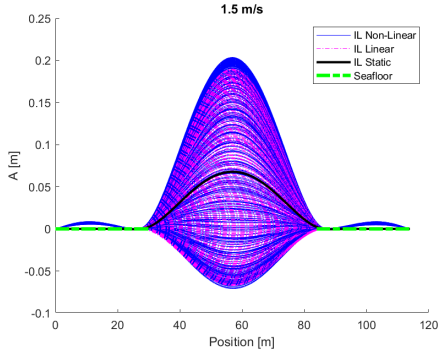

(c) IL - 1.5 m/s

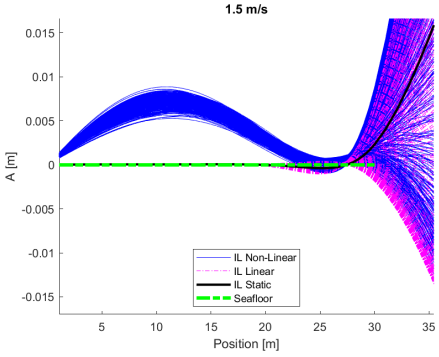

(d) IL - 1.5 m/s (zoom at the left shoulder)

Figure B.174: Comparative snapshots of the calculated responses for the two soil models at 1.5 m/s.

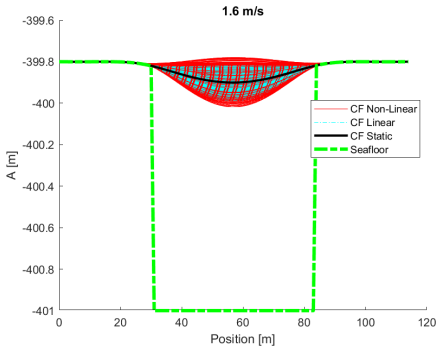

(a) CF - 1.6 m/s

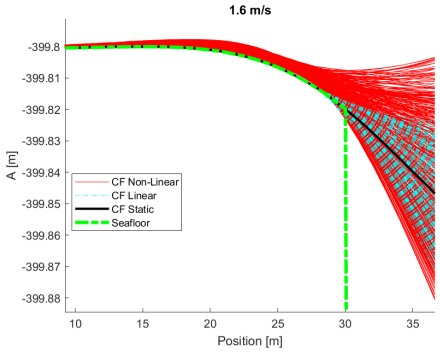

(b) CF - 1.6 m/s (zoom at the left shoulder)

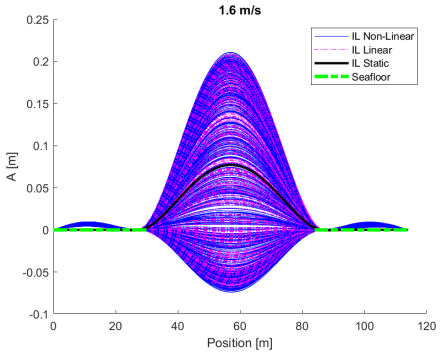

(c) IL - 1.6 m/s

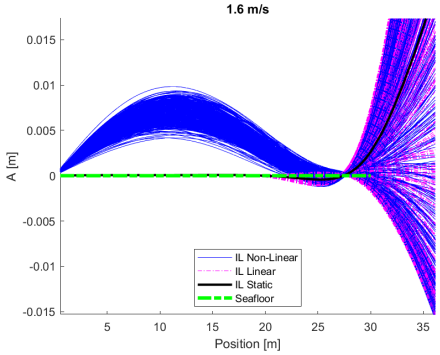

(d) IL - 1.6 m/s (zoom at the left shoulder)

Figure B.175: Comparative snapshots of the calculated responses for the two soil models at 1.6 m/s.

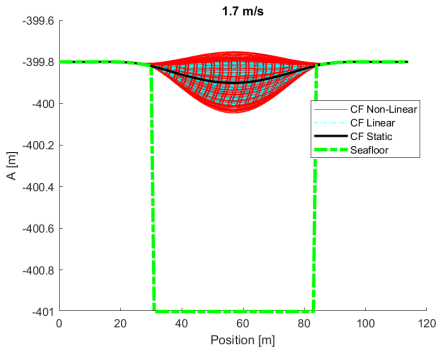

(a) CF - 1.7 m/s

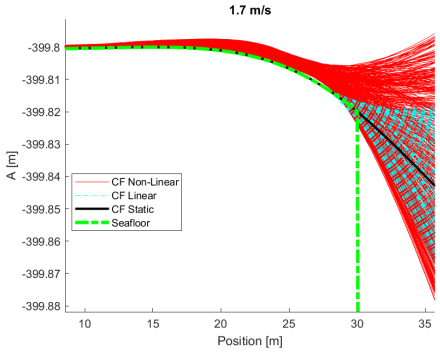

(b) CF - 1.7 m/s (zoom at the left shoulder)

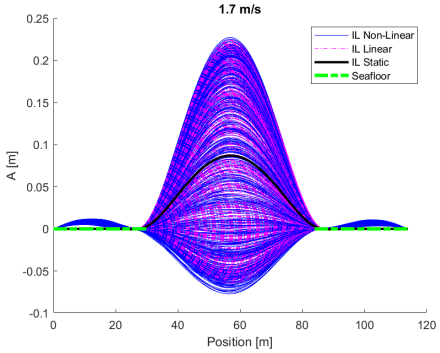

(c) IL - 1.7 m/s

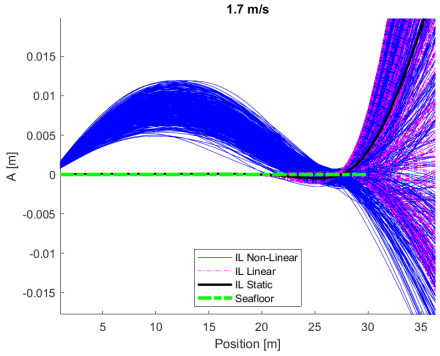

(d) IL - 1.7 m/s (zoom at the left shoulder)

Figure B.176: Comparative snapshots of the calculated responses for the two soil models at 1.7 m/s.

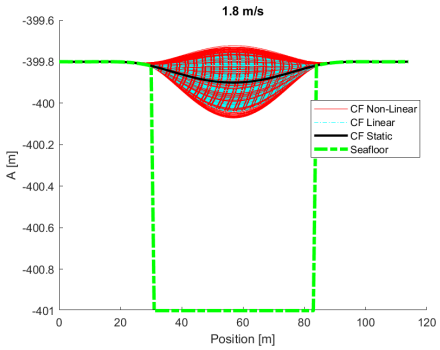

(a) CF - 1.8 m/s

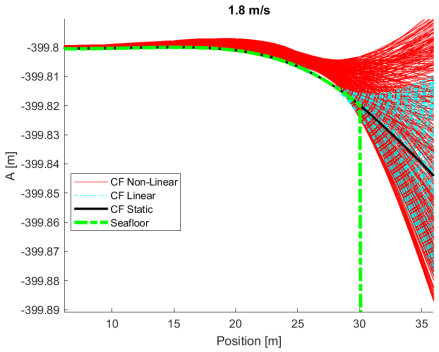

(b) CF - 1.8 m/s (zoom at the left shoulder)

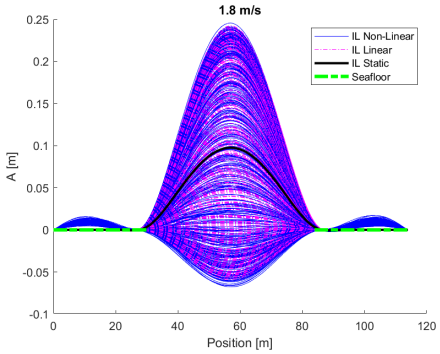

(c) IL - 1.8 m/s

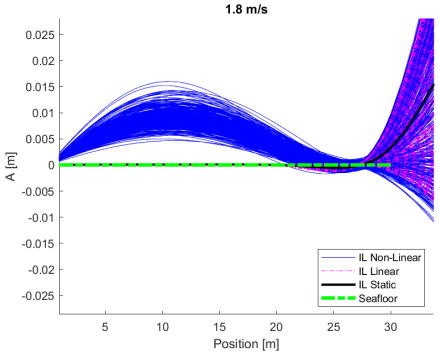

(d) IL - 1.8 m/s (zoom at the left shoulder)

Figure B.177: Comparative snapshots of the calculated responses for the two soil models at 1.8 m/s.

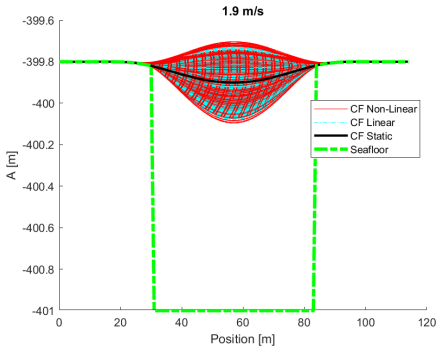

(a) CF - 1.9 m/s

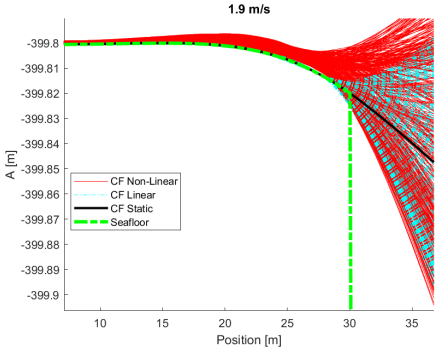

(b) CF - 1.9 m/s (zoom at the left shoulder)

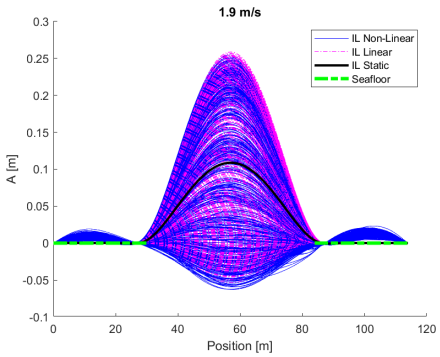

(c) IL - 1.9 m/s

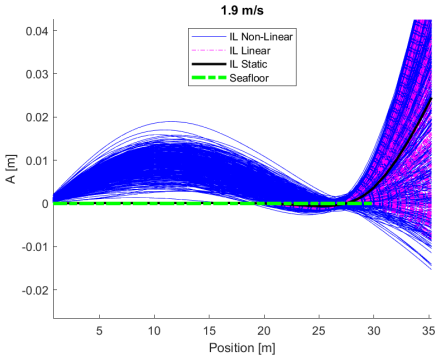

(d) IL - 1.9 m/s (zoom at the left shoulder)

Figure B.178: Comparative snapshots of the calculated responses for the two soil models at 1.9 m/s.

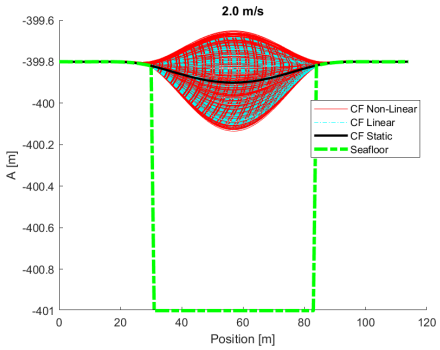

(a) CF - 2.0 m/s

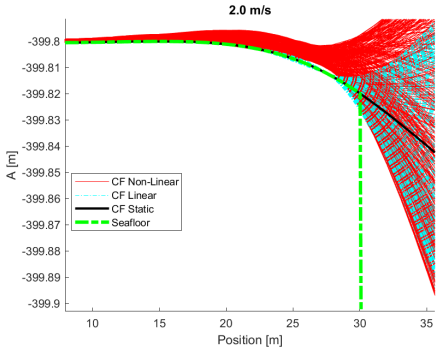

(b) CF - 2.0 m/s (zoom at the left shoulder)

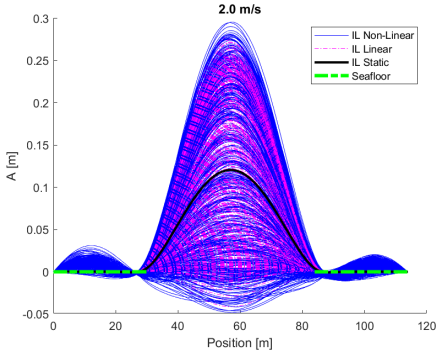

(c) IL - 2.0 m/s

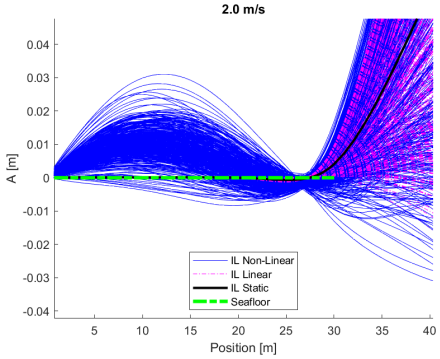

(d) IL - 2.0 m/s (zoom at the left shoulder)

Figure B.179: Comparative snapshots of the calculated responses for the two soil models at 2.0 m/s.

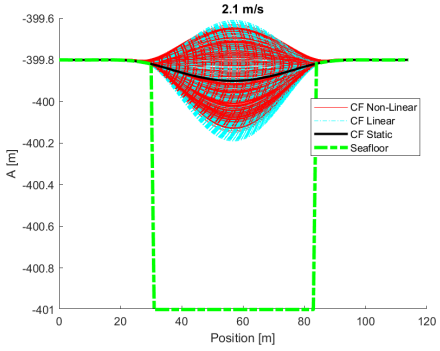

(a) CF - 2.1 m/s

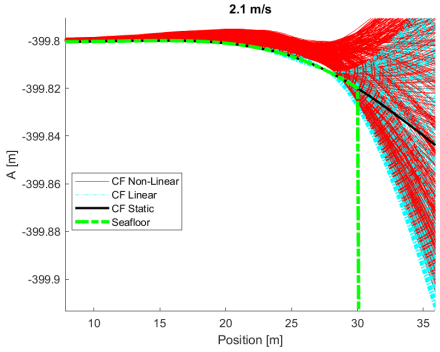

(b) CF - 2.1 m/s (zoom at the left shoulder)

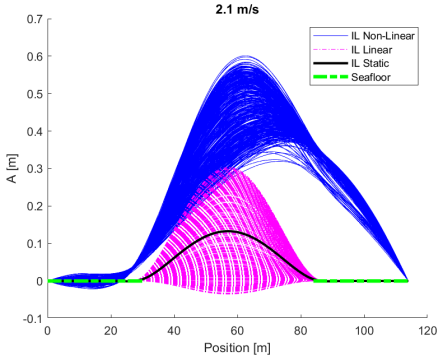

(c) IL - 2.1 m/s

Figure B.180: Comparative snapshots of the calculated responses for the two soil models at 2.1 m/s.

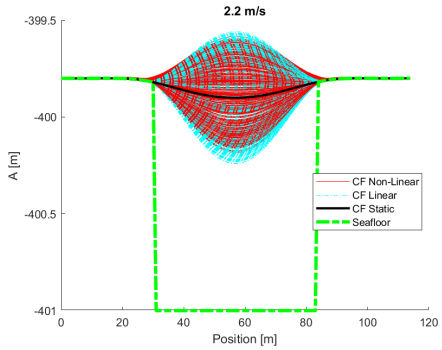

(a) CF - 2.2 m/s

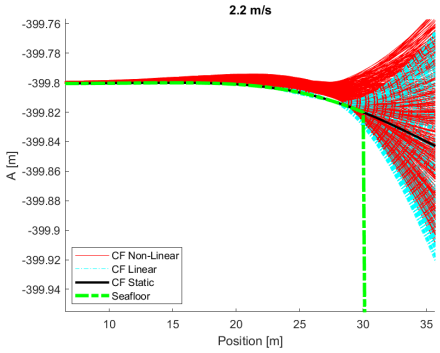

(b) CF - 2.2 m/s (zoom at the left shoulder)

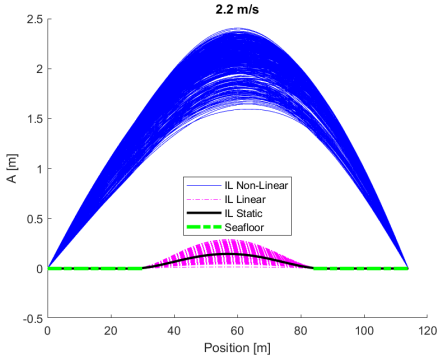

(c) IL - 2.2 m/s

Figure B.181: Comparative snapshots of the calculated responses for the two soil models at 2.2 m/s.

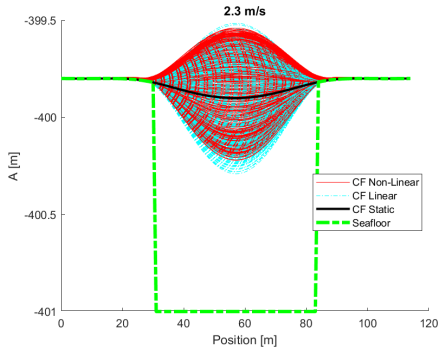

(a) CF - 2.3 m/s

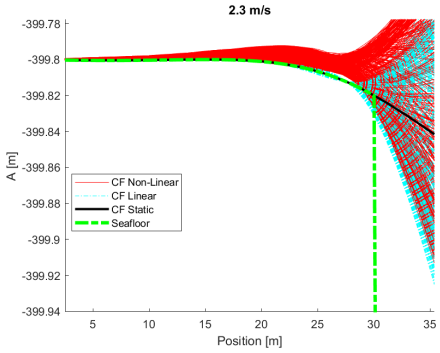

(b) CF - 2.3 m/s (zoom at the left shoulder)

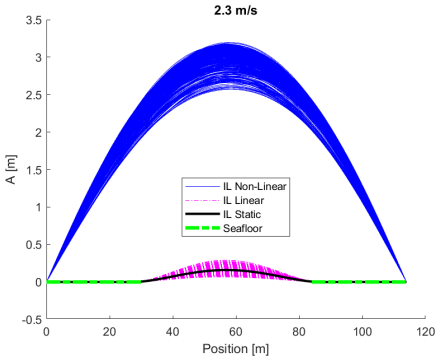

(c) IL - 2.3 m/s

Figure B.182: Comparative snapshots of the calculated responses for the two soil models at 2.3 m/s.

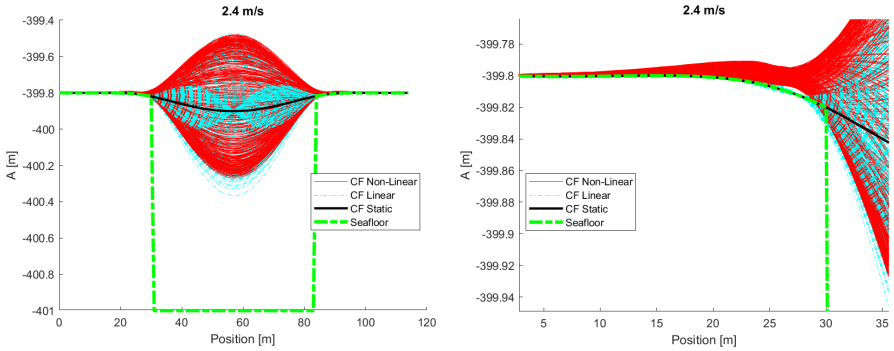

(a) CF - 2.4 m/s

(b) CF - 2.4 m/s (zoom at the left shoulder)

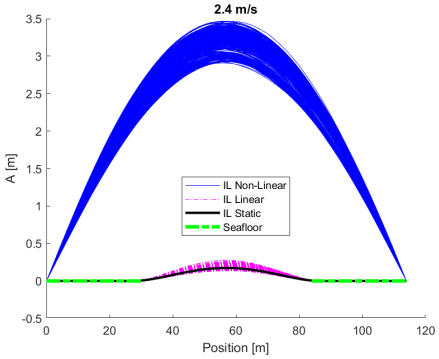

(c) IL - 2.4 m/s

Figure B.183: Comparative snapshots of the calculated responses for the two soil models at 2.4 m/s.

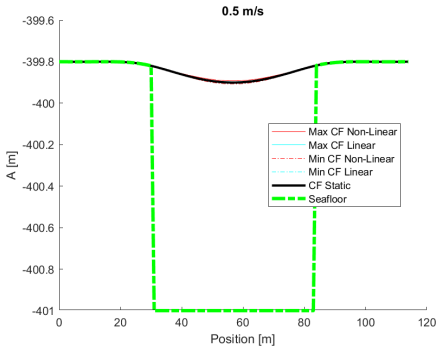

(a) CF - 0.5 m/s

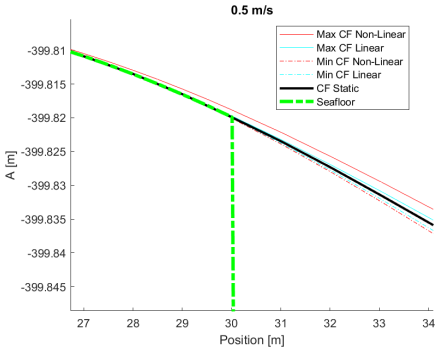

(b) CF - 0.5 m/s (zoom at the left shoulder)

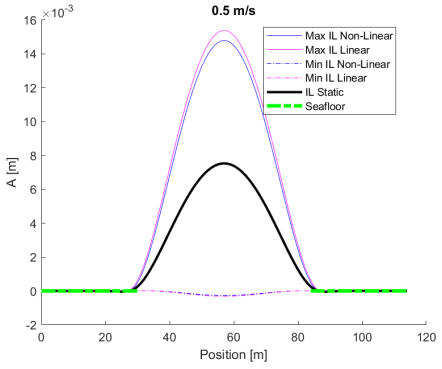

(c) IL - 0.5 m/s

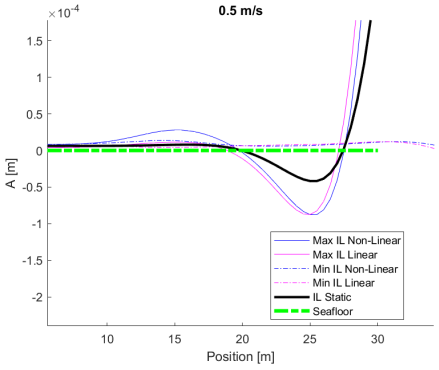

(d) IL - 0.5 m/s (zoom at the left shoulder)

Figure B.184: Comparative snapshots of the max and min responses for the two soil models at 0.5 m/s.

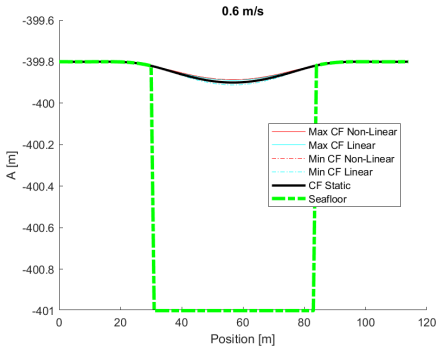

(a) CF - 0.6 m/s

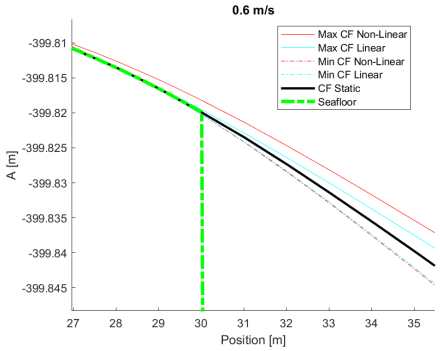

(b) CF - 0.6 m/s (zoom at the left shoulder)

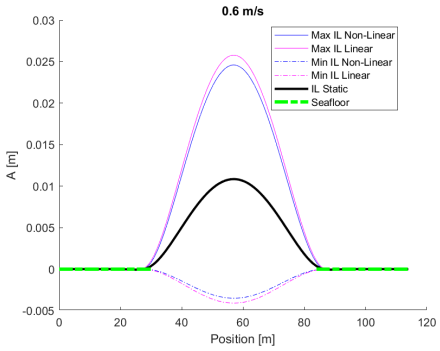

(c) IL - 0.6 m/s

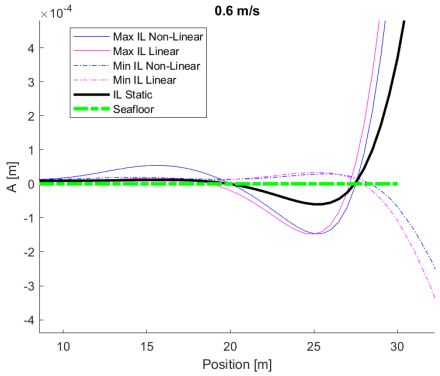

(d) IL - 0.6 m/s (zoom at the left shoulder)

Figure B.185: Comparative snapshots of the max and min responses for the two soil models at 0.6 m/s.

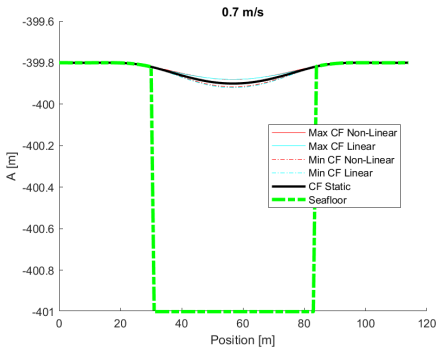

(a) CF - 0.7 m/s

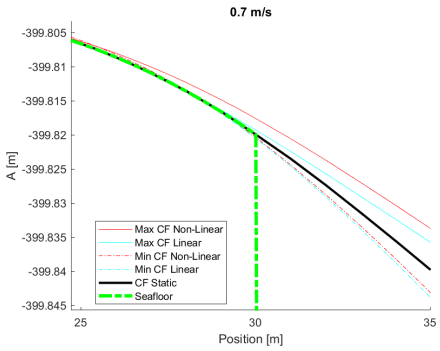

(b) CF - 0.7 m/s (zoom at the left shoulder)

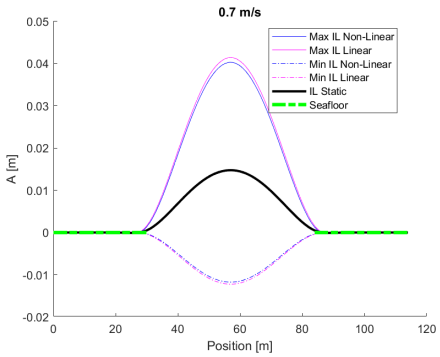

(c) IL - 0.7 m/s

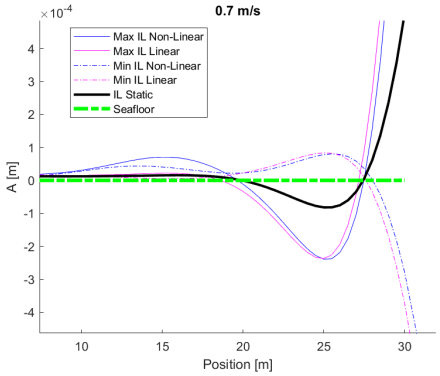

(d) IL - 0.7 m/s (zoom at the left shoulder)

Figure B.186: Comparative snapshots of the max and min responses for the two soil models at 0.7 m/s.

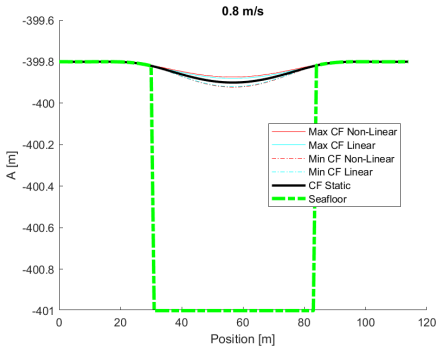

(a) CF - 0.8 m/s

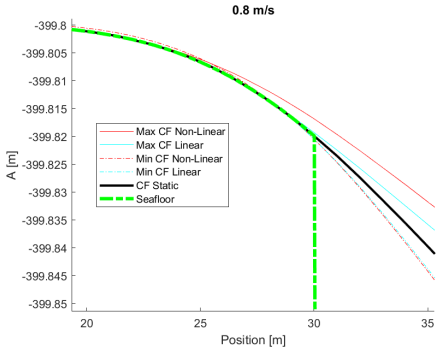

(b) CF - 0.8 m/s (zoom at the left shoulder)

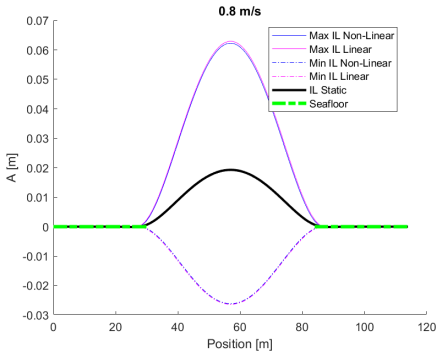

(c) IL - 0.8 m/s

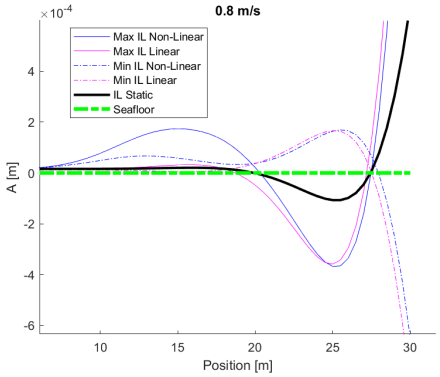

(d) IL - 0.8 m/s (zoom at the left shoulder)

Figure B.187: Comparative snapshots of the max and min responses for the two soil models at 0.8 m/s.

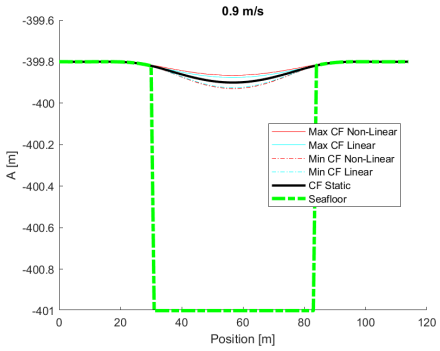

(a) CF - 0.9 m/s

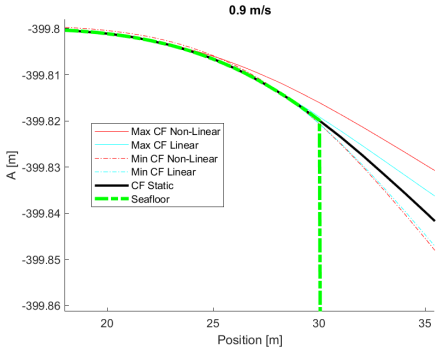

(b) CF - 0.9 m/s (zoom at the left shoulder)

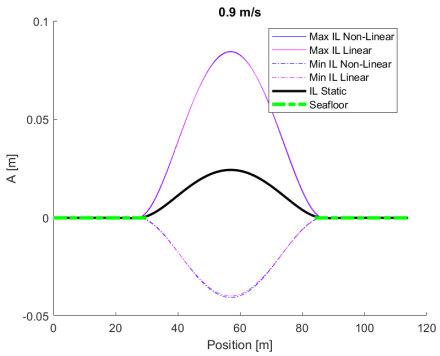

(c) IL - 0.9 m/s

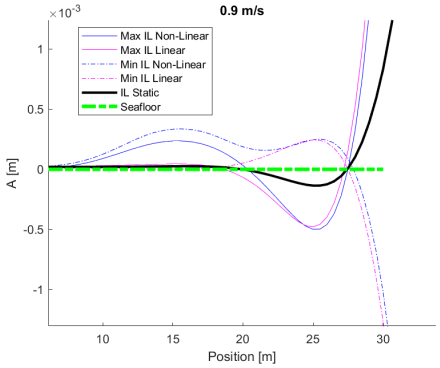

(d) IL - 0.9 m/s (zoom at the left shoulder)

Figure B.188: Comparative snapshots of the max and min responses for the two soil models at 0.9 m/s.

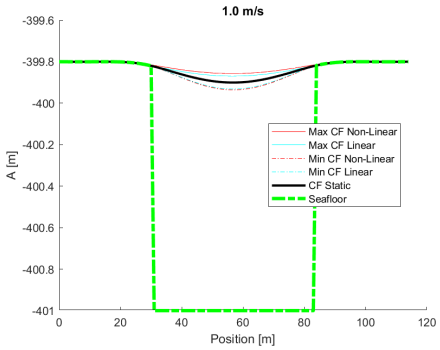

(a) CF - 1.0 m/s

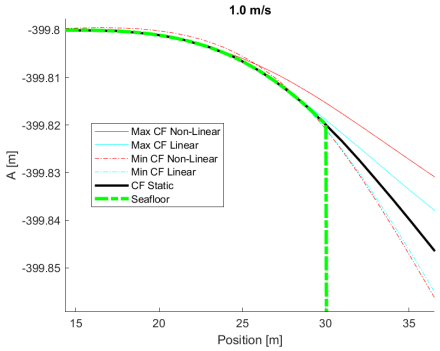

(b) CF - 1.0 m/s (zoom at the left shoulder)

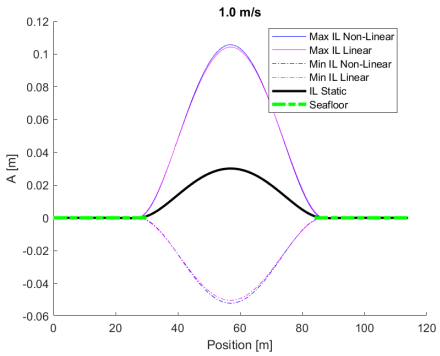

(c) IL - 1.0 m/s

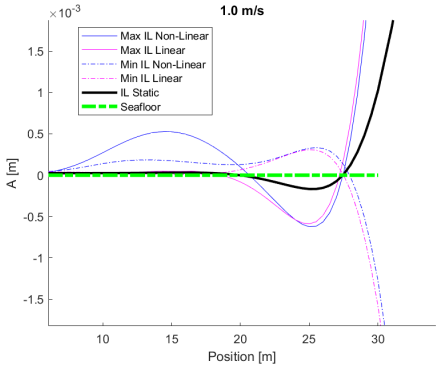

(d) IL - 1.0 m/s (zoom at the left shoulder)

Figure B.189: Comparative snapshots of the max and min responses for the two soil models at 1.0 m/s.

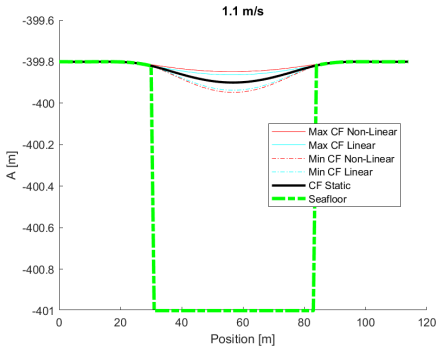

(a) CF - 1.1 m/s

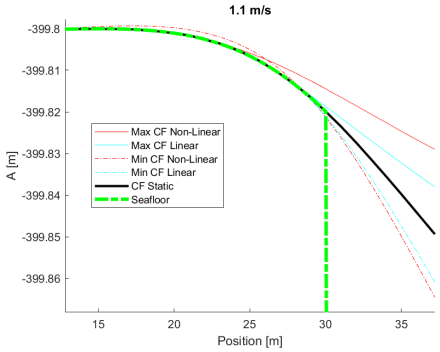

(b) CF - 1.1 m/s (zoom at the left shoulder)

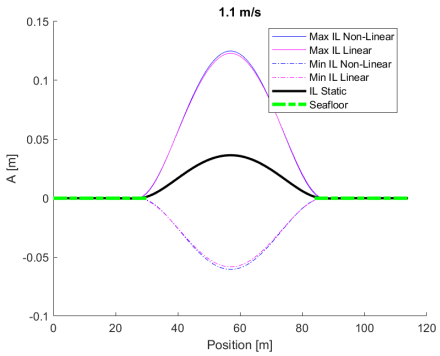

(c) IL - 1.1 m/s

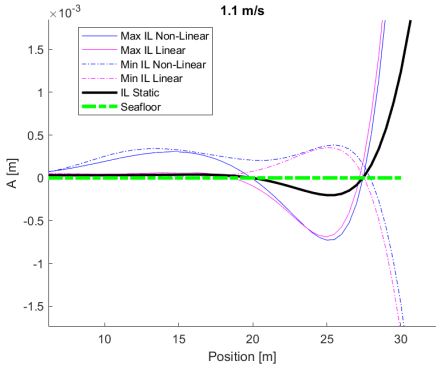

(d) IL - 1.1 m/s (zoom at the left shoulder)

Figure B.190: Comparative snapshots of the max and min responses for the two soil models at 1.1 m/s.

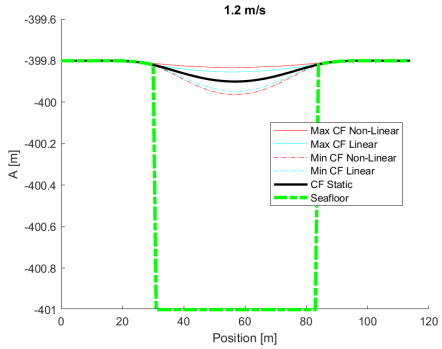

(a) CF - 1.2 m/s

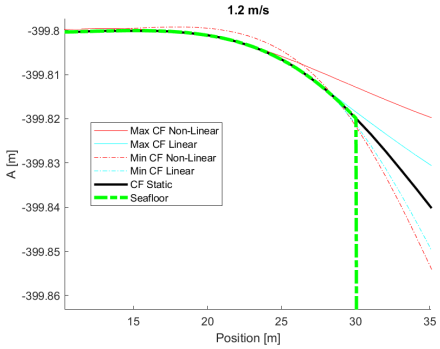

(b) CF - 1.2 m/s (zoom at the left shoulder)

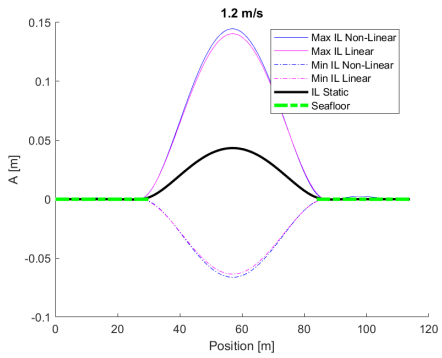

(c) IL - 1.2 m/s

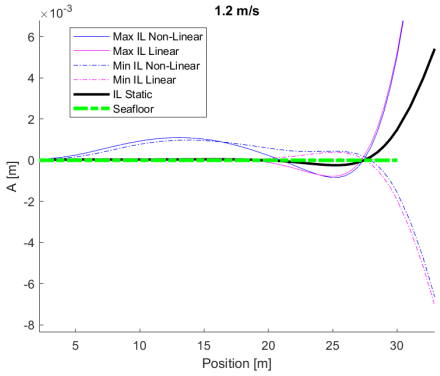

(d) IL - 1.2 m/s (zoom at the left shoulder)

Figure B.191: Comparative snapshots of the max and min responses for the two soil models at 1.2 m/s.

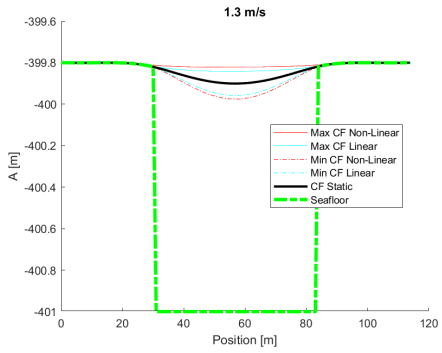

(a) CF - 1.3 m/s

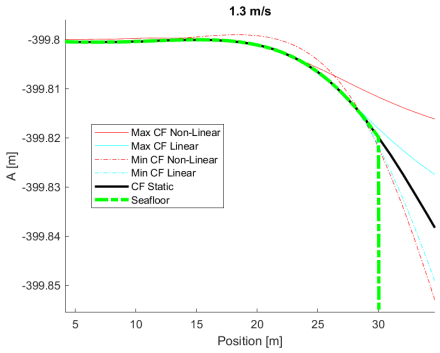

(b) CF - 1.3 m/s (zoom at the left shoulder)

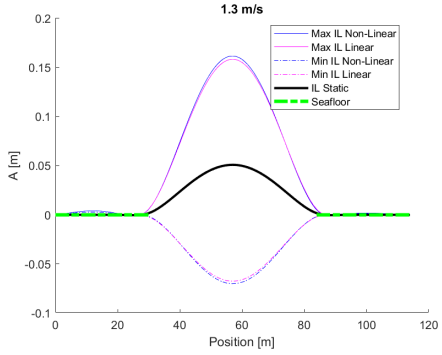

(c) IL - 1.3 m/s

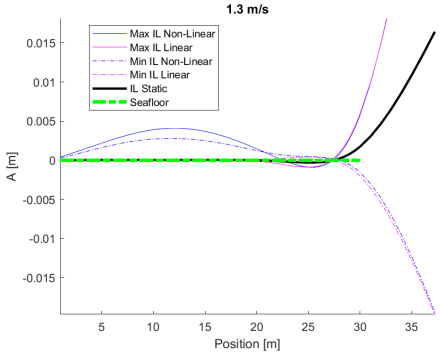

(d) IL - 1.3 m/s (zoom at the left shoulder)

Figure B.192: Comparative snapshots of the max and min responses for the two soil models at 1.3 m/s.

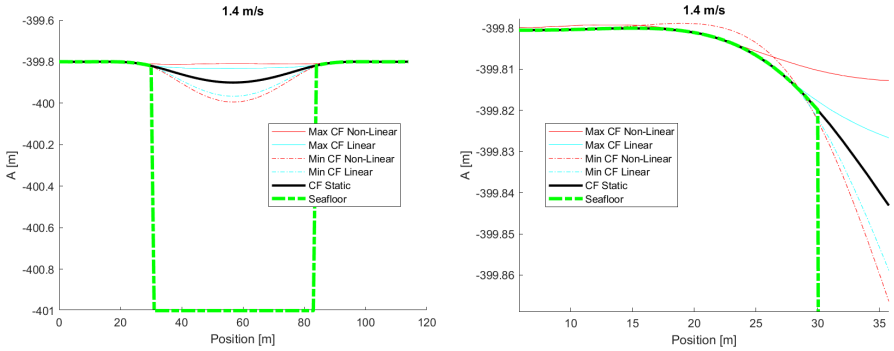

(a) CF - 1.4 m/s

(b) CF - 1.4 m/s (zoom at the left shoulder)

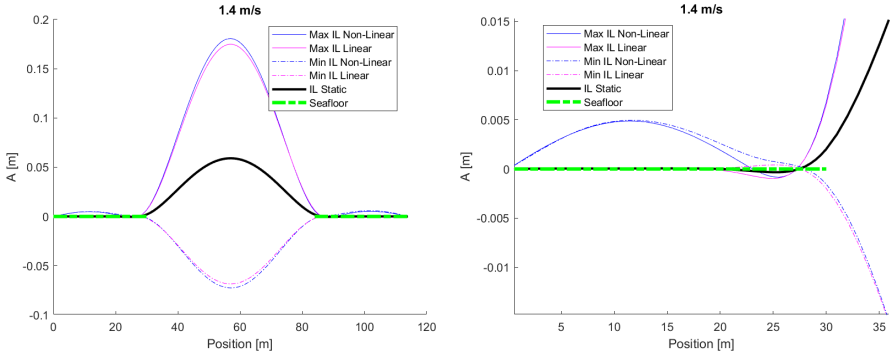

(c) IL - 1.4 m/s

(d) IL - 1.4 m/s (zoom at the left shoulder)

Figure B.193: Comparative snapshots of the max and min responses for the two soil models at 1.4 m/s.

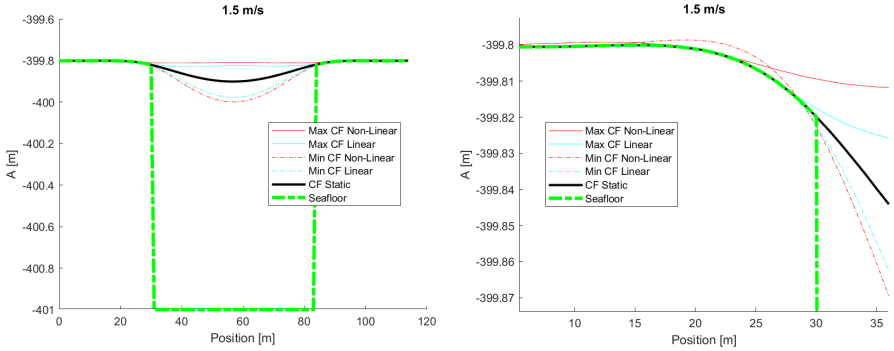

(a) CF - 1.5 m/s

(b) CF - 1.5 m/s (zoom at the left shoulder)

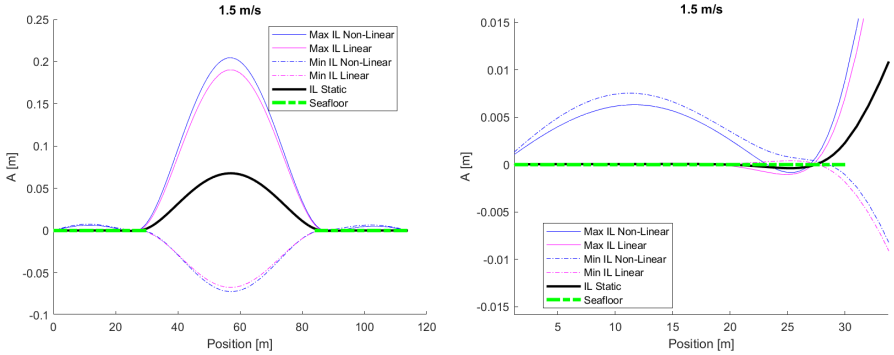

(c) IL - 1.5 m/s

(d) IL - 1.5 m/s (zoom at the left shoulder)

Figure B.194: Comparative snapshots of the max and min responses for the two soil models at 1.5 m/s.

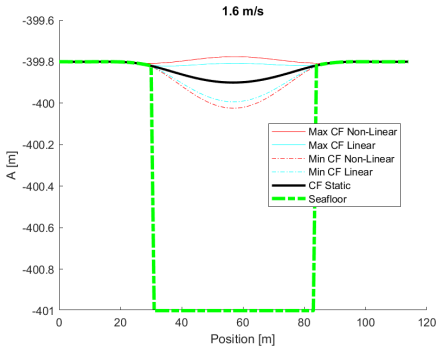

(a) CF - 1.6 m/s

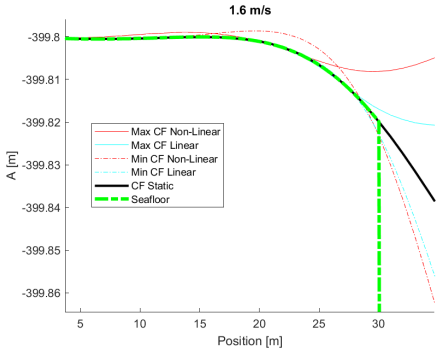

(b) CF - 1.6 m/s (zoom at the left shoulder)

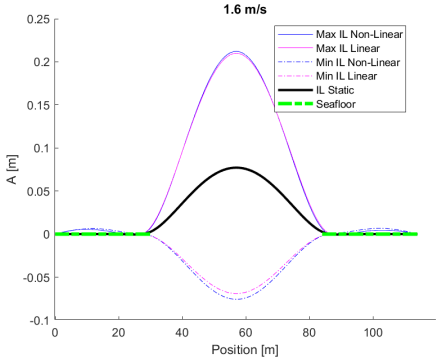

(c) IL - 1.6 m/s

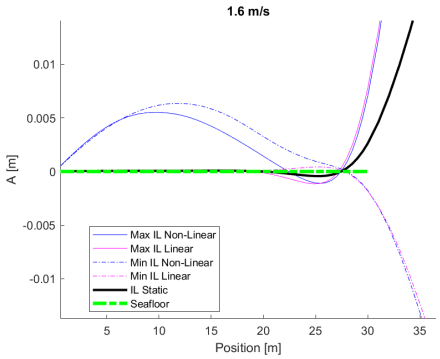

(d) IL - 1.6 m/s (zoom at the left shoulder)

Figure B.195: Comparative snapshots of the max and min responses for the two soil models at 1.6 m/s.

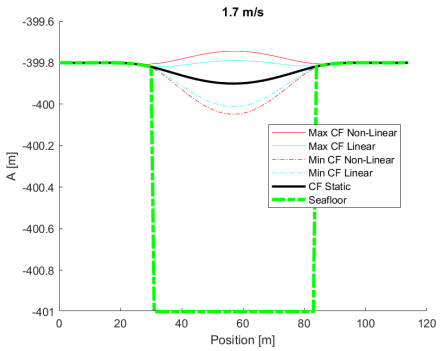

(a) CF - 1.7 m/s

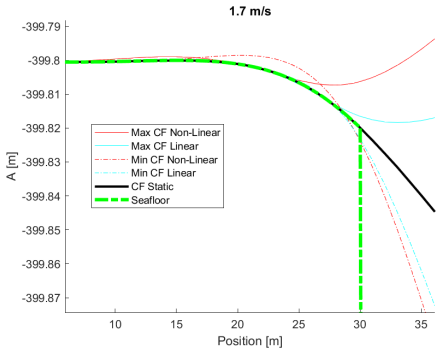

(b) CF - 1.7 m/s (zoom at the left shoulder)

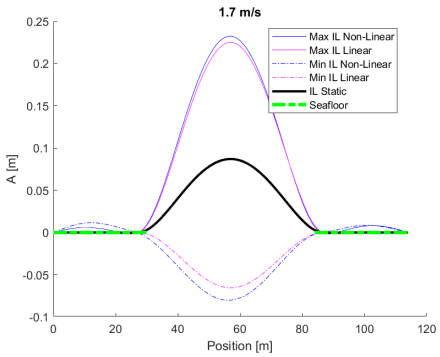

(c) IL - 1.7 m/s

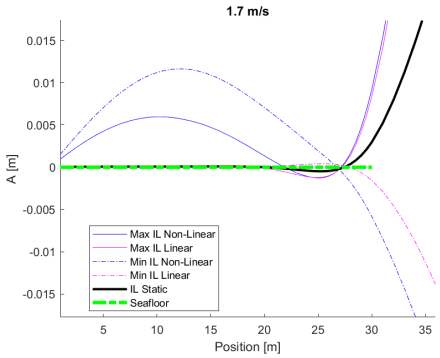

(d) IL - 1.7 m/s (zoom at the left shoulder)

Figure B.196: Comparative snapshots of the max and min responses for the two soil models at 1.7 m/s.

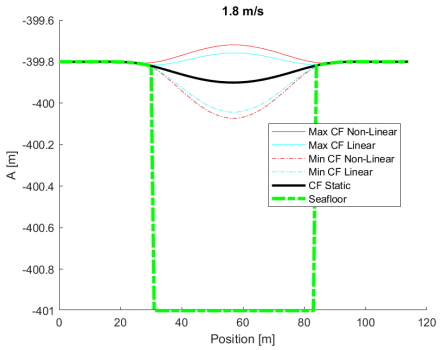

(a) CF - 1.8 m/s

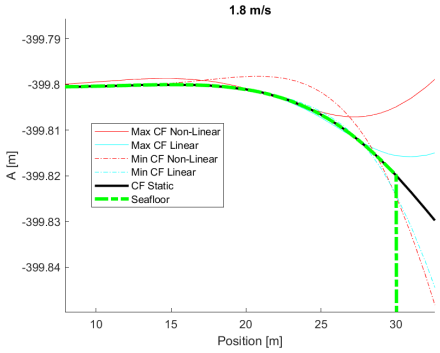

(b) CF - 1.8 m/s (zoom at the left shoulder)

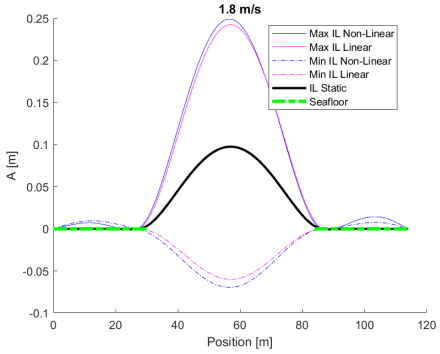

(c) IL - 1.8 m/s

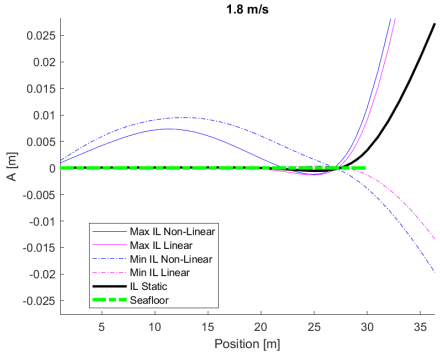

(d) IL - 1.8 m/s (zoom at the left shoulder)

Figure B.197: Comparative snapshots of the max and min responses for the two soil models at 1.8 m/s.

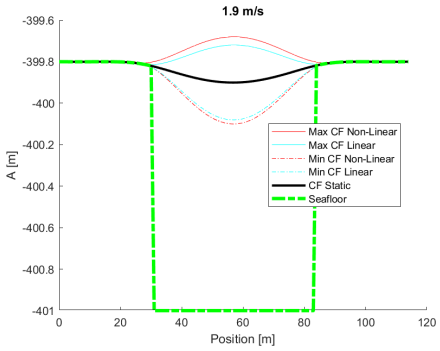

(a) CF - 1.9 m/s

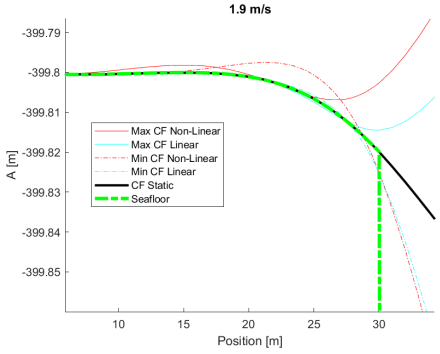

(b) CF - 1.9 m/s (zoom at the left shoulder)

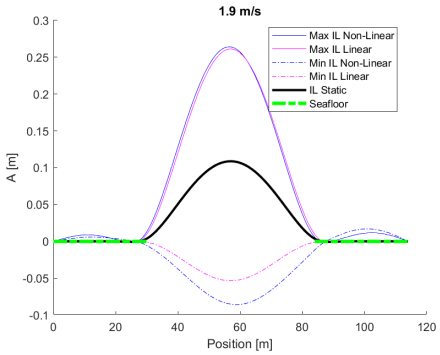

(c) IL - 1.9 m/s

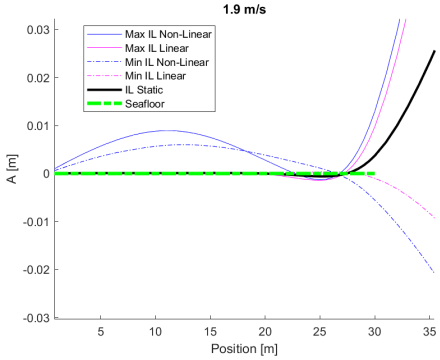

(d) IL - 1.9 m/s (zoom at the left shoulder)

Figure B.198: Comparative snapshots of the max and min responses for the two soil models at 1.9 m/s.

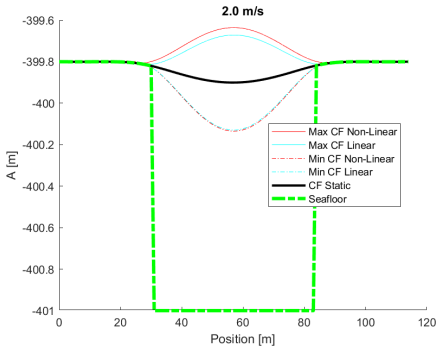

(a) CF - 2.0 m/s

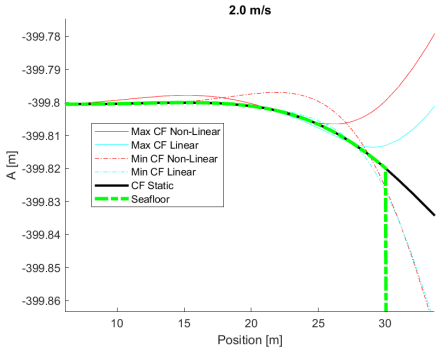

(b) CF - 2.0 m/s (zoom at the left shoulder)

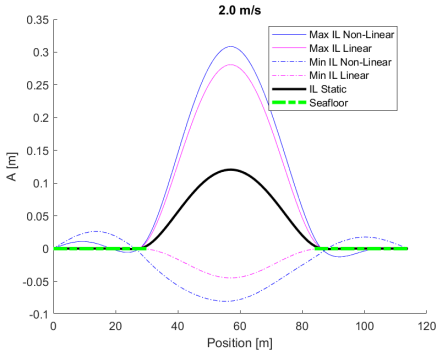

(c) IL - 2.0 m/s

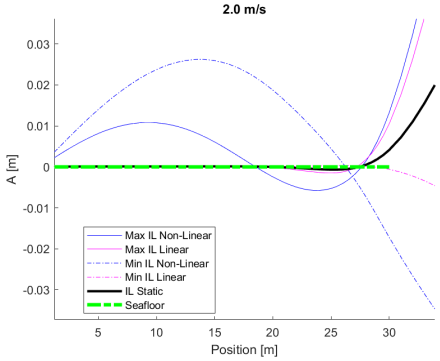

(d) IL - 2.0 m/s (zoom at the left shoulder)

Figure B.199: Comparative snapshots of the max and min responses for the two soil models at 2.0 m/s.

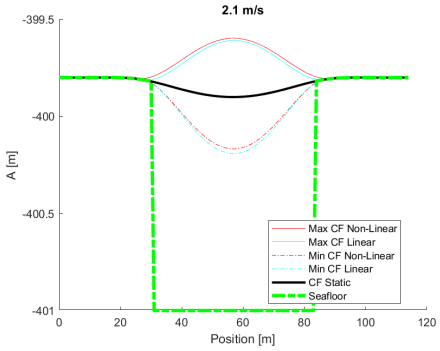

(a) CF - 2.1 m/s

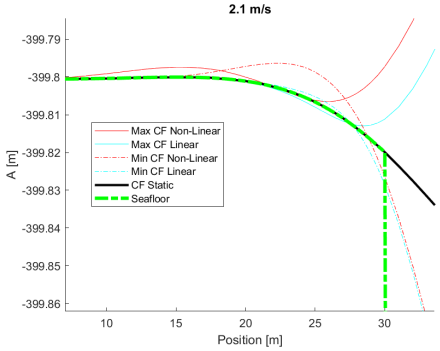

(b) CF - 2.1 m/s (zoom at the left shoulder)

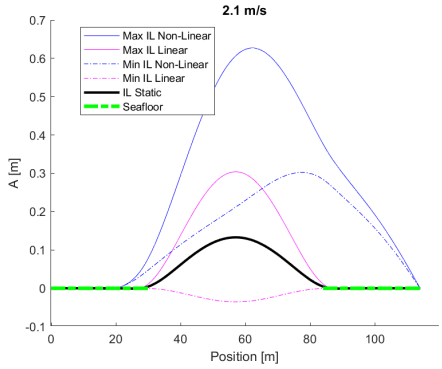

(c) IL - 2.1 m/s

Figure B.200: Comparative snapshots of the max and min responses for the two soil models at 2.1 m/s.

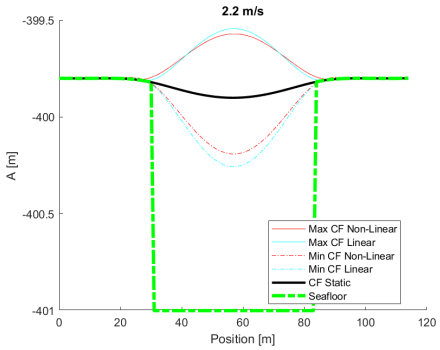

(a) CF - 2.2 m/s

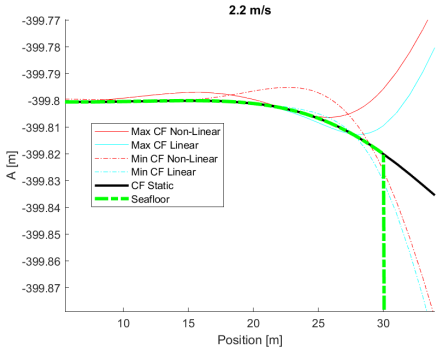

(b) CF - 2.2 m/s (zoom at the left shoulder)

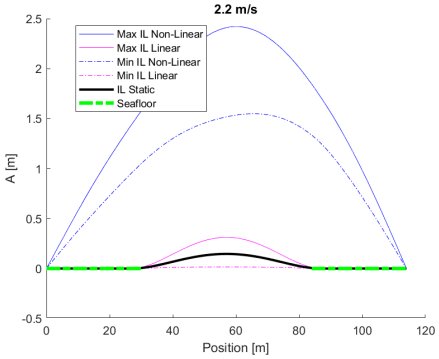

(c) IL - 2.2 m/s

Figure B.201: Comparative snapshots of the max and min responses for the two soil models at 2.2 m/s.

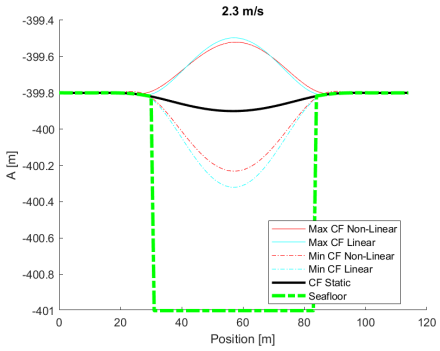

(a) CF - 2.3 m/s

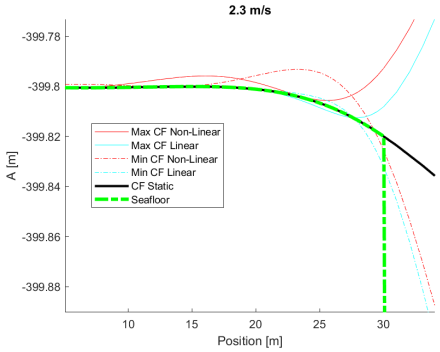

(b) CF - 2.3 m/s (zoom at the left shoulder)

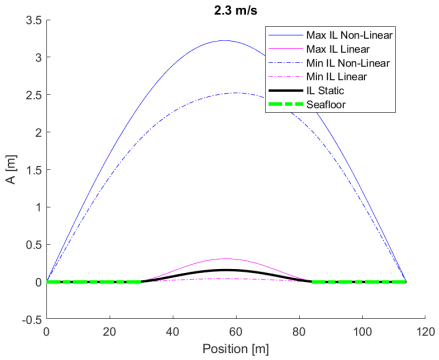

(c) IL - 2.3 m/s

Figure B.202: Comparative snapshots of the max and min responses for the two soil models at 2.3 m/s.

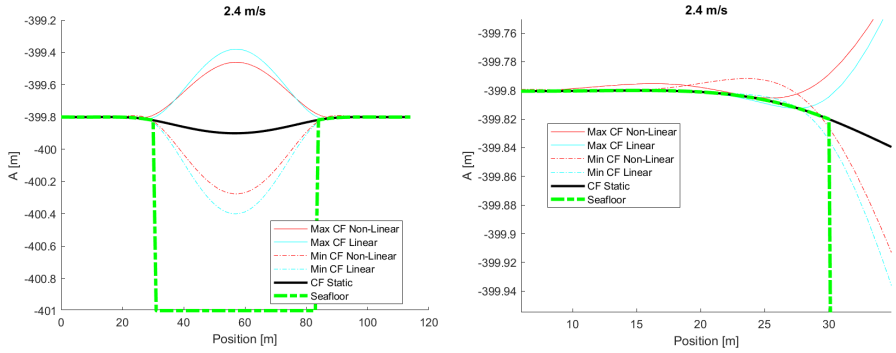

(a) CF - 2.4 m/s

(b) CF - 2.4 m/s (zoom at the left shoulder)

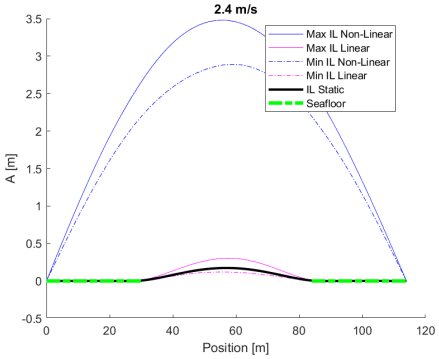

(c) IL - 2.4 m/s

Figure B.203: Comparative snapshots of the max and min responses for the two soil models at 2.4 m/s.

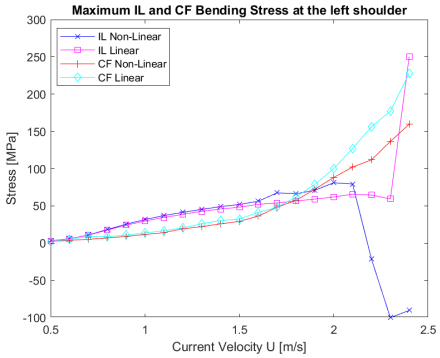

(a) Maximum Bending Stress at the left shoulder

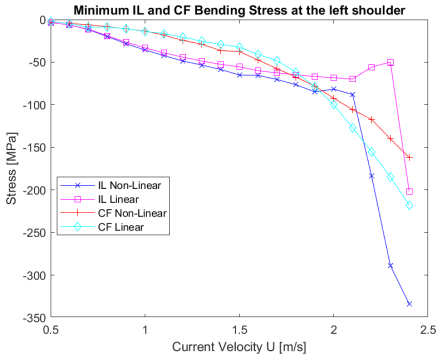

(b) Minimum Bending Stress at the left shoulder

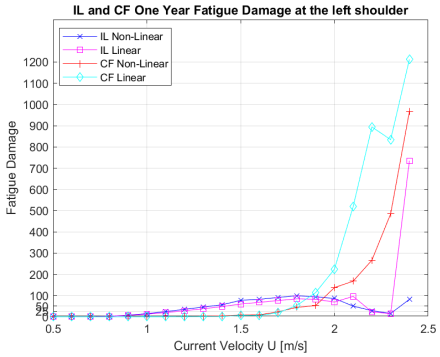

(c) Fatigue Damage Accumulation at the left shoulder

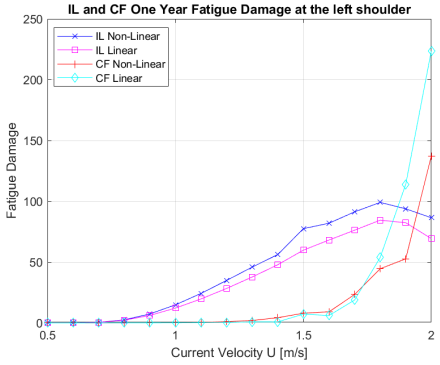

(d) Fatigue Damage Accumulation at the left shoulder (zoom at velocities up to 2.0 m/s)

Figure B.204: Comparative plots of the calculated Bending Stress and Fatigue Damage at the left shoulder.

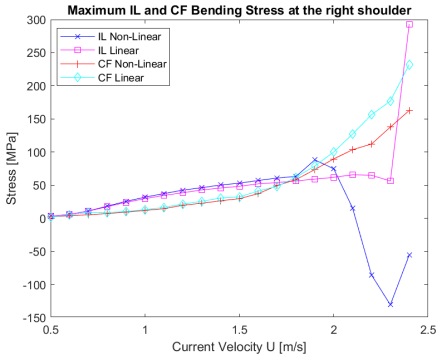

(a) Maximum Bending Stress at the right shoulder

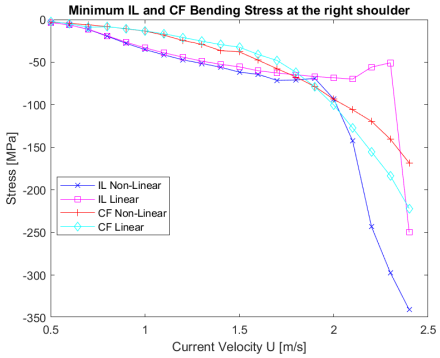

(b) Minimum Bending Stress at the right shoulder

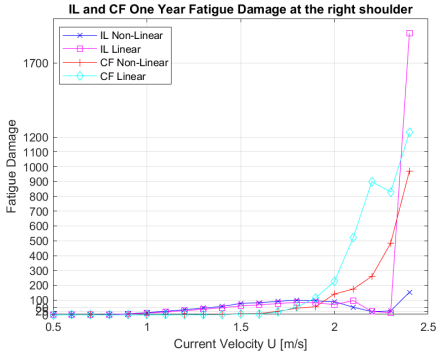

(c) Fatigue Damage Accumulation at the right shoulder

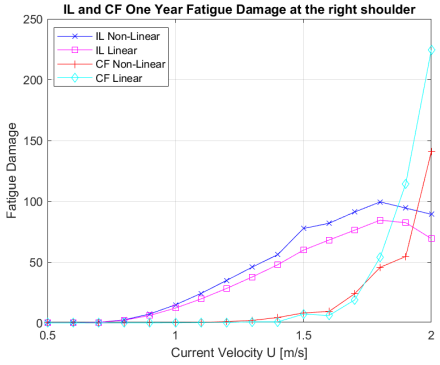

(d) Fatigue Damage Accumulation at the right shoulder (zoom at velocities up to 2.0 m/s)

Figure B.205: Comparative plots of the calculated Bending Stress and Fatigue Damage at the right shoulder.

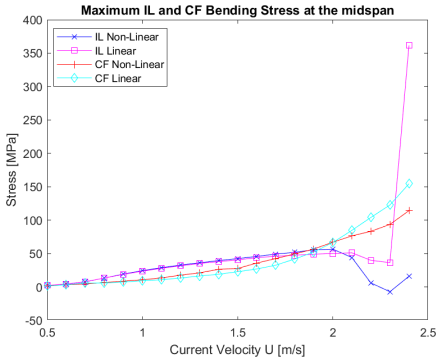

(a) Maximum Bending Stress at the midspan

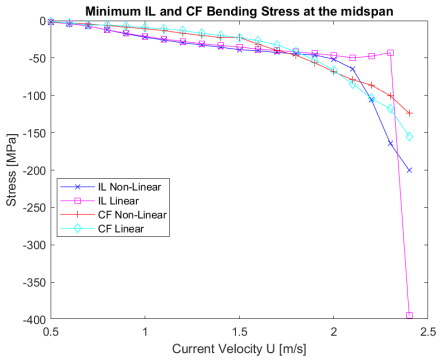

(b) Minimum Bending Stress at the midspan

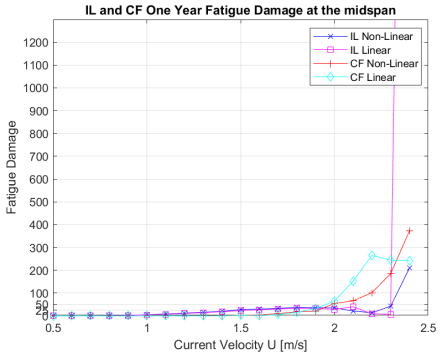

(c) Fatigue Damage Accumulation at the midspan

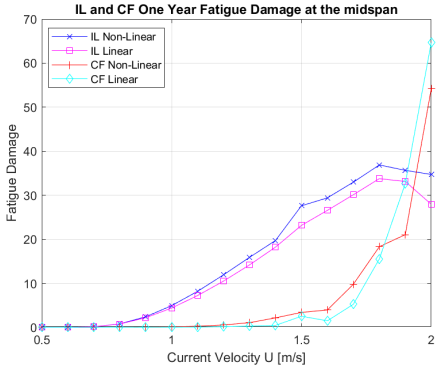

(d) Fatigue Damage Accumulation at the midspan (zoom at velocities up to 2.0 m/s)

Figure B.206: Comparative plots of the calculated Bending Stress and Fatigue Damage at the midspan.

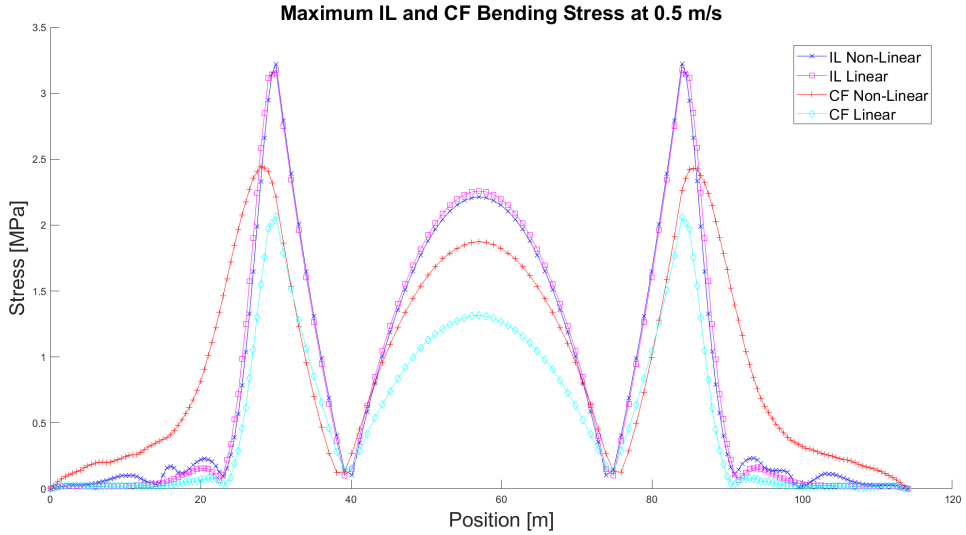

(a) CF and IL Maximum Bending Stress Distribution at 0.5 m/s

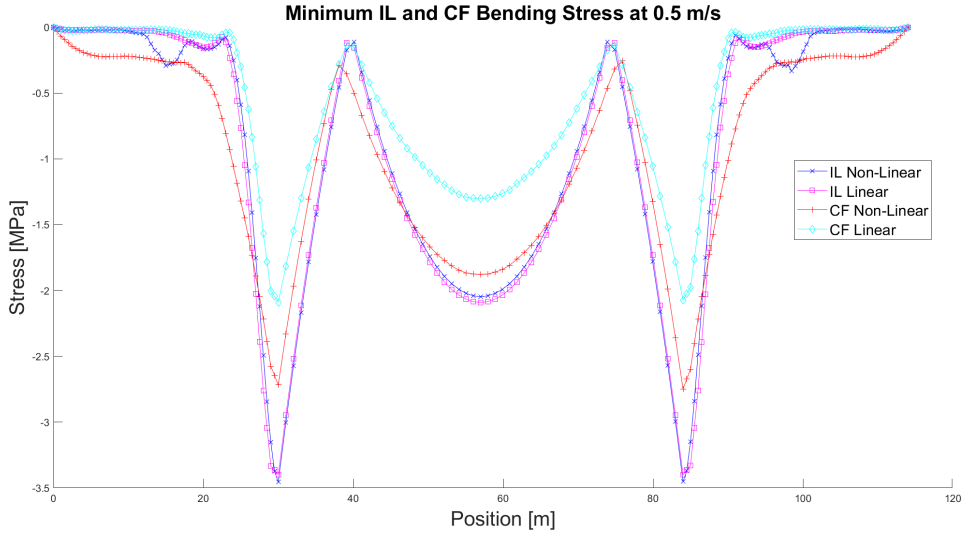

(b) CF and IL Minimum Bending Stress Distribution at 0.5 m/s

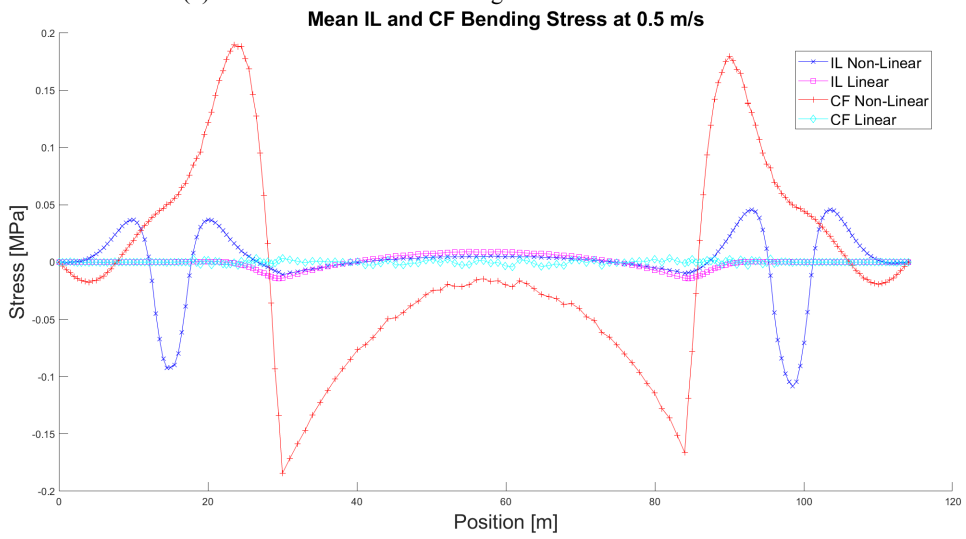

(c) CF and IL Mean Bending Stress Distribution at 0.5 m/s

Figure B.207: Comparative plots of the calculated bending stress distribution for the two soil models and $\zeta_{soil} = 8\%$ at 0.5 m/s.

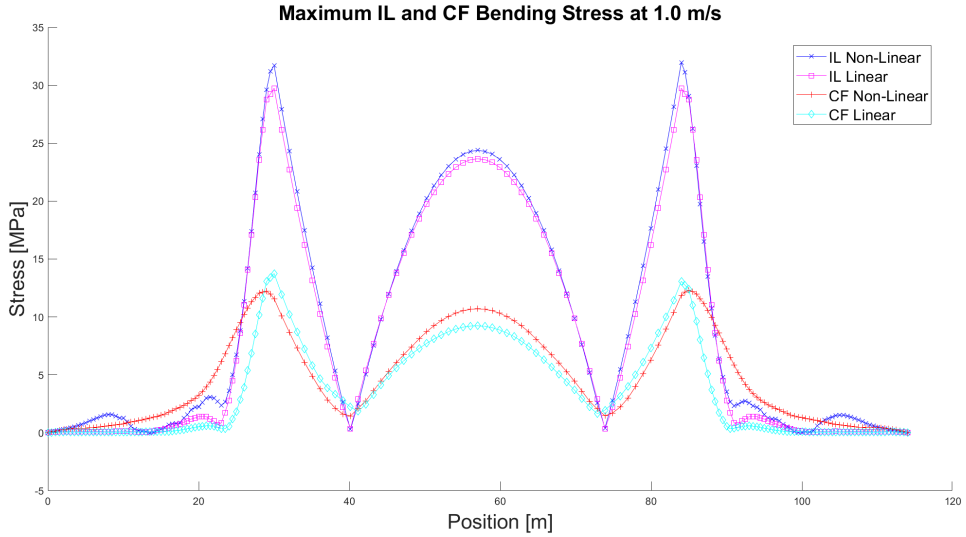

(a) CF and IL Maximum Bending Stress Distribution at 1.0 m/s

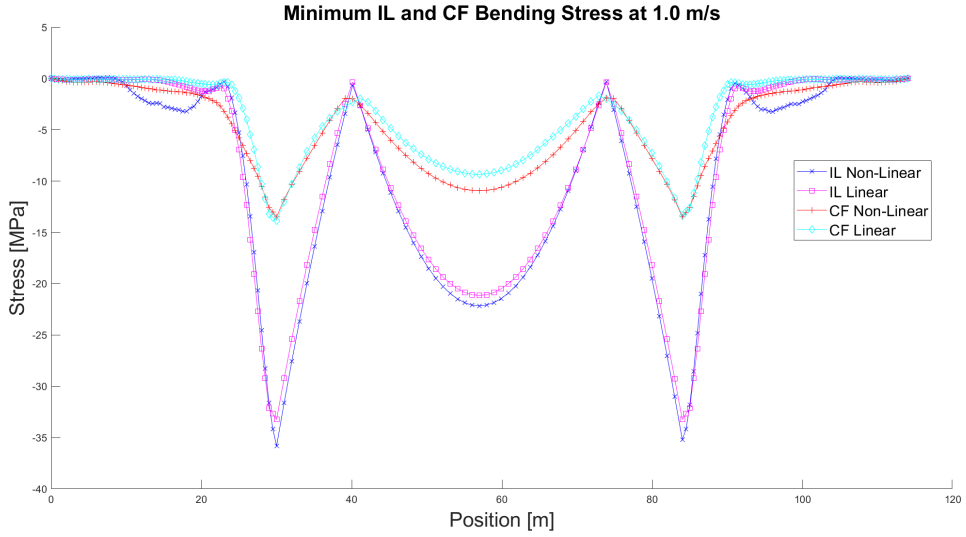

(b) CF and IL Minimum Bending Stress Distribution at 1.0 m/s

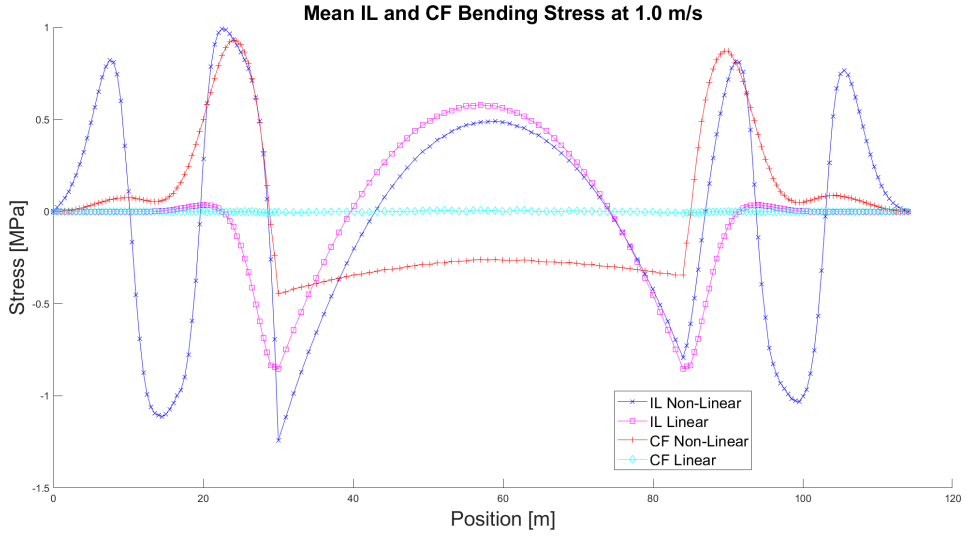

(c) CF and IL Mean Bending Stress Distribution at 1.0 m/s

Figure B.208: Comparative plots of the calculated bending stress distribution for the two soil models and $\zeta_{soil} = 8\%$ at 1.0 m/s.

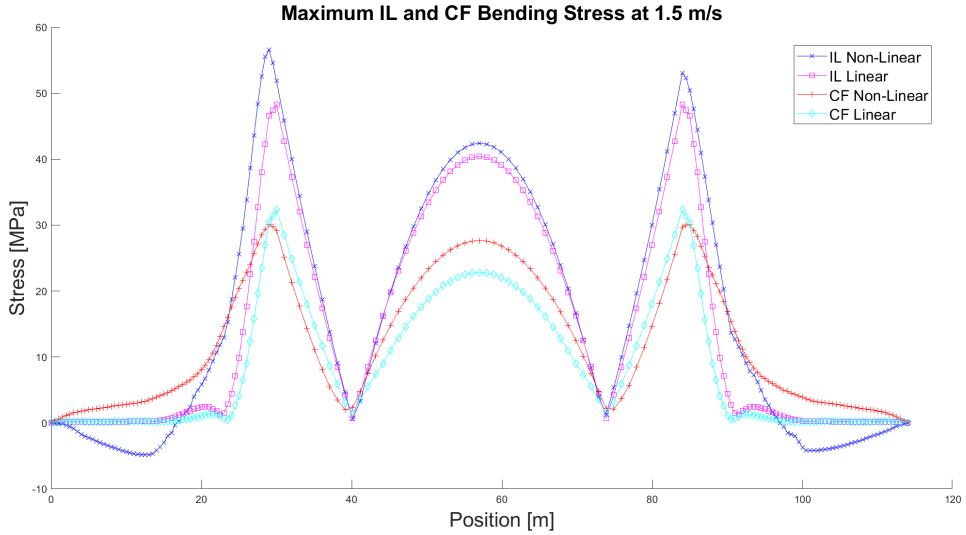

(a) CF and IL Maximum Bending Stress Distribution at 1.5 m/s

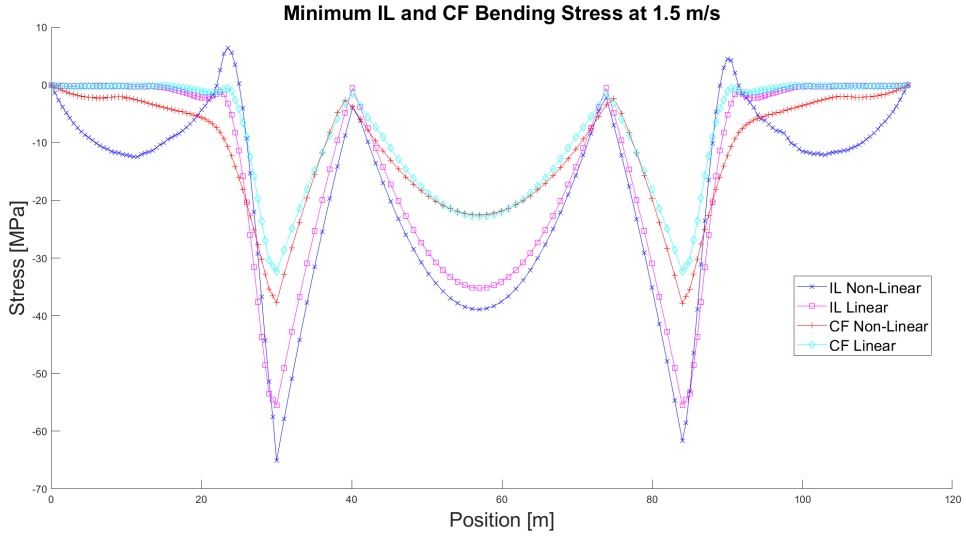

(b) CF and IL Minimum Bending Stress Distribution at 1.5 m/s

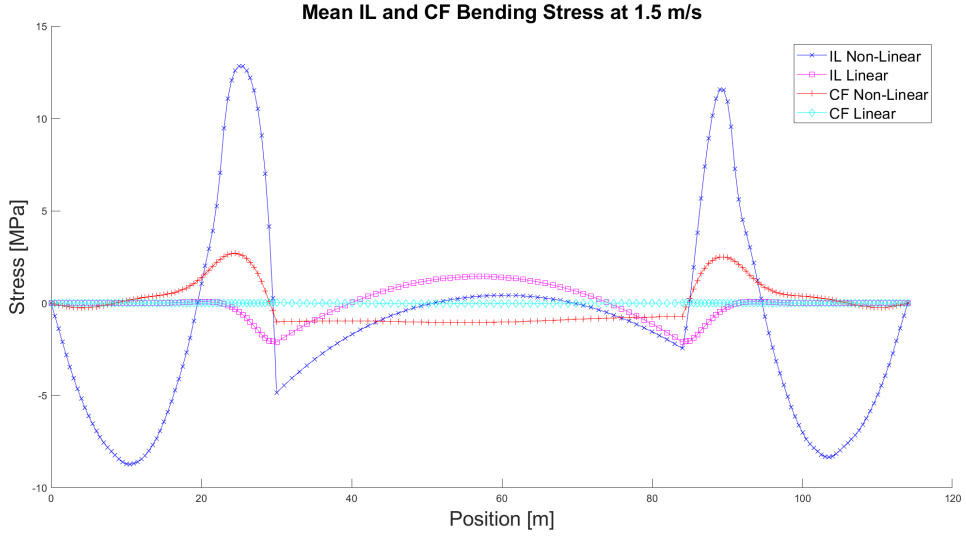

(c) CF and IL Mean Bending Stress Distribution at 1.5 m/s

Figure B.209: Comparative plots of the calculated bending stress distribution for the two soil models and $\zeta_{soil} = 8\%$ at 1.5 m/s.

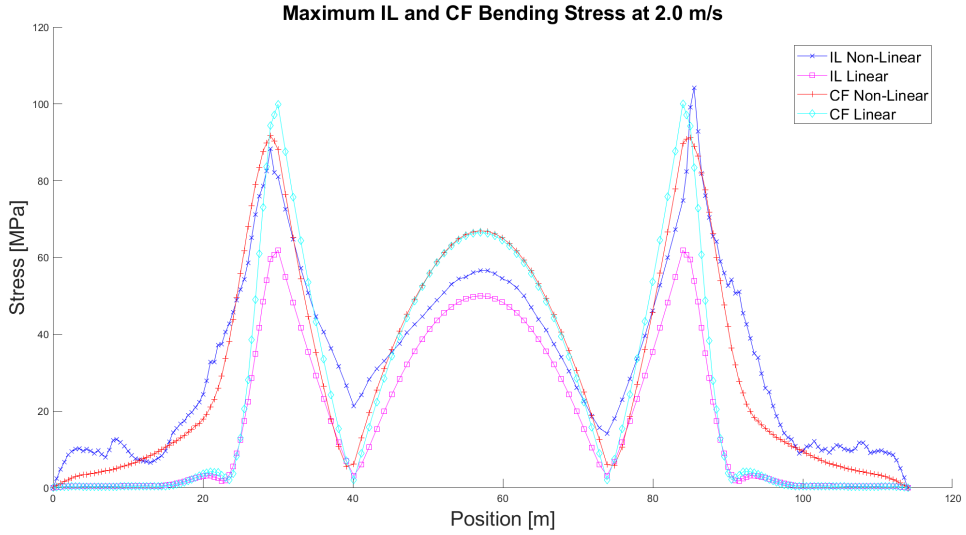

(a) CF and IL Maximum Bending Stress Distribution at 2.0 m/s

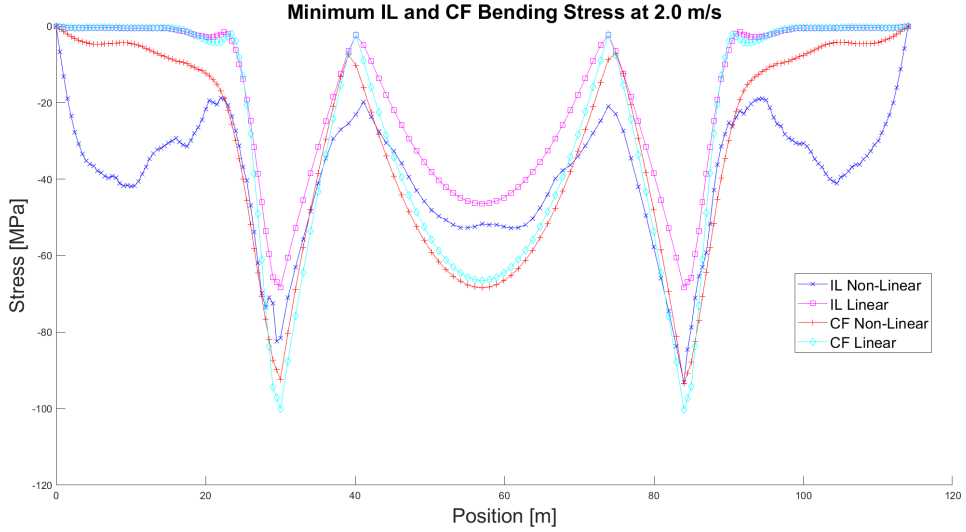

(b) CF and IL Minimum Bending Stress Distribution at 2.0 m/s

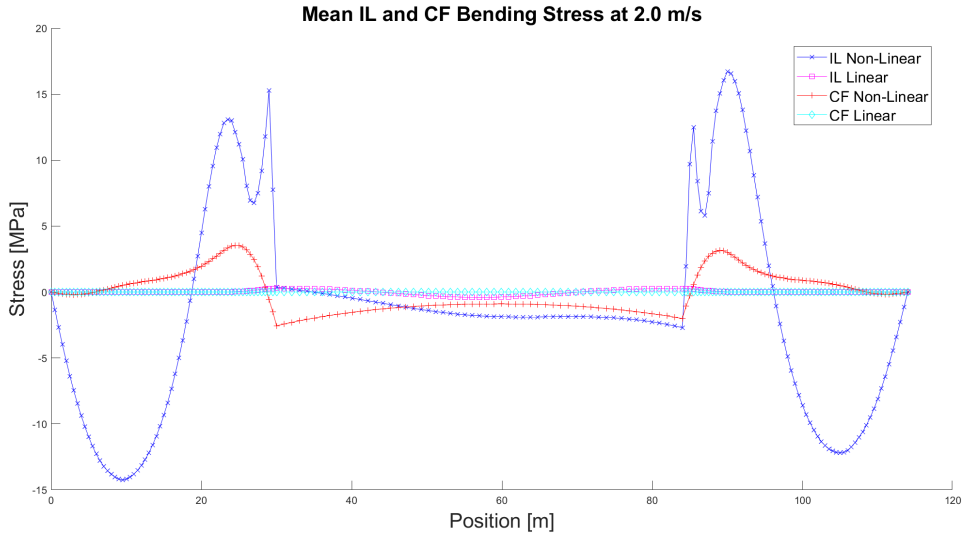

(c) CF and IL Mean Bending Stress Distribution at 2.0 m/s

Figure B.210: Comparative plots of the calculated bending stress distribution for the two soil models and $\zeta_{soil} = 8\%$ at 2.0 m/s.

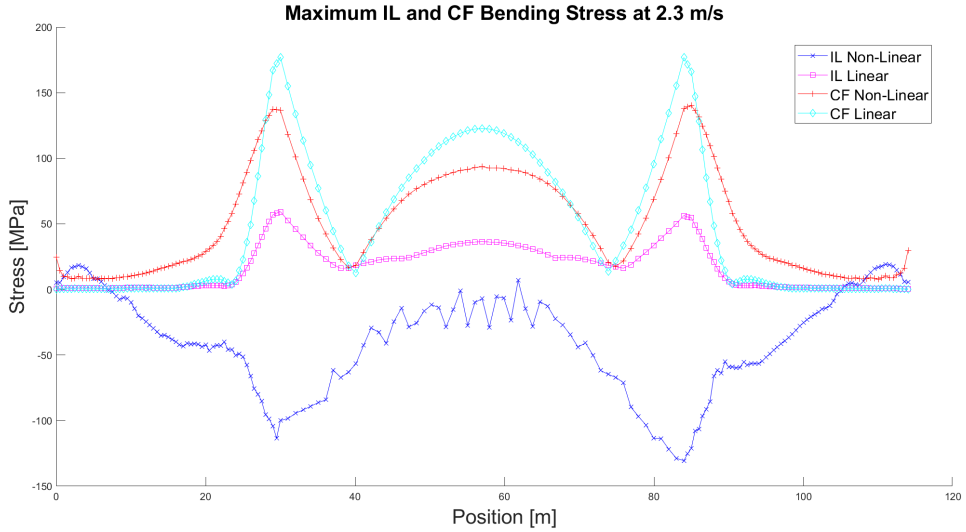

(a) CF and IL Maximum Bending Stress Distribution at 2.3 m/s

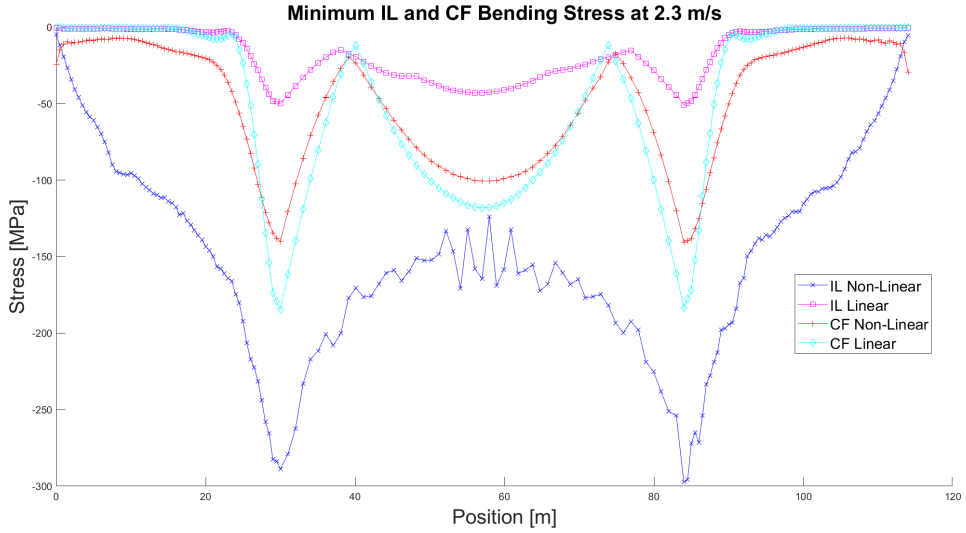

(b) CF and IL Minimum Bending Stress Distribution at 2.3 m/s

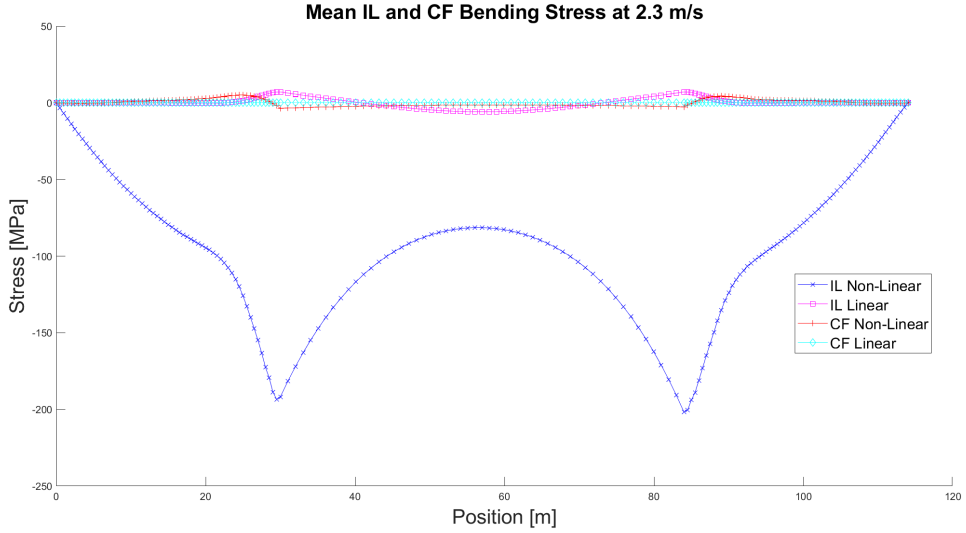

(c) CF and IL Mean Bending Stress Distribution at 2.3 m/s

Figure B.211: Comparative plots of the calculated bending stress distribution for the two soil models and $\zeta_{soil} = 8\%$ at 2.3 m/s.

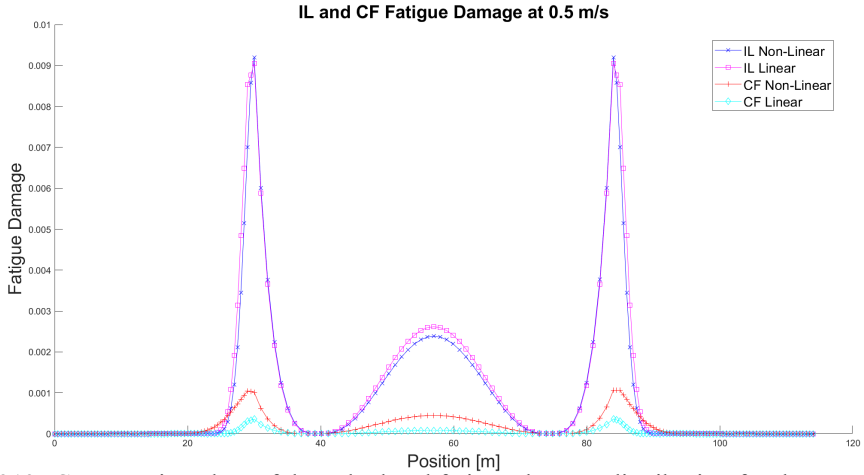

Figure B.212: Comparative plots of the calculated fatigue damage distribution for the two soil model and $\zeta_{soil} = 8\%$ at current velocity 0.5 m/s.

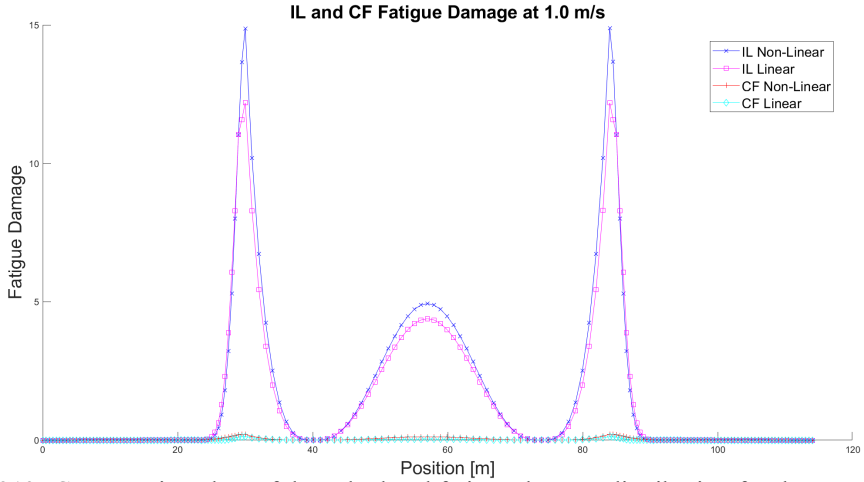

Figure B.213: Comparative plots of the calculated fatigue damage distribution for the two soil model and $\zeta_{soil} = 8\%$ at current velocity 1.0 m/s.

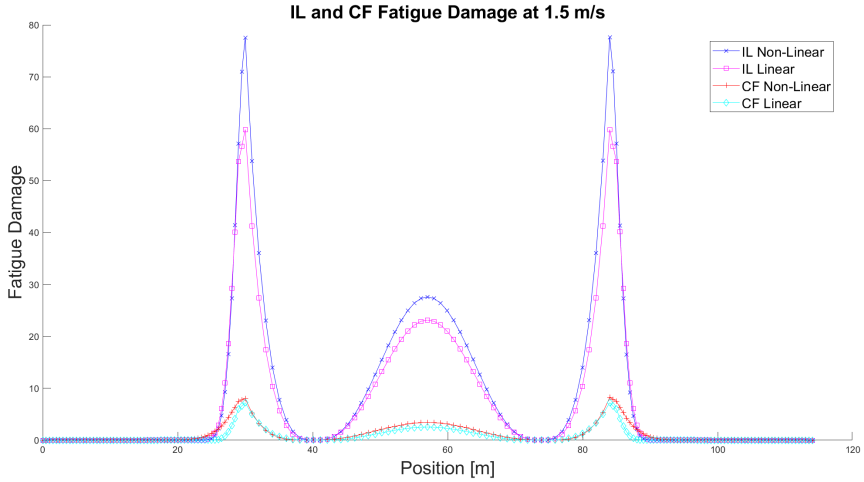

Figure B.214: Comparative plots of the calculated fatigue damage distribution for the two soil model and $\zeta_{soil} = 8\%$ at current velocity 1.5 m/s.

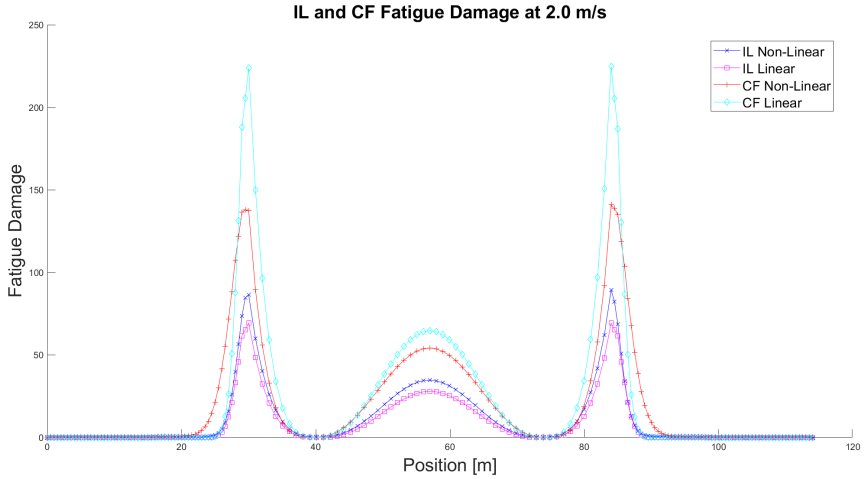

Figure B.215: Comparative plots of the calculated fatigue damage distribution for the two soil model and $\zeta_{soil} = 8\%$ at current velocity 2.0 m/s.

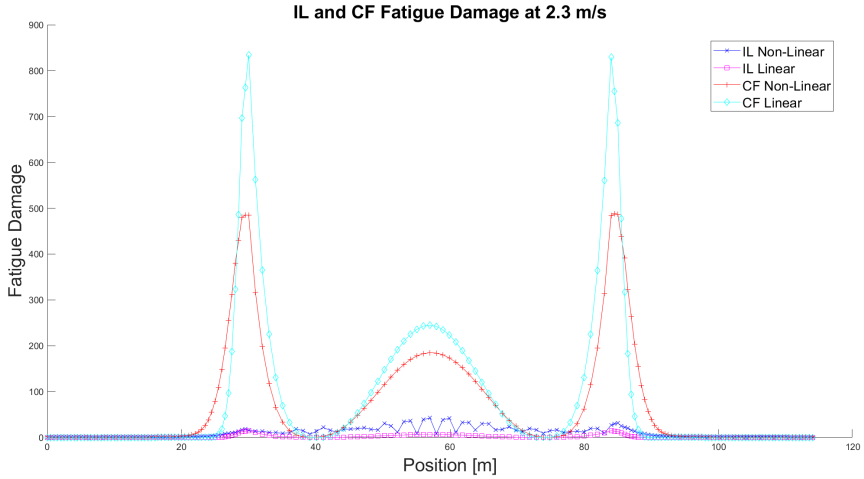

Figure B.216: Comparative plots of the calculated fatigue damage distribution for the two soil model and $\zeta_{soil} = 8\%$ at current velocity 2.3 m/s.

B.7 Overall Comparison - Total set of Results

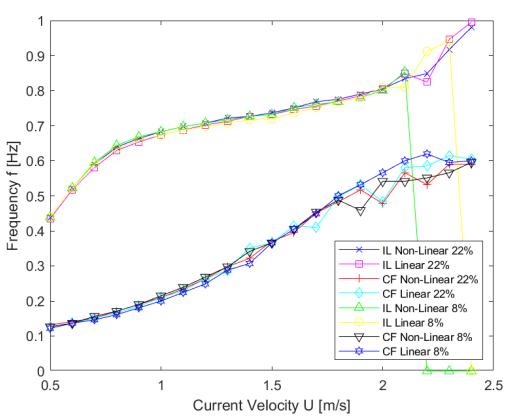

(a) Response Frequency vs Current Velocity

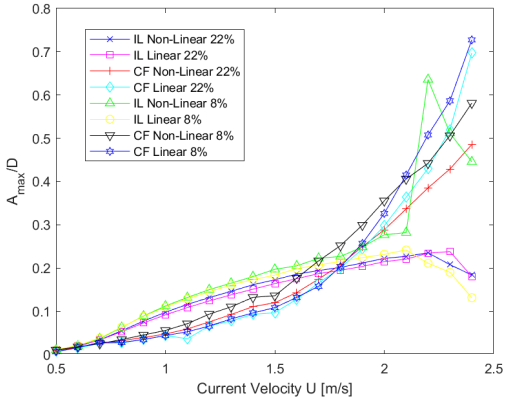

(b) Maximum response amplitude vs Current Velocity

Figure B.217: Comparative plots of the dominant response frequencies and the maximum response amplitudes for all the examined cases.

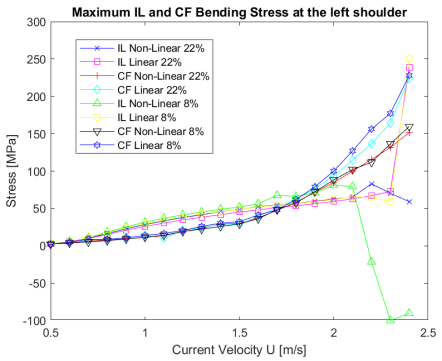

(a) Maximum Bending Stress at the left shoulder

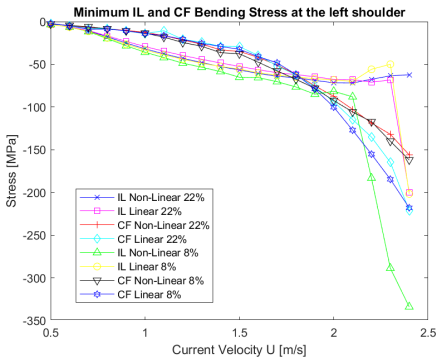

(b) Minimum Bending Stress at the left shoulder

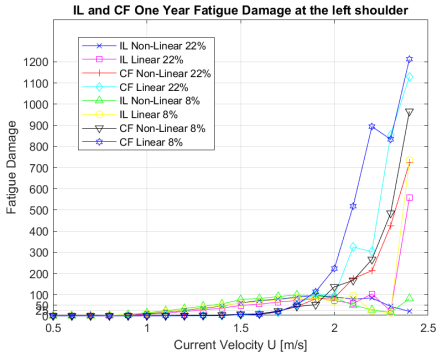

(c) Fatigue Damage Accumulation at the left shoulder

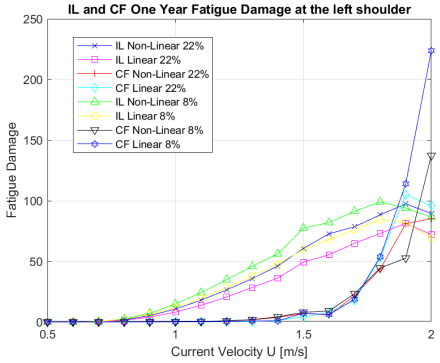

(d) Fatigue Damage Accumulation at the left shoulder (zoom at velocities up to 2.0 m/s)

Figure B.218: Comparative plots of the calculated Bending Stress and Fatigue Damage at the left shoulder for all the examined cases.

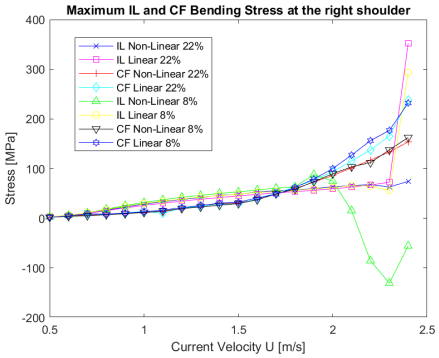

(a) Maximum Bending Stress at the right shoulder

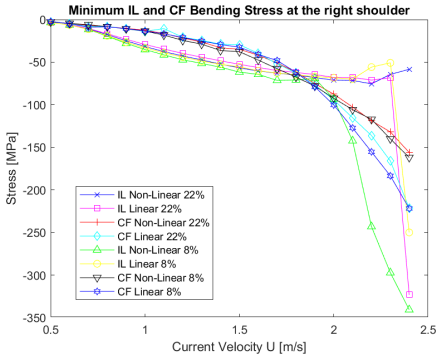

(b) Minimum Bending Stress at the right shoulder

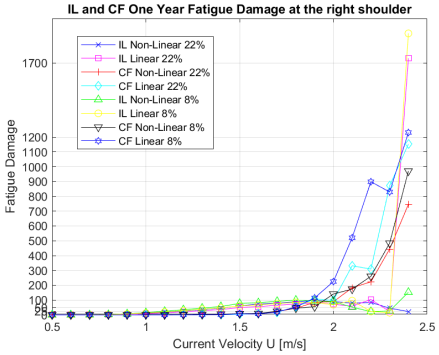

(c) Fatigue Damage Accumulation at the right shoulder

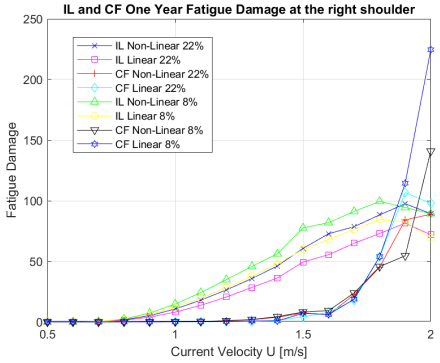

(d) Fatigue Damage Accumulation at the right shoulder (zoom at velocities up to 2.0 m/s)

Figure B.219: Comparative plots of the calculated Bending Stress and Fatigue Damage at the right shoulder for all the examined cases.

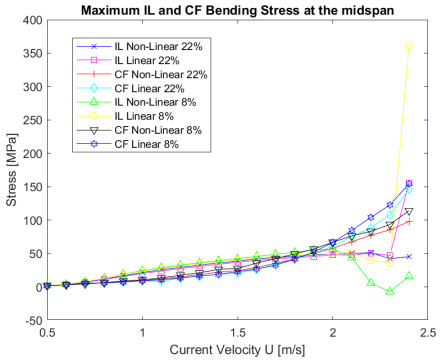

(a) Maximum Bending Stress at the midspan

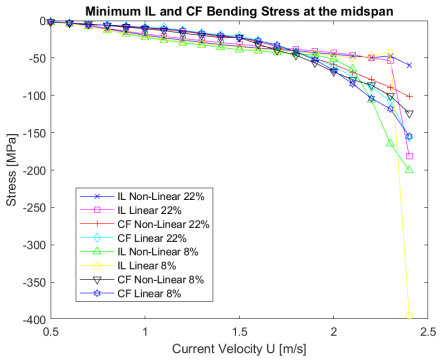

(b) Minimum Bending Stress at the midspan

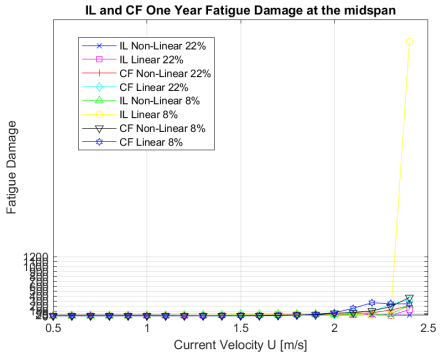

(c) Fatigue Damage Accumulation at the midspan

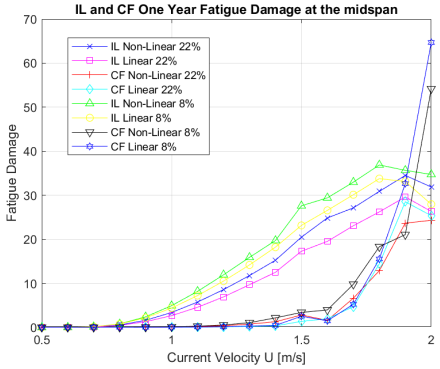

(d) Fatigue Damage Accumulation at the midspan (zoom at velocities up to 2.0 m/s)

Figure B.220: Comparative plots of the calculated Bending Stress and Fatigue Damage at the midspan for all the examined cases.

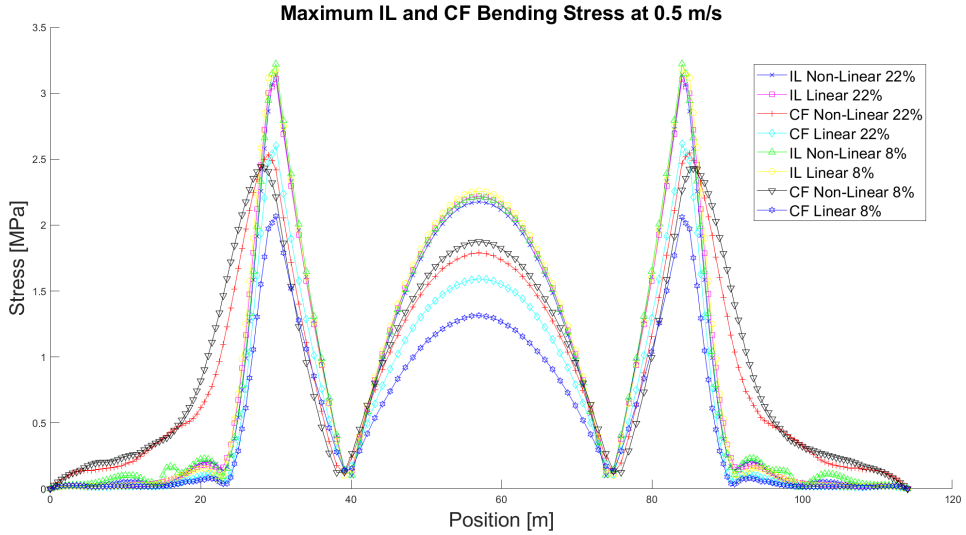

(a) CF and IL Maximum Bending Stress Distribution at 0.5 m/s

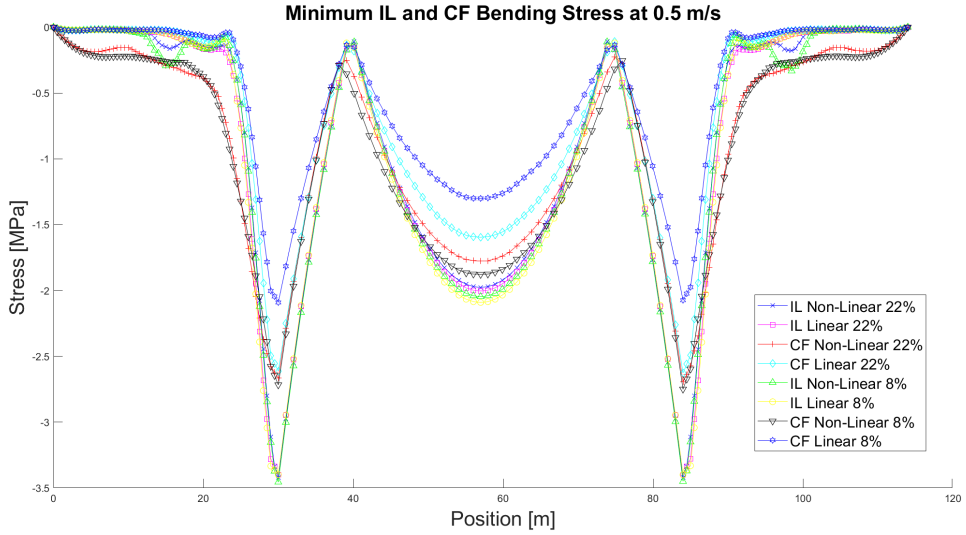

(b) CF and IL Minimum Bending Stress Distribution at 0.5 m/s

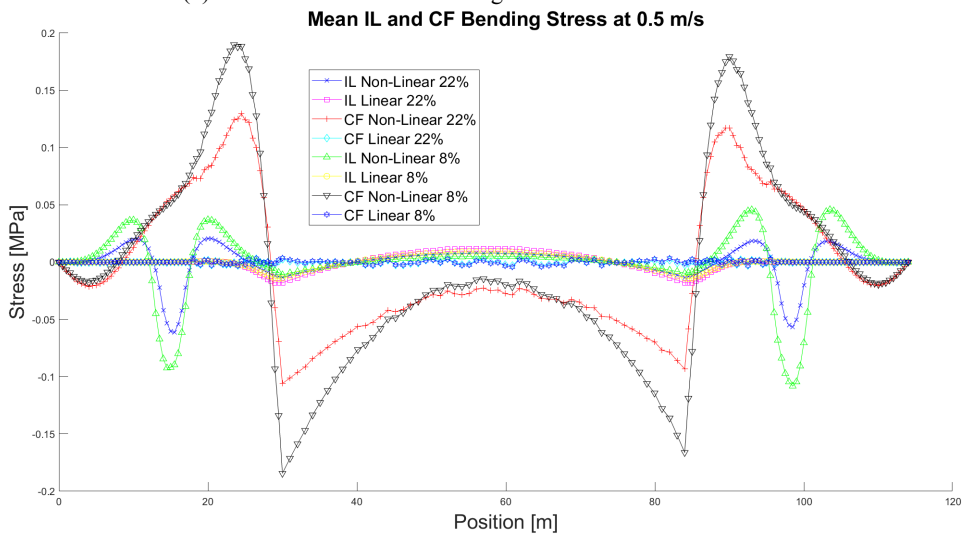

(c) CF and IL Mean Bending Stress Distribution at 0.5 m/s

Figure B.221: Comparative plots of the calculated bending stress distribution for all the examined cases at 0.5 m/s.

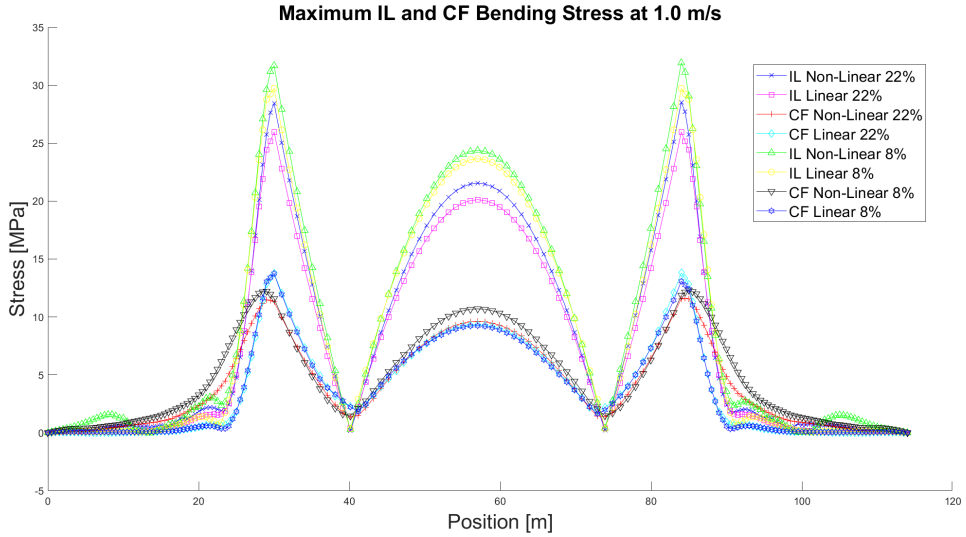

(a) CF and IL Maximum Bending Stress Distribution at 1.0 m/s

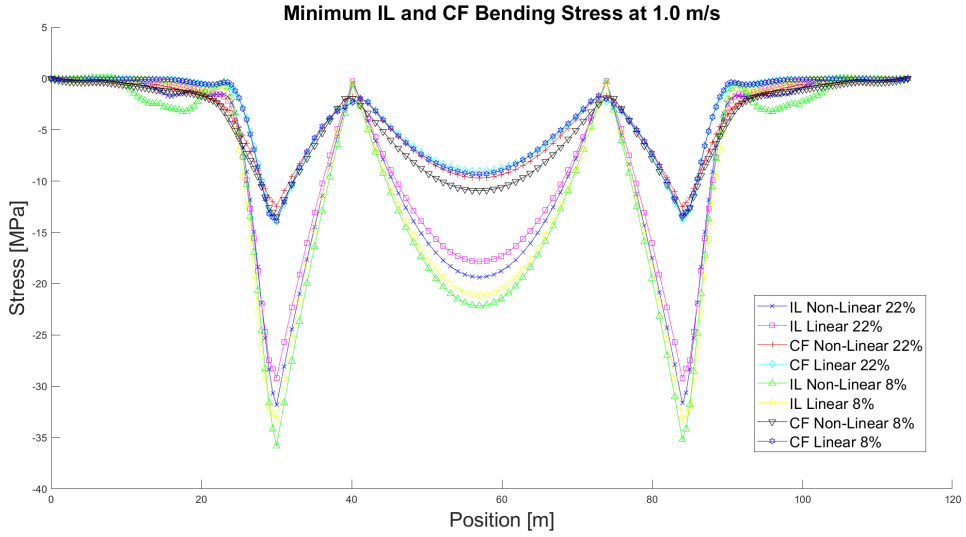

(b) CF and IL Minimum Bending Stress Distribution at 1.0 m/s

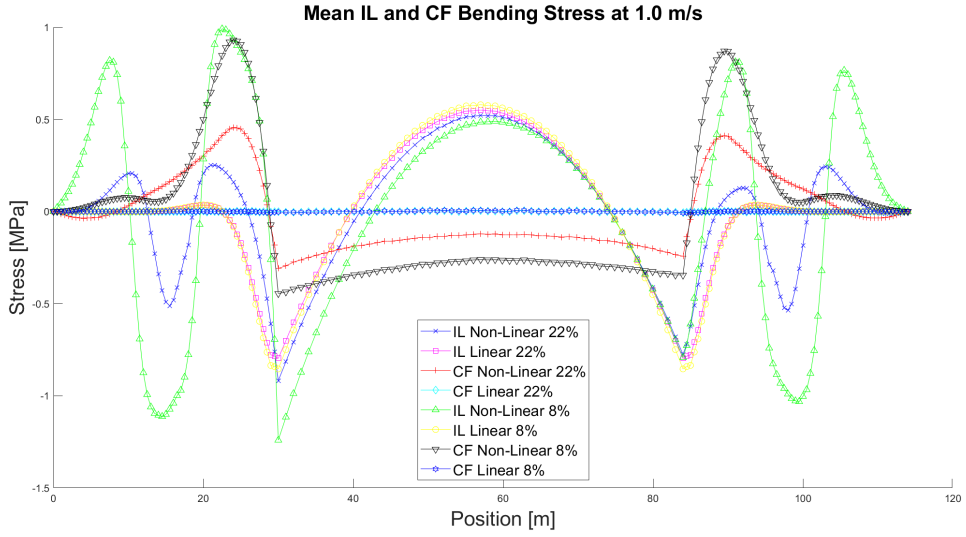

(c) CF and IL Mean Bending Stress Distribution at 1.0 m/s

Figure B.222: Comparative plots of the calculated bending stress distribution for all the examined cases at 1.0 m/s.

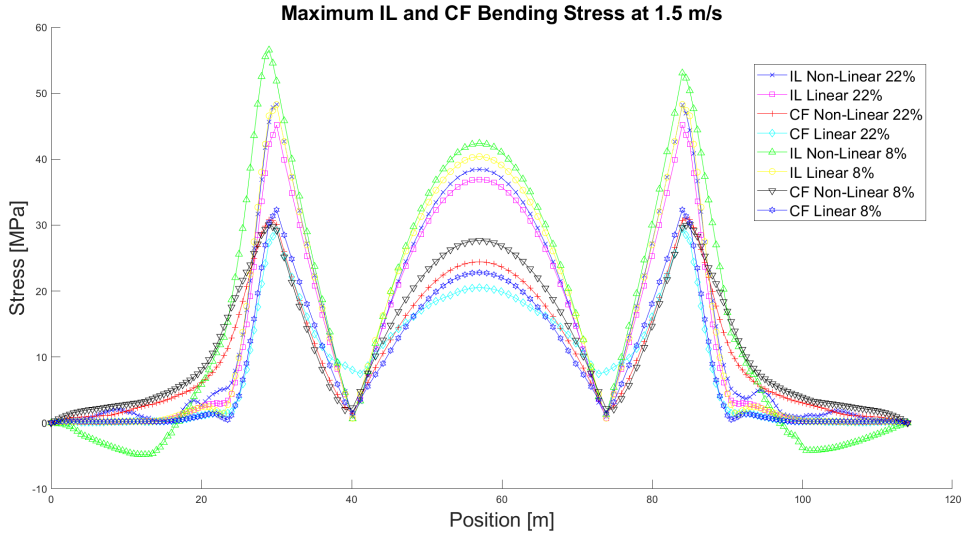

(a) CF and IL Maximum Bending Stress Distribution at 1.5 m/s

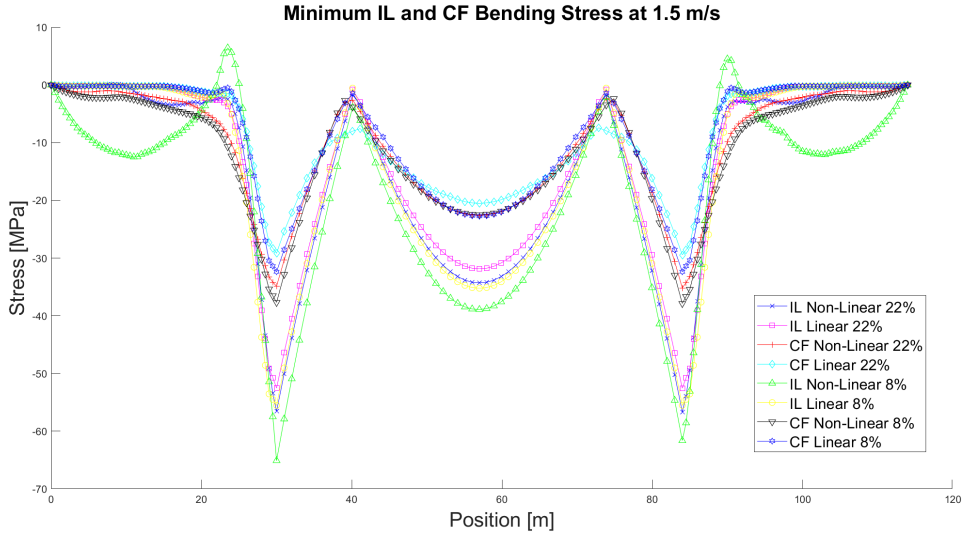

(b) CF and IL Minimum Bending Stress Distribution at 1.5 m/s

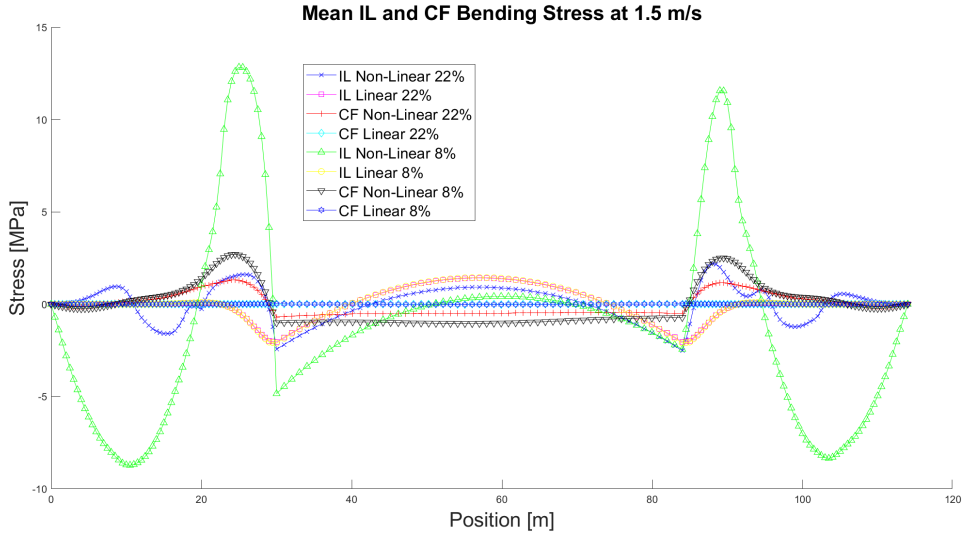

(c) CF and IL Mean Bending Stress Distribution at 1.5 m/s

Figure B.223: Comparative plots of the calculated bending stress distribution for all the examined cases at 1.5 m/s.

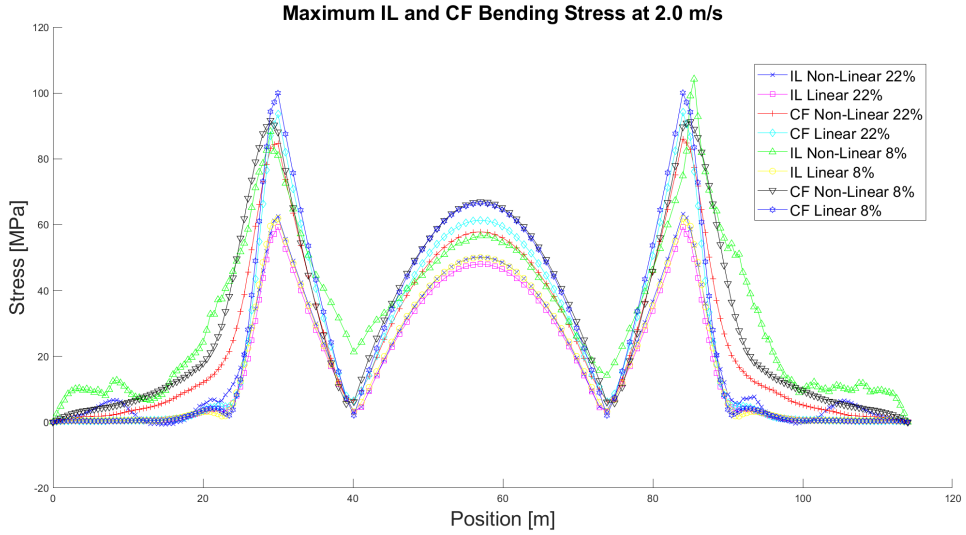

(a) CF and IL Maximum Bending Stress Distribution at 2.0 m/s

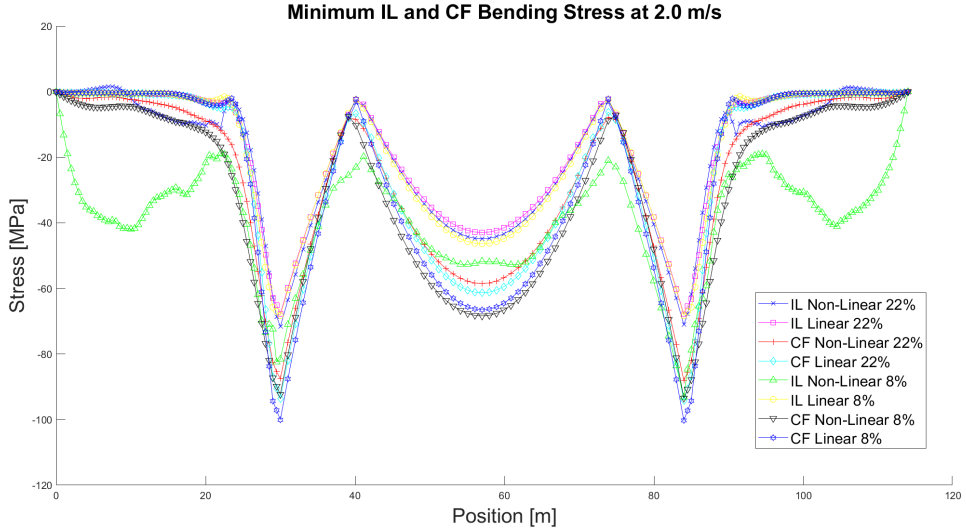

(b) CF and IL Minimum Bending Stress Distribution at 2.0 m/s

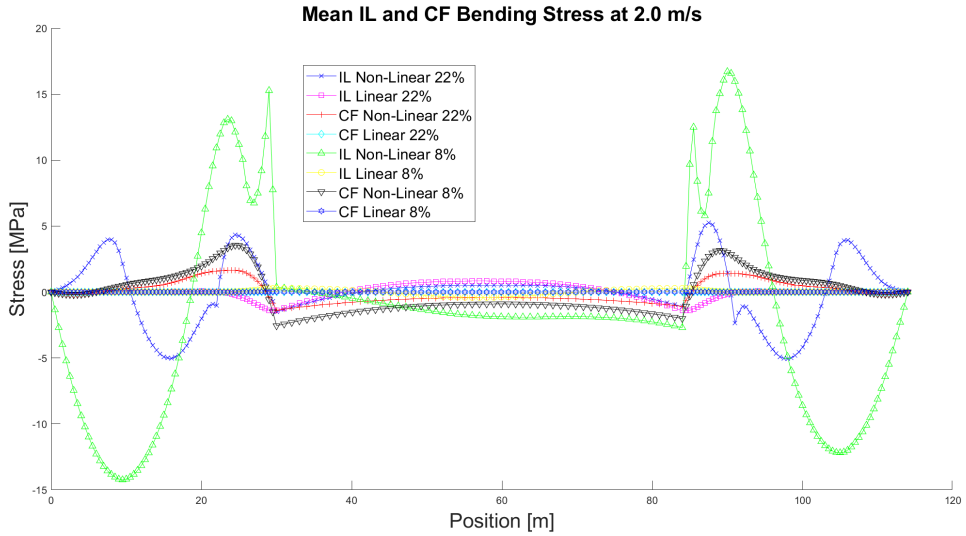

(c) CF and IL Mean Bending Stress Distribution at 2.0 m/s

Figure B.224: Comparative plots of the calculated bending stress distribution for all the examined cases at 2.0 m/s.

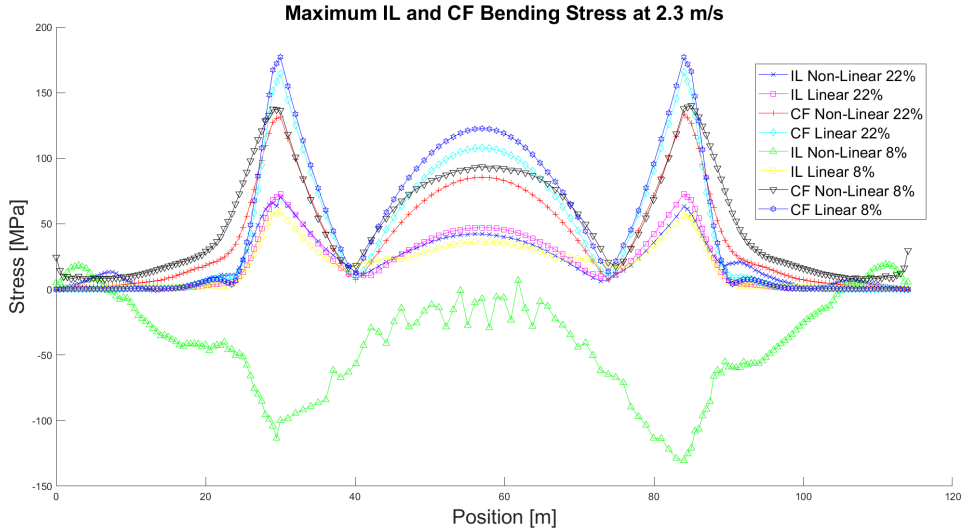

(a) CF and IL Maximum Bending Stress Distribution at 2.3 m/s

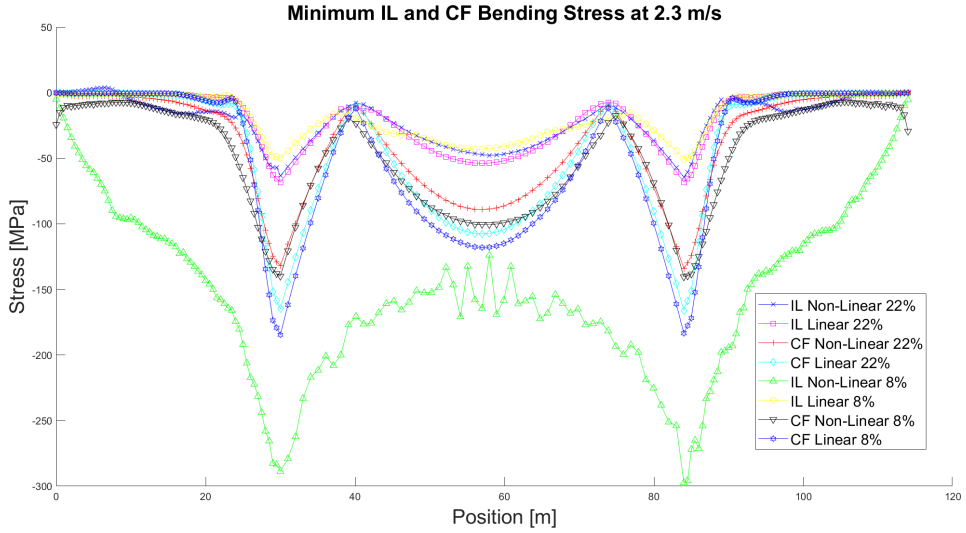

(b) CF and IL Minimum Bending Stress Distribution at 2.3 m/s

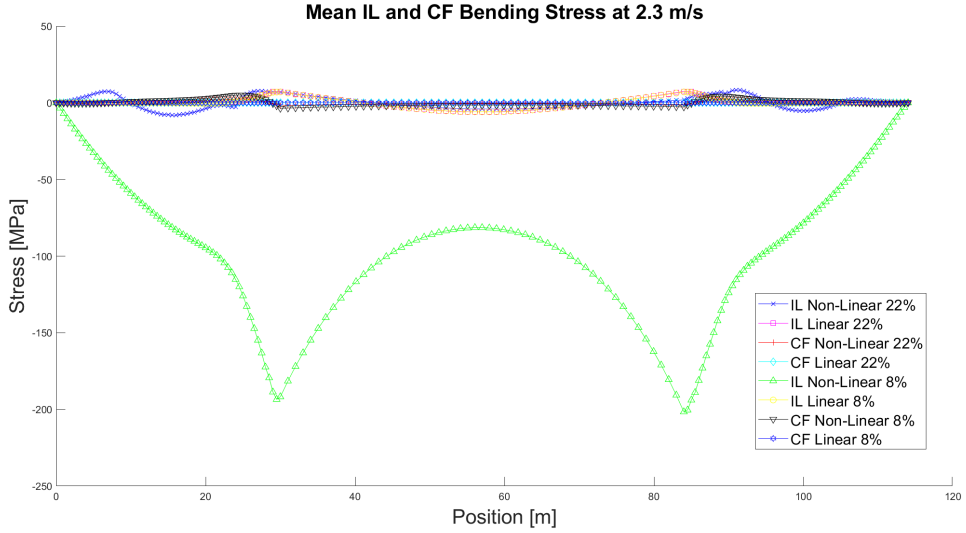

(c) CF and IL Mean Bending Stress Distribution at 2.3 m/s

Figure B.225: Comparative plots of the calculated bending stress distribution for all the examined cases at 2.3 m/s.

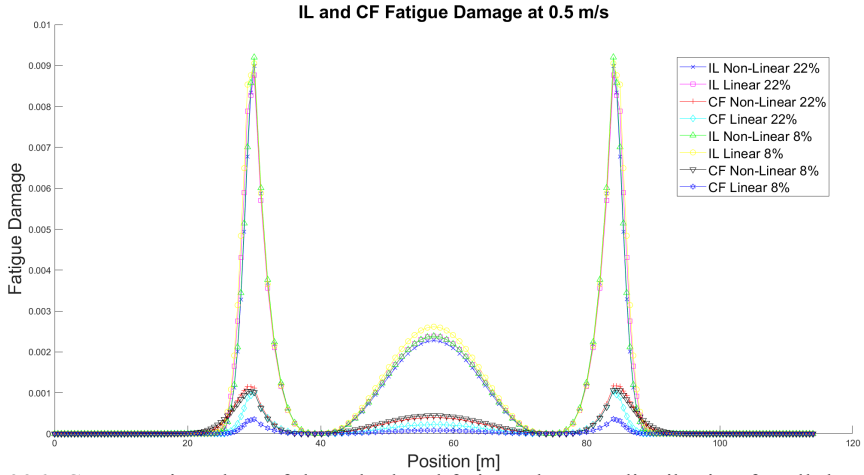

Figure B.226: Comparative plots of the calculated fatigue damage distribution for all the examined cases at 0.5 m/s.

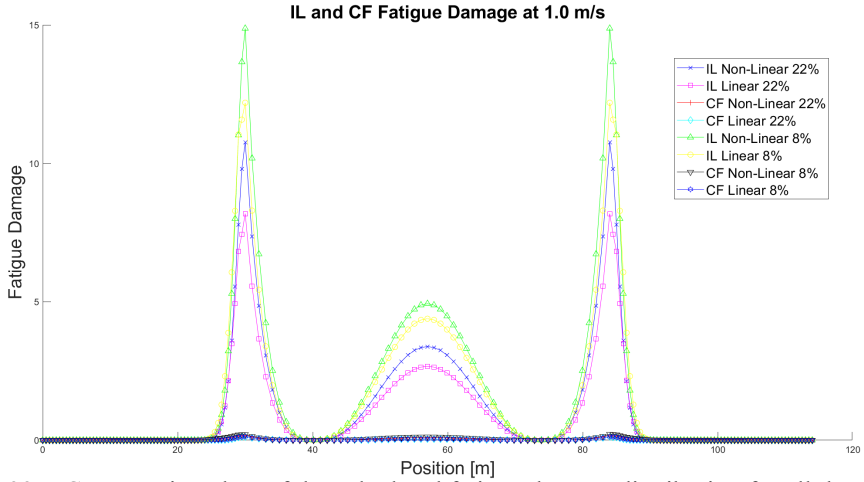

Figure B.227: Comparative plots of the calculated fatigue damage distribution for all the examined cases at 1.0 m/s.

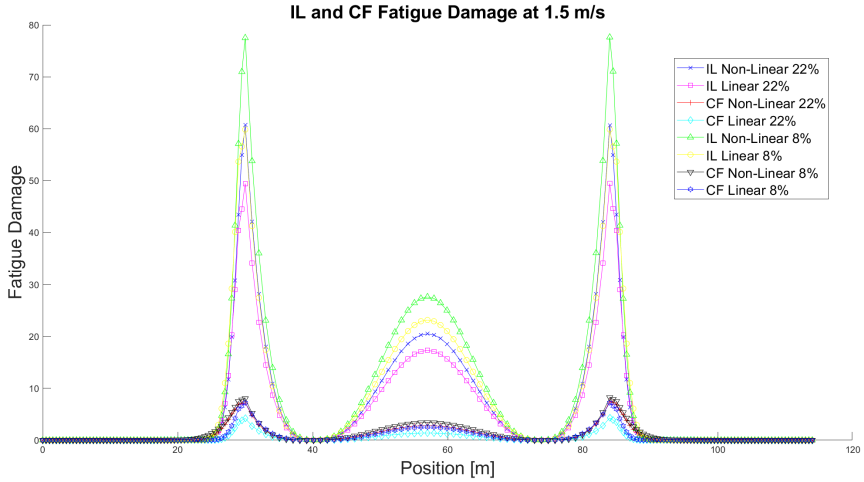

Figure B.228: Comparative plots of the calculated fatigue damage distribution for all the examined cases at 1.5 m/s.

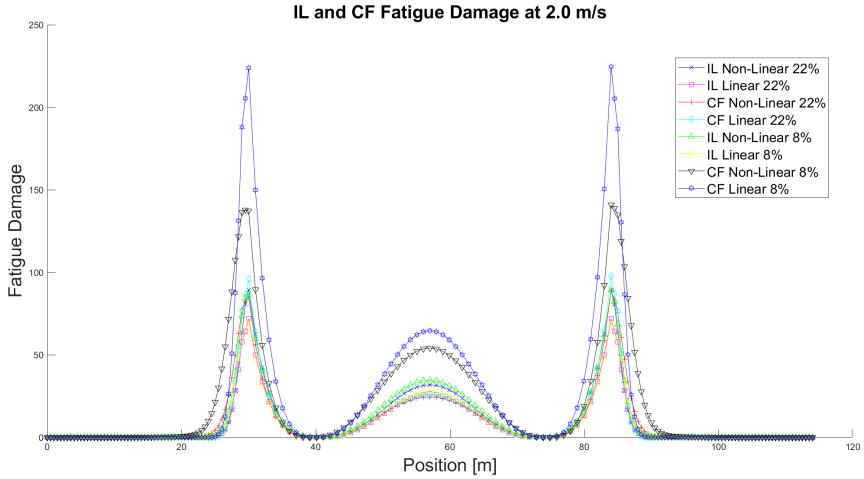

Figure B.229: Comparative plots of the calculated fatigue damage distribution for all the examined cases at 2.0 m/s.

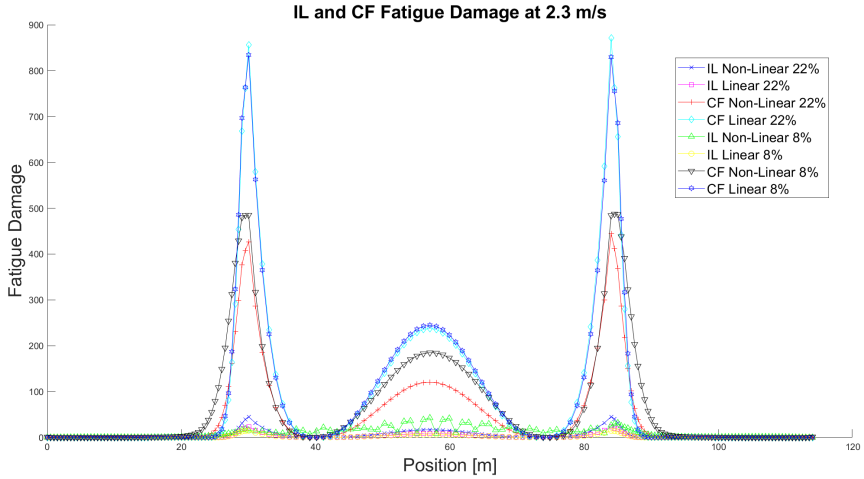

Figure B.230: Comparative plots of the calculated fatigue damage distribution for all the examined cases at 2.3 m/s.

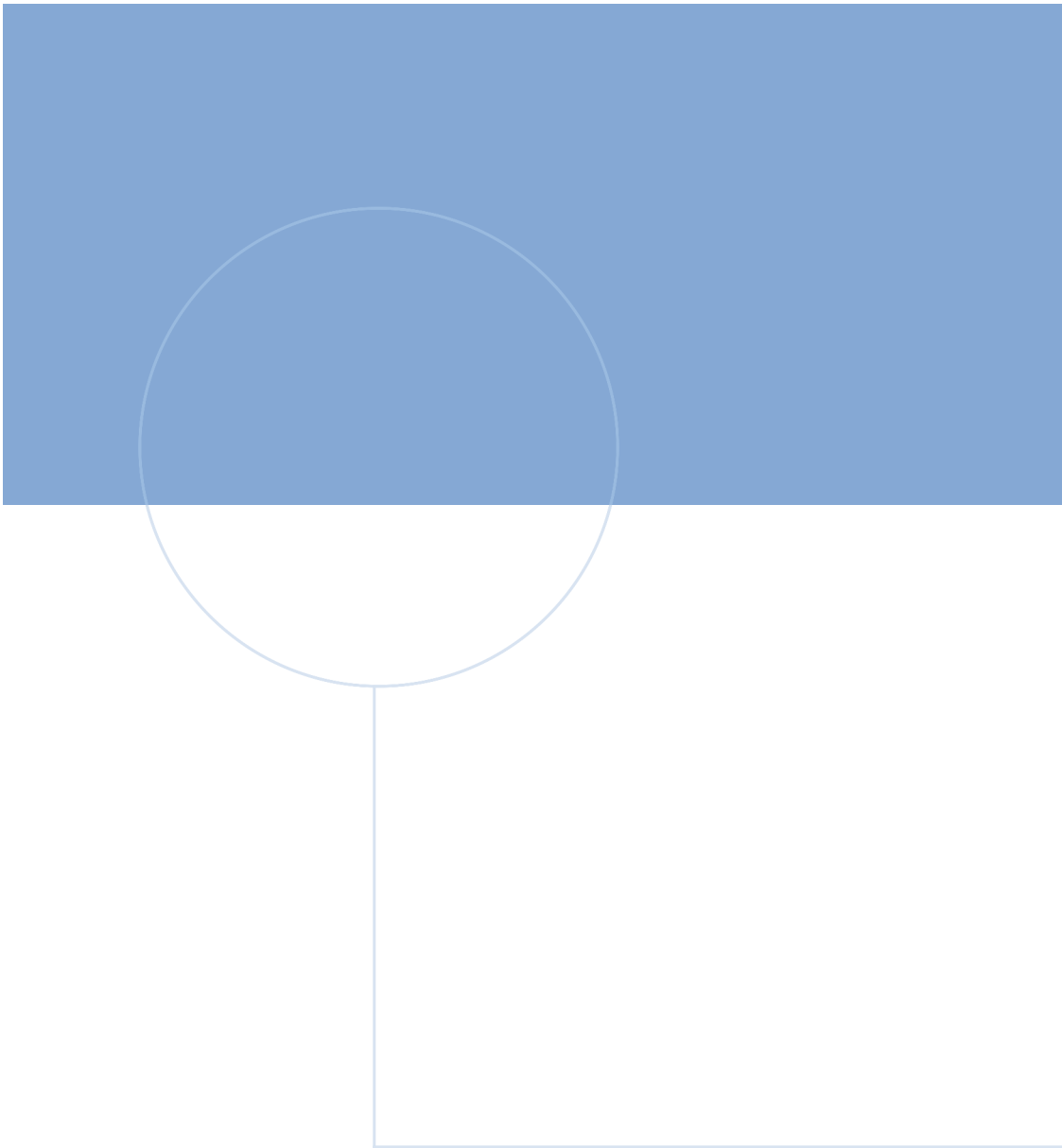

NTNU
Kunnskap for en bedre verden

DTU Technical University of Denmark